LASER PHYSICS®

Editor-in-Chief
Alexander M. Prokhorov

Director of the General Physics Institute
Member of the Russian Academy of Sciences

International Journal of Theoretical and Experimental Laser Research and Application Published in Cooperation with Institutes Involved in Laser Research

Laser Physics

Editor-in-Chief
Alexander M. Prokhorov

Director, General Physics Institute, Russian Academy of Sciences
Member of the Russian Academy of Sciences

Editorial Office, Astro, Ltd.: Tel./Fax: 7-(095) 148-2780; 7-(095) 324-2033; E-mail: yevseyev@theor.mephi.msk.su

EDITORIAL BOARD

Access the Laser Physics web site at **http://www.maik.rssi.ru/journals/lasphys.htm**

Laser Physics is abstracted or/and indexed in *Current Contents, SciSearch,* and *Research Alert.*

REPORT DOCUMENTATION PAGE

Form Approved OMB No. 0704-0188

1. AGENCY USE ONLY (Leave blank)	2. REPORT DATE	3. REPORT TYPE AND DATES COVERED
	1998	Conference Proceedings

4. TITLE AND SUBTITLE

Sixth International Workshop on Laser Physics (LPHYS '97)

5. FUNDING NUMBERS

F6170897W0181

6. AUTHOR(S)

Conference Committee

7. PERFORMING ORGANIZATION NAME(S) AND ADDRESS(ES)

Russian Academy of Sciences
38 Vavilov St.
Moscow 117942
Russia

8. PERFORMING ORGANIZATION REPORT NUMBER

N/A

9. SPONSORING/MONITORING AGENCY NAME(S) AND ADDRESS(ES)

EOARD
PSC 802 BOX 14
FPO 09499-0200

10. SPONSORING/MONITORING AGENCY REPORT NUMBER

CSP 97-1054

11. SUPPLEMENTARY NOTES

12a. DISTRIBUTION/AVAILABILITY STATEMENT

Approved for public release; distribution is unlimited.

12b. DISTRIBUTION CODE

A

13. ABSTRACT (Maximum 200 words)

The Final Proceedings for International Workshop on Laser Physics, 4 August 1997 - 8 August 1997

The Topics covered include: New laser sources, measurement and diagnostics, lasers in R&D, communications and informatics, lasers in medicine.

19980617 112

14. SUBJECT TERMS

Lasers, C3I, Control System

15. NUMBER OF PAGES

362

16. PRICE CODE

N/A

17. SECURITY CLASSIFICATION OF REPORT	18. SECURITY CLASSIFICATION OF THIS PAGE	19. SECURITY CLASSIFICATION OF ABSTRACT	20. LIMITATION OF ABSTRACT
UNCLASSIFIED	UNCLASSIFIED	UNCLASSIFIED	UL

Contents

The Proceedings of the Sixth International Workshop on Laser Physics (LPHYS'97), Prague, August 4-8, 1997

Laser Methods in Medicine

Physics of Solid State Lasers

Lasers and Physics of Thin Films

Comments

Information

Quantum Optics of a Single Atom

H. Walther

Sektion Physik der Universität München and Max-Planck-Institut für Quantenoptik, Garching, 85748 Fed. Rep. of Germany
e-mail: Herbert.Walther@mpq.mpg.de
Received August 19, 1997

Abstract—In this paper recent experiments with the one-atom maser or micromaser are reviewed. They deal with the dynamical behavior of the field at parameter values where the field undergoes phase transitions. Furthermore atomic interferences are observed in the micromaser when the inversion of the atoms leaving the cavity is measured while the cavity frequency is scanned across the atomic resonance. The interferences are due to the nonadiabatic mixing of dressed states at the entrance and exit holes of the maser cavity. They are associated with the dynamics of the atom-field interaction, show quantum jumps, and demonstrate bistability of the micromaser field. In the second part of the paper experiments on the resonance fluorescence of a single trapped $^{24}Mg^+$-ion at low excitation intensity are discussed. The measurements were performed by heterodyning the fluorescent radiation with a sideband of the single mode laser radiation used to excite the ion, resulting in a linewidth of 0.7 Hz. Under identical experimental conditions, the antibunching in the photon statistics of the fluorescent radiation was also investigated. Heterodyne detection and photon correlation measurement are complementary featuring either the wave or the particle nature of the radiation. A brief outlook on new experiments with ultracold atoms in cavities and traps is given.

1. EXPERIMENTS WITH THE ONE-ATOM MASER

The one-atom maser or micromaser is an ideal device for the study of the resonant interaction of a single atom with a single mode of a superconducting niobium cavity [1–4]. In the experiments values of the quality factor as high as 3×10^{10} have been achieved for the resonant mode, corresponding to an average lifetime of a photon in the cavity of 0.2 s. The photon lifetime is thus much longer than the interaction time of an atom with the maser field; during the atom passes through the cavity the only change of the cavity field that occurs is due to the atom-field interaction. The atoms used in the experiments are rubidium Rydberg atoms pumped by laser excitation into the upper level of the maser transition, which is usually induced between neighboring Rydberg states. In the experiments the atom–field interaction is probed by observing the population in the upper and lower maser levels after the atoms have left the cavity. The field in the cavity consists only of single or a few photons depending on the atomic flux. Nevertheless, it is possible to study the interaction in considerable detail. The dynamics of the atom-field interaction treated with the Jaynes–Cummings model was investigated by selecting and varying the velocity of the pump atoms [2]. The counting statistics of the pump atoms emerging from the cavity allowed us to measure the non-classical character of the cavity field [3, 4] predicted by the micromaser theory. The maser field can be investigated in this way since there is entanglement between the maser field and the state in which the atom leaves the cavity [5, 6]. It also has been observed that under suitable experimental conditions the maser field exhibits metastability and hysteresis [7]. The first of the maser experiments have

been performed at cavity temperatures of 2 or 0.5 K. In the more recent experiments the temperature was reduced to roughly 0.1 K by using an improved setup in a dilution refrigerator [7]. For a review of the previous work see Raithel *et al.* [9].

In the following the experiments on quantum jumps of the micromaser field and on the observation of atomic interferences in the cavity [8] are reviewed. New experiments on the correlation of atoms after the interaction with the cavity field will be discussed also. Interesting new experiments get possible if ultracold atoms are used to pump the micromaser. In the case that the kinetic energy of the atoms get comparable to the interaction energy between atoms and field the motion of the atoms has to be quantized leading to new interesting features which are briefly discussed in this paper.

1.1 Quantum Jumps and Atomic Interferences in the Micromaser

Under steady-state conditions, the photon statistics $P(n)$ of the field of the micromaser is essentially determined by the pump parameter, $\Theta = N_{ex}^{1/2} \Omega t_{int}/2$ [9–11]. Here, N_{ex} is the average number of atoms that enter the cavity during τ_{cav}, Ω the vacuum Rabi flopping frequency, and t_{int} is the atom-cavity interaction time. The quantity $\langle v \rangle = \langle n \rangle / N_{ex}$ shows the following generic behavior (see Fig. 1): It suddenly increases at the maser threshold value $\Theta = 1$, and reaches a maximum for $\Theta \approx 2$ (denoted by a in Fig. 1). At threshold the characteristics of a continuous phase transition [10, 11] are displayed. As Θ further increases, $\langle v \rangle$ decreases and reaches a minimum at $\Theta \approx 2\pi$, and then abruptly increases to a second maximum (b in Fig. 1). This general
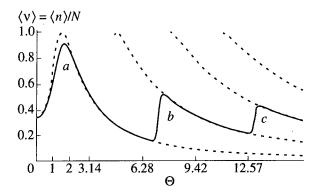
Fig. 1. Mean value of $v = n/N_{ex}$ versus the pump parameter

$\Theta = \Omega t_{int} \sqrt{N_{ex}} /2$, where the value of Θ is changed via N_{ex}. The solid line represents the micromaser solution for $\Omega = 36$ kHz, $t_{int} = 35$ μs, and temperature $T = 0.15$ K. The dotted lines are semiclassical steady-state solutions corresponding to fixed stable gain = loss equilibrium photon numbers [12]. The crossing points between a line $\Theta = $ const and the dotted lines correspond to the values where minima in the Fokker–Planck potential $V(v)$ occur.

type of behavior recurs roughly at integer multiples of 2π, but becomes less pronounced with increasing Θ. The reason for the periodic maxima of $\langle v \rangle$ is that for integer multiples of $\Theta = 2\pi$ the pump atoms perform an almost integer number of full Rabi flopping cycles, and start to flip over at a slightly larger value of Θ, thus leading to enhanced photon emission. The periodic maxima in $\langle v \rangle$ for $\Theta = 2\pi$, 4π, and so on can be interpreted as first-order phase transitions [10, 11]. The field strongly fluctuates for all phase transitions (a, b, and c in Fig. 1), the large photon number fluctuations for $\Theta \approx 2\pi$ and multiples thereof being caused by the presence of two maxima in the photon number distribution $P(n)$ at photon numbers n_l and n_h ($n_l < n_h$).

The phenomenon of the two coexisting maxima in $P(n)$ was also studied in a semiheuristic Fokker–Planck (FP) approach [10, 11]. There, the photon number distribution $P(n)$ is replaced by a probability function $P(v, \tau)$ with continuous variables $\tau = t/\tau_{cav}$ and $v(n) = n/N_{ex}$, the latter replacing the photon number n. The steady-state solution obtained for $P(v, \tau)$, $\tau \gg 1$, can be constructed by means of an effective potential $V(v)$ showing minima at positions where maxima of $P(v, \tau)$, $\tau \gg 1$, are found. Close to $\Theta = 2\pi$ and multiples thereof, the effective potential $V(v)$ exhibits two equally attractive minima located at stable gain-loss equilibrium points of maser operation [12] (see Fig. 1). The mechanism at the phase transitions mentioned is always the same: A minimum of $V(v)$ loses its global character when Θ is increased, and is replaced in this role by the next one. This reasoning is a variation of the Landau theory of first-order phase transitions, with $\sqrt{v}$ being the order parameter. This analogy actually leads to the notion that in the limit $N_{ex} \longrightarrow \infty$ the change of the micromaser field around integer multiples $\Theta = 2\pi$ can be interpreted as first-order phase transitions.

Close to first-order phase transitions long field evolution time constants are expected [10, 11]. This phenomenon was experimentally demonstrated in [7], as well as related phenomena, such as spontaneous quantum jumps between equally attractive minima of $V(v)$, bistability, and hysteresis. Some of those phenomena are also predicted in the two-photon micromaser [13], for which qualitative evidence of first-order phase transitions and hysteresis is reported.

The experimental setup used is shown in Fig. 2. It is similar to that described by Rempe and Walther [4] and Benson, Raithel and Walther [7]. As before, [85]Rb atoms were used to pump the maser. They are excited from the $5S_{1/2}$, $F = 3$ ground state to $63P_{3/2}$, $m_J = \pm 1/2$ states by linearly polarized light of a frequency-doubled cw ring dye laser. The polarization of the laser light is linear
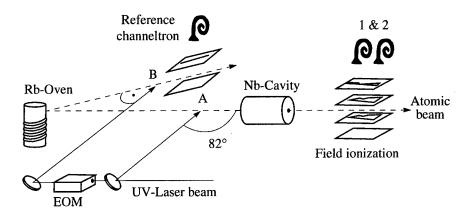
Fig. 2. Sketch of the experimental setup. The rubidium atoms emerge from an atomic beam oven and are excited at an angle of 82° at location A. After interaction with the cavity field, they enter a state-selective field ionization region, where channeltrons 1 and 2 detect atoms in the upper and lower maser levels, respectively. A small fraction of the UV radiation passes through an electro-optic modulator (EOM), which generates sidebands of the UV radiation. The blueshifted sideband is used to stabilize the frequency of the laser onto the Doppler-free resonance monitored with a secondary atomic beam produced by the same oven (location B).

and parallel to the likewise linearly polarized maser field, and therefore only $\Delta m_J = 0$ transitions are excited. Superconducting niobium cavities resonant with the transition to the $61D_{3/2}$, $m_J = \pm 1/2$ states were used; the corresponding resonance frequency is 21.506 GHz. The experiments were performed in a $^3\text{He}/^4\text{He}$ dilution refrigerator with cavity temperatures T $\approx$ 0.15 K. The cavity Q values ranged from 4×10^9 to 8×10^9. The velocity of the Rydberg atoms and thus their interaction time t_{int} with the cavity field were preselected by exciting a particular velocity subgroup with the laser. For this purpose, the laser beam irradiated the atomic beam at an angle of approximately 82°. As a consequence, the UV laser light (linewidth $\approx$ 2 MHz) is blueshifted by 50–200 MHz by the Doppler effect, depending on the velocity of the atoms.

Information on the maser field and interaction of the atoms in the cavity can be obtained solely by state-selective field ionization of the atoms in the upper or lower maser level after they have passed through the cavity. The field ionization detector was recently modified, so that there is now a detection efficiency of $\eta =$ (35 $\pm$ 5)%. For different t_{int} the atomic inversion has been measured as a function of the pump rate by comparing the results with micromaser theory [10, 11], the coupling constant Ω is found to be $\Omega = (40 \pm 10)$ krad/s.

Depending on the parameter range, essentially three regimes of the field evolution time constant τ_{field} can be distinguished. Here we only discuss the results for intermediate time constants. The maser was operated under steady-state conditions close to the second first-order phase transition (c in Fig. 1). The interaction time was $t_{int} = 47$ µs and the cavity decay time $\tau_{cav} = 60$ ms. The value of N_{ex} necessary to reach the second first-order phase transition was $N_{ex} \approx 200$. For these parameters, the two maxima in P(n) are manifested in spontaneous jumps of the maser field between the two maxima with a time constant of ≈ 5 s. This fact and the relatively large pump rate led to the clearly observable field jumps shown in Fig. 3. Because of the large cavity field decay time, the average number of atoms in the cavity was still as low as 0.17. The two discrete values for the counting rates correspond to the metastable operating points of the maser, which correspond to ≈ 70 and ≈ 140 photons. In the FP description, the two values correspond to two equally attractive minima in the FP potential $V(v)$. If one considers, for instance, the counting rate of lower-state atoms (CT2 in Fig. 3), the lower (higher) plateaus correspond to time intervals in the low (high) field metastable operating point. If the actual photon number distribution is averaged over a time interval containing many spontaneous field jumps, the steady-state result $P(n)$ of the micromaser theory is recovered.

In the parameter ranges where switching occurs much faster than in the case shown in Fig. 3 the individual jumps cannot be resolved, therefore different methods have to be used for the measurement. Furthermore
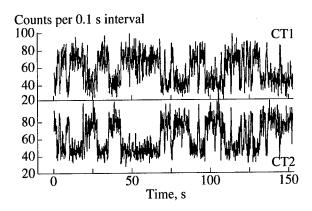
Fig. 3. Quantum jumps between two equally stable operation points of the maser field. The channeltron counts are plotted versus time (CT1 = upper state and CT2 = lower state signals).

hysteresis is observed at the maser parameters for which the field jumps occur. Owing to lack of space these results cannot be discussed here. For a complete survey on the performed experiments it is referred to [7].

As next topic we would like to discuss the observation of atomic interferences in the micromaser [8]. Since a non-classical field is generated in the maser cavity, we were able for the first time to investigate atomic interference phenomena under the influence of non-classical radiation; owing to the bistable behavior of the maser field the interferences display quantum jumps, thus the quantum nature of the field gets directly visible in the interference fringes. Interferences occur since a coherent superposition of dressed states is produced by mixing the states at the entrance and exit holes of the cavity. Inside the cavity the dressed states develop differently in time, giving rise to Ramsey-type interferences [14] when the maser cavity is tuned through resonance.

The setup used in the experiment is identical to the one described before [7]. However, the flux of atoms through the cavity is by a factor of 5–10 higher than in the previous experiments, where the $63P_{3/2}$–$61D_{5/2}$ transition was used. For the experiments the Q-value of the cavity was 6×10^9 corresponding to a photon decay time of 42 ms.

Figure 4 shows the standard maser resonance in the uppermost plot which is obtained when the resonator frequency is tuned. At large values of N_{ex} ($N_{ex} > 89$) sharp, periodic structures appear. These typically consist of a smooth wing on the low-frequency side, and a vertical step on the high-frequency side. The clarity of the pattern rapidly decreases when N_{ex} increases to 190 or beyond. We will see later that these structures have to be interpreted as interferences. It can be seen that the atom-field resonance frequency is red-shifted with increasing N_{ex}, the shift reaching 200 kHz for $N_{ex} = 190$. Under these conditions there are roughly 100 photons on the average in the cavity. The large red-shift cannot be explained by AC Stark effect, which for 100 photons
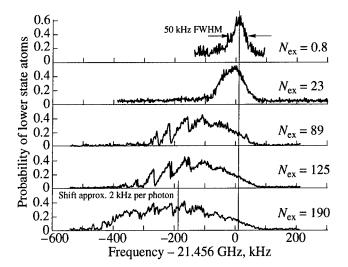
Fig. 4. Shift of the maser resonance $63P_{3/2}$–$61D_{5/2}$ for fast atoms ($t_{int} = 35$ μs). The upper plot shows the maser line for low pump rate ($N_{ex} < 1$).The FWHM linewidth (50 kHz) sets an upper limit of ≈ 5 mV/cm for the residual electric stray fields in the center of the cavity. The lower resonance lines are taken for the indicated large values of N_{ex}.The plots show that the center of the maser line shifts by about 2 kHz per photon. In addition, there is considerable field-induced line broadening which is approximately proportional to $\sqrt{N_{ex}}$. For $N_{ex} \geq 89$ the lines display periodic structures, which are discussed in the text.

would amount to about one kHz for the transition used. Therefore it is obvious that other reasons must be responsible for the observed shift.

It is known from previous maser experiments that there are small static electric fields in the entrance and exit holes of the cavity. It is supposed that this field is generated by patch effects at the surface of the niobium metal caused by rubidium deposits caused by the atomic beam or by microcrystallites formed when the cavities are tempered after machining. The tempering process is necessary to achieve high quality factors. The influence of those stray fields is only observable in the cavity holes; in the center of the cavity they are negligible owing to the large atomwall distances.

When the interaction time t_{int} between the atoms and the cavity field is increased the interference structure disappears for $t_{int} > 47$ μs [8]. This is due to the fact that there is no non-adiabatic mixing any more between the substates when the atoms get too slow.

In order to understand the observed structures, the Jaynes–Cummings dynamics of the atoms in the cavity has to be analyzed. This treatment is more involved than that in connection with previous experiments, since the higher maser field requires detailed consideration of the field in the periphery of the cavity, where the additional influence of stray electric fields is more important.

The usual formalism for the description of the coupling of an atom to the radiation field is the dressed atom approach [15], leading to splitting of the coupled atomfield states, depending on the vacuum Rabi-flopping frequency Ω, the photon number n, and the atomfield detuning δ. We face a special situation at the entrance and exit holes of the cavity. There we have a position-dependent variation of the cavity field, as a consequence of which Ω is position-dependent. An additional variation results from the stray electric fields in the entrance and exit holes. Owing to the Stark-effect these fields lead to a position-dependent atom-field detuning δ.

The Jaynes–Cummings Hamiltonian only couples pairs of dressed states. Therefore, it is sufficient to consider the dynamics within such a pair. In our case, prior to the atom-field interaction the system is in one of the two dressed states. For parameters corresponding to the periodic substructures in Fig. 4 the dressed states are mixed only at the beginning of the atom-field interaction and at the end. The mixing at the beginning creates a coherent superposition of the dressed states. Afterwards the system develops adiabatically, whereby the two dressed states accumulate a differential dynamic phase Φ which strongly depends on the cavity frequency. The mixing of the dressed states at the entrance and exit holes of the cavity, in combination with the intermediate adiabatic evolution, generates a situation similar to a Ramsey two-field interaction.

The maximum differential dynamic phase Φ solely resulting from dressed-state coupling by the maser field is roughly 4π under the experimental conditions used here. This is not sufficient to explain the interference pattern of Fig. 4, where we have at least six maxima corresponding to a differential phase of 12π. This means that an additional energy shift differently affecting upper and lower maser states is present. Such a phenomenon can be caused by the above mentioned small static electric fields present in the holes of the cavity. The static field causes a position-dependent detuning δ of the atomic transition from the cavity resonance; as a consequence we get an additional differential dynamic phase Φ. In order to interpret the periodic substructures as a result of the variation of Φ with the cavity frequency, the phase Φ has to be calculated from the atomic dynamics in the maser field.

The quantitative calculation can be performed on the basis of the micromaser theory. The calculations reproduce the experimental finding that the maser line shifts to lower frequencies when N_{ex} is increased [8]. The mechanism for that can be explained as follows: the high-frequency edge of the maser line does not shift with N_{ex} at all, since this part of the resonance is produced in the central region of the cavity, where practically no static electric fields are present. The low-frequency cut-off of the structure is determined by the location where the mixing of the dressed states occurs. With decreasing cavity frequency those points shift

closer to the entrance and exit holes, with the difference between the particular cavity frequency and the unperturbed atomic resonance frequency giving a measure of the static electric field at the mixing locations. Closer to the holes the passage behavior of the atoms through the mixing locations gets nonadiabatic for the following reasons: firstly, the maser field strength reduces towards the holes. This leads to reduced repulsion of the dressed states. Secondly, the stray electric field strongly increases towards the holes. This implies a larger differential slope of the dressed state energies at the mixing locations, and therefore leads to a stronger non-adiabatic passage. At the same time the observed signal extends further to the low frequency spectral region. Since the photon emission probabilities are decreasing towards lower frequencies their behavior finally defines the low-frequency boundary of the maser resonance line. With increasing N_{ex} the photon number n increases. As for larger values of n the photon emission probabilities get larger, also an increasing N_{ex} leads to an extension of the range of the signal to lower frequencies. This theoretical expectation is in agreement with the experimental observation.

In the experiment it is also found that the maser line shifts towards lower frequencies with increasing t_{int}. This result also follows from the developed model: the redshift increases with t_{int} since a longer interaction time leads to a more adiabatic behavior in the same way as a larger N_{ex} does.

The calculations reveal that on the vertical steps displayed in the signal the photon number distribution has two distinctly separate maxima similar to those observed at the phase transition points discussed above. Therefore, the maser field should exhibit hysteresis and metastability under the present conditions as well. The hysteresis indeed shows up when the cavity frequency is linearly scanned up and down with a modest scan rate [9]. When the maser is operated in steady-state and the cavity frequency is fixed to the steep side of one of the fringes we also observe spontaneous jumps of the maser field between two metastable field states.

The calculations also show that on the smooth wings of the more pronounced interference fringes the photon number distribution $P(n)$ of the maser field is strongly sub-Poissonian. This leads us to the conclusion that we observe Ramsey-type interferences induced by a nonclassical radiation field. The sub-Poissonian character of $P(n)$ results from the fact that on the smooth wings of the fringes the photon gain reduces when the photon number is increased. This feedback mechanism stabilizes the photon number resulting in a sub-Poissonian photon distribution.

1.2 Entanglement in the Micromaser

Owing to the interaction of the Rydberg atom with the maser field there is an entanglement between field and state in which a particular atom is leaving the cav-

ity. This entanglement was studied in several papers, see, e.g. [16] and [6]. Furthermore there is a correlation between the states of the atoms leaving the cavity subsequently. If, e.g., atoms in the lower maser level are studied [17] an anticorrelation is observed in a region for the pump parameter Θ where sub-Poissonian photon statistics is present in the maser field. Recently measurements [18] of these pair correlations have been performed giving a rather good agreement with the theoretical predictions by Briegel et al. [19]. The pair correlations disappear when the time interval between subsequent atoms get larger than the storage time of a photon in the cavity.

1.3 The One-Atom Maser and Ultracold Atoms

The photon emission probability in a micromaser changes drastically when the kinetic energy of the pumping atoms is comparable to the atom-field interaction energy. In this situation, the atomic center-of-mass motion has to be treated quantum mechanically and the de Broglie wavelength of the atom inside the cavity is an important physical parameter. The interplay between reflection and transmission of the atoms leads to a new mechanism for induced emission [20–23]. In the ordinary maser, stimulated emission prevails as the mechanism for amplification of radiation; but in the case of ultracold atoms the physics of the induced emission process is intimately associated with the quantization of the CM motion (taken to be in the z direction). For this reason we distinguish between the usual stimulated emission maser physics and that characterized by the present quantized-z-motion induced emission, and call the process of Microwave Amplification via z-motion induced Emission of Radiation (MAZER) the mazer action.

The physical mechanism responsible for the induced emission is the longitudinal force that the atoms experience upon passing into a high-Q cavity due to the abrupt change in the atom-field interaction. Different dressed-state components of the combined atom-field system encounter different potentials and experience different longitudinal forces.

A photon is emitted by an excited atom when the de Broglie wavelength fits resonantly into the cavity. These resonances lead to the new process. A master equation for the mazer has been derived [20–23]. We note that the probability for emission by an excited thermal atom (stimulated maser emission) is very different from the emission probability as given by the de Broglie resonances (induced mazer emission). The photon emission probability depends in the special case of ultracold atoms on $\sqrt[4]{n+1}$ instead of $\sqrt{n+1}$ as observed for the usual micromaser. This results from the interplay between the ultracold atoms and the potential well of the dressed atom potential [20–23].

2. ION TRAP EXPERIMENTS

Besides the experiments performed with atoms in a cavity the trapped ion techniques provide another way to investigate quantum phenomena in radiation atom interaction. In the following some new experiments and new possibilities will be reviewed.

2.1 Resonance Fluorescence of a Single Atom

Resonance fluorescence of an atom is a basic process in radiation-atom interactions, and has therefore always generated considerable interest. The methods of experimental investigation have changed continuously due to the availability of new experimental tools. A considerable step forward occurred when tunable and narrow band dye laser radiation became available. These laser sources are sufficiently intense to easily saturate an atomic transition. In addition, the lasers provide highly monochromatic light with coherence times much longer than typical natural lifetimes of excited atomic states. Excitation spectra with laser light using well collimated atomic beam lead to a width being practically the natural width of the resonance transition, therefore it became possible to investigate the frequency spectrum of the fluorescence radiation with high resolution. However, the spectrograph used to analyze the reemitted radiation was a Fabry–Perot interferometer, the resolution of which did reach the natural width of the atoms, but was insufficient to reach the laser linewidth, see e.g. Hartig et al. [24] and Cresser et al. [25]. A considerable progress in this direction was achieved by investigating the fluorescence spectrum of ultra-cold atoms in an optical lattice in a heterodyne experiment [26]. In these measurements a linewidth of 1 kHz was achieved, however, the quantum aspects of the resonance fluorescence such as antibunched photon statistics cannot be investigated under these conditions since they wash out when more than one atom is involved.

Thus the ideal experiment requires a single atom to be investigated. Since some time it is known that ion traps allow to study the fluorescence from a single laser cooled particle practically at rest, thus providing the ideal case for the spectroscopic investigation of the resonance fluorescence. The other essential ingredient for achievement of high resolution is the measurement of the frequency spectrum by heterodyning the scattered radiation with laser light as demonstrated with many cold atoms [26]. Such an optimal experiment with a single trapped Mg^+ ion is described in this paper. The measurement of the spectrum of the fluorescent radiation at low excitation intensities is presented. Furthermore, the photon correlation of the fluorescent light has been investigated under practically identical excitation conditions. The comparison of the two results shows a very interesting aspect of complementarity since the heterodyne measurement corresponds to a "wave" detection of the radiation whereas the measurement of the photon correlation is a "particle" detection scheme. It will be shown that under the same excitation conditions the wave detection provides the properties of a classical atom, i.e. a driven oscillator, whereas the particle or photon detection displays the quantum properties of the atom. Whether the atom displays classical or quantum properties thus depends on the method of observation.

The spectrum of the fluorescence radiation is given by the Fourier transform of the first order correlation function of the field operators, whereas the photon statistics and photon correlation is obtained from the second order correlation function. The corresponding operators do not commute, thus the respective observations are complementary. Present theory on the spectra of fluorescent radiation following monochromatic laser excitation can be summarized as follows: fluorescence radiation obtained with low incident intensity is also monochromatic owing to energy conservation. In this case, elastic scattering dominates the spectrum and thus one should measure a monochromatic line at the same frequency as the driving laser field. The atom stays in the ground state most of the time and absorption and emission must be considered as one process with the atom in principle behaving as a classical oscillator. This case was treated on the basis of a quantized field many years ago by Heitler [27]. With increasing intensity upper and lower states become more strongly coupled leading to an inelastic component, which increases with the square of the intensity. At low intensities, the elastic part dominates since it depends linearly on the intensity. As the intensity of the exciting light increases, the atom spends more time in the upper state and the effect of the vacuum fluctuations comes into play through spontaneous emission. The inelastic component is added to the spectrum, and the elastic component goes through a maximum where the Rabi flopping frequency $\Omega = \Gamma/\sqrt{2}$ (Γ is the natural linewidth) and then disappears with growing Ω. The inelastic part of the spectrum gradually broadens as Ω increases and for $\Omega > \Gamma/2$ sidebands begin to appear [25, 28].

The experimental study of the problem requires, as mentioned above, a Doppler-free observation. In order to measure the frequency distribution, the fluorescent light has to be investigated by means of a high resolution spectrometer. The first experiments of this type were performed by Schuda et al. [29] and later by Walther et al. [30], Hartig et al. [24] and Ezekiel et al. [31]. In all these experiments, the excitation was performed by single-mode dye laser radiation, with the scattered radiation from a well collimated atomic beam observed and analyzed by a Fabry-Perot interferometer. Experiments to investigate the elastic part of the resonance fluorescence giving a resolution better than the natural linewidth have been performed by Gibbs et al. [32] and Cresser et al. [25].

The first experiments which investigated antibunching in resonance fluorescence were also performed by

means of laser-excited collimated atomic beams. The initial results obtained by Kimble, Dagenais, and Mandel [33] showed that the second-order correlation function $g^{(2)}(t)$ had a positive slope which is characteristic of photon antibunching. However, $g^{(2)}(0)$ was larger than $g^{(2)}(t)$ for $t \longrightarrow \infty$ due to number fluctuations in the atomic beam and to the finite interaction time of the atoms [34, 35]. Further refinement of the analysis of the experiment was provided by Dagenais and Mandel [35]. Rateike *et al.* [36] used a longer interaction time for an experiment in which they measured the photon correlation at very low laser intensities (see Cresser *et al.* [25] for a review). Later, photon antibunching was measured using a single trapped ion in an experiment which avoids the disadvantages of atom number statistics and finite interaction time between atom and laser field [37].

As pointed out in many papers photon antibunching is a purely quantum phenomenon (see e.g. Cresser *et al.* [25] and Walls [38]). The fluorescence of a single ion displays the additional nonclassical property that the variance of the photon number is smaller than its mean value (i.e., it is sub-Poissonian) [37, 39].

The trap used for the present experiment was a modified Paul-trap, called an endcap-trap [40]. The trap consists of two solid copper–beryllium cylinders (diameter 0.5 mm) arranged colinearly with a separation of 0.56 mm. These correspond to the cap electrodes of a traditional Paul trap, whereas the ring electrode is replaced by two hollow cylinders, one of which is concentric with each of the cylindrical endcaps. Their inner and outer diameters are 1 and 2 mm, respectively and they are electrically isolated from the cap electrodes. The fractional anharmonicity of this trap configuration, determined by the deviation of the real potential from the ideal quadrupole field is below 0.1% (see Schrama *et al.* [40]). The trap is driven at a frequency of 24 MHz with typical secular frequencies in the *xy* plane of approximately 4 MHz. This required a radio-frequency voltage with an amplitude on the order of 300 V to be applied between the cylinders and the endcaps.

The measurements were performed using the $3^2S_{1/2}$–$3^2P_{3/2}$ transition of the 24 Mg$^+$-ion at a wavelength of 280 nm. The heterodyne measurement is performed as follows. The dye laser excites the trapped ion while the fluorescence is observed in a direction of about 54° to the exciting laser beam. However, both the observation direction and the laser beam are in a plane perpendicular to the symmetry axis of the trap. A fraction of the laser radiation is removed with a beamsplitter and then frequency shifted [by 137 MHz with an acousto-optic modulator (AOM)] to serve as the local oscillator. An example of a heterodyne signal is displayed in Fig. 5. The signal is the narrowest optical heterodyne spectrum of resonance fluorescence reported to date. Thus our experiment provides the most compelling confirmation of Weisskopf's prediction of a coherent component in resonance fluorescence. The linewidth observed implies that exciting laser and fluorescent light

Heterodyne signal, μV
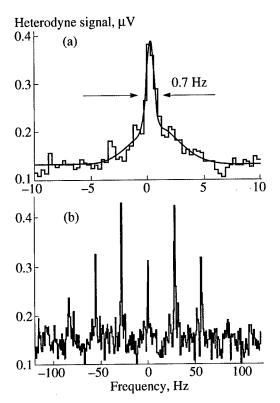
Fig. 5. Heterodyne spectrum of a single trapped 24 Mg$^+$-ion. Left side: Resolution bandwidth 0.5 Hz. The solid line is a Lorentzian fit to the experimental data; the peak appears on top of a small pedestal being 4 Hz wide. The latter signal is due to random phase fluctuations in the spatially separated sections of the light paths of local oscillator and fluorescent light; they are generated by variable air currents in the laboratory. Right side: Heterodyne spectrum of the coherent peak with sidebands generated by mechanical vibrations of the mount holding the trap. The vibrations are due to the operation of a rotary pump in the laboratory. For details see [42].

are coherent over a length of 400000 km. Further details on the experiment are given in [41] and [42].

Investigation of photon correlations employed the ordinary Hanbury–Brown and Twiss setup. The setup was essentially the same as described by Diedrich and Walther [37]. The results are shown and discussed in [41] also.

In conclusion, we have presented the first high-resolution heterodyne measurement of the elastic peak in resonance fluorescence of a single ion. At identical experimental parameters we have also measured antibunching in the photon correlation of the scattered field. Together, both measurements show that, in the limit of weak excitation, the fluorescence light differs from the excitation radiation in the second-order correlation but not in the first order correlation. However, the elastic component of resonance fluorescence combines an extremely narrow frequency spectrum with antibunched photon statistics, which means that the fluorescence radiation is not second-order coherent as expected from a classical point of view [43]. The heterodyne and

the photon correlation measurement are complementary since they emphasize either the classical wave properties or the quantum properties of resonance fluorescence, respectively.

2.2 The Ion-Trap Laser

There have been several theoretical papers on one-atom lasers in the past [44–47]. This system provides a testing ground for new theoretical concepts and results in the quantum theory of the laser. Examples are atomic coherence effects [48] and dynamic (i.e., self-generated) quantum-noise reduction [49, 50, 47]. All these aspects are a consequence of a pump process whose complex nature is not accounted for in the standard treatment of the laser. So far there is one experiment where laser action could be demonstrated with one atom at a time in the optical resonator [51]. A weak beam of excited atoms was used.

A formidable challenge for an experiment is to perform a similar experiment with a trapped ion in the cavity. Mirrors with an ultrahigh finesse are required, and a strong atom–field coupling is needed. After the emission of a photon, the ion has to be pumped before the next stimulated emission can occur. Similar as in the resonance fluorescence experiments which show antibunching, [33, 37] there is a certain time gap during which the ion is unable to add another photon to the laser field. It has been shown [47] that this time gap plays a significant role in the production of a field with sub-Poissonian photon statistics.

We have investigated the theoretical basis for an experimental realization of the ion trap laser. Our analysis takes into account details such as the multi-level structure, the coupling strengths and the parameters of the resonator. It has been a problem to find an ion with an appropriate level scheme. We could show that it is possible to produce a laser field with the parameters of a single Ca^+ ion. This one-atom laser displays several features, which are not found in conventional lasers: the development of two thresholds, sub-Poissonian statistics, lasing without inversion and self-quenching. The details of this work are reported in [52, 53]. In a subsequent paper [54] also the center-of-mass motion of the trapped ion was quantized. This leads to additional features of the ion trap laser, especially a multiple vacuum Rabi-splitting is observed.

3. CONCLUSIONS

In this paper recent experiments with single atoms in cavities and traps are reviewed. It is especially pointed out that using ultracold atoms will lead to new and interesting aspects in atom-matter interaction. The possibility that now ultracold atoms are available bring such experiments into reach in the near future.

REFERENCES

1. Meschede, D., Walther, H., and Müller, G., 1985, *Phys. Rev. Lett.*, **54**, 551.
2. Rempe, G., Walther, H., and Klein, N., 1987, *Phys. Rev. Lett.*, **58**, 353.
3. Rempe, G., Schmidt-Kaler, F., and Walther, H., 1990, *Phys. Rev. Lett.*, **64**, 2783.
4. Rempe, G. and Walther, H., 1990, *Phys. Rev. A*, **42**, 1650.
5. Wagner, C., Brecha, R.J., Schenzle, A., and Walther, H., 1993, *Phys. Rev. A*, **47**, 5068.
6. Löffler, M., Englert, B.-G., and Walther, H., 1996, *Appl. Phys. B*, **63**, 511.
7. Benson, O., Raithel, G., and Walther, H., 1994, *Phys. Rev. Lett.*, **72**, 3506.
8. Raithel, G., Benson, O., and Walther, H., 1995, *Phys. Rev. Lett.*, **75**, 3446.
9. Raithel, G., Wagner, C., Walther, H., *et al.*, 1994, *Advances in Atomic, Molecular, and Optical Physics*, Supplement 2, Berman, P., Ed. (New York: Academic), p. 57.
10. Filipowicz, P., Javanainen, J., and Meystre, P., 1986, *Phys. Rev. A*, **34**, 3077.
11. Lugiato, L.A., Scully, M.O., and Walther, H., 1987, *Phys. Rev. A*, **36**, 740.
12. P. Meystre, 1992, *Progress in Optics*, Wolf, E., Ed. (New York: Elsevier Science), vol. 30, p. 261.
13. Raimond, J.M., Brune, M., Davidovich, L., *et al.*, 1989, *Atomic Physics*, **11**, 441.
14. Ramsey, N.F., 1956, *Molecular Beams* (Oxford: Clarendon), p. 124.
15. Cohen-Tannoudji, C., Dupont-Roc, J., and Grynberg, G., 1992, *Atom–Photon Interactions* (New York: John Wiley and Sons), p. 407.
16. Wagner, C., Schenzle, A., and Walther, H., 1994, *Opt. Commun.*, **107**, 318.
17. Walther, H., 1992, *Phys. Reports*, **219**, 263.
18. Weidinger, M., Benson, O., and Walther, H., to be published.
19. Briegel, H.-J., Englert, B.-G., Sterpi, N., and Walther, H., 1994, *Phys. Rev. A*, **49**, 2962.
20. Scully, M.O., Meyer, G.M., and Walther, H., 1996, *Phys. Rev. Lett.*, **76**, 4144.
21. Meyer, G.M., Scully, M.O., and Walther, H., *Phys. Rev. A* (in press).
22. Löffler, M., Meyer, G.M., Schröder, M., *et al.*, *Phys. Rev. A*, in print.
23. Schröder, M., Vogel, K., Schleich, W.P., *et al.*, *Phys. Rev. A* (in press).
24. Hartig, W., Rasmussen, W., Schieder, R., and Walther, H., 1976, *Z. Physik A*, **278**, 205.
25. Cresser, J.D., Häger, J., Leuchs, G., *et al.*, 1982, *Topics in Current Physics*, **27**, 21.
26. Jessen, P.S., Gerz, C., Lett, P.D., *et al.*, 1992, *Phys. Rev. Lett.*, **69**, 49.
27. Heitler, W., 1954, *The Quantum Theory of Radiation*, 3rd ed. (Oxford: Oxford Univ. Press), p. 196.
28. Mollow, B.R., 1969, *Phys. Rev.*, **188**, 1969.
29. Schuda, F., Stroud, C., Jr., and Hercher, M., 1974, *J. Phys. B*, **1**, L198.

30. Walther, H., 1975, *Lecture Notes in Physics*, **43**, 358.

31. Wu, F.Y., Grove, R.E., and Ezekiel, S., 1975, *Phys. Rev. Lett.*, **35**, 1426; Grove, R.E., Wu, F.Y., and Ezekiel, S., 1977, *Phys. Rev. Lett. A*, **15**, 227.

32. Gibbs, H.M. and Venkatesan, T.N.C., 1976, *Opt. Commun.*, **17**, 87.

33. Kimble, H.J., Dagenais, M., and Mandel, L., 1977, *Phys. Rev. Lett.*, **39**, 691.

34. Jakeman, E., Pike, E.R., Pusey, P. N., and Vaugham, J.M., 1977, *J. Phys. A*, **10**, L257.

35. Kimble, H.J., Dagenais, M., and Mandel, L., 1978, *Phys. Rev. A*, **18**, 201; Dagenais, M. and Mandel, L., 1978, *Phys. Rev. A*, **18**, 2217.

36. Rateike, F.M., Leuchs, G., and Walther, H., results cited in Ref. 21.

37. Diedrich, F. and Walther, H., 1987, *Phys. Rev. Lett.*, **58**, 203.

38. Walls, D.F., 1979, *Nature*, **280**, 451.

39. Short, R. and Mandel, L., 1983, *Phys. Rev. Lett.*, **51**, 384; 1984, *Coherence and Quantum Optics V*, Mandel, L. and Wolf, E., Eds. (New York: Plenum), p. 671.

40. Schrama, C.A., Peik, E., Smith, W.W., and Walther, H., 1993, *Opt. Commun.*, **101**, 32.

41. Höffges, J.T., Baldauf, H.W., Eichler, T., *et al.*, 1997, *Opt. Commun.*, **133**, 170.

42. Höffges, J.T., Baldauf, H.W., Lange, W., and Walther, H., *J. Mod. Opt.* (in press).

43. Loudon, R., 1980, *Rep. Prog. Phys.*, **43**, 913.

44. Mu, Y. and Savage, C.M., 1992, *Phys. Rev. A*, **46**, 5944.

45. Ginzel, C., Briegel, H.-J., Martini, U., *et al.*, 1993, *Phys. Rev. A*, **48**, 732.

46. Pellizzari, T. and Ritsch, H., 1994, *J. Mod. Opt.*, **41**, 609; 1994, *Phys. Rev. Lett.*, **72**, 3973; Horak, P., Gheri, K.M., and Ritsch, H., 1995, *Phys. Rev. A*, **51**, 3257.

47. Briegel, H.-J., Meyer, G.M., and Englert, B.-G., 1996, *Phys. Rev. A*, **53**, 1143; 1996, *Europhys. Lett.*, **33**, 515.

48. For a recent review see Arimondo, E., 1996, *Progress in Optics*, vol. XXXV, Wolf, E., Ed. (Amsterdam: Elsevier), p. 257.

49. Khazanov, A. M., Koganov, G.A., and Gordov, E.P., 1990, *Phys. Rev. A*, **42**, 3065; Ralph, T.C. and Savage, C.M., 1991, *Phys. Rev. A*, **44**, 7809; Ritsch, H., Zoller, P., Gardiner, C.W., and Walls, D.F., 1991, *Phys. Rev. A*, **44**, 3361.

50. Gheri, K.M. and Walls, D.F., 1992, *Phys. Rev. A*, **45**, 6675; Ritsch, H. and Marte, M.A.M., 1993, *Phys. Rev. A*, **47**, 2354.

51. An, K., Childs, J.J., Dasari, R.R., and Feld, M.S., 1994, *Phys. Rev. Lett.*, **73**, 3375.

52. Meyer, G.M., Briegel, H.-J., and Walher, H., 1997, *Europhys. Lett.*, **37**, 317.

53. Meyer, G.M., Löffler, M., and Walther, H., 1997, *Phys. Rev. A*, **56**, R1099.

54. Löffler, M., Meyer, G.M., and Walther, H., to be published.

Generation of Quantum Photon States by an Active Microcavity Trap

F. De Martini, O. Jedrkiewicz, and P. Mataloni

Dipartimento di Fisica, Universita di Roma "La Sapienza," Istituto Nazionale di Fisica Nucleare
and Istituto Nazionale di Fisica della Materia, P. le A. Moro 2-00185 Roma, Italy
e-mail: P.Mataloni@CASPUR.IT
Received August 6, 1997

Abstract—Nonclassical radiation has been generated in an active Fabry-Perot dye microcavity excited by a femtosecond laser. Generation of single-photon states over the forward cavity mode, with a nonclassical sub-Poissonian distribution has been demonstrated in these conditions. By multiple excitation of the active medium collective emission phenomena are expected because of the superradiant coupling occurring within the transverse area of coherence of the microcavity. In particular, we have experimentally verified, with femtosecond temporal resolution, the principle of relativistic causality within the process of two-dipole superradiance by transverse interaction in conditions of strong microcavity confinement.

The generation of nonclassical light in an active microcavity has been recently demonstrated in our laboratory [1, 2]. With these experiments it has been shown that a Fabry-Perot dye microcavity, with length $d = m\lambda_0/2$ (where λ_0 represents the wavelength of emission of the dye solution and $m \longrightarrow 1$ is the cavity order) can behave as a generator of quantum radiation when a very small number of active molecules is excited by a femtosecond laser pulse. In these experimental conditions single photon, states (Fock states), are emitted over the forward cavity mode with sub-Poissonian distribution. The process of coupling of the molecular emission to a single-mode cavity has been studied in the context of a semiclassical Rabi approach and it has been demonstrated that each excitation pulse is found to be a π *pulse* for the overall dynamics [2]. Then, if a single molecule interacts with that pulse, the excitation does not have time to cycle more than once within the molecular four-level system, whose quantum efficiency of the absorption emission cycle is nearly equal to 1 [3]. This process, which leads to the emission of no more than one photon over the forward cavity mode for each excitation pulse, is precisely the origin of the mechanism of self-regularization and determines the *antibunched* character of the emitted radiation [4].

The single-molecule excitation process can be reproduced n-times within the same device by multiple focusing within the macroscopic transverse extension 1_c of the same field mode [5, 6]. Let us suppose, for example, that two equal dipoles are excited by two identical, delayed femtosecond pulses and assume that they are localized on the symmetry plane of the microcavity at a mutual transverse distance $R = |\mathbf{R}|$ (Fig. 1). Provided that $R < 1_c$, the field involved in the inter atomic coupling belongs to the cavity forward mode and transverse coupling between the two quantum objects can occur via a quantum mechanical process such as stimulated emission or superradiance. As a con-

sequence, the emitted, indistinguishable singlephotons do belong to the same space-time extension of the output field mode, i.e., they form a quantum Fock state [7]. The knowledge of this physical process could possibly bring us to conceive monolithic arrays of transverse interacting microlasers or optical active multiplexers acting with spatially modulated coupling. As far as the fundamental aspects of this phenomenon are concerned, one interesting question is what is the "speed" at which the transverse interaction between the two quantum objects is estabilished. The theory of this process, reported in [7], in the framework of the nonrelativistic quantum theory, predicts that the spontaneous emission dynamics of the excited molecules are strongly coupled by relativistically causal, superradiant interactions acting with a retardation time R/c, *shorter* than the coherence-time of the field emitted by the microcavity. The explicit expression of the two-dipole correlation amplitude is, in the case of two equal
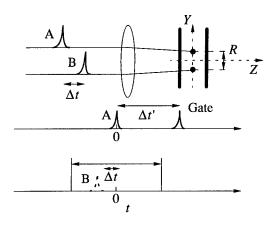
Fig. 1. Correlation experiment: temporal sequence of the femtosecond pulses.

dipoles aligned along the **X**-axis, perpendicular to the plane **YZ** in Fig. 1,

$$D(t - R_n/c) \equiv \pi \left\{ \frac{k_0^2}{R} - \frac{ik_0}{R^2} + \frac{1}{R^3} \right\}$$

$$\times \exp(ik_0 R)\theta(ct - R)$$

$$+ 2\pi \sum_{n=1}^{+\infty} (-1)^n |r|^n \left\{ \frac{k_0^2}{R_n} - \frac{ik_0}{R_n^2} + \frac{1}{R_n^3} \right\}$$

$$\times \exp(ik_0 R_n)\theta(ct - R_n)$$

(1)

with $k_0 = \frac{2\pi}{\lambda_0}$ and $R_n = \sqrt{R^2 + (nd)^2}$. In this expression the retardation, and then the *relativistic causality*, is expressed by the appearance of the Heaviside step functions: $\theta(z) = 1$, for $z > 0$, and $\theta(z) = 0$, $z < 0$. The first term in the above expression corresponds to a retarded direct interatom correlation over the distance R in free space. The second term represents the interference with alternate signs, of increasingly retarded contributions leading to a peculiar *quasi-oscillatory* response and corresponds to the interaction of one dipole with the infinite reflected images of the other. Such behavior is found to be strongly dependent on the finesse f and on the ratio $\gamma = R/1_c$, expressing for $\gamma < 1$ the coexistence of the atoms within the same transverse cavity mode.

The result corresponding to the dipoles aligned along the **Y**-axis is given by the expression

$$D(t - R_n/c) = 4\pi^2 \left\{ \frac{ik_0}{R^2} - \frac{1}{R^3} \right\}$$

$$\times \exp(ik_0 R)\theta(ct - R) + 4\pi^2$$

(2)

$$\times \sum_{n=1}^{\infty} (-|r|)^n \left\{ (nd)^2 \left[\frac{k_0^2}{R_n^3} - i\frac{k_0}{R_n^4} + \frac{1}{R_n^5} \right] + 2 \left[\frac{ik_0}{R_n^2} - \frac{1}{R_n^3} \right] \right\}$$

$$\times \exp(ik_0 R_n)\theta(ct - R_n).$$

Note in this second case the absence of the long-range interaction term proportional to R^{-1}.

Following these theoretical results we expect an onset of the correlation amplitude at a temporal delay R/c. Since in a high-finesse microcavity $R \le 1_c$ can be larger than 100 μm [6], the expected retardation time is in the sub-picosecond time scale.

The problem of transverse interaction in a microcavity has been previously investigated in the time domain in the case of coupling via stimulated emission among two microlasers excited by a femtosecond laser [8]. The experiment we present in this work, which adopts the same experimental layout of that work, concerns the case of two dipoles emitting spontaneously and interacting over the transverse distance R within the microcavity by superradiant coupling.

The 100-fs pulses generated by a 20 Hz amplified CPM dye laser were split by two 50/50 beamsplitters into three different optical paths, mutually delayed by means of two step-by-step translation stages with resolution of 1 μm. The two main excitation beams, properly attenuated by a set of neutral density filters, were focused by a lens ($f = 7.5$ cm) on the plane of an active microcavity in two different focal spot sizes with diameter 15 μm, at a mutual transverse distance R. This could be changed by slightly adjusting the angle between the two pump beams. The experiment was carried out by varying R in the range 0–200 μm, which nearly corresponds to the maximum spatial extension of the field mode. An asymmetric Fabry-Perot microcavity, terminated by two multilayer dielectric mirrors with reflectivities $|r_1|^2 = 0.99998$ and $|r_2|^2 = 0.995$ respectively, was aligned in resonance with the wavelength of emission ($\lambda_0 = 702$ nm) of a drop of ethylene glycol solution of Oxazine 725, squeezed between the two mirrors. A value of the finesse $f \cong 1000$ and an equivalent cavity order $m = 15$ were measured by preliminary characterization of the spectral transmission of the interferometer and of its output pulse shape when operating as a microlaser [9]. Let us look in detail at the experimental procedure we followed in this work: two linearly polarized identical femtosecond laser pulses, A and B, excite with a variable delay t two different regions of the microcavity located at a distance $R = |R| \le 1_c$ (Fig. 1). Because of their random orientation, the excitation probability is larger for the molecules whose dipole moments are parallel to the pump polarization. For a single molecule with dipole moment μ, the excitation probability is proportional to $\cos^2\beta$, where β is the angle between μ and the pumping electric field. It has been demonstrated that, because of the long orientational diffusion time, the excited dipoles are frozen in their position just after femtosecond excitation, with the result that the emitted radiation keeps the same polarization of the pump [10]. In this way the two ensembles of excited molecules can be considered equivalent to two identical parallel dipoles which can be coupled by transverse mutual interaction. By a simple rotation of the pump polarization we can investigate experimentally the two relevant cases of dipoles oriented along the **Y** direction (parallel to **R**) and the **X** direction (perpendicular to **R**). The single-photon radiation is emitted by the two systems with the characteristic time $T \cong 3$ ns [11] on the common output cavity mode [12], with an intrinsic indistinguishability between the origin of the two emissions. Following the theory, the enhancement of the total emission rate should occur for $\Delta t = \eta' R/c$ where $\eta' = 1.43$ is the index of refraction of the active medium. Because of the intrinsic symmetry of the problem, the enhancement is expected either for positive or negative values of Δt. However, because of dephasing and non radiative emission
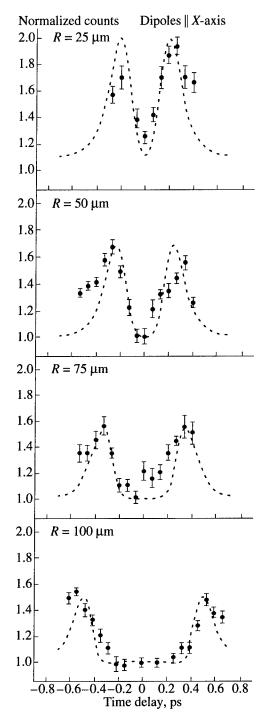
Fig. 2. Counting rate vs. time delay of the excitation pulses. Dipoles oriented along the X-axis.

Fig. 3. Counting rate vs. time delay of the excitation pulses. Dipoles oriented along the Y-axis.

of the dye molecules, this effect would be washed out if observed in a time interval of the order of the radiative lifetime T. As a consequence, a nonlinear femtosecond optical gate, with single-photon sensitivity, was assessed for this purpose by us. Following its scheme, the microcavity single-photon signal was mixed in a second-order nonlinear crystal ($LiIO_3$, thickness = 1 mm) with a properly delayed laser pulse, in order to generate the sum frequency signal. Single UV scattered photons, corresponding to the ultrafast gate, were measured with a quantum efficiency of 40% and with a noise count rate of less than 2×10^{-4}, mainly given by the second harmonic of the laser pulse. In summary, by referring to Fig. 1, a third femtosecond laser pulse creates the probe gate in the nonlinear crystal at a fixed delay $\Delta t'$ (nearly 5 ps) with respect to the first excitation pulse A.

Correlation amplitude
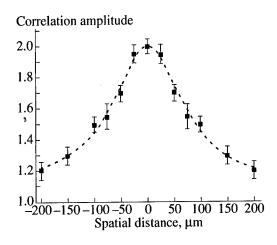
Fig. 4. Spatial extension of the electromagnetic field mode. (The data corresponding to $R > 0$ are reported also for $R < 0$.)

The experiment was performed in the following way: for each value of the temporal delay Δt, 7000 gate samples were collected for each of the three cases: signal given by the simultaneous presence of pulses A and B, S_{AB}, and signal given by the presence of only the pulse A (S_A) or pulse B (S_B). This allows us to calculate the normalized counting rate $S_{AB}/(S_A + S_B)$ for each value of Δt. We expect $S_{AB}/(S_A + S_B) = 1$ in the absence of correlation. The experimental results relative to the case of excited dipoles oriented in the **X** direction are reported in Fig. 2 for $R = 25, 50, 75$ and $100 \, \mu m$. Similar results are shown in Fig. 3 for the case of dipoles parallel to the **Y**-axis. The second case corresponds to a strong inhibition of the "free-space" direct interaction between the two systems because the two dipoles cannot exchange *directly* photons emitted over the forward cavity mode. As a consequence, any observed enhancement in the emission rate must be attributed in this case to the microcavity confinement. The experimental results can be compared with the theoretical curves obtained by the convolution of the correlation signal with a Gaussian-shape excitation pulse of 0.1 ps duration. In this theoretical fit we took in account the strong effect of dipole decoherence due to the short dephasing time ($T_2 \cong 0.1$ ps) of the dye molecules at room temperature [13]. The good agreement between theory and experiment demonstrates the causality effect in the

transverse interaction, especially for the case of dipoles oriented along the **X**-axis, where the presence of the long-range interaction term proportional to R^{-1} is responsible for the observed enhancement of the coupling process. We performed other measurements in this particular case, for $R = 0, 150$ and $200 \, \mu m$, always confirming the causality effect. All the results are summarized in Fig. 4, where the maximum correlation amplitude is reported as a function of the spatial distance R. The experimental point fits very well with a Lorentzian curve which gives, in a first approximation, the spatial profile of the electromagnetic field mode.

ACKNOWLEDGMENTS

REFERENCES

1. De Martini, F., Di Giuseppe, G., and Marrocco, M., 1996, *Phys. Rev. Lett.*, **76**, 900.
2. De Martini, F., Jedrkiewicz, O., and Mataloni, P., *J. Mod. Opt.*, (in press).
3. Svelto, O., 1989, *Principles of Lasers* (New York: Plenum); 1997, *J. Mod. Opt.*, **44**, issue 11/12.
4. Loudon, R., 1983, *The Quantum Theory of Light* (Oxford: Clarendon).
5. De Martini, F., Marrocco, M., and Murra, D., 1990, *Phys. Rev. Lett.*, **65**, 1853.
6. Aiello, A., De Martini, F., Marrocco, M., and Mataloni, P., 1995, *Opt. Lett.*, **20**, 1492.
7. De Martini, F. and Giangrasso, M., 1995, *Appl. Phys. B* **60**, S49.
8. Aiello, A., De Martini, F., Giangrasso, M., and Mataloni, P., 1995, *Quantum Semiclassical Opt.*, **7**, 677.
9. Mataloni, P., Aiello, A., Murra, D., and De Martini, F., 1994, *Appl. Phys. Lett.*, **65**, 1891.
10. Aiello, A., De Martini, F., and Mataloni, P., 1996, *Opt. Lett.*, **21**, 149.
11. Ciancaleoni, S., De Martini, F., and Mataloni, P., 1996, *Quantum Interferometry* (Weinheim: VCH).
12. Ciancaleoni, S., Mataloni, P., Jedrkiewicz, O., and Mataloni, P., 1997, *Opt. Soc. Am. B*, **14**, 1556.
13. de Brito Cruz, C.H., Fork, R.L., Knox, W.H., and Shank, C.V., 1986, *Chem. Phys. Lett.*, **32**, 341.

Laser Cooling of Impurity Crystals

S. N. Andrianov and V. V. Samartsev

Kazan Physicotechnical Institute, Russian Academy of Sciences, Sibirskii trakt 10/7, Kazan, 420029 Russia
e-mail: samartsev@dionis.kfti.kcn.ru
Received October 9, 1997

Abstract—Laser cooling of impurity molecular crystals excited at the edge of the absorption line is considered. A sample is cooled through a system of resonant phonons. The expression for the final temperature of cooling is derived in both low- and high-frequency approximations. The kinetics of cooling is analyzed in a weakly nonequilibrium situation.

1. INTRODUCTION

Presently, laser cooling has become a highly developed branch of science, which is of considerable importance for fundamental science and applications [1, 2]. However, only the laser cooling of gas media has been investigated thus far. Several recent theoretical [3–6] and experimental [7, 8] studies have been devoted to laser cooling in condensed phase. Epstein *et al.* have implemented cooling of heavy metal–fluoride glass doped with trivalent ytterbium ions [7]. Clark and Rumbles [8] have cooled a liquid solution of Rhodamine 101 in acid-containing ethanol. Both experiments were performed at room temperature, and the authors of these papers attribute the cooling effect to the excitation at the edge of the absorption line of impurity particles. Andrianov and Samartsev [5] considered laser cooling of an isolated phonon mode in a mixed molecular crystal through excitation at the edge of the line and examined the possibility to cool a pure molecular crystal with the help of the exciton mechanism. Oraevskii [6] and Zadernovskii and Rivlin [3] have analyzed laser cooling of free carriers in semiconductors. In this paper, we will theoretically study laser cooling of a molecular crystal through the impurity subsystem.

2. KINETIC EQUATIONS

Anisotropic impurity molecules are involved in vibrational librations with respect to their equilibrium positions in a molecular crystal. Since the direction of their transition dipole moment is unambiguously related to molecular symmetry axes, these librations modulate the constant of interaction of a molecule with the electromagnetic field, which gives rise to the so-called indirect transitions, when a phonon is absorbed or emitted simultaneously with a photon.

The Hamiltonian of anisotropic molecules in a molecular crystal can be written as [9]

$$H = H_0 + H_1, \tag{1}$$

where

$$H_0 = H_d + H_f + H_l \tag{2}$$

is the main Hamiltonian and

$$H_1 = H_{df} + H'_{df} \tag{3}$$

is the Hamiltonian of perturbation. Here,

$$H_d = \sum_j \hbar \omega_0 S_j^z \tag{4}$$

is the Hamiltonian of impurity molecules in the two-level model, where j is the number of an impurity molecule, ω_0 is the frequency of an electronic transition, and S_j^z is the operator of the effective spin $S = 1/2$ (z-projection);

$$H_f = \sum_k \hbar \omega_k a_k^+ a_k \tag{5}$$

is the Hamiltonian of the electromagnetic field in the secondary-quantized form, where ω_k is the frequency of the k mode of the electromagnetic field and a_k^+ and a_k are the operators of creation and annihilation of quanta from the k mode of the electromagnetic field;

$$H_l = \sum_q \hbar \Omega_q b_q^+ b_q \tag{6}$$

is the Hamiltonian of the lattice, where Ω_q is the phonon frequency of the q mode and b_q^+ and b_q are the operators of creation and annihilation of a phonon from the q mode;

$$H_{df} = \sum_{jk} (q_k e^{i\mathbf{kr}_j} S_j^+ a_k + q_k^* e^{-i\mathbf{kr}_j} S_j^- a_k^+) \tag{7}$$

is the Hamiltonian of interaction between molecules and the electromagnetic field in the rotating-wave approximation, where q_k is the coupling constant for the k mode, $\mathbf{k}$ is the wave vector of a photon from the k mode, $\mathbf{r}$ is the radius vector of the jth molecule, and $S_j^\pm$

are the operators raising and reducing the z-projection of the effective spin; and

$$H_{df}^l = \sum_{jkq} \{ h_{kq} e^{i(k-q)r_j} S_j^+ a_k (b_q + b_q^+) $$

$$+ h_{kq}^* e^{-i(k-q)r_j} S_j^- a_k^+ (b_q + b_q^+) \} \tag{8}$$

is the Hamiltonian of interaction between molecules and the electromagnetic field in the presence of lattice vibrations, where h_{kq} is the relevant coupling constant.

Using the method of nonequilibrium statistical operator [10, 11], we can introduce the following dynamic variables D_m: the operator of the number of photons in the kth mode,

$$n_k = a_k^+ a_k; \tag{9}$$

the operator of the number of phonons in the qth mode,

$$n_q = b_q^+ b_q; \tag{10}$$

and the operator of the collective population difference between the working electronic levels,

$$R_z = 2 \sum_j S_j^z; \tag{11}$$

Dynamic variables represent independent integrals of motion,

$$[D_m, H_0] = [D_m, D_{m'}] = 0, \tag{12}$$

for all $m \neq m'$. Therefore, the kinetic equations are written as

$$\frac{d\langle D_m \rangle}{dt} = \frac{1}{\hbar^2} \int_{-\infty}^{0} e^{\varepsilon t} \langle [H_1(t), [D_m, H_1]] \rangle_q dt, \tag{13}$$

where the parameter ε takes into account the irreversible character of the processes under study (we should let this parameter tend to zero after the integration) and $\langle ... \rangle_q$ denotes the averaging over the quasi-equilibrium statistical operator

$$\rho_q = Q^{-1} \exp\left[-\sum_m \beta_m D_m \right], \tag{14}$$

where

$$Q = Sp \exp\left[-\sum_m \beta_m D_m \right] \tag{15}$$

is the normalizing factor, β_m are the inverse temperatures of the relevant subsystems, and

$$\langle D_m \rangle = \langle D_m \rangle_q \tag{16}$$

In accordance with the method of nonequilibrium statistical operator,

$$H_1(t) = e^{\frac{i}{\hbar} H_0 t} H_1 e^{-\frac{i}{\hbar} H_0 t} \tag{17}$$

describes the time dependence of operators involved in (13).

In the spatially homogeneous case, we can substitute operators (1)–(11) into expressions (13)–(17) to derive the following set of kinetic equations:

$$\frac{d\langle n_k \rangle}{dt} = \left\{ \sum_q \left[\frac{\langle n_q \rangle + 1}{\tau_1^s(kq)} + \frac{\langle n_q \rangle}{\tau_1^{as}(kq)} + \frac{\langle n_k \rangle}{\tau_1^s(kq)} \right] \right.$$

$$+ \frac{1}{\tau_1(k)} \left\} \frac{\langle R_z \rangle + N}{2} + \left\{ \sum_q \left[\frac{1}{\tau_1^s(kq)} + \frac{1}{\tau_1^{as}(kq)} \right] \right. \tag{18}$$

$$\times \langle n_q \rangle + \frac{1}{\tau_1(k)} \right\} \langle n_k \rangle \langle R_z \rangle$$

$$+ \sum_q \frac{\langle n_k \rangle}{\tau_1^{as}(kq)} \frac{\langle R_z \rangle - N}{2} - \frac{\langle n_k \rangle - \bar{n}_k}{\tau_k},$$

$$\frac{d\langle n_q \rangle}{dt} = \sum_k \left[\frac{\langle n_q \rangle + 1}{\tau_1^s(kq)} - \frac{\langle n_q \rangle}{\tau_1^{as}(kq)} + \frac{\langle n_k \rangle}{\tau_1^s(kq)} \right] \frac{\langle R_z \rangle + N}{2}$$

$$+ \sum_k \left[\frac{1}{\tau_1^s(kq)} - \frac{1}{\tau_1^{as}(kq)} \right] \langle n_k \rangle \langle n_q \rangle \langle R_z \rangle \tag{19}$$

$$- \sum_k \frac{\langle n_k \rangle}{\tau_1^{as}(kq)} \frac{\langle R_z \rangle - N}{2} - \frac{\langle n_q \rangle - \bar{n}_q}{\tau_q},$$

$$\frac{d\langle R_z \rangle}{dt} = -\left\{ \sum_{kq} \left[\frac{\langle n_q \rangle + 1}{\tau_1^s(kq)} + \frac{\langle n_q \rangle}{\tau_1^{as}(kq)} + \frac{\langle n_k \rangle}{\tau_1^s(kq)} \right] \right.$$

$$+ \frac{1}{\tau_1(k)} \right\} (\langle R_z \rangle + N) - 2\left\{ \sum_{kq} \left[\frac{1}{\tau_1^s(kq)} + \frac{1}{\tau_1^{as}(kq)} \right] \right. \tag{20}$$

$$\times \langle n_q \rangle + \frac{1}{\tau_1(k)} \right\} \langle n_k \rangle \langle R_z \rangle - \sum_{kq} \frac{\langle n_k \rangle}{\tau_1^{as}(kq)} (\langle R_z \rangle - N),$$

where

$$\frac{1}{\tau_1(k)} = \frac{2\pi}{\hbar^2} |g_k|^2 \delta(\omega_0 - \omega_k) \tag{21}$$

is the inverse time of spontaneous emission through direct transitions of a photon in the kth mode,

$$\frac{1}{\tau_1^s(kq)} = \frac{2\pi}{\hbar^2} |h_{kq}|^2 \delta(\omega_0 - \omega_k - \Omega_q) \tag{22}$$

is the inverse time of spontaneous emission through Stokes indirect transitions of a photon in the kth mode and a phonon in the qth mode,

$$\frac{1}{\tau_1^{as}(kq)} = \frac{2\pi}{\hbar^2} |h_{kq}|^2 \delta(\omega_0 - \omega_k + \Omega_q) \tag{23}$$

is the inverse time of spontaneous emission through anti-Stokes indirect transitions of a photon in the kth mode with absorption of a phonon in the qth mode, τ_k is the time of flight for a photon in the kth mode, τ_q is the passage time for a phonon in the qth mode, $\bar{n}_k$ is the mean number of photons in the kth mode determined by the external source, and $\bar{n}_q$ is the mean number of phonons in the qth mode determined by the interaction with a thermostat.

Using the properties of delta functions in expressions (21)–(23), we can derive the following conservation law from equations (18)–(20):

$$\sum_k \hbar\omega_k \frac{d\langle n_k \rangle}{dt} + \sum_q \hbar\Omega_q \frac{d\langle n_q \rangle}{dt} + \frac{\hbar\omega_0}{2}\frac{d\langle R_z \rangle}{dt}$$
$$= \sum_k \hbar\omega_k \frac{\bar{n}_k - \langle n_k \rangle}{\tau_k} + \sum_q \hbar\Omega_q \frac{\bar{n}_q - \langle n_q \rangle}{\tau_q}. \qquad (24)$$

In the stationary case, when all the derivatives are equal to zero, relation (24) gives the following energy-conservation law:

$$\sum_k \hbar\omega_k \frac{\bar{n}_k - \langle n_k \rangle}{\tau_k} + \sum_q \hbar\Omega_q \frac{\langle n_q \rangle - \bar{n}_q}{\tau_q} = 0. \qquad (25)$$

Let us suppose that excitation occurs at frequency ω_l, which falls in the long-wavelength wing, and radiation is emitted at the same frequency and at a higher frequency ω_f corresponding to the line center. Then, equation (25) is reduced to

$$\hbar\omega_l \frac{\bar{n}_l - \langle n_l \rangle}{\tau_l} = \hbar\omega_f \frac{\langle n_f \rangle}{\tau_f} + \hbar\Omega_q \frac{\bar{n}_q - \langle n_q \rangle}{\tau_q}, \qquad (26)$$

where $\Omega_q = \omega_f - \omega_l$. Equations (18)–(20) also give the law of excitation conservation:

$$\sum_k \frac{d\langle n_k \rangle}{dt} + \frac{1}{2}\frac{d\langle R_z \rangle}{dt} = \sum_k \frac{\bar{n}_k - \langle n_k \rangle}{\tau_k}. \qquad (27)$$

Consequently, in the stationary regime under the above-specified conditions, we have

$$\frac{\bar{n}_l - \langle n_l \rangle}{\tau_l} = \frac{\langle n_f \rangle}{\tau_f}, \qquad (28)$$

which allows us to rewrite (26) in the form

$$\hbar(\omega_f - \omega_l)\frac{\bar{n}_l - \langle n_l \rangle}{\tau_l} = \hbar\Omega_q \frac{\bar{n}_q - \langle n_q \rangle}{\tau_q}. \qquad (29)$$

Denoting the right-hand side of equation (29) as P_{cool} and introducing a quantity

$$P_{abs} = \hbar\omega_l \frac{\bar{n}_l - \langle n_l \rangle}{\tau_l}, \qquad (30)$$

we find that the relation between the power of cooling P_{cool} and the absorbed power P_{abs} that follows from (29) coincides with the relation employed without substantiation in experimental study [7],

$$P_{cool} = P_{abs}\frac{\lambda_l - \lambda_f}{\lambda_f}. \qquad (31)$$

On the other hand, the quantity

$$A = -\frac{\hbar\omega_l}{\tau_l}\bar{n}_l \qquad (32)$$

can be considered as the negative work done by an external source on the system of resonant phonons to extract positive heat

$$Q_2 = \frac{\hbar\Omega_q}{\tau_q}(\bar{n}_q - \langle n_q \rangle) \qquad (33)$$

from a sample and return negative heat

$$Q_1 = -\frac{\hbar\omega_f}{\tau_f}\langle n_f \rangle - \frac{\hbar\omega_l}{\tau_l}\langle n_l \rangle \qquad (34)$$

with spontaneous radiation emission into the ambient medium. Thus, equation (26) is reduced to the conventional equation of a cooler:

$$A = Q_1 + Q_2. \qquad (35)$$

Here, the sample is a cold body, the system of resonant phonons is a working body, the thermostat is a hot body, and the work is the excitation of molecules at the long-wavelength edge. In accordance with the formula derived above, incident laser radiation can cool a solid sample through the system of resonant phonons.

3. STATIONARY SOLUTIONS

Let us consider the set of equations (18)–(20) again. If τ_k is less than all the characteristic times of the system, i.e., photons rapidly leave the sample, equation (18) shows that $\langle n_k \rangle = \bar{n}_k$, and equations (19) and (20) are reduced to

$$\frac{d\langle n_q \rangle}{dt} = \left[\frac{\langle n_q \rangle + 1}{\tau_1^s(q)} - \frac{\langle n_q \rangle}{\tau_1^{as}(q)} + \frac{1}{\tau_s(q)}\right]\frac{\langle R_z \rangle + N}{2}$$
$$+ \left[\frac{1}{\tau_s(q)} - \frac{1}{\tau_{as}(q)}\right]\langle n_q \rangle\langle R_z \rangle + \frac{N - \langle R_z \rangle}{2\tau_{as}(q)} - \frac{\langle n_q \rangle - \bar{n}_q}{\tau_q}, \qquad (37)$$

$$\frac{d\langle R_z \rangle}{dt} = -(N + \langle R_z \rangle)$$
$$\times \left\{\frac{1}{\tau_1} + \sum_q \left[\frac{\langle n_q \rangle + 1}{\tau_1^s(q)} + \frac{\langle n_q \rangle}{\tau_1^{as}(q)} + \frac{1}{\tau_s(q)}\right]\right\} - 2\langle R_z \rangle$$
$$\left\{\frac{1}{\tau_1} + \sum_q \left[\frac{1}{\tau_s(q)} + \frac{1}{\tau_{as}(q)}\right]\langle n_q \rangle\right\} + \sum_q \frac{N - \langle R_z \rangle}{\tau_{as}(q)}, \qquad (38)$$

$$\frac{1}{\tau_1} = \sum_k \frac{1}{\tau_1(k)}, \quad \frac{1}{\tau_1^s(q)} = \sum_k \frac{1}{\tau_1^s(kq)},$$

$$\frac{1}{\tau_1^{as}(q)} = \sum_k \frac{1}{\tau_1^{as}(kq)}, \quad \frac{1}{\tau_s(q)} = \sum_k \frac{\langle n_k \rangle}{\tau_1^s(kq)}, \quad (39)$$

$$\frac{1}{\tau_{as}(q)} = \sum_k \frac{\langle n_k \rangle}{\tau_1^{as}(kq)}, \quad \frac{1}{\tau_r} = \sum_k \frac{\langle n_k \rangle}{\tau_1}.$$

In the approximation of weak electron–phonon coupling, we can consider a situation when all indirect transitions occur through the states of pseudolocalized phonons. Pseudolocalized phonons are defined as quanta of hybrid vibrational motion emerging through the electrostatic interaction from low-frequency optical librations of anisotropic impurity molecules, which modulate the constant of electron–photon coupling via resonant acoustic phonons of the host crystal. Therefore, such phonons will be considered as resonant phonons that represent the states of the entire crystal. These states are characterized by a high spectral density ρ and are manifested within a narrow spectral interval Δ as narrow peaks in the long-wavelength wing of the absorption line. Within the framework of this approximation, we can rewrite the set of equations (37) and (38) for time intervals greater than the formation time of pseudolocalized phonons as

$$\frac{d\langle n \rangle}{dt} = \left(\frac{\langle n \rangle + 1}{\tau_1^s} - \frac{\langle n \rangle}{\tau_1^{as}} + \frac{1}{\tau_s} \right) \frac{\langle R_z \rangle + N}{2}$$

$$+ \left(\frac{1}{\tau_s} - \frac{1}{\tau_{as}} \right) \langle n \rangle \langle R_z \rangle + \frac{N - \langle R_z \rangle}{2\tau_{as}} - \frac{\langle n \rangle - \bar{n}}{\tau_1}, \quad (40)$$

$$\frac{d\langle R_z \rangle}{dt} = -\left[\frac{1}{\tau_1} + M\left(\frac{\langle n \rangle + 1}{\tau_1^s} + \frac{\langle n \rangle}{\tau_1^{as}} + \frac{1}{\tau_s} \right) \right](N + \langle R_z \rangle)$$

$$- \left[\frac{2}{\tau_r} + 2M\left(\frac{1}{\tau_s} + \frac{1}{\tau_{as}} \right) \langle n \rangle \right] \langle R_z \rangle + \frac{M}{\tau_{as}}(N - \langle R_z \rangle), \quad (41)$$

where $\langle n \rangle$ is the number of resonant phonons, τ_l is their thermalization time, and $M = \rho\Delta$ is the number of their states.

Consider the case when excitation is implemented through an indirect Stokes transition. Such an excitation corresponds to experiments [7, 8]. In this case, the numbers of all the photons, except for the photons with frequency $\omega_0 - \Omega_0$, should be set equal to zero. Then, the set of equations (40) and (41) is reduced to the following set of equations:

$$\frac{d\langle n \rangle}{dt} = \left(\frac{\langle n \rangle + 1}{\tau_1^s} - \frac{\langle n \rangle}{\tau_1^{as}} + \frac{1}{\tau_s} \right) \frac{\langle R_z \rangle + N}{2}$$

$$+ \frac{1}{\tau_s} \langle n \rangle \langle R_z \rangle - \frac{\langle n \rangle - \bar{n}}{\tau_l}, \quad (42)$$

$$\frac{d\langle R_z \rangle}{dt} = -\left[\frac{1}{\tau_1} + M\left(\frac{\langle n \rangle + 1}{\tau_1^s} + \frac{\langle n \rangle}{\tau_1^{as}} + \frac{1}{\tau_s} \right) \right]$$

$$\times (N + \langle R_z \rangle) - 2M\frac{\langle n \rangle}{\tau_s}\langle R_z \rangle. \quad (43)$$

The stationary solution to the set of equations (42) and (43) can be written as

$$\langle R_z \rangle_{st} = -\frac{\left(\frac{2M\langle n \rangle_{st}}{\tau_1^{as}} + \frac{1}{\tau_1} \right)}{2M\left(\frac{N}{\tau_1^{as}} + \frac{1}{\tau_l} \right)\langle n \rangle_{st} + \frac{N}{\tau_1} - \frac{2M\bar{n}}{\tau_l}}, \quad (44)$$

$$\langle n \rangle_{st} = \frac{-a + b\bar{n} + \sqrt{(a - b\bar{n})^2 + c\bar{n}}}{2\left[b + \frac{2MN}{\tau_s\tau_1^{as}} \right]}, \quad (45)$$

where

$$a = \frac{1}{\tau_1}\left(\frac{1}{\tau_l} + \frac{N}{\tau_s} \right) + \frac{M}{\tau_l}\left(\frac{1}{\tau_s} + \frac{1}{\tau_1^s} \right), \quad (46)$$

$$b = \frac{M}{\tau_l}\left(\frac{2}{\tau_s} + \frac{1}{\tau_1^s} + \frac{1}{\tau_1^{as}} \right), \quad (47)$$

and

$$c = \frac{4}{\tau_l}\left(b + \frac{2MN}{\tau_s\tau_1^{as}} \right)\left(\frac{M}{\tau_1^s} + \frac{M}{\tau_s} + \frac{1}{\tau_1} \right). \quad (48)$$

In the approximation of low temperatures, $\bar{n} \ll 1$, expression (45) can be rewritten in the following form:

$$\langle n \rangle_{st} = \frac{\frac{1}{\tau_l}\left(\frac{M}{\tau_1^s} + \frac{M}{\tau_s} + \frac{1}{\tau_1} \right)\left[1 + \frac{\bar{n}}{2a^2}\left(b - \frac{c}{2a} \right) \right]}{\frac{1}{\tau_l}\left(\frac{M}{\tau_1^s} + \frac{M}{\tau_s} + \frac{1}{\tau_1} \right) + \frac{N}{\tau_1\tau_s}}\bar{n}. \quad (49)$$

Thus, anti-Stokes processes manifest themselves only in the second order in n_0. Ignoring these processes, we derive

$$\langle n \rangle_{st} = \bar{n}\frac{[\tau_s\tau_1^s + M\tau_1(\tau_s + \tau_1^s)]}{\tau_s\tau_1^s + M\tau_1(\tau_s + \tau_1^s) + N\tau_1^s\tau_l}. \quad (50)$$

When the source of field is not very weak, we have $\langle n_k \rangle \gg 1$ and $\tau_s \ll \tau_1^s$. Then, for large times of heating, $N\tau_l \gg M\tau_1$, we find that

$$\langle n \rangle_{st} = \frac{\tau_1}{\tau_l}\left(\frac{M}{N} \right)\bar{n}. \quad (51)$$

In the approximation of high temperatures, we have $\bar{n} \gg 1$, and formulas (45)–(48) yield

$$\langle n \rangle_{st} = \bar{n} - \left(\frac{N}{M} \right)\frac{\frac{1}{\tau_1}\left(\frac{2}{\tau_s} + \frac{1}{\tau_1^s} \right) - \frac{2M}{\tau_1^{as}}\left(\frac{1}{\tau_s} + \frac{1}{\tau_1^s} + \frac{1}{\tau_1} \right)}{\frac{\tau_s}{\tau_l}\left(\frac{2}{\tau_s} + \frac{1}{\tau_1^s} + \frac{1}{\tau_1^{as}} \right)^2}. \quad (52)$$

For $\tau_s \ll \tau_1^s$, τ_1^{as} and $\tau_1 \ll \tau_1^{as}/M$, expression (52) can be simplified,

$$\langle n \rangle_{st} = n_0 - \frac{\tau_l}{\tau_1}\left(\frac{N}{M}\right). \qquad (53)$$

Formulas (51)–(53) demonstrate that, in both low- and high-temperature approximations, laser cooling decreases the number of phonons.

In the high-temperature approximation, we can consider an arbitrary phonon dispersion. Summation of equations (37) and (38) in q yields

$$\frac{d\langle n \rangle}{dt} = \frac{N + \langle R_z \rangle}{2}\left[F_1^s(T) - F_1^{as}(T) + \frac{1}{T_1^s} + \frac{1}{T_s}\right]$$
$$+ \langle R_z \rangle[F_s(T) - F_{as}(T)] + \frac{N - \langle R_z \rangle}{2T_{as}} - F_l(T) + F_l(T_0) \qquad (54)$$

and

$$\frac{d\langle R_z \rangle}{dt} = -(N + \langle R_z \rangle)\left[F_1^s(T) + F_1^{as}(T) + \frac{1}{T_1^s}\right.$$
$$\left.+ \frac{1}{T_s} + \frac{1}{\tau_1}\right] - 2\langle R_z \rangle\left[F_s(T) + F_{as}(T) + \frac{1}{\tau_r}\right] + \frac{N - \langle R_z \rangle}{T_{as}}, \qquad (55)$$

where

$$\langle n \rangle = \sum_q \langle n_q \rangle$$

$$\frac{1}{T_1^s} = \sum_q \frac{1}{\tau_1^s(q)}, \quad \frac{1}{T_s} = \sum_q \frac{1}{\tau_s(q)}, \quad \frac{1}{T_{as}} = \sum_q \frac{1}{\tau_{as}(q)},$$

$$F_1^s(T) = \sum_q \frac{\langle n_q \rangle}{\tau_1^s(q)}, \quad F_1^{as}(T) = \sum_q \frac{\langle n_q \rangle}{\tau_1^{as}(q)}, \qquad (56)$$

$$F_s(T) = \sum_q \frac{\langle n_q \rangle}{\tau_s(q)}, \quad F_{as}(T) = \sum_q \frac{\langle m_q \rangle}{\tau_{as}(q)},$$

$$F_l(T) = \sum_q \frac{\langle n_q \rangle}{\tau_l(q)}.$$

Ignoring anti-Stokes processes in the stationary regime, we can derive the following equation for the temperature T_r of resonant phonons:

$$F_s(T_r)\{2\tau_1[F_l(T_r) - F_l(T_s)]\} + \{\tau_1[F_l(T_r) - F_l(T_s)]$$
$$+ N\}\left[F_1^s(T_r) + \frac{1}{T_1^s} + \frac{1}{T_s} + \frac{1}{\tau_1}\right] = 0. \qquad (57)$$

Equation (57) can be solved numerically through the comparison of theoretical predictions with experimental data.

4. CONCLUSION

Thus, we have considered laser cooling of an impurity crystal at the edge of the line. In our opinion, the main advantage of laser cooling over conventional cooling stems from the frequency and spatial selectivity of laser cooling. If impurity molecules and the host crystal have the same vibrational structure, then pseudolocalized phonons may arise in a crystal. Since such phonons are characterized by a low mobility and are spectrally isolated, they enhance the efficiency of cooling. Such phonons can be cooled by laser radiation with an appropriate frequency. Then, with proper thermal insulation, the entire crystal can be cooled through the states of these resonant phonons.

ACKNOWLEDGMENTS

REFERENCES

1. Minogin, V.G. and Letokhov, V.S., 1986, *Pressure of Light on Atoms* (Moscow: Nauka) (in Russian).
2. Letokhov, V.S. and Chebotayev, V.P., 1990, *Nonlinear Laser Spectroscopy of Ultrahigh Resolution* (Moscow: Nauka) (in Russian).
3. Zadernovskii, A.A. and Rivlin, L.A., 1996, *Kvantovaya Elektron.*, **23**, 1131.
4. Andrianov, S.N. and Samartsev, V.V., 1996, *Laser Phys.*, **6**, 759.
5. Andrianov, S.N. and Samartsev, V.V., 1996, *Laser Phys.*, **6**, 949.
6. Oraevskii, A.N., 1996, *Kvantovaya Elektron.*, **23**, 1045.
7. Epstein, R.I., Buchwald, M.I., Edwards, B.S., *et al.*, 1995, *Nature*, **377**, 500.
8. Clark, J.L. and Rumbles, G., 1996, *Phys. Rev. Lett.*, **76**, 2037.
9. Davydov, A.S., 1976, *Theory of Solids* (Moscow: Nauka) (in Russian).
10. Zubarev, D.N., 1971, *Nonequilibrium Statistical Thermodynamics* (Moscow: Nauka) (in Russian).
11. Akhiezer, A.I. and Peletminskii, S.V., 1977, *Methods of Statistical Physics* (Moscow: Nauka) (in Russian).

MODERN TRENDS
IN LASER PHYSICS

Stability Analysis of Nonlinear Dynamics in Spin Masers

V. I. Yukalov*, J. A. Gonzalez*, **, and C. L. Dias*

* *International Centre of Condensed Matter Physics, University of Brasilia, CP 04513, Brasilia, DF 70919-970 Brazil*
** *Centro de Fizica, Instituto Venezolano de Investigaciones Cientificas, Apartado 21827, Caracas 1020 A, Venezuela*
e-mail: yukalov@solids.iccmp.br
Received August 5, 1997

Abstract—The stability analysis is presented for nonlinear spin dynamics of spin masers. The features of long-time relaxation are studied. The possibility of achieving a stationary regime of coherent radiation is discussed.

1. INTRODUCTION

Coherent radiation from an ensemble of nuclear spins has been observed in experiments with several substances: from Al nuclear spins in Ruby (Al_2O_3) [1] and from proton spins in propanediol ($C_3H_8O_2$) [2, 3], butanol (C_4H_9OH), and ammonia (NH_3) [4]. Because of many similarities with atomic and molecular superradiance, coherent radiation from spins can be called spin superradiance. At initial time, nuclear spins must be polarized forming a nonequilibrium nuclear magnet. The theory of spin superradiance by nuclear magnets was developed in [5–7]. The mathematical basis of this theory is the method of scale separation [6–8] permitting an accurate solution of complicated nonlinear systems of differential and integrodifferential equations.

For describing fast transient processes of nonlinear spin dynamics [5–7], some small relaxation parameters can be omitted. This allows one to obtain analytic solutions to evolution equations and to give the complete classification of fast relaxation regimes with relaxation times shorter or of the order of the spin–spin dephasing time. However, as is known, one has to be very cautious dealing with nonlinear differential equations. It may happen that neglecting even quite small terms drastically changes the behaviour of solutions. Therefore, in the present paper we aim at answering the following questions.

(i) What qualitative changes, in the behaviour of solutions, appear when we omit, from the evolution equations of spin maser, the terms containing damping parameters much smaller than the spin–spin damping constant? Even if there are no radical changes for nuclear magnets, this question can be of importance for other materials for which the omitted parameters can be not as negligible as for nuclear magnets. For example, these parameters can be quite different for the system of electron spins in a high-quality resonator [9, 10], or for model systems [11].

(ii) Even if the omission of small damping parameters does not change much the properties of short-time transient processes, it, certainly, should essentially influence long-time relaxation. What are the features of this long-time relaxation?

(iii) Is it possible to realize a stationary regime of coherent spin radiation? If so, can this stationary radiation be comparable, in its power, with that of the transient superradiance?

2. EVOLUTION EQUATIONS

The system of N nuclear spins is described [12] by the Hamiltonian

$$\hat{H} = \frac{1}{2}\sum_{i \neq j}^{N} H_{ij} - \mu \sum_{i=1}^{N} \mathbf{B} \cdot \mathbf{S}_i \qquad (1)$$

with the dipole interactions

$$H_{ij} = \frac{\mu^2}{r_{ij}^3}[\mathbf{S}_i \cdot \mathbf{S}_j - 3(\mathbf{S}_i \cdot \mathbf{n}_{ij})(\mathbf{S}_j \cdot \mathbf{n}_{ij})], \qquad (2)$$

in which μ is a nuclear magneton, $\mathbf{S}$ is a spin operator, and

$$r_{ij} \equiv |\mathbf{r}_{ij}|, \quad \mathbf{n}_{ij} \equiv \frac{\mathbf{r}_{ij}}{r_{ij}}, \quad \mathbf{r}_{ij} = \mathbf{r}_i - \mathbf{r}_j.$$

The total magnetic field

$$\mathbf{B} = \mathbf{H}_0 + \mathbf{H}, \quad \mathbf{H}_0 = H_0 \mathbf{e}_z, \quad \mathbf{H} = H\mathbf{e}_x \qquad (3)$$

consists of two parts: The first is an external magnetic field and the second is a field of the coil of a resonance electric circuit. The latter is characterized by resistance R, inductance L, and capacity C. The coil, surrounding the sample, has n turns of cross section A_0 over a length l. The magnetic field inside the coil,

$$H = \frac{4\pi n}{cl} j, \qquad (4)$$

is formed by an electric current satisfying the Kirchhoff equation

$$\frac{dj}{dt} + Rj + \frac{1}{C}\int_0^t j(\tau) d\tau = -\frac{d\Phi}{dt} + E_f, \qquad (5)$$

in which E_f is an electromotive force and Φ is the magnetic flux

$$\Phi = \frac{4\pi}{c} n A_0 \eta \rho \frac{\mu}{N} \sum_{i=1}^{N} \langle S_i^x \rangle,$$

where η is a filling factor, ρ is the spin density, and $\langle \cdot \rangle$ means statistical averaging with an initial statistical operator $\hat{\rho}(0)$.

Introduce the notion for the resonator circuit natural frequency ω and the spin Zeeman frequency ω_0, respectively,

$$\omega \equiv \frac{1}{\sqrt{LC}}, \quad \omega_0 \equiv \frac{\mu H_0}{\hbar}. \tag{6}$$

Define the resonator ringing width γ_3,

$$\gamma_3 \equiv \frac{\omega}{2Q}, \quad Q \equiv \frac{\omega L}{R}, \tag{7}$$

Q being the resonator quality factor.

We shall consider the evolution equations for the average transverse magnetization

$$u \equiv \frac{1}{N} \sum_{j=1}^{N} \langle S_j^x - i S_j^y \rangle \tag{8}$$

and the average longitudinal magnetization

$$s \equiv \frac{1}{N} \sum_{j=1}^{N} \langle S_j^z \rangle. \tag{9}$$

Also, we shall need the dimensionless resonator field

$$h \equiv \frac{\mu H}{\hbar \gamma_3} \tag{10}$$

and driving force

$$f \equiv \frac{c\mu E_f}{n A_0 \hbar \gamma_3^2}. \tag{11}$$

For the latter, we assume the standard form

$$f = f_0 \cos \omega t, \quad f_0 \equiv \frac{c\mu E_0}{n A_0 \hbar \gamma_3^2}. \tag{12}$$

The characteristic damping widths of the system are the spin–lattice relaxation parameter γ_1, the spin–spin dephasing parameter γ_2, the inhomogeneous dipole broadening γ_*, and the resonator ringing width γ_3. These parameters are small as compared to the corresponding frequencies:

$$\frac{\gamma_1}{\omega_0} \ll 1, \quad \frac{\gamma_2}{\omega_0} \ll 1, \quad \frac{\gamma_*}{\omega_0} \ll 1, \quad \frac{\gamma_3}{\omega} \ll 1. \tag{13}$$

In the quasi-resonance case, the resonator natural frequency is close to the Zeeman spin frequency,

$$\frac{|\Delta|}{\omega_0} \ll 1, \quad \Delta \equiv \omega - \omega_0, \tag{14}$$

that is, the detuning from the resonance is small.

The existence of the small parameters in (13) provides grounds for using the method of scale separation [6–8]. Applying this method, we classify, first, the sought functions onto fast and slow. In our case, the functions u and h are fast, while s and $|u|$ are slow. Then, the equations for the fast functions are solved with the slow functions kept as quasi-integrals of motion. The found solutions for the fast functions are substituted into the equations for the slow functions. The right-hand sides of the latter equations are averaged over the time period $T_0 \equiv 2\pi/\omega_0$, which is the shortest among all characteristic times. In addition, we average over local spin fluctuations presented by random Gaussian fields. The averaged equations are written for the slow functions

$$z = s, \quad v = |u|, \tag{15}$$

and for the convenient combination

$$w = v^2 - 2\varepsilon_* z, \quad \varepsilon_* \equiv \frac{\gamma_*^2}{\omega_0^2}. \tag{16}$$

This results in the equations

$$\frac{dz}{dt} = g\gamma_2 w - \gamma_s - \gamma_1(z - \zeta) - \gamma_f z \tag{17}$$

and

$$\frac{dw}{dt} = -2\gamma_2 w - 2(g\gamma_2 w - \gamma_s)z + 2\gamma_f z^2, \tag{18}$$

in which γ_s and γ_f are the relaxation widths due to the correlation between spins and the resonator field [7], and

$$g \equiv \frac{\pi^2 \eta \rho \mu^2}{\hbar \gamma_2} \frac{(\gamma_2 - \gamma_3)^2}{(\gamma_2 - \gamma_3)^2 + \Delta^2} \tag{19}$$

is the coupling constant describing the coupling between the spin system and the resonator. The constant ζ in (17) is a stationary magnetization along the z-axis. This could be either an internal magnetization of the sample or a magnetization supported by external fields and by special methods, like dynamic nuclear polarization. In what follows, we assume that $\zeta \geq 0$.

The values of γ_s and γ_f are very small as compared to γ_2. In addition, at low temperature, the spin–lattice damping parameter γ_1 is also much smaller than γ_2. Thus, we have the following small parameters:

$$\frac{\gamma_1}{\gamma_2} \ll 1, \quad \frac{\gamma_s}{\gamma_2} \ll 1, \quad \frac{\gamma_f}{\gamma_2} \ll 1. \tag{20}$$

If we put $\gamma_1 = \gamma_s = \gamma_f = 0$ in (17) and (18), then the latter can be solved exactly [7] yielding

$$z = \frac{\gamma_0}{g\gamma_2}\tanh\left(\frac{t-t_0}{\tau_0}\right) - \frac{1}{g}, \qquad (21)$$

$$w = \left(\frac{\gamma_0}{g\gamma_2}\right)^2 \operatorname{sech}^2\left(\frac{t-t_0}{\tau_0}\right), \qquad (22)$$

where γ_0 and t_0 are defined by the initial conditions

$$z(0) = z_0, \quad w(0) = w_0 = v_0^2 - 2\varepsilon_* z_0, \qquad (23)$$

which give

$$\gamma_0^2 = \gamma_2^2(1 + gz_0)^2 + (g\gamma_2)^2 w_0, \quad \tau_0 \equiv \frac{1}{\gamma_0}, \qquad (24)$$

$$t_0 = \frac{\tau_0}{2}\ln\left|\frac{\gamma_0 - \gamma_2(1 + gz_0)}{\gamma_0 + \gamma_2(1 + gz_0)}\right|. \qquad (25)$$

Here, we shall consider the influence of the terms γ_1, γ_2, and γ_f dropped in [7].

3. PHASE ANALYSIS

Equations (17) and (18) can be written in the form

$$\frac{dz}{dt} = F_1, \quad \frac{dw}{dt} = F_2, \qquad (26)$$

with the right-hand sides

$$F_1 = g\gamma_2 w - \gamma_s - \gamma_1(z - \zeta) - \gamma_f z,$$
$$F_2 = -2\gamma_2 w - 2(g\gamma_2 w - \gamma_s)z + 2\gamma_f z^2. \qquad (27)$$

The fixed points z^* and w^* are defined by the equations

$$F_1(z^*, w^*) = F_2(z^*, w^*) = 0. \qquad (28)$$

Note that, according to relation (16), if $z \le 0$ then $w > 0$. Therefore, if (28) has several solutions then one has to select those of them that satisfy the condition

$$w^* > 0 \quad (z^* \le 0). \qquad (29)$$

Asymptotic stability of solutions is characterized by the eigenvalues of the Jacobian matrix

$$J_{ij} = \begin{bmatrix} \dfrac{\partial F_1}{\partial z} & \dfrac{\partial F_1}{\partial w} \\[2mm] \dfrac{\partial F_2}{\partial z} & \dfrac{\partial F_2}{\partial w} \end{bmatrix} \qquad (30)$$

evaluated at the fixed points $z = z^*$ and $w = w^*$. It is convenient to separate several particular cases in the stability analysis.

(i) $\gamma_1 = \gamma_s = \gamma_f = 0$. In this case the system of equations (17) and (18) is structurally unstable, since the fixed points are degenerate. Really, the fixed-point

equations in (28) possess an infinite set of solutions

$$z^* \in [0, \infty), \quad w^* = 0.$$

The eigenvalues of the Jacobi matrix (30), called the Lyapunov exponents, are

$$\lambda_1 = 0, \quad \lambda_2 = -2\gamma_2.$$

The existence of a zero eigenvalue means translational invariance along the line $w = 0$ and is the manifestation of the structural instability [13, 14]. The actual limit of z, as $t \longrightarrow \infty$, can be found from (21) yielding

$$\lim_{t \to \infty} z(t) = \sqrt{\left(z_0 + \frac{1}{g}\right)^2 + w_0} - \frac{1}{g}.$$

The corresponding phase portrait is shown in Fig. 1a.

(ii) $\gamma_1 \ne 0$, $\gamma_s = \gamma_f = 0$. The dynamics, as compared to the previous case, undergoes a bifurcation because the flux in the phase space (z, w) changes topologically. Equation (28) gives two fixed points. But only one of them,

$$z^* = \zeta, \quad w^* = 0,$$

is in the physically meaningful region satisfying condition (29). The Lyapunov exponents are

$$\lambda_1 = -\gamma_1, \quad \lambda_2 = -2\gamma_2(1 + g\zeta).$$

Hence, the fixed point is a stable node. The flux is depicted in Fig. 1b All trajectories with initial conditions in the quadrants I, II, and IV tend to the stable node; the relaxation times being $|\lambda_1|^{-1}$ and $|\lambda_2|^{-1}$. The quadrant III is unphysical, since there the condition that $w > 0$ at $z \le 0$ is not satisfied.

(iii) $\gamma_1 = \gamma_s = 0$, $\gamma_f \ne 0$. The fixed point is

$$z^* = 0, \quad w^* = 0.$$

The Lyapunov exponents are

$$\lambda_1 = -\gamma_f, \quad \lambda_2 = -2\gamma_2,$$

showing that the fixed point is a stable node. The corresponding phase portrait is given in Fig. 1c.

(iv) $\gamma_1 \ne 0$, $\gamma_s = 0$, $\gamma_f \ne 0$. This case is similar to (ii), but with a slightly different fixed point

$$z^* = \zeta, \quad w^* = \frac{\gamma_f \zeta^2}{\gamma_2(1 + g\zeta)},$$

being also a stable node. Here, we have taken into account the inequality $\gamma_f \ll \gamma_1$. The phase portrait is presented in Fig. 1d.

(v) $\gamma_1 = 0$, $\gamma_s \ne 0$, $\gamma_f = 0$. Then (28) gives the fixed point

$$z^* = \frac{1 + g}{g}, \quad w^* = \frac{\gamma_s}{g}.$$

However, since $\lambda_1 < 0$ and $\lambda_2 > 0$, all trajectories are unstable and tend to the unphysical region as is shown in Fig. 1e.
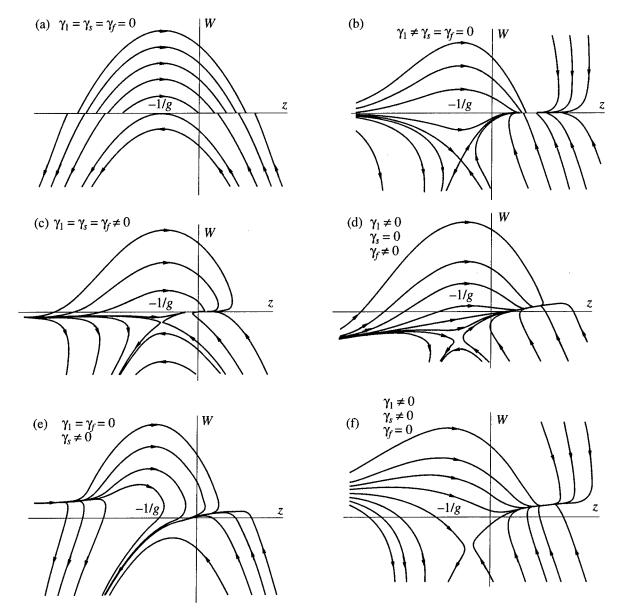
Fig. 1. The phase portrait for the different cases.

(vi) $\gamma_1 \neq 0$, $\gamma_s \neq 0$, $\gamma_f = 0$. The phase portrait, given in Fig. 1f, is topologically equivalent to that of case (iv), provided the condition

$$\frac{\gamma_s}{\gamma_1} < \frac{(1 + g\zeta)^2}{4g}$$

holds true. If this inequality is not valid, we again get an unstable situation as in case (v).

(vii) $\gamma_1 \neq 0$, $\gamma_s \neq 0$, $\gamma_f \neq 0$. This is the general and the most interesting case. For the fixed point we have

$$z^* = \zeta + \frac{\gamma_s}{\gamma_1(1 + g\zeta)},$$

$$w^* = \frac{\zeta(\gamma_s + \gamma_f \zeta)}{\gamma_2(1 + g\zeta)}, \tag{31}$$

where, to simplify the expressions, we accepted that γ_s, $\gamma_f \ll \gamma$. For the Lyapunov exponents we find

$$\lambda_1 = -\gamma_1\left(1 - 2g\frac{\gamma_2}{\gamma_1}\delta\right),$$

$$\lambda_2 = -2\gamma_2(1 + g\zeta + g\delta), \tag{32}$$

where

$$\delta \equiv \left(\frac{1}{1 + g\zeta}\right)\frac{\gamma_s + \gamma_f\zeta(1 + g\zeta)}{2\gamma_2(1 + g\zeta) - \gamma_1}.$$

It is interesting to understand whether it is feasible to achieve, in the stationary regime, a coherent current power comparable to that occurring in the transient process [7]. The current power $P \sim v^2$. Remembering rela-
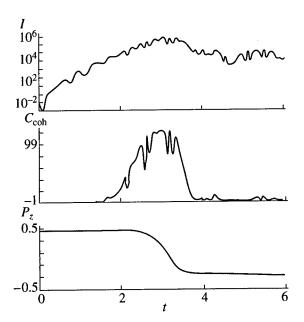
Fig. 2. Radiation intensity, I, in arbitrary units, coherence coefficient C_{coh}, and p_z vs. time for $g \sim 1$ and $f_0 = 0$.

Fig. 3. Coherence coefficient C_{coh}, radiation intensity I, and p_z as functions of time for $g = 0$, $\omega_0 = \omega$, and different f_0. The solid line is for $f_0 = 0.5$, the dashed line is for $f_0 = 2$, and the solid line with crosses is for $f_0 = 5$.

tion (16), between v^2 and w given by (22), we have in the transient process $v(t_0) \approx m_0 \equiv \sqrt{v_0^2 + z_0^2}$. For $\zeta \geq 0$, it follows from (31) that the optimal condition for getting the maximal coherent power is $\gamma_s = 0$ and $g = 0$. Then $v^2(\infty) \approx (\gamma_f/\gamma_2)\zeta^2$. The ratio of the corresponding powers is

$$\frac{P(\infty)}{P(t_0)} = \frac{\gamma_f}{\gamma_2}\left(\frac{\zeta}{m_0}\right)^2. \qquad (33)$$

As far as $\gamma_f \ll \gamma_1$ and $\gamma_1 \ll \gamma_2$, expression (33) shows that $P(\infty) \ll P(t_0)$ even if ζ reaches m_0.

Consider the case when the pumping electromotive force, defined in (12), is so strong that $\gamma_f \gg \gamma_1$. Then the fixed point would be

$$z^* = \frac{\gamma_s + \gamma_1\zeta}{\gamma_f}, \quad w^* = \frac{(\gamma_s + \gamma_1\zeta)(2\gamma_s + \gamma_1\zeta)}{\gamma_2(\gamma_f + g\gamma_s)}. \qquad (34)$$

The maximal coherence is achieved for $\gamma_s = 0$. Thence

$$w^* = \frac{\gamma_1^2}{\gamma_2\gamma_f}\zeta^2.$$

Comparing the current powers of the stationary and transient processes, we obtain

$$\frac{P(\infty)}{P(t_0)} = \frac{\gamma_1^2}{\gamma_2\gamma_f}\left(\frac{\zeta}{m_0}\right)^2. \qquad (35)$$

Recall that $\gamma_1 \ll \gamma_2$, and here, by assumption, $\gamma_1 \ll \gamma_f$. Therefore, again $P(\infty) \ll P(t_0)$. Thus, in any case, the current power in the stationary regime is much less than that of the transient process.

Fig. 4. The same functions as in Fig. 8 for $g = 0$, $\omega_0 = \omega$, and different initial polarizations $p_z(0) = -z_0$.

4. TWO-STAGE RELAXATION

Recall, first, that for the occurrence of the short-time relaxation, as is shown in [7], it is necessary to have nonzero initial magnetization $m_0 = \sqrt{z_0^2 + v_0^2} > 0$. Then transient processes happen during the time $t_0 + \tau_0$, which is less or of the order of $T_2 \equiv \gamma_2^{-1}$. In the presence of the spin–lattice damping γ_1, there exists the long-time relaxation process with the relaxation time $T_1 \equiv \gamma_1^{-1}$.

This late relaxation process occurs at any initial magnetization including zero; it is either incoherent or may be coherent but with the current power much less than the maximal power reached in the transient regime. These two relaxational regimes, fast transient and slow late, are clearly seen in the presented figures.

The damping parameters γ_s and γ_f are due to the existence of the driving electromotive force (12). The latter, as we noticed above, can create stationary coherence, although with the power much weaker than that of the transient regime. The role of the driving force at short times is illustrated in Figs. 2–4, where $I = I(t)$ is the intensity of magnetodipole radiation, which is proportional to the current power $P(t)$, the function $C_{coh} = C_{coh}(t)$ is the coherence coefficient [15], and $p_z = -z(t)$. As is seen, the driving force cannot extend an essential level of coherence longer than for $4T_2$. A more detailed analysis of time dependence of radiation characteristics during the transient regime was accomplished in [16–18].

5. CONCLUSION

The nonlinear dynamics in spin masers has been studied by using the phase-space analysis. For considering fast transient processes occurring at times shorter or of the order of the spin–spin dephasing time T_2, it is admissible to put zero the small damping parameters γ_s, γ_f, and γ_1. However, these parameters are important for describing long-time relaxation. Without those parameters, the system of equations (17) and (18) is structurally unstable. The structural stability is recovered if at least one of the parameters γ_f or γ_1 is nonzero. The damping parameter γ_s alone is not able to make the system of equations stable [see case (v)]. When all damping parameters are nonzero, the dynamical system always possesses an attractor, a stable node. Emphasize again that to have a stable node it is sufficient that γ_1 and γ_2 be nonzero. The presence of the parameters γ_s and γ_f can lead to the formation of stationary coherence, even starting from the state with zero magnetization. But the stationary current power never becomes comparable with that existing in the transient regime. Probably, the most interesting effect which the driving force, providing nonzero values for γ_s and γ_f, can lead to is the extension of the transient interval of coherence up to $4T_2$.

Note in conclusion that coherent radiation effects similar to those occurring in nuclear magnets can exist in ferroelectrics coupled with a resonator [8]. It would be interesting to analyse whether such effects can arise in materials having both magnetic and ferroelectric properties [19], as well as in other complex magnetic systems such as dilute magnetic alloys [20].

REFERENCES

1. Bösiger, P., Brun, E., and Meier, D., 1978, *Phys. Rev. A*, **18**, 671.
2. Kiselev, J.F., Prudkoglyad, A.F., Shumovsky, A.S., and Yukalov, V.I., 1988, *Mod. Phys. Lett. B*, **1**, 409.
3. Kiselev, Y.F., Prudkoglyad, A.F., Shumovsky, A.S., and Yukalov, V.I., 1988, *Sov. Phys. JETP*, **67**, 413.
4. Reichertz, L. *et al.*, 1994, *Nucl. Instrum. Methods Phys. Res. A*, **340**, 278.
5. Yukalov, V.I., 1995, *Phys. Rev. Lett.*, **75**, 3000.
6. Yukalov, V.I., 1955, *Laser Phys.*, **5**, 970.
7. Yukalov, V.I., 1996, *Phys. Rev. B*, **53**, 9232.
8. Yukalov, V.I., 1993, *Laser Phys.*, **3**, 870.
9. Yukalov, V.I., 1992, *Laser Phys.*, **2**, 559.
10. Fokina, N.P., Khutsishvili, K.O., Chkhaidze, S.G., and Lomidze, A.M., 1995, *Fiz. Tverd. Tela*, **37**, 1910.
11. Mizrahi, S.S., Dodonov, V.V., and Otero, D., 1996, *Mod. Phys. Lett. B*, **10**, 1339.
12. Slichter, C.P., 1980, *Principles of Magnetic Resonance* (Berlin: Springer).
13. Andronov, A.A., Vitt, E.A., and Khaikin, S.E., 1966, *Theory of Oscillations* (Oxford: Pergamon).
14. Guckenheimer, J. and Holmes, P.L., 1986, *Nonlinear Oscillations, Dynamical Systems, and Bifurcations of Vector Fields* (Berlin: Springer).
15. Yukalov, V.I., 1990, *J. Mod. Opt.*, **37**, 1361.
16. Belozerova, T.S., Henner, V.K., and Yukalov, V.I., 1992, *Laser Phys.*, **2**, 545.
17. Belozerova, T.S., Henner, V.K., and Yukalov, V.I., 1992, *Comput. Phys. Commun.*, **73**, 151.
18. Belozerova, T.S., Henner, V.K., and Yukalov, V.I., 1992, *Phys. Rev. B*, **46**, 682.
19. Smolensky, G.A. and Chupis, I.E., 1982, *Usp. Fiz. Nauk*, **137**, 415.
20. Fermin, J.R., 1995, *Physica B*, **212**, 423.

Remote Sensing of Planet Earth Challenges For Solid-State Lasers

Norman P. Barnes

NASA Langley Research Center, Hampton, VA 23681 USA
e-mail: n.p.barnes@larc.nasa.gov
Received August 6, 1997

Abstract—Global remote sensing of Planet Earth over protracted time intervals is necessary if the global community wishes to adopt reasoned responses to anthropogenically induced changes in the environment. Laser remote sensors using solid-state lasers can measure many of the Earth variables, such as the ozone levels, needed to describe the health of Planet Earth from orbit. However, the lasers are usually highly specialized devices, often requiring unusual wavelengths, tuning capability, dual pulse capability, as well as high efficiency and reliability. Laser remote sensing techniques are covered along with an example of the development being performed at NASA Langley on a specific laser system for remote sensing.

1. INTRODUCTION

Remote sensing of Planet Earth is necessary to monitor its long-term health. NASA sponsored a workshop at which parameters germane to the health of Planet Earth were identified. These parameters were referred to as essential Earth variables. Many of the essential Earth variables are amenable to laser remote sensing techniques. NASA is developing the requisite laser technology in order to be able to deploy instruments to measure many of the essential Earth variables from space.

Increasing evidence indicates that there are anthropogenic induced changes in the environment. One change is the appearance of the O_3 hole, especially in the Antarctic. While not universally accepted, the O_3 hole is usually associated with chlorofluorocarbons. To prevent further degradation in the stratospheric O_3 layer, the production of chlorofluorocarbons has been curtailed. Another change is the trend toward global warming. Evidence for global warming trends have been
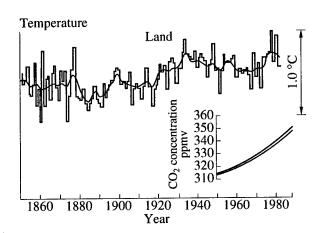
gathered for over 100 years. A sample of this trend appears in Figure 1. Because of the large variability, warming trends can be difficult to interpret.

Global warming can be correlated with increased greenhouse gases, such as CO_2. CO_2 levels have been measured over the last 40 years and indicate a definite rise; however, a causal relationship is not firmly established. Global warming would probably trigger significant shifts in global weather patterns and a rise in the sea level caused by melting icecaps. A rise in the sea level of even a half of a meter would cause widespread coastal flooding. If reduced CO_2 emission is deemed to be the appropriate response, the economic impact could be huge. Consequently, continued monitoring of the temperature and the greenhouse gases is prudent.

Remote sensors deployed in satellites can be a cost-effective method of obtaining global coverage of the essential Earth variables. In order to obtain sufficient data globally, atmospheric variables must be measured at least on a 250 by 250 km horizontal grid and with a 1.0 km vertical resolution. If ground stations were to be employed in each grid, there would be over 8100 of them. On the other hand, a single polar orbiting satellite can interrogate much of the Earth on a daily basis. In addition, a satellite can obtain accurate measurements of atmospheric variables at high altitudes since the optical signal does not have to pass through the lower part of the atmosphere and suffer the concomitant degradation.

2. REMOTE SENSING TECHNIQUES

Laser remote sensing instruments can measure several of the essential Earth variables using a variety of techniques. Aerosol particle density, such as water droplets, can be measured by propagating a laser beam through the atmosphere and collecting the photons backscattered by the aerosol particles. Backscattered

Fig. 1. History of average global temperature and CO_2 concentration.

Wavelength requirements for remote sensing

Atmospheric constituent	Possible wavelengths μm
H_2O	0.73, 0.83, 0.94, 2.05
CO_2	2.05–2.30, 4.0–4.6
CO	2.3–2.4, 4.5–5.0
CH_4	3.1–3.7
O_3	0.28–0.32, 9.3–10.0
Density/temperature	0.76

signal level is proportional to the aerosol density. By using backscattered radiation, the receiver can be colocated with the transmitter, thus providing a self-contained system. Aerosol density can be measured as a function of range using time-of-flight techniques.

Atmospheric constituents can be measured using two tunable laser transmitters and receivers with a differential absorption technique. The first laser is tuned off atmospheric absorption peaks and measures the aerosol density, as described above. A second laser is tuned to an absorption peak of the atmospheric constituent of interest. As it propagates through the atmosphere, it is backscattered and received in the same manner as the first beam but it is also attenuated by being absorbed. By rationing the received backscattered signals, the absorption and thus the concentration of the atmospheric constituent can be measured. As before, the concentration as a function of range can be determined using time-of-flight techniques.

Many of the atmospheric constituents can be measured using the differential absorption technique. H_2O vapor density is currently being measured using a Ti : Al_2O_3 laser tuned to the water vapor absorption peaks near 0.82 μm. However, stronger H_2O vapor absorption exists around 0.94 μm where it may be possible to use a Nd laser operating on the $^4F_{3/2}$ to $^4I_{9/2}$ transition. O_3 can most conveniently be measured in the near ultraviolet, ~0.3 μm, but it may also be possible to use the infrared absorption features around 10.0 μm in some cases. Greenhouse gases, such as CO_2, CH_4, and CO as well as H_2O can conveniently be addressed in the mid-infrared region of the spectrum, 2.0 to 5.0 μm. Laser wavelength requirements for different applications are summarized in the table.

Wind speed can be determined by measuring the Doppler shift of the backscattered radiation. Doppler shifts can be readily measured using heterodyne techniques. In this case, the heterodyne beat frequency is directly proportional to the radial component of the speed. Doppler shifts can also be measured using a filter with a sharp edge in the transmission versus wavelength curve. In the latter case, the transmission through the filter is linearly proportional to the radial component of the wind speed. By making several measurements of the radial component of the wind speed from different directions, the wind velocity can be measured.

Distances can be measured using time-of-flight techniques with a pulsed laser or a modulated continuous-wave laser. In the pulsed case, the resolution is related to the pulse length; the shorter the pulse length, the greater the resolution. Ice cap thickness and tectonic plate motion can be measured using ranging techniques. Once a satellite is in orbit, the orbital parameters can be determined quite accurately. By using laser ranging techniques, the distance of the ground can be determined. In turn, this can be used to measure altitude of the ground return and hence ice cap thickness. Tectonic plate motion, being so small, would probably utilize two retroreflectors, one on each of the tectonic plates. By illuminating both retroreflectors with the same pulse and measuring the temporal difference in their return as a function of time, tectonic plate motion can be measured.

3. LASER REQUIREMENTS

Lasers needed for remote sensing are highly specialized devices. For differential absorption measurements, the wavelength must be tuned to the correct atmospheric absorption feature with a tolerance of about 1.0 pm. Similarly, the linewidth must be on the order of 1.0 pm or less. For wind speed measurements using heterodyne techniques, the linewidth must be on the order of 0.01 pm. For differential absorption measurements, the laser transmitter must be able to produce two pulses in rapid succession, about 300 to 400 μs apart. Each of the pulses of the pulse pair must be accurately tuned to its specific wavelength for the absorption measurement. Pulse length requirements for remote sensing lasers can range from pici- to microseconds. Short pulse lengths are required for ranging accuracy. On the other hand, long pulse lengths are needed to preserve the very narrow spectral bandwidths needed for wind sensing. Laser efficiency needs to be high since power is at a premium on a satellite. Typically, an electrical-to-optical efficiency in excess of 0.05 including frequency conversion processes is needed. Reliability for 10^9 shots or more is needed to achieve a 5-year operational lifetime. Finally, the laser must be compact and lightweight to minimize launch costs.

Development of these virtually unique laser systems is an opportunity for the laser researcher. As an example, the work being performed at NASA Langley in the development of a 0.94-μm laser for the remote sensing of H_2O vapor is described. For efficiency and reliability reasons, it is desirable to have a laser that is directly pumped by laser diode arrays. It is well known that Nd : YAG can operate at 0.946 μm on the $^4F_{3/2}$ to $^4I_{9/2}$ transition and it is directly pumpable with existing laser diodes. However, the peak emission wavelength of Nd : YAG does not correspond to an absorption peak of a H_2O line. In addition, there is intense completion from the much stronger transition at 1.064 μm on the $^4F_{3/2}$ to $^4I_{11/2}$ transition. To make a

Wavelength in micrometers
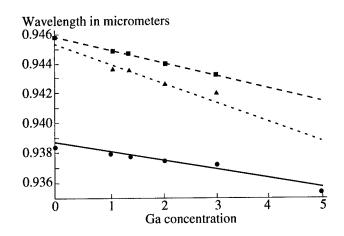
Fig. 2. Compositional tuning of Nd : YGAG. Two sets of data for the R_1 to Z_5 transitions represent the line splitting.

useful laser for remote sensing, these problems must be solved.

4. LASER DEVELOPMENT FOR WATER VAPOR MEASUREMENTS

Obtaining the optimum wavelength for remote sensing of H_2O can be addressed by using compositional tuning. That is, the wavelength can be tuned by selecting the laser material. To demonstrate this technique, various compositions of Nd : YGAG were grown and evaluated spectroscopically. Nd : YGAG represents Nd : $Y_3(Ga_xAl_{1-x})_5O_{12}$ where Ga is substituted for Al in the basic Nd : YAG structure. Wavelengths of the R_1 to Z_5 and R_2 to Z_5 transitions are plotted versus Ga concentration in Fig. 2. From the figure it can be seen that any wavelength between 0.946 and 0.938 µm should be possible on the R_1 to Z_5 transition. A similar evaluation was done for Nd : GYAG where Nd : GYAG represents Nd : $(Gd_xY_{1-x})_3Al_5O_{12}$. In this case, not all compositions are possible since Gd is substantially larger than Y.

For efficient laser performance, the strong competition of the $^4F_{3/2}$ to $^4I_{11/2}$ transition must be suppressed. Since the emission cross section of the 0.946-µm transition is so much lower and the thermal population of the lower laser level is nonnegligible, a modest gain at 0.946 µm may lead to an unsustainable gain at 1.064 µm. At moderate pump energies, amplified spontaneous emission can limit the gain while at high pump energies parasitic lasing at 1.064 µm can occur.

Modeling showed that amplified spontaneous emission effects could be observed by measuring the gain as a function of time. To accomplish this, a continuous-wave 1.064-µm probe beam was used to measure the gain of a flashlamp-pumped Nd : YAG laser rod. Gain was determined by measuring the transmitted 1.064-µm probe power as a function of time. By dividing the transmitted probe power signal by the transmitted probe power signal before the onset of pumping, gain as a function of time was measured.

Gain, after cessation of the pump pulse, decays away faster than exponentially, as shown in Fig. 3. In essence, this is caused by amplified spontaneous emission. A spontaneously emitted photon will induce other excited Nd atoms to emit a photon before it escapes the pumped volume, that is, the spontaneously emitted photon is amplified. As the gain is decreased, the amplified spontaneous emission decreases and the decay becomes exponential.

A model of the amplified spontaneous emission process was derived and found to agree well with the measured decay curves. Gain, as a function of time, was measured for various pump energies. Two of these measured curves, with the associated model curves, are shown in Fig. 3. Agreement between curves is viewed as highly encouraging.

Gain is limited by amplified spontaneous emission effects. Peak gain at 1.064 µm was measured as a function of the electrical energy delivered to the flashlamp. Results of these measurements indicate that peak gain coefficient and length products above about 3.0 are

Gain coefficient length product

Time in seconds
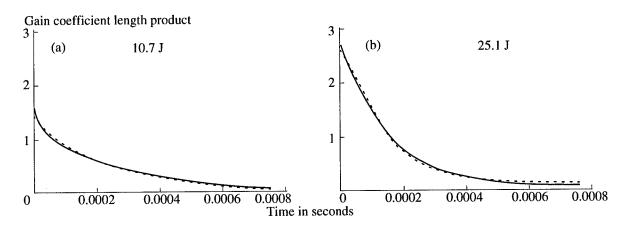
Fig. 3. Gain coefficient length product at 1.064 µm for a 38 mm laser rod versus time for two levels of pumping. Solid line represents the data while dashed line represents the curve fit of the model.

Laser output energy in mJ
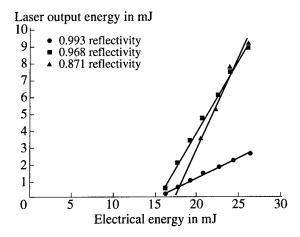
Fig. 4. Performance of Nd : YAG at 0.946 μm. Various output mirror reflectivities.

increasingly difficult to sustain. Increases in the electrical energy produce diminishing increases in the gain coefficient and length product. However, there does not appear to be an asymptotic value for the gain coefficient and length product which would indicate parasitic lasing.

A small population in the lower laser level of the $^4F_{3/2}$ to $^4I_{9/2}$ transition can cause significant amplified spontaneous emission problems. A small-signal gain coefficient, g_0, of this transition can be shown to be

$$g_0 = \sigma_e(\gamma N_2 - (\gamma - 1)C_A N_s),$$

where σ_e is the effective emission cross section, N_2 is the upper laser level population density, C_A is the concentration of active atoms, N_s is the number density of available Nd sites, and

$$\gamma = 1 - Z_1/Z_2.$$

In the latter expression, Z_1 and Z_2 are the thermal occupation factors, or Boltzmann factors, of the lower and upper laser levels, respectively. At low levels of pumping, the gain coefficient at 0.946 μm is negative because of the thermal population of the lower laser level. Consequently, at an absolute minimum, the pumping must be strong enough to achieve optical transparency, that is,

$$N_{2OT} = (\gamma - 1)C_A N_s/\gamma.$$

At this level of pumping, the gain coefficient and length product on the 1.064-μm transition is $\sigma_e(1.064)N_{2OT}l$, where l is the length of the laser material. If this product exceeds approximately 3.0, amplified spontaneous emission could seriously deplete the population density of the upper laser level.

To mitigate these effects, a short, small-diameter laser rod was used. By doing this, a high level of inversion could be achieved without exceeding gain length products where amplified spontaneous emission is a serious problem. For the experiments described above, a 5.0 by 38.0 mm laser rod was flashlamp pumped in a flooded cavity. Undoped YAG was bonded into the ends of the laser rod in order to be able to hold the rod in the cavity. By using undoped ends, the ground-state absorption in the unpumped ends of the laser rod could be avoided.

Laser performance on the 0.946-μm transition achieved in this arrangement was substantially better than other performance reported in the literature. A typical laser output energy versus electrical energy is shown in Fig. 4. With this configuration, at a temperature of 290° K, a threshold of 17 J and a slope efficiency of 0.003 was achieved. In comparison, other researchers [1] achieved a threshold of 62 J and a slope efficiency of 0.0013 at a temperature 248° K. With further improvements in geometry afforded by laser diode pumping, substantially better performance is expected.

5. SUMMARY

In summary, NASA is developing remote sensors to monitor the health of Planet Earth. Essential Earth variables which can be monitored using laser techniques include aerosol particles, H_2O vapor, O_3, greenhouse gases, wind speed, ice cap thickness, and tectonic plate motion. However, the lasers required for these sensors are often highly specialized devices, requiring precise tuning, narrow linewidth, double pulse formats, as well as high efficiency and reliability. Development of such lasers can be an opportunity for the laser research community.

NASA Langley is developing a specialized laser for remote sensing of H_2O at 0.94 μm. For this, two developments were necessary: a compositionally tuned laser material around 0.946 μm and a method of mitigating the effects of amplified spontaneous emission. Apparently, continuous tuning on the R_1 to Z_5 has been achieved with Nd : YGAG from 0.938 to 0.946 μm. Using a Nd : YAG laser, a threshold of 17 J and a slope efficiency of 0.003 has been achieved at 290° K. Thus, both of the initial objectives have been met and work is proceeding on combining these developments and proceeding with laser diode pumping.

REFERENCES

1. Dimov, S., Pelik, E., and Walther, H., 1991, *Appl. Phys. B.*, **53**, 6.

Coherent Control of Photoabsorption: Application to Real Atoms

Takashi Nakajima*, Jian Zhang**, and P. Lambropoulos,** ***

* *The Institute of Physical and Chemical Research (RIKEN), 2-1 Hirosawa, Wako, Saitama, 351-01 Japan*
e-mail: tnakajim@postman.riken.go.jp

** *Max-Planck-Institut fur Quantenoptik, Garching, D 85748 Germany*

*** *F.O.R.TH., Institute of Electronic Structure and Laser and Department of Physics, University of Crete, P.O. Box 1527,
Heraklion 711 10, Crete, Greece*

Received August 7, 1997

Abstract—In this paper we present the subject covered in the talk at the 6th International Workshop on Laser Physics. After a brief review on the control of photoabsorption processes, we show numerical results for real atoms such as Na and Ca, showing the experimentally achievable control of photoionization yield into different ionic channels. A scheme utilizing the laser detunings instead of the laser phase is also briefly discussed.

1. INTRODUCTION

The control of light–matter interactions has been the subject of intense study in the last several years. Various schemes have been devised for that. Those schemes could be classified into two categories. Some of them utilize the coherent property of radiation and hence such a subject is often called "coherent control." The others utilize the alteration of radiation modes by changing the boundary condition, which is termed "cavity QED." Among the schemes in coherent control, the most well-known schemes include pump–probe [1], counter-intuitive pulse delay [2], lasing without inversion and electromagnetically induced transparency [3, 4], and the phase control schemes [5–13]. Briefly, the pump–probe scheme explores the system evolution in the time domain by making use of the short pulse and the variable pulse delay. In the counter-intuitive pulse sequence the system (typically a three-level Λ system) is prepared in a dark state followed by the adiabatic evolution in order to achieve an efficient population transfer to the initially unoccupied third state. Lasing without inversion and electromagnetically induced transparency can be realized by creating the asymmetry between the absorption and emission profiles due to the laser-induced coherence. Phase control utilizes the interference between more than two transition paths, which can be manipulated to be constructive/destructive by the proper choice of the relative phase of two lasers.

In this paper we first overview the various schemes for phase control and then proceed to apply the basic idea to the Na and Ca atoms. The application of the laser detuning considered in recent papers [14–16] is also briefly discussed.

2. PHASE CONTROL: OVERVIEW

The prototype scheme for phase control is presented in Fig. 1a. Two bound states $|1\rangle$ and $|2\rangle$ are coupled by laser fields $E(t)$:

$$E(t) = (\varepsilon_a e^{i\omega_a t} + \varepsilon_b e^{i(\omega_b t + \phi)}) + \text{c.c.} \qquad (1)$$

The two frequency components have relations $\omega_b = 3\omega_a$, and the relative phase between them is given by ϕ. We have assumed that the two fields have the same polarization vector and have written the above equation in a scalar form. Technically speaking, such phase-correlated fields can be obtained from a single laser with frequency ω_a by tripling it through a third-harmonic process. Then the fields with ω_a and ω_b ($=3\omega_a$) are necessarily phase-correlated due to the phase-matching condition during the nonlinear optical processes. Note that the relative phase ϕ can be controlled by sending both beams into another gas cell. By changing the gas pressure, the relative phase between the fields can be varied as a result of the different refractive indices at frequencies ω_a and ω_b. Introducing the dipole matrices D_a and D_b between $|1\rangle$ and $|2\rangle$ coupled by three- and single-photon absorption of ω_a and ω_b, respectively, the total transition amplitude T can be written as

$$T = |D_a + e^{i\phi}D_b|^2 = |D_a|^2 + |D_b|^2 + 2\cos\phi D_a D_b. \qquad (2)$$

It is indeed the last term containing ϕ which is responsible for the phase control of photoabsorption processes. Such a principle is still valid if the upper bound
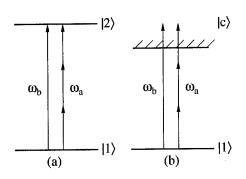
Fig. 1. Prototype scheme for phase control for (a) bound–bound and (b) bound–continuum transitions. The lower and the upper states are coupled by three-photon with frequency ω_a and single-photon of its third harmonic ω_b ($=3\omega_a$).
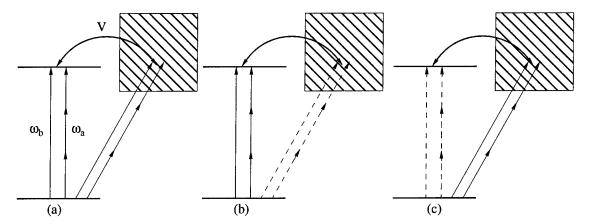
Fig. 2. Extended scheme for phase control for bound–autoionizing transition. The shaded box represents an atomic continuum. The electrostatic coupling (configuration interaction) between the discrete and continuum components of the autoionizing state is denoted by V. Starting from a general case depicted in (a), the cancellations of the direct transition to the continuum and the discrete parts of the autoionizing state are achieved in (b) and (c), respectively, by the proper choice of laser intensities and relative phase.

state $|2\rangle$ is replaced by a continuum $|c\rangle$ (Fig. 1b) as we have demonstrated in [8].

We now place the two schemes (Figs. 1a, 1b) on top of each other, and obtain the scheme depicted in Fig. 2a. Note that the upper state becomes a superposition of a discrete state and a continuum, which is nothing but an *autoionizing state* as described by Fano [17]. Therefore an autoionizing state represents a prototype of channel interactions for phase control [9]. It is not difficult to imagine that such channel interactions may be significantly controlled by the proper choice of the laser intensities and the relative phase. Two extreme cases are illustrated in Figs. 2b and 2c. In Fig. 2b the transition amplitude directly to the continuum part of the autoionizing state is canceled, leading to the symmetric Lorentzian ionization profile [9]. On the other hand, in Fig. 2c the transition amplitude to the discrete part of the autoionizing state is canceled, and the ionization
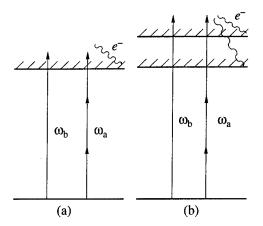
profile has been shown to become flat with a window at zero detuning [9]. It should be noted that such cancellations are always possible by carefully choosing laser intensities as long as the involved continuum is only one [9]. In reality, depending on atoms and transition levels considered, the upper state might not be represented just by "single-discrete and single-continuum," but might exhibit a more-than-one-channel behavior. Such a case is discussed in the next section. We simply note at this point that, even in such a more complicated case, dramatic phase-sensitive effects can be seen as we show later on.

3. PHASE CONTROL: MULTICHANNEL CASE

The schemes described in the previous section can be easily extended to the multichannel case [10]. The level diagram for such a case is given in Figs. 3a and 3b. In Fig. 3a, the final state lies above the ground ionic state but below the first excited ionic state. Atoms excited to such a state are left in the ground ionic state but may eject photoelectrons with different angular momentum εl. What can be controlled by changing the relative phase ϕ is the ratio of the number of photoelectrons belonging to the different continua. Note, however, that such a ratio cannot be experimentally measured by simply taking the angle-integrated ionization signal, since those continua are energetically degenerate. It is essential to measure the photoelectron angular distribution. In Fig. 3b, the final state lies above the first excited ionic state, and atoms excited to such a state have two ionic states to decay. In this case, it is possible to control the photoionization yields into two ionic states. The ratio of ionization into different channels is defined as a branching ratio, which depends on the photon frequency and the number of photons involved. Therefore, in general, the ionization to the same final state energy gives the different branching ratios for the three ω_a photon absorption and a single ω_b $(=3\omega_a)$ photon absorp-

Fig. 3. Level scheme of phase control involving multiple channels. (a) The final state consists of more than one continua εl, but all of them belong to the same ionic state. (b) The final state consists of more than one continua belonging to more than one ionic states.

tion. There are two reasons for that. The first reason is that the final states seen by three-photon and single-photon absorptions involve different continua in terms of angular momentum. Generally speaking, there exist incoherent channels which are accessible only by three-photon absorption because of the dipole-transition selection rule on the total angular J. The second reason is that near-resonant effects might occur for three-photon absorption at an intermediate state. If the near-resonance occurs at intermediate states, a particular ionization path may be enhanced or de-enhanced, depending on the photon frequency ω_a. We note that these two effects also exist for the case in Fig. 3a. After these considerations, it should be clear that, if the atom is subject to two fields with frequencies ω_a and ω_b ($=3\omega_a$) and the two fields are not phase-correlated, the branching ratio depends on the intensity ratio of two fields. On the other hand, if they are phase-correlated, the branching ratio varies even at fixed intensities as a function of the relative phase. In the former case, the ionization yield into each channel simply becomes the incoherent summation of those by the two fields, and in the latter case it becomes the coherent summation of those. In both cases the branching ratio does vary, assuming that the branching ratio by each field is different from each other, which is usually the case. We now show a few representative numerical results. An example corresponding to Fig. 3a is presented in Fig. 4 for the Na atom, in which the final state is embedded in two continua, i.e., ϵp and ϵf. Note that the ϵs continuum is a coherent channel, while the ϵf is an incoherent continuum accessible only by the three-photon absorption from the ground state. Figure 4a shows the variation of the ratio of ionization into the ϵp and ϵf continua as a function of the final state energy at the relative phases $\phi = 0$ (solid line) and $\phi = \pi$ (dashed line). Although the ionization into the ϵf continuum is an incoherent process, the ionization yield into it varies as a function of final state energy due to the near-resonant effects stated above. The resonance structure near 48000 cm^{-1} comes from the variation of the incoherent ionization together with the phase-sensitive variation of the ionization into the ϵp continuum. The small peak near 50000 cm^{-1} is due to the strong ionization through the $3s \longrightarrow 5s \longrightarrow \epsilon p$ path by the three-photon absorption. When the final state energy is near 51000 cm^{-1} (51800 cm^{-1}), the photon frequency ω_a becomes close to the atomic transition frequency to the $3p$ ($4d$) states at the one- (two-) photon absorption (Fig. 4b), and given the chosen laser intensities $I_a = 10^8$ W/cm^2 and $I_b = 10^2$ W/cm^2, the three-photon ionization becomes dominant. Therefore the phase effect is very small at such final state energies and laser intensities. In Fig. 5 we show a representative result corresponding to the scheme given in Fig. 3b for the Ca atom. Again we see the significant phase effect in terms of the variation of the branching ratio of photoionization into two ionic states Ca$^+$ $4s$ and $3d$. The profile of the phase-sensitive branching ratio exhibits a much more complicated structure compared with that for
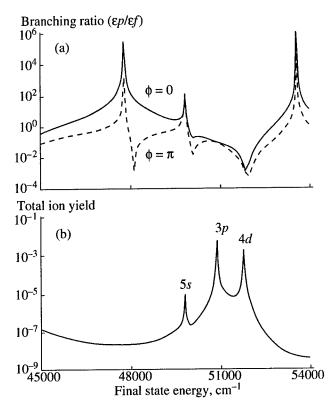
Fig. 4. Numerical example for the Na atom, corresponding to Fig. 3a. Laser intensities $I_a = 10^8$ W/cm^2 and $I_b = 10^2$ W/cm^2, 10-ns square pulse. (a) Variation of the branching ratio into two continua ϵp and ϵf as a function of final state energy at (solid line) $\phi = 0$ and (dashed line) $\phi = \pi$. (b) Variation of the "phase-averaged" (i.e., incoherent) total ionization yield as a function of final state energy. $5s$, $3p$, and $4d$ in the graph indicate that the resonances occur for the three-photon process at the second, first, and second intermediate states, respectively.
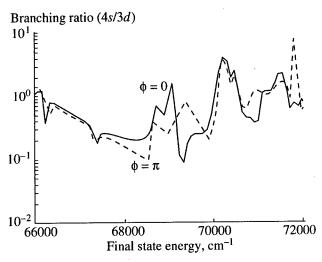
Fig. 5. Numerical example for the Ca atom, corresponding to Fig. 3b. Laser intensities $I_a = 10^8$ W/cm^2 and $I_b = 10^3$ W/cm^2, 10-ns square pulse. Variation of the branching ratio into two ionic states Ca$^+$ $4s$ and $3d$ is plotted as a function of final state energy at (solid line) $\phi = 0$ and (dashed line) $\phi = \pi$.
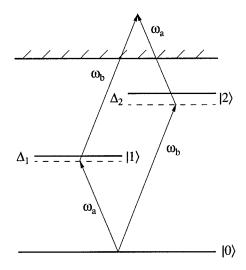
Fig. 6. Prototype level scheme for detuning control.

Fig. 7. Variation of the total ionization yield as a function of detuning Δ_1 for various Δ_2 calculated for the Na atom. $I_a = 10^3$ W/cm^2, $I_b = 10^4$ W/cm^2, and the laser pulse is taken to be 10-ns Gaussian.

4. DETUNING CONTROL

Recently a less restrictive scheme for controlling the photoabsorption processes has been suggested [14] and demonstrated [15, 16]. The level scheme is described in Fig. 6. The atom in the ground state $|0\rangle$ is dipole-coupled to the excited states $|1\rangle$ and $|2\rangle$ by two lasers with frequencies ω_a and ω_b, respectively, which are chosen to be close to the atomic transition frequency between $|0\rangle$ and $|1\rangle$, and $|0\rangle$ and $|2\rangle$. Furthermore, if the laser frequencies satisfy the condition that $\hbar(\omega_a + \omega_b)$ exceeds the ionization energy, the photoionization occurs through two paths, i.e., $|0\rangle \longrightarrow |1\rangle \longrightarrow$ continuum and $|0\rangle \longrightarrow |2\rangle \longrightarrow$ continuum. Hence, an interference effect can be expected in terms of the ionization signal. The sign and the strength of such an interference depend on the detunings and intensities of the two lasers. For illustration, the ionization yield is plotted in Fig. 7 for the Na atom as a function of detuning Δ_1 for various values of Δ_2. $|0\rangle$, $|1\rangle$, and $|2\rangle$ have been chosen to be $3s_{1/2}$, $3p_{1/2}$, and $4p_{1/2}$ of Na, respectively. The incoherent ionization by absorbing two ω_b photons has been included in the calculation. We have assumed that some atoms in the excited states $|1\rangle$ and $|2\rangle$ go back directly to the ground state $|0\rangle$ by spontaneous decay, whose rates are known to be 16 and 110 ns, respectively, for $3p$ and $4p$ of Na. We have ignored, however, the dephasing effect due to the laser bandwidth. Note that there is no incoherent channel in this case due to the choice of the intermediate states $3p_{1/2}$ and $4p_{1/2}$. It is clear that the ionization profile is symmetric Lorentzian (see Fig. 7a) when one of the transition paths is dominant over the other at a large detuning. How much detuning may be considered to be sufficiently large depends on the transition strengths through two paths, or laser intensities. In the example shown in Fig. 7,
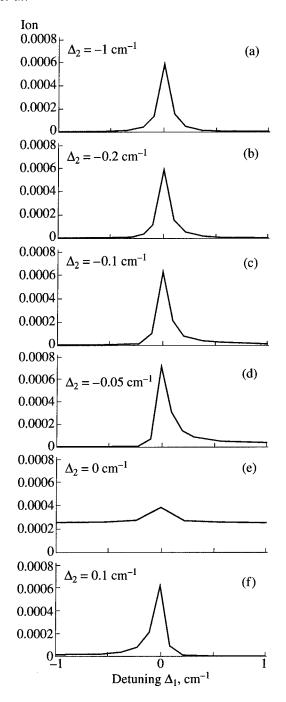
the Na atom (see Fig. 4) due to the more channels involved for the case of Ca atom.

$|\Delta_2| = 1$ cm^{-1} is sufficiently large in this sense. As the detuning Δ_2 becomes smaller (Figs. 7b–7d), the profile begins to reveal an asymmetry, which means that the two ionization paths are competing with each other and the interference is taking place. In Fig. 7e the profile becomes symmetric again since one of the paths is exactly on resonance. When the sign of the detuning Δ_2

is reversed, the asymmetry of the profile is also reversed (Figs. 7c and 7f).

5. SUMMARY

In summary, we have overviewed the schemes for controlling the branching ratio of photoionization products. A few illustrative examples have been presented for the schemes of phase control together with numerical results based on real atoms Na and Ca. We have shown that the control of the relative phase of the laser fields leads to the significant change of ionization profile and the branching ratio. A less restrictive scheme, which utilizes the control of detuning from the near-resonant intermediate states, has been briefly discussed with the illustrative numerical results for the Na atom. We have seen the variation of the ionization profile as the detunings are varied.

ACKNOWLEDGMENTS

REFERENCES

1. Tannor, D.J. and Rice, S.A., 1988, *Adv. Chem. Phys.*, **70**, 441.
2. Schiemann, S., Kuhn, A., Steuerwald, S., and Bergmann, K., 1993, *Phys. Rev. Lett.*, **71**, 3637.
3. Harris, S.E., 1989, *Phys. Rev. Lett.*, **62**, 1033.
4. Boller, K.-J., Imamoglu, A., and Harris, S.E., 1991, *Phys. Rev. Lett.*, **66**, 2593.
5. Brumer, P. and Shapiro, M., 1992, *Ann. Rev. Phys. Chem.*, **43**, 257.
6. Chen, C., Yin, Y., and Elliott, D.S., 1990, *Phys. Rev. Lett.*, **64**, 507.
7. Yin, Y., Chen, C., and Elliott, D.S., 1992, *Phys. Rev. Lett.*, **69**, 2353.
8. Nakajima, T., Lambropoulos, P., Cavalieri, S., and Matera, M., 1992, *Phys. Rev. A*, **46**, 7315.
9. Nakajima, T. and Lambropoulos, P., 1993, *Phys. Rev. Lett.*, **70**, 1081; 1994, *Phys. Rev. A*, **50**, 595.
10. Nakajima, T., Zhang, J., and Lambropoulos, P., 1997, *J. Phys. B*, **30**, 1077.
11. Kleiman, V.D., Zhu, L., Li, X., and Gordon, R.J., 1995, *J. Chem. Phys.*, **102**, 5863.
12. Kleiman, V.D., Zhu, L., Allen, J., and Gordon, R.J., 1995, *J. Chem. Phys.*, **103**, 10800.
13. Wang, X., Bersohn, R., Takahashi, K., *et al.*, 1996, *J. Chem. Phys.*, **105**, 2992.
14. Chen, Z., Brumer, P., and Shapiro, M., 1992, *Chem. Phys. Lett.*, **198**, 498.
15. Pratt, S.T., 1996, *J. Chem. Phys.*, **104**, 5776.
16. Wang, F., Chen, C., and Elliott, D.S., 1996, *Phys. Rev. Lett.*, **77**, 2416.
17. Fano, U., 1961, *Phys. Rev.*, **124**, 1866.

Microparticles as Laser Sources and Bistable Elements

L. A. Kotomtseva, G. P. Lednyeva, and L. G. Astafieva

B. I. Stepanov Institute of Physics, National Academy of Sciences of Belarus, pr. F. Skaryna 70, Minsk, 220072 Belarus
e-mail: kotomts@dragon.bas-net.by
Received August 3, 1997

Abstract—Theoretical models for consideration of spherical and cylindrical microparticle as a laser source and a bistable element are proposed. For two types of transversal electric (TE) and transversal magnetic (TM) modes of a microlaser under the action of radiation with the frequency of pumping, the basic system of equations for the interaction of the substance with light at the frequency of laser is given. Steady states and their instabilities for spherical and cylindrical particles are described. Action of external signal on the steady states and their bistability are considered.

1. INTRODUCTION

Microparticles as compact sources of coherent light and nonlinear elements with high efficiency are very attractive for many practical applications. The advantages of microcavities due to their very high quality factor and easy fitting to the optical fiber and other elements of microsystems are evident. Such systems simultaneously radiate on some space modes and concentrate very high energy in small volume and promise good prospectives for modern microoptics and optical communications.

Theoretical models for the description of two types of transversal electric (TE) and transversal magnetic (TM) modes of a spherical microlaser under the action of the pumping radiation have been proposed by authors in [1–3]. Their steady states and instabilities have been described on the basis of the semiclassical equations for the nonlinear interaction of the field with the substance with their modification to the geometry of particle.

We propose results of consideration of modes for the solid-state particles-glass or plastic doped with dye spheres and cylindrical microparticles under the action of pumping radiation. The spatial distribution of intensity is given with taking into account the morphoplogy-dependent resonances for the components of field expressed through the Debye potentials. Detailed consideration of the solutions for the radiation inside a spherical microparticle, for example, of the electric field, gives for the size parameter $\varepsilon = 2\pi a/\lambda > 1$ at mode number l much higher than unity very intensive radiation in two areas of the diametral zone of the sphere. Such resonances have been intensively studied and are known as morphology-dependent resonances [4–7]. The effects of modes pulling and pushing for their steady states in microlaser are described. Dependence of the quality factor for the definite mode upon its number and order for the spherical or cylindrical harmonics for various sizes, lengths of waves, and other parameters is demonstrated. Results of the stability analysis for the spherical and cylindrical lasers are proposed.

The action of the external radiation leads to the appearance of bistability in the dependence of the laser intensity upon the external signal. We show the results of solving this problem for the definite mode in a spherical particle.

2. BASIC SYSTEM OF EQUATIONS

Theoretical consideration of the laser action in a spherical microparticle on the basis of semiclassical equations can be done with the help of the system of coupled equations for the interaction of light with an active medium. Maxwell equations must take into account the action of the substance of the active medium. Equations for the medium interacting with light must describe relaxation and spectral properties of the substance for transition from the upper excited level of the energy to the lower one at the frequency of lasing. For the dipole interaction of the substance with light, we use a semiclassical system of equations for electric field **E**, polarization **P**, and inversion of populations y for the active medium:

$$\nabla \times \nabla \times \mathbf{E} = \frac{4\pi\sigma}{v^2}\frac{\partial \mathbf{E}}{\partial t} + \frac{1}{v^2}\frac{\partial^2}{\partial t^2}(\mathbf{E} + 4\pi\mathbf{P}), \quad (1)$$

$$\frac{\partial^2 \mathbf{P}}{\partial t^2} + 2\gamma\frac{\partial \mathbf{P}}{\partial t} + (\gamma^2 + \omega_a^2)\mathbf{P} = \frac{2N\omega_a|d|^2}{3h}\mathbf{E}y, \quad (2)$$

$$\frac{\partial y}{\partial t} = \frac{2\mathbf{E}}{h\omega_a N}\left(\frac{\partial \mathbf{P}}{\partial t} + \gamma\mathbf{P}\right) - D(y - y_0). \quad (3)$$

Here, ∇ is the vector differential operator, v is the phase velocity of light in the medium of particle, D and γ are the rates of decay of populations and of polarization of the active medium, ω_a is the frequency of transition in the active medium, N is the concentration of active particles, y_0 is the nonsaturated inversion of populations achievable under the action of pumping, and $|d|$ is the modulus of the matrix element of the dipole moment of transition in the molecule of particle.

With the help of the angular momentum operator $L = (1/i)\mathbf{r} \times \nabla$, we introduce new variables

$$\eta = L \bullet \nabla \times \mathbf{E}, \quad \Phi = L \bullet \nabla \times \mathbf{P}, \qquad (4)$$

and for slowly varying in time (but not in space) electrical field and polarization

$$\mathbf{E} = \mathbf{e}e^{i\omega t} + \mathbf{e}*e^{-i\omega t}, \quad \mathbf{P} = \mathbf{p}e^{i\omega t} + \mathbf{p}*e^{-i\omega t} \qquad (5)$$

with

$$\eta = \Pi(\mathbf{r}, t)e^{i\omega t} + \text{c.c.}, \quad \Phi = \Gamma(\mathbf{r}, t)e^{i\omega t} + \text{c.c.}, \qquad (6)$$

and for the angular distribution of modes in the nonlinear system the same as in the linear problem for our sphere, we write

$$\Pi = \sum_l \sum_{m=-l}^{l} q_l(r, t) Y_{lm}(\vartheta, \varphi), \qquad (7)$$

$$\Gamma = \sum_l \sum_{m=-l}^{l} w_l(r, t) Y_{lm}(\vartheta, \varphi). \qquad (8)$$

Here, Y_{lm} are spherical harmonics.

Macroscopic polarization is created by all excited modes, and inversion of populations is under the action of all modes. To be able to understand a single-mode problem we suppose that different angular modes are separated in space and do not interact one with others. Then we can consider one angular mode with a definite number l and a definite order n. For example, let it be the magnetic wave or the transversal electric wave $E_r = 0$. For this mode we can write

$$e_\vartheta = iq_l(r, t)S_l(\vartheta), \quad e_\varphi = -iq_l(r, t)Q_l(\vartheta), \qquad (9)$$

$$p_\vartheta = iw_l(r, t)S_l(\vartheta), \quad p_\varphi = -iw_l(r, t)Q_l(\vartheta). \qquad (10)$$

Here,

$$Q_l(\vartheta) = P_l^{(l)}(\cos\vartheta)/\sin\vartheta,$$

$$S_l(\vartheta) = -P_l^{(l)'}(\cos\vartheta)\sin\vartheta.$$

Then we can rewrite equations (1)–(3) for sizeless variables:

$$\frac{1}{r^2}\frac{\partial}{\partial r}\left(r^2\frac{\partial q_l}{\partial r}\right) + \left[k_1^2 a^2 + \frac{l(l+1)}{r^2}\right]q_l - 2i\omega\frac{\partial q_l}{\partial t} \qquad (11)$$

$$= i\rho\omega q_l - \omega w_l,$$

$$\frac{\partial w_l}{\partial t} + [\gamma + i(\omega - \omega_a)]w_l + ikq_l = 0, \qquad (12)$$

$$\frac{\partial k}{\partial t} = D(k_0 - k) + iD\gamma Y_l^2(q_l w_l^* - q_l^* w_l)/2. \qquad (13)$$

Here $k_1 = 2\pi m/\lambda$ is the complex wave number for the light inside a particle with complex refractive index m. New variables correspond to previous ones:

$$r \Leftrightarrow r/a, \quad t \Leftrightarrow tv/a, \quad D \Leftrightarrow Da/v, \quad \gamma \Leftrightarrow \gamma a/v,$$

$$q_l \Leftrightarrow \frac{|d|q_l}{h\sqrt{3\gamma D}}, \quad w_l \Leftrightarrow \frac{4\pi\omega|d|aw_l}{vh\sqrt{3\gamma D}},$$

$$k \Leftrightarrow \frac{4\pi\omega N|d|^2 a^2 y}{3v^2 h}, \qquad (14)$$

$$\omega \Leftrightarrow \omega a/v, \quad \rho \Leftrightarrow \frac{4\pi\sigma}{v}a, \quad Y_l^2 = S_l^2(\vartheta) + Q_l^2(\vartheta).$$

It is the basic system of equations for the single-mode laser on the spherical microparticle. The action of pumping is taken into account in the rate of decay of populations of active medium D with the help of the corresponding correlations and in the nonsaturated inversion of populations k_0 [8].

For a cylindrical microparticle, for example, for the optical fiber with radius a much less than its length, we can write for the magnetic wave with $E_r = 0$

$$e_\varphi = -iq_l(r, t)\sin(l\varphi), \quad p_\varphi = -iw_l(r, t)\sin(l\varphi), \qquad (15)$$

and we obtain the next equation for the field in the cylindrical particle:

$$\frac{1}{r}\frac{\partial}{\partial r}\left(r\frac{\partial q_l}{\partial r}\right) + \left(k_1^2 a^2 - \frac{l^2}{r^2}\right)q_1 - 2i\omega\frac{\partial q_l}{\partial t} \qquad (16)$$

$$= i\rho\omega q_l - \omega w_l.$$

The system (12)–(13), (16) is the basic system for a single-mode fiber laser.

3. PUMPING OF A MICROPARTICLE

Pumping of the active medium is taken as laser monochromatic light which normally falls on a particle (sphere or cylinder) in the direction of the Z-axis. Its distribution in the equatorial plane of the sphere for the light polarized at 45° to the plane in which it falls is given in Fig. 1 for the radius of spherical particle $a = 7.56 \mu m$ with complex refraction index $m - i\kappa = 1.33 - i \times 3 \times 10^{-8}$ and $\lambda = 0.532 \mu m$. The relative intensity of radiation is obtained for the field as the sum of all spherical harmonics. It is seen that the main area with the highest intensity is near the principal diameter in a shadow area close to the exit out of the sphere, and the second, less in intensity and square, area is concentrated near the entrance of light into the sphere. Detailed tuning of the size parameter $\varepsilon = 2\pi a/\lambda$ with change of this value in the fourth or the fifth sign permits us to get morphology-dependent resonances for the definite number of resonance l and the order of solution n. The relative intensity of the resonances is two or

Intensity, arb. units
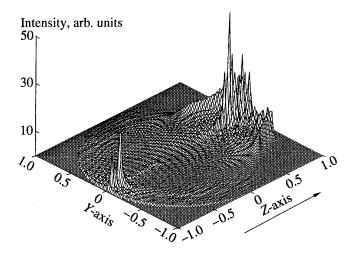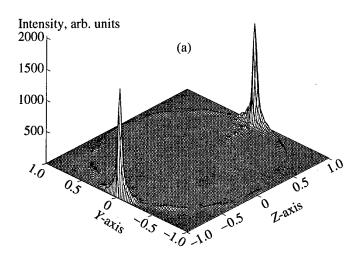
Fig. 1. Distribution of the intensity of light in the equatorial plane of the sphere with radius $a = 7.56$ μm at $\lambda = 532$ μm.

Intensity, arb. units

Intensity, arb. units
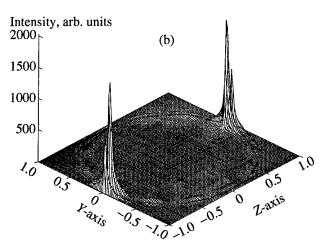
Fig. 2. Intensity of light inside a spherical particle with radius $a = 7.56$ μm, $m = 1.33 - i \times 10^{-8}$ for the mode with $l = 96$, (a) $n = 1$, (b) 2.

more orders higher than in Fig. 1. Areas of such high resonances are very small and their selectivity in space is very high. As pumping light for the laser action of microparticle situation in Fig. 1 can be the most appropriate due to relatively high intensity in wide area. This light excites an upper laser level through the additional energy levels, as it is usually considered for traditional lasers on the basis of three of four level scheme of energy levels [8].

4. STEADY STATES

For zero time derivatives in equations (11)–(13) we can write the steady solutions for a single mode in the sphere:

$$k = k_0/(1 + \gamma^2 c_l^2 \psi_l^2 Y_l^2 / \delta^2),$$
$$\delta^2 = \gamma^2 + (\omega - \omega_a)^2, \tag{17}$$

$$w_l = -(\omega - \omega_a + i\gamma)kq_l/\delta^2.$$

Here, ψ_λ is the Ricatti–Bessel function and c_l is the coefficient for the field inside the particle.

For the field we can write solution of equation (17) with the help of Green functions as a sum of solutions of the homogeneous equation and a partial solution that can be written through the table integrals. In another way this solution can be written due to boundary conditions on the surface of a particle. Radiation out of the particle for $r > a$ is

$$q_l = \bar{b}_l \xi(k_0 r),$$
$$\bar{b}_l = b_l + k_1 c_1 \int_0^a (k - \rho)\psi_l^2(k_1 r')dr', \quad k_0 = \frac{2\pi}{\lambda}, \tag{18}$$

where b_1 is the solution of the linear problem and ξ is the Ricatti–Hunkel function. Inside the particle for $r < a$,

$$q_l = \bar{c}_l \psi(k_1 r), \tag{19}$$

and from the boundary conditions for $r = a$ we obtain

$$\bar{c}_l = \frac{\bar{b}_l \xi_l(k_0 a)}{\psi_l(k_1 a)}. \tag{20}$$

Solution of (17) and (19) gives us steady values for the amplitude of the field q_l and, consequently, for the frequency of the steady state.

The distribution of the laser field inside a particle in the equatorial plane of a spherical particle is given in Fig. 2 for the definite mode with number $l = 96$ and order $n = 1$ (Fig. 2a), 2 (Fig. 2b).

Solution for the cylindrical particle for definite size is given in Fig. 3 for $l = 70$ and $n = 1$.
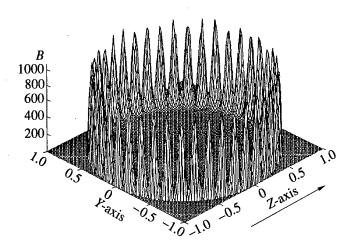
Fig. 3. Distribution of light inside a cylinder with $\varepsilon = 2\pi a/\lambda = 57.369$, $m = 1.31 - i \times 10^{-6}$, $l = 70$, $n = 1$.

5. BISTABILITY OF THE STEADY STATE UNDER THE EXTERNAL SIGNAL

For a particle under the action of the external field Fe^{if}, solution of the basic system gives us a cubic equation for q_l, namely,

$$q_l^3 - \frac{F\sin(\alpha - f)}{\rho}q_l^2 + \frac{\rho(\omega - \omega_a)^2 + k\gamma^2}{\rho\gamma^2 Y_l^2}q_l$$
$$- \frac{F[\gamma^2 + (\omega - \omega_a)^2]\sin(\alpha - f)}{\rho\gamma^2 Y_l^2} = 0. \tag{21}$$

This equation can have three positive roots for a wide area of parameters. Such bistability appears due to the external signal, which changes the steady state. This effect can be important for a particle surrounded with other light sources.

REFERENCES

1. Lednyeva, G.P., 1994, *Opt. Spektrosk.*, **76**, 506.

2. Lednyeva, G.P. and Astafieva, L.G., 1996, *Opt. Spektrosk.*, **80**, 858.

3. Kotomtseva L.A. and Lednyeva G.P., 1997, in *Diffractive Optics and Optical Microsystems* (New York: Plenum), p. 83. *Proc. 20th International School on Quantum Electronics*, (Plenum) (in press).

4. Bennett, H.S. and Rosasco, G.J., 1978, *Appl. Opt.*, **17**, 491.

5. Chylek, P., Kiehl, J.T., and Ko, M.K.W., 1978, *Appl. Opt.*, **17**, 3019.

6. Bennett, R.E., Barber, P.W., Owen, J.F., and Chang, R.K., 1980, *Phys. Rev. Lett.*, **44**, 475.

7. Prishivalko, A.P., Astafieva, L.G., Lednyeva, G.P., *et al.*, 1984, *J. Appl. Spectrosc.*, **41**, 1184.

8. Samson, A.M., Kotomtseva, L.A., and Loiko, N.A., 1990, *Self-Sustained Oscillations in Lasers* (Minsk: Nauka i Tekhnika) (in Russian).

Ultrahigh-Power Lasers and Their Industrial Applications

K. Schröder and D. Schuöcker

Department of Laser Technology, University of Technology Vienna, Arsenal, Objekt 207, Wien A-1030, Austria
e-mail: kschroed@et.tuwien.ac.at
Received August 5, 1997

Abstract—In this paper, concepts for industrial high-power lasers in the range of 100 kW and their applications in engineering are discussed. Considering different laser types and excitation techniques, the rf-excited fast-flow coaxial CO_2 laser is identified as the most promising candidate which can fulfill the requirements for an industrial very high power laser source. Based on an industrial 6 kW laser of this kind, the potential of this concept with respect to very high beam powers is demonstrated, where a modular design is proposed. The suggested 100-kW CO_2 laser consists of four modules, each formed by a radial blower of 15000 m³/h flow rate and two discharge sections powered with 62.5 kW rf each. Afterwards a flow mechanical simulation of the suggested laser module is presented, which yields flow velocity, temperature, mass density, and pressure inside the discharge section at the rated power input. Following, potential applications of 100-kW lasers are discussed, where applications in decontamination and decommissioning, in deep penetration welding of heavy sections, in surface treatment, in assisting of metal forming and in cleaning/paint stripping are identified as the most realistic applications.

1. INTRODUCTION

Since the CO_2 laser was introduced in 1964, the available beam power has increased from a few milliwatts to values above 100 kW [1] continuous-wave. In the field of industrial applications, however, only powers up to approximately 20 kW are being used although industrial lasers of more than twice this power are in principle available.

When considering the distribution of lasers with respect to output power and field of application, it can be concluded that most of the lasers are used for cutting at beam powers of up to about 2.5 kW. The number of applications of beam powers up to approximately 6 kW, e.g., in welding or surface treatment, is significantly lower; however, it is increasing steadily. Applications up to 12 kW can only be found for a very small number of examples such as in heavy-section welding. Finally, industrial lasers with powers above 12 kW are presently mostly used for research and development means, where almost no industrial users can be found.

Due to this situation it must be looked for the reasons for the existing gap between the availability of very high power lasers and the acceptance by industrial users. Surely, the main reason for this discrepancy is the high expenses connected with laser applications, which are composed of investment, operating, and maintenance costs.

As the most important criterion for applying lasers is the economical aspect, it must be tried to reduce the cost of the laser source as far as possible, however, without losing the advantages of the laser radiation for materials processing. Studies of the cost of beam energy have shown that CO_2 lasers are by far the cheapest beam sources, followed by Nd : YAG lasers at twice the cost and COILs (Chemical Oxygen Iodine Lasers)

at four times the cost [2]. Also, from the technical point of view, the CO_2 laser is the best candidate for a 100-kW source, since no principal limitations for scaling CO_2 lasers up to very high beam powers are obvious at present. As a consequence, the most important problem which must be considered is not the implementation of the beam power itself, but the identification of a concept which can be realized at reasonable costs.

Since the specifications demanded from the laser source are closely connected to the envisaged processing techniques, it is necessary to develop the laser source and potential applications in parallel. Since this approach requires investigations on a broad basis, a EUREKA project (EU: 1390) has been launched, where partners both from industry and from research institutions deal with the related questions.

As all preceding estimations have demonstrated that the CO_2 laser scheme represents both from the economical and the technical point of view the best approach for a 100-kW laser source, only this one will be considered in the following sections.

2. BASIC CONCEPTS FOR 100-kW CO_2 LASERS

2.1. General Considerations

When high-power lasers in the range of 100-kW are considered, the first interest concerns the efficiency of the conversion from the power supplied to the laser into laser radiation. If an efficiency for the conversion from line power to laser radiation (plug efficiency) of 10% is assumed, which is a very good value for a CO_2 laser, there is the requirement for 1 MW of power supply. Since only 100 kW are transferred to laser radiation, the remaining 900 kW are transformed to heat and must be removed by a cooling system.

Industrial lasers are usually driven by electric power, which means that the laser amplifying medium is formed by a gas discharge, where about half of the total power consumption, that is 500 kW, is dissipated in this region. A fraction of 100 kW from this power is emitted as laser radiation, where the remaining 400 kW are heating up the laser gas and must be removed. The currently used technique for the removal of this heat is convective cooling by a fast gas flow. But also diffusion cooled systems have recently shown a remarkable ability for heat dissipation [3] so that they should also be considered. And, finally, gas-dynamic lasers have a high potential for achieving high beam powers. However, it is difficult to control them according to the requirements of an industrial environment. Consequently, fast flow (subsonic) and diffusion cooled concepts are the most promising candidates for industrial 100-kW lasers. Among these lasers it has to be distinguished between dc and rf excitation, where for rf excitation also the range of the excitation frequency must be considered.

2.2. Cooling Techniques

Since the removal of the heat losses from the active region is the dominating problem in a high-power laser, the different cooling techniques shall be treated first.

The usual technique for heat removal from the active region used in industrial high-power lasers is convective cooling where the laser gas passes the active medium at a high mass flow and is cooled afterwards in a heat exchanger. The mass flow must be established in a way that the temperature increase of the laser gas remains below the limit where the lasing process gets too inefficient. In order to provide a low gas consumption, the gas flow system is operated in a closed loop where the gas is replaced only at a slow rate in order to compensate for the decomposition and pollution of the laser gas.

In order to produce the high mass flow required for sufficient cooling, either a high flow velocity at a low cross section or a relatively small velocity and a large cross section can be chosen. The first approach is utilized in so-called fast-axial-flow lasers which are usually operating with gas discharges in circular tubes where the gas flows in the direction of the axis of the tubes. In this design, the optical axis of the laser resonator corresponds to the axis of the flow tube, which gives an almost perfect cylindrical symmetry of the laser resonator and thus a high beam quality can be achieved. The other option with large flow cross section and low velocity is used in so-called transverse-flow lasers. In this type, the gas flow is oriented perpendicular to the optical axis of the resonator. This kind of laser shows the potential of realizing large active volumes and, thus, high beam powers, where, however, no symmetry of the active medium can be achieved and, thus, a poor beam quality must be expected.

A compromise between axial-flow and transverse-flow lasers can be achieved by using annular gain media [4] where the gas flow is applied in axial direction. This design shows, on the one hand a cylindrical symmetry, which provides advantages with respect to the beam quality, on the other hand, a large cross section of the active medium is obtained and, thus, high mass flows can easily be applied. For this reason, this type of laser is assumed as the most promising concept for a 100-kW CO_2 laser and will be discussed in more detail in Section 2.5.

The upper limit for the mass flow in fast-flow lasers is reached when the flow velocity required for sufficient cooling approaches the velocity of sound. When the Mach number comes in the vicinity of 1, the flow becomes highly compressible, which gives a high pressure loss and, thus, a demand for blowers capable of handling this compression. In addition, shock waves may form which damage the discharge vessel, components of the optical resonator, or the blower. As a consequence, that high flow velocities must be avoided although in this regime the heat dissipation is very effective (see Section 3).

In this context, also the blower technology has to be considered. While in older fast-flow lasers root blowers have mainly been used, in modern systems radial blowers are preferred, since they show minor vibrations and produce less contamination of the laser gas. These blowers contain typically one to three stages, depending on the pressure ratio they are designed for. Blowers of this kind are available for flow rates up to 6000 m^3/h at a pressure ratio of 1.4. Due to the steeply inclined pressure–volume flow characteristics, they provide a stable operation for the unignited case, as well as for different power levels. Radial blowers, however, cannot be scaled arbitrarily; it is assumed that at approximately 12000–15000 m^3/h a limit will be reached [5]. For higher volume flows, axial blowers, similar to gas turbines, must be used. The operation of such blowers, however, is much more critical than that of radial ones, since they show very flat characteristics and, thus, need turbine blades which can be adjusted to the setting of the laser for a stable operation.

Since convective cooling requires high-performance blowers, which represent expensive parts of a laser systems, it would be of great interest to find ways to replace these components. For this purpose, a technique known as "diffusion cooling," which has been studied with low-power lasers, has recently been suggested also for high-power lasers [3]. This cooling technique utilizes the heat conduction in the laser plasma which is placed between large-area electrodes at a very small distance in the order of 2 mm or even less. By using an efficient water cooling system for the electrodes, a temperature gradient and, thus, a heat flow directed to the electrodes builds up which dissipates the heat losses from the discharge region.

Depending on the cooling technique and the design of the active medium, four feasible concepts for 100-kW CO_2 lasers are remaining: the axial-flow laser with cylindrical discharge tubes, the axial-flow laser with an annular medium, the transverse-flow laser, and finally the diffusion-cooled laser. For each concept, important consequences with respect to the optical resonator and the excitation technique must be considered. Since a high beam quality is one of the essential requirements for modern laser systems which cannot be provided by transverse-flow lasers, they will be excluded in the following.

2.3. Excitation Techniques

Among the electric excitation techniques for high-power CO_2 lasers, dc excitation is the oldest one. This method uses high-voltage power supplies which are connected to the electrodes of the discharge. In order to stabilize the discharge, ballast resistors are required which are responsible for ohmic losses and, thus, for a poor overall efficiency of the system.

Another disadvantage of dc-excited lasers is the low power density of 10–20 W/cm^3 in the plasma, which would yield a bulky design at high output powers. In addition, the stabilization of such discharges requires a highly turbulent flow and, thus, a blower which is able to produce a high pressure ratio. With radial blowers, this can only be obtained by multistage designs, which are more expensive than blowers designed for rf-excited lasers (see below).

As a consequence, dc excitation is mainly used at low to moderate powers, where advantages of the cheap and simple design of the power supply outweigh the poor discharge properties and the bulky size.

A newer technique for energizing the laser plasma is rf excitation. In fast-flow laser systems, this provides high power densities up to 50 W/cm^3 and large plasma volumes, yielding up to 10 W/cm^3 optical output. The coupling of the rf power to the plasma is achieved by electrodes which are situated at the outside of the discharge vessel, where the electric current flows through the dielectric discharge tube as a displacement current. The excitation frequency must be chosen depending on the availability of cheap, reliable, and efficient power generators. In addition, the discharge behavior at different frequencies must be considered. According to these criteria, 27.12 MHz are usually preferred for the excitation of fast-flow lasers.

Diffusion-cooled systems, however, must be operated at excitation frequencies in the vhf range, e.g., around 100 MHz, since a stable operation of gas discharges at an electrode spacing of 2 mm or less cannot be achieved at lower frequencies. In this case, the power input into the plasma scales with the electrode area and can yield an optical output of up to about 2 W/cm^2 at 2-mm electrode separation [3]. Consequently, elec-

trode layouts with large areas must be used, such as coaxial [6] or star-shaped [7] systems.

2.4. Extraction of Laser Radiation

In dependence on the shape of the active region of the laser, the optical resonator must be chosen properly in order to obtain both an efficient extraction of laser radiation and a high beam quality.

These requirements can be fulfilled best with the conventional fast-axial-flow design, where conventional resonators consisting of one spherical mirror, one plane output coupler, and eventually several folding mirrors can be applied. These advantageous properties with respect to the beam extraction are obtained at the cost of a rather complicated and, thus, expensive design, which makes this approach unrealistic for very high beam powers.

Coaxial systems, on the contrary, show a simple design with respect to the gas-flow system and the excitation technique. Since an annular aperture of the active medium is obtained, however, conventional resonator designs cannot be applied any more, and new, sophisticated concepts for the optical resonator must be developed. In the 6-kW range, for example, resonators with toric end mirrors and plane out-coupling windows have proven to give a beam quality which is excellently suited for welding applications [8]. For very high output powers, however, output couplers covering the whole annular aperture are no more feasible, and, thus, new solutions must be found, e.g., with internal axicons [9] or with excentric coupling apertures [10].

Also diffusion-cooled lasers show complicated forms of the aperture of the plasma, and, thus, the layout of the optical resonator is assumed to be the crucial point of this concept.

2.5. Coaxial Fast-Flow Laser

As mentioned above, the coaxial design is one of the most promising laser concepts for achieving 100-kW beam power. As already discussed, this design allows a cylinder symmetrical layout of both the flow and the optical system. In addition, a large cross section for the flow can be achieved enabling high mass flows for cooling means.

The operation of an industrial 6-kW laser using this design has already been proved, and this system is commercially available. A photograph of this system and a schematic drawing are shown in Fig. 1.

The streamline design of the inner electrode and an optimized gas circulation system help to reduce the pressure losses within the electrode system and make it possible to use only one turbo blower with 6000 m^3/h for the 6-kW system. This radial blower has two axial inlets and two radial outlets admitting a design according to Fig. 1. One main heat exchanger at the exhaust of

the discharge section removes the heat produced by the discharge and two auxiliary coolers dissipate the compression heat generated by the pump.

For the excitation of the laser plasma, two rf generators operated at a rated power of 25 kW each are used.

The optical resonator consists of one toric end mirror and a plane zinc-selenide out-coupling window and produces a beam which can be focused to a spot diameter of less than 450 μm with a 10-inch focusing lens [8], giving excellent welds in steel up to a thickness of 6 mm.

Theoretical calculations have shown that the coaxial design can easily be extended to provide an optical output power capacity of 100 kW [11]. In order to come along with available blowers or with blowers which will be available in the near future, respectively, a modular design must be realized, e.g., consisting of four modules similar to those shown in Fig. 1, each contributing 25 kW of beam power. Each section could be operated by a radial blower of 15000 m³/h, which is assumed to be the upper limit for radial blowers. A detailed flow mechanical treatment of a module of this kind is given in Section 3.
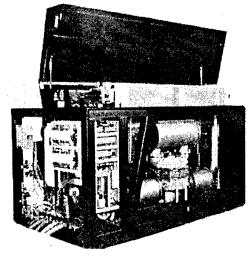
3. FLUID MECHANICAL BEHAVIOR OF A FAST-FLOW HIGH-POWER GAS-TRANSPORT LASER

CO_2 lasers provide an excitational efficiency of less than 20%, meaning that more than 80% of the pumping power has to be dissipated. Since in CO_2 lasers the gas temperature must remain below approximately 450 K in order to avoid a thermal population of the lower laser level and, thus, an interference of the lasing process. In gas-transport lasers, this heat removal is achieved by a closed-loop gas-circulation system, where the laser gas is first heated by the gas discharge in the lasing region and afterwards cooled by a gas–liquid heat exchanger. In order to limit the temperature increase of the laser gas between the inlet into the discharge section of the laser and the outlet, the flow rate of the gas must be chosen properly. For a rough estimation of the required flow rate, it can be assumed that the laser gas mixture with the initial mass density ρ_0, the temperature T_0, and the specific enthalpy h is entering the discharge tube of the diameter D at the velocity v_0 and, thus, the volume flow $G_0 = \pi D^2 v_0/4$.

The overall power balance of the discharge section must consider the power input by the gas flow at the temperature T_0 entering the tube; the heat input by the gas discharge P_{diss}; and finally the heat removal by the hot gas leaving the discharge section at the temperature T_1, the volume flow G_1, and the mass density ρ_1:

$$G_0\rho_0 h(T_0) + P_{diss} = G_1\rho_1 h(T_1). \qquad (1)$$

Considering the continuity of the stationary flow, $G_0\rho_0 = G_1\rho_1$, and assuming a linear dependence of the enthalpy
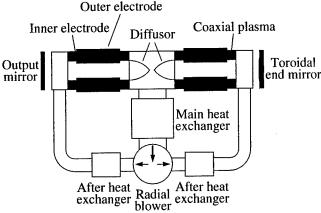
Fig. 1. Coaxial laser consisting of two discharge sections, one radial blower (two axial inputs operated in parallel, two radial outputs), one main heat exchanger, and two auxiliary heat exchangers. The discharges are powered by rf generators at 27.12 MHz. (Upper) Photograph of an industrial 6-kW coaxial CO_2 laser (Developed at the Department of Laser Technology in cooperation with the company Wild Kärnten GmbH). (Lower) Schematic representation of the gas circulation system of the coaxial laser.

$h(T) = c_p T$ on the absolute temperature T, where c_p means the specific heat at constant pressure, the required flow rate G_0 for a temperature rise $T_1 - T_0$ of the laser gas during its passage through the discharge section can be calculated from (1)

$$G_0 = \frac{P_{diss}}{\rho_0 c_p(T_1 - T_0)}. \qquad (2)$$

For a 100-kW CO_2 laser operating at optimum conditions, an excitation efficiency of 20% can be assumed meaning that 500 kW of pumping power must be applied where $P_{diss} = 400$ kW is to be dissipated by the gas flow. In order to calculate the required volume flow for this situation, c_p and ρ_0 must first be estimated for the laser gas mixture, where the well-known formulas for a mixture consisting of components with the atomic

weights M_i, the specific heat capacities c_{pi}, and the mixing ratios k_i (referred to the volume) are used [12]:

$$c_p = \frac{\sum_i c_{pi} M_i k_i}{\sum_i M_i k_i}, \tag{3}$$

$$\rho_0 = \frac{p_0 \sum_i M_i k_i}{RT}. \tag{4}$$

For a typical laser gas mixture of 4.5% carbon dioxide, 13.5% nitrogen, and 82% helium at an ambient temperature of $T_0 = 300$ K and a pressure of $p_0 = 150$ mbar, these mixing formulas yield $c_p = 2500$ J/(kg K) and $\rho_0 = 0.054$ kg/m^3. Thus, for a maximum temperature rise of 150 K, a volume flow of $G_0 = 20$ m^3/s can be calculated from these values. This very rough calculation, however, considers only the increase of the enthalpy of the laser gas, but neglects the rise of the kinetic energy of the heated gas. Under real conditions this kinetic energy has to be subtracted from the enthalpy of the gas leaving the discharge region, which means that the temperature must be lower than that one predicted by this very simple power balance. For this reason, a smaller volume flow than that one calculated will be sufficient.

A more realistic understanding of the properties of the flow in the discharge section can be obtained by a detailed treatment based on fluid mechanical considerations. Since blowers of the required volume flow in the order of 20 m^3/s, however, are far from being available on an industrial level, the system must be split up into smaller modules which can be handled by the technology of today or where the solutions are at least foreseeable for the near future. Considering that blowers at a volume flow of 10000 m^3/h = 2.8 m^3/s will very soon be available [5], it shall be assumed that volume flows of 4 to 5 m^3/s could be realized in the medium term which is also the time frame for realizing an industrial 100-kW laser. Thus, a design consisting of four modules, each operating at an input power of 125 kW and at a volume flow of 5 m^3/s will be the basis for this setup in a first approach. Using the symmetric setup given in Fig. 1, each module consists of two discharge sections which are powered by 62.5 kW rf, meaning that at an efficiency of 20% $P_{diss} = 50$ kW must be dissipated by the gas circulation system. For each section, a volume flow of 2.5 m^3/h is available accordingly. Since these flow rates were obtained by neglecting the energy dissipated by the kinetic energy of the flow, a detailed analysis of the flow will yield lower values.

In order to find a self-consistent description of the fluid mechanical processes inside the discharge region of the laser, a one-dimensional stationary flow of an ideal gas with constant specific heat capacity will be assumed. Therefore, the state quantities ρ, p, T and the velocity v depend only on the axial coordinate, say, x. Under these assumptions the flow is described by the equation of continuity (5), the momentum equation (6), the energy equation (7) and the state equation (8):

$$\rho v = \rho_0 v_0, \tag{5}$$

$$\frac{dp}{dx} = -\frac{f}{D_{hyd}} \frac{\rho v^2}{2}, \tag{6}$$

$$\frac{d}{dx}\left(v\frac{\rho v^2}{2} + v\rho c_p T\right) = \frac{dP_{diss}}{dV}, \tag{7}$$

$$\frac{p}{\rho} = \frac{RT}{\sum_i k_i M_i}. \tag{8}$$

Due to the continuity equation (5), the mass flow ρv is constant and equal to the initial mass flow $\rho_0 v_0$ at the entrance of the discharge region.

The momentum equation (6) describes the pressure loss because of friction with the walls of the tube, where f means the friction factor and D_{hyd}, the hydraulic diameter of the discharge tube. In the case of a turbulent flow in a coaxial channel, the hydraulic diameter corresponds with the difference of outer and inner radius of the annular system, whereas the friction factor is given by Blasius' formula [13], with Re $= vD_{hyd}\rho/\eta$ meaning the Reynolds number:

$$f = \frac{0.316}{Re^{0.25}} \quad \text{for} \quad 5000 < Re < 80000. \tag{9}$$

The dynamic viscosity η of the laser gas mixture has been calculated from the viscosities of the individual components given by Sutherland's formula [14] and by using the mixing formula derived from kinetic gas theory [15].

The energy equation (7) balances the kinetic energy of the gas flow, the enthalpy, and the loss energy fed into the gas discharge per unit volume and unit time. The power density $(dP/dV)_{diss}$ is limited by instabilities of the gas discharge and may reach up to 40 W/cm^3, when a total input power density of 50 W/cm^3 at an excitation efficiency of 20% is assumed [16].

Finally, the state equation (8) describes the relation between the pressure p, the temperature T, and the mass density ρ of the laser gas mixture, which is assumed to be ideal. The mixing ratios of helium, carbon dioxide, and nitrogen are considered according to the well-known theory [12].

The set of equations (5)–(8) has been evaluated for a typical coaxial discharge section as given in Fig. 2. Eight of these sections would be capable of producing an output of about 100 kW cw. Each of these sections is 30 cm long and has an outer diameter of 12 cm.

In order to get a homogeneous field distribution and a high flow velocity, the spacing between inner and outer tube is chosen relatively small and amounts to 16 mm. In order to get a good efficiency of the conversion of electric power to optical output, the power density in an rf-excited gas discharge should approach the upper limit of 50 W/cm^3 as close as possible. Since stability problems must be expected in the vicinity of this limit, 40 W/cm^3 is assumed, which is considered to be a save value. At an excitation efficiency of 20%, this means a power density of the heat losses of 32 W/cm^3, giving 50.2 kW for the whole volume, which has to be dissipated by the gas flow. For the typical laser gas mixture of 4.5% carbon dioxide, 13.5% nitrogen, and 82% helium at an ambient temperature of $T_0 = 300$ K and a pressure of $p_0 = 150$ mbar, this gives a flow velocity of about 400 m/s, corresponding to a Mach number of $M = 0.61$ at the inlet of the discharge section. With these initial conditions, the flow behavior given by Fig. 3 is obtained.

As is demonstrated by this figure, the flow is accelerated up to about 700 m/s according to $M = 0.90$ on its way through the discharge section. The pressure drops from 150 to 119 mbar connected with a reduction of the mass density from 0.054 to 0.031 kg/m^3. The most interesting result is the temperature rise from 300 to 412 K, which is much less than would be expected according to (2), neglecting the kinetic energy carried with the flow. Balancing the gas flow which enters the discharge section and the flow leaving this volume (see the table), it can be seen that, in fact, a great amount of heating energy is transferred to kinetic energy of the flow.

As can be concluded from this table, in the present example, 31.8 kW is converted to heat, meaning an increase of the gas temperature, and 18.3 kW, to kinetic energy, which is more than one third of the total dissipated power.

Since the increase of the gas temperature must be limited to about 150 K in order to avoid a reduction of the efficiency of the lasing process, the predicted transfer of heating energy to kinetic energy improves the performance of the system considerably. Equation (7) shows that the kinetic energy per unit time transported by the flow increases with the third power of the flow velocity, which means that the latter must be increased as far as possible in order to get a low temperature rise of the laser gas for a given heating input and mass flow. A natural limit for this velocity is the velocity of sound, which must not be approached too closely, as mentioned already.

4. APPLICATIONS OF 100-kW CO_2 LASERS

4.1. Influence of the Properties of the Laser Beam on the Application Process

Since laser technology is usually involved with high costs compared to conventional techniques, the advan-
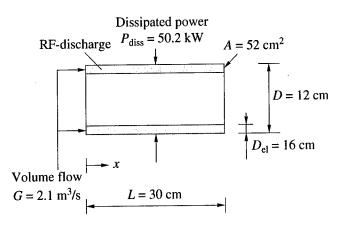
Fig. 2. Dimensions of one of the eight discharge sections of the 100-kW laser (two sections per blower).
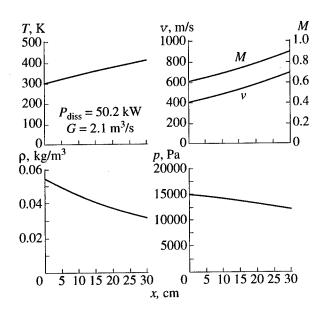
Fig. 3. Simulation results for temperature T, flow velocity v (Mach number M), mass density ρ, and pressure p in the discharge section according to Fig. 2.

tages of laser radiation must always be utilized in some way in order to justify the high expenses. This means, for example, that using the laser as a simple heat source usually is not economical. Thus, it is necessary to be aware of the outstanding properties of laser beams which can be applied in material processing:

Energy balance of the gas flow

Input	Kinetic energy per unit time	9.2 kW	59.4 kW
	Dissipated heat per unit time	50.2 kW	
	Enthalpy per unit time (reference)	0.0 kW	
Output	Kinetic energy per unit time	27.5 kW	59.4 kW
	Enthalpy per unit time (reference)	31.9 kW	

- High radiance
- Small spectral bandwidth
- Pulsability

The high radiance of laser beams is the most obvious property which gives the possibility to achieve high power densities by focusing the beam. At a given raw beam diameter D and a focal length f of the focusing optics, the smallest focal spot radius and, thus, the highest power density can be achieved for a Gaussian beam [17]. The ratio between this optimum value for the focal spot radius and the larger one which is obtained for a "real" laser beam is called the K number. Alternatively, the M^2 value is in use too. With the F number of the focusing optics, defined as the ratio f/D between the focal length f and the raw beam diameter D at the focusing lens, the focal spot radius w_0 is given by (10), where λ means the wavelength of the laser radiation. For a laser beam of the power P, this gives the power density p according to (11) in the focal spot [17]. Above and beyond the focal spot, the power density is reduced, which is described by the Rayleigh length z_r. This number gives the distance at which the power density has reduced to half of the maximum value in the focal spot and defines the focal depth. It can be calculated by using (12)

$$w_0 = \frac{2\lambda F}{\pi K},$$ (10)

$$p = \frac{\pi K^2 P}{2\lambda^2 F^2},$$ (11)

$$z_r = \frac{4\lambda F^2}{\pi K^2}.$$ (12)

When thinking about applications of high-power CO_2 lasers in the range of 100-kW beam power with the focused beam, usually thick workpieces are to be processed, which requires a high focal depth and, thus, high F numbers, e.g., $F = 10$. Taking this value as constant, formulas (10)–(12) show that the focal spot radius depends on the fraction $(1/K)$, the power density on $(K^2 P)$, and the Rayleigh length on $(1/K^2)$. In order to obtain a high power density, it is thus not sufficient to increase the output power, but a good beam quality must be provided too. The focal depth, on the other hand, increases with decreasing beam quality, which may be helpful for penetrating thick materials.

The small spectral bandwidth may be of interest when materials shall be treated selectively. For cleaning or paint stripping applications, for example, the layers which have to be removed show a high absorption for the radiation of the CO_2 laser, whereas the base material, e.g., a metal, reflects the beam very effectively and, thus, is not damaged by the laser beam.

The pulsability of lasers allows one to produce temperature profiles which differ considerably from those produced by continuous-wave sources such as electric torches, gas flames, or high-power arc lamps. This, in general, allows one to produce temperature gradients or rates of heating and cooling which are very steep. This facilitates exactly localized transformation processes in the material or small heat-affected zones, respectively.

4.2. Laser Cutting

Fusion and oxygen cutting of metals with the CO_2 laser are the best introduced processes of high-power lasers. These applications require a power density of about 10^7 W/cm². For obtaining a small kerf width, lasers operating in the fundamental mode ($K \approx 1$) are required, that is why lasers with an output power of 2.5 kW at maximum are preferred.

When higher laser powers are to be applied, this means either an increased focal spot diameter or a higher power density. Because of technical restrictions which cause a degradation of the beam mode at high output powers, the power density usually even degrades compared to lasers of lower powers meaning a considerable increase of the focal spot diameter. As a consequence, the thickness of the materials which can be cut increases but the quality of the cut is reduced, meaning nonparallel edges, formation of striations, and dross. At smaller thicknesses of the workpieces, an increase of the feed rate can be predicted, where the quality of the cut, however, remains poor.

Since the quality of laser cuts is one of the economical main advantages of this technology, cutting applications of 100-kW lasers in manufacturing engineering seem to be of minor interest.

For very high beam powers, however, additional applications can be considered where the quality of the cuts is of no relevance. One example for this category are decontamination and decommissioning (D & D) applications which are assumed to be of great interest in the near future [18]. In the field of dismantling of nuclear plants, it is most important to cut heavy sections of arbitrary composition. Besides, it is very important that the laser process can be remote controlled, which makes it possible that personnel need not enter the contaminated area. Another advantage of laser cutting in this field is the fact that there is no mechanical contact between the workpiece and the tool. That is why no tools are contaminated and, thus, less waste is produced.

4.3. Laser Welding

The welding process most commonly used with lasers is deep penetration welding where the pressure of the metal vapor forms a hole in the melt, the so-called keyhole, which enables the beam to reach deep regions of the workpiece, thus enabling to join thick materials. In order to form the keyhole, power densities of 10^6 to 10^7 W/cm² are required. When approaching this power density, however, the formation of a plasma must be considered which reduces the coupling of the

laser radiation to the workpiece and interferes with the deep penetration welding effect. Consequently, it is one of the main tasks when developing welding processes for very high beam powers to get a proper control of the plasma formation. This can be achieved by adding shielding and assisting gases to the interaction zone of laser beam and workpiece. Under the condition that no plasma shielding occurs, much power can be coupled into the workpiece where the keyhole gives the possibility to reach deep regions of the workpiece too.

The increase of the focal spot diameter, which is a consequence of the reduced beam quality of high-power lasers, meaning a great drawback in the field of laser cutting, has sometimes even an advantageous effect on the welding process. Since the laser beam and the edges of the workpieces have to be aligned in a way that the beam is incident on both edges at any time, this requires a high precision of both the preparation of the workpieces and the handling system. With an increased focal spot, the latter requirements are obviously easier to fulfill, which means a more simple preparation of the welding seam and an easier alignment of the workpiece with respect to the laser beam.

For welding heavy sections, a high focal depth, meaning a large F number, is required. Due to (11), this means a high value of (K^2P) in order to get the required power density, and, thus, a high value of K has to be demanded. In the case of a 100-kW CO_2 laser ($\lambda = 10.6$ μm) and a power density of 10^7 W/cm^2, for example, a K number of about 0.1 is necessary, which is assumed to be a very good beam quality of a laser of this kind.

Since laser welding of heavy sections is assumed to be one of the most realistic applications of a 100-kW laser, a high beam quality must be one of the main design requirements.

4.4. Laser Surface Treatment

In surface treatment applications, the defocused beam is used which means that the applied power densities are far below those required for cutting and welding; typically they amount to 10^4 W/cm^2. In order to get the desired metallurgical effects, the temperature gradient as well as the heating and cooling rates must be adjusted by selecting the focal spot dimensions, the applied power, and the feed rates properly. In this field, the laser shows some advantages over competing techniques since the processed contours are defined very precisely. Besides, the total heat input can be very small giving no adverse effects like distortions or extended heat-affected zones.

With high beam powers available, the processing speed and the focal area can be increased accordingly, giving the possibility of high-speed processing of large areas.

As an example, re-annealing of railroad track with a laser mounted on a train carriage has already been discussed and is assumed to be a way to rework old tracks.

In the field of surface treatment, the beam quality of the laser only is of minor interest and, thus, the requirements for the laser source are less restrictive. Here, the laser acts more as a source for high irradiance instead of high radiance. The competition, therefore, by conventional techniques is quite large in this field so that only in some specialized applications will the laser be the better choice. As a consequence, a 100-kW laser source should primarily be designed for applications with high beam quality, since in this regime there are obvious advantages over conventional techniques.

4.5. New Applications

Apart from scaling the well-known applications of laser radiation up to very high beam powers, it can be thought about some new applications which can only be realized with such beam powers and, thus, are not yet developed satisfactorily. Since it is not feasible to increase the power density of a 100-kW laser above values which can be reached with lasers at moderate output powers, the main useful effect of high beam powers is the increased irradiated area and the high total power input. This may speed up some applications to a level where they get economical on an industrial level.

One example in this field is cleaning and paint stripping with the laser. These applications are already used in the restoration of fine arts, where the radiation of pulsed Nd : YAG lasers is applied via a hand-held processing head. Paint stripping, e.g., from the fuselage of aircrafts during regular maintenance, has recently been introduced by using CO_2 TEA lasers. Especially for applications of this kind high average power TEA lasers have been developed [19] which are capable of stripping 8 m^2/h, where it is known that about 90 J/cm^2 are required to remove the 100-μm-thick layers.

For cleaning and paint stripping applications, it is necessary to work with pulsed lasers in order to prevent the base material from being thermally loaded. As a consequence, the peak power of the laser pulses must be very high when reasonable ablation rates shall be obtained.

When using a very high power cw laser, the power density does reach the desired level, but measures must be taken to reduce the interaction time with the surface of the workpiece in order to avoid overheating. This can be reached by using scanner optics which sweeps the beam over a large surface area. Considering that the interaction time and the power density are set properly, the removal rate of 90 J/cm^2 would yield a paint stripping capacity of 400 m^2/h, when 100 kW beam power is assumed.

Further applications can be found in metal forming technology, where the laser beam heats up the workpiece

locally causing a transition between the range of cold working and hot working. It is well known that heating a metal above its recrystallization temperature reduces the yield stress and increases the elongation at fracture, which allows higher logarithmic deformations and reduced mechanical forces for forming hot materials. Compared to conventional hot working, where the whole workpiece must be heated, the process of laser-assisted forming provides the advantage of selective heating of the workpiece. This can be done directly in the forming press, saving a lot of time. Besides, adverse effects to the material properties caused by the (slow) heating process can be avoided. One example for an application in this field is laser-assisted deep drawing (LADD) [20].

Finally, **laser-assisted D & D** (decontamination and decommissioning) is assumed to be a field for the application of 100-kW lasers. Apart from cutting in D & D, which has already been mentioned, processes like ablation or glazing must be considered too. Ablation can be used to separate the waste depending on the degree of contamination and, thus, to provide an adequate removal or processing, respectively. Glazing with the laser may be a useful way to contain the waste and prepare it for removal. In all cases, it is advantageous that the processes do not involve any mechanical contact between tool and workpiece and that they can be remote controlled.

5. CONCLUSIONS

The coaxial fast-flow laser has proven as a good concept for a 100-kW CO_2 laser. The large cross section of the discharge section allows high mass flows at low pressure losses, which allows the efficient use of radial blowers. Also the rf excitation for pumping the active medium can be achieved at a good stability and a high power density, which is due to the cylindrical symmetry.

Industrial applications of 100-kW CO_2 lasers can be found in deep penetration welding, surface treatment, and laser-assisted forming cleaning/paint stripping, where, however, the cost of the laser process must be minimized in order to be able to compete with conventional techniques.

REFERENCES

1. Lander, M.L., Maxwell, K.J., Reilly, J.P., and Hull, R.J., 1996, *Proc. SPIE*, **3092**, 186.

2. Von Bülow, H. and Schall, W.O., 1994, *Proc. SPIE*, **2502**, 258.

3. Hall, D.R. and Baker, H.J., 1994, *Proc. SPIE*, **2502**, 12.

4. Schröder, K. and Schuöcker, D., 1991, *Infrared Phys.*, **32**, 417.

5. Diedrichsen, Fa. Becker GmbH, private communication.

6. Habich, U., 1992, Diffusionsgekühlte CO_2-Laser, *Dissertation* (Aachen: RWTH).

7. Yelden, E.F., Seguin, H.J.J., Capjack, C.E., and Nikumb, S.K., 1991, *Opt. Commun.*, **82**, 503.

8. Bohrer, M., Basalka, H., and Schuöcker, D., 1997, *Proc. LASER'97* (Berlin: Springer).

9. Chodzko, R.A. *et al.*, 1980, *Appl. Opt.*, **19**, 778.

10. Ehrlichmann, D., Habich, U., Plum, H.-D., and Loosen, P., 1997, *Technical Digest of the CLEO'97*.

11. Schuöcker, D. and Schröder, K., 1994, *Proc. LANE'94* (Bamberg: Meisenbach).

12. Kuchling, H., 1969, *Buch- und Zeit-Verlagsgesellschaft*.

13. Streeter, V.L. and Xylie, E.B., 1985, *Fluid Mechanics* (New York: McGraw-Hill).

14. Schlichting, H., 1965, *Grenzschichttheorie* (Karlsruhe: G. Braun).

15. Bird, Stewart, and Lightfoot, 1960, *Transport Phenomena* (New York: Wiley).

16. Hall, D.R. and Baker, H.J., 1988, *Proc. SPIE*, **1031**, 60.

17. Migliore, L., 1996, *Laser Materials Processing* (New York: Marcel Dekker).

18. Vetrovec, J., Hindy, N.H., Subbaraman, G., and Spiegel, L., 1996, *Proc. SPIE*, **3092**, 780.

19. Schweizer, G. and Werner, L., 1994, *Proc SPIE*, **2502**, 57.

20. Schuöcker, D. and Schröder, K., 1997, *Proc. LANE'97* (in press).

Nonstationary Effects in Laser Ablation of Indium: Calculations Based on Spatial Moments Technique

N. Arnold*, B. Luk'yanchuk**, N. Bityurin***, and D. Bäuerle*

* Angewandte Physik, Johannes Kepler Universität Linz, Linz, A-4040 Austria
e-mail: nikida.arnold@jk.uni-linz.ac.at
e-mail: dieter.baeuerle@jk.uni-linz.ac.at
** General Physics Institute, Russian Academy of Sciences, Moscow, 117942 Russia
e-mail: lukyanch@kapella.gpi.ru
*** Institute of Applied Physics, Russian Academy of Sciences, Nizhnii Novgorod, 603600 Russia
e-mail: bit@appl.sci-nnov.ru
Received August 7, 1997

Abstract—The nonstationary averaging technique (spatial moments technique) is used for the solution of nonlinear heat equation describing laser ablation. The temperature dependencies of material parameters and the temporal profile of laser beam are taken into account. Nonstationary heat equation is reduced to three ordinary differential equations for the surface temperature, spatial width of the enthalpy distribution, and the ablated depth. Calculations have been done for laser ablation of indium, where we study the influence of the duration and temporal profile of the laser pulse on the threshold fluence, Φ_{th}, the influence of temperature dependencies in material parameters on the overall ablation kinetics (ablated depth versus laser fluence), the duration of the surface melt presence, etc.

1. INTRODUCTION

Laser ablation is used in many technological applications like micropatterning (for microelectronics, micromechanics, etc.), pulsed laser deposition including multilayer structures with atomic thickness, like X-ray mirrors, formation of nanoclusters, etc. [1–4].

To optimize these applications it is important to understand the fundamental aspects of laser–matter interaction. The coupling mechanisms of the laser light to the ablated sample can be very complex. They are related to the change of thermophysical and optical characteristics during laser heating, phase transitions, hydrodynamic effects, absorption of radiation within the plume, optical breakdown of vapor, plasma formation etc. Many of these effects are accompanied by numerous instabilities [5]. It is clear that there are no simple analytical formulas which can be easily applied to a given experimental situation.

The situation becomes even more complex for ultrashort (subpicosecond) laser pulses where nonlinear absorption, critical phenomena, different temperatures of electron gas and lattice come into play [5]. Meanwhile, shorter laser pulses are used to produce better ablation characteristics.

To analyze numerous effects in laser ablation, both, the experimental investigations and the theoretical simulations are needed. For the effective feedback between theory and the experiment one should develop semianalytical methods of "intermediate power," which should be flexible, applicable for quantitative analysis of experimental data and can be done within seconds on a PC. Now there is a big gap between the primitive theoretical analysis related to the solution of the linear heat equation and direct numerical solution of nonlinear heat equation (or hydrodynamics equations) by finite-differences or finite-elements technique with the help of powerful computers. In the first case the analysis is oversimplified and cannot be used sometimes even for qualitative consideration. In the second case the analysis refers to some particular problems and is not flexible, one cannot apply this technique for a fast analysis of experimental data.

The first question which should be clarified during the analysis is related to the ejection mechanism: is it purely thermal surface vaporization, or do other mechanisms (hydrodynamics, nonequilibrium excitation of electrons, phonons, etc.) contribute to the ejection? The lack of real quantitative analysis of experimental data in the broad range of parameters (especially in the field of polymer ablation) leads to many speculations and discussions. It is especially important for short laser pulses where new effects are expected during the transition from nanosecond to femtosecond ablation regime. The border for these effects lies probably in the subpicosecond range and depends on the material.

In the present paper we applied the nonstationary averaging (moments technique) to solve the nonlinear heat equation, where one takes into account

– arbitrary *temperature dependencies* of material parameters, such as the specific heat, thermal conductivity, absorptivity, absorption coefficient, etc.;

– arbitrary *temporal profiles* of the laser pulse;

– strong (Arrhenius-type) dependence of the ablation velocity on the temperature of the ablation front, which leads to a *nonsteady movement* of the ablation boundary during the (single) pulse;

– *screening* of the incoming radiation by the ablated product;

– influence of the ablation (vaporization) enthalpy on the heating process;

– influence of melting and/or other phase transformations.

Not included are hydrodynamic effects, nonlinear optical effects, optical breakdown, nonequilibrium distribution in the lattice and electron gas, and thermally induced stresses.

Calculations have been done for laser ablation of indium. Here, thermal properties change strongly below and at the melting point. At the same time (apart from absorption coefficient, which behavior is difficult to estimate) they are almost constant at elevated temperatures. Calculations have been done for the radiation with 248 nm (KrF excimer laser) where the experimental data on subpicosecond laser ablation were published recently [6]. We study the influence of the duration and temporal profile of the laser pulse on the threshold fluence, Φ_{th}, the influence of temperature dependencies in material parameters on the overall ablation kinetics (ablated depth versus laser fluence), the duration of the surface melt presence, etc. At higher fluences one can expect the change in ablation kinetics related to hydrodynamic effects (for nanosecond ablation) and to the critical phenomena (for picosecond ablation regime).

2. THE MODEL

For the analysis of laser ablation process the following approximation is often used. It is assumed that after a certain delay time the ablation proceeds (quasi) stationary i.e., with constant ablation velocity v. The delay time is found from the nonstationary heat equation with $v = 0$ [1, 5, 7, 8]. In reality, one should solve the *nonstationary* heat conduction problem with $v = v(t)$ for all times. An accurate description of nonstationary effects in ablation and nonlinearities related to temperature dependencies of parameters represents the main problem for the theoretical analysis.

We start with one-dimensional problem which is relevant for sufficiently short laser pulses and nonfocused beams [1]. We write it in the moving reference frame fixed with the ablation front, and in terms of enthalpy per unit mass H:

$$\rho\frac{\partial H}{\partial t} = \rho v\frac{\partial H}{\partial z} + \frac{\partial}{\partial z}\left(\kappa\frac{\partial T}{\partial z}\right) - \frac{\partial I}{\partial z} \equiv B[T], \quad (1)$$

where we introduced the notation $B[T]$ for the right-hand side. The density of solid ρ is considered as constant, while the heat capacity c, heat conductivity κ, and the source term $(-\partial I/\partial z)$ may significantly depend on

temperature T. The intensity I, within the solid shall obey Bouguer–Beer equation:

$$\frac{\partial I}{\partial z} = -\alpha I, \quad I|_{z=0} = I_s, \quad (2)$$

where α is the absorption coefficient and I_s is the intensity absorbed at the surface. In some cases [1, 7], I_s can be related to laser pulse intensity $I_0 = I_0(t)$ by

$$I_s = I_0 A(T_s)\exp[-\alpha_g h], \quad (3)$$

where A is the (temperature-dependent) absorptivity, and α_g is the vapor absorption coefficient, recalculated to the density of solid. The exponential term describes the shielding of radiation by the ablated material with thickness $h(t) = \int_0^t v(t_1)dt_1$. The surface evaporation (ablation) rate v is given by [7, 8]

$$v = v_0\exp\left[-\frac{T_a}{T_s}\right], \quad (4)$$

where T_a is the activation temperature (in Kelvin), v_0 is preexponential factor (by the order of sound velocity), which can be considered as a constant.

The heat equation (1) should be solved together with boundary conditions. At the surface $z = 0$ it reads [7, 9]

$$\kappa\frac{\partial T}{\partial z}\bigg|_{z=0} = \rho v[L - H_s + H_{vs}]. \quad (5)$$

Here, L is latent heat of vaporization and H_v and H are enthalpies of vapor and solid, respectively

$$H_v(T) = \int_{T_\infty}^T c_p(T_1)dT_1, \quad H(T) = \int_{T_\infty}^T c(T_1)dT_1, \quad (6)$$

where c_p and c are the heat capacities for vapor and solid, and T_∞ initial temperature. Index s indicates the surface value, i.e., $H_{vs} = H_v(T_s)$, $H_s = H(T_s)$, etc.

The second boundary condition $T(z \longrightarrow \infty) \longrightarrow T_\infty$ and initial condition $T(t = 0) = T_\infty$ are trivial.

Using the second relation (6) between H and T the boundary condition (5) can be rewritten for the value of surface enthalpy gradient:

$$\frac{\partial H}{\partial z}\bigg|_{z=0} = \frac{v}{D_s}(L - H_s + H_{vs}) \equiv J_s. \quad (7)$$

Here, $D = \kappa/c\rho$ is thermal diffusivity, $D_s = D(T_s)$, and we introduced the notation J_s for brevity.

Though somewhat simplified [7, 9], this model is still acceptable for the *quantitative analysis* of experimental data. In the present form it contains nonlinearities and nonstationary effects which can be analyzed by numerical solution with the help of finite-element technique (see e.g., [2]). This analysis requires big computational time and is not flexible. With the moment technique [10] which we will use in the further analysis,

this problem can be reduced to three coupled nonlinear *ordinary differential equations* with a small loss in accuracy. These equations can be solved by fast Runge–Kutta algorithms which are a routine part of many computational packages. Therefore, we obtain a fast tool for the quantitative simulation of thermal effects in laser ablation.

3. MOMENTS METHOD

The idea of "moments method" or "nonstationary averaging" method (see, e.g., [10]) is close to Galerkin method for approximate solution of nonlinear problems. This technique, was successfully applied, e.g., to problems in laser thermochemistry [11]. Here, we apply this technique for the analysis of laser ablation. The details of the procedure and the validation of the method's accuracy will be discussed elsewhere [12].

The idea of the method is simple. The exact solution of the boundary-value problem (1)–(6) fulfills (1) identically. If we use some approximate trial solution $H = H_p(z, t)$ the identity (1) will be violated and will result in the residue R:

$$\rho \frac{\partial H_p}{\partial t} - B[T_p] \equiv R[H_p]. \qquad (8)$$

Nevertheless, we can use $H_p(z, t)$ as an approximate solution, if we demand that it fulfills the "conservation laws" for the moments M_n:

$$\frac{dM_n}{dt} - \int_0^\infty z^n B[T(H_p(z, t))]dz = 0, \qquad (9)$$

$$\text{where } M_n = \int_0^\infty z^n H_p(z, t)dz.$$

The total number of equations (9) should be equal to the total number of unknown time-dependent functions which characterize $H_p(z, t)$. Equations (9) minimize residue R along the directions z^n within the functional space.

The difference between the Galerkin and moment methods refers to physics. There is no general algorithm for the choice of the trial function. The Galerkin method varies the trial functions in such a way that their combination is as close as possible to the "true solution." Some conservation law may not be fulfilled during the procedure. The moments method suggests less efficient approximation to the true solution, but it warrants that during the evolution certain conservation laws hold. As a result, the set of equations produced by the moment method usually has a clear physical sense.

For example, in (9), the equation for M_0 reflects the time-dependent energy balance, while equation for M_1 reflects the local energy balance with respect to some characteristic length.

We will consider two time-dependent parameters— surface temperature $T_s(t)$ (and associated surface enthalpy $H_s \equiv H[T_s(t)]$) and characteristic length $l(t)$ for the enthalpy distribution. These two quantities yield the most important information about the *distribution of internal energy* within the solid, which, as we believe, governs the ablation process. According to (9) we introduce two moments of *enthalpy* distribution:

$$M_0(t) = \int_0^\infty H(z, t)dz,$$

$$\text{and } M_1(t) = \int_0^\infty z H(z, t)dz. \qquad (10)$$

Integration of equation (10) with (5) yields

$$\rho \frac{dM_0}{dt} = -\rho v H_s - \rho v[L - H_{vs} + H_s] + I_s, \qquad (11)$$

and

$$\rho \frac{dM_1}{dt} = -\rho v M_0 + \int_{T_\infty}^{T_s(t)} \kappa(T)dT + \frac{I_s}{\alpha}. \qquad (12)$$

The integral in the right-hand side is typical for the Kirchhoff transform [1]. We set the trial solution $H_p(z, t)$ in the following form:

$$H_p(z, t) = \frac{1}{1 - \alpha l}[H_s + J_s l]\exp[-\alpha z]$$

$$- \frac{1}{1 - \alpha l}[\alpha l H_s + J_s l]\exp\left[-\frac{z}{l}\right]. \qquad (13)$$

This form satisfies boundary condition (13) and obvious requirement $H_p(z = 0, t) \equiv H_s(t)$. The first term in (13) describes the change of the enthalpy distribution with characteristic scale related to absorption of radiation, while the second term describes the changes related to heat conduction. From the physical point of view $l(t)$ represents the thermal length. Substitution of (13) into (10) yields

$$M_0 = (l + \alpha^{-1})H_s + \alpha^{-1}l J_s,$$

$$M_1 = (l^2 + l\alpha^{-1} + \alpha^{-2})H_s + (l + \alpha^{-1})\alpha^{-1}l J_s. \qquad (14)$$

Now, we can substitute (14) into (11), (12) to obtain two ordinary differential equations for T_s and l. Note that J_s, as well as H_s, depends on surface temperature T_s via (7) and (6). It is not necessary to resolve the resulting equations with respect to dl/dt and dT_s/dt for the numerical computations which have been done with *Mathematica* software package [13].

The third equation for the thickness of ablated material [which we need for the description of the screening effect, see (3)] is given by

$$\frac{dh}{dt} = v. \qquad (15)$$

Thus, the initial boundary-value problem is reduced to three ordinary differential equations for T_s, l, and h which should be solved with corresponding initial conditions. The study [12] shows, that this solution describes known analytical solutions with accuracy 5–10%. It also describes well the influence of the temperature-dependent $c(T)$, $\kappa(T)$, and $A(T)$ and, to a lower extent, $\alpha(T)$.

4. LASER ABLATION OF INDIUM: NUMERICAL SIMULATION

With laser ablation of metals one can often subdivide the fluences used in the ablation experiments into three regions:

(i) subthreshold ablation with $\Phi \ll \Phi_{th}$, where $\Delta h \propto \exp[-B/\Phi]$;
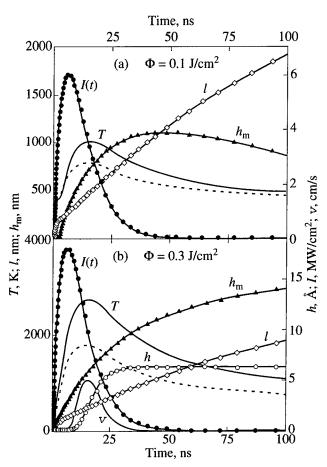
Fig. 1. Calculated dynamics of heating and ablation: (a) Φ = 100 mJ/cm² (subthreshold fluence) and (b) Φ = 300 mJ/cm². The surface temperature T_s (solid line), thermal length l (diamonds), and position of melt h_m (filled triangles) refer to the left axis, while the thickness of ablated material h (open circles), laser intensity I (filled circles), and the ablation velocity v (solid line) refer to the right axis. The temperature dependencies of $c(T)$, $\kappa(T)$, and $v(T)$ are given in the Appendix. The analytical temperature (18) is shown by dotted line. Initial temperature is T_∞ = 300 K. The value of absorptivity is A = 1, and the absorption coefficient is α = $\alpha(T_\infty)$; t_{FWHM} = 15 ns.

(ii) near-threshold region with $\Phi \geq \Phi_{th}$, where $\Delta h \propto \Phi$;

(iii) region of developed ablation, $\Phi \geq (3–5)\Phi_{th}$, where the screening becomes important. For this region $\Delta h \propto \log[\Phi]$. An optical breakdown occurs at still higher fluences and highly ionized plasma forms near the target, which changes the ablation kinetics dramatically.

In the last two regions certain approximate solutions can be found [7, 14]. Above the threshold, the overall kinetics of thermal ablation is not very sensitive to nonstationary effects and material parameters. It is guided mainly by the overall energy conservation law and by the plasma properties at higher fluences. In this work we will be concerned with subthreshold ablation. Here ablation is essentially nonstationary and depends heavily on the material properties and pulse characteristics. This makes it difficult to write any approximate formulas for this region. To find ablated depth one has to calculate the integral

$$\Delta h = \int_{0}^{t \gg t_l} v(t)dt. \tag{16}$$

This can be done easily with the help of moments method, the calculations with which can be carried out as fast as the calculations with approximate analytical formulas. The advantage of the moments method is also that we may describe with equal ease the experimental data in the intermediate situations, where no approximations exists.

We apply the developed method to the ablation of indium. The calculations are performed for KrF excimer laser (λ = 248 nm). Thermal and optical properties used in calculations are summarized in the Appendix. Indium has a low melting temperature, almost constant thermal conductivity, and the specific heat above the melting point. Ablation data have been measured for the background temperature below and above the melting point both for ns and fs laser pulses [6]. This makes indium an attractive model system.

The hydrodynamic effects are weak for the ns pulses near the threshold. They can become more pronounced with higher fluences (higher recoil pressures) and multipulse irradiation [15–17]. In fact, developed hydrodynamic effects for ns laser pulse can be seen on the SEM photography, shown in [6]. Similar effects were found in ns experiments for bismuth and lead [15].

We approximate the temporal profile of the excimer laser pulse by a smooth function [1]

$$I(t) = I_0 \frac{t}{t_l} \exp\left[-\frac{t}{t_l}\right]. \tag{17}$$

The laser fluence is given by $\Phi = I_0 t_l$. Note, that $t_l \approx 0.409 t_{FWHM}$ (the duration of the pulse defined at the full widths at half maximum). Below, this pulse is referred

to as "excimer" pulse. The analytical solution of the linear heat equation $T_{an}(t)$ presented for comparison in the first figure is given by

$$T_{an}(t)$$

$$= T_\infty + \frac{\alpha}{\rho c}\int_0^t I(t - t_1)\exp[\alpha^2 Dt_1]\mathrm{erfc}\sqrt{\alpha^2 Dt_1}\,dt_1, \quad (18)$$

where parameters of the material are taken at $T = T_\infty$.

Figure 1 shows the *calculated* time dependencies of different quantities in a single ns pulse. In Fig. 1a ablation is absent, while in Fig. 1b several angstroms are ablated. The following features are worth noting.

(i) The rate of heating slows down near the melting point.

(ii) Melt exists extremely long after the end of the laser pulse ($\Delta t_m \gg t_l$). This is especially typical for indium with its low T_m and ΔH_m and high thermal conductivity, which allows one to melt a big volume. The flat tail in $T_s(t)$ dependence is due to the release of the latent heat of solidification.

(iii) The estimations of the surface temperature based on the analytical solution (18) of the heat equation may lead to big mistakes.

(iv) Ablation is *essentially* nonstationary. Ablation velocity is by no means constant during the pulse. Thermal length increases all the way during and after the pulse and is not very sensitive to the onset of ablation.

The last fact indicates that, for the parameters used here, ablation *cannot* be described by a quasi-stationary wave. It also suggests that the ablation threshold and rate may noticeably depend on the temporal profile and duration of the laser pulse.

Figure 2 demonstrates that the shape of the pulse influences the maximal temperature and the ablated depth significantly. This is due to the fact that with metals and ns laser pulses, T_{max} (near the threshold) is determined by heat conduction. This results in higher temperatures for more "compact" pulses, without tails, which lead to the unnecessary energy losses to the heating of material. The most compact pulse is the rectangular one. This is similar to the theoretical analysis [18], where it was shown, that the deepest melting (with fixed fluence and characteristic duration) is provided by the rectangular pulse. One can see that the ablation curves almost coincide for the rectangular pulse, and for the excimer pulse (17), with *twice* as small t_{FWHM} (dashed line). It is interesting to note that, although the maximal *temperature* for the short excimer pulse is slightly *lower*, the ablated *depth* is *higher*. Indeed, though the maximal ablation velocity is higher for the rectangular pulse, the effective width of the $v(t)$ is bigger for excimer pulse. As a result *integral* in (16) has higher value for a *smoother* excimer pulse.

With higher fluences the maximal temperature grows slower and the ablated depth becomes linear with
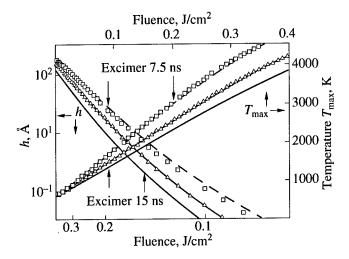
Fig. 2. The influence of the pulse shape onto the ablation. Three pulse shapes were used: rectangular, symmetric triangular, and smooth excimer pulse (17). Dashed lines refer to excimer pulse with t_{FWHM} = 7.5 ns. In all other cases t_{FWHM} = 15 ns. Initial temperature is T_∞ = 600 K. Other parameters are the same as in Fig. 1. The plots for the maximal temperature (right axis) vs. fluence (top axis) are shown in linear scale. The plot for the ablated thickness per pulse is shown in Arrhenius coordinates, i.e., log(h) (left axis) vs. inverse fluence $1/\Phi$ (bottom axis).

the fluence (as long as screening and hydrodynamics effects are negligible) due to latent heat of vaporization. The transition to this regime (which can be considered as an ablation threshold) occurs above $\Phi = 0.3$ J/cm² when the amount of ablated material per pulse exceeds 100 Å. This threshold significantly depends on the pulse shape. Thus, with *the same* t_{FWHM} experiments can show *different* threshold fluences. It is important, for example, for excimer lasers, where the pulse shapes can vary strongly. We emphasized the importance of the temporal shape of the laser pulse previously [1, 18, 19].

Another interesting feature of Fig. 2 is that the "Arrhenius plot" log(h) versus $1/\Phi$ is *steeper* than linear below the Φ_{th}, in spite of the fact that the temperature *is linear* with fluence in this region. The slope of log(h) versus $1/\Phi$ dependence is influenced by the pulse shape and duration. The reason for this is again the widening of the temporal region with $v(t) \neq 0$ in the integral (16). For the analysis of the experimental data, one also has to have in mind that with many excimer lasers t_{FWHM} increases with the output pulse energy.

Figure 3 illustrates the influence of temperature dependences in $A(T)$ and $\alpha(T)$ onto ablation curves. As in Fig. 2, for simplicity calculations are performed for *liquid* indium. With ns pulses $\alpha^2 Dt_l \gg 1$, and absorption is essentially surface. This holds even for smaller values of α at elevated temperatures (see the Appendix). As a result, $\alpha(T)$ dependence makes only a minor difference for ns pulses. The difference, which can be seen in the figure, is almost entirely due to $A(T)$ dependence, and is "accumulated" during the initial stage of heating,
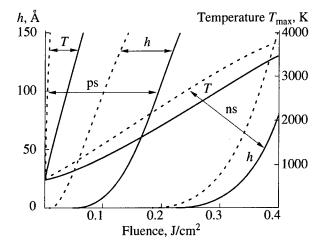
Fig. 3. The influence of temperature dependencies in A and α onto the ablation. For ns pulses the solid curves refer to the temperature-dependent coefficients. Dotted lines refer to $A = 1$. For ps pulses solid curves refer to $\alpha = 10^5$ cm^{-1}, while dotted lines, to $\alpha = 1.2 \times 10^6$ cm^{-1}. The absorptivity for ps pulses is $A = 1$. Initial temperature is $T_\infty = 600$ K in all cases. Other parameters are the same as in Fig. 1.
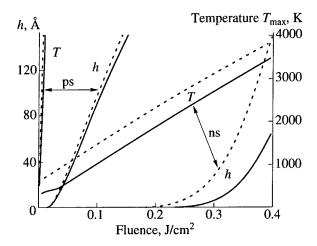
Fig. 4. The influence of the initial temperature T_∞ onto the ablation. Solid curves refer to $T_\infty = 300$ K and dotted curves, to $T_\infty = 600$ K. Absorptivity is $A = 1$, and the absorption coefficient is $\alpha = 1.2 \times 10^6$ cm^{-1} for all curves.

when the absorptivity is significantly smaller than one (A.7). One can also see a faster than linear increase in the T_{max} at low fluences, where absorptivity strongly increases with temperature.

The analysis of the ps pulses (with $\alpha^2 Dt_l \ll 1$) with the present model has a more qualitative character. Thermal *surface* evaporation model can be applied to ps pulses near and below the threshold only. This is related to several factors. According to [5], electron–phonon thermalization occurs within subpicosecond range. As a result, the temperatures much higher than the boiling temperature, and probably even the critical

temperature T_k, are reached already at low fluences. This leads to the following complications.

(i) With temperature approaching T_k, the distinction between the condensed and the solid phase disappears. This results in the decrease in the vaporization enthalpy $\Delta H = L - H_{vs} + H_s$ (which is equal *zero* at the critical temperature). At the same time, specific heat tends to infinity at T_k [20]. Above T_k only one phase exists. The material does not have the time to fly out of the laser beam, and provides very strong screening even at relatively low temperatures. With high fluences, it is more realistic to assume simply that all material heated above T_k is ablated.

(ii) The moment method in its present form adopted for the brevity in this work yields rather big mistakes in the case of short pulses $\alpha^2 Dt_l \ll 1$, when α strongly changes with temperature [12].

(iii) Besides, optical parameters of indium at high temperatures are known only from the extrapolations.

For these reasons, we present in Fig. 3 the results for $A(T)$ and two constant values of α. Temperature dependence of absorptivity does not influence the ablation curves, because with ps pulses, already at low fluences the temperatures are so high that $A \approx 1$ [see (A.7)]. Dependence $\alpha(T)$, to the contrary, is very important. The maximal surface temperature is proportional to α in this region (calorimetric solution). This about triples ablation threshold when α is decreased from 1.2×10^6 to 10^5 cm^{-1}. The temperature for $\alpha(T)$ dependence given by (A.8) lies between the dotted and the solid curve, while the behavior of the ablated depth near the threshold is quite similar to that for $\alpha = 10^5$ cm^{-1}, due to high temperatures achieved in this region.

Thus, high-temperature behavior of the absorption coefficient (which is usually *not* known from the direct measurements) is extremely important for the determination of ablation threshold in the ps pulses, and unimportant in the ns case. The $A(T)$ dependence, to the contrary, influences the ns threshold, but not the ps one.

Figure 4 shows the influence of the ambient temperature onto the ablation curves. With ns pulses, the main difference stems from two factors:

(i) Thermal conductivity of liquid phase is about twice as small as for the solid indium. This yields a reduction in the slope in initial part of $T(\Phi)$ dependence for $T_\infty = 600$ K.

(ii) The necessity to heat over 300 more Kelvin when heating starts from $T_\infty = 300$ K. The heat of fusion is anomalously small for indium and is less important than these factors.

The fluences necessary for the developed ablation from solid and liquid phases differ by some 20–25%. The relative difference becomes more pronounced for very small ablated depths.

This is not the case with ps pulses, where the curves for the temperature and the ablated depth almost coincide for both T_∞. The reason is that, with ps pulses, due

Table

Parameter	Value	Units
Atomic number, A	49	
Atomic weight, M	114.76	g/mole
Density, ρ	7.3	g/cm^3
Melting temperature, T_m	430	K
Vaporization (boiling) temperature, T_v (corresponds to saturated vapor pressure $P = 1$ atm.)	2340	K
Latent heat of fusion, ΔH_m	28.5	J/g
Latent heat of vaporization, ΔH_v	1960	J/g
The Debye temperature, T_D	108	K

to their short duration, ablated depth comparable to that of ns pulses is achieved at higher ablation velocities, that is, at higher temperatures. In this case 300 K difference in the background temperature is less important. Besides, the heat conduction plays less important role in ps pulses. It determines the cooling time of the surface, i.e., enters the ablated depth almost linearly. In ns pulses, it determines the maximal temperature, and as a result exponentially influences the ablated depth.

Thus, we should consider that laser ablation of indium with nanosecond pulses seems to be purely thermal although the temperature dependencies of material parameters strongly influence ablation rate. On the contrary, with subpicosecond pulses some other effects (not included into the discussed model) play an important role.

Effects related to the difference in electron and lattice temperature [21][1] seem to be the most important as well as the critical phenomena (heating above the critical temperature).

5. CONCLUSIONS

Numerical simulations of nonstationary effects in thermal surface laser ablation of indium are performed on the basis of the nonstationary averaging technique. Nonstationary effects influence the kinetics of laser ablation differently for nanosecond and picosecond laser pulses. Below we summarize the results.

– There exists a big difference in characteristic temperatures during the ablation by ns and ps pulses. For ps pulses temperatures are significantly higher and probably exceed critical temperature. This may render surface ablation model irrelevant already near the ablation threshold.

– Experimentally measured ablation threshold for ps pulses [6] is significantly higher than expected from the data based on room temperature values of absorption coefficient. This is probably due to a significant decrease in absorption coefficient with temperature.

– There exists a big difference in the ablation rates for ns ablation of solid and liquid indium, while for ps pulses this difference is practically absent.

– With indium, the kinetics of ablation with ns pulses is sensitive to the nonlinearities caused by the temperature dependencies in thermal conductivity and absorptivity. At the same time it is not sensitive to temperature dependence in absorption coefficient. With ps pulses, only the temperature dependence in the absorption coefficient strongly influences kinetics.

– Ablation threshold and near-threshold kinetics of nanosecond laser ablation (unlike the picosecond one) are sensitive to the temporal shape of laser pulse. Subthreshold ablated depth may deviate from the Arrhenius dependence on fluence due to nonstationary effects, and the slope of this Arrhenius dependence depends noticeably on the pulse shape.

ACKNOWLEDGMENTS

APPENDIX: THERMOPHYSICAL AND OPTICAL PROPERTIES OF INDIUM

(a) The table summarizes the parameters of indium which were taken as constant in calculations. The data were taken from [22, 23].

(b) **Specific heat** $c(T)$. The algorithm uses the analytical integration for the enthalpy. Thus, the specific heat (as well as the thermal conductivity) was fitted by the functions which allow analytical integration. The coefficients were found by the minimization of

---

[1] We should mention that the moments technique was used in [21] to estimate ablated layer thickness under simplified assumptions (one-temperature approximation with constant material parameters).

least-square deviation. The interpolation holds within 250–3000 K. $c(T)$ is measured in J/g K and T, in K,

$$c_p(T) = 0.25 + 1.19 \times 10^{-2} \arctan\left[\frac{T - T_m}{\Delta T}\right]$$
$$- 1.49 \times 10^{-5} T \arctan\left[\frac{T - T_m}{\Delta T}\right], \quad\quad (A.1)$$

The temperature width of melting $\Delta T = 0.01 T_m \approx 43$ K was introduced to smoothen steplike changes in parameters near T_m. The constant specific heat approximation with $c_p \approx 0.24$ J/gK results in less than 4% difference in the calculated temperature, and can be used as well. The Debye interpolation formula [20], as well as the Dulong–Petit law, deviates from the experimental data. These deviations are probably caused by anharmonicity.

The latent heat of fusion was taken into account by the "specific heat of melting" which was written in a Lorentzian form

$$c_m(T) = \frac{\Delta H_m}{\pi} \frac{\Delta T}{\Delta T^2 + (T - T_m)^2}. \quad\quad (A.2)$$

The total specific heat is given by

$$c(T) = c_p(T) + c_m(T). \quad\quad (A.3)$$

(c) Thermal conductivity $\kappa(T)$. The interpolation formula was taken in the form

$$\kappa(T) = 0.396 - 0.23\left(\arctan\left[\frac{T - T_m}{\Delta T}\right] - \frac{\pi}{2}\right)$$
$$+ 2.6 \times 10^{-4} T\left(\arctan\left[\frac{T - T_m}{\Delta T}\right] - \frac{\pi}{2}\right). \quad\quad (A.4)$$

It includes jump at the melting temperature and fits experimental data [23, 24] with sufficient accuracy within the region from 250–3000 K.

(d) Surface evaporation rate. According to [22],the evaporation rate is given by

$$v(T) = v_1\sqrt{\frac{300}{T}}\exp\left[-\frac{T_a}{T}\right], \quad\quad (A.5)$$

where $T_a = 28000$ K and $v_1 = 4.2 \times 10^5$ cm/s. Without loss of accuracy the value $v_0 = 1.5 \times 10^5$ can be used in (4) for the whole preexponential factor (its value at boiling temperature). The activation energy is in agreement with measurements on saturated vapor pressure, which yields $T_a = 29000$ K [22].

(e) Optical properties of indium. The data given in [22] yield too high value of $A \sim 0.4$–0.6. The ideal films of indium prepared in ultrahigh vacuum conditions and well annealed show a big reflectivity (see [25, 26]). Using Drude theory we extrapolate data [23] for 298 K to the wavelength of KrF excimer laser ($\lambda = 248$ nm, $\hbar\omega = 5$ eV). It yields $A = 0.16$ for the absorptivity and $\alpha = 1.2 \times 10^6$ cm^{-1} for the absorption coefficient.

We use the Drude formulas for the calculation of the temperature dependencies and the relation $\sigma(T)T =$ const which should be fulfilled above the Debye temperature [27]. We assume that this approximation holds for indium above 300 K.

To find the jump in the optical characteristics at melting temperature we can use the continuity of the Wiedemann–Franz ratio $\kappa(T)/T\sigma(T)$ across the melting point [24]:

$$\left.\frac{\sigma_s}{\sigma_l}\right|_{T = T_m} = \left.\frac{\kappa_s}{\kappa_l}\right|_{T = T_m} = 2.1. \quad\quad (A.6)$$

This yields jump in absorptivity up to $A \approx 0.4$ at melting temperature. For the smooth interpolation of absorptivity above the melting temperature we used

$$A(T) = 1 - 0.6\exp\left[\frac{T_m - T}{1200}\right]. \quad\quad (A.7)$$

The jump in α is small and almost does not influence the heating. It was not included in the interpolation which we used:

$$\alpha(T) = \frac{10^6}{\alpha_0 + \alpha_1 T}[\text{cm}^{-1}], \quad\quad (A.8)$$

where $\alpha_0 = 0.582, \quad \alpha_1 = 7.813 \times 10^{-4}$.

REFERENCES

1. Bäuerle, D., 1996, *Laser Processing and Chemistry*, 2nd ed. (Berlin: Springer).
2. 1996, *Laser Ablation*, Fogarassy, E., Geohegan, D., and Stuke, M., Eds. (Amsterdam: North-Holland).
3. 1992, *Laser Ablation of Electronic Materials*, Fogarassy, E. and Lazare, S., Eds. (Amsterdam: North-Holland).
4. Gaponov, S.V., 1985, *Sov. Phys. Uspekhi*, **28**, 522.
5. Anisimov, S.I. and Khokhlov, V.A., 1995, *Instabilities in Laser–Matter Interaction* (Boca Raton: CRC).
6. Preuss, S., Demchuk, A., and Stuke, M., 1995, *Appl. Phys. A*, **61**, 33.
7. Anisimov, S.I., Imas, Ya.A., Romanov, G.S., and Khodyko, Yu.V., 1971, *Action of High-Power Radiation on Metals* (Springfield, VA: National Technical Information Service).
8. Sobol, E.N., 1995, *Phase Transformations and Ablation in Laser-Treated Solids* (New York: John Wiley).
9. Luk'yanchuk, B., Bityurin, N., Himmelbauer, M., and Arnold, N., 1997, *Nucl. Instrum. Meth. B*, **122**, 347.
10. Zwillinger, D., 1989, *Handbook of Differential Equations*, (Boston: Academic).
11. Karlov, N.V., Kirichenko, N.A., and Luk'yanchuk, B.S., 1997, *Laser Thermochemistry*, 2nd ed., (Cambridge Interscience Press).
12. Arnold, N., Luk'yanchuk, B., and Bityrin, N., 1998, *Appl. Surf. Sci.* (in press).
13. Wolfram, S., 1991, *Mathematica*, 2nd ed., (Addison-Wesley).

14. Tokarev, V.N., Lunney, J.G., Marine, W., and Sentis, M., 1995, *J. Appl. Phys.*, **78**, 1241.

15. Vedenov, A.A., and Gladush, G.G., 1985, *Physical Processes in Laser-Treated Materials*, (Moscow: Energoatomizdat) (in Russian).

16. Yth, C.S., 1974, *Phys. Fluids*, **14**, 1936.

17. H. Ven, Shui, 1978, *Phys. Fluids*, **21**, 2174.

18. Bunkin, F.V., Kirichenko, N.A., and Luk'yanchuk, B.S., 1978, *Preprint Lebedev Physical Institute*, no. 146, Moscow, USSR; 1980, *Fiz. Khim. Obrabotki Materialov*, **5**, 7.

19. Luk'yanchuk, B., Bityurin, N., Anisimov, S., *et al.*, 1996, *Appl. Phys. A*, **62**, 397.

20. Landau, L.D. and Lifshitz, E.M., 1980, *Statistical Physics*, (Pergamon), part 1.

21. Anisimov, S.I. and Rethfeld, B., 1997, *Proc. SPIE*, **3093**, 192.

22. 1973, *American Institute of Physics Handbook*, 3rd ed., Gray, D.E., Ed. (Mc Graw-Hill).

23. 1980, *Landolt-Bornstein New Series*, Madelung, O. Ed. (Berlin: Springer).

24. Goldratt, E. and Greenfield, A.J., 1980, *J. Phys. F*, **10**, 295.

25. Koyama, R.Y., Smith, N.V., and Spicer, W.E., 1973, *Phys. Rev. B*, **8**, 2426.

26. Lemonuier, J.C., Jezequel, G., and Thomas, J., 1975, *J. Phys. C*, **8**, 2818.

27. Lifshitz, E.M. and Pitaevsky, L.P., 1981, *Physical Kinetics*, (Pergamon).

Electron Spectra of Above-Threshold Ionization in Elliptically Polarized Laser Fields

W. Becker*,[1], M. Kleber**, A. Lohr**, G. G. Paulus***,
H. Walther***,[2], and F. Zacher***

*Max-Born-Institut, 12474 Berlin, Germany
e-mail: wbecker@mbi-berlin.de
**Physik-Department, Technische Universität München, Garching, 85747 Germany
***Max-Planck-Institut für Quantenoptik, Garching, 85748 Germany
Received September 16, 1997

Abstract—Measurements of electron spectra of above-threshold ionization in an elliptically polarized laser field are reported and discussed in terms of theoretical models. For low energies, the electron yields in the direction of the large component of the elliptically polarized field first decrease when the ellipticity increases and then rise again when circular polarization is approached. A classical explanation of this effect is provided. The same electron yields display, while they are decreasing as a function of the ellipticity, characteristic shoulders and ripples. These features can be related to quantum mechanical interference of electrons tunneling out into the continuum at different times within one cycle of the field. Electron yields for high energies, those that are part of the plateau, drop very quickly with increasing ellipticity at a rate almost independent of the energy. This is fully explained by spreading of the electronic wave function. A first example of the electron spectrum as a function of energy and angle of emission for fixed ellipticity is presented, too.

1. INTRODUCTION

The electronic spectra recorded in above-threshold ionization (ATI) (for a recent review, see [1]) display many qualitative features that do not depend on the individual atom. Typically, these are large-scale effects that dominate the overall appearance of the spectrum. Examples include the suppression of the low-energy peaks in, long-pulse ATI [2], the typical differences between ATI caused by linear versus circular polarization [3], and in high-energy ATI the plateau [4] and the associated side lobes [5] in the angular distributions. The plateau and its cutoff in high-harmonic generation (HHG) is another case in point [6]. All of these phenomena have in common that basically they are manifestations of simple classical physics. Quantum mechanics is, of course, responsible for the very existence of separate peaks and, certainly, for many of the details (as yet poorly understood) of the spectra which do depend on the atomic species. Part of the reason of why there is so little visible evidence of quantum mechanics in the spectra is the thus far limited means of probing the system. In particular, one of the decisive parameters, viz. the intensity of the incident laser field, has no well defined value in actual experiments. Hence, any feature of ATI that has, in principle, a sensitive dependence on the intensity tends to be smoothed over in the data, often beyond recognition. In this work we exploit the existence

of an additional parameter which can be controlled very well in experiments: the ellipticity of the laser field.

Ellipticity will be seen to introduce further examples of the kind of almost classical effects which are so typical of ATI. Some other effects, also to be discussed in this paper, can still be understood in terms of classical trajectories provided quantum mechanical wave packet spreading is taken into account. However, the most interesting effect of ellipticity will be that it allows to track quantum mechanical interference of different tunneling trajectories [7]. These interferences are ubiquitous in ATI as well as, presumably, HHG. Usually, however, they are not visible owing to the broad intensity distribution of the laser field. Varying the ellipticity in a controlled manner brings them into the open.

The paper is organized as follows. In the next Section, we describe the experiment and briefly review the results. We observe characteristic ripples in the dependence of the ATI rate for fixed energy and direction of emission as a function of the ellipticity of the ionizing field. In the third Section, we discuss several theoretical concepts to be used later on in the analysis of the experimental data. First, we investigate symmetries of the exact matrix element for multiphoton ionization into a given channel due to an elliptically polarized field. We then check whether or not these symmetries are obeyed by the KFR approximation and/or an improved approximation that allows for rescattering. Second, we evaluate the KFR matrix element by a saddle point approximation. The saddle points lend themselves to a semiclassical physical interpretation: they specify the time at which the electron is "born" in the continuum via

---

[1] Also at Center for Advanced Studies, Department of Physics and Astronomy, University of New Mexico, Albuquerque, NM, 87131 USA.
[2] Also at Sektion Physik der Ludwig-Maximilians Universität München, Am Coulombwall 1, Garching, 85747 Germany.

tunneling and the associated tunneling time. The expression for the ionization rate in terms of the saddle points makes it evident that the contributions from different saddle points interfere, constructively or destructively. Third, we review the "simple man's" model and extend it in order to account for finite-range effects of the binding potential on the angular spectrum. Finally, we review the "Gaussian overlap model" which is useful in the analysis of the ellipticity dependence of the ATI spectra at high energies when the rescattering mechanism is dominant. In the fourth Section, we scrutinize the experimental data in the light of the models introduced earlier.

2. EXPERIMENTS

Our experimental setup consists of a femtosecond laser system, the vacuum chamber with the electron spectrometer, and a computer that controls the experiment and collects the data. The pulses are generated in a colliding-pulse mode-locked ring dye laser with chirp compensation by four prisms. It delivers 50fs pulses with a repetition rate of 100 MHz and a wavelength of 630 nm. A two-stage multipass dye amplifier pumped by a copper-vapor laser raises the energy to about 15 μJ per pulse at a repetition rate of 6.2 kHz. After recompression in a prism sequence, 50-fs FWHM pulse duration can be achieved. The laser beam is focused with a 120 mm achromat inside the vacuum chamber. The beam waist of the focus is about 12 μm FWHM. This leads to a peak intensity of 1.6×10^{14} W/cm^2.

The electron spectrometer uses time-of-flight analysis. The atoms leaving a very fine nozzle with a diameter down to 10 μm are ionized by the laser pulses. The photoelectrons then travel through a flight region of 40 cm length and double shielded by cryoperm. Finally they are detected by a microchannel plate at right angles to the incident laser radiation with a collecting angle of 5°. By means of a cryopump the background pressure in the vacuum chamber is held below 10^{-8} Torr.

Special emphasis was given to the resolution of the spectrometer and to its collection efficiency. The flight times of the photoelectrons are measured by a FAST7886 multiscaler capable of recording many electrons per laser shot without dead time and with a resolution of 500 ps. In addition, for each laser shot, the fastest electron is recorded with 100 ps time resolution by a time-to-amplitude converter the output of which is digitized. Since time resolution is most critical for fast electrons on the one hand and since the number of these electrons is very small on the other, the spectrometer is well adapted to the problem of measuring high-order ATI spectra.

A program, partially in assembler and running on a Pentium-PC, was written to control the time-to-amplitude converter as well as the multiscaler and to collect the data. In addition the computer controls one or two

rotary stages with a half- or a quarter-wave plate to manipulate the laser polarization. Typically we use 73 different positions of the rotary stage and move it every 20000 laser shots. In the case of photoelectron angular distributions this corresponds to an angular resolution of 2.5°. Thus the computer mimics 73 different multichannel analyzers. In order to minimize systematic errors due to possible long-term drifts in the experimental apparatus, the spectra corresponding to the different directions (or ellipticities) of the laser polarization are measured at quasi the same time, that means the rotary stage scans its typically 73 positions several times.

Besides the photoelectrons, the energy of each laser pulse is also registered by a photodiode. Thus the influence of intensity fluctuations can be monitored. A measurement of an angular distribution or an ellipticity distribution takes one to three hours. The gas pressure is adjusted so that no space charge effect is visible. This corresponds to an electron count rate of less than 10 s^{-1} for that position of the rotary stage that corresponds to the strongest spectrum. About 30×10^6 electrons are recorded for such a measurement.

For the discussion of the data it is useful to discriminate between "direct" and "rescattered" electrons. Direct electrons leave the field region without significant interaction with the binding potential after they have emerged in the continuum. In the context of the classical "simple man's" model [8], for linear polarization, their energy cannot exceed twice the ponderomotive potential U_p. In contrast, rescattered electrons have been subject to substantial interaction with the binding potential after having made a major excursion away from the parent ion. In the process of rescattering they
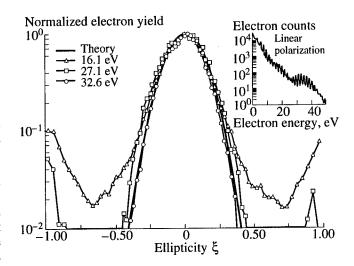
Fig. 1. Measured ellipticity distributions for xenon at an intensity of 0.8×10^{14} W/cm^2. Here and in the following Figs. 2 and 3 the data are taken in the direction of the large axis of the polarization of the field. The data are normalized to unity for zero ellipticity. The thick solid line labelled "theory" gives the result of the Gausian overlap model. The inset depicts the energy spectrum for linear polarization.
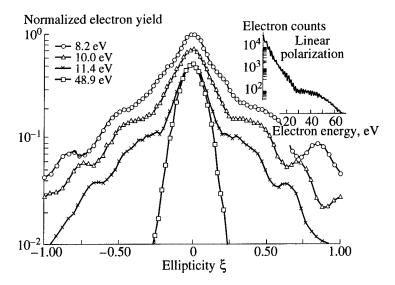
Fig. 2. Measured ellipticity distributions for xenon at an intensity of 1.2×10^{14} W/cm^2. The curves are slightly separated in the vertical direction for visual convenience.
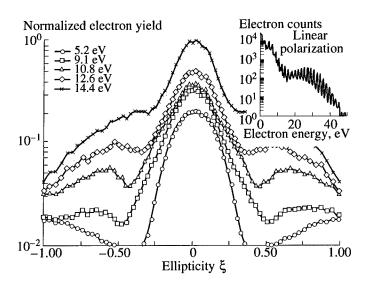
Fig. 3. Measured ellipticity distributions for argon at an intensity of 0.8×10^{14} W/cm^2.

may acquire energies, again for linear polarization, as high as 10 U_p [9]. The distinction between direct and rescattered electrons is somewhat vague, both in theory and even for a short-range potential, and even more so in reality, particularly in the intermediate energy range. Still we believe it is useful in view of the physical picture it communicates. It becomes more precise within the theoretical context discussed below.

Figures 1 to 3 display typical experimental results. In each case, electron counts *in the direction of the large axis* of the polarization ellipse are given in arbitrary units on a logarithmic scale as a function of the ellipticity ξ of the incident laser field. The ellipticity varies from left circular via linear to right circular. The experimental setup is such that the intensity is held con-

stant as the ellipticity is tuned. The ellipticity distributions of direct and rescattered electrons have a very different appearance. The count rate of the *rescattered* electrons drops very quickly with increasing ellipticity (cf. Fig. 1). The shape of this relative decrease is largely independent of the electron energy. Ulimately, when the ellipticity approaches unity, the electron yields for not too high energies rise again and reach a local maximum for circular polarization. Figure 2 displays yields of direct electrons. Their count rates decrease as well as the ellipticity rises from zero, but much more gradually and in a nonmonotonic fashion. The overall decrease has superimposed oscillations which move to lower ellipticities when the electron energy is raised. In this process the oscillations degenerate into shoulders and

finally become indiscernible. The spectra of Figs. 1 and 2 were taken for xenon. Figure 3 shows spectra of direct electrons from irradiation of argon. Essentially the same structures are recovered, in particular the ripples which move to lower ellipticity for increasing energy. All of these features will be explained below and traced to different physical origins.

Figure 4 is the only angular distribution shown in this paper, all other results concerning emission in the direction of the large axis of the polarization ellipse of the field. The figure details, for a fixed ellipticity of $\xi = 0.36$ of the driving field, the angular distribution for angles from $-90°$ to $90°$ with respect to the large axis and electron energies from 0 to 50 eV in the form of a density plot. More examples of angular distributions for nonzero ellipticity will be presented and discussed elsewhere. Here we will be satisfied just with highlighting a few of the most conspicuous features. The figure covers both direct and rescattered electrons. The lack of left–right symmetry for both is obvious. A peak structure of the spectrum is well developed except for the lower energies at positive angles. A ripplelike structure is visible for the low-energy electrons in the region of negative angles. It moves towards smaller angles with increasing energy. Emission of the plateau electrons is maximal at an angle of about 20° with respect to the large axis. The angular distribution with respect to its center at this angle exhibits a marked asymmetry.

3. THEORETICAL CONSIDERATIONS

In all that follows, we will consider the monochromatic elliptically polarized field

$$\mathbf{E}(t) = \frac{E_L}{\sqrt{1 + \xi^2}}(\hat{\mathbf{x}}\sin\omega t - \xi\hat{\mathbf{y}}\cos\omega t) \qquad (1)$$

with ellipticity ξ. Its vector potential is

$$\mathbf{A}(t) = a(\hat{\mathbf{x}}\cos\omega t + \xi\hat{\mathbf{y}}\sin\omega t) \qquad (2)$$

with $a = E_L/(\omega\sqrt{1 + \xi^2})$. We defined the field such that its ponderomotive potential

$$U_p = e^2\langle\mathbf{A}(t)^2\rangle/2m \qquad (3)$$

is independent of the ellipticity. For later use we still introduce the parameter

$$\zeta = \frac{1 - \xi^2}{1 + \xi^2}. \qquad (4)$$

3.1. Symmetries

In the interaction representation, the exact matrix element for multiphoton ionization to a state with asymptotic momentum $\mathbf{p}$ can be expressed as

$$M(\mathbf{p}, \xi) = \langle\mathbf{p}|T\exp\left\{-i\int_{-\infty}^{\infty} d\tau H_I(\tau)\right\}|0\rangle, \qquad (5)$$

$\xi = 0.36$
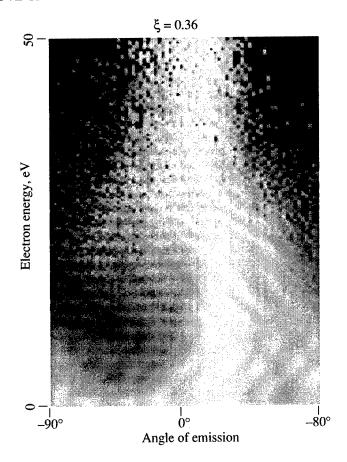
Fig. 4. Measured angular distribution of ATI in xenon for angles from $-90°$ to $90°$ (horizontal axis) with respect to the large axis of the incident elliptically polarized field and for electron energies from 0 to 50 eV (vertical axis). The incident field has an ellipticity of $\xi = 0.36$, the intensity is approximately 1.0×10^{14} W/cm^2. The rate of emission is indicated on a gray scale which is renormalized for each electron energy. That implies, the rates of emission for *different* energies cannot be directly compared.

where $|0\rangle$ and $\mathbf{p}\rangle$ denote the initial bound state and final scattering state with asymptotic momentum $\mathbf{p}$, respectively, in the given atomic binding potential $V(\mathbf{r})$. H_I denotes the interaction operator with the external laser field. In the length gauge,

$$H_I(t) = e^{iH_0t}(-e\mathbf{r}\cdot\mathbf{E}(t))e^{-iH_0t} \qquad (6)$$

with the atomic Hamiltonian $H_0 = \mathbf{p}^2/2m + V(\mathbf{r})$. First, we notice that the matrix element (5) is independent of the sign of the momentum component p_z which is perpendicular to the plane of the polarization. For the time being, we will suppress the dependence on p_z in what follows, so that $\mathbf{p} = (p_x, p_y)$ refers to just the momentum in the plane of the polarization. If the atomic Hamiltonian H_0 obeys parity symmetry and the initial ground state is an eigenstate of parity, then it is intuitively obvious and easy to show that

$$M(\mathbf{p}, \xi) \doteq M(-\mathbf{p}, \xi). \qquad (7)$$

The equality holds, in general, only up to a phase which we indicate here and below by writing $\hat{=}$. In order to prove the inversion symmetry (7) we write

$$M(-\mathbf{p}, \xi) = \langle \mathbf{p}|PT\exp\left\{-i\int_{-\infty}^{\infty} d\tau H_I(\tau)\right\}PP|0\rangle, \quad (8)$$

where P indicates the parity operation in the plane of the polarization, $P^2 = 1$ and $P|0\rangle = \pm|0\rangle$. Carrying out the parity operation in (8) flips the sign of the exponent in the time-ordered exponential. Substituting subsequently $\tau \longrightarrow \tau + T/2$ with T the period of the field yields another change of sign so that

$$PT\exp\left\{-i\int_{-\infty}^{\infty} d\tau H_I(\tau)\right\}P$$

$$= e^{iH_0T/2}T\exp\left\{-i\int_{-\infty}^{\infty} d\tau H_I(\tau)\right\}e^{-iH_0T/2}. \quad (9)$$

The two exponentials that sandwich the time-ordered exponential on the right-hand side of (9) yield phases when applied to the respective states in (8). This completes the proof of the inversion symmetry (7) of the spectrum. In obtaining (9) we used the particular form of the field (1) which changes its sign upon a translation in time by half a period. In general, for example, for a two-color field which does not exhibit an analogous symmetry, equation (9) will not hold and, consequently, there is no inversion symmetry (7) in the spectrum (see, e.g. [10]).

What happens to the spectrum if we change the sign of the ellipticity? Let P_i denote reflection about the i-axis within the plane of the polarization, e.g., $P_x\mathbf{p} = (-p_x, p_y)$. Then, along the same lines as above, we can easily prove the symmetry

$$M(\mathbf{p}, -\xi) \hat{=} M(P_i\mathbf{p}, \xi) \quad (10)$$

for $i = x$ or $i = y$. Now, if $\mathbf{p}$ is parallel to either the x-axis or the y-axis (the two axes of the polarization ellipse) then $P_i\mathbf{p} = -\mathbf{p}$ and with the help of the symmetry (7) we prove the property

$$M(\mathbf{p}, -\xi) \hat{=} M(\mathbf{p}, \xi). \quad (11)$$

For general momenta, however, a change of the handedness of the field (1) does change the spectrum.

The above considerations apply to the exact matrix element. Approximations may induce additional symmetries or disobey symmetries of the exact matrix element. Below we will investigate the symmetry properties both of the KFR-matrix elements [11–13] and of an improved version [15] that allows for one additional interaction with the binding potential so that rescatter-

ing, for example, is included. The KFR matrix element, in the form given in [14], can be represented as

$$M^{(0)}(\mathbf{p}, \xi) = -i\int_{-\infty}^{\infty} dt\langle\psi_\mathbf{p}^{(V)}(t)|V|\psi_0(t)\rangle \quad (12)$$

with, in the length gauge, the Volkov wave function

$$\psi_\mathbf{p}^{(V)} = (2\pi)^{-3/2}e^{i(\mathbf{p}-e\mathbf{A}(t))\mathbf{r}}e^{-iS_\mathbf{p}(t)}. \quad (13)$$

In the velocity gauge, the exponential $\exp(-ie\mathbf{A}(t)\mathbf{r})$ in (13) is absent. The second exponent in (13), viz.,

$$S_\mathbf{p}(t) = \frac{1}{2m}\int^t d\tau(\mathbf{p} - e\mathbf{A}(\tau))^2 \quad (14)$$

(to be understood as the indefinite integral) is the action of the charged particle moving in the field with the time-averaged (canonical) momentum $\mathbf{p}$.

The above-mentioned improved version [15] is

$$M^{(1)}(\mathbf{p}, \xi)$$

$$= -i\int_{-\infty}^{\infty} dt\int_{-\infty}^{t} dt'\langle\psi_\mathbf{p}^{(V)}(t)|VU^{(V)}(t, t')V|\psi_0(t')\rangle. \quad (15)$$

The quantity $U^{(V)}(t, t')$ is the Volkov time-evolution operator having the representation in position space

$$U^{(V)}(\mathbf{r}t, \mathbf{r}'t') = \left(\frac{im}{2\pi(t-t')}\right)^{3/2}e^{iS(\mathbf{r}t, \mathbf{r}'t')}. \quad (16)$$

The (gauge-dependent) action $S(\mathbf{r}t, \mathbf{r}', t')$ is that of a particle trajectory moving from the position $\mathbf{r}'$ at time t' to the position $\mathbf{r}$ at the later time t subject to the vector potential (2); for an explicit representation, see, e.g., [16]. It should be emphasized that $M^{(1)}$ is not to be added to $M^{(0)}$, but is an improved approximation which contains $M^{(0)}$. Expressions similar to (15) can be found in [17, 18].

First, we will inspect the symmetry properties of the KFR matrix element $M_\mathbf{p}^{(0)}$. Under the same conditions as above one can ascertain that the inversion symmetry (7) holds for both $M^{(0)}$ and $M^{(1)}$, that is,

$$M^{(i)}(\mathbf{p}, \xi) \hat{=} M^{(i)}(-\mathbf{p}, \xi) \quad (i = 0, 1), \quad (17)$$

Substituting $t \longrightarrow -t$ in (12) we find

$$M^{(0)}(\mathbf{p}, \xi) \hat{=} M^{(0)}(\mathbf{p}, -\xi)^* \quad (18)$$

for *arbitrary* momenta $\mathbf{p}$. This implies that the entire electron spectrum is, in this approximation, independent of the handedness of the field. For the exact spectrum, this applies only for emission in the direction of one or the other axis of the polarization ellipse. (Notice, that $M^{(0)}$ also obeys the symmetry (11); for momenta in

the x- or y-direction, the matrix element $M^{(0)}$ is real). Similarly, we can get

$$M^{(0)}(P_i\mathbf{p}, \xi) \triangleq M^{(0)}(\mathbf{p}, \xi)^* \quad (i = x, y) \qquad (19)$$

for arbitrary momenta $\mathbf{p}$. This leads to the prediction of a *fourfold* symmetry of the spectrum in the plane of the polarization. The independence of the helicity demonstrated above as well as the fourfold symmetry (19) are artifacts of the KFR approximation (12) using the Volkov plane wave (13) for the description of the final state. The symmetries (18) and (19) are invalidated already if a Coulomb–Volkov state is taken in place of the plane-wave Volkov state or, in case of a zero-range binding potential, if the exact scattering state is used which contains an outgoing s-wave in addition to the plane wave. Similarly, the improved approximation (15) destroys the symmetries (18) and (19). This is due to the occurrence of the two times t and t' in the matrix element (15) which satisfy $t \geq t'$ which is not invariant under time reversal. In general, the electron must be able to experience the binding potential $V(\mathbf{r})$ more than once, via rescattering or the presence of a scattering phase, in order that the artificial helicity symmetry or the fourfold symmetry be absent.

In experiments with elliptical polarization [19] the fourfold symmetry (19) was, indeed, found to be violated while the twofold symmetry (7) as well as the independence of helicity for emission along the axis (11) was found to hold. These experiments which were carried out almost ten years ago were restricted to what we now call the direct electrons. Various explanations of the violation of the fourfold symmetry were given [20–22] which can all be subsumed under effects that are due the nonzero range of the binding potential.

3.2. A Saddle Point Approximation to the ATI Rates

For a periodic field such as (1) with $T = 2\pi/\omega$ the action satisfies

$$S_\mathbf{p}(t + T) - S_\mathbf{p}(t) = T\left(\frac{1}{2m}\mathbf{p}^2 + U_p\right). \qquad (20)$$

With the help of this periodicity property of the action we can rewrite the lowest-order KFR matrix element such that the temporal integration extends over just one period:

$$M^{(0)}(\mathbf{p}, \xi) = -2\pi i \sum_n \delta\left(\frac{1}{2m}\mathbf{p}^2 + |E_0| + U_p - n\omega\right)$$

$$\times \int_0^T dt \langle \mathbf{p} - e\mathbf{A}(t)|V|0\rangle e^{i|E_0|t} e^{iS_\mathbf{p}(t)} \qquad (21)$$

$$\equiv \sum_n \delta\left(\frac{1}{2m}\mathbf{p}^2 + |E_0| + U_p - n\omega\right)M_n^{(0)}(\xi).$$

In contrast to (5) the ket $\langle\mathbf{p}|$ here denotes a plane-wave state. To a surprisingly good approximation, this matrix element is determined by the saddle points of the phase, specified by

$$\frac{\partial}{\partial t}(-i\Phi(t)) \equiv \frac{\partial}{\partial t}(|E_0|t + S_\mathbf{p}(t))$$

$$= |E_0| + \frac{1}{2m}(\mathbf{p} - e\mathbf{A}(t))^2 = 0, \qquad (22)$$

or, explicitly, for the vector potential (2), by

$$|E_0| + \frac{1}{2m}$$

$$\times [(p_x - ea\cos\omega t)^2 + (p_y - ea\xi\sin\omega t)^2 + p_z^2] = 0. \qquad (23)$$

Obviously, this equation has no real solutions for t. Any symmetry of the kinetic energy is transferred to the saddle points. Since $(\cos(z))^* = \cos(z^*)$ while $(\sin(z))^* = -\sin(z^*)$, provided t is a solution of (23), then $T - t^*$ is another solution. For general momenta, (23) yields a quartic equation for either $\cos\omega t$ or $\sin\omega t$, and this is the only symmetry relating the various saddle points to each other.

If $p_y = 0$ or $\xi = 0$, or if $p_x = 0$, then (23) reduces to a quadratic equation in $\cos\omega t$ or $\sin\omega t$, respectively. In the first case, the solutions are determined by

$$\cos\omega t = (4m\zeta(1 - \xi^2)U_p)^{-1/2}$$

$$\times [p_x \pm \{\xi^2 p_x^2 - (1 - \xi^2)(2m|E_0| + p_z^2)$$

$$- 4m\xi^2\zeta U_p\}^{1/2}] \quad (p_y = 0), \qquad (24)$$

where the parameter ζ is defined above in (4). Given any solution t, $T - t$ is another solution, and the solutions for t come in complex conjugate pairs. There is a limiting value ξ_0 of the ellipticity [defined by the zero of the second square root in (24)] with the following property: for $0 \leq |\xi| \leq \xi_0$, there are two pairs of solutions situated symmetrically with respect to $\text{Re}\,\omega t = T/2$; on the other hand, for $1 \geq |\xi| \geq \xi_0$, all solutions are real with $|\cos\omega t| > 1$ and, consequently, $\text{Re}\,\omega t = T/2$. Figure 5 displays an example of the trajectories of the saddle points in the complex ωt-plane as a function of ξ. For $p_x = 0$, the analog of (24) is

$$\sin\omega t = (4m\zeta(1 - \xi^2)U_p)^{-1/2}[-\xi p_y$$

$$\pm \{p_y^2 + (2m|E_0| + p_z^2)(1 - \xi^2) + 4m\zeta U_p\}^{1/2}] \qquad (25)$$

$$(p_x = 0).$$

Now with any solution t, $T/2 - t$ and $t^* + T/2$ are additional solutions. In contrast to $\cos\omega t$ from (24), the solutions $\sin\omega t$ are real for any ξ. They all have $\text{Re}\,\omega t = T/4$ or $3T/4$. For increasing ξ, one moves closer to and the other one away from the real axis, as it does in Fig. 5
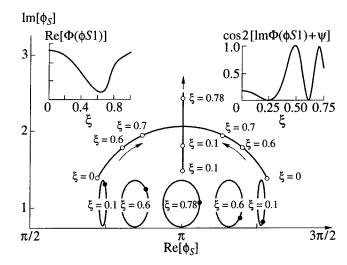
Fig. 5. Positions of the saddle points ϕ_S in the upper half complex ϕ-plane in the interval $\pi/2 \leq \mathrm{Re}\phi \leq 3\pi/2$, calculated from (24) for the conditions of Fig. 6 and $n = 17$. The arrows indicate the motion of the saddle points for increasing ξ. For several values of the ellipticity, insets depict the polarization ellipse with the emission times $\omega t = \mathrm{Re}\phi_S$ marked by solid dots. For $0 \leq \xi \leq \xi_0$, there are two such positions whose contributions interfere. For $\xi_0 \leq \xi \leq 1$, there is just one corresponding to emission at $\omega t = \pi$. Emission at $\omega t = 0$ has its drift velocity in the opposite direction and does not interfere with the former. For $n = 17$, the limiting value is $\xi_0 = 0.755$. Additional insets depict, for $n = 17$, the magnitude and the squared cosine of the approximation (27). Notice that the ellipticities where the cosine vanishes or is maximal precisely agree with the minima and maxima, respectively, of the ellipticity distributions of Fig. 6.

for $\xi \geq \xi_0$. Finally, for circular polarization, there is just one solution,

$$\cos(\omega t - \delta)$$
$$= (2p_T\sqrt{2mU_p})^{-1}[2m(|E_0| + U_p) + p_T^2 + p_z^2], \quad (26)$$

which is real and whose magnitude is larger than unity. This solution holds for arbitrary momenta. Here $p_T = \sqrt{p_x^2 + p_y^2}$ is the component of the momentum in the plane of the polarization and $\tan\delta = p_y/p_x$.

In all three cases we notice that the component p_z of the momentum orthogonal to the plane of the polarization enters the equations such that the corresponding kinetic energy $p_z^2/2m$ adds to the binding energy $|E_0|$. Hence, in this context varying p_z is equivalent to tuning the binding energy.

Having determined the saddle points for the cases of foremost interest we are now in a position to write down the corresponding approximation to the matrix element (21). The result is particularly simple for a zero-range potential for which the matrix element $\langle \mathbf{p} - e\mathbf{A}(t)|V|0\rangle$ is just a constant independent of the saddle points and of $\mathbf{p}$. The original contour of integration over time in the

matrix element (21) is the real axis. For the case mentioned above where $0 < |\xi| < \xi_0$, the contour may be deformed into the upper half complex plane so that it passes through the two saddle points depicted in Fig. 5. In the vicinity of the saddle points the integral may be approximated by a Gaussian. With some nonexponential and nonoscillatory factors left out this yields

$$M_n^{(0)}(\xi)$$

$$\sim \exp[\mathrm{Re}\Phi(\phi_{S1})]\cos\left[\mathrm{Im}\Phi(\phi_{S1}) - \frac{1}{2}\arg(\sin\phi_{S1})\right]. \quad (27)$$

Here, $\phi_{S1} \equiv \arccos\cos\omega t$ denotes one of the saddle points determined from (24), namely the one with $\mathrm{Im}\phi_{S1} > 0$ and $0 < \mathrm{Re}\phi_{S1} < \pi$. This holds for $0 < |\xi| < \xi_0$. For $|\xi| > \xi_0$, the contour is to be routed through one saddle point only, the one above and closest to the real axis. As a consequence, the cosine in (27) is absent. The form (27) is the one given by Leubner [23]; for an alternative form, cf. Reiss [13].

The saddle points $\phi_S = \omega(t_R + it_I)$ and the approximation based on them have more than formal significance. The real part t_R specifies the time within the period of the field (1) when in the context of a semiclassical limit the electron enters the continuum via tunneling. Notice that the saddle points depend on the electron energy $E = \mathbf{p}^2/2m = n\hbar\omega - U_p - |E_0|$ and also on the direction of emission (here, in all explicit results, both the experimental and the calculated ones, emission is always considered in the direction of the large component of the field, so that $p_y = p_z = 0$). If the statement is turned around it implies that in order to acquire a certain energy and direction the electron must enter the continuum at the appropriate time. For $0 < |\xi| < \xi_0$, there are two relevant saddle points and, correspondingly, two such times within one period. The contributions from these two times to the matrix element $M_n^{(0)}(\xi)$ do not add incoherently. Rather they interfere as is illustrated by the presence of the cosine in the approximation (27). For $\xi_0 < |\xi| < 1$, just one saddle point contributes to $M_n^{(0)}(\xi)$. Consequently, there is no cosine in (27) and no interference. The imaginary part t_I is related to the tunneling time or the tunneling probability in much the same way as in the situation of tunneling in a field that is independent of time (cf. [24, 25]).

For emission in the direction of the small component of the field ($p_x = 0$) the saddle points are determined by (25). Their configuration is always like that for $\xi_0 < |\xi| < 1$ and emission in the direction of the large component ($p_y = 0$). Hence, just one saddle point contributes, and there is no interference. For emission in any other direction in the (p_x, p_y)-plane, the saddle points have to be determined from the fourth-order equation (23). Since the relevant saddle points will, in general, have different imaginary parts, complete destructive interference cannot occur. This case has not been analyzed in detail yet. Notice also, that in this case

use of the zero-range potential in $M^{(0)}$ is questionable since this generates the artificial fourfold symmetry.

3.3. The "Simple Man's" Model Revisited

A classical model helps understanding some of the gross features of the angular distributions. The frequently cited simple man assumes that an electron enters the continuum at some time with zero velocity and is subsequently accelerated by the electric field (1). If he neglects the binding potential, then the electron's velocity at the later time t_0 has the components

$$m\dot{x} = -ea(\cos\omega t - \cos\omega t_0),$$
$$m\dot{y} = -\xi ea(\sin\omega t - \sin\omega t_0). \tag{28}$$

The drift velocity of the electron in the field is the time average of the preceding expression, indicated by the notation $\langle ... \rangle$,

$$m\langle \dot{x} \rangle = ea\cos\omega t_0 = \sqrt{\frac{2mU_p}{1+\xi^2}}\cos\omega t_0,$$
$$m\langle \dot{y} \rangle = \xi ea\sin\omega t_0 = \xi\sqrt{\frac{2mU_p}{1+\xi^2}}\sin\omega t_0. \tag{29}$$

If no further interaction with the binding potential occurs, the electron leaves the pulse (which we assume to be short enough that the electron is swept over by the pulse rather than leaving it by its side) at an angle given by

$$\tan\vartheta = \frac{\langle \dot{y} \rangle}{\langle \dot{x} \rangle} = \xi\tan\omega t_0. \tag{30}$$

In the tunneling regime, electrons are preferentially injected in the continuum at times t_0 when the electric field (1) is near its maximum value, that is near $\omega t_0 = \pi/2$. For these electrons, (30) implies that $\vartheta \longrightarrow \pi/2$, that is, these electrons leave the field region in the direction of the *small* component of the elliptically polarized field. This at first glance counterintuitive result is easy to understand: for these electrons the drift velocity (29) in the direction of the large component of the field is zero while it is maximal in the direction of the small component. The implications for the KFR amplitude have been worked out in detail [27].

It is easy to realize, too, that this model produces a fourfold symmetry for the electron's angular distribution. We get a distribution of angles ϑ by assuming a distribution of initial times t_0. This latter distribution may be uniform (in the multiphoton regime) or biased towards those times where the field is maximal (in the tunneling regime). However, as long as it only depends on the absolute value of the field (1) at the time t_0 the angular distribution will be symmetric upon $\vartheta \longrightarrow \pi - \vartheta$.

In order to get an idea of how the continued presence of the binding potential affects the electronic angular distribution the simple man might extend his reasoning as follows. Assume that the electron, at some distance r_0 from its site of injection at the center of the

binding potential, has to overcome a spherical potential step of height $e\Phi$. Assume further that the azimuthal component of the velocity is continuous in this process while the electron is slowed down in the radial direction. Let t_1 denote the time at which the electron for the first time reaches the distance r_0. Rather than by (28), its velocity is now governed by

$$m\dot{x} = -ea(\cos\omega t - \cos\omega t_0) + ea\alpha_x\theta(t-t_1),$$
$$m\dot{y} = -\xi ea(\sin\omega t - \sin\omega t_0) + ea\xi\alpha_y\theta(t-t_1), \tag{31}$$

where $\theta(t-t_1)$ denotes the step function. The aforementioned continuity of the azimuthal component of the velocity requires that

$$\frac{\xi\alpha_y}{\alpha_x} = \frac{y}{x}. \tag{32}$$

A second condition for α_x and α_y is provided by the change in kinetic energy that occurs at the potential step. The model is completely analogous to optical refraction at the boundary between different media. It includes the possibility of total refraction in case the electron's kinetic energy is insufficient to overcome the step. For simplicity, we will ignore those electrons below. If treated exactly, this model constitutes a formidable problem in nonlinear mechanics; for the complexities of the much simpler problem of a one-dimensional infinitely deep well, compare, e.g., [26].

In a realistic situation, for sufficiently high laser intensity and a potential step of the order of $\hbar\omega$ or lower, the time difference $\omega(t_1 - t_0)$ is small compared to unity. In this event we can get an analytical approximation for the angle of emission. A lengthy, but rather straightforward calculation yields

$$\tan\vartheta = \xi\tan(\omega t_0 + \sigma) \tag{33}$$

in place of the above expression (30). The shift σ is determined by

$$\tan\sigma = \frac{e\Phi}{4U_p}\left(\frac{d}{r_0}\right)^{1/2}\left(\frac{1+\xi^2}{\sin^2\omega t_0 + \xi^2\cos^2\omega t_0}\right)^{3/4}. \tag{34}$$

Here, we introduced the distance $d = ea\sqrt{1+\xi^2}/2m\omega$ to set the scale for the oscillatory motion of the electron in the laser field (1), and U_p denotes its ponderomotive potential (3). Notice that the limit $r_0 \longrightarrow 0$ in (34) is ruled out, owing to the approximations made in the derivation of (34). In this case, the electrons have no time to gain any energy, so they are unable to climb the potential step.

Equations (33) and (34) no longer obey the fourfold symmetry. For a uniform distribution of initial times t_0, it would still hold were it not for the last term in (34). Without this term, the shift σ could be removed from (33) just by resetting the clock. In the tunneling regime, however, the times t_0 are weighted in relation to the maxima of the field, and this is not possible, anyway.

3.4. The Gaussian Overlap Model

If rescattering is the origin of a particular part of the ATI spectrum, then an increase of the ellipticity clearly reduces the count rate, since the returning electron's impact parameter increases with increasing ellipticity so that rescattering becomes less efficient. The essence of this is brought out by a model that assumes that the count rate is proportional to the square of the overlap between the wave function of the returning electron and that of the parent ion [28, 29]. This model has worked well in describing the decrease of high-harmonic generation near the cutoff with increasing ellipticity.

We describe the electron that has been created in the continuum by the Gaussian wave function

$$\Psi_{a_0}(\mathbf{r}, t = 0) = (a_0\sqrt{\pi})^{-3/2}\exp\left(-\frac{\mathbf{r}^2}{2a_0^2}\right) \qquad (35)$$

such that the starting width of the associated probability distribution is a_0. Provided the electron is subject only to the field (1) the center of its wave packet follows the classical trajectory of a charged particle in this field. Assume that the ellipticity ξ is not too large. Then the wave function of the returning electron upon its closest approach to its parent ion at the time t is

$$\Psi_{a(t)}(\mathbf{r}, t)$$

$$= (a(t)\sqrt{\pi})^{-3/2}\exp\left(-\frac{x^2 + (y - y_d)^2 + z^2}{2a(t)^2}\right). \qquad (36)$$

The electron misses its parent ion by the distance y_d [along the direction of the small component of the

Normalized electron yield
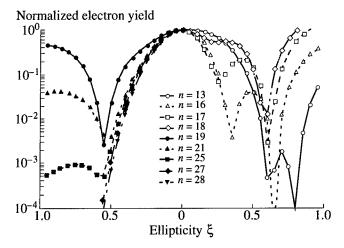
Fig. 6. Calculated ellipticity distributions in the direction of the large axis of the elliptically polarized field for a zero-range atom with the improved Keldysh approximation (15). The parameters are $E_0 = 15.76$ eV corresponding to argon, $\hbar\omega = 1.96$ eV, and $U_p = 3.68$ eV. Yields are given for various energies E labelled by the number n of photons absorbed from the ground state, $E = n\hbar\omega - E_0 - U_p$.

field (1)] and the associated wave packet has acquired the width

$$a(t)^2 = a_0^2 + \frac{t^2}{ma_0^2}. \qquad (37)$$

For simplicity, we model the parent ion by a Gaussian wave function just like (35), however, with a_0 replaced by $r_0 = 1/2\kappa$ corresponding to a zero-range binding potential with binding energy $E_0 = -\kappa^2/2m$. The overlap of these two wave functions is

$$O(y_d) = \int d^3\mathbf{r}\Psi_{a(t)}(\mathbf{r}, t)^*\Psi_{r_0}(\mathbf{r}, t = 0)$$

$$= \left(\frac{2r_0 a(t)}{r_0^2 + a(t)^2}\right)^{3/2}\exp\left(-\frac{y_d^2}{r_0^2 + a(t)^2}\right). \qquad (38)$$

Now, the model assumes that the efficiency of rescattering is reduced by the ratio

$$R = \left|\frac{O(y_d = 0)}{O(y_d)}\right|^2 = \exp\left(\frac{y_d^2}{r_0^2 + a(t)^2}\right). \qquad (39)$$

The question remains of what to take for the initial width a_0. It has been argued [29] that this should be the width at the exit of the tunnel of the wave packet of an electron ionized from a bound state with binding energy E_0 by a uniform static electric field F. This yields the expression

$$a_0^2 = \frac{1}{\kappa^2} + \frac{2|E_0|}{\kappa F}. \qquad (40)$$

With this width (and only with this width) the model has produced excellent agreement with calculations of harmonic generation in elliptically polarized fields near the end of the plateau. It may seem contradictory that we set the electronic wave packet free at the position of the parent ion, but with a width corresponding to the exit of the tunnel. However, this has worked very well even in the multiphoton regime where (due to the oscillating field) the electron never reaches the exit of the tunnel (calculated for the static field). For strong fields, on the other hand, the exit of the tunnel is close to the parent ion's position so that taking one or the other makes little difference.

4. DISCUSSION

First, we report the result of a calculation using the improved KFR expression (15) which incorporates rescattering effects to first order. As the atomic potential we employ a zero-range potential with the binding energy of 15.8 eV corresponding to argon. Figure 6 shows normalized electron yields in the direction of the large component of the elliptically polarized field for various electron energies as a function of the ellipticity. The symmetry (11) holds for $M^{(1)}$ as well as for $M^{(0)}$ provided emission in the direction of either one axis of the polarization ellipse is considered. Therefore, Fig. 6

only gives results for positive ellipticity. The right-hand side of the figure shows the yields of direct electrons— those that leave the field region without further significant interaction with the binding potential—while the left-hand side deals with rescattered electrons. The behavior of these two groups is markedly different. The transition from one to the other is quite well defined and happens around $n = 18$ and $n = 19$ where n is the number of photons absorbed from the ground state, $n\hbar\omega = E + U_p + |E_0|$.

4.1. Rescattered Electrons

For these electrons, the yields drop quickly while ellipticity increases up to a value of slightly larger than 0.5. Up to this point, the decrease is largely independent of the respective energy. Thereafter, the yields rise again, the more so the lower the energy. The calculation of Fig. 6 agrees with the experimental data depicted in Fig. 1. The latter also displays the result of the Gaussian overlap model of Section 3.4 which can be seen to provide an almost perfect fit. The underlying physics is the same as in the related cases of the ellipticity dependence of HHG and nonsequential double ionization [28]: the larger the ellipticity the smaller the overlap between the wave packet of the returning electron with the parent ion. If so, why does the decrease terminate and the rates even start rising again, at least for some of the lower energies, at the aforementioned ellipticity of about 0.5? The answer is that the electrons responsible for this are direct electrons. Since, however, the spectrum of direct electrons very quickly drops with increasing energy (its classical cutoff is at $2U_p$), the yield of these electrons drops steeply with increasing n. For $n = 19$, direct and rescattered electrons are about equally important and the yields for linear and for circular polarization are, in the context of this model, comparable. The energy corresponding to $n = 19$ is about $5U_p$ and this marks in this case the transition into the plateau.
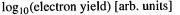
The energy where this transition occurs is not universal: it has varied from as high as $8U_p$ for low intensity in xenon [5] to $2.5U_p$ at high intensity in helium [30].

4.2. Direct Electrons

Figures 2 and 3 show that the emission rates for the direct electrons drop with increasing ellipticity, too, but at a lesser rate than the rescattered electrons. Also, the physical origin is different. For the direct electrons, it can be found in the simple man's model as expressed in (30): the closer in time to the peak of the field the electrons are born and the higher the ellipticity of the field the larger is the angle they make with the direction of the large component of the field. The electrons dodge the large component and escape on the side. Since both the measurements and the calculations deal with emission in the direction of the large component, the rates in this direction drop with increasing ellipticity. Figure 4 which is the only one in this paper to exhibit an angular distribution shows where the electrons go: off the direc-

tion of the large component as predicted by the simple man's model. As the ellipticity increases further the decrease of the rates is finally reversed and the rates of the direct electrons rise again when circular polarization is approached. This again has a simple reason: for circular polarization all directions are equivalent; the electron cannot dodge the field any more.

However, the most interesting feature of the experimental data presented in Fig. 2 is the ripplelike structure in the ellipticity dependence of ATI yields for specified energy that moves towards lower ellipticity when the energy increases. This structure is well matched by the calculation of Fig. 6 which shows for the lower energies a similar structure having the same tendency in moving. The calculation is based upon the improved KFR expression (15). Since, however, the relevant electron energies are quite low the zeroth-order expression (21) should provide a good description already. For the latter, in turn, we may resort to the saddle point approximation (27). Indeed the saddle point approximation gives an excellent fit to the latter as long as $n \leq 17$ for the case of Fig. 6. In particular, the pronounced dips exhibited by the result of the complete calculation precisely coincide with the zeroes of the cosine in the approximation (27). An example is given in the inset in Fig. 5. This makes it possible to trace the dips to their physical origin: destructive interference of electrons that tunnel out into the continuum at those two times t_R that are compatible with their respective energy and direction of emission.

log$_{10}$(electron yield) [arb. units]
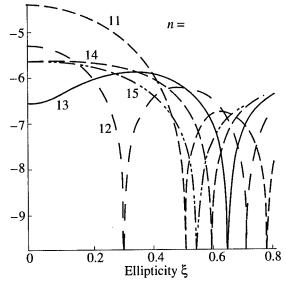
Fig. 7. Dependence of the ellipticity distributions on the electron energy, calculated with the saddlepoint approximation (27) for the parameters of Fig. 2, $\epsilon = |E_0|/\hbar\omega = 6.12$ (xenon) and $\eta = U_p/\hbar\omega = 2.29$. The curves are labelled by the number n of photons absorbed from the ground state. The ellipticities for which the destructive interferences occur move toward smaller values for increasing energy.

$\log_{10}$(electron yield)[arb. units]
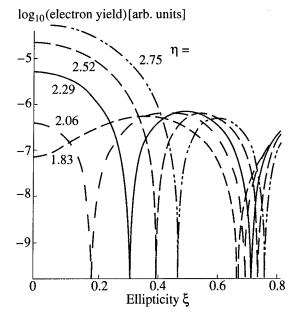
Fig. 8. Same as Fig. 7, but the energy is kept constant ($n = 12$) and the intensity varies. The curves are labelled by the value of $\eta = U_p/\hbar\omega$. The negative interference for large ellipticity does not as strongly depend on the intensity as the one for smaller ellipticity.

$\log_{10}$(electron yield)[arb. units]
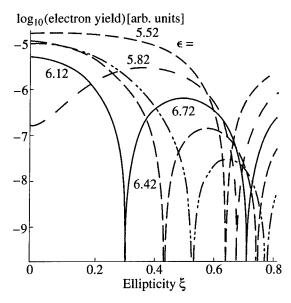
Fig. 9. Same as Fig. 7, but the energy ($n = 12$) and the intensity ($U_p/\hbar\omega = 2.29$) are kept constant while the binding energy varies. The curves are labelled by the value of $\epsilon = |E_0|/\hbar\omega$.

Figures 7 to 9 give results of calculations now based exclusively on the KFR rate $M^{(0)}$ in the saddle point approximation (27), for the parameters corresponding to the experiment of Fig. 2 with an estimated peak intensity corresponding to $U_p = 2.29\hbar\omega$. The lowest peak given in Fig. 7 ($n = 11$) displays two dips both of which move to lower ellipticities for increasing n. The

lower one moves fast and has already degenerated into a shoulder for $n = 13$ while the higher one moves much more slowly. In order to get an understanding of the dependence of the dips on intensity we show in Fig. 8 the peak with $n = 12$ as a function of the intensity. We observe the same dependence: the dip at the comparatively low ellipticity reacts very sensitively to the change in intensity as opposed to the one at higher ellipticity. An actual experiment averages over a certain range of intensities. Consequently, in the experimental data the dip at the lower ellipticity tends to flatten into a shoulder. This is indeed visible in the data. In contrast, the dip at the higher ellipticity survives the averaging. The positions of the shoulder at low ellipticity and the dip at high ellipticity in the data of Fig. 2 roughly agree with the result of the saddle point calculation of Fig. 7. Finally, Fig. 9 shows the dependence of a given ATI peak on the binding energy for fixed intensity. This is relevant to a comparison between this simple theory and experimental data: in a KFR description it is not quite obvious which value to assign to the binding energy since the model does not properly take the Rydberg series into account which effects a gradual transition into the continuum. Hence features of a KFR model that strongly depend on the value of the binding energy may not be realistic [31]. Figure 9 displays the same behavior already familiar from the dependence on intensity and emission energy.

The motion of the saddle points can be partially understood in terms of the simple man's model. As discussed above, electrons enjoy the highest tunneling probability at the peaks of the electric field. Born, however, at $\omega t_0 = \pi/2$ or $3\pi/2$ they have zero drift velocity in the x-direction, cf. (29). In order to have a nonzero drift momentum in this direction they must be born at a time ωt_0 somewhat later than $\pi/2$ or somewhat earlier than $3\pi/2$, the later (or the earlier) so the higher the drift momentum is to be. From some point on (quantitatively determined by the zero of the second square root in (24) there is only *one* choice left: the electron has to be born at $\omega t_0 = 0$ or π in order to have the maximum possible drift momentum in the x-direction. These classical arguments can do no more than pointing into the right direction: classically, a given value of ωt_0 determines everything, the electron's energy and direction of emission. Hence, classically, emission in the direction of the large field component ($p_y = p_z = 0$) enforces $\omega t_0 = 0$ or π regardless of the energy. Quantum mechanics relaxes the rigidity of the classical model.

The interferences discussed above are not a phenomenon restricted to remote corners of the ATI realm. In fact, they are ubiquitous, though hard to observe in actual experiments. Figure 10 shows the result of a calculation of the ATI spectrum for a linearly polarized driving field on the basis of the improved Keldysh approximation (15). It models the recent experimental data of Walker *et al.* [30]. Both the direct electrons at energies below about $2.5U_p$ and the rescattered elec-

trons at higher energies show a sequence of very pronounced dips. The spectrum at low energies including the precise positions of the dips can be exactly reproduced by the saddle point approximation (27). Hence they are due to the same interference mechanism as discussed so far. This is an example of interferences as a function of the electron's energy. Similarly, interferences can be analyzed for fixed energy and a linearly polarized driving field as a function of the direction of emission [32]. However, as discussed above at the very end of Section 3.2, in this case the interference will not be completely destructive. All of these interferences are extremely sensitively dependent on the intensity and will be very hard to observe in any standard experiment. In fact, the data of [30] did not resolve the interferences. Finally, coming back to Fig. 10, we draw attention to the dips within the plateau which have a very similar appearance and should have a related origin. Since they are due to rescattering, however, their analysis is more involved. For the closely related case of HHG, it has been suggested that they are due to interfering tunneling trajectories as well [33].

The ripples in the ellipticity dependence of the ATI rates are strongly reminiscent of those observed in photodetachment of H⁻ in the presence of an additional static uniform electric field [34] and, indeed, these are caused by a similar quantum interference. In the photodetachment experiment, an electron is promoted up into the continuum by the absorption of one photon of the laser field (whose energy exceeds the binding energy of H⁻). As opposed to the simple man's model described above where the electron was assumed to start its journey with zero velocity, here the electron is set free with a noticeable energy overshoot. The corresponding initial velocity is uniformly distributed. In a one-dimensional picture, the electron may start with its velocity going either up or down the incline formed by the potential of the static electric field. If it moves up it will be bent around by the field later on and then interfere with the electron that started moving down right away, constructively or destructively depending on the magnitude of the static field.

4.3. Emission at Arbitrary Angles

We will conclude by briefly discussing a measurement of angular distributions for fixed nonzero ellipticity exhibited in Fig. 4. The lack of any left–right symmetry, that is the absence of the fourfold symmetry (19), is immediately obvious. It is a common feature of both direct and rescattered electrons. Qualitatively, this agrees with the prediction (33) of the modified simple man's model. A more quantitative analysis of the angular distributions is not straightforward owing to the fact that the simple KFR approximation (12) even with a finite-range potential does predict the fourfold symmetry. However, one may argue that the KFR approximation may still be used to predict the existence or even the positions of destructive interferences as they were
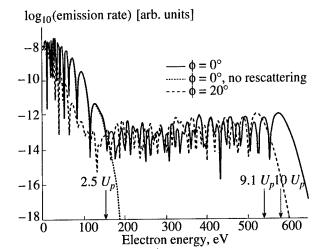
Fig. 10. ATI spectrum for linear polarization calculated with the improved Keldysh approximation (15) for the parameters of the recent experiment [30] in helium at $\hbar\omega = 1.58$ eV and 10^{15} W/cm². Yields are calculated in the direction of the electric-field vector ($\phi = 0°$) as well as at an angle of $20°$ with respect to the former. The arrows at $10U_p$ and $9.1U_p$ specify the classical cutoff for $\phi = 0°$ and $\phi = 20°$, respectively. The arrow at $2.5U_p$ marks the energy for which (for $\phi = 0°$) rescattered electrons start making a significant contribution, that is, where the results of (15) (for $\phi = 0°$ given by the thin solid line) start to differ from those of (21).

discussed above. Then, the general quartic equation (23) must be solved in order to determine the saddle points, and the simple approximation (27) no longer holds. Complete destructive interference becomes unlikely, but remnants of its on-axis manifestation should still exist. In fact, the lower left corner of Fig. 4 (negative angles, low energy) displays moving ripples that may be due to this mechanism.

5. CONCLUSIONS

We have shown that using an elliptically polarized laser field reveals several novel facets of above-threshold ionization. In particular, it allows for the observation of quantum interferences in the ATI spectra. They are due to the fact that for an electron to leave the field region with a specific energy in a specific direction it has to tunnel into the continuum at specific times during the cycle of the driving laser field. Depending on the situation, there is just one such time or there are two. In the latter case, the electrons from these two times interfere. If the interference is destructive, then it leads to a pronounced dip in the spectrum. This is observable, and has been observed in the data presented, provided it survives the average over intensity which is inherent in the experimental data. These interferences may open up a novel quantitative and experimentally feasible approach to the investigation of time-dependent tunneling.

ACKNOWLEDGMENTS

REFERENCES

1. DiMauro, L.F. and Agostini, P., 1995, *Adv. At. Mol. Opt. Phys.*, **35**, 79.

2. Kruit, P., Kimman, J., Muller, H.G., and van der Wiel, M.J., 1983, *Phys. Rev. A*, **28**, 248.

3. Bucksbaum, P.H., Bashkansky, M., Freeman, R.R., and McIlrath, T.J., 1986, *Phys. Rev. Lett.*, **56**, 2590.

4. Paulus, G.G., Nicklich, W., Xu, H., *et al.*, 1994, *Phys. Rev. Lett.*, **72**, 2851.

5. Yang, B., Schafer, K.J., Walker, B., *et al.*, 1993, *Phys. Rev. Lett.*, **71**, 3770.

6. Ferray, M., L'Huillier, A., Li, X.F., *et al.*, 1988, *J. Phys. B*, **21**, L31.

7. Paulus, G.G., Zacher, F., Walther, H., *et al.*, 1997, submitted for publication.

8. van Linden van den Heuvell, H.B. and Muller, H.G., 1988, *Studies in Modern Optics No. 8, Multiphoton Processes*, Smith, S.J. and Knight, P.L., Eds. (Cambridge: Cambridge Univ. Press), p. 25.

9. Paulus, G.G., Becker, W., Nicklich, W., and Walther, H., 1994, *J. Phys. B*, **27**, L703.

10. Paulus, G.G., Becker, W., and Walther, H., 1995, *Phys. Rev. A*, **52**, 4043.

11. Keldysh, L.V., 1964, *Zh. Eksp. Teor. Fiz.*, **47**, 1945 [*Sov. Phys. JETP*, **20**, 1307].

12. Faisal, F.H.M., 1973, *J. Phys. B*, **6**, L89.

13. Reiss, H.R., 1980, *Phys. Rev. A*, **22**, 1786.

14. Peremolov, A.M., Popov, V.S., and Terent'ev, M.V., 1966, *Zh. Eksp. Teor. Phys.*, **50**, 1393 [*Sov. Phys. JETP*, **24**, 207].

15. Lohr, A., Kleber, M., Kopold, R., and Becker, W., 1997, *Phys. Rev. A*, **55**, R4003.

16. Becker, W., Lohr, A., and Kleber, M., 1995, *Quantum Semiclass. Opt.*, **7**, 423.

17. Bao, D., Chen, S.G., and Liu, J., 1996, *Appl. Phys. B*, **62**, 313.

18. Faisal, F.H.M. and Becker, A., 1997, *Laser Phys.*, **7**, 684.

19. Bashkansky, M., Bucksbaum, P.H., and Schumacher, D.W., 1988, *Phys. Rev. Lett.*, **60**, 2458.

20. Basile, S., Trombetta, F., and Ferrante, G., 1988, *Phys. Rev. Lett.*, **61**, 2435.

21. Lambropoulos, P. and Tang, X., 1988, *Phys. Rev. Lett.*, **61**, 2506.

22. Muller, H.G., Petite, G., and Agostini, P., 1988, *Phys. Rev. Lett.*, **61**, 2507.

23. Leubner, C., 1981, *Phys. Rev. A*, **23**, 2877.

24. Hauge, H.E. and Støvneng, J.A., 1989, *Rev. Mod. Phys.*, **59**, 917.

25. Banks, T. *et al.*, 1973, *Phys. Rev. D*, **8**, 3346.

26. Fuka, M.Z., McIver, J.K., Becker, W., *et al.*, 1995, *Phys. Rev. E*, **51**, 1935.

27. Goreslavskii, S.P. and Popruzhenko, S.V., 1996, *Zh. Eksp. Teor. Fiz.*, **110**, 1200 [*JETP*, **83**, 661].

28. Dietrich, P., Burnett, N.H., Ivanov, M., and Corkum, P.B., 1994, *Phys. Rev. A*, **50**, R3585.

29. Gottlieb, B., Lohr, A., Becker, W., and Kleber, M., 1996, *Phys. Rev. A*, **54**, R1022.

30. Walker, B., Sheehy, B., Kulander, K. C., *et al.*, 1996, *Phys. Rev. Lett.*, **77**, 5031.

31. Ivanov, M.Yu., Brabec, Th., and Burnett, N., 1996, *Phys. Rev. A*, **54**, 742.

32. Gribakin, G.F. and Kuchiev, M.Yu., 1997, *Phys. Rev. A*, **55**, 3760.

33. Lewenstein, M., Salieres, P., and L'Huillier, A., 1995, *Phys. Rev. A*, **52**, 4747.

34. Bryant, H.C., Mohaghegi, A., Stewart, J.E., *et al.*, 1987, *Phys. Rev. Lett.*, **58**, 2412.

Correlation, Energy Sharing, and Formation of the "Knee" in Nonsequential Double Ionization of He in Intense Laser Fields

A. Becker* and F. H. M. Faisal**

Fakultät für Physik, Universität Bielefeld, Bielefeld, D-33501 Germany
* e-mail: abecker@physik.uni-bielefeld.de
** e-mail: ffaisal@physik.uni-bielefeld.de
Received August 14, 1997

Abstract—In this paper we discuss the role of electron–electron correlation and the associated energy sharing mechanism for the nonsequential double ionization of He in intense laser fields in order to clarify the origin of the unexpectedly large probabilities of the process that have been observed experimentally. The analysis is based on the leading Feynman diagram of the process, obtained from the Intense-Field Many-Body S-Matrix Theory, that is used here to derive a simple model formula for the total rate of the laser-induced double ionization, by extending the diagram to all orders and summing them approximately. The theory is applied to calculate the single and double ionization rates per neutral He atom as well as the single ionization rate per He^+ ion. Comparison of the single ionization ATI spectrum with that measured for He atom shows excellent agreement with the present calculation and confirms the importance of the role of rescattering from the ionic core for the high-energy tail of the spectrum. Finally, the predictions of the present model formula for the double ionization process show a remarkably good agreement with the data for He at 780 nm and over a wide range of intensity, obtained by Walker *et al.* (1994). It is shown by solving the rate-equations involving the rates of the three processes that the origin of the ubiquitous "knee" structure in the double ionization signal (in the transition region between the nonsequential and the sequential regimes of intensity) results from a competition between depletion of the neutral atom and the dominance of the stepwise process at very high intensities. The basic mechanism of absorption of field energy by one electron and the sharing of this energy by the other electron via the e–e correlation, as proposed by us earlier, is thus further confirmed by the present analysis of the experimental data.

1. INTRODUCTION

Observation of nonsequential double ionization of He in intense laser fields [1–8] has introduced a new element in intense field physics, namely the role of Coulomb correlation between the two electrons on the probability of laser-induced double ionization of atoms. The theoretical challenge of simultaneously accounting for the combined influence of the nonlinear electron–field coupling *and* the electron–electron correlation is being currently approached by direct simulation of the time-dependent Schrödinger equation on a large space–time grid [9–11] as well as by several model investigations (e.g., [12–14] and references cited therein). As an alternative systematic approach to direct integration of the response of many-electron systems to an intense laser field, we have recently developed the Intense-Field Many-Body S-Matrix Theory [15–17]. Using Feynman's diagrammatic technique we have already analyzed the lowest order term of the S-matrix series for the double ionization process [15–17] and could identify the leading diagram for the process [15–18]. Furthermore, we have extended this lowest order diagram systematically to all orders and presented a first estimation of the total rates of laser-induced double ionization [14]. Here, we investigate these diagrams, propose a simple model formula for the total rates of

the process [19], and compare the predicted single- and double-ionization rates *per atom*, as well as the single- and double-ionization *yields*, and the *ratio* of nonsequential double ionization to single ionization for He, with the experimental data.

2. ENERGY-SHARING DIAGRAM

We shall not repeat the analysis of the Intense-Field Many-Body S-matrix series for the laser-induced double ionization process, the details of which are given and discussed elsewhere [15–17], but present the systematic extension of the leading diagram in the S-matrix series in Fig. 1 (cf. [14]). This diagram includes the essential physical steps of the energy sharing mechanism of nonsequential double ionization, that we have identified by analyzing the lowest order term of the S-matrix series [15–17]. We note that a similar process has been investigated independently by Kuchiev [20]. Reading the diagram in Fig. 1 from the bottom upwards (the assumed direction of the flow of time) we see first that one of the electrons, say electron (1), absorbs (virtually) a large number of photons in an ATI-like one-electron process and goes into the intermediate Volkov states of momenta {k}, while, at the same time, the second electron propagates in the intermediate eigenstates,
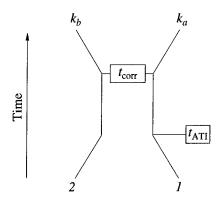
Fig. 1. Energy-sharing diagram for laser-induced double ionization of He. The flow of time is assumed from the bottom upwards, as indicated; straight lines stand for the evolution of the two electrons, (1) and (2). t_{ATI} is the full one-electron ATI-like electron–field interaction operator and t_{corr} incorporates the e–e correlation operator to all orders (cf. Figs. 2a and 2b, respectively); $\mathbf{k}_a$ and $\mathbf{k}_b$ are the final momenta.

Fig. 2. Diagrams showing (a) the extension of the electron–field interaction in the t_{ATI}-matrix, including in the higher orders the rescattering interactions of the Volkov electron with the screened potential V_s, and (b) the generalization of the e–e correlation interaction, V_c, to all orders in the t_{corr}-matrix. The other symbols have the same significance as in Fig. 1.

$\{j\}$, of the residual ion. The first-order term of the corresponding full one-electron t_{ATI}-matrix (cf. Fig. 2a) involves the interaction of the active electron with the field only, while in the higher orders it propagates in the intermediate Volkov states and rescatters from the potential $V_s = \langle\Phi_j(\mathbf{r}_2)| - \dfrac{1}{r_1} + \dfrac{1}{r_{12}} |\Phi_j(\mathbf{r}_2)\rangle$, where $\Phi_j(\mathbf{r}_2)$ is the wavefunction of the intermediate jth state of the He$^+$ ion. Following this ATI-like process the first electron shares its absorbed photon energy with the second electron through the electron–electron correlation interaction, $V_c = 1/r_{12}$ (see Fig. 1), generalized to all orders in the t_{corr}-matrix, as shown in Fig. 2b.

3. MODEL FORMULA

The analytical amplitude corresponding to the diagram in Fig. 1 can be expressed as (cf. [14])

$$S(t, -\infty) = -i\int_{-\infty}^{t} dt' \exp\left(i\frac{k_a^2 + k_b^2}{2}t'\right)$$

$$\times \langle\Psi_{\mathbf{k}_a}^C(\mathbf{r}_1)\Psi_{\mathbf{k}_b}^C(\mathbf{r}_2)|t_{\mathrm{corr}}\int_{-\infty}^{t'} dt_1 G^0(t', t_1) \tag{1}$$

$$\times t_{ATI}|\Phi_i(\mathbf{r}_1, \mathbf{r}_2)\rangle\exp(iE_B t_1),$$

where $\Phi_i(\mathbf{r}_1, \mathbf{r}_2)$ is the initial state wavefunction and E_B is the binding energy of the atom. $\Psi_{\mathbf{k}_a}^C(\mathbf{r}_1)$ and $\Psi_{\mathbf{k}_b}^C(\mathbf{r}_2)$ are the Coulomb wavefunctions of momenta $\mathbf{k}_a$ and $\mathbf{k}_b$, respectively, and $G^0(t', t_1)$ is the intermediate

ionic $\otimes$ Volkov Green's function (cf. [15, 22]):

$$G^0(t', t_1) = -i\Theta(t' - t_1)\sum_{\{j\}}(2\pi)^{-3}\int d\mathbf{k} \tag{2}$$

$$\times |\Phi_j^C(\mathbf{r}_2, t')\Phi_{\mathbf{k}}^V(\mathbf{r}_1, t')\rangle\langle\Phi_j^C(\mathbf{r}_2, t_1)\Phi_{\mathbf{k}}^V(\mathbf{r}_1, t_1)|,$$

where $\Phi_{\mathbf{k}}^V(\mathbf{r}_1, t)$ is the Volkov state of the free electron of momentum $\mathbf{k}$ [23].

Using the Floquet representation for the Volkov Green's function (cf. [15, 22, 24]), carrying out the t_1- and t'-time integrations and taking the limit $t \longrightarrow \infty$ the amplitude (1) can be written for a linearly polarized laser field as

$$S(\infty, -\infty) = -2\pi i$$

$$\times \sum_{N=-\infty}^{\infty} \delta\left(N\omega - E_B - \frac{k_a^2 + k_b^2}{2}\right)T^{(N)} \tag{3}$$

with

$$T^{(N)} = \sum_{n=-\infty}^{\infty}\int d\mathbf{k}\sum_{\{j\}}T_{\mathrm{corr}}(\mathbf{k}_a, \mathbf{k}_b; \mathbf{k}, j)$$

$$\times \frac{J_{n-N}\left(\boldsymbol{\alpha}_0\cdot\mathbf{k}; \dfrac{U_p}{2\omega}\right)}{\dfrac{k^2}{2} + (E_B - E_j) + U_p - n\omega + i0}T_{ATI}(\mathbf{k}, j; i). \tag{4}$$

$T_{\mathrm{corr}}(\mathbf{k}_a, \mathbf{k}_b; \mathbf{k}, j)$ is the matrix element of the (field-free) energy sharing process via e–e correlation (cf. t_{corr} in Fig. 2b) between the intermediate ionic $\otimes$ free electron continuum state and the two-electron state of momenta $\mathbf{k}_a$ and $\mathbf{k}_b$; $T_{ATI}(\mathbf{k}, j; i)$ is the T-matrix element of the one-electron ATI process (cf. t_{ATI} in Fig. 2a). $J_n(a; b)$ is the generalized Bessel function of two arguments (e.g., [25, 26]), E_j is the energy of the intermediate jth state of the ion, $\alpha_0 = \sqrt{I}/\omega^2$ is the quiver radius, and $U_p = I/4\omega^2$ is the ponderomotive energy.

To proceed further, we first carry out the k-integration in (4) assuming the pole approximation and estimate the $\hat{\Omega}_k$-integration by the major contribution for emission of the electron along the polarization axis $\hat{\epsilon}$ in the ATI-like process. In former calculations [17, 18] we found quite generally that the intermediate ground state of the He$^+$ ion dominates greatly over the excited intermediate states; thus, we further neglect the latter ones. We obtain from the amplitude for the double ionization process, (3) and (4):

$$S(\infty, -\infty)$$

$$= -2\pi i \sum_{n=n_0}^{\infty} \sum_{m=-\infty}^{\infty} \delta\left((n+m)\omega - E_B - \frac{k_a^2 + k_b^2}{2}\right)$$

$$\times T_{\text{corr}}(\mathbf{k}_a, \mathbf{k}_b; \mathbf{k}_n \parallel \hat{\epsilon}, 1s) J_{-m}\left(\alpha_0 k_n; \frac{U_p}{2\omega}\right)$$

$$\times (-i\pi) k_n T_{ATI}(\mathbf{k}_n \parallel \hat{\epsilon}, 1s; i)$$

with $\dfrac{k_n^2}{2} = n\omega - (E_B - E_{1s}) - U_p$ and $m = N - n$. The total

rates of double ionization per He atom, i.e., the total probability per unit time, can then be expressed as (we further neglect the mixed terms in the sum over m)

$$\Gamma^{++} = \sum_{n=n_0}^{\infty} \Gamma_{\text{corr}}^{(n)} \frac{\pi k_n}{2} \Gamma^{(n)}(\mathbf{k}_n \parallel \hat{\epsilon}),\qquad(6)$$

where

$$\Gamma_{\text{corr}}^{(n)} = \sum_{m=-\infty}^{\infty} \Gamma_{\text{corr}}(E_{n,m}) J_m^2\left(\alpha_0 k_{n,m}; \frac{U_p}{2\omega}\right)\qquad(7)$$

with

$$E_{n,m} = \frac{k_{n,m}^2}{2} = \frac{k_n^2}{2} + m\omega + U_p.\qquad(8)$$

The above expression, (6), for the total rate of double ionization, Γ^{++}, based on the diagram in Fig. 1, enables one to carry out calculations in a relatively simple manner. This is due to the fact that the contribution from each n to the process can be calculated independently and added together in the end. We note that formula (6) is a quantum version of the semiclassical formula obtained by us earlier [14]. The factor $\Gamma^{(n)}(\mathbf{k}_n \parallel \hat{\epsilon})$ is nothing but the n-photon one-electron differential ATI rate (per atomic electron) parallel to the polarization axis. It can be calculated as for any effective one-electron system, e.g., (a) by exact numerical simulation, or it can even be obtained from (b) the experimental measurement of the single-electron ATI spectrum over a sufficiently wide range of energy and intensity, or it may be (c) estimated by approximately evaluating the

diagram in Fig. 2a (as will be done in the present application below). The factor $\Gamma_{\text{corr}}^{(n)}$ is the rate of energy sharing between the intermediate Volkov electron and the residual ionic electron via the e–e correlation. It includes a sum according to the possibility of absorption or emission of m additional photons of the Volkov electron during its propagation in the laser field. This results in an infinite set of intermediate "incident" energies, $E_{n,m}$, of the "active" electron, for a final "e–2e"-like energy sharing reaction process. $\Gamma_{\text{corr}}(E_{n,m})$ is the (field-free) rate of sharing of the energy $E_{n,m}$ by the residual ionic electron (in the ground state of the ion) via the e–e correlation. At the end of this energy sharing process the 'incident' electron emerges with the momentum $\mathbf{k}_a$ and the ionic electron emerges with the momentum $\mathbf{k}_b$. This rate is weighted by the square of a generalized Bessel function, as given by (7). $\Gamma_{\text{corr}}(E_{n,m})$ can also be obtained independently, either, as in the theory of "e–2e" reactions (e.g., [27, 28] and references cited therein) or, more simply, from the available semiempirical formulas, e.g., that due to Lotz [29].

4. ATI SPECTRUM AND 'RESCATTERING'

For the present purpose we have estimated the single-electron ATI rates in He, $\Gamma^{(n)}(\mathbf{k}_n)$, by evaluating the diagrams in Fig. 2a approximately as follows: the integrals over the coordinates, $\mathbf{r}_1$ and $\mathbf{r}_2$, are calculated analytically. The integrations over the intermediate momenta in successive order are carried out by assuming the pole approximation and taking the contribution along the polarization axis. We note that these steps are similar to those we have used while estimating the k-integration in the double ionization amplitude [cf. the paragraph below (4)]. Finally we neglect the mixed terms, corresponding to an averaging over many rapidly changing

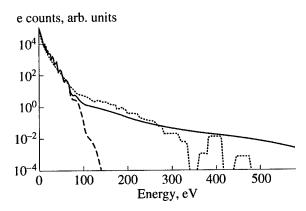e counts, arb. units

Fig. 3. Single-electron angle-integrated ATI rates per He atom as a function of the electron energy at a laser wavelength of 780 nm and an intensity of 8.5×10^{14} W/cm^2. The theoretical rates with (solid line) and without rescattering (dashed line) have been scaled for the purpose of comparison to the experimental data (dotted line, from [8]) at $E = 1.8$ eV.
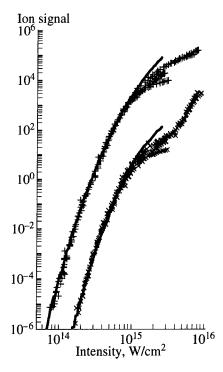
Ion signal

Fig. 4. Theoretical rates per atom of laser-induced single (left-hand curve) and double ionization (right-hand curve), obtained from the present energy-sharing model formula, (6), as a function of intensity at a laser wavelength of 780 nm. The theoretical predictions are compared with the experimental He^+ ("+") and He^{++} yields ("×"), measured by Walker et al. [7]. The intensities used in the calculations have been shifted by a factor of 0.87 within the experimental accuracy. The rates have been scaled by matching the theoretical result for single ionization with the experimental data point at the saturation intensity, $I = 0.8 \times 10^{15}$ W/cm^2.

interference terms, while squaring and summing the successive partial t_{ATI}-matrix elements.

In Fig. 3 we present the angle-integrated ATI spectrum of laser-induced single ionization of He at a wavelength $\lambda = 780$ nm and an intensity $I = 0.85 \times 10^{15}$ W/cm^2. The theoretical rates per atom (solid line), predicted by the present theory, are compared as a function of the electron energy, with the experimental data obtained by Sheehy et al. [8] (dotted line). For the purpose of comparison we have taken the experimental data from [8] and scaled the theoretical rates by matching the value at a point, $E = 1.8$ eV, with the experimental signal at that point. It is seen from the comparison that the calculated rates and the measured signal are in a remarkably good agreement with each other over a wide range of energies. The result further shows the qualitative difference brought about in the spectrum by the influence of rescattering. This can be seen by comparing the spectrum obtained without rescattering (dashed line) with that obtained by including the first-order rescattering (solid line). In fact, the results are very similar up to about 70 eV then they differ greatly with increasing energy: the results of the 1-rescattering calculation

exceed the no-rescattering results at high energies by many orders of magnitude. We point out that the contribution of higher order rescattering, that can be included relatively simply in the present model calculation, has been estimated to be less than a per cent with respect to the 1-rescattering result. Finally, we may note that a change of the slope in the ATI spectrum due to the rescattering of the emitted electron with the residual (ionic) core has also been observed in numerical simulations in H atom [30] and some other model calculations (e.g., [14, 31–33] and references cited therein).

5. SINGLE IONIZATION AND NONSEQUENTIAL DOUBLE IONIZATION

In this section we apply the model formula, (6), to analyze the experimental data obtained for the single and non-sequential double ionization of He at a laser wavelength of 780 nm and in a domain of intensity between about 10^{14} and 10^{16} W/cm^2 [7]. In view of the good agreement between the calculated results for the ATI spectrum and the experimental data, shown in Fig. 3, we shall use below, the 1-rescattering results for $\Gamma^{(n)}(\mathbf{k}_n \parallel \hat{\varepsilon})$. We shall also approximate $\Gamma_{corr}(E_{n,m})$, cf. (7), by the well-known Lotz formula [29] for the "e–2e" reaction in He^+ ion. The total (energy integrated) rates (per atom or ion) of single ionization of He atom and He^+ ion, respectively, have been calculated using the well-known KFR amplitude [25, 34, 35]; we note that this corresponds to the no-rescattering approximation of the present theory of ATI amplitude discussed above.

5.1. Rates Per Atom

In Fig. 4 we present the theoretical rates per atom of laser-induced single ionization (left-hand curve) and double ionization (right-hand curve) of neutral He, obtained from the present model formula, as a function of the laser intensity at a wavelength of 780 nm and compare them with the corresponding experimental signals of single ("+") and double ionization ("×") obtained by Walker et al. [7]. We note that the calculated rates have been shifted by a factor of 0.87 in intensity, in accordance with the accuracy of the intensity measurement in the experiment [7]. For the purpose of comparison we have scaled the theoretical rates per He atom by matching the single ionization rate at the saturation intensity, $I = 0.8 \times 10^{15}$ W/cm^2, with the corresponding single ionization data point. It is seen from the figure that the results predicted by the present theory and the measured signals for both single and double ionization are in remarkably good agreement with each other, right up to the saturation intensity. The difference between theoretical rates per atom and the experimental ion yields at intensities above the saturation intensity can be shown to be due to the depletion of the neutral target atoms initially present in interaction volume.

5.2. Ion Yields

Thus, given the excellent agreement between the theoretical rates per atom and the experimental data in the sub-saturation region (see Fig. 3), we can use these results further to evaluate the He^+ and He^{++} yields. To this end, we have first calculated a spatial average of the rates per atom, assuming a Gaussian beam profile, and then solved the coupled rate equations of the three processes, assuming a Gaussian pulse with a pulse length of 160 fs. We have also scaled the rates by a constant factor to match the single ionization rate with the observed saturation rate for production of He^+ at 0.8×10^{15} W/cm^2 [36]. Finally, we have taken account of the usual $I^{\frac{3}{2}}$-expansion of the Gaussian focal volume beyond the saturation points [7, 38].

In Fig. 5 we present the calculated He^+ ion signal (left-hand solid curve) and the He^{++} ion signal (right-hand solid curve), along with the experimental He^+ ("+") and He^{++} yields ("x") measured by Walker *et al.* [7]. From the comparison it is clearly seen that the calculated and the experimental yields for both the single and the double ionization are in remarkably good agreement for the intensities considered in the experiment. To the best of our knowledge, this is the first time such a good agreement could be obtained for the ion yields over the entire intensity range, from a theory giving the basic rates per atom of single ionization, as well as of nonsequential and sequential double ionization of He.

5.3. Origin of the "Knee" Structure

Note the occurrence of the ubiquitous "knee" structure in the He^{++} yield in Fig. 5. From the comparison of the results with (right-hand solid curve) and without (dotted curve) the contribution of the nonsequential double ionization, it is seen that below 0.8×10^{15} W/cm^2 the production of He^{++} ion arises from the nonsequential double ionization of the neutral He atom alone. Beyond this intensity the nonsequential double ionization is influenced by the depletion of He atom in the interaction volume, which results in a significant change of the slope of the He^{++} yield. In the saturation regime with increasing intensity the nonsequential production of He^{++} ion competes with the single ionization of He^+ ion. From the figure it is seen that the latter process dominates at intensities above about 4×10^{15} W/cm^2, which results in a second change of the slope of the He^{++} yield, giving rise to the "knee" structure. The "knee" structure appears, therefore, to be due to the joint processes of saturation of the nonsequential production of He^{++} ion, followed by the dominance of its sequential production. We note that the prediction of accurate nonsequential double ionization rates per atom is the single most important ingredient for the agreement obtained here between the theoretical results and the experimental yields.
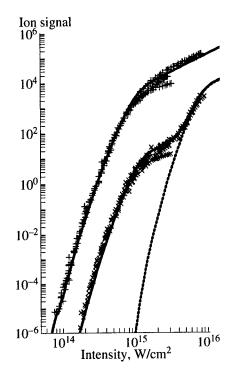
Fig. 5. Comparison of the calculated He^+ (left-hand solid curve) and He^{++} yields (right-hand solid curve) with the experimental He^+ ("+") and He^{++} yields ("x"). Note the occurrence of the "knee" structure in the He^{++} yields, both in the theoretical result and in the experimental data, which is not present if the contribution of nonsequential double ionization is neglected (dotted line).
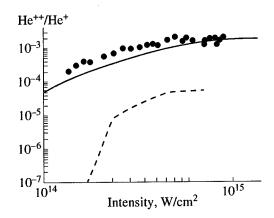
Fig. 6. Ratio of double to single ionization as a function of the laser intensity. The predictions of the present theory (solid line) are shown along with the experimental data ("•," from [7, 8]) and compared with that of an extended "simple man's model" (dashed line, from [8]) [8, 39].

5.4. Ratio of Double to Single Ionization

A sensitive test of the results of nonsequential double ionization is provided by the He^{++}/He^+ ratio as a function of the laser intensity. In Fig. 6 we show the predictions of the present theory (solid line) and compare them with the measured ratio ("x," from [7, 8]).

The comparison shows that the theoretical and experimental results are in reasonable agreement with each other. The significance of this agreement becomes obvious by the comparison with the best results of this ratio obtained so far from an extension of the early "simple man's model" (dashed line, from [8]) (cf. [8, 39]), which underestimates the experimental data by more than an order of magnitude.

5.5. The Energy-Sharing Mechanism

In view of the present agreement between the predictions of the energy sharing model formula, (6), and the experimental data over the entire range of measured intensities (in particular, at subsaturation intensities) we may emphasize the role of e–e correlation and the associated energy-sharing mechanism for the nonsequential double ionization of He in intense laser fields at a laser wavelength of 780 nm. As discussed above the mechanism consists in the sharing of photon energy initially absorbed by one electron (in an intermediate ATI-like process) by the other via the e–e correlation until they both have enough energy to escape together from the binding force of the nucleus. This result confirms the conclusions of our earlier analysis of the process [14–18, 22]. It should be noted that the nonsequential double ionization process is a prototype of a "cooperative" quantum phenomenon at its most rudimentary form: two-particle joint escape by energy sharing via the e–e correlation.

CONCLUSIONS

We have obtained a simple model expression for the total rate of laser-induced nonsequential double ionization of atoms by extending the previously identified leading diagram for the process to all orders and summing them approximately. The model formula, (6), is applied to analyze the nonsequential double ionization data of He, obtained by Walker et al. [7], at 780 nm. Comparison between the experimental data and the model predictions shows a remarkable agreement with both the single- and double-ionization processes over the entire range of intensities considered in the experiment, including the formation of the "knee" structure. The analysis carried out reveals the central importance of e–e correlation effects in the intermediate and final states for the laser-induced nonsequential double ionization process considered.

ACKNOWLEDGMENTS

REFERENCES

1. Augst, S., Meyerhofer, D.D., Strickland, D., and Chin, S.L., 1991, *J. Opt. Soc. Am. B*, **8**, 858.

2. Fittinghoff, D.N., Bolton, P.R., Chang, B., and Kulander, K.C., 1992, *Phys. Rev. Lett.*, **69**, 2642.

3. Peatross, J., Buerke, B., and Meyerhofer, D.D., 1993, *Phys. Rev. A*, **47**, 1517.

4. Walker, B., Mevel, E., Yang, B., et al., 1993, *Phys. Rev. A*, **48**, R894.

5. Kondo, K., Sagisaka, A., Tamida, T., et al., 1993, *Phys. Rev. A*, **48**, R2531.

6. Fittinghoff, D.N., Bolton, P.R., Chang, B., and Kulander, K.C., 1994, *Phys. Rev. A*, **49**, 2174.

7. Walker, B., Sheehy, B., DiMauro, L.F., et al., 1994, *Phys. Rev. Lett.*, **73**, 1227.

8. Sheehy, B., Walker, B., Lafon, R., et al., 1997, *Multiphoton Processes 1996*, Int. Phys. Conf. Ser., no. 154, Lambropoulos, P. and Walther, H., Eds. (Bristol: IOP), 106.

9. Parker, J., Taylor, K.T., Clark, C.W., and Blodgett-Ford, S., 1996, *J. Phys. B*, **29**, L33.

10. Taylor, K.T., Parker, J.S., Dundas, D.,et al., 1997, *Multiphoton Processes 1996*, Int. Phys. Conf. Ser., no. 154, Lambropoulos, P. and Walther, H., Eds. (Bristol: IOP), 56.

11. Dimou, L. and Faisal, F.H.M., 1996, *ICOMP VII, September 30–October 4, Garmisch-Partenkirchen, Book of Abstracts*, Lambropoulos, P. and Walther, H., Eds., A33.

12. Watson, J.B., Sanpera, A., Burnett, K., et al., 1997, *Multiphoton Processes 1996*, Int. Phys. Conf. Ser., no. 154, Lambropoulos, P. and Walther, H., Eds. (Bristol: IOP), 132.

13. Watson, J.B., Sanpera, A., Lappas, D.G., et al., 1997, *Phys. Rev. Lett.*, **78**, 1884.

14. Faisal, F.H.M. and Becker, A., 1997, *Laser Phys.*, **7**, 684.

15. Faisal, F.H.M. and Becker, A., 1996, *Selected Topics on Electron Physics*, Campbell, D.M. and Kleinpoppen, H., Eds. (New York: Plenum), 397.

16. Faisal, F.H.M., and Becker, A., 1997, *Multiphoton Processes 1996*, Int. Phys. Conf. Ser., no. 154, Lambropoulos, P. and Walther, H., Eds. (Bristol: IOP), 118.

17. Becker, A., 1997, *PhD Thesis* (Universität Bielefeld).

18. Becker, A. and Faisal, F.H.M., 1996, *J. Phys. B*, **29**, L197.

19. This formula removes a classical trajectory approximation used earlier [14] in part of the amplitude, by a fully quantum expression [cf. Eqs. (6)–(8)].

20. Kuchiev, M.Yu., 1987, *Sov. Phys. JETP Lett.*, **45**, 404; 1995, *J. Phys. B*, **28**, 5093; *Phys. Lett. A*, **212**, 77. We note, however that application of his formula to the double ionization processes yields results which deviate significantly from the experimental data (see [21]).

21. Talebpour, A., Chien, C.Y., Liang, Y., et al., 1997, *J. Phys. B*, **30**, 1721.

22. Faisal, F.H.M. and Becker, A., 1996, *Super-Intense Laser-Atom Physics IV*, Muller, H.G. and Federov, M.V., Eds. (Dordrecht: Kluwer Academic), 317.

23. Wolkow, D.M., 1935, *Zeit. f. Phys.*, **94**, 250.

24. Becker, A. and Faisal, F.H.M., 1994, *Phys. Rev. A*, **50**, 3256.

25. Reiss, H.R., 1980, *Phys. Rev. A*, **22**, 1786.

26. Faisal, F.H.M., 1989, *Comp. Phys. Rep.*, **9**, no. 2.

27. Jetzke, S. and Faisal, F.H.M., 1992, *J. Phys. B*, **25**, 1543; 1992, *ibid.*, **25**, L269.

28. Becker, A., Jetzke, S., and Faisal, F.H.M., 1994, *Hyperfine Interactions*, **89**, 83; Becker, A., 1994, *Diplom Thesis* (Universitat Bielefeld).

29. Lotz, W., 1968, *Zeit. f. Phys.*, 216, 241; 1970, *ibid.*, **232**, 101.

30. Cormier, E. and Lambropoulos, P., 1997, *J. Phys. B*, **30**, 77.

31. Lohr, A., Becker, W., and Kleber, M., 1997, *Multiphoton Processes 1996*, Lambropoulos, P. and Walther, H., Eds., (Bristol: IOP), 87.

32. Kaminski, J.Z. and Ehlotzky, F., 1997, *J. Phys. B*, **30**, 69.

33. Lohr, A., Kleber, M., Kopold, R., and Becker, W., 1997, *Phys. Rev. A*, **55**, R4003.

34. Keldysh, L.V., 1964, *Zh. Eksp. Teor. Fiz.*, **47**, 1945 [1965, *Sov. Phys. JETP*, **20**, 1307].

35. Faisal, F.H.M., 1973, *J. Phys. B*, **6**, L89.

36. The factor may be interpreted as a modification of the KFR rates at the saturation intensity, arising from a non-vanishing asymptotic Coulomb charge (cf. [37]).

37. Krainov, V.P., 1997, *J. Opt. Soc. Am. B*, **14**, 425.

38. Cervenan, M.R. and Isenor, N.R., 1975, *Opt. Commun.*, **13**, 175.

39. Corkum, P.B., 1993, *Phys. Rev. Lett.*, **71**, 1994.

Coulomb Correction to the Volkov Solution

J. Bauer*,**

* *Centrum Fizyki Teoretycznej PAN, Al. Lotników 32/46, Warsaw 02-668, Poland*
** *Katedra Fizyki Jądrowej i Bezpieczeństwa Radiacyjnego Uniwersytetu Łódzkiego,
Ul. Pomorska 149/153, Łódź, 90-236 Poland*
e-mail: bauer@krysia.uni.lodz.pl
Received August 6, 1997

Abstract—A simple analytical approximation exists for the wave function of an unbound electron interacting both with a strong, circularly polarized laser field and an atomic Coulomb potential [1]. This wave function is the Volkov state with a first-order Coulomb correction coming from some perturbative expansion of the potential in the Kramers–Henneberger reference frame [2–4]. The expansion is valid if the distance from the center of the Coulomb force is smaller than the classical radius of motion of a free electron in a plane-wave field. We generalize this approach for any elliptic polarization. The total photoionization rate in the strong-field approximation grows more for linear than for circular polarization due to Coulomb correction.

An exact analytical solution of the Schrödinger equation, for a charged particle interacting both with an attractive Coulomb potential and a plane-wave electromagnetic field, has never been found. This equation is exactly solvable if one of the fields vanishes. Thus, when either field dominates, the other one can be treated perturbatively. In the present paper, we fix our attention on the situation when the radiation field dominates the Coulomb potential. This is true for the final state of an outgoing electron in a process of a strong-field photoionization or photodetachment. The exact solution of the Schrödinger equation for a free, charged particle oscillating in a plane-wave electromagnetic field is known as the Volkov or Gordon–Volkov wave function [5, 6]. In this equation, the field depends only on time (the dipole approximation). The Volkov wave function has been used in many approximate calculations concerning ionization of atoms [7–9] and other applications (see also references in [1]). Many authors have introduced corrections due to Coulomb potential to the Volkov-type solutions in various ways [1, 7, 10–17].

The Coulomb correction of Reiss and Krainov [1] has a very simple form, derivation, and physical interpretation. The Volkov wave function with this correction is applicable when the laser field is strong enough to force the unbound electron to move in an almost circular orbit at a distance much larger than atomic radius from the nucleus. The improved wave function differs from an ordinary nonrelativistic Volkov state only by a simple shift in energy. But this leads to significant changes in the description of strong-field ionization. For typical laser frequencies, applied in experiments, the lower applicability limit of radiation intensity decreases considerably in the strong-field approximation (SFA). Moreover, at this lower intensity limit, the growth of the total ionization rate due to Coulomb correction may be of even a few orders of magnitude. As intensity grows, the difference between the Coulomb-

corrected strong-field approximation (CSFA) and the ordinary SFA vanishes. When intensity acquires the lower applicability limit of the ordinary SFA, both ionization rates are very close to each other. In this way, the CSFA confirms the validity of the SFA. There is the only weakness of the CSFA, that it is limited only to the circular polarization. Below we show how to overcome this limitation.

The Schrödinger equation to be solved is

$$\left[i\frac{\partial}{\partial t} - \frac{1}{2}\left(-i\nabla + \frac{1}{c}\mathbf{A}(t)\right)^2 - V(\mathbf{r})\right]\Psi(\mathbf{r}, t) = 0, \quad (1)$$

with

$$V(\mathbf{r}) = -\frac{Z}{r} \quad (2)$$

(atomic units are used throughout the paper), Z is the charge of the nucleus, the distance between the electron and the nucleus is $r = |\mathbf{r}|$, and $\mathbf{A}(t)$ is the vector potential for electromagnetic field in radiation gauge, in the dipole approximation, with the boundary condition $\lim_{t \to \pm\infty} \mathbf{A}(t) = \mathbf{0}$. The field propagates as an elliptically polarized plane wave of frequency ω in the direction of the z-axis,

$$\mathbf{A}(t)$$
$$= a(\hat{e}_x\cos(\omega t)\cos(\xi/2) \pm \hat{e}_y\sin(\omega t)\sin(\xi/2)). \quad (3)$$

In equation (3), $\hat{e}_x$ and $\hat{e}_y$ are real unit vectors along the x- and y-axes. Polarization is described by the ellipticity ξ ($0 \leq \xi \leq \pi/2$, $\xi = 0$ for linear and $\xi = \pi/2$ for circular polarization). The upper and the lower signs in equation (3) refer to the right and the left elliptic polarization, respectively. (Note that, according to (3), the radiation intensity $I = (a\omega/c)^2$ in atomic units for any polarization.) The vector potential $\mathbf{A}(t)$ is a linear com-

bination of two vector potentials, one for the right and the other for the left circular polarization:

$$\mathbf{A}(t) = \lambda_R \mathbf{A}_R(t) + \lambda_L \mathbf{A}_L(t), \qquad (4)$$

where λ_R, λ_L are real and nonnegative, and $\lambda_R^2 + \lambda_L^2 = 1$ [$\mathbf{A}_R(t)$, $\mathbf{A}_L(t)$ are also given by equation (3) with $\xi = \pi/2$, the plus and the minus sign, respectively]. We can assume, without a loss of generality, that $\lambda_R \geq \lambda_L$, and, hence, $1 \geq \lambda_R \geq 1/\sqrt{2}$. Now we apply the KH transformation to the frame of reference whose origin moves with the vector

$$\boldsymbol{\alpha}_R(t) = -\frac{\lambda_R}{c} \int_{-\infty}^{t} \mathbf{A}_R(\tau)d\tau, \qquad (5)$$

given by the stronger circular component of the vector potential. The KH transformation is a unitary one, given by the operator

$$\hat{U} = \exp\left[-i\boldsymbol{\alpha}_R(t)\mathbf{p} + i\int_{-\infty}^{t} \frac{\lambda_R^2 \mathbf{A}_R(\tau)^2}{2c^2}d\tau\right]. \qquad (6)$$

We transform equation (1) according to the well-known prescription for the wave functions and the operators ($\Phi = \hat{U}\Psi$, and $\hat{O}' = \hat{U}\hat{O}\hat{U}^{-1}$). The transformed equation is

$$i\frac{\partial}{\partial t}\Phi(\mathbf{r}, t) = \left[\frac{1}{2}\left(-i\nabla + \frac{\lambda_L}{c}\mathbf{A}_L(t)\right)^2 \right.$$
$$\left. + \frac{\lambda_R \lambda_L}{c^2}\mathbf{A}_R(t)\mathbf{A}_L(t) + V(\mathbf{r} - \boldsymbol{\alpha}_R(t))\right]\Phi(\mathbf{r}, t). \qquad (7)$$

Applying the approximation

$$V(\mathbf{r} - \boldsymbol{\alpha}_R(t)) = -\frac{Z}{|\mathbf{r} - \boldsymbol{\alpha}_R(t)|} \cong -\frac{Z}{|\boldsymbol{\alpha}_R(t)|} = -\frac{Z}{\alpha_R}, \qquad (8)$$

we make equation (7) solvable. Instead of $\lambda_R \mathbf{A}_R(t)$, we could also use the weaker circular component $\lambda_L \mathbf{A}_L(t)$ of the vector potential (if $\lambda_L \neq 0$), in equations (5)–(7). But, apparently, the exactness of approximation (8) would be worse then. The solution of equation (7), with approximation (8), is just a Volkov vector times some function of time. Returning, through the inverse unitary transformation, to the original wave function Ψ, we obtain

$$\Psi_{\mathbf{p}}^{CV}(\mathbf{r}, t) = \Psi_{\mathbf{p}}^{V}(\mathbf{r}, t)\exp\left(i\frac{Z}{\alpha_R}t\right)$$
$$= \frac{1}{\sqrt{V}}\exp\left[i\mathbf{p}\mathbf{r} - \frac{i}{2}\int_{-\infty}^{t}\left(\mathbf{p} + \frac{1}{c}\mathbf{A}(\tau)\right)^2 d\tau + i\frac{Z}{\alpha_R}t\right]. \qquad (9)$$

This modified Volkov solution may be applied in the S matrix element, to calculate ionization rate in the SFA. One can easily understand this change as a simple radiation frequency, intensity, and polarization (through the parameter $\lambda_R = \cos(\xi/2 - \pi/4)$) dependent decrease of the binding energy [1]:

$$E_B(\omega, I) = E_B - \frac{Z}{\alpha_R(\omega, I)} = E_B - \sqrt{2}\frac{Z\omega^2}{\lambda_R\sqrt{I}}. \qquad (10)$$

For the linear polarization, the shift is greater ($\lambda_R = 1/\sqrt{2}$) than for the circular one ($\lambda_R = 1$). Thus, the SFA total ionization rate grows more for the linear polarization than for the circular one, due to Coulomb correction. For the circular polarization, our calculation reduces to that of Reiss and Krainov [1].

REFERENCES

1. Reiss, H.R. and Krainov, V.P., 1994, *Phys. Rev. A*, **50**, R910.
2. Pauli, W. and Fierz, M., 1938, *Nuovo Cimento*, **15**, 167.
3. Kramers, H.A., 1956, *Collected Scientific Papers* (Amsterdam: North-Holland).
4. Henneberger, W.C., 1968, *Phys. Rev. Lett.*, **21**, 838.
5. Gordon, W., 1926, *Z. Phys.*, **40**, 117.
6. Volkov, D.M., 1935, *Z. Phys.*, **94**, 250.
7. Keldysh, L.V., 1964, *Zh. Eksp. Teor. Fiz.*, **47**, 1945 [1965, *Sov. Phys. JETP*, **20**, 1307].
8. Nikishov, A.I. and Ritus, V.I., 1966, *Zh. Eksp. Teor. Fiz.*, **50**, 255 [1966, *Sov. Phys. JETP*, **23**, 168].
9. Reiss, H.R., 1980, *Phys. Rev. A*, **22**, 1786; Reiss, H.R., 1987, *J. Phys. B*, **20**, L79; Reiss, H.R., 1992, *Phys. Rev. A*, **46**, 391.
10. Perelomov, A.M., Popov, V.S., and Terent'ev, M.V., 1966, *Zh. Eksp. Teor. Fiz.*, **50**, 1393 [1966, *Sov. Phys. JETP*, **23**, 924].
11. Nikishov, A.I. and Ritus, V.I., 1967, *Zh. Eksp. Teor. Fiz.*, **52**, 223 [1967, *Sov. Phys. JETP*, **25**, 145].
12. Perry, M.D., Szoke, A., Landen, O.L., and Campbell, E.M., 1988, *Phys. Rev. Lett.*, **60**, 1270.
13. Basile, S., Trombetta, F., Ferrante, G., et al., 1988, *Phys. Rev., A*, **37**, 1050; Basile, S., Trombetta, F., and Ferrante, G., 1988, *Phys. Rev. Lett.*, **61**, 2435.
14. Pan, L., 1989, *J. Mod. Opt.*, **36**, 877.
15. Mittleman, M.H., 1994, *Phys. Rev. A*, **50**, 3249.
16. Krainov, V.P. and Shokri, B., 1995, *Zh. Eksp. Teor. Fiz.*, **107**, 1180; Krainov, V.P., 1997, *J. Opt. Soc. Am. B*, **14**, 425.
17. Kamiński, J.Z., Jaroń, A., and Ehlotzky, F., 1996, *Phys. Rev. A*, **53**, 1756.

Photoelectron Energy Spectra in Photodetachment Assisted by a Bichromatic Low-Frequency Field

S. Bivona, R. Burlon, and C. Leone

INFM (Istituto Nazionale di Fisica della Materia) and Dipartimento di Energetica e Applicazioni di Fisica, Viale delle Scienze, Palermo, 90128 Italy

e-mail: Burlon@cuc.unipa.it

Received September 2, 1997

Abstract—We report on the effect of the relative phase of two low-frequency (LF) fields assisting the photodetachment of a negative atomic ion by a weak electromagnetic field, when a large number of LF photons is exchanged. In the case in which the frequencies of the LF fields are commensurate, the photodetachment probability amplitude is obtained as a coherent sum of partial amplitudes, each of which is associated to processes in which a different number of LF photons leading to the same final state of the ejected electron is exchanged. As a result, photoelectron energy spectra and angular distributions are found that are strongly affected by the relative phase the LF fields.

INTRODUCTION

It is well established that when two radiation fields with well defined relative phase illuminate an atomic system, provided each of the fields may excite the system to the same final state, the transition rate may be controlled by varying the relative phase of the driving fields. Over the last decade, quantum control of elementary processes is different areas of physics and photochemistry, based on quantum interference, has been object of both theoretical and experimental studies [1].

Recently we have investigated the effect of the relative phase of a low-frequency (LF) bichromatic field

$$\mathbf{E}(t) = E_1[\sin\omega_1 t + \sin(\omega_2 t + \delta)]\mathbf{z} \qquad (1)$$

(with $\mathbf{z}$ a unit vector along the z-axis) on the photodetachment of negative ion H⁻ by one high frequency (HF) photon with energy $\hbar\omega_H$ of the order of 1 eV [2]. When $\omega_2 = 2\omega_1$, the electron may be detached into the same final state through different routes and, because of the coherent interference of the respective transition amplitudes, angular distribution were found that exhibit polar asymmetry. The asymmetry results to be more pronounced when the vector potential $\mathbf{A}(t)$ associated to the bichromatic field has its maximal polar asymmetry, i.e., when $\langle A^3(t)\rangle$ is maximum, the brackets denoting the temporal average over the period of the field having the lowest frequency. The calculation were carried out with such LF field parameters that the photoelectron could exchange a little amount of the LF photons. In this regime the total yield was found to be weakly dependent on the relative phase δ.

The present paper is aimed at investigating the effect of the relative phase δ on the photodetachment of H⁻ when the photoelectrons may exchange a large amount of LF photons. This occurs when the ponderomotive energy of the bichromatic field is much larger than the photon energies of the LF laser fields. In this regime,

during the photodetachment event, the bichromatic LF field may be assumed to act as a static field. Experimental observation of photodetachment of negative ion [3] have corroborated this assumption. It was found that a sizeable total photocurrent may establish even if the photon energy $\hbar\omega_H$ is lower than the electron affinity $-I_0$ of the unperturbed ion, indicating that the photoelectron may tunnel through the barrier formed by the LF fields. In this picture, when $\hbar\omega_H$ is enough smaller than $-I_0$, the largest probability of tunnelling occurs at the peak of the LF radiation field. Therefore, in the presence of the bichromatic field, the total photocurrent is expected to depend on δ, as the maximum value of the bichromatic electric field may be controlled by the relative phase.

When the photodetachment takes place in the presence of a monochromatic field, the probability amplitude describing the process results to be either an even or an odd function of the average momentum $\mathbf{q}$ of the ejected photoelectron, according as an odd or an even number of LF photons is respectively exchanged. Consequently, due to the definite parity of the probability amplitude, the differential cross section of the process is invariant under the transformation $\mathbf{q} \longrightarrow -\mathbf{q}$.

In the presence of an additional field of commensurate frequency, the active electron may be ejected through different routes; in each of them different combinations of number of LF photons with frequency ω_1 and $n\omega_1$ may be exchanged leading to the same final state. The resulting transition amplitudes will result as a coherent sum of partial transition amplitudes each of them, being connected with one of the possible routes, is either an even or odd function of q. Hence, the angular distribution of the electrons may result not to be invariant under the transformation $\mathbf{q} \longrightarrow -\mathbf{q}$. In fact, it can be shown that the electron angular distribution result to be invariant under the operation $\mathbf{q} \longrightarrow -\mathbf{q}$, when it is possible to find such a temporal translation τ

that, putting $t' = t + \tau$, $\mathbf{A}(t')$ results equal to $-\mathbf{A}(-t')$. Thus, the symmetry properties of the angular distribution are related to the behavior of the classical velocity $\mathbf{v}$ of the electron (in fact, changing $\mathbf{q}$ into $-\mathbf{q}$ and $\mathbf{A}$ into $-\mathbf{A}$, $\mathbf{v}$ goes into $-\mathbf{v}$).

Another peculiar feature that characterizes the photodetachment event in the presence of a single mode radiation field, when $\hbar\omega_H > -I_0$, is that the total cross section as a function of ω_H oscillates about the values found when the LF field is turned off. This result may be explained [4, 5] in terms of interference of the wave associated to the direct motion of the ejected electron and the one that reflects by the effective barrier created by the LF field whose characteristic height has been evaluated to be 2Δ, Δ being the ponderomotive potential associated to the LF field. The presence of a bichromatic field assisting the photodetachment does not alter this picture. Now the electrons during their ejection are reflected by a barrier whose effective height, being the sum of the two ponderomotive potential pertinent to the fields, does not depend on their relative phase. Hence, the frequency ω_H at which the wiggles in the curves showing the cross sections as a function of the HF photon energy are expected to disappear should be independent of the relative phase δ.

Before closing this section, we want to remark that the effects connected with the rescattering of the ejected electron by the residual atom will be ignored. They have been proved to play a role in experiments of above threshold ionization (ATI) where an abrupt change of the slope of the ATI spectra due to the inverse bremsstrahlung was observed to occur in the region of highest energy where the electron population was found to be order of magnitude below the one of the most intense peak [6]. Below, in order to simplify our treatment, the negative ion will be modelled by a one-electron system that moves in a zero-range potential.

EVALUATION OF THE DETACHMENT AMPLITUDES

Details of the theoretical treatment presented here, based on the theory of two-color photodetachment, may be found elsewhere [7]. Here we limit ourselves to outline the main steps leading to the S-matrix of the process in which the negative ion, initially in its ground state, is detached by the joint action of both the HF and the bichromatic fields, the former being treated perturbatively.

In the E-gauge the Schrödinger equation of the electron moving in the presence of a static atomic potential and the radiation fields is

$$\left[i\hbar\frac{\delta}{\delta t} - H_0 - W(t)\right]\psi(r, t) = 0, \tag{2}$$

where

$$H_0 = \frac{\hat{p}^2}{2m} + V(r) \tag{3}$$

is the unperturbed Hamiltonian whose eigenstates and eingenvalues are respectively denoted by u_a^0 and I_a^0 and

$$W(t) = W_H + W_L \tag{4}$$

with

$$W_j(t) = e\mathbf{E}_j(t) \cdot \mathbf{r}, \quad (j = H, L), \tag{5}$$

represents the interaction of the electron of the two fields.

In (5) $E_H(t)$ and $E_L(t)$ are, respectively, the HF and the LF electric fields, the last one taken as in (1). The complete retarded Green function associated to (2) satisfies the following equation

$$\left[i\hbar\frac{\partial}{\partial t} - H_0 - W(t)\right]G^+(\mathbf{r}, t; \mathbf{r}', t')$$

$$= i\hbar\delta(\mathbf{r} - \mathbf{r}')\delta(t - t'). \tag{6}$$

Assuming that at the time t' the negative ion is in its ground state Ψ_i^0, at the instant $t > t'$, the electron wavefunction in the presence of both the HF and LF fields may be written as $[x = (\mathbf{r}, t)]$

$$\psi^+(x) = \int d^3r' G^+(x; x')u_i^0\exp(-iI_i^0 t') \tag{7}$$

$$(t \geq t').$$

The S-matrix of the process under consideration is

$$S_{fi} = \lim_{\substack{t \to +\infty \\ t' \to -\infty}} \langle\psi_f^0(t)|\psi^+(t')\rangle \tag{8}$$

with Ψ_f^0 the wavefunction of the detached electron moving under the only action of the short-range potential.

By expanding G^+ in terms of the complete retarded Green's function $g^+(\mathbf{r}, t; \mathbf{r}', t')$ associated to the Hamiltonian of the negative ion in the presence of the LF field, satisfying the equation

$$\left[i\hbar\frac{\partial}{\partial t} - H_0 - W_L\right]g^+(r, t; r', t')$$

$$= i\hbar\delta(r - r')\delta(t - t'), \tag{9}$$

and substituting this expansion into (8), equation (7) and the one giving the S-matrix, respectively, become

$$\psi^+(x) = \phi_{i,L}(x) - \frac{i}{\hbar}\int d^4x' g^+(x; x')W_H(x)\psi^+(x'), \tag{10}$$

$$S_{fi} = \langle\psi_f^0|\Phi_{i,L}\rangle - \frac{i}{\hbar}\int_{-\infty}^{+\infty} dt\langle\Phi_{f,L}|W_H|\psi_i^+\rangle, \tag{11}$$

with

$$\Phi_{i,L}(r, t) = \lim_{t' \to -\infty}\int d^3r' g^+(\mathbf{r}, t; \mathbf{r}', t')\psi_i^0(\mathbf{r}', t'), \tag{12a}$$

$$\Phi_{f,L}(r'',t'') = \lim_{t\to\infty}\int d^3\mathbf{r}g^+(\mathbf{r},t;r'',t'')\psi_f^0(\mathbf{r},t), \quad (12b)$$

the exact wavefunctions of the electron moving in the short-range potential in the presence of the LF radiation only, that tends to Ψ_i^0 for $t' \longrightarrow -\infty$ and to Ψ_f^0 for $t'' \longrightarrow +\infty$.

In order to simplify our problem, we approximate the electron–atom potential by the zero-range potential

$$V(r) = \frac{2\pi}{mh}\delta(\mathbf{r})\frac{\partial}{\partial r} \quad (13)$$

that supports only a bound state with energy $I_0 = -(b^2/2m)$, which in our calculations will be chosen to be -0.75 eV, equal to the binding energy of H^-. The wavefunction of the field-free bound state is, then, taken as

$$u_0(r) = B\left[\frac{b}{2\pi}\right]^{1/2}\frac{\exp(-br)}{r}, \quad (14)$$

where B is an empirical constant equal to $(2.65)^{1/2}$ [8].

Following Becker *et al.* [9], we choose such frequencies and intensities of the radiation fields that states different from the initial state are not populated when the HF photon detaches the electron. Then Ψ^+ of (10) is approximated by the wavefunction of the bare bound state

$$\psi^+ \cong \exp\left\{-\frac{i}{\hbar}I_0 t\right\}u_0(r). \quad (15)$$

Further, by neglecting the interaction of the ejected electron with the atomic potential, $\Phi_{f,L}$ may be approximated by the Volkov wavefunction

$$\Phi_{f,L}(\mathbf{r},t) = \exp\{i[\mathbf{q} - \mathbf{K}_L(\omega_1 t, \omega_2 t + \delta)]\cdot\mathbf{r}\}$$

$$\times \exp\left[-\frac{i}{2\hbar m}\int^t[\mathbf{q} - \mathbf{K}_L(\omega_1 t', \omega_2 t' + \delta)]^2 dt'\right], \quad (16)$$

where

$$\mathbf{K}_L(\alpha,\beta) = \frac{e\mathbf{E}_1}{\hbar\omega}\cos\alpha + \frac{e\mathbf{E}_2}{\hbar\omega}\cos\beta, \quad (17)$$

$\hbar\mathbf{K}_L(\omega_1 t, \omega_2 t + \delta)$ is the oscillating momentum imparted to the ejected electron by the bichromatic LF radiation field and $\hbar[\mathbf{q} + \mathbf{K}_L(\omega_1 t, \omega_2 t + \delta)]$ is the momentum of the ejected electron.

We note that, as already said in the introduction, effects due to inverse bremsstrahlung have been reported in ATI experiments where the formation of so-called rings in the angular distribution of the photoelectron, as well as abrupt changes in the far wings of their energy spectra, have been attributed to the rescattering of the electron by the atomic nucleus. In the case our concern, these effects are expected to play a negligible role as the total photocurrent for each photodetachment

channel will be taken under consideration. With the above assumptions the S-matrix becomes

$$S_{if} = -2\pi i\sum_{n_1}\sum_{n_2}\delta\left(\frac{\hbar^2 q^2}{2m} - n_1\hbar\omega_1 - n_2\hbar\omega_2\right.$$

$$\left. - \hbar\omega_H - I_0 + \Delta_L\right)T_{n_1,n_2}(q,\delta), \quad (18)$$

where T_{n_1,n_2} is the transition amplitude of the process in which the ejected electron absorbs one HF photons and exchanges n_1 photon of frequency ω_1 and n_2 photons of frequency ω_2. It may be written as (hereafter atomic units will be used)

$$T_{n_1,n_2}(q,\delta) = \frac{\exp(in_2\delta)}{(2\pi)^2}$$

$$\times\int_{-\pi}^{+\pi} d\alpha\int_{-\pi}^{+\pi} d\beta f_{n_1 n_2}(\alpha,\beta)M(q,\alpha,\beta), \quad (19)$$

where

$$f_{n_1 n_2}(\alpha,\beta) = \exp\left\{-in_1\alpha - in_2\beta + i\lambda_q(\alpha,\beta)\right.$$

$$(20a)$$

$$\left. + i\rho(\alpha,\beta) + i\frac{E_1 E_2}{\omega_1^2 - \omega_2^2}\left[\frac{\sin(\alpha+\beta)}{\omega_2} - \frac{\sin(\alpha-\beta)}{\omega_1}\right]\right\},$$

$$M(q,\alpha,\beta) = -iB\left(\frac{b}{\pi^2}\right)^{1/2}$$

$$\times\frac{E_{0H}[\mathbf{q} + \mathbf{K}_L(\alpha,\beta)]\cdot\hat{\mathbf{z}}}{\{b^2 + [q + K_L(\alpha\beta)]^2\}^2}, \quad (20b)$$

$$\lambda_q(\alpha,\beta) = \left[\frac{E_1}{\omega_1}\sin\alpha + \frac{E_2}{\omega_2}\sin\beta\right]\frac{e}{\hbar}q_z, \quad (20c)$$

$$\rho(\alpha,\beta) = \frac{e^2 E_1^2}{8m\omega_1^2}\sin 2\alpha + \frac{e^2 E_2^2}{8m\omega_2^2}\sin 2\beta, \quad (20d)$$

$$\Delta = \frac{e^2 E_1^2}{4m\omega_1^2} + \frac{e^2 E_2^2}{4m\omega_2^2}, \quad (20e)$$

and E_{0H} is the amplitude of the HF electric field taken as

$$\mathbf{E}_H = \hat{\mathbf{z}}E_{0H}\sin\omega_H t. \quad (20f)$$

As the relative phase δ enters (19) just through a factor phase, the photodetachment cross section will not depend on δ. Moreover, it is very easy to show that $T_{n1,n2}(\mathbf{q},\delta) = (-1)^{n1+n2+1}T_{n1,n2}(-\mathbf{q},\delta)$. Consequently, the photoelectron angular distribution result to be invariant under the inversion of the direction of the electron canonical momentum.

For $\omega_2 = 2\omega_1$, the same electron final state may be realized by the interference of all the possible transitions in which the numbers n_1 and n_2, associated respectively with processes in which photons of energies ω_1 and ω_2 are exchanged, combine giving $n_1 + 2n_2 = N$. Hence, the probability amplitudes of the process in which the electron absorbs one HF photon and exchanges the energy $N\omega_1$ with the bichromatic field may be written as the following coherent sum:

$$T_N = \sum_{n_2} T_{N-2n_2, n_2}(q, \delta). \tag{21}$$

Proceeding in the usual way, the corresponding partial differential and total cross sections with absorption of photodetachment into the channel characterized by the number N are obtained as

$$\frac{d\sigma(N, \varphi)}{d\Omega} = \frac{m\omega_H e^2 q_N}{\hbar^2 c}|T_N|^2, \tag{22}$$

$$\sigma(N, \delta) = \int_\Omega d\Omega \frac{d\sigma(N, \delta)}{d\Omega}, \tag{23}$$

with

$$\frac{q_N^2}{2} = N\omega_1 + \omega_H + I_0 - \Delta_L \tag{24}$$

the energy of the ejected electron.

From this last equation it follows that the photoelectron energy spectra consist of a series of peaks evenly separated by the energy ω_1. By summing over all the photodetachment channels the differential and total photodetachment yields are obtained as

$$\frac{d\sigma(\delta)}{d\Omega} = \sum_N \frac{d\sigma(N, \delta)}{d\Omega} \tag{25}$$

and

$$\sigma(\delta) = \sum_N \sigma(N, \delta). \tag{26}$$

By concluding this section, we observe that the transition amplitudes T_N, (21), are not invariant under the transformation $q \longrightarrow -q$ as it is a result of a coherent sum of terms that are either symmetric or antisymmetric under the transformation $q \longrightarrow -q$ [2]. Consequently, the angular distribution of the photoelectrons, which have exchanged an energy $N\omega_1$ with the bichromatic field, exhibits a polar asymmetry. We remark that, when, together with the inversion of q, the relative phase δ is changed of π ($\delta \longrightarrow \delta + \pi$), the differential cross section of (22) does not change, implying that the rate of forward ejection for a phase δ is the same as the backward one when the phase is changed into $\delta + \pi$. Further for $\delta = \pi/2$, the differential cross section, (22), exhibits polar symmetry as it is invariant under the transformation $q \longrightarrow -q$. Finally, we note that the dif-

ferential cross section, (22), is invariant under reflection of δ about $\delta = 0$ and $\delta = \pi$.

RESULTS AND COMMENTS

In this section we present selected calculations that show the effect of the relative phase δ on the photodetachment process in the highly nonlinear regime, in which the detached electron may exchange a large amount of energy $N\omega_1$ with the bichromatic LF field.

To facilitate the discussion of the results, in Fig. 1 we report the temporal shapes of the oscillating electric field and the vector potential for different values of δ.

In Fig. 2 we show the ratio $R = \sigma(\pi/2)/\sigma(0)$ of the total yield, (26), evaluated at $\delta = \pi/2$ and $\delta = 0$, as a function of ω_H, for different values of the intensity ad frequency of the bichromatic LF field. We remark that, by varying ω_1, the values of the ratio R do not change appreciably, while considerable modifications appear when the intensities of the LF bichromatic field are varied keeping fixed the value of ω_1. The poor sensitivity of the values R to the variation of ω_1 can be considered as the consequence that the LF field acts like a static electric field until after the ejection of the photoelectron. For $\hbar\omega_H < -I_0$ the ratio R depend strongly on the relative phase and its values increase when the intensities of the bichromatic LF field increases. For $\hbar\omega_H > -I_0$ the ratio R becomes almost equal to 1 for any value of ω_H, and the total photocurrent is independent of the relative phase δ. For values of ω_H of the order of the field-free affinity $-I_0$, the values of R oscillate about the value $R = 1$. In the region $\omega_H < I_0$ the total yield at $\delta = \pi/2$ is greater than the one found when $\delta = 0$. This behavior may be interpreted as a manifestation of the fact that the photoelectrons tunnel through the quasi-static, time-dependent potential barrier originated by the LF field, the ejection probability being highest at the peak of the electric field strength. In fact as shown in Fig. 1, the maximum of the field strength at $\delta = \pi/2$ is higher than the one when $\delta = 0$ and, accordingly, the above outlined interpretation of the photodetachment dynamics follows.

While for $\omega_H > -I_0$ the total yield is not greatly affected by the relative phase δ, a quite different behavior is exhibited by the energy distribution of the photoelectron. In Fig. 3 we show electron energy spectra evaluated at different values of the relative phase δ and HF photon energy ω_H. For $\omega_H < -I_0$ the spectra show a very similar shape at different values of the relative phase δ, though the values of the cross sections are notably affected by the relative phase. According to the picture that the electrons are detached by tunnelling through the barrier produced by the LF electric field, the photodetachment probability decreases rapidly as the energy of photoelectrons increases.

For $\omega_H > -I_0$ the shape of the spectra is strongly affected by the relative phase δ. We remark that considerable modifications occur when the value of δ is
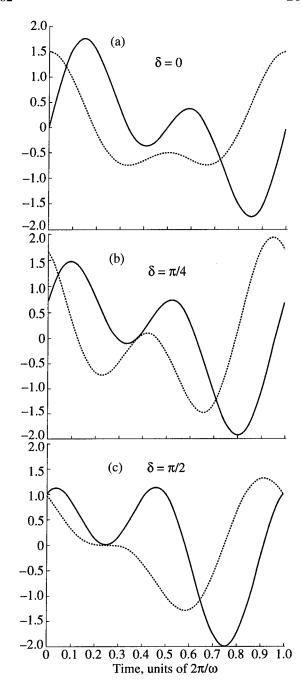
Fig. 1. Time-dependent electric field (full line) $E(t) = E_1[\sin\omega_1 t + \sin(2\omega_1 t + \delta)]$ and vector potential (dotted line) $A(t) = A_1[\cos\omega_1 t + 0.5\cos(2\omega_1 t + \delta)]$ for different phases δ, in units of E_1 and A_1 respectively.
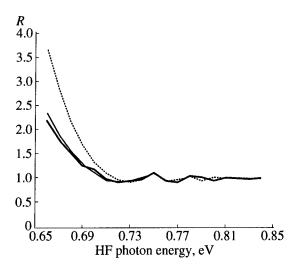

Fig. 2. Ratio $R = \sigma(\pi/2)/\sigma(0)$ of the total yield, (26), evaluated at $\delta = \pi/2$ and $\delta = 0$, as a function of the HF photon energy $\hbar\omega_H$ for different values of the intensity and frequency of the LF field. Thick curve: $\omega_1 = 0.004$ eV; the intensities of the LF fields are $I_1 = I_2 = 10^7$ W/cm^2. Thin curve: $\omega_1 = 0.003$ eV; $I_1 = I_2 = 10^7$ W/cm^2. Dotted curve: $\omega_1 = 0.004$ eV; $I_1 = I_2 = 5 \times 10^7$ W/cm^2.

A further distinctive feature of the energy spectra is the onset of a plateau whose extension is determined, at fixed value of ω_H, by the relative phase δ and the ponderomotive shift Δ.

In order to better illustrate some of these features and to get an insight into the dynamics underlying the photodetachment event, we put (19) in the following form, valid for $\omega_2 = 2\omega_1$:

$$T_N = \frac{1}{2\pi}\int_{-\pi}^{+\pi} \exp\left\{-iN\alpha + i\frac{\zeta(\alpha)}{\omega_1}\right\}\tilde{M}(q_N, \alpha)d\alpha \quad (27)$$

with

$$\zeta(\alpha) = \left(-\frac{q^2}{2} + \Delta_1 + \Delta_2\right)\alpha + \frac{1}{2}\int^{\alpha}[\mathbf{q} + \mathbf{K}_L(\alpha')]^2 d\alpha', \quad (28)$$

$$\tilde{M}(q_N, \alpha, \delta) = M(q_N, \alpha, 2\alpha + \delta). \quad (29)$$

The main contribution to the integral comes from the points of stationary phase satisfying

$$\frac{1}{2}[\mathbf{q} + \mathbf{K}_L(\alpha_s)]^2 = \omega_H - I_0 \quad (30)$$

from which it follows

$$q_N\cos\vartheta + K_L(\alpha)$$
$$= \pm\sqrt{2[(\omega_H + I_0)\cos^2\theta - (N\omega_1 - \Delta_L)\sin^2\theta]}, \quad (30a)$$

where θ denotes the angle between $\mathbf{q}_N$ and $\mathbf{z}$, and the signs of the right-hand side of (17a) are respectively

changed from 0 to $\pi/2$. For $\delta = \pi/2$ the energy spectrum shows a pronounced, narrow maximum when the photoelectron absorbs by the bichromatic field such an amount of energy $N\omega_1$ almost equal to Δ. At, roughly, the same energy, the energy spectra calculated for $\delta = 0$ show a minimum, while two maxima located, respectively, at lower and higher energy appear. The energy separation of such maxima increases by increasing ω_H.

Fig. 3. (a) Photodetachment cross sections (PCS) versus the photodetachment channel N, evaluated at $\omega_H = 0.68$ eV, for two different values of the relative phase δ of the LF fields. The calculations have been carried out at the same value of the LF fields amplitudes, for $\omega_1 = 0.004$ eV and $\omega_2 = 2\omega_1$. The intensity of the radiation field at frequency ω_1 has been taken $I_1 = 10^7$ W/cm$_2$. The lines are a guide for the eye. Thin line: $\delta = 0$; thick line $\delta = \pi/2$. The amount of energy the photoelectrons exchange with the LF fields is given by $N\omega_1$. (b) $\hbar\omega_H = 0.90$ eV; (c) $\hbar\omega_H = 1.5$ eV.

Fig. 4. (a) Angular distributions of the total yield of the photoelectrons evaluated at the HF photon energy $\hbar\omega_H = 0.68$ eV; thick line $\delta = \pi/2$, thin line: $\delta = \pi/4$, dotted line: $\delta = 0$. The intensities and frequencies of the LF field are as in Fig. 3; (b) $\hbar\omega_H = 0.90$ eV; (c) $\hbar\omega_H = 1.5$ eV. Thick line: $\delta = \pi/2$, dotted line: $\delta = 0$.

associated to the values the projection of the kinetic momentum of the photoelectron along the z-axis takes at $\omega_1 t_s = \alpha_s$. For the values of ω_H taken under consideration in the present paper, $\omega_H > I_0$, α_s may result to be real or complex, the integral of (15) becoming vanishing small in the latter case. This certainly happens when

the square root (17a) becomes imaginary, i.e. when the values of θ fall into the angular interval defined by

$$\tan^2\theta > \frac{(\omega_H - |I_0|)}{N\omega_1 - \Delta_L}. \tag{31}$$

Therefore, in this interval, whose extension results to be independent of the relative phase δ, the differential

photodetachment cross sections are expected to be very small. By (30) it is also possible to estimate the cut-off energy of the plateau that establishes in the energy spectra. For real α_s, the maximum value of q is obtained when the canonical momentum is antiparallel to $\mathbf{K}_L$. Its modulus in very easily found to be

$$q = \sqrt{2(\omega_H - |I_0|)} + K_{LM}, \qquad (32)$$

where K_{LM} is the amplitude of the quivering momentum imparted to the electron by the LF fields. Values of q greater than the one given by the above relation are obtained only for complex α, when the photodetachment amplitude probability becomes very small. Substitution of q_N in (32) allows us to determine the values of N beyond which the photodetachment cross sections fall of orders of magnitudes. Moreover, provided $(2\omega_H - |I_0|)^{1/2} > K_{LM}$, by replacing in (24) K_L with $-K_L$ and substituting the resulting value of q in (24), a value of N is found that, roughly determines the lower limit of the energy spectrum. Hence, the extension of the photoelectron energy spectrum beyond which the values of the cross section fall of order of magnitudes is approximately estimated to be (in units of ω_1)

$$\Delta N \simeq \frac{2}{\omega_1} \sqrt{2(\omega_H - |I_0|)} K_{LM}. \qquad (33)$$

For the cross sections shown in Fig. 3c lower and upper values of N estimated by means of (24) result to be respectively $N = -135$ and 342 for $\delta = \pi/2$, and $N = -146$ and 403 for $\delta = 0$, in very good agreement with the numerical evaluation carried out by (27).

The angular distributions of the total yield of the photoelectron are shown in Figs. 4. For three different values of the energy of the HF photons ($\omega_H = -0.68$ eV, 0.9 eV, 1.5 eV) ad three different values of the relative phase ($\delta = 0$; $\pi/4$; $\pi/2$). We remark that the polar asymmetry exhibited by the angular distributions reduces when δ increases from 0 to $\pi/2$. In fact, because of the particular choice of the temporal behavior of the bichromatic field, when $\delta = \pi/2$, the photodetachment amplitude probability into the channel characterized by the number N transforms according to $T_N(\mathbf{q}) = i^N T_N(-\mathbf{q})$, from which a photoelectron current results that is equal in both the forwards ad backwards directions. As already discussed in the introductions, this properties follows from the circumstances when $\delta = \pi/2$ it is possible to final such a temporal translation τ ($\tau = -\pi/\omega_1$) that under the successive transformations $t \longrightarrow t + \tau$ and $t \longrightarrow -t$, the potential vector inverts its sign, as well as the instantaneous velocity of the photoelectron, when $\mathbf{q} \longrightarrow -\mathbf{q}$. By increasing ω_H, the polar asymmetry reduces for any value of δ until it practically vanishes. This results by the fact that when the HF energy photon increases ad the quiver velocity of the electron becomes a small fraction of its average velocity, ad the photoelectron fluxes in the forwards ad backwards directions are almost equal for every value of the relative phase δ. Moreover, for increasing ω_H, the angular

distribution of the total yield becomes almost equal to the field free one, the effect of the phase δ reducing to controlling the redistribution of the photoelectrons into different ejection channels.

In conclusion, we have proposed a photodetachment scheme for observing interference effects caused by the simultaneous action of a two-color low-frequency field during the photodetachment event. Loosely speaking, the HF field may be considered as a probe testing the continuum embedded in the LF fields. By changing their relative phase δ, the structure of the continuum changes too, and considerable modifications are found to occur in the angular distributions of the ejected electrons when $\omega_H < -I_0$ as well as in their energy spectra.

REFERENCES

1. Ce Chen, Yi-Yian-Yin, and Elliot, D.S., 1990, *Phys. Rev. Lett.*, **64**, 507; Schumacher, D.W., Weihe, F., Muller, H.G., and Bucksbaum, P.H., 1994, *Phys. Rev. Lett.*, **73**, 1344; Nakajima, T. and Lampropoulos, P., 1993, *Phys. Rev. Lett.*, **70**, 1081; Baranova, N.B., Beterov, I.M., Zel'dovich, B.Ya., *et al.*, *JETP Lett.*, **55**, 439; Sheeky, B., Walker, B., and Di Mauro, L.F., 1995, *Phys. Rev. Lett.*, **74**, 4799; Dupont, E., Corkum, P.B., Lin, H.C., *et al.*, 1995, *Phys. Rev. Lett.*, **74**, 3586; Schumacher, D.W. and Bucksbaum, P.H., 1996, *Phys. Rev. A*, **54**, 4271.

2. Leone, C., Bivona, S., and Burlon, R., 1996, *Laser Phys.*, **6**, 526.

3. Larson, D.J., Armstron, P.S., Baruch, M.C., *et al.*, 1989, in *Abstract of the Fifteenth International Conference on the Physics of Electronic and Atomic Collisions* (Amsterdam: North-Holland), p. 513.

4. Bugacov, A., Piraux, P., Pont, M., and Shakeshaft, R., 1992, *Phys. Rev. A*, **45**, 3041.

5. Bivona, S., Burlon, R., and Leone, C., 1992, *Phys. Rev. A*, **45**, 3268; 1993, *ibidem A*, **48**, R3441.

6. Becker, W., Lohr, A., and Kleber, M., 1994, *J. Phys. B*, **27**, L325.

7. Leone, C., Bivona, S., Burlon, R., and Ferrante, G., 1988, *Phys. Rev. A*, **38**, 5642; Door, M. and Shakeshaft, R., 1987, *Phys. Rev. A*, **36**, 421.

8. Armstrong, B.H., 1963, *Phys. Rev.*, **131**, 1132; Du, M.L. and Delos, J.B., 1988, *Phys. Rev. A*, **38**, 5609.

9. Becker, W., Lang, S., and McIver, J.K., 1994, *Phys. Rev. A*, **50**, 1540.

Interference Stabilization of Rydberg Atoms: Analytical Investigation and Numerical Simulations

O. V. Tikhonova*, E. A. Volkova*, A. M. Popov*, and M. V. Fedorov**

Skobeltsyn Research Institute of Nuclear Physics, Moscow State University, Vorob'evy gory, Moscow, 119899 Russia
e-mail: ovt@mics.msu.su
** General Physics Institute, Russian Academy of Sciences, ul. Vavilova 38, Moscow, 117942 Russia*
e-mail: fedorov@theor.gpi.ru
Received October 16, 1997

Abstract—Strong-field ionization of Rydberg atoms is studied both analytically and numerically. The analytical investigation is based on the quasi-classical (WKB) approach and is free from the often used Rotating Wave and Pole approximations. The numerical method used allows us to solve directly the nonstationary Schrödinger equation for a 3D hydrogen Rydberg atom in a strong linearly polarized electromagnetic field. The results of analytical and exact numerical solutions are compared and are shown to be in a very good agreement with each other. The effect of interference stabilization is confirmed to occur.

INTRODUCTION

Stabilization of atoms is one of the most interesting features of strong-field ionization. The main known mechanisms of stabilization (suppression of ionization) are the (adiabatic) Kramers–Henneberger stabilization [1, 2] and interference stabilization (IS) [3–5]. IS of Rydberg atoms is known to arise due to field-induced Λ-type transitions (via the continuum) between neighboring Rydberg levels. Because of such transitions, coherent repopulation of Rydberg states and destructive interference of Rydberg–continuum transitions take place. As a result, in the strong-field limit, the time of ionization differs dramatically from the Fermi Golden Rule and its dependence on the field strength takes the form of the "death-valley" [3, 4] or "death-plateau" [6, 7] curves. It should be emphasized that the death-valley and death-plateau predictions correspond to different regimes of IS and it is crucially important to make a reasonable choice between these two predictions of the earlier works. This is one of the goals of this paper. In addition, it should be mentioned that in the most of the earlier theoretical works the Rotating Wave and Pole Approximations (RWA and PA) were used. Unfortunately, in the case of strong field, these approximations do not seem to be rigorously justified. This is the reason for searching new approaches to the theory of IS free from both RWA and PA. Such an approach, based on the quasi-classical (WKB) approximation was suggested in [8, 9] and is further developed in this paper. As a result, some new features of IS are discovered and the death-plateau regime of IS is obtained.

Moreover, an alternative method of investigation used and described in this work is the direct numerical integration of the nonstationary Schrödinger equation for a 3D Rydberg atom in a laser field. The results of such numerical simulations are compared with analytical predictions of our theory and a very good agreement

is found. This fact is interpreted as a direct confirmation of IS in its death-plateau form and helps to make choice in favor of IS when the existing experimental data on strong-field stabilization of atom [10, 11] are analyzed.

THE QUASI-CLASSICAL APPROACH TO THE STRONG-FIELD SOLUTION OF THE SCHRÖDINGER EQUATION

The WKB, or quasi-classical approximation, is known to be very fruitful for theoretical description of bound–free atomic transitions. Most often, this approximation is used only to simplify the atomic wave functions of initial and final field-free states entering the matrix elements of bound–free transitions [12, 13]. In this paper, the quasi-classical approach is used directly to solve the nonstationary Schrödinger equation for an atomic electron in the presence of the Coulomb potential and laser field. Using such a method, rather simple analytical expressions for partial probabilities of above-threshold ionization and for the total probability of ionization are found and the details of time–space distribution of the photoelectron density in the continuum are analyzed.

The main idea of the quasi-classical approach [5, 8, 13] can be formulated as an assumption that the field-induced Rydberg–continuum transitions occur mainly in the region of electron–nuclear distances r of the order of the so-called quasi-classical length r_q, where

$$r_q = \omega^{-2/3}, \qquad (1)$$

atomic units are used here and throughout the paper. This quasi-classical length is typically much larger than unity and usually is much shorter than the size of the Rydberg orbit $r_{max} = 2n^2$, $r_q \gg 1$, and $r_q \ll r_{max}$ at $\omega \ll 1$, $\omega > 1/2n^2$. Under these conditions, the centrifugal energy in the Schrödinger equation, estimated at $r \sim r_q$,
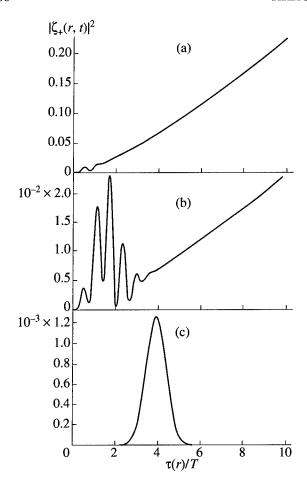
Fig. 1. The electron population in the continuum vs. the electron–nucleus distance r for (a) $t = 0$, (b) $1.5T$, and (c) $4T$; r is in units of $\tau(r) = \sqrt{2}\, r^{3/2}/3$ and $\tau(r)$ is in units of Gaussian pulse duration T.

appears to be much smaller than the Coulomb potential energy $1/r$, if only average angular momentum is smaller than $\omega^{-1/3} \gg 1$ [12]. This approximation gives rise to the approximation of slow angular motion [5, 8, 9], under which the centrifugal energy is dropped at all from the atomic Hamiltonian. As the result, the original three-dimensional Schrödinger equation can be reduced to the one-dimensional radial equation

$$i\frac{\partial x(r, t;\, \theta)}{\partial t}$$

$$= \left[-\frac{1}{2}\frac{\partial^2}{\partial r^2} - \frac{1}{r} + \cos(\theta)\varepsilon_0(t)r\sin(\omega t) \right] \chi(r, t;\, \theta), \qquad (2)$$

where $\chi = rR$ and R is the electron radial wave function; in a light field both χ and R depend parametrically on the angle θ between the field-strength vector ε_0 and electron position vector $\mathbf{r}$, $\varepsilon_0(t)$ is a slow field-strength amplitude describing how a light pulse is switched on and off. Below, in all the intermediate formulas, to shorten notations, $\cos\theta$ is dropped from the product

$\varepsilon_0(t)\cos\theta$. However, in the final results this product is written down explicitly and the following procedure of averaging is performed.

With the wave function of the initially populated field-free Rydberg state taken as the initial condition for the Schrödinger equation (2), the latter can be solved first at a frozen angle θ ($\theta = \text{const}$) [5, 8, 9]. Then the results obtained are averaged over θ.

Expanding the results obtained in [8, 9] for any instant of time t the electron density of the kth ATI peak can be written in the following form:

$$\overline{\rho_k(r, t)} = \frac{\sqrt{r}}{2^{3/2}\pi n^3}$$

$$\times \{ J_k^2[|\zeta_+(r, t)|] + J_k^2[|\zeta_-(r, t)|] \}, \qquad (3)$$

where $J_k(x)$ is the cylindrical Bessel function,

$$\zeta_+(r, t) \sim 2\frac{i^{5/3}2^{2/3}\varepsilon_0[t - \tau(r)]}{3^{1/3}\omega^{5/3}}\Gamma\!\left(\frac{2}{3}\right) + \frac{i r \varepsilon_0(t)}{\omega}, \qquad (4)$$

$$\zeta_-(r, t) \sim \frac{i r \varepsilon_0(t)}{\omega}, \qquad (5)$$

$\Gamma(x)$ is the Euler Γ-function.

The bar over $\rho_k(r, t)$ in (3) means that very fast oscillations in r are averaged out. The variable $\tau(r)$ in (4) has a very simple interpretation. This is the classical time of motion for an electron in the Coulomb potential: $\tau(r) =$

$$\frac{\sqrt{2}}{3}\, r^{3/2} \text{ for } r \ll r_{\text{max}}.$$

Figures 1a–1c show the continuum population in dependence on $\tau(r)$ for three different instants of time t for the Gaussian laser pulse of duration T. Two different parts of the continuum population can be distinguished. They are referred to "temporary" and "irreversible" population. The temporary population is formed in a wide range of electron–nucleus distances r ($0 < r < r_{\text{max}}$). It follows adiabatically the laser pulse envelope and returns back to bound states when the field is off. For the Gaussian pulse envelope this temporary population is negligibly small when the time is much longer than the pulse duration T (Fig. 1c). In contrast, the irreversible population remains in the continuum and never returns to bound states even at time much longer than the pulse duration of ionizing light field. This part of population appears in the continuum in the range of distances r shorter or of the order of the quasi-classical length r_q and takes the form of a wave packet of a diverging spherical wave (Fig. 1c). The center of mass of the wave packet of irreversible ionization is moving into the direction of larger r. It should be mentioned that temporary part of population appears to be significantly suppressed in the strong field limit when $\varepsilon_0 \geq \omega^{5/3}$ (Figs. 2a–2c). As for the irreversible population, only the shape of the

wave packet is modified: the double-peak and, then, multipeak structure is found to arise in the growing field strength (Figs. 2d–2f).

The total probability of ionization, found when the laser pulse has gone, i.e., at $t \gg T$, follows from (3)–(5) and has the form

$$W_i = \frac{1}{2t_K} \int\limits_{-\infty}^{\infty} dt \left[1 - J_0^2 \left(\frac{2^{2/3}3^{1/6}\Gamma\left(\frac{2}{3}\right)\varepsilon_0(t)}{\omega^{5/3}} \right) \right], \quad (6)$$

where $t_K = 2\pi n^3$ is the Kepler period for the initial state.

Remembering now that, in fact, $\varepsilon_0(t)$ should be understood as $\varepsilon_0(t)\cos\theta$ and the probability (6) has to be averaged over θ, let us write down the final results for a case of a square pulse of a duration T

$$\overline{W}_i = \overline{\Gamma}_i \times T, \quad (7)$$

where $\overline{\Gamma}_i$ is the averaged nonlinear rate of ionization

$$\overline{\Gamma}_i = \frac{1}{2t_K} \left[1 - \int\limits_0^1 dx J_0^2(\zeta x) \right] \quad (8)$$

and

$$\zeta = \frac{2^{2/3}3^{1/6}\Gamma\left(\frac{2}{3}\right)\varepsilon_0}{\omega^{5/3}} \quad (9)$$

is the field parameter proportional to the laser field strength ε_0. The time of ionization $\bar{t}_i$ corresponding to the rate $\overline{\Gamma}_i$ (8) can be determined as $\bar{t}_i = \dfrac{1}{2\overline{\Gamma}_i}$.

The dependencies $\overline{\Gamma}_i(\zeta)$ and $\bar{t}_i(\zeta)$ are shown in Figs. 3a and 3b. The functions $\overline{\Gamma}_i(\zeta)$ and $\bar{t}_i(\zeta)$ are seen to be monotonous and to exhibit a kind of a saturation at the asymptotic levels $1/2t_K$ and t_K, respectively. The saturation can be interpreted as the strong-field stabilization of the Rydberg atom: if the pulse duration T is shorter than the Kepler period t_K, the atom remains partially nonionized, independently on the laser field strength. The saturation-type mechanism of the strong-field IS agrees with the death-plateau regime of IS [5, 6] though the method of analysis in [5] is absolutely different from that described above. We assume that the saturation or death-plateau regime of IS is intrinsic feature of a strong field ionization of 3D atoms. This behaviour can contrast with that of model 1D atoms to be investigated separately. Below the results of analytical quasi-classical investigation are compared with those of a direct numerical solution of the real 3D hydrogen atom.
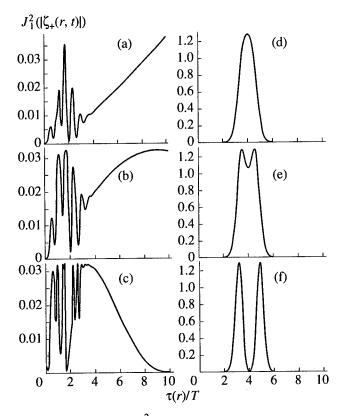
Fig. 2. The function $J_1^2\,[|\zeta_+(r,\,t)|]$ determining the strong-field photoelectron distribution in the first ATI peak, for (a–c) $t = 1.5T$ and (d–f) $t = 4T$ and for (a) $\varepsilon_0/\omega^{5/3} = 1$, (b) 1.5, (c) 2.35, (d) 0.03, (e) 0.86, and (f) 1.72.
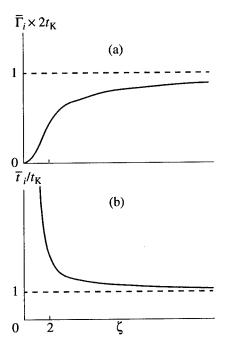
Fig. 3. (a) The rate of ionization averaged over θ, $\overline{\Gamma}_i$, and (b) the correspondent "average" time of ionization $\bar{t}_i = 1/(2\overline{\Gamma}_i)$ versus the field parameter ζ (9).
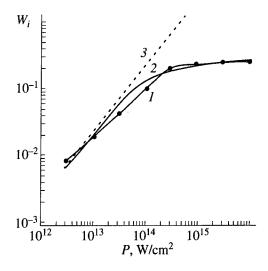
Fig. 4. The probability of ionization W_i in dependence on laser intensity P found from numerical calculations (1), analytical theory (2), and Fermi Golden Rule (3); the data are obtained in the case of symmetric trapezoidal pulse envelope with the pulse plateau duration $T_p = 10T_f$ and ramps equal to $2T_f$ ($\omega = 5$ eV).

Fig. 5. The probability of ionization W_i in dependence on the principal quantum number of the initial state n.

THE RESULTS OF NUMERICAL SIMULATIONS

The direct numerical solution of the nonstationary Schrödinger equation was obtained for the three-dimensional excited hydrogen atom in a linearly polarized electromagnetic field. The details of calculations performed can be found in [14]. As an initial condition the atom is supposed to be in an excited state, characterized by some definite principal and orbital momentum quantum numbers n and l. The found nonstationary wave function obeying the Schrödinger equation was expanded in a series of field-free atomic states. The coefficients of expansion were interpr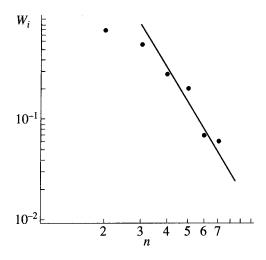eted as time-dependent probability amplitudes to find an atom in atomic states. It should be emphasized that such an expansion is not needed to find the numerical solution of the nonstationary Schrödinger equation; it is used only to interpret the results obtained and to study transitions between different (n, l) states. In the case of linearly polarized electromagnetic field the problem is symmetric over azimuthal angle φ, the transitions

The probability of ionization calculated for different laser intensities P and frequencies ω but for a given value of parameter $V = \varepsilon_0/\omega^{5/3}$, $V = 1.57$, in the case of square pulse of duration T_p

$\hbar\omega$, eV	T_p, opt. cycl.	P, W/cm^2	W_i
1.0	3	1.41×10^{12}	0.478
2.0	6	1.41×10^{13}	0.392
3.0	9	5.46×10^{13}	0.345
4.0	12	1.43×10^{14}	0.301
5.0	15	3.0×10^{14}	0.245

changing the projection of orbital moment are forbidden and the corresponding quantum number m is conserved (in our calculations it was taken to be $m = 0$).

The calculations were performed for different laser frequencies in the region from 1 to 5 eV in a wide range of laser intensities for the symmetric trapezoidal pulse envelope $\varepsilon_0(t)$ with ramps of $2T_f$ (T_f is the duration of an optical cycle) and pulse plateau duration T_p.

The main result of calculations is the dependence of ionization probability on the laser intensity (Fig. 4). The three curves of this picture are the probability of ionization obtained from the direct numerical calculations (curve *1*), from analytical theory [(6) averaged over θ] (curve *2*) and from Fermi Golden Rule for the case of $\omega = 5$ eV and symmetric trapezoidal pulse envelope with pulse plateau duration $T_p = 10T_f$. A perfect coincidence between the analytical theory and direct numerical calculations is found in the range of intensities when the field is strong $\varepsilon_0/\omega^{5/3} > 1$. The probability of ionization is seen to saturate at a level, which is much less than unity. This means that in our calculations stabilization is demonstrated to occur and to agree with the "death-plateau" regime of IS predicted by analytical theory described above. Both exact calculation and analytical theory give the results coinciding with Fermi Golden Rule in the low-field limit. But it should be emphasized that the deviations from Fermi Golden Rule appear already in the range of field strengths much less than the atomic field, if only the field parameter (9) $\zeta \geq 1$.

According to the analytical theory, the probability of ionization depends on the field strength ε_0 and frequency ω only via the parameter $V = \varepsilon_0/\omega^{5/3}$ [see (6) and (8)]. This conclusion is checked and confirmed by our numerical calculation, the results of which are given in the table. The probability of ionization presented in this table was obtained for different laser intensities and frequencies but for a given value of V,
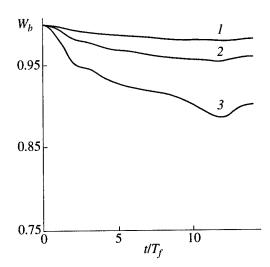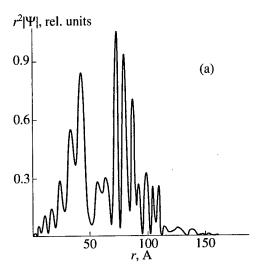
Fig. 6. The probability W_b for an atom to be found in bound states in dependence on time t (in units of T_f) during the laser pulse for intensity P = (1) 10^{13}, (2) 3×10^{13}, and (3) 10^{14} W/cm^2.

$V = 1.57$. In this table the values of the probability W_i calculated for the square pulse are close to each other, whereas the laser intensity is changing in two orders of magnitude. The observed small deviations from the law W_i = const are likely to be explained by a few number of optical cycles in the laser pulse for the case of low frequencies.

Another important conclusion of the quasi-classical (WKB) theory concerns the dependence $W_i \sim n^{-3}$ for the probability of ionization. Our numerical data (Fig. 5) fit this law pretty well at $n \geq 4$. That is why the excited states with the principal quantum numbers $n \geq 4$ can be considered to be real Rydberg states in terms of agreement with theory of IS.

The results of numerical calculations shown in Fig. 6 demonstrate directly the above discussed phenomenon of the temporary population of the continuum. The probability for the system to be found in bound states is presented as a function of time (in optical cycles) during the trapezoidal laser pulse for different laser intensities. In addition to an actual ionization, there is a partial return of population back to bound states towards the end of the pulse. In agreement with the analytical predictions, the temporary part of population repeats the trapezoidal shape of the pulse and has maximal value in the range of medium intensities when the field is not strong ($\varepsilon < \omega^{5/3}$). In the strong-field limit this returning population is suppressed and only the wave packet of an actual ionization exists in the continuum. The numerically calculated strong-field structure of this wave packet is shown in Fig. 7a. Being averaged over fast oscillations, the curve of this picture reveals the double-peak structure of the wave packet in the case of strong field (see Fig. 7a) in agreement with analytical theory (compare with Fig. 2f). The center of mass of the wave packet moves into the direction of larger r
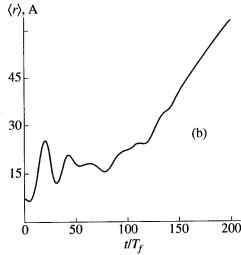
Fig. 7. The space structure of the wave packet in the continuum (a) in relative units and (b) the time-dependent mean coordinate of its center of mass.

in the after-pulse regime. Such a behavior is confirmed by monotonous increase of the mean electron–nucleus distance for the electron in the continuum calculated in dependence on time when the pulse is over (Fig. 7b).

In our numerical calculations, the population of states with different principal quantum numbers n and orbital quantum numbers l and transitions between them can be easy investigated. Figure 8 shows the distribution of population obtained at the end of the laser pulse over different bound (n, l) states with $l = 0, 1, 2$ $(ns, np, nd$ states) for low (Fig. 8a), medium (Fig. 8b), and high (Fig. 8c) laser intensities. Transitions from the initial $5s$ state to different ns and nd states, especially to $5s$ and $6s$ states, are seen to be very efficient in a strong field. This means that λ-type transitions from the initial state to neighboring levels are proved to occur. Excitations of Rydberg states of the same parity $(s, d, g, \ldots)$ as the initial one $(5s)$ is easily interpreted as occurring due to λ-type transitions via the continuum. On the other hand, excitation of odd (p) Rydberg states is also
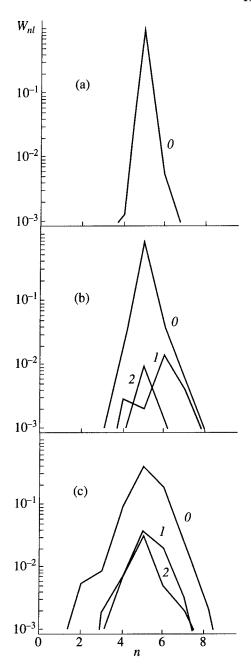
Fig. 8. The probability W_{nl} for an atom to be found in (n, l) states at the end of the laser pulse for different laser intensities P: (a) $P = 10^{13}$, (b) 10^{14}, and (c) 3×10^{14} W/cm^2; the calculations are performed for symmetric trapezoidal pulse envelope with the pulse plateau duration $T_p = 10 T_f$ and ramps equal to $2T_f$ ($\omega = 5$ eV).

Fig. 9. The probability W_{nl} for an atom to be found in (n, l) states at the end of the laser pulse for different plateau durations T_p of trapezoidal pulse envelope: (a) $T_p = 5T_f$, (b) $20T_f$; laser intensity is equal to 3×10^{14} W/cm^2.

seen pretty well in the results of calculations. The process has to be interpreted as a direct one-photon absorption (emission) of a photon ω with simultaneous transition $E_n \longrightarrow E_{n'}$ forbidden by the energy conservation rule. The results of calculations show that this restriction is rather efficiently removed in the case of strong fields (because of a large value of matrix element for bound–bound transitions) and very short pulses

(because of a wide enough spectral width). Nonresonant $5s \longrightarrow np$ transitions are most pronounced in the case of super short laser pulse (of trapezoidal envelope) with $T_p = 5T_f$ (Fig. 9a), but they are relatively small in the case of longer laser pulse with $T_p = 20T_f$ (Fig. 9b). It should be mentioned that until now such nonresonant transitions were never taken into account or discovered in analytical theories of IS. The contribution of different states into the total residual probability to find an atom in any bound state when the pulse is over can be analyzed with the help of data presented in Figs. 10 and 11. Relative probabilities to find an atom in any bound state with arbitrary principal quantum numbers n but given orbital numbers l ($l = 1, 2, 3$) are shown in Fig. 10 as a function of plateau pulse duration T_p. The relative population of nonresonantly excited p states is found to decrease with the increase of laser pulse duration, whereas the residual probability for d states appears to grow monotonously. The behavior of the residual probability in the case of even orbital numbers is similar to that obtained in earlier analytical investigations of IS [6, 7]. Because of this similarity, the interference mechanism of stabilization observed by results of our numer-
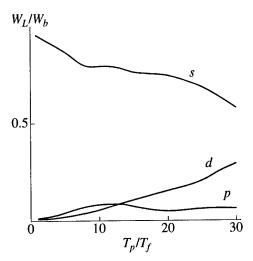
Fig. 10. Relative residual probabilities of finding an atom in bound states with arbitrary principal quantum numbers n but given orbital numbers $l = s, p, d$ in dependence on the plateau duration T_p of the trapezoidal pulse envelope; laser intensity is equal to 3×10^{14} W/cm^2.

Fig. 11. Residual probabilities of finding an atom in bound states with arbitrary orbital quantum numbers l but given principal quantum number $n = 4, 5, 6$ in dependence on plateau duration T_p of the trapezoidal pulse envelope; laser intensity is equal to 3×10^{14} W/cm^2.

ical simulations can be considered as a strong support of the idea about close connection between IS and repopulation of Rydberg levels due to Λ-type transitions.

Moreover, the dependencies of partial residual probabilities for given principal quantum number n (arbitrary orbital numbers) on the plateau duration T_p found in our calculations are also very close to those obtained from analytical studies of IS [3, 4]. According to [3, 4] the populations of Rydberg states with different principal quantum numbers n oscillate in time. The period of the oscillations depends on n and for $n = n_0$ is equal to Kepler period $t_K = 2\pi n_0^3$. For other states the ratio of their oscillation periods corresponds to the inverse ratio of their energy deviations from the initial energy level E_{n_0}.

The results obtained from numerical calculations and presented in Fig. 11 show that for a given n the residual probabilities W_{nl} summed over l are characterized by oscillating dependencies on the plateau duration T_p. The period of oscillations is close to the Kepler period (≈ 23 optical cycles) in the case of $n_0 = 5$. In the case of $n = 6$ and $n = 4$ the oscillation periods are different from t_K and from each other but they are also of the order of the Kepler period. Their ratio is equal to 1.85, in a good agreement with the ratio of $|E_n - E_{n_0}|^{-1}$ calculated for $n_0 = 5$, $n = 6$, and $n = 4$. Thus, there is a close similarity between our calculations and analytical investigations based on the consideration of Λ-type transitions. Therefore, we conclude that the dynamics of the system is mostly determined by Λ-type transitions with an admixture of direct nonresonant transitions between neighboring Rydberg levels occurring in the case of supershort pulses. Apart from nonresonant transitions, these results can be considered as a confir-

mation of the main ideas and predictions of the analytical theory of IS described above.
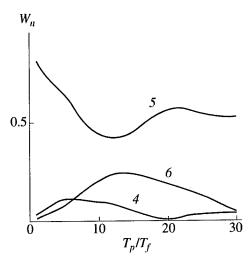
CONCLUSIONS

In conclusion, strong-field ionization of a Rydberg atom was investigated both analytically and via direct numerical solution of the nonstationary Schrödinger equation. The existence of temporary population and the motion of the irreversible ionization wave packet away from the nucleus is seen both in analytical and numerical calculations. The numerical calculations performed demonstrate a very good agreement with the analytical theory. In particular, the analytical and numerical curves of ionization probability versus laser intensity perfectly coincide in a strong field region. In the numerical calculations Λ-type transitions between different Rydberg states are prove to be a reason for the stabilization found. Thus, the predictions of the analytical theory concerning the interference stabilization of Rydberg atoms were confirmed.

By returning to the question formulated in the Introduction about an option between the death-valley and death-plateau regimes of IS and strong-field ionization, we can use the results of this work to make a clear choice in favor of the death-plateau or "saturation" regime. This conclusion is assumed to be valid for 3D atoms, though different regimes can be expected to occur in model 1D atoms.

In addition, the direct numerical solution has shown that in the case of strong and very short pulses the process of photoionization is accompanied by very efficient nonresonant transitions between Rydberg levels. E.g., excitation of Rydberg np-states from the originally populated $5s$-state appears to be highly pronounced, though in terms of perturbation theory such

transitions would correspond to a direct absorption of a photon ω forbidden by the energy conservation law. An extremely high efficiency of such nonresonant transitions found in numerical calculations is beyond the framework of any existing analytical theories and deserves further investigation.

REFERENCES

1. Gavrila, M., 1992, in *Atoms Intense Laser Field*, Gavrila, M., Ed. (New York: Academic), p. 435.
2. Gavrila, M. and Kaminski, J., 1984, *Phys. Rev. Lett.*, **52**, 613.
3. Fedorov, M.V. and Movsesian, A.M., 1988, *J. Phys. B*, **21**, L155.
4. Fedorov, M.V., 1993, *Laser Phys.*, **3**, 219.
5. Fedorov, M.V., 1994, *J. Phys. B*, **27**, 4145.
6. Fedorov, M.V., Tegranchi, M.-M., and Fedorov, S.M., 1996, *J. Phys. B*, **29**, 2907.
7. Woiczik, A. and Parzynski, R., 1997, *Laser Phys.*, **7**, 551.
8. Tikhonova, O.V. and Fedorov, M.V., 1997, *Laser Phys.*, **7**, 574.
9. Tikhonova, O.V. and Fedorov, M.V., *Acta Physica Polonica* (in press).
10. Jones, R.R., Schumacher, D., and Bucksbaum, P., 1993, *Phys. Rev. A*, **47**, R49.
11. Hoogenraad, J., *et al.*, 1994, *Phys. Rev. A*, **50**, 4133.
12. Delone, N.B., Goreslavsky, S.P., and Krainov, V.P., 1983, *J. Phys. B*, **16**, 2369; 1989, *J. Phys. B*, **22**, 2941.
13. Adams, M., Fedorov, M.V., Krainov, V.P., and Meyerhofer, D.D., 1995, *Phys. Rev. A*, **52**, 125.
14. Volkova, E.A., Popov, A.M., and Tikhonova, O.V., 1998, *JETP* (in press).

Wave Packet Motion in Relativistic Electric Fields

Q. Su, B. A. Smetanko[1], and R. Grobe

Intense Laser Physics Theory Unit and Department of Physics, Illinois State University, Normal, IL 61790-4560 USA
E-mail: qcsu@entropy.phy.ilstu.edu
Received August 4, 1997

Abstract—We investigate the relativistic and the quantum mechanical corrections to the motion of an electron wave packet in the presence of an intense static electric field. In contrast to the predictions of the (nonrelativistic) Schrödinger theory, the rate of the spatial wave packet spreading can be altered when the electron's response to the field requires a relativistic treatment. The spreading rate in the field's polarization direction as well as in the transverse directions is reduced and the wave function develops an asymmetric shape. We compare analytical but approximate results for the time evolution of the position, the width, and the skewness with the predictions obtained from the direct numerical integration of the Dirac equation.

1. INTRODUCTION

In atomic, molecular, and optical physics the effects of relativity were discussed mainly in the context of the atomic and molecular structure and the energy levels [1, 2]. The magnitude of the relativistic corrections to the precise energy of spectroscopic lines, however, is rather small. In the area of heavy-ion collisions, relativistic contributions are typically much larger and, especially for atoms with large nuclear charges Z, these effects can be quite significant [3]. Theoretical studies that include the numerical solution of the time-dependent Dirac equation have aided experimental observations of signals including electron–positron pair productions [4]. Relativistic contributions have also been considered in the studies of the electron motion in the operation of free-electron lasers [5].

Up to a few years ago only a limited number of works have been devoted to the case for which a relativistic treatment is required due to the interaction of an atom with a strong laser field. Pioneering works by Reiss [6] were among the first to incorporate the relativistic acceleration of electrons by the action of strong laser source into a theoretical description to compute ionization rates for the hydrogen atom. More recent studies were motivated by the availability of high-intensity lasers and some initial experimental evidence indicated deviations from the nonrelativistic behavior [7].

Theoretical studies have shown that the ionization rate of atoms in certain dressed states can be a decreasing function of the intensity if the laser fields are sufficiently strong [8–10]. Large-scale numerical simulations for the ionization of hydrogen have demonstrated that the ionization can be suppressed in realistic laser pulses [11–13]. Later, several research groups have confirmed this so-called stabilization phenomenon which also motivated several experiments [14]. An important question which is not fully understood today

concerns the fate of stabilization in the fully relativistic regime [15, 16].

As a first step in systematically exploring the role of relativistic corrections in the motion of an atomic electron in strong laser fields, we have analyzed a very simple system: a free electron wave packet in a static electric field [17]. This system has the advantage that it allows for more transparent analysis of relativistic phenomena without any interfering effects due to the magnetic field, the atomic Coulomb field, or temporal characteristics of the finite laser pulse. In this work we report on our first results. Our approximate analytical results were obtained from the square root Klein–Gordon-type Schrödinger equation and the applicability of this approach was tested by comparing our predictions with the results obtained from the exact numerical wave function solutions of the Dirac equation.

Our main findings include a significant suppression of the growth pattern of the second-order moments, i.e., the spatial width of the electron wave packet. Furthermore, we find that the wave packet in the direction of the polarization axis of the field becomes practically "frozen" in the long-time limit as electron approaches the speed of light. The suppression of the width is also present in the transverse directions, but to a lesser extent. To the best of our knowledge, these characteristics of relativistic wave packet spreading have not been discussed previously. Dodonov and Mizrahi [18] have shown that the variance of the physical coordinate of a relativistic particle must be greater than one half of its Compton length provided the average value of the energy in the wave packet is much smaller than twice the rest energy mc^2. For a review on localization, superluminal spreading, and a discussion of the violation of Einstein causality in this context, see [19]. In addition, we have also analyzed the third-order moment that characterizes the asymmetry of the wave packet and found it becomes nonzero as a result of the steepening of the front edge of the wave packet.

---

[1] Undergraduate research assistant.

This paper is organized as follows: In Section 2 we introduce the physical system for our numerical calculations and motivate the use of a relativistic Schrödinger equation for our approximate analytical investigations. We derive and solve the Heisenberg equations for the position operator and show that the coupling between the three coordinate directions conserves the relativistic momentum but not the kinetic velocity for the direction perpendicular to the external field. In Section 3 we investigate the second-order moments as a function of time and point out an interesting finite long-time limit. In Section 4 we discuss the third-order moment. Our approximate analytical results that were obtained from the Heisenberg equations derived from a square root Klein–Gordon-type Hamiltonian have been compared with the predictions obtained from the exact numerical solution to the Dirac equation. These numerical solutions allow us also to predict the contributions due to spin and electron–positron pair production. In the Appendix we discuss the connection of the relativistic quantum phenomena to the dynamics of a classical distribution of electrons. In Section 5 we offer a direct interpretation of these results, a comment on experiments, and conclude with a summary.

2. THE QUANTUM WAVE PACKET IN AN ELECTRIC FIELD

2.1 Exact Numerical Approach

In the case of a constant electromagnetic field, we may choose, without loss of generality, a reference frame in which only the electric component is present. The interaction of an electron with a static electric field **E** in the x-direction is described by the vector potential

$$\mathbf{A}(t) = -c\mathbf{E}t = -cEt\hat{e}_x. \tag{2.1}$$

The quantum motion of the electron in such a field has to satisfy the time-dependent Dirac equation given by

$$i\hbar\frac{\partial}{\partial t}\Psi(\mathbf{r}, t)$$
$$= \left[mc\vec{\alpha}\left(\mathbf{p} - \frac{q}{c}\mathbf{A}(t)\right) + \vec{\beta}mc^2\right]\Psi(r, t), \tag{2.2}$$

where $\Psi(\mathbf{r}, t)$ denotes the well-known four-spinor and $\vec{\alpha}$ and $\vec{\beta}$ are the 4×4 Dirac matrices [20].

To solve this equation in time, each of the three spatial variables x, y, and z has been discretized into 64–512 space points. The spinor $\Psi(\mathbf{r}, t)$ is then represented numerically by a vector with typically 4×128^3 components. The time-dependent Dirac equation has been solved via a generalized split-operator Fourier technique on a cray supercomputer. For details of the numerical method, see [21].

Before we discuss our analytical results, let us mention first the initial state used in the numerical calculations. We have chosen an initial quantum wave function of the simple form:

$$\Psi(\mathbf{r}, t = 0)$$
$$= [2\pi\sigma^2]^{-3/4}(\exp[-(r/2\sigma)^2], 0, 0, 0). \tag{2.3}$$

The initial spatial uncertainty of $\Delta x = \Delta y = \Delta z = \sigma$ was chosen to be a tenth of the Bohr radius, $\sigma = 5.3 \times 10^{-12}$ m (0.1 a.u.); this corresponds to a momentum width of $\Delta p_x = \Delta p_y = \Delta p_z \approx 5 \times 10^{-22}$ kg m/s (5 a.u.). The momentum width is small enough such that contributions of the Dirac states with negative energy (Dirac sea) are practically negligible in the initial state. Contributions of the negative-mass states are only relevant if the electron's extension is smaller than the Compton wavelength ($\hbar/mc = 2.43 \times 10^{-12}$ m) and quantum effects like the Zitterbewegung play a role [22].

2.2 Approximate Analytical Description

In order to obtain some analytical results, we will neglect the spin as well as the possibility of positron–electron pair production. We will analyze the spinless (relativistic) Schrödinger equation with the square root Klein–Gordon-type Hamiltonian [23]:

$$i\hbar\frac{\partial}{\partial t}\Psi(\mathbf{r}, t) = \sqrt{\left[m^2c^4 + c^2\left(\mathbf{p} - \frac{q}{c}\mathbf{A}\right)^2\right]}\Psi(\mathbf{r}, t). \tag{2.4}$$

We then use our exact numerical solutions to the Dirac equation to test the validity of this approximate approach. Such a Schrödinger equation has the well-known Volkov–Gordon solution:

$$\Phi_k(\mathbf{r}, t) = (2\pi)^{-3/2}$$
$$\times \exp\left\{-i\int^t \sqrt{\left[m^2c^4 + c^2\left(\hbar k - \frac{q}{c}\mathbf{A}(t')\right)^2\right]}dt'/\hbar\right\} \tag{2.5}$$
$$\times \exp\{i\mathbf{k} \cdot \mathbf{r}\}.$$

Volkov states, however, are spatially not localized and therefore of no immediate practical use in studying the temporal evolution of wave packets. The Volkov states could be applied to find the time evolution of a wave packet $\Psi(\mathbf{r}, t = 0)$:

$$\Psi(\mathbf{r}, t)$$
$$= \int d^3k\Phi_k(\mathbf{r}, t)\int d^3x'\Phi_k(\mathbf{r}', t = 0)\Psi(\mathbf{r}', t = 0). \tag{2.6}$$

Using this approach we did not find it easy to judge which characteristics of the solution depend on the specific properties of the initial-state wave function and which characteristics are generally valid. We have not

managed to significantly simplify the sixfold integrals in (2.6) to obtain some useful insight without any additional approximations. It seems that in order to investigate the time evolution of Volkov wave packets one has to rely on numerical methods.

It turns out, however, that it is more advantageous to analyze the Heisenberg equations of motion, e.g., $i\hbar\dfrac{d}{dt}\mathbf{r} = [\mathbf{r}, H]$ for the position operator. The operator equations can be solved fully analytically and we obtain

$$x(t) = x + \frac{1}{qE}\sqrt{[m^2c^4 + c^2(\mathbf{p} + q\mathbf{E}t)^2]}$$
$$- \frac{1}{qE}\sqrt{[m^2c^4 + c^2\mathbf{p}^2]},$$
(2.7a)

$$y(t) = y + \frac{cp_y}{qE}\ln\{[p_x + qEt$$
$$+ \sqrt{[m^2c^2 + (\mathbf{p} + q\mathbf{E}t)^2]}]/[p_x + \sqrt{[m^2c^2 + \mathbf{p}^2]}]\},$$
(2.7b)

$$z(t) = z + \frac{cp_z}{qE}\ln\{[p_x + qEt$$
$$+ \sqrt{[m^2c^2 + (\mathbf{p} + q\mathbf{E}t)^2]}]/[p_x + \sqrt{[m^2c^2 + \mathbf{p}^2]}]\}.$$
(2.7c)

The omission of the time argument for the operators on the right-hand side indicates the (usual) operators in the Schrödinger picture. The symmetry between the solution in the y- and z-directions, transverse to the electric field, is expected. The nonrelativistic limit can be easily obtained from (2.7) for $c \longrightarrow \infty$ leading to the solutions $\mathbf{r}_{NR}(t) = \mathbf{r} + \dfrac{\mathbf{p}}{m}t + \dfrac{q\mathbf{E}}{2m}t^2$. The relativistic solutions are formally identical to the solutions for a single classical electron trajectory. However, the time-dependent expectation values $\langle\mathbf{r}\rangle(t)$ differ from the solution for a classical particle. For a more thorough comparison of the relativistic classical and quantum mechanical predictions, see Appendix A.

As the Hamiltonian in (2.4) commutes with each of the canonical momenta p_x, p_y, and p_z, the momentum operators are conserved under the time evolution. The velocities, $\dot{x}$, $\dot{y}$, and $\dot{z}$, however, are not conserved. In the long-time limit, $\dot{x} \longrightarrow c$, whereas $\dot{y} \longrightarrow 0$ and $\dot{z} \longrightarrow 0$ as one can easily verify from the time derivative of (2.7). This is interesting. Although the force due to the electric field points in the x-direction, the motion in the perpendicular (y, z) plane is also influenced by the field. This is a direct consequence of the fact that the total velocity $v(t) = \sqrt{[\dot{x}^2 + \dot{y}^2 + \dot{z}^2]}$ cannot exceed the speed of light c. As the velocity grows in the x-direction, the particle must be decelerated in the transverse directions. The same argument can be also illustrated using

the concept of the time-dependent relativistic mass defined as $m_r \equiv m/\sqrt{[1 - (v/c)^2]}$. The Heisenberg equations for the three relativistic momenta lead to

$$\frac{d}{dt}m_r\dot{\mathbf{r}} = q\mathbf{E}.$$
(2.8)

The three components are nonlinearly coupled through the common velocity-dependent mass m_r. As this mass increases and approaches infinity, the two velocities $\dot{y}$ and $\dot{z}$ have to approach zero in order to conserve the relativistic momentum in the transverse directions.

3. SECOND-ORDER MOMENTS: SUPPRESSION OF WAVE PACKET SPREADING

Let us now analyze the evolution of the second-order moments defined by $\Delta x^2 = \langle(x - \langle x\rangle)^2\rangle$ and similarly for y and z. To simplify the notation, we restrict our analysis to those initial quantum states that are symmetric in their spatial and momentum representation: $\Psi(\mathbf{r}, t = 0) = \Psi(-\mathbf{r}, t = 0)$ and $\phi(\mathbf{p}, t = 0) = \phi(-\mathbf{p}, t = 0)$. Using the operator solutions (2.7), one can find the time evolution of the second-order moments:

$$\Delta x(t)^2 = \Delta x^2 + \langle(\Delta f_x)^2\rangle,$$
(3.1a)

$$\Delta y(t)^2 = \Delta y^2 + \langle(\Delta f_y)^2\rangle,$$
(3.1b)

$$\Delta z(t)^2 = \Delta z^2 + \langle(\Delta f_z)^2\rangle,$$
(3.1c)

where the variances of the functions f are given by

$$\Delta f_x \equiv \frac{c}{qE}[\sqrt{(\mathbf{p} + q\mathbf{E}t)^2 + m^2c^2} - \sqrt{\mathbf{p}^2 + m^2c^2}$$
$$- \langle\sqrt{(\mathbf{p} + q\mathbf{E}t)^2 + m^2c^2}\rangle + \langle\sqrt{\mathbf{p}^2 + m^2c^2}\rangle],$$
(3.1d)

$$\Delta f_y \equiv \frac{cp_y}{qE}\left[\ln\left[\frac{p_x + qEt + \sqrt{(\mathbf{p} + q\mathbf{E}t)^2 + m^2c^2}}{p_x + \sqrt{\mathbf{p}^2 + m^2c^2}}\right]\right.$$
$$\left. - \left\langle\ln\left[\frac{p_x + qEt + \sqrt{(\mathbf{p} + q\mathbf{E}t)^2 + m^2c^2}}{p_x + \sqrt{\mathbf{p}^2 + m^2c^2}}\right]\right\rangle\right],$$
(3.1e)

$$\Delta f_z \equiv \frac{cp_z}{qE}\left[\ln\left[\frac{p_x + qEt + \sqrt{(\mathbf{p} + q\mathbf{E}t)^2 + m^2c^2}}{p_x + \sqrt{\mathbf{p}^2 + m^2c^2}}\right]\right.$$
$$\left. - \left\langle\ln\left[\frac{p_x + qEt + \sqrt{(\mathbf{p} + q\mathbf{E}t)^2 + m^2c^2}}{p_x + \sqrt{\mathbf{p}^2 + m^2c^2}}\right]\right\rangle\right].$$
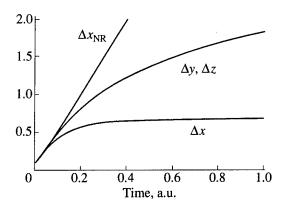(3.1f)

Fig. 1. Relativistic reduction of wave packet spreading. The graphs show the temporal growth pattern of the spatial width obtained from (3.1) $\Delta x(t)$, $\Delta y(t)$, and $\Delta z(t)$ together with the nonrelativistic width $\Delta x_{NR}(t)$. Superimposed on the graphs for $\Delta x(t)$, $\Delta y(t)$, and $\Delta z(t)$ are the width determined from the time-dependent wave function solution obtained from the full Dirac equation (2.2) (dashed lines). The two graphs are indistinguishable. [E = 1000 a.u., initial quantum state as in (2.3) with $\sigma = \Delta x(t = 0) = 0.1$ a.u.]
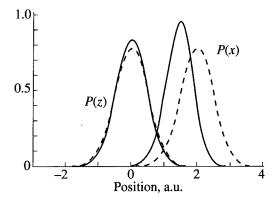

Fig. 2. Spatial probability distributions. Displayed are the spatial probability distributions $P(x, t) \equiv \sum_i \int dy\, dz |\Psi_i(x, y, z, t)|^2$ and $P(z, t) \equiv \sum_i \int dx\, dy |\Psi_i(x, y, z, t)|^2$ in the x and z direction at time $t = 0.1$ a.u. For comparison, the dashed lines show the corresponding distributions obtained from the nonrelativistic Schrödinger time evolution. The initial wave packet was centered initially at $\mathbf{r} = (-3, 0, 0)$. The nonrelativistic wave packet has moved to $x(t = 0.1 \text{ a.u.}) = -3$ a.u. $+ Et^2/2 = 2$ a.u. (Same parameters as in Fig. 1.)

Due to the square root of the operators in the expectation values at $t = 0$, all higher-order moments of the momentum contribute to determine the time evolution of the width. One can easily see that in the nonrelativistic limit these equations reduce to $\Delta x_{NR}(t)^2 = \Delta x^2 + \Delta p_x^2 t^2/m^2$, and similarly for y and z.

The long-time limit is of interest in the relativistic case. The first of expressions (3.1) has an interesting finite limit:

$$\Delta x(t \longrightarrow \infty)^2 = \Delta x^2 + \frac{1}{q^2 E^2}[c^2 \langle p_x^2 + \mathbf{p}^2 \rangle + m^2 c^4]$$

$$- \frac{1}{q^2 E^2} \langle \sqrt{[m^2 c^4 + c^2 \mathbf{p}^2]} \rangle^2 . \tag{3.2}$$

The spatial variances in the transverse directions diverge logarithmically in accord with $\Delta z(t \longrightarrow \infty)^2 =$

$$\Delta z^2 + \frac{c^2 \langle p_z^2 \rangle}{q^2 E^2} \ln^2\left[\frac{2qEt}{mc}\right] \text{ for the } z\text{-direction. As the}$$

electron approaches the speed of light, the spreading gets significantly reduced. The spatial probability distribution in the x-direction gets "frozen." If we assume that our initial wave packet is at rest such that basically all initial velocity contributions are much smaller than c, expression (3.2) simplifies to

$$\Delta x(t \longrightarrow \infty)^2 = \Delta x^2 + \langle p_x^2 \rangle \frac{c^2}{q^2 E^2}. \tag{3.3}$$

This expression has a direct interpretation. The time it takes a non-relativistic particle that is initially at rest to

exceed the velocity of light is $t^* = \dfrac{mc}{qE}$. If we assume that during this time the wave packet extends its width according to (the nonrelativistic formula) $\Delta x_{NR}(t)^2 = \Delta x^2 + \langle p_x^2 \rangle t^2/m^2$, then we obtain expression (3.3) for the final relativistic width with $t = t^*$. From this reasoning one could expect the nonrelativistic Schrödinger theory to roughly agree with the relativistic theory for times up to $t = t^*$. The fact that the final width is inversely proportional to E is also expected. The electron approaches c quicker and the time that is available for the wave packet to spread is shorter for larger E fields.

Let us now illustrate our results graphically. For better clarity we present our data in atomic units, for which $|q| = \hbar = m = 1$ and $c \approx 137$. The expectation values in (3.1) of the form $\langle \sqrt{...} \rangle$ were evaluated numerically in the Fourier space. As an initial state we used the first component of the Dirac state of (2.3). For the electric field strength we chose $E = 1000$ a.u. (ca. 5×10^{12} V/cm) corresponding to the time $t^* = 0.137$ a.u.

In Fig. 1 we show the evolution of the variance in three coordinate directions according to the analytical prediction of the relativistic Schrödinger theory (3.1). For comparison we have also included the predictions of the nonrelativistic (Schrödinger) theory $\Delta x_{NR}(t) = \Delta y_{NR}(t) = \Delta z_{NR}(t)$. For short times both theories agree but when the electron approaches the speed of light, the spreading in all three directions is severely suppressed. The spreading in the transverse direction y and z is reduced significantly logarithmically, whereas the spreading in the longitudinal x direction approaches the final value according to (3.3) $\Delta x(t \longrightarrow \infty) = 0.6935$.

In Fig. 1 we also compare the validity of our analytical approach for these parameters with the results obtained from the full solution to the Dirac equation on a numerical grid. Due to the limit in our numerical grid size as well as the memory restrictions, we have traced the time evolution of our Dirac wave packet to only $t = 0.3$ a.u. We have used this wave function to compute the spatial variances. The calculated widths are practically indistinguishable with those obtained from the Heisenberg equations. The agreement between our exact Dirac theory (dashed lines) and the (approximate) relativistic Schrödinger theory used for our analytical analysis is superb. Furthermore, the wave function has been projected on the negative-energy eigenstates and we found that during the entire interaction the fraction of population in the negative-energy Dirac sea remained negligible. In addition, the monotonic time evolution of the first-order moment (not presented) also confirms that effects due to the Zitterbewegung are not so important here.

In Fig. 2 we display the spatial probability distribution of the Dirac wave packet in the x and z directions. The distribution along the x-axis is defined as $P(x, t) \equiv \sum_i \int dy\, dz |\Psi_i(x, y, z, t)|^2$, where the summation goes over the four spinor components and the integration over the two complementary coordinate directions y and z. The wave packet in the x as well as z directions shows a significant reduction in spreading compared to the nonrelativistic spreading (dashed lines).

4. THIRD-ORDER MOMENTS: ASYMMETRIC WAVE PACKET SPREADING

Let us now investigate the third-order moments and demonstrate that the spatial probability distribution becomes asymmetric with respect to its "central" peak. The Schrödinger theory would predict that an initially symmetric wave packet remains symmetric as a function of time, independent of the speed of the center of mass even when the velocity of the center approaches c. In the relativistic case, however, we expect that a symmetric state becomes spatially asymmetric. The velocity of the front edge depends on the speed of the central peak and the spreading velocity. If the central peak approaches the speed of light, the spreading at the front of the wave packet must be reduced in order not to violate any causality as the leading part of the wave packet cannot propagate with a velocity larger than c. This raises an interesting question whether information can be transported by the front edge of a wave packet. Chiao and coworkers have investigated the possibility to obtain "superluminal" velocities in the propagation of wave packets in dispersive media [24].

A direct measure of the deviation from a symmetrical distribution is the coefficient of skewness, defined from the third-order moment of the spatial coordinates: $\mu_3 \equiv \langle(x - \langle x \rangle)^3 \rangle / \Delta x^3$. This provides a dimensionless measure of the asymmetry of a probability density. For
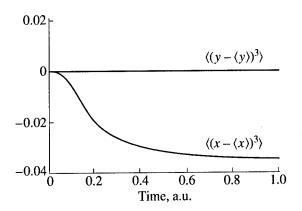

Fig. 3. Third-order moments. We show the third-order moments of the wave packet as a function of time according to (4.1). (Same parameters as in Fig. 1.)

reasons of symmetry we expect this coefficient to remain zero in the direction perpendicular to the electric field. In the direction of the external force, however, we might expect a steepening of the front edge portion of the wave packet.

To answer this question unambiguously, we have determined also the third-order moments from the operator solution (2.7) as

$$\langle (x - \langle x^3 \rangle) \rangle (t) \\ = 2\mathrm{Re}[\langle \Delta f_x (\Delta x)^2 \rangle] + \langle (\Delta f_x)^3 \rangle + \langle \Delta x \Delta f_x \Delta x \rangle, \tag{4.1}$$

where $\mathrm{Re}[\ldots]$ denotes the real part of $[\ldots]$, and Δf_x has the same meaning as in (3.1d). As the spatial distribution gets frozen in the x-direction in the long-time limit, the third-order moment approaches a time-independent limit

$$\langle (x - \langle x^3 \rangle) \rangle (t \longrightarrow \infty) = -\frac{3c^2 \langle p_x^2 \rangle^2}{mq^3 E^3}. \tag{4.2}$$

To keep this expression as simple as possible we have again assumed that all moments in $\mathbf{p}$ are initially much less than mc.

The results of (4.1) are presented in Fig. 3. The numerical result obtained from the time-dependent Dirac state (obtained from Section 2.1) is plotted in the same figure. Note that there is no visible difference between states evolved from the square root Klein–Gordon-type Hamiltonian in (2.4) and the Dirac Hamiltonian in (2.2). The negative sign in the third-order moment is a result of the steepened edge for the spatial distribution $P(x)$ toward increasing x values. This is the result of an acceleration due to the static field in that direction. The vanishing third-order moments found for the transverse directions indicate the spatial symmetry is maintained during the evolution of the wave packet in y and z. Finally, the third-order moment approaches the constant value predicted by (4.2) with a value of $\Delta x^3(t \longrightarrow \infty) = -0.0351$. For graphical examples of
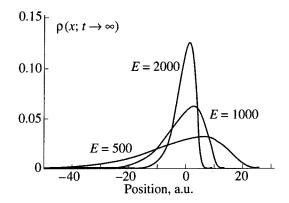
Fig. 4. Classical distribution functions in the long-time limit. Displayed are the classical densities $\rho(x, t \longrightarrow \infty)$ for three different values of the electric field strength in the long-time limit. The predicted steepening of the propagation front is clearly visible. The distributions were shifted to fit on the same plot. (E = 500, 1000, and 2000 a.u.; σ_x = 0.1 a.u.; and σ_p = 50 a.u.)

skewed spatial densities, we refer the reader to Fig. 4 discussed in the Appendix.

5. DISCUSSION

The observed suppression of the wave packet spreading can be interpreted if we analyze the time evolution of the velocity distribution of the wave packet. In the nonrelativistic limit this distribution remains shape-invariant while the center of this distribution follows the constantly accelerated motion. When the velocity contributions approach c, the acceleration is reduced and the distribution in velocity becomes more narrow. Asymptotically, the distribution approaches a narrow peak centered at c for which the spread in velocity is zero. As the dispersion in the velocity is the source for the spatial spreading, a narrowing in the velocity distribution has to be accompanied by a reduction in spatial spreading. We should mention here that the zero velocity width accompanied with a finite width in position space does not violate any quantum uncertainty relation. The commutator between the velocity operator and the position operator is not constant. The product of the two uncertainties $\Delta \dot{x} \Delta x$ therefore has no positive lower limit. The usual uncertainty product $\Delta p_x \Delta x$, however, grows as a function of time as the canonical momentum is conserved under the time evolution.

We should also point out that the relativistic spreading width reduction should not be confused with the well-known Lorentz contraction, which occurs if the wave packet is observed from a moving coordinate frame. Of course, the width observed from a moving frame is smaller compared to that observed in the packet's own rest frame, this effect is different than the one reported here. In our case the reduction of the spreading is a dynamical effect due to the presence of an external force. Furthermore, a simple Lorentz con-

traction would predict a symmetric density for which the coefficient of skewness is zero.

An important, if not the most important, question concerns the possibility of an experimental verification of our theoretical predictions. As mentioned in the Introduction, laser field strengths are available that are so strong that the electron's motion can become relativistic. The initial width of ca. $\sigma = 5.3 \times 10^{-12}$ m chosen in our numerical simulations agrees roughly with that of the ground-state wave function of the hydrogen-like Ne^{9+} ion. In strong-field experiments one can think of the role of the atom as a mere vehicle to carry the atomic electrons into the laser focus without changing the shape of the wave functions. As the atom approaches higher and higher intensities of the laser pulse, more and more of its weaker bound electrons are stripped off. In previous work on intense field ionization, it has been pointed out that the nonrelativistic spreading of the wave packet can be an important ionization mechanism in the superintense field stabilization regime [25, 26]. In this regime the suppression of spreading could lead to a reduced ionization rate. But at the present time this is just a speculation, and our description is too simplistic to allow for truly reliable predictions of the complicated atom–laser dynamics in the relativistic regime.

To summarize, our numerical solutions to the Dirac equation for an electron in a time-independent electric field show that the rate of wave packet spreading can be reduced. This effect is most pronounced in the direction of the external field but it is also manifested in the plane perpendicular to the field. Furthermore, the wave packet develops an asymmetric profile, which is caused by a steepening of the wave front along the propagation direction.

ACKNOWLEDGMENTS

APPENDIX A

Due to the nonlinearity induced by the relativistic mass, the direct classical–quantum correspondence principle does not apply and a single classical trajec-

tory does not follow exactly the quantum expectation values $\langle x \rangle(t)$ and $\langle p \rangle(t)$. If the quantum motion is compared with a classical statistical ensemble, however, the relativistic quantum dynamics in a static electric field can be described essentially in terms of classical mechanics. As is well known, the (nonrelativistic) quantum mechanical spreading of a wave packet has its direct classical counterpart. In order to keep our notation as transparent as possible, we restrict our discussion here to only one spatial dimension. A generalization to the full three-dimensional motion is straightforward. The classical Hamilton function is

$$H_{cl} = \sqrt{[m^2 c^4 + c^2 (p + qEt)^2]}. \qquad (A.1)$$

The single trajectory depends on the initial conditions $x(t = 0) \equiv x_0$ and $p(t = 0) \equiv p_0$ and has the solution

$$x_{cl}(t) = x_0 + \frac{1}{qE} \qquad (A.2)$$
$$\times [\sqrt{[m^2 c^4 + c^2 (p_0 + qEt)^2]} - \sqrt{[m^2 c^4 + c^2 p_0^2]}].$$

The time evolution of the classical probability distribution $\rho(x, p; t)$ is determined by the Liouville equation $\frac{\partial}{\partial t} \rho(x, p; t) = \{H_{cl}, \rho\}_{x,p}$, where $\{H_{cl}, \rho\}_{x,p} \equiv$

$\frac{\partial}{\partial x} H_{cl} \frac{\partial}{\partial p} \rho - \frac{\partial}{\partial p} H_{cl} \frac{\partial}{\partial x} \rho$ is the Poisson brackets of statistical mechanics [27]. For the relativistic motion in a constant E-field this equation takes the form:

$$\frac{\partial}{\partial t} \rho(x, p; t) \qquad (A.3)$$
$$= -c^2 (p + qEt) / \sqrt{[m^2 c^4 + c^2 (p + qEt)^2]} \frac{\partial}{\partial x} \rho(x, p; t).$$

If we assume that the classical ensemble is initially in the state $\rho(x, p, t = 0) \equiv \rho_0(x, p)$, the Liouville equation can be solved easily, as the Hamilton function is only a function of the canonical momentum:

$$\rho(x, p; t) = \rho_0(x - f(p, t), p), \qquad (A.4)$$

where $f(p, t)$ denotes the function $f(p, t) = \frac{1}{qE} \times$

$[\sqrt{m^2 c^4 + c^2 (p + qEt)^2} - \sqrt{m^2 c^4 + c^2 p^2}].$

The nonrelativistic spreading can be obtained directly from (A.4) in the limit $c \longrightarrow \infty$. In this limit $f(p, t)$ approaches $\frac{1}{2qmE} [(p + qEt)^2 - p^2] = \frac{p}{m} t + \frac{qE}{2m} t^2$.

Let us now focus on the spatial density defined by the integral of $\rho(x, p; t)$ over the momentum $\rho(x; t) \equiv$

$\int dp\, \rho(x, p; t) = \int dp\, \rho_0(x - f(p, t), p)$. In contrast to the nonrelativistic limit, for which one can obtain analytical results for $\rho(x, t)$ for various initial distributions ρ_0, such as Gaussians, we did not find any closed-form

solutions for the time evolution of the probability density in the relativistic case. In order to demonstrate the relativistic suppression of spreading, we have used an initial ensemble with Gaussian function dependency in

coordinate and momentum: $\rho_0(x, p) = \frac{1}{2\pi\sigma_x\sigma_p} \times$

$\exp[-(x/\sigma_x)^2/2]\exp[-(p/\sigma_p)^2/2]$. This classical ensemble has all average values $\langle x^n \rangle_{cl}$ and $\langle p^m \rangle_{cl}$ identical to the corresponding quantum expectation values of the wave function $\Psi(x) = [2\pi\sigma_x^2]^{-1/4}\exp[-(x/2\sigma_x)^2]$ if the classical widths are related by $\sigma_p = \hbar/(2\sigma_x)$. This wave function is the one-dimensional analog of the one used in the calculations in Sections 2–4.

For the nonrelativistic limit the time dependence of the spatial density can be obtained by integrating $\rho_0(x - f(p, t), p)$ over p:

$$\rho(x; t)$$
$$= \frac{1}{\sigma_x(t)\sqrt{2\pi}} \exp\left[-\frac{1}{2}\left(\left(x - \frac{qE}{2m}t^2\right) \Big/ \sigma_x(t)\right)^2\right] \qquad (A.5)$$

with the well-known spreading relation $\sigma_x(t)^2 \equiv \sigma_x^2 + \frac{\sigma_p^2}{m^2} t^2$. Please note that the more general relation

$\langle \Delta x^2 \rangle_{cl}(t) = \langle \Delta x^2 \rangle_{cl} + \frac{\langle \Delta p^2 \rangle_{cl}}{m^2} t^2$ holds for any classical

distribution.

In Fig. 4 we have calculated the spatial density numerically for the relativistic case. The initial distribution was a (symmetric) Gaussian in momentum and position with $\sigma_x = 0.1$ a.u. and $\sigma_p = 50$ a.u. We show the asymptotic shape of the density $\rho(x; t \longrightarrow \infty)$ for three values of the electric field strengths E. The figure shows that the distribution can develop a quite asymmetric profile due to a steepening of the propagation front of the wave packet. The central peak of the distribution has been shifted close to zero for convenience. The graphs demonstrate again our findings from Section 3 about the inverse relation of the final width to the electric field strength E [compare with (3.3)].

In Fig. 5 we present a direct comparison of the predictions for the one-dimensional classical ensemble $\rho(x; t)$ with the corresponding distribution $P(x, t)$ obtained from the quantum solution of the Dirac equation at time $t = 0.3$ a.u. The classical distribution is shown by the dashed line and it is practically indistinguishable from the quantum probability of the Dirac wave function. This suggests strongly that for our parameter regime the entire quantum evolution can be very well described by a classical probability distribution. It also suggests that the dynamics in the longitudinal direction depends only very weakly on the dynamics
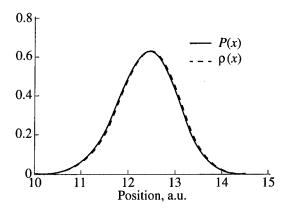
Fig. 5. Quantum versus classical spatial densities. Direct comparison of the spatial probability distribution of the Dirac wave packet $P(x, t)$ with that of the classical ensemble $\rho(x, t)$ taken at time $t = 0.3$ a.u. At this time the width has increased by roughly a factor of six, whereas the nonrelativistic width has grown by a factor of 15, as is shown in Fig. 1. Note that the full width at half maximum is $\sqrt{8\ln 2}\,\sigma_x$. [The two distributions were centered initially at $\mathbf{r} = (-14, 0, 0)$. Same parameters as in Fig. 1, $E = 1000$ a.u., $\sigma_x = 0.1$ a.u., and $\sigma_p = 5$ a.u.]

in the transverse directions. A one-dimensional model is therefore expected to work well.

The close similarity between the relativistic quantum and classical ensemble dynamics can be also demonstrated independently of the choice of the initial states if we compare the time evolution of the ensemble averages with the quantum expectation values. The equations of motion for the classical average values defined by $\langle x^n p^m \rangle_{cl} \equiv \iint dx\, dp\, x^n p^m \rho(x, p; t)$ are

$$\frac{\partial}{\partial t}\langle x^n p^m \rangle_{cl} = \iint dx dp\, x^n p^m \frac{\partial}{\partial t}\rho(x, p; t)$$

$$= -\iint dx dp\, x^n p^m \frac{\partial}{\partial p}H_{cl}\frac{\partial}{\partial x}\rho(x, p; t)$$

$$= \iint dx dp\, n x^{n-1} p^m \frac{\partial}{\partial p}H_{cl}\rho(x, p; t) \tag{A.6}$$

$$= n\langle x^{n-1} p^m c^2 (p + qEt)/\sqrt{[m^2 c^4 + c^2(p + qEt)^2]}\rangle_{cl}.$$

With the exception of the classical symmetry $\langle x^n p^m \rangle_{cl} = \langle p^m x^n \rangle_{cl}$, these equations are identical to those obtained from the Heisenberg equations of motions in the quantum case. In other words, if a classical ensemble can be identified whose initial average values for all moments in x and p agree with those of the corresponding initial quantum state, then the classical average values remain identical to the corresponding quantum expectation values for all times. For example, the classical spreading in the longitudinal direction has an identical form to that of the quantum mechanical case:

$$\langle \Delta x^2 \rangle_{cl}(t) = \langle \Delta x^2 \rangle_{cl} + \langle \Delta f(p, t)^2 \rangle_{cl}. \tag{A.7}$$

REFERENCES

1. Bethe, H.A. and Salpeter, E.E., 1977, *Quantum Mechanics of One- and Two-Electron Atoms* (Plenum).
2. Cowan, R.D., 1981, *The Theory of Atomic Structure and Spectra* (Univ. California Press).
3. For a review, see 1987, *Physics of Strong Fields*, Nato ASI series B, vol. 513, Greiner, W., Ed. (Plenum).
4. For numerical solutions to the Dirac equation in heavy-ion collisions, see Becker, U., Grün, N., and Schneid, W., 1983, *J. Phys. B*, **16**, 1967; Becker, U., Grun, N., Schneid, W., and Soff, G., 1986, *Phys. Rev. Lett.*, **56**, 2016; Bottcher, C., Strayer, M.R., Umar, A.S., and Reinhard, P.G., 1989, *Phys. Rev. A*, **40**, 4182; Momberger, K., Grun, N., and Scheid, W., 1991, *Z. Phys. D*, **18**, 133.
5. McIver, J.K. and Fedorov, M.V., 1979, *Sov. Phys. JETP*, **49**, 1012.
6. For a review, see Reiss, H.R., 1992, *Prog. Quantum Electron*, **16**, 1. See also Reiss, H.R., 1990, *J. Opt. Soc. Am. B*, **7**, 574.
7. For recent experimental works using high-power laser sources, see Perry, M.D. and Mourou, G., 1994, *Science*, **264**, 917; Boyer, K. and Rhodes, C.K., 1994, *J. Phys. B*, **27**, L633; Moore, C.I., Knauer, J.P., and Meyerhofer, D.D., 1995, *Phys. Rev. Lett.*, **74**, 2439; Monot, P., Auguste, T., Gibbon, P., *et al.* 1995, *Phys. Rev. Lett.*, **74**, 2953.
8. Gersten, J.I. and Mittleman, 1976, *J. Phys. B*, **9**, 2561.
9. Gavrila, M. and Kaminski, J.Z., 1984, *Phys. Rev. Lett.*, **52**, 613; Pont, M., Walet, N., Gavrila, M., and McCurdy, C.W., 1988, *Phys. Rev. Lett.*, **61**, 939.
10. Fedorov, M.V. and Movsesian, A.M., 1988, *J. Phys. B*, **21**, L155.
11. Su, Q., Eberly, J.H., and Javanainen, J., 1990, *Phys. Rev. Lett.*, **64**, 862; Su, Q. and Eberly, J.H., 1991, *Phys. Rev. A*, **43**, 2474; Law, C.K., Su, Q., and Eberly, J.H., 1991, *Phys. Rev. A*, **44**, 7844; Su, Q. and Eberly, J.H., 1992, *Laser Phys.*, **2**, 598; Su, Q., 1993, *Laser Phys.*, **3**, 241; Su, Q., Irving, B.P., Johnson, C.W., and Eberly, J.H., 1996, *J. Phys. B*, **29**, 5755.
12. Dörr, M., Potvliege, R.M., and Shakeshaft, R., 1990, *Phys. Rev. Lett.*, **64**, 2003; Kulander, K.C., Schafer, K.J., and Krause, J.L., 1991, *Phys. Rev. Lett.*, **66**, 2601; Dorr, M., Potvliege, R.M., and Shakeshaft, R., 1991, *Phys. Rev. A*, **43**, 3729.
13. For review articles, see 1992, *Atoms in Intense Laser Fields*, Gavrila, M., Ed. (Academic).
14. De Boer, M.P., Hoogenraad, J.H., Vrijen, R.B., *et al.* 1993, *Phys. Rev. Lett.*, **71**, 3263; van Druten, N.J., Constantinescu, R.C., Schins, J.M., *et al.* 1997, Phys. Rev. A, **55**.
15. For a classical treatment of relativistic ionization, see, e.g., Grochmalicki, J., Lewenstein, M., Wilkens, M., and Rzazewski, K., 1990, *J. Opt. Soc. Am. B*, **7**, 607; Keitel, C.H. and Knight, P.L., 1995, *Phys. Rev. A*, **51**, 1420.
16. For work on a quantum mechanical description of relativistic ionization, see, e.g., Faisal, F.H.M. and Radozycki, T., 1993, *Phys. Rev. A*, **47**, 4464; 1993, *Phys. Rev. A* **48**, 554; Horbatsch, M., 1993, *Z. Phys. D*, **25**, 305; Keitel, C.H., Knight, P.L., and Burnett, K., 1993, *Europhys. Lett.*, **24**, 539; Crawford, D.P. and Reiss, H.R., 1994,

Phys. Rev. A, **50**, 1844; Protopapas, M., Keitel, C.H., and Knight, P.L., 1996, *J. Phys. B*, **29**, L591.

17. For early work on free electrons in relativistic fields, see Brown, L.S. and Kibble, T.W.B., 1964, *Phys. Rev. A*, **133**, 705; Eberly, J.H. and Sleeper, A., 1968, *Phys. Rev. A*, **176**, 1570; Eberly, J.H., 1969, *Progress in Optics 7*, Wolf, E., Ed. (Amsterdam: North-Holland) p. 359; Satachik, A. and Schappert, E.S., 1970, *Phys. Rev. D*, **1**, 2738.

18. Dodonov, V.V. and Mizrahi, S.S., 1993, *Phys. Lett. A*, **177**, 394.

19. Thaller, B., 1992, *The Dirac Equation* (Springer).

20. Bjorken, J.D. and Drell, S.D., 1964, *Relativistic Quantum Mechanics* (McGraw-Hill).

21. For technical details of the numerical algorithm, see Smetanko, B.A., Su, Q., and Grobe, R., *Comm. Comp. Phys.* (to be submitted).

22. Miloni, P.W., 1994, *The Quantum Vacuum* (Academic).

23. For a review on the particle interpretations of relativistic theories, see Feshbach H. and Villars, F., 1958, *Rev. Mod. Phys.*, **30**, 24.

24. For reviews on "superluminal" propagation of wave packets see Chiao, R.Y., Kwiat, P.G., and Steinberg, A., 1993, *Scientific Am.*, 52 (August); Chiao, R.Y., 1994, *Quantum Opt.*, **6**, 359.

25. Grobe, R. and Fedorov, M.V., 1992, *Phys. Rev. Lett.*, **68**, 2592; 1993, *J. Phys. B*, **26**, 1181; 1993, *Laser Phys.*, **3**, 265.

26. Katsouleas, T. and Mori, W.B., 1993, *Phys. Rev. Lett.*, **70**, 1561; Grobe, R. and Fedorov, M.V., 1993, *Phys. Rev. Lett.*, **70**, 1562.

27. For a review see, e.g., Goldstein, H., 1981, *Classical Mechanics* (Addison-Wesley), chapter 9.8.

Laser-Assisted Scattering of Polarized Electrons at High Field Intensities

C. Szymanowski*, R. Taïeb, and A. Maquet

Laboratoire de Chimie Physique—Matière et Rayonnement, 11 rue Pierre et Marie Curie, Université P. et M. Curie Paris VI, Paris Cedex 05, F-75231 France

* e-mail: szymanow@ccr.jussieu.fr

Received August 4, 1997

Abstract—Qualitative and quantitative results of a relativistic calculation of the S-matrix transition amplitudes and cross sections for Mott scattering of initially polarized electrons in the presence of an ultraintense single-mode laser field are presented. Exact Dirac–Volkov wave functions within a circularly polarized light field are used to describe the "dressed" electron and the collisional stage with the Coulomb potential is treated in the first-Born approximation. We discuss the influence of the laser field on the degree of polarization of the scattered electrons, depending on its intensity, and consider effects arising in different geometries in ultrastrong fields.

Recent experiments on laser-induced processes in ultrahigh intensity fields, namely, well beyond the atomic field strength intensity of about 3.5×10^{16} W/cm^2, obtained via short-pulse laser systems have clearly given evidence of relativistic effects [1]. In fact, it has been well-known since the theoretical work on free electrons in ultrastrong electromagnetic fields [2] that, for intensities in the range 10^{18}–10^{20} W/cm^2, in the near-infrared frequency domain, the averaged quiver energy of the electron becomes comparable to its rest energy. Here, the relativistic mass shift, the breakdown of the electric dipole approximation, the roles of the magnetic field component of the laser field and the electron spin may become of significance. On the one hand, the search for spin-specific effects has been relatively scarce and especially under certain assumptions for other purposes [3]. On the other hand, it is expected that spin-dependent relativistic Mott scattering provides a clear distinction between simple kinematics and spin–orbit coupling effects [4]. The purpose of this letter is to show that the modifications of the polarization degree in Mott scattering of polarized electrons due to the presence of an ultraintense field can provide a remarkable signature of spin effects in electron–laser interaction.

Concerning laser-assisted electron–atom collisions, most experimental and theoretical studies were restricted to the nonrelativistic regime and low-frequency fields, where it has been already recognized that, as a general consequence of the infrared divergence of QED, large numbers of photons can be exchanged between the field and the projectile-target system. An extension of the first-Born nonrelativistic treatment [5] to the relativistic domain was formally derived for unpolarized electrons [6]. There have been as well theoretical investigations of relativistic scattering in multimode fields [7]. Recently, for the monochromatic case, the explicit derivation of the S-matrix element in first-order Born approximation for Coulomb scattering of Dirac–Volkov electrons has been used in order to discuss the differential cross section for unpolarized electrons in detail [4]. These results show, notably in comparison to more simplified approaches (spinless particle and nonrelativistic limit), the importance of the full Dirac approach, especially in the case of ultraintense laser fields.

Before we present the most interesting results of our investigation regarding laser-assisted Mott scattering of polarized electrons, we sketch the principal steps of our treatment. The solutions to the Dirac equation for an electron with four-momentum p^μ inside an electromagnetic plane wave are well known [8, 9]. They read for the case of circular polarization of the field propagating along the $\hat{e}_z$ direction

$$\psi_q = \langle x|q \rangle = \left[1 + \frac{\cancel{k}\cancel{A}}{2c(kp)} \right] \frac{u}{\sqrt{2QV}}$$

$$\times \exp\left[-i(qx) - i \int_0^{kx} \frac{(pA)}{c(kp)} d\phi \right], \quad (1)$$

where u represents a free electron bispinor satisfying the Dirac equation without field and which is normalized by $\bar{u}u = u^*\gamma^0 u = 2c^2$. Here the Feynman slash notation is used, and V is the normalization volume. The physical significance of $q^\mu = (Q/c, \mathbf{q})$ is the averaged four-momentum (dressed momentum) of the particle inside the laser field with vector potential $A^\mu = (0, A_x\cos(kx), A_y\sin(kx), 0)$ with wave four-vector k^μ: $q^\mu = p^\mu - k^\mu[A^2/2(kp)c^2]$. From the free bispinors u the two helicity states of the bare electrons can be obtained by using the projection operators

$$\Sigma^{(\pm)} = \frac{1 \pm \gamma^5 \cancel{s}}{2} \quad (2)$$

with $\gamma^5 = i\gamma^0\gamma^1\gamma^2\gamma^3$, the γ^i denoting Dirac matrices, and the Lorentz-boosted spin four-vector $s^\mu = (|\mathbf{p}|/c, E\mathbf{p}/c^2|\mathbf{p}|)$.

For Coulomb scattering the S-matrix element for the transition $|q\rangle \longrightarrow |q'\rangle$ of the dressed electrons is, in first-Born approximation,

$$T_{q' \leftarrow q} = \frac{iZ}{c}\int d^4x \bar\Psi_{q'}\frac{\gamma^0}{|\mathbf{x}|}\Psi_q. \tag{3}$$

For the high energies of the incoming projectiles in ultrastrong fields, the first-order calculation is certainly valid. Since the four-vector potential A^μ of the intense laser field does not change in the collision process, the Volkov electron in the final state $|q'\rangle$ will have the same invariant effective mass as in the initial state $|q\rangle$ and, hence, the following condition fixing the outgoing momentum $\mathbf{q'}$ holds:

$$q^\mu q_\mu = q'^\mu q'_\mu = \left(1 - \frac{A^2}{c^4}\right)c^2. \tag{4}$$

In the absence of the laser this equation reduces to the elastic condition $|\mathbf{p}| = |\mathbf{p'}|$ obtained in ordinary Mott scattering using energy and mass conservation.

The differential cross section $d\sigma^{(\pm)}$ for the scattering of right-handed (positive helicity) electrons, described by the bispinor $u^{(+)}$, with (−) or without (+) spin flip is

$$d\sigma^{(\pm)} = \frac{Z^2}{c^2}\left| \int d^4x \bar{u}'^{(\pm)}\left[1 + \frac{A\!\!\!/k\!\!\!/}{2c(p'k)}\right]\frac{\gamma^0}{|\mathbf{x}|} \right.$$

$$\times \left[1 + \frac{k\!\!\!/A\!\!\!/}{2c(pk)}\right]u^{(+)}\exp\left[-i(q-q')x - i\int_0^{kx}\frac{(pA)}{c(kp)}d\phi \right. \tag{5}$$

$$\left. + i\int_0^{kx}\frac{(p'A)}{c(kp')}d\phi\right]\bigg|^2 \frac{|\mathbf{q'}|dQ'do}{32\pi^3c^4|\mathbf{q}|T}.$$

Here, the density of final states $|\mathbf{q'}\rangle$ in phase space divided by time T and the incoming flux of electrons have been used and o denotes the solid angle.

The main steps in the explicit calculation of the cross section are as follows: The time dependence of the phase in the matrix element (3), which arise from the $A\!\!\!/$ factors, can be recast by using trigonometric relations and the generating function of ordinary Bessel functions J_n. The differential cross section is then obtained under the form of a sum over Fourier components, the order of which being associated to the net number of exchanged photons. Each corresponding partial cross section is then expressed via well-known Fourier transform integrals of the potential $1/|\mathbf{x}|$. The

appropriate expression for the square of the δ-function occurring in this formula is obtained by the usual procedure [9]. This leads to the expression

$$\frac{d\sigma^{(\pm)}}{do} = \sum_n \frac{d\sigma^{(n,\pm)}}{do}\bigg|_{Q' = Q + n\omega}, \tag{6}$$

where $\mathbf{q'}$ is fixed through condition (4). The differential cross section $d\sigma^{(n,\pm)}/do$ for each net n-photon process is

$$\frac{d\sigma^{(n,\pm)}}{do} = \frac{Z^2|\mathbf{q'}|}{c^2|\mathbf{q}|}\frac{1}{|\mathbf{q} - \mathbf{q'} + n\mathbf{k}|^4}\bigg| [\bar{u}'^{(\pm)}\gamma^0 u^{(+)}]J_n(\zeta)$$

$$\times e^{(in\phi_0)} + \left[\bar{u}'^{(\pm)}\frac{A\!\!\!/_x k\!\!\!/}{2c(kp')}\gamma_0 u^{(+)} + \bar{u}'^{(\pm)}\gamma^0\frac{k\!\!\!/A\!\!\!/_x}{2c(kp)}u^{(+)}\right]$$

$$\times \frac{1}{2}\{J_{n+1}(\zeta)e^{[i(n+1)\phi_0]} + J_{n-1}(\zeta)e^{[i(n-1)\phi_0]}\}$$

$$+ \left[\bar{u}'^{(\pm)}\frac{A\!\!\!/_y k\!\!\!/}{2c(kp')}\gamma^0 u^{(+)} + \bar{u}'^{(\pm)}\gamma^0\frac{k\!\!\!/A\!\!\!/_y}{2c(kp)}u^{(+)}\right] \tag{7}$$

$$\times \frac{1}{2i}\{J_{n+1}(\zeta)e^{[i(n+1)\phi_0]} - J_{n-1}(\zeta)e^{[i(n-1)\phi_0]}\}$$

$$- \frac{A^2}{4c^2(kp)(kp')}[\bar{u}'^{(\pm)}k\!\!\!/\gamma^0 k\!\!\!/u^{(+)}]J_n(\zeta)e^{(in\phi_0)}\bigg|^2,$$

where $\zeta = \{[(pA_x/c(kp) - p'A_x/c(kp'))]^2 + [pA_y/c(kp) - p'A_y/c(kp')]^2\}^{1/2}$ and $\phi_0 = \arccos\{[pA_x/(kp) - p'A_x/(kp')]/c\zeta\}$. We note that without laser field, (6) with (7) reduces, after integration over the final energy variable, to the well-known polarized (first-Born) Mott cross section for potential scattering.

Coming back to the laser-assisted cross section, we observe two features: The effect of the vector potential is contained in both the arguments of the Bessel functions and in prefactors in front of them. The latter originate from the Volkov terms acting on the free bispinor in (1) and do not depend on the net number of exchanged photons. In addition to these weight factors the squared amplitude for each n-photon energy transfer is given in terms of squares and products of Bessel functions whose magnitudes govern the corresponding differential cross section.

In order to calculate the different transition amplitudes between polarized spin states, the standard trace technique is used. Using the spin projection operators (2), traces of the following form have to be evaluated:

$$\left|\bar{u}'^{(\pm)}...\gamma...u^{(+)}\right|^2 = \frac{1}{4}\text{Tr}[...\gamma...(1 \pm \gamma^5 s\!\!\!/') \tag{8}$$

$$\times (c p\!\!\!/' + c^2)...\gamma...(1 + \gamma^5 s\!\!\!/)(c p\!\!\!/ + c^2)],$$

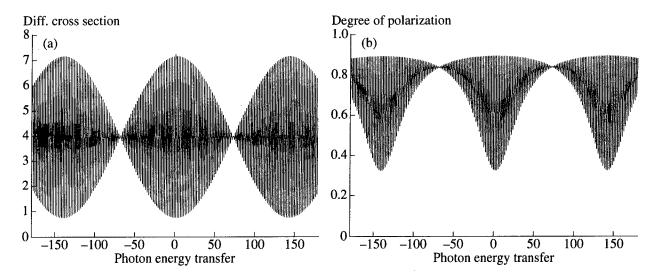Diff. cross section

Degree of polarization

Fig. 1. (a) Envelope of unpolarized differential cross section $d\sigma/do$ scaled in 10^{-14} a.u. as a function of energy transfer $Q' - Q$ scaled in units of the laser photon energy ω for an electrical field strength of $E = \omega c = 5.89$ a.u. or vector potential $A = c^2 = 18769$ a.u. (b) Degree of polarization $P^{(n)}$ after $\pi/2$-scattering (solid line) as a function of energy transfer $Q' - Q$ around the elastic energy peak scaled in units of the laser photon energy ω for the same electrical field strength. The incoming electrons are right-handed polarized and their energy is $W = 4c^2$.

where the occurring dyadics of bispinors have been written in terms of energy projection operators.

Let us first consider the case of a measurement which does not distinguish between final spin projection states. This means that only the operator $(1 + \gamma^5 \not{f})$ in (8) occurs. An explicit calculation of theses traces in order to evaluate (7) shows that all additional traces involving γ^5 vanish or cancel mutually, and the unpolarized cross section [4] is recovered. This corresponds to the well-known feature of ordinary Mott scattering that in first order, the differential cross section for unpolarized and polarized beams is identical [10].

The derivation of the explicit formula for the spin-flip $d\sigma^{(-)}/do$ and nonflip $d\sigma^{(+)}/do$ cross sections from (7) has led to the calculation of a large number of different traces over products of up to 8 γ-matrices. The final expressions are rather lengthy and will be omitted here.

We are especially interested in the degree of polarization of the electrons after the scattering event. This

Degree of polarization P^{tot} after $\pi/2$-scattering of right-handed polarized electrons for different kinetic energies W of the electrons and several electric field strengths E

W_{kin}	$E = 0$ a.u.	$E = 0.05$ a.u.	$E = 0.1$ a.u.	$E = 0.5$ a.u.
100 a.u.	0.00531	0.00452	0.00377	0.00205
c^2	0.60000	0.59468	0.58931	0.52012
$4c^2$	0.92308	0.92017	0.91716	0.82421

quantity is defined for right-handed electrons as

$$P^{(n)} = \left(\frac{d\sigma^{(n,+)}}{do} - \frac{d\sigma^{(n,-)}}{do} \right) \Big/ \left(\frac{d\sigma^{(n,+)}}{do} + \frac{d\sigma^{(n,-)}}{do} \right). \quad (9)$$

Notably in very strong laser fields a large number of photons can be exchanged during the collision process. In order to compare the values obtained for a particular field strength to the ordinary Mott case, the quantity

$$P^{tot} = \left(\frac{d\sigma^{Mott}}{do} \right)^{-1} \sum_n P^{(n)} \frac{d\sigma^{(n)}}{do} \quad (10)$$

is considered which weights the degree of polarization of each net n-photon process by its unpolarized cross section.

We have performed simulations in a wide range of parameters of laser intensities and for an angular frequency of $\omega = 0.043$ a.u., corresponding to the neodymium laser using different scattering geometries. However, in order to illustrate the main features of our results we will restrict here to the case of $\pi/2$-scattering when the incoming right-handed electron is propagating in the plane of polarization: $\mathbf{k} \cdot \mathbf{q} = 0$.

Under these conditions, in the table for several electric field strength the comparable value P^{tot} is compiled for $\pi/2$-scattering into the plane of polarization, $\mathbf{k} \cdot \mathbf{q}' = 0$, depending on the initial kinetic energy $W_{kin} = cp_0 - c^2$ of the electrons. It is realized that the overall effect of the laser field, even at relatively low laser intensities, is to further reduce the degree of polarization as compared with the effect of the spin–orbit coupling in ordi-

nary (field-free) Mott scattering. This depolarization effect is due to the spin precession in the field which effectively reduces the degree of polarization.

We turn now to the scattering events in which relatively small numbers of photons are exchanged which corresponds to the central part of the spectrum of the energy distribution of scattered electrons around the elastic peak of net zero photon exchange. In the strong field regime, the Bessel functions reach their principal asymptotic limit with $\zeta \gg n$, and the envelope of the differential cross section exhibits regular oscillations as plotted in Fig. 1a. The corresponding oscillations in the degree of polarization for scattering into the plane of polarization can be seen in Fig. 1b: Though slightly reduced in comparison to the field-free case, the maximal degree of polarization is obtained when the contribution from the first factor ($\propto 1$) contained in the Volkov prefactor in (1) dominates the cross section. When the cross section becomes small, the degree of polarization drops down as well. In this case the contribution from the factor $\propto 1$ of the Volkov prefactor becomes comparable to the contributions from the second part ($\propto A$) associated to the spin–laser interaction.

While this is an influence of the laser field on an energy scale defined by the laser photon energy and, hence, small compared to the kinetic energy of the projectile, a notable effect arises when the scattering geometry is changed with respect to the wave vector $\mathbf{k}$: In Fig. 2 the differential cross section summed over a small window around the elastic peak is shown as a function of $\vartheta = \angle(\mathbf{k}, \mathbf{q}')$. As in the absence of a laser field, for high energies of the projectiles the $\pi/2$-scattering is reduced by the Mott factor due to spin–orbit coupling. However, for ultraintense fields and in the propagation direction of the laser, meaning ϑ close to zero, there is a strong enhancement of $d\sigma/do$ mainly due to the contributions arising from the second part of the Volkov prefactor ($\propto A$) [4]. This can be seen more clearly in the inset. It is realized in Fig. 2 that this corresponds to an enhancement of spin-flip against nonflip processes. In order to illustrate this behavior even further, the corresponding degree of polarization is shown in Fig. 3. Here, it can be clearly seen that around the propagation direction $\mathbf{k}$ of the field the degree of polarization is strongly reduced even below zero. This is a remarkable result in comparison to ordinary Mott scattering where in the limit of high projectile energies no depolarization takes place.

In brief, our calculations show that the influence of the external field during a laser-assisted electron–atom collision process is to reduce the degree of polarization even stronger than the effect due to spin–orbit coupling in ordinary Mott scattering. A particularly interesting situation is the scattering into the propagation direction of the laser where it is found that the degree of polarization can even drop remarkably below zero.
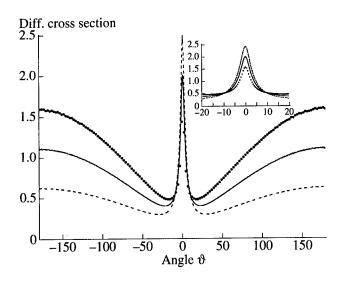
Diff. cross section

Fig. 2. Summed differential cross sections $d\sigma/do$ scaled in 10^{-14} a.u. of ± 100 peaks around the elastic one as a function of the angle ϑ between the light propagation and the final momentum for an electrical field strength of $E = \omega c = 5.89$ a.u. The solid line denotes the result averaged over the two polarization states, the dashed one sketches the value for spin-flipped electrons $d\sigma^{(-)}/do$, and the dotted one is the result for the no-spin-flip process $d\sigma^{(+)}/do$. The incoming electrons are right-handed polarized and their energy is $W = 4c^2$. In the inset a magnification of the central peak around $\vartheta = 0$ is shown.

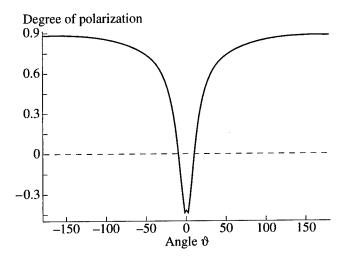Degree of polarization

Fig. 3. Degree of polarization averaged over ± 100 peaks around the elastic one as a function of the angle ϑ between the light propagation and the final momentum for an electrical field strength of $E = \omega c = 5.89$ a.u. The incoming electrons are right-handed polarized and their energy is $W = 4c^2$. The scattering angle is $\pi/2$.

ACKNOWLEDGMENTS

CRB CHRX CT 940470. The Laboratoire de Chimie Physique—Matière et Rayonnement is Unité de Recherche Associée au CNRS (URA 176).

REFERENCES

1. Bula, C. *et al.*, 1996, *Phys. Rev. Lett.*, **76**, 3116; Norreys, P.A. *et al.*, 1996, *Phys. Rev. Lett.*, **76**, 1832; Monot, P. *et al.*, 1995, *Phys. Rev. Lett.*, **74**, 2953; Moore, C.I., Knauer, J.P., and Meyerhofer, D.D., 1995, *Phys. Rev. Lett.*, **74**, 2439.

2. Brown, L.S. and Kibble, T.W.B., 1964, *Phys. Rev. A*, **133**, 705; Nikishov, A.I. and Ritus, V.I., 1964, *Zh. Eksp. Teor. Fiz.*, **46**, 776 [1964, *Sov. Phys. JETP*, **19**, 529]; Eberly, J.H., 1969, *Progress in Optics 7*, Wolf, E., Ed. (Amsterdam: North-Holland).

3. Krstic, P.S. and Mittleman, M.H., 1992, *Phys. Rev. A*, **45**, 6514; Latinne, O., Joachain, C.J., and Dörr, M., 1994, *Europhys. Lett.*, **26**, 333.

4. Szymanowski, C. *et al.*, 1997, *Phys. Rev. A*, 3846.

5. Bunkin, F.V. and Fedorov, M.V., 1965, *Zh. Eksp. Teor. Fiz.*, **49**, 1215 [1966, *Sov. Phys. JETP*, **22**, 844].

6. Denisov, M.M. and Fedorov, M.V., 1967, *Zh. Eksp. Teor. Fiz.*, **53**, 1340 [1968, *Sov. Phys. JETP*, **26** 779].

7. Roshchupkin, S.P., 1996, *Zh. Eksp. Teor. Fiz.*, 109, 337 [1996, *JETP*, **82**, 177]; Zhou, F. and Rosenberg, L., 1992, *Phys. Rev. A*, **45**, 7818.

8. Volkov, D.M., 1935, *Z. Phys.*, **94**, 250.

9. Berestetzkii, V.B., Lifshitz, E.M., and Pitaevskii, L.P., 1982, *Quantum Electrodynamics*, 2nd ed. (Oxford: Pergamon).

10. Bjorken, J.D. and Drell, S.D., 1964, *Relativistic Quantum Mechanics* (New York: McGraw-Hill).

Nuclear Excitation and Decay at the Superstrong Laser Field

M. Yu. Romanovsky[1]

Humboldt University, Institute of Physics, Berlin, 10099 Germany

Received July, 5, 1997

Abstract—The classical interaction of particles connected by a central potential in a superstrong laser field is investigated. It is shown that bound charged particle or the group of particles can change their energy under the action of such field. Transitions between bound states are treated classically; the spectrum of unperturbed bound states is supposedly known. The energy obtained by the particles above the bound energy can provide their decay. The introduced approach is used for the first rough description of the possible direct nuclear excitation and decay by superstrong laser field.

1. INTRODUCTION

A classical two-particles system with the central attracting potential shows a bound state(s) if it has an internal motion: a simple angular revolution. Particles fall on each other in the absence of this internal rotation. On the other hand, the classical bound systems can exist in presence of an external field if their internal rotation is absent. For example, one can conceive a special classical bound system "ion–electron(s)" in presence of the strong circularly polarized laser field, which provides the electrons with the necessary rotation [1]. Such a system is bound regardless of the presence of internal angular motion.

With the notable exception of S-state systems, most systems in nature exhibit an angular motion. These systems are of interest not only in attractive electric force contexts, but also in cosmology with the Newtonian problem of revolving gravitating bodies around a masses center. At the same time, atom and ion systems with Coulomb interaction between nucleus and moving electrons also fall in this category. The next level in this description is within the nucleus where one or several strongly bound nucleons can be excited above complete shells. In principle, the inner-nucleons (quark) motion can be considered in this perspective.

With the exception of the gravitational motion, a strong polarized laser field can perturb any internal motion of charged particles. Indeed, let us consider a system of a particle with mass m and charge q which revolves along the circular orbit with the radius r_0 and with the frequency Ω. This system can acquire additional angular momentum $\Delta M = m r_0^2 \omega/2$ during the half-period of laser radiation, where ω is the angular frequency of laser radiation. If the radiation is linearly polarized, this particle acquires the same moment with opposite sign during the next half-period, so that with such a laser, no time-cumulative effects occur. Nevertheless, such accumulation is principally possible if the

radiation is elliptically polarized, most evidently with circular polarization where (like in [1]) an increment of the angular moment of the revolved particle occurs uniformly in time. In order to simplify following calculations, we suppose here and below that the vector Ω is parallel the wave vector of the laser field, i.e., circulations with frequencies Ω and ω are coaxial. Therefore, the energy which the particle acquires during the period of laser radiation is $\Delta E_T \sim 2 m r_0^2 \Omega \omega$. If the effect is accumulated like for the circularly polarized laser radiation, the total energy change can be $\Delta E_T \sim 2 m r_0^2 \Omega \omega^2 \tau_i$ when τ_i is the laser pulse duration. This value is not small, if one considers that for lower quadruple nuclear levels where Ω corresponds to 100 keV, ω corresponds to 1 eV, under $\tau_i \sim 1$ ps, $r_0 \sim 5 \times 10^{-13}$ cm, $m = m_N$ (nucleon mass) we have that $\Delta E_T \sim 40$ keV. This estimation is very optimistic, because the system has also to be able to absorb this energy. There are no problems in a classical case, because the considered particle simply changes its orbit. At the same time, all considered systems look rather quantized when this energy can change by a jump only. Consequently, this energy "absorption" process needs another interpretation.

The general way to describe each system is to solve its Schrödinger equation for a general wave function. In our case it has a time-dependent Hamiltonian and it is not clear how to solve it even numerically. At the same time, it is possible to search solutions of the general Schrödinger equation for any system operator describing some measured system parameter. We need the equation for the distance operator $(\tilde{r})$; it is

$$d\tilde{r}/dt = [\tilde{H}, \tilde{r}],$$

where $\tilde{H}$ is Hamiltonian of the system. This equation can be reduced using the expansion of the operator $\tilde{r}$ over the momenta series. Then it is possible to study mean values of this operator (the radius of particle orbit in our case), the variance (smearing) of the particle over space, and all higher momenta. The simplest approximation

[1] Permanent address: General Physics Institute, Russian Academy of Sciences, Moscow, 117942 Russia

of the problem is to solve the equation for the operator mean value **r**. It is known that this is the equation of Newton's second law (see, for example, [2]):

$$dr/dt = -\partial U/\partial r,$$

where U is the potential energy of the system.

Finally, the classical interpretation of the quantum angular motion perturbation can be the following: the perturbation is simply the appearance of the system in an another eigenstate. The unperturbed energy spectrum is supposed known. The concentration of considered systems at the initial and all others states can be changed under the influence of the laser field. The rate of this change must be interpreted as the transition rate and it physically means that not all particles in the interaction volume receive the additional energy from the external electromagnetic field simultaneously: when one of them is receiving energy, others are "waiting." It is a normal quantum mechanics approach to substitute the distribution over time by the distribution over an ensemble. This approach is valid if the final part of the excited systems is small [2]. We will solve equations of Newton's second law taking these considerations into account.

We suppose that the first rough description of systems connected by the central potential at the superstrong laser field can be simply classical. It is known that the (quasi-) classical description of systems is enough if systems are in states with a large principal quantum number. A cross-verification for this approach can be obtained if the expressions for the transition rates contain observable values only (like a transition energy ΔE) and unmeasurable values (like the depth of a potential well U_0) do not come into play.

Notice that the ability of systems to absorb energy can differ strongly even in a classical case. In particular, if there is some resonance in the system, the energy can rise in time significantly. The nonresonant energy absorption is comparably much less. The presence of resonance in the problem can also be used as a cross-verification of the effect existence.

2. THE FIRST- AND SECOND-ORDER EQUATIONS FOR A SYSTEMS MOTION

If the laser field is applied to a two-body system, it will move the system as a whole as well as give it some additional rotation. Let the largest body (the nucleus skeleton with completed shells) have mass M and charge $\tilde{Q}$ and the excited particle mass m and charge $\tilde{q}$. Let **R** and **r** be their respective coordinates and the force between them $\mathbf{F}_n(|\mathbf{R} - \mathbf{r}|)$. We have

$$M\ddot{\mathbf{R}} = -\mathbf{F}_n(|\mathbf{R} - \mathbf{r}|) + \tilde{Q}\mathbf{E}(\mathbf{R}),$$
$$m\ddot{\mathbf{r}} = \mathbf{F}_n(|\mathbf{R} - \mathbf{r}|) + \tilde{q}\mathbf{E}(\mathbf{r}), \tag{1}$$

where **E** is the vector of the laser field strength amplitude and Newton's third law is taken into account. The

sign means the time differentiation. The laser wavelength λ is always much more than the characteristic size of the system $|\mathbf{R} - \mathbf{r}|$ and $|\mathbf{R} - \mathbf{r}| \sim 10^{-8}$ cm is much less than $\lambda \sim 10^{-4}$ cm already for atoms. This means that $\mathbf{E}(\mathbf{R}) = \mathbf{E}(\mathbf{r})$. If we now shift to center-mass coordinates, $\mathbf{R}_{cm} = (M\mathbf{R} + m\mathbf{r})/(M + m)$ and we have

$$(M + m)\ddot{\mathbf{R}}_{cm} = (\tilde{Q} + \tilde{q})\mathbf{E}(\mathbf{R} = \mathbf{r}). \tag{2}$$

This equation describes center mass oscillations in field **E** of the equivalent body with mass $(M + m)$ and charge $(\tilde{Q} + \tilde{q})$. The second equation for $\Delta\mathbf{r} = \mathbf{R} - \mathbf{r}$ looks

$$\Delta\ddot{\mathbf{r}} = (1/\mu)\mathbf{F}_n(|\Delta\mathbf{r}|) + (\tilde{q}/m - \tilde{Q}/M)\mathbf{E}(\mathbf{r}). \tag{3}$$

Here, μ is reduced mass, $\mu = Mm/(M + m)$, the $\tilde{q}_{eff}$ is effective charge:

$$\tilde{q}_{eff} = (\tilde{q}M - \tilde{Q}m)/(m + M). \tag{4}$$

For example, for the nucleus with total number of protons Z, total number of nucleons A, the number of protons in the excited particle (this can be several nucleons) q, and the total number of nucleons p, the effective charge is

$$\tilde{q}_{eff} = qe(1 - pZ/qA), \tag{4a}$$

where e is electron charge. Normally, the maximal value of $\tilde{q}_{eff}$ is achieved when the excited particle contains protons only (this is nuclear example): $q = p$. In such case $\tilde{q}_{eff}^{max} = qe(1 - Z/A) \simeq 3qe/5$ for heavy nuclei since $A \sim 2.5Z$ under $A > 150$. At the same time, $\tilde{q}_{eff}$ can also be zero and even change the sign compared to $\tilde{q}$. For instance, $p \geq 3$, $q = 1$ implies $\tilde{q}_{eff} = q(1 - pZ/A)$ which has already the opposite sign.

From (3) we derive that $\mathbf{E}(\mathbf{R}) = \mathbf{E}(\mathbf{r})$ which holds with $\Delta r/\lambda$ accuracy. If the oscillation velocity of particle in the laser field becomes close to the light one c, the next terms of expansion over $\Delta r/\lambda$ become nonzero (they appear on the harmonics of main frequency ω). In the following, we will consider systems in which equation (3) is accurate enough under present intensities of laser field. Note that for nuclei these terms should be taken into account if the intensity of laser radiation $I > 10^{25}$ W/cm^2.

We will take equation (3) as a starting point for the following analysis. For ease of notation we will now denote $\Delta\mathbf{r}$ as **r** and $\tilde{q}_{eff}$ as q respectively. We thus obtain the original system of equations in Cartesian coordinates under our suggestions ($\mathbf{\Omega} \parallel \mathbf{\omega}$) for elliptically polarized laser radiation:

$$\mu\ddot{x} = -(\partial U/\partial x) + qE_{x0}\cos\omega t,$$
$$\mu\ddot{y} = -(\partial U/\partial z) + qE_{y0}\sin\omega t, \tag{5}$$
$$\mu\ddot{z} = -(\partial U/\partial z).$$

We suppose here that the radiation has the left polarization versus the vector Ω, E_{x0}, and E_{y0} are the amplitudes of laser wave. In accordance with [1], we turn to cylindrical coordinates: $x = r\cos\phi$, $y = r\sin\phi$. Let us denote

$$A = \ddot{r} - r^2\dot{\phi} + \partial U/\mu\partial r, \quad B = 2\dot{r}\dot{\phi} + r\ddot{\phi},$$
$$C = qE_{x0}/\mu. \quad D = qE_{y0}/\mu. \tag{6}$$

The solution of these equation will be

$$A = C\cos\omega t\cos\phi + D\sin\omega t\sin\phi,$$
$$B = D\sin\omega t\cos\phi - C\cos\omega t\sin\phi. \tag{7}$$

Let us linearize equation (7) for following analysis in order to receive the zeroth, first, and second orders consequent iterations over the field E_0. Suppose $r = r_0 + \Delta r$; $\phi = \phi_0 + \Delta\phi$, the potential energy expansion should be taken till the quadratic terms over Δr inclusive. Then the first equation (7a) will be

$$\Delta\ddot{r} - (r_0 + \Delta r)(\dot{\phi}_0 + \Delta\dot{\phi})^2 + \frac{1}{\mu}\left(\frac{\partial U}{\partial r}\right)_{r=r_0} + \frac{\Delta r}{\mu}\left(\frac{\partial^2 U}{\partial r^2}\right)_{r=r_0}$$
$$+ \frac{(\Delta r)^2}{2\mu}\left(\frac{\partial^3 U}{\partial r^3}\right)_{r=r_0} = \frac{q(E_{x0} + E_{y0})}{2\mu} \tag{8}$$
$$\times \cos[(\omega t - \phi_0) - \Delta\phi] + \frac{q(E_{x0} - E_{y0})}{2\mu}$$
$$\times \cos[(\omega t + \phi_0) + \Delta\phi]$$

and the second,

$$2\Delta\dot{r}(\dot{\phi}_0 + \Delta\dot{\phi}) + (r_0 + \Delta r)(\ddot{\phi}_0 + \Delta\dot{\phi})$$
$$= \frac{q(E_{y0} - E_{y0})}{2\mu}\sin[(\omega t + \phi_0) + \Delta\phi] \tag{9}$$
$$- \frac{q(E_{x0} + E_{y0})}{2\mu}\sin[(\omega t - \phi_0) - \Delta\phi].$$

Only two terms in the first equation

$$r_0\dot{\phi}_0^2 + \frac{1}{\mu}\left(\frac{\partial U}{\partial r}\right)_{r=r_0},$$

are not small over Δr and $\Delta\phi$ (they are of zero orders over E_0); these terms describe nonperturbated classical motion of the particle with the mass μ along the orbit with the radius r_0. Thus, $\dot{\phi}_0 = \Omega$ is the frequency of this motion, and

$$\Omega^2 = \frac{1}{\mu r_0}\left(\frac{\partial U}{\partial r}\right)_{r=r_0}. \tag{10}$$

Therefore, we have $\ddot{\phi}_0 = 0$ in (9b). Keeping in (8) and (9) only linear terms over Δr and $\Delta\phi$ ($\Delta\phi$ under the sign

of trigonometrical function is equal to zero here), we have the first iteration: the linear field approximation,

$$\Delta\ddot{r}_1 + \Omega_1^2\Delta r_1 = \left(\frac{3\Omega + \omega}{\Omega - \omega}\right)\cos[(\Omega - \omega)t]\frac{q(E_{x0} + E_{y0})}{2\mu}$$
$$+ \left(\frac{3\Omega - \omega}{\Omega + \omega}\right)\cos[(\Omega - \omega)t]\frac{q(E_{y0} - E_{x0})}{2\mu},$$

$$\Delta\ddot{\phi}_1 + \Omega_1^2\Delta\phi_1$$
$$= -\frac{(\Omega + \omega)^2 + 2\Omega(\Omega + \omega) + 4\Omega^2 - \Omega_1^2}{(\Omega + \omega)^2} \tag{11}$$
$$\times \sin[(\Omega + \omega)t]\frac{q(E_{x0} + E_{y0})}{2\mu r_0}$$
$$+ \frac{(\Omega - \omega)^2 + 2\Omega(\Omega - \omega) + 4\Omega^2 - \Omega_1^2}{(\Omega - \omega)^2}$$
$$\times \sin[(\Omega - \omega)t]\frac{q(E_{y0} - E_{x0})}{2\mu r_0},$$

where $\Omega_1^2 = 3\Omega^2 + \frac{1}{\mu}\left(\frac{\partial^2 U}{\partial r^2}\right)_{r=r_0}$. It is clear that when the polarization is linear the effect is absent [both right parts of (11) are equal to zero]. Thus, we get the equations of the first approximation over the laser field for perturbations Δr and $\Delta\phi$. If Ω_1 does not get close to frequencies multiple of $(\Omega \pm \omega)$: $2(\Omega \pm \omega)$, $3(\Omega \pm \omega)$ etc., it is not necessary to make any further approximation and the first one is sufficient. This first approximation describes perturbations of internal orbital motion with frequency Ω (10).

Next-order corrections give a sufficient physical effect in presence of a resonance only. It is easy to see that the system energy has second-order corrections, which can increase in time. If we consider this correction, we obtain the second iteration equation introducing (11) into (9). Since the equations for the elliptical polarization will be very awkward, we present the result for the circular polarization only. The results would be the same. We have

$$\Delta\ddot{r}_2 + \Omega_1^2\Delta r_2$$
$$= \cos[2(\Omega \pm \omega)t]\left[a - b + c + \frac{d\Omega}{(\Omega \pm \omega)}\right] - \frac{a + b + c}{2},$$

$$\Delta\ddot{\phi}_2 + \Omega_1^2\Delta\dot{\phi}_2 = \frac{\Omega}{r_0}(a + b + c) \tag{12}$$
$$+ \cos[2(\Omega \pm \omega)t]\frac{1}{r_0}\left\{d\left[(\Omega \pm \omega) + \frac{4\Omega^2 - \Omega_1^2}{(\Omega \pm \omega)}\right]\right.$$
$$\left. + \Omega(a + b + c)\right\}.$$

Here,

$$a = 2(\Omega \pm \omega)\Omega$$

$$\times (q^2 E_0^2 [1 + 2\Omega/(\Omega \pm \omega)]$$

$$\times [1 + 2\Omega/(\Omega \pm \omega)$$

$$+ (4\Omega^2 - \Omega_1^2)/(\Omega \pm \omega)^2])/(\mu^2 r_0 (\Omega_1^2 - \Omega^2)^2),$$

$$b = \frac{q^2 E_0^2 [1 + 2\Omega/(\Omega \pm \omega) + (4\Omega_1^2 - \Omega^2)/(\Omega \pm \omega)^2]}{2\mu^2 r_0 (\Omega_1^2 - \Omega^2)},$$

$$c = \frac{1}{2\mu}\left(\frac{\partial^3 U}{\partial r^3}\right)_{r = r_0} \frac{q^2 E_0^2 [1 + 2\Omega/(\Omega \pm \omega)]^2}{\mu^2 (\Omega_1^2 - \Omega^2)^2},$$

$$d = (q^2 E_0^2 [1 + 2\Omega/(\Omega \pm \omega)$$

$$+ (4\Omega_1^2 - \Omega^2)/(\Omega \pm \omega)^2]$$

$$\times \{-(\Omega_1^2 - \Omega^2)/2 - (\Omega \pm \omega)^2$$

$$\times [1 + 2\Omega/(\Omega \pm \omega)]\})/(\mu^2 r_0 (\Omega_1^2 - \Omega^2)^2).$$

Note that the presence of constant terms for Δr_2 and $\Delta \phi_2$ in (12) implies a Stark's shift of the energy, proportional to E_0^2.

We see that both the first- and the second-order perturbations appear at the frequency Ω_1 which is essentially different from Ω. The same can be shown for the third- and high-order perturbations so that any resonance can appear when $\Omega_1 = \Omega \pm \omega$, $2(\Omega \pm \omega)$, $3(\Omega \pm \omega)$, etc.

3. CENTRAL POTENTIALS PROVIDING RESONANCE EXCITATION

The resonance condition for Δr_2 and $\Delta \phi_2$ in (12) is $\Omega_1 = 2(\Omega \pm \omega) \simeq 2\Omega$. The same conditions for higher corrections are $\Omega_1 \simeq (3, 4, \ldots)\Omega$. Generally speaking, the expression $\Omega_1 = n'\Omega$ (n' is integer, $n' = 1, 2, 3, \ldots$) provides an equation for the function $U(r)$. Solving it, we have

$$U = \alpha_{n'} r^{n'^2 - 2} + U_{n'0}, \qquad (13)$$

where, each n' corresponds to a definite potential U. For $n' = 0$, $U_0 = \alpha_0/r^2$ is the centrifugal-like potential. This potential always arises if the system is not in the S-state. Above that, the nuclear kern repulsing potential can be described in the same manner. This potential arises in many nuclear models as well as even in quantum chro-

modynamics (QCD). The centrifugal potential describes quasi-free behavior of Δr_2^0 and $\Delta \phi_2^0$: they behave like Cartesian coordinates of free particles in plasmas. These values renormalize total values of Δr_2 and $\Delta \phi_2$ and Ω_1 remains unchanged. Thus, (11) and (12) remain unchangeable under the transition to the coordinates system rotated with an arbitrary angular velocity!

For $n' = 1$ the value $U_1 = \alpha_1/r$ is a Coulomb-like potential. Whether the potential of nuclear forces can also have such a component is an issue which still needs to be addressed extensively.

The value $n' = 2$ corresponds to the $U_2 = \alpha_2 r^2$ oscillator potential. This term always arises in the expansion of a real limited-in-zero potential in the Taylor series and often is general. For nuclei, the nonisotropic three-dimensional oscillator potential is known as Nilsen's potential, the same potential is used in QCD too. Note, that the Coulomb repulsing potential can be included in this term U_2 if the excited particle is located "inside" or "at the edge" of a nucleus and an electric charge is distributed more or less uniformly inside a nucleus.

Potentials with $n' \geq 3$ ($U_3 = \alpha_3 r^7$, $U_4 = \alpha_4 r^{14}$, etc.) are "box-like" potentials that are typical for the nucleus–nucleon interactions. It seems that the realistic approximation for our problem is to take the total interaction potential $U = U_2 + \Delta U$ when the last term can be large enough compared with the main one and it can conveniently be expressed in the $\alpha_3 r^7$ notation.

4. CLASSICAL TRANSITIONS RATE

The resonance in (12) is expected to occur under $\Omega_1 = 2(\Omega \pm \omega)$, or $\Omega_1 \simeq 2\Omega$ and at a first look, it is simply force resonance when the resonant solution Δr_2 grows linearly in time,

$$\Delta r_2 = \Delta r_2^{max} \cos[2(\Omega \pm \omega)t]$$

$$= \frac{t}{2\Omega_1}\left[a - b + c + \frac{d\Omega}{(\Omega \pm \omega)}\right]\cos\Omega_1 t.$$

Let us use the value $E_0 = m r_0^2 \Omega^2$ for the energy of initial state and the value $E_1 = m r_1^2 \Omega^2$ for the excited state. The excitation mostly implies the change in the orbit radius. It is easy to see from (9a) and (9b) that the frequency change is the next order infinitesimal. The value ΔE, $\Delta E = E_1 - E_0 = m(r_1^2 - r_0^2)\Omega^2 \simeq 2m r_0 \Delta r \Omega^2$ under E_1, $E_0 \gg \Delta E$, corresponds to the transition between states with large principal quantum numbers. As mentioned above, this fact proves the validity of the classical approach. The expression $\Delta r = \Delta r_2^{max}$, or $\Delta r_2^{max}/r_0 \simeq \Delta E/2E_0$ corresponds to this transition. The transition

rate can be determined as $\Delta r_2^{max}/tr_0 = W$. In the potential $U = \alpha_2 r^2 + \Delta U$, we have

$$W = \frac{c}{2\Omega_1 r_0} = \left(\frac{\partial^3 U}{\partial r^3}\right)_{r = r_0} \frac{q^2 E_0^2}{8\mu^3 \Omega^5 r_0}, \qquad (14)$$

where we use that $\left[a - b + \dfrac{d\Omega}{(\Omega \pm \omega)}\right] = 0$. Expression (14) shows that the excitation in the pure oscillator potential is impossible. This fact is easy to obtain without any perturbation theory, because in this case the problem becomes linear.

5. CONDITIONS OF THE SYSTEM RESONANT PARAMETRIC EXCITATION

As we mentioned, the resonance arisen in the system under $\Omega_1 = 2(\Omega \pm \omega)$ looks like a force (as well as under $\Omega_1 = \Omega \pm \omega$). Physically, it is not so. Indeed, the system has internal rotation at the frequency Ω, i.e., coordinates x and y are harmonically changed. According to (10)–(12), we can write $r = r_0\exp(i\phi)$. Here, $\phi = \Omega t + \Delta\dot\phi_1 t + \Delta\dot\phi_2 t + \ldots$. The unperturbed equation for r is

$$\ddot r + \Omega^2 r = 0.$$

At the next step we should take into account perturbations $\Delta\dot\phi_1$, $\Delta\dot\phi_2$, etc. The first-order correction $\Delta\dot\phi_1$ over the laser field is described by equations (11). It does not lead to any resonance because $\Delta\dot\phi_1 \sim \cos\Omega t$. The second-order correction $\Delta\dot\phi_2$ (12) perturbs internal rotation frequency approximately twice a period $2\pi/\Omega$: this is a condition for the arising of some parametric resonance. The frequency of parametric changes of Δr is equal to $2(\Omega \pm \omega) + \Delta\dot\phi_2$. The parametric excitation arises in some area of detunings over the frequency Ω_1 which is determined by the modulation depth $\Delta\dot\phi_2/\Omega$. Let us consider two cases: the small frequency deviation $\Omega_1 \simeq 2\Omega$ and large one $\Omega_1 \neq 2\Omega$.

The parametric resonance growth as a function of the radius r is $r_0\exp\Lambda t$. Usually $\Lambda t \ll 1$, and we have $r = r_0 + \Delta r$, $\Delta r = r_0\Lambda t$. Under the exact parametric resonance we have that $\Lambda_{max} = W$ from (14): this W is determined for the force resonance. Note that the parametric excitation exists under nonzero detuning too. The detuning width is determined by the first Floquet zone and increases with the growth of the modulation depth $\Delta\dot\phi_2/\Omega$. Thus the parametric resonance is always excited under enough large modulation depth $\sim E_0^2$.

Under the small frequency deviation, the parametric resonance appears if $\left|\Delta\dot\phi_2^{max}\right| \geq |\Omega_1/2 - \Omega|$ (compare with the force resonance condition $\Omega_1 = 2(\Omega \pm \omega)$):

$$\Delta\dot\phi_2^{max} = \frac{\Omega}{[\Omega_1^2 - 4(\Omega \pm \omega)^2]}\left(\frac{\partial^3 U}{\partial r^3}\right)_{r = r_0}$$
$$\times \frac{q^2 E_0^2[1 + 2\Omega/(\Omega \pm \omega)]^2}{2\mu^3 r_0(\Omega_1^2 - \Omega^2)^2}. \qquad (15)$$

The value $\left(\dfrac{\partial^3 U}{\partial r^3}\right)_{r = r_0}$ is not known. If we take term $U_3 = \alpha_3 r^7$ as ΔU (see above), we obtain $\left(\dfrac{\partial^3 U}{\partial r^3}\right)_{r = r_0} = 210\Delta U/r_0^3$. Therefore, it follows from (15) for $\Omega_1 \simeq 2\Omega$ that

$$8\Omega_0\omega \gg \frac{1}{\mu}\left(\frac{\partial^2 \Delta U}{\partial r^2}\right)_{r = r_0}, \quad \frac{1}{\mu r_0}\left(\frac{\partial\Delta U}{\partial r}\right)_{r = r_0},$$

and $\Delta\dot\phi_2^{max} \geq \omega$. Since $\Omega_0 = 2\alpha_2$, we have that the intensity of laser radiation must be more than some threshold value:

$$I \geq I_{th} = \frac{\mu\omega^2 c E_0}{420\pi k q^2}. \qquad (16a)$$

Here, E_0 is taken equal to $U_2^0 = mr_0^2\Omega^2$ and has the meaning of the initial state energy. To satisfy the condition $\Omega_1 \simeq 2\Omega$, we suppose that the value k is determined from the expression $420\pi k = 0.01$. Under $\Delta E \sim 100$ keV, $\omega \simeq 1.8 \times 10^{15}$ s^{-1}, $q = e$, we have $I_{th} = 4 \times 10^{22}$ W/cm^2. Consequently, the parametric resonance for our condition under $I \geq I_{th}$ is always excited when $\Delta U \ll U_2$ and k is small enough. The case $k = 0$ corresponds to the oscillator potential when the excitation is no longer possible ($I_{th} = \infty$).

In case of strong frequency deviation

$$8\Omega_0\omega \ll \frac{1}{\mu}\left(\frac{\partial^2 \Delta U}{\partial r^2}\right)_{r = r_0}, \quad \frac{1}{\mu r_0}\left(\frac{\partial\Delta U}{\partial r}\right)_{r = r_0},$$

the laser intensity should be larger than I'_{th},

$$I'_{th} = \frac{\mu c E_0 \Delta\Omega^2}{8\pi k' q^2}, \qquad (16b)$$

where $\Delta\Omega^2 = \dfrac{1}{\mu r_0}\left(\dfrac{\partial\Delta U}{\partial r}\right)_{r = r_0}$, $k' = n'(n' - 1)(n' - 2)/2(n'^2 + 2n')$, and with the additional conditions that

$\Delta\Omega \leq \Omega_0$, $r_0 \simeq 5 \times 10^{-13}$ cm, $I'_{th} \sim 10^{28}$ W/cm^2. This value of the threshold intensity is an absolute value and it does not require condition $\Delta U \ll U_2$ to be satisfied. Nevertheless, in this case the motion becomes relativistic. Note that the values (16a) and (16b) contain the depth of potential well E_0 and require the following explanation when "effective" oscillator potential is used (see below).

As we note above, under the exact parametric resonance $\Lambda_{max} = W$, taking ΔU as $U_3 = \alpha_3 r^7$, we have ($W = W_2$ is the rate of the second-order transition)

$$W_2 = \frac{420\pi k q^2 I}{mc\Omega\Delta E}. \tag{17}$$

How to connect Ω with ΔE? The ground state of a three-dimensional oscillator has an energy $3\hbar\Omega'/2$. The value Ω' describes the energy difference between equidistant spectrum levels. At the same time, we determine Ω as the unperturbed internal revolution frequency. Therefore, we have to equalize Ω to the value $\Omega'(N' + 3/2)$, where N' is the principal quantum number of the initial state. Of course, our system can be in one of excited states and N' can be nonzero; furthermore, since $\hbar\Omega' = \Delta E$, Ω has the value $\Delta E(N' + 3/2)/\hbar$. Finally, we have

$$W_2 = \frac{420\pi k q^2 \hbar I}{(N' + 3/2)mc(\Delta E)^2}. \tag{17a}$$

When $N' \gg 1$, this expression determines the rate of transition between levels when an energy difference is much less then both eigenvalues of the two considered energy levels. It can be seen that this expression does not include any nondirectly observable values like whole levels energies E_0, E_1, etc. This is a cross-verification of the developed approach as we said above.

6. PHYSICAL INTERPRETATION AND ESTIMATIONS

Expression (17) looks like the rate of photoexcitation (or photoinization, if we want to describe decay processes) by a monochromatic radiation with frequency $\sim\Delta E/\hbar$ and even coincides with it when one would be written in corresponding view. Since the equations for the first-order perturbation (11), the second-order ones (12), etc. do not change under the transition to the rotating coordinates system, we can conclude that the considered effect is the photoeffect for the excited particle with charge q_{eff}. The initial rotation of this particle around the nuclear remainder is changed in the rotating coordinates system on the rotating field, of course, with the same angular frequency $\Omega \sim \Delta E/\hbar$. Instead of the fine-structure constant for the photoeffect, (17) contains the value k which has the same role like above-mentioned fine-structure constant (with some multiplicator). The opportunity to consider this constant k like something close to the constant of strong interaction is not clear yet.

Since the laser field directly modulates the shape of the revolved particle orbit, the nuclei transitions can be connected with the collective excitations. The excitation with a frequency close to Ω produces a single perturbation of the orbit of charged particles within a period since the period of the nonperturbed motion is comparable with that of the perturbation, i.e., the system can be thought as receiving an additional dipole moment. Therefore, it should be interpreted as the giant resonance, which is conceivable since its width is very high. Energies of the giant resonance are 10–20 MeV as a rule; therefore, it is hard to expect any observable induced dipole moment.

The excitation at frequency close to 2Ω changes the orbit twice a period and the orbit looks like the shape of quadruple oscillations in this case. The characteristic energies are much less here (0.1–1 MeV); therefore, it is impossible to exclude the occurrence of the resonant excitation. The rate of these transitions is described by formulas (17) or (17a). It is possible to speak about octopole transitions in principle. They should clearly arise when the oscillator term is less than U_3. The rate of this transition will be $\sim E^3$ and $(\Delta E)^3$, but its value will be very small because $\Delta E > 1$ MeV for octopole transitions in nuclei.

In order to receive quantitative estimations of the yielded value, it is necessary to calculate in first place how many particles can be in the volume of interaction, i.e., the measure of the volume for very large I ($\geq 10^{18}$ W/cm^2). It is known that the radiation with such intensity is self-channeled in plasmas [3] and each gaseous medium becomes plasma in a field of such intensity during a few periods of laser radiation. The diameter of channel when the radiation is propagated is ~ 8–10 wavelengths and its length L can reach 50 diffraction lengths L_d [4]

Since $L_d = 2\pi r_c^2/\lambda$, r_c is the channel radius here, $r_c \sim 4\lambda$, we have that $L_d \simeq 16\pi\lambda$. For L/L_d it holds $L/L_d = G \leq 50$ (see [4]); therefore, the volume of interaction V_{int} is

$$V_{int} = \pi r_c^2 L_d G = 256\pi G\lambda^3.$$

This gives $V_{int} = 4.02 \times 10^4\lambda^3$ under $G = 50$. Only heavy nuclei have quadruple excitations with transition energies $\Delta E \sim 0.1$–1 MeV. Therefore, the density of initial gas target can not be very high, because rapid ionization leads to an appearance of a lot of free electrons. The density of these electrons can exceed the critical density n_{cr} for this laser wavelength and stop the laser radiation propagation. Practically, the initial gas density should be about atmospheric one.

The second question arises about how bound electrons which remained in the ion, screen the nucleus from the action of laser radiation. Taking the radius of ions as $r_i \sim 10^{-10}$ cm, the electron density inside the ion n_e will be $n_e \sim 10/r_i^3 \sim 10^{31}$ cm^{-3}. For Nd laser, it gives dumping factor "into the ion" $\sim \lambda(n_e/n_{cr})^{1/2} \sim 10^{-9}$ cm, which is more than ion size. This estimation was done

for free electrons and the radiation penetration depth for bound electrons is expected to be larger. Thus, for estimations of the field amplitude acting on the nucleus, we can take its amplitude in the vacuum right before the target.

The present level of laser pulse radiation intensities permits us to expect quadruple nuclear excitations if the nonharmonic part of the nuclear potential is small enough to hit to the resonance peak [see (16a)]. We think, therefore, that it would be good to use in first experiments nuclei with more or less equidistant spectra of the lowest quadruple states. As criterion, we take the differences between $(2+ \longrightarrow 0+)$ and $(4+ \longrightarrow 2+)$ transitions: real k here is simply the ratio $\{E(4+ \longrightarrow 2+) - E(2+ \longrightarrow 0+)\}/\{E(4+ \longrightarrow 2+) + E(2+ \longrightarrow 0+)\}$. Note here that all our considerations were done for bare nuclei. Experimentally, the superstrong laser radiation leads to a rapid ionization of atoms, as we mentioned above. Each electron in an atom gives some contribution to the nuclear potential which can be proportional to Δr, $(\Delta r)^2$, etc. The term proportional to Δr influences the difference $\Omega_1 - 2\Omega$. The effective energy shift is high enough especially for S-electrons. This shift can give an optimal "hit" to the parametric resonance even for large k. But in general this issue needs to be addressed in another work.

Also it would be experimentally better if the normal state of media with these nuclei were gaseous. The nuclei of normally gaseous media which fulfill this lowest unharmonic criterion are ^{40}Ar, ^{132}Xe, and ^{134}Xe. Note that the best nucleus from the used criterion point of view is ^{128}Te, which is normally a metal.

Let us estimate the probability of the excitation of the 2^+ state of argon nucleus ^{40}Ar, $\Delta E = 1432$ keV, $k = 0.01$. Here, we should suppose $N' = 0$ for which the application of the developed theory would be limited. Nevertheless, it is reasonable to expect that the corresponding results will represent the real situation at least half-quantitatively. Taking the nuclei density $n_n = 2.67 \times 10^{19}$ cm^{-3}, the total number of particles in the volume of interaction $N = V_{int}n_n$ becomes 1.3×10^{12}. The time of excitation $t_{Ar} = W_2^{-1}$. Taking into account the shell structure of this argon nucleus, we have to suppose that the excited particles contain no more than 2 protons, $q_{eff} = 1.1e$, $m \simeq 1.9m_N$ (nucleon mass). We have

$$t_{Ar} \simeq 2.1 \times 10^{13}/I[\text{W/cm}^2],$$

where I is measured in watts per square centimeter. Taking $I = 10^{18}$ W/cm^2 and $\tau_i = 1$ ps, we have total number of excited argon nuclei per shot:

$$N_{Ar}^{exc} = N\tau_i/t = 0.6 \times 10^5.$$

We supposed here that the total Nd-laser pulse energy ~1 J and about the half of laser pulse energy hits the channel.

For the same excitation of ^{132}Xe, we have $\Delta E = 668$ keV, $k = 0.03$. There are four protons above the complete proton shell and there are not enough (only 4 neutrons) in the neutron one. We suppose that the excited particles contain 4 protons, $q_{eff} = 2.36e$, $m \simeq 3.9m_N$ (nucleon mass). We have

$$t_{^{132}\text{Xe}} \simeq 6.5 \times 10^{11}/I[\text{W/cm}^2].$$

For the above-mentioned I and τ_i,

$$N_{^{132}\text{Xe}}^{exc} = N\tau_i/t_{^{132}\text{Xe}} = 2.0 \times 10^6.$$

For the same excitation of ^{134}Xe, the corresponding values are $\Delta E = 847$ keV, $k = 0.05$. There are four protons above the complete proton shell and there are not enough (only 2 neutrons) in the neutron one. We suppose that the excited particles contain 4 protons, $q_{eff} = 2.39e$, $m \simeq 3.9m_N$ (nucleon mass). We have

$$t_{^{134}\text{Xe}} \simeq 6.1 \times 10^{11}/I[\text{W/cm}^2].$$

For the above-mentioned I and τ_i

$$N_{^{134}\text{Xe}}^{exc} = N\tau_i/t_{^{134}\text{Xe}} = 1.2 \times 10^6.$$

For the same excitation of ^{128}Te, we have $\Delta E = 742$ keV, $k = 0.007$. This nucleus has the lowest unharmonic ratio from all even–even nuclei. There are two protons above the complete proton shell and there are not enough (only 6 neutrons) in the neutron one. We suppose that the excited particles contain 2 protons, $q_{eff} = 1.19e$, $m \simeq 1.97m_N$ (nucleon mass). We have

$$t_{^{128}\text{Te}} \simeq 6.5 \times 10^{12}/I[\text{W/cm}^2].$$

For the above-mentioned I and τ_i

$$N_{^{128}\text{Te}}^{exc} = N\tau_i/t_{^{128}\text{Te}} = 1.8 \times 10^5.$$

Each excited nucleus emits one γ-quantum with the corresponding energy; therefore, the total number of γ-quanta should coincide with N^{exc}. The angular distribution of emitted quanta is expected to be $1 + \cos^2\vartheta$, where ϑ is the angle between the observation line and the wave vector.

Let us estimate rates of transitions to a continuum, i.e. decay-like processes. Formulas (17) and (17a) are not directly applied to them. As it usually occurs for decay processes, the particle which is leaving the system has the eigenstate near the continuum. It is far from the potential well bottom and the potential shape here is far from the oscillator one. Indeed, this particle feels the shape of the potential well between this initial bound state with energy E_0 and the continuum $E_1 = 0$ only. It means that we can change real potential well $U_{n'}$, with the effective oscillator one $U_2^{eff} = \alpha_2^{eff}r^2 - U_0'$.

We can require that U_2^{eff} should be equal to $U_{n'}$, under r_1 and r_2:

$$U_2^{eff}(r_1) = U_{n'}(r_1) = E_0$$

$$\text{and } U_2^{eff}(r_2) = U_{n'}(r_2) = E_1 = 0.$$

These two equations determine U_0'. If we take $U_{n'} = \alpha_{n'} r^{n'^2-2} - U_0$ (see above), we have for $n \gg 2$ that

$$U_0' \simeq n'U_0/2(E_1 - E_0) = n'U_0/2\Delta E. \tag{18}$$

The effective principal quantum number N' can be determined as

$$N' \simeq U_0'/\Delta E. \tag{18a}$$

The effective unharmonic ratio k^{eff} can be determined as the difference between U_2^{eff} and $U_{n'}$, at the point $(r_1 + r_2)/2$, divided by the value $U_{n'}$, at the same point. We have

$$k^{eff} = \frac{3\Delta E}{4U_0}\left(1 - \frac{3}{n'}\right). \tag{18b}$$

From the classical point of view, the particle slips in the "potential well" and simply leaves the well under the definite "amplitude of oscillations." It means that the shape of the potential well should be close to the oscillator one in order to satisfy the resonance condition (15). For the decay processes this is not so unusual because the excited system should obtain the energy which is equal to or larger than ΔE. Thus, we can use values N' and k^{eff} for the computation of the transition rates to unbound states from the bound ones.

Let us estimate now the probability of the deuteron decay. The nuclei density can be taken about $n_{cr}/2$, $n_n \simeq 5 \times 10^{20}$ cm^{-3}, $N_D = 2.6 \times 10^{13}$. The deuteron has just one bound state near the top of the potential well. The depth of a deuteron potential well E_0 is ~30 MeV, the difference between the ground state E_1 and the continuum E_2 is $E_2 - E_1 = \Delta E = 2.23$ MeV. Taking $n' = 7$ (see above), we can write the following approximations for $E_0' \sim 105$ MeV and $N' \simeq 47$. The value k^{eff} for deuteron is about 0.032, $q_{eff} = e/2$, $m = m_N/2$. The total decay time t_D is

$$t_D = 3.6 \times 10^{14}/I[\text{W/cm}^2].$$

Taking $I = 10^{18}$ W/cm^2 and $\tau_i = 1$ ps, we have the total number of decayed deuterons about 0.73×10^5 (per shot). Free neutrons can be traced during the experiment.

At the subnucleon level, there is another type of transition to the almost continuous spectrum. This is the transition "nucleon–barion resonance." From the QCD point of view, it is, very roughly, the one-quark

excitation. Thus, it is conceivable to compute transition rates using the developed classical approach. For the bottom Δ-resonance the value ΔE is equal to 232 MeV, $U_0 - \Delta E = m_N c^2 = 940$ MeV, $q_{eff} \sim e/3$ from (4). We have from (18a) and (18b) that the value $k^{eff} \simeq 0.085$ and $N' \simeq 18$ (see what mentioned above for deuterons). Taking hydrogen as a target gas, nuclei density n_n can be up to $n_{cr}/2$. If we take constituent mass of a quark as $\mu \sim 2m_N/9$, we obtain

$$t_\Delta \simeq 1.06 \times 10^{18}/I[\text{W/cm}^2]$$

and $N_\Delta^{exc} \simeq 25$ per laser shot. At the same time, if we set the current mass to μ, we obtain that N_Δ^{exc} is 60 times as large: $N_\Delta^{exc} \simeq 1.5 \times 10^3$.

Experiments could be aimed at tracing extremely hard (232 MeV) γ-quanta. The probability of the γ-emission is about 1/100 per one Δ-barion decay. Similarly, π-mesons (~99% decays) could be traced as well.

7. OBSTACLES TO EXPERIMENTAL VERIFICATION

Within the same kind of nuclear excitation, other processes may lead to the emission of γ-quanta. There are two such processes: the direct Coulomb excitation of quadruple transition by nuclei–nuclei impacts, where high-energy nuclei arise at the laser channel and repel each other [5]. The second process is the bremsstrahlung due to relativistic electron–ion collisions [6].

Each laser channel provides the strong transversal outflow of stripped atoms. The characteristic velocity of this flux is [5] v:

$$v = (4\pi n Q^2/M_i)^{1/2} r_c/\sqrt{2e}.$$

Here, M_i is mass of ion (practically, it is the mass of the nucleus under investigation), Q is ion charge, n is ions density in the channel, e is the base of natural logarithm. During the pumping pulse, this flux will provide the quadruple excitation of nuclei located near the "wall" of the channel, the depth of the ring of possibly excited nuclei d is $v\tau_i$. The expected force of an ionization of atoms in the channel is about 10, so that $v \sim 10^9$ cm/s for ^{134}Xe. The value d is about 10 μm. The number of nuclei which are Coulomb-excited during the pumping pulse is $N_c^{exc} \sim d r_c^2 V_{int} n^2 \sigma(E2)/(d + r_c)^2$, $\sigma(E2)$ is the cross section of the Coulomb excitation of the first quadruple level. The value $\sigma(E2)$ is about 10–100 mb for such v [7], and N_c^{exc} is no more than 400. The angular distribution of the photons emitted by Coulomb-excited nuclei is expected to be more or less isotropical. Thus, the direct Coulomb excitation of quadruple transition by nuclei–nuclei impacts cannot compete with our process.

Two part of plasma electron component can provide the hard bremsstrahlung. The first one arises when electrons are repelled from the channel at the pumping pulse front due to the ponderomotive force. The maximal energy of such electron is about the maximal oscillating energy of the electron at the electromagnetic wave as typically for the ponderomotive force. For 1-J, 1-ps pulse of Nd-glass laser this maximal energy is about 100 keV. Thus, this part of electrons cannot provide any bremsstrahlung in an energy band of 0.5–1.5 MeV for considered nuclei.

At the same time, it is known that there is the strong acceleration of electrons in the wake of the superstrong laser pulse; observed energies E_e were up to several MeV [6]. The total power of bremsstrahlung P is

$$P = \iint_{V\omega} dV d\omega n n_e v_{rel} d\sigma(\omega)\hbar\omega.$$

Here, v_{rel} is relative velocity of collided particles (electron and ion), n_e is electron density, $\sigma(\omega)$ is the bremsstrahlung cross section, ω is the quanta frequency. If we want to know the total power at the frequencies band between ω_1 and ω_2, we need to calculate the frequency integral over these limits. The considered case is relativistic, $v_{rel} \simeq c$. Setting the frequency range to $[0.9\omega, 1.1\omega]$, the total energy of bremsstrahlung becomes $E = P\tau_i \leq 1$ erg. All radiation propagates in the cone with an angle $\chi \sim m_e c^2/E_e$, from the laser propagation direction, where m_e and E_e are the unperturbed electron mass and electron energy, respectively. The value χ is no larger than several degrees. It is easy to separate this radiation from the investigated one by a space filter. So, we can avoid the competition with the investigated nuclear excitations processes using time and space separations.

A number of free neutrons also can appear due to the deuteron–deuteron impacts by the $(D + D \longrightarrow n + {}^3He)$ reaction. The cross section of this process σ_D is about 100 mb. The number of neutrons which appear by deuteron–deuteron collisions during the pumping pulse is

$N_N = d r_c^2 V_{int} n^2 \sigma_D/(r_c + d)^2$. Here, we took into account the decrement of the projectiles flux due to the cylindric symmetry. If we take $n = n_{cr}/2$, v will be $\sim 0.35 \times 10^{10}$ cm/s, $d \sim 35$ μm, and the total number of free neutrons is no larger than 3×10^4. This value is comparable with the expected quantity of free neutrons in the laser-stimulated decay process. Indeed, neutrons appearing due to collisions are much hotter than the latter, thus providing an effective criterion to verify the result of the experiment.

Since the energy of particles emitted by the channel cannot achieve several hundreds MeV, it is impossible to expect any Δ-barion excitations except as above considered.

8. CONCLUSION

The regular classical perturbation procedure was applied to the system of a body in a central potential which is excited by a superstrong laser field. The excitations of a nucleon in the nucleus potential, a quark in the QCD potential and the nuclei decay were roughly estimated. The transition rates of excitations were introduced in the classical theory and determined. The transitions to the excited states and to the continuous spectra are the same from the classical point of view; therefore, the developed theory could be applied to decay processes.

Necessary levels of laser intensities are routinely realized at present. The classical approach can be checked experimentally for the validity of quantitative estimations. Nuclear excitations to the bound state were interpreted as induced quadruple ones. They can be realized for large enough numbers of particles in the volume of interaction. Of course, not every nuclear quadruple transition can be excited because a precise "hit" to the parametric resonance peak is needed. We suppose that it would be better to take nuclei with more or less equidistant spectra for low excited states for the first experiments. The nuclear decay and subnuclear excitations also look possible and a high experimental yield can be expected. The realization of such laser-induced nuclear and, may be, subnuclear excitations and decays can be an attractive alternative for some experiments in high-energies physics on a large-scale accelerator facility.

REFERENCES

1. Korobkin, V.V. and Romanovsky, M.Yu., 1992, *Phys. Lett. A*, **171**, 215.
2. Davydov, A.S., 1973, *Quantum Mechanics*, 2nd ed., (Moscow: Nauka) (in Russian).
3. Borisov, A.B., Borovskiy, A.V., Shiryaev, O.B., *et al.*, 1992, *Phys. Rev. A*, **45**, 5830.
4. Borovskiy, A.V., Galkin, A.L., Karpov, V.B., *et al.*, 1995, *Trudy IOFAN*, **50**, 83.
5. Romanovsky, M.Yu., Korobkin, V.V., and Borovskiy, A.V., 1996, *5th Int. Conf. on X-Ray Lasers Programme and Abstracts*, Svanberg, S. and Wahlstrom, C.-G., Eds. (Lund, Sweden), p. 37.
6. Umstadter, D., Kim, J.K., and Dodd, E., 1996, *Phys. Rev. Lett.*, **76**, 2073.
7. Alder, K., Bohr, A., Huus, T., *et al.*, 1956, *Rev. Mod. Phys.*, **28**, 432.

Dynamics of a Molecular Hydrogen Ion in Infrared Laser Fields

A. M. Popov, O. V. Tikhonova, and E. A. Volkova

D. V. Skobel'tsin Institute of Nuclear Physics, Moscow State University, Moscow, 119899 Russia
e-mail: popov@mics.msu.su
Received October 16, 1997

Abstract—The method of numerical simulation is employed to investigate the dissociation dynamics of elementary molecular systems (H_2^+ and D_2^+ ions) in an intense infrared laser field. The approximation of n terms is developed for the description of the dynamics of a molecular system in a strong electromagnetic field. The results of calculations carried out within the framework of the approximation of n terms are compared with the results of the exact numerical solution of the relevant two-body problem. The dependence of the dissociation probability on radiation intensity and frequency is discussed. A quasi-static model is proposed for the dissociation of molecules in an infrared field. This model employs the basis of field-dressed states. It is demonstrated that the quasi-static model provides a physical explanation for the dependence of the dissociation probability on the intensity and frequency of laser radiation.

1. INTRODUCTION

Currently, direct numerical integration of the time-dependent Schrödinger equation for a quantum system in the field of an electromagnetic wave is one of the main methods for studying the dynamics of atomic and molecular systems in high-intensity laser fields [1–3].

The complexity of molecular systems relative to atomic systems gives rise to a variety of phenomena that occur in molecular systems under the action of laser fields due to the difference in frequencies characteristic of natural vibrations of electronic and nuclear subsystems in a molecule. Therefore, direct numerical solution of the problem concerning the action of an ultrashort laser pulse on an elementary molecular system—molecular hydrogen ion H_2^+—is of undeniable interest [4–6]. However, such simulations require too much computation time even with modern computers, which prevents this approach from being used at the moment for the systematic computation of the behavior of even elementary molecules in high-intensity laser fields. Therefore, we encounter an urgent problem of developing approximate models that would allow an adequate description of the action of a strong electromagnetic field on molecules.

In this paper, the method of numerical simulation is employed to investigate the dissociation of various molecular hydrogen ions (H_2^+ and D_2^+) in a strong infrared (IR) laser field. The results of calculations carried out with the use of various models are compared with the results obtained by direct numerical integration of the time-dependent Schrödinger equation for a molecular system in the field of an electromagnetic wave. The dependences of dissociation probabilities on the intensity and frequency of laser radiation are investigated for H_2^+ and D_2^+ ions within the framework of

the model of n terms. A quasi-static model that provides an adequate description of the dissociation of molecules in a low-frequency IR field is proposed.

2. MOLECULAR HYDROGEN ION: STATIONARY STATES

In this paper, we restrict our consideration to a one-dimensional model of a molecular system where an electron moves only along the axis of the molecule and nuclei can be involved only in vibrational motion [6].

In the frame of reference related to the center of mass, the Hamiltonian of a molecule H_0 has the following form:

$$H_0 = -\frac{\hbar^2}{2m}\frac{\partial^2}{\partial x^2} - \frac{\hbar^2}{2\mu}\frac{\partial^2}{\partial R^2} + V_e(x, R) + e^2/R, \quad (1)$$

where x is the coordinate of the electron; R is the distance between the nuclei; $\mu = \xi M$ is the reduced mass of the molecule; M is the mass of the proton; and ξ is a factor that takes the values of 1/2 and 1 for H_2^+ and D_2^+ molecules, respectively. Similar to [6], the expression for the electron potential energy $V_e(x, R)$ was chosen in the form

$$V_e(x, R) = -\frac{e^2}{\sqrt{(R/2 - x)^2 + \alpha^2}} - \frac{e^2}{\sqrt{(R/2 + x)^2 + \alpha^2}},$$

where $\alpha = 0.943a_0$ is the parameter of smoothing and a_0 is the Bohr radius.

Using the adiabatic approximation based on the smallness of the parameter m/M, we can construct a complete set of functions describing the stationary states of the Hamiltonian H_0 in the form [7]

$$\Phi_{nv}(x, R) = \phi_{nv}(R)\varphi_n(x, R), \quad (2)$$

where $\varphi_n(x, R)$ ($n = 1, 2, 3, ...$) is the electron wave function and $\phi_{nv}(R)$ is the nuclear wave function that belongs to the nth electronic term and that can be found from the solution of the equation

$$\left[-\frac{\hbar^2}{2\mu}\frac{\partial^2}{\partial R^2} + V_{eff}^{(n)}(R) \right]\phi_{nv}(R) = E_{nv}\phi_{nv}(R). \quad (3)$$

Here,

$$V_{eff}^{(n)}(R) = \frac{e^2}{R} + E_e^{(n)}(R) \quad (4)$$

is the effective potential energy of nucleus interaction that takes into account the electron energy of the system $E_e^{(n)}(R)$ and $v = 0, 1, 2, ...$ is the vibrational quantum number.

Figure 1 displays several $V_{eff}^{(n)}(R)$ dependences for low-energy terms. The table presents several energies E_{nv} for the ground electronic term ($n = 1$). The total numbers of vibrational states in the discrete spectrum for this term are equal to 19 and 25 for H_2^+ and D_2^+, respectively.

3. INTERACTION WITH THE FIELD OF AN ELECTROMAGNETIC WAVE

In the dipole approximation, the interaction of a molecular system with the field of an electromagnetic wave is written as

$$W = -D\varepsilon(t)\cos\omega t, \quad (5)$$

where D is the operator of the dipole moment, $\varepsilon(t)$ is the amplitude of the electric field in the wave slowly varying in time, and ω is the frequency.

In the frame of reference related to the center of mass, the dipole moment of the nuclear subsystem is identically equal to zero for homonuclear molecules, and the electric field acts only on the electronic subsystem of a molecule:

$$D = d_e = -ex. \quad (6)$$

Therefore, transitions between different vibrational states are forbidden within the same electronic term, and vibrational states can be populated only through multiphoton transitions via other electronic states.

In calculations, we assumed that the amplitude of the electric field in the wave is described by

$$\varepsilon(t) = \begin{cases} \varepsilon_0\dfrac{t}{\tau_f}, & 0 < t < \tau_f \\ \varepsilon_0, & \tau_f \le t < \tau + \tau_f \\ \varepsilon_0\left(1 - \dfrac{t - (\tau + \tau_f)}{\tau_f}\right), & \tau + \tau_f \le t < \tau + 2\tau_f, \end{cases} \quad (7)$$
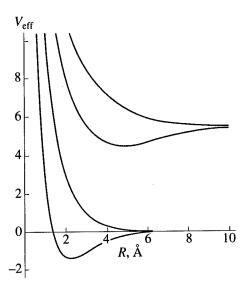

Fig. 1. Effective potential interaction energies of nuclei in a model molecular hydrogen ion for the electronic states with $i = 1, 2, 3$, and 4.

where τ_f is the duration of the leading and trailing edges of the pulse and τ is the duration of the plateau at the top of the pulse.

The energy of the quantum of electromagnetic radiation was chosen within the range $\hbar\omega = 0.12$–0.96 eV in such a manner that the durations τ_f and τ were multiple of the field period $T = 2\pi/\omega$. Specifically, for $\hbar\omega = 0.12$ eV, which corresponds to the energy of a CO_2-laser quantum, we set $\tau_f = 2T$ and $\tau = 5T$.

In the one-dimensional case, the dynamics of a molecular system in the field of an electromagnetic wave is described by a two-particle wave function $\Psi(x, R, t)$, which can be found from the solution of the time-dependent Schrödinger equation

$$i\hbar\frac{\partial\Psi(x, R, t)}{\partial t} = [H_0 - D\varepsilon(t)\cos\omega t]\Psi(x, R, t). \quad (8)$$

As demonstrated in [6], the wave functions that describe the stationary states of a system in the absence of the field can be approximated with a high accuracy by wave functions derived in the adiabatic approximation (2).

Energy levels E_{1v} (eV) of model H_2^+ and D_2^+ ions that belong to the ground electronic term of a molecule

V	H_2^+	D_2^+
0	−1.355	−1.373
1	−1.236	−1.288
2	−1.120	−1.204
3	−1.009	−1.123

Therefore, the initial condition for (8) was chosen in the form

$$\Psi(x, R, t = 0) = \phi_{1v}(R)\phi_1(x, R), \qquad (9)$$

which corresponds to the ground electronic state of a molecule and the vibrational state with number v. It was usually assumed that $v = 0$.

In [8], we employed the method of direct numerical integration to find the solution to equation (8) subject to initial condition (9) for laser pulses in the visible and IR frequency ranges. It was shown that dissociation processes compete with ionization in the visible range, whereas for IR radiation, there exists a range of laser intensities where the ionization probability of a molecular system is negligibly small as compared with its dissociation probability.

In studying the action of IR radiation on H_2^+ and D_2^+ in this paper, we will restrict our consideration to the range of intensities where we can ignore the ionization process.

As mentioned above, exact solution of this problem requires much computation time. Therefore, it is of interest to consider various approximate models. We investigated two approximate models that describe the dissociation process in a molecular system in an IR field—approximation of n terms, which takes into consideration n electronic states of a molecule unperturbed by the field, and a quasi-static model, which is based on the assumption that the electronic subsystem of a molecule is adjusted in accordance with the instantaneous strength of the electric field in the wave. We will discuss the efficiency of the considered models based on the comparison of model predictions with the results of exact simulations [8].

4. RESULTS AND DISCUSSION

4.1. Approximation of n Terms: Comparison with the Results of Exact Simulations

Let us expand the total wave function $\Psi(x, R, t)$ of a molecule in the set of electronic terms $\{\phi_i(x, R)\}$ unperturbed by the field:

$$\Psi(x, R, t) = \sum_i \alpha_i(R, t)\phi_i(x, R). \qquad (10)$$

Then, using the adiabatic approximation for expansion coefficients $\alpha_i(R, t)$, we can readily derive the following set of equations [7]:

$$i\hbar\frac{\partial\alpha_i}{\partial t} = \left[-\frac{\hbar^2}{2\mu}\frac{\partial^2}{\partial R^2} + V_{eff}^{(i)}(R)\right]\alpha_i + \sum_{j \neq i}\alpha_j W_{ij}, \qquad (11)$$

where $W_{ij} = -d_{ij}(R)\varepsilon(t)\cos\omega t$; d_{ji} is the matrix element of the electron dipole moment of the system, which parametrically depends on the nuclear coordinate; and $V_{eff}^{(i)}$ is the effective potential energy of interaction between the nuclei for the ith electronic state of a molecule, which is described by expression (4).

The set of functions $\{\alpha_i(R, t)\}$ is a manifold of nuclear wave functions that correspond to nonstationary states for various electronic terms of a molecule. The last term in (11) describes transitions between different electronic states in a molecule (transitions from one term to another) under the action of the field of the electromagnetic wave. If summation in (10) includes integration over the states of the electronic continuum, then the set (11) is identical to the initial equation (8) within the range where the adiabatic approximation is applicable. Truncating the set (11) and restricting our consideration to a moderate number of electronic terms in expansion (10), we can appreciably simplify the problem under study. Analysis of ionization and dissociation of H_2^+ and D_2^+ molecules performed in [8] has demonstrated that, for intensities $\sim 10^{13}$ W/cm^2, the ionization probability of a molecule is low as compared with its dissociation probability in the IR frequency range. Therefore, we can ignore transitions to the electronic continuum in (11).

Initial conditions to the set (11) equivalent to condition (9) are written as

$$\begin{cases} \alpha_1(R, t = 0) = \phi_{1v}(R) \\ \alpha_i(R, t = 0) = 0, \quad i = 2, 3, 4, \dots. \end{cases} \qquad (12)$$

In the absence of the ionization process, the normalization condition

$$\sum_i W_i = 1$$

is satisfied, where

$$W_i = \int|\alpha_i(R, t)|^2 dR \qquad (13)$$

is the probability to find a molecule in the ith electronic term.

Thus, within the considered approximation, the solution to the exact two-particle Schrödinger equation on a two-dimensional net can be replaced by the solution to a set of n one-dimensional equations, which allows us to considerably simplify the problem in the case of moderate n. Evidently, the number of terms that should be taken into account is determined by parameters of laser radiation. To find the number of expansion terms that should be kept in (10), in [9], we have calculated the dynamics of an H_2^+ molecule in the field of a CO_2 laser ($\hbar\omega = 0.12$ eV) in the range of intensities $P = 4 \times 10^{12}$–2×10^{13} W/cm^2 within the framework of the approximation of n terms ($n = 2, 3, \dots$) using the technique described in [6, 8]. Comparison of the results of two-body simulations with the data obtained within the framework of the approximation of n terms in the considered range of parameters has demonstrated that no less than four terms should be taken into account in (10).

The dissociation probability was calculated in accordance with the formula

$$W_D = 1 - \sum_v W_{1v}, \qquad (14)$$

where summation is performed over all vibrational states of the ground electronic term. We employ this formula based on the results of exact simulations, which have shown that the excitation probabilities W_{3v} for the states in the discrete spectrum are negligibly small for an excited bound term. This finding is a consequence of the Franck–Condon principle and the large difference in the distances between the nuclei for these terms (see also [8]).

Figure 2 displays the $W_D(P)$ dependences for the studied H_2^+ and D_2^+ systems in the case when the quantum energy is $\hbar\omega = 0.12$ eV. As can be seen from the presented plots, the increase in the mass of nuclei lowers the dissociation probability of D_2^+ as compared with the dissociation probability of H_2^+ due to the lower velocity of the nuclear wave packet for a decaying molecular term.

We should also point to a characteristic step in the $W_D(P)$ dependence revealed for the H_2^+ system. The origin of this step will be discussed in the following section within the framework of the quasi-static model of dissociation.

Now, let us discuss the dependence of the dissociation probability on the frequency of laser radiation. We have investigated this dependence within the range $\hbar\omega = 0.12$–0.96 eV assuming that the shape and the duration of the laser pulse remain unchanged, so that the edges and the plateau of the laser pulse included integer numbers of optical cycles of laser radiation. The results of such calculations for H_2^+ with $P = 1.4 \times 10^{13}$ W/cm^2 are presented in Fig. 3. The dissociation probability rapidly grows within the range of quantum energies $\hbar\omega \geq 0.5$ eV, which may be due to the decrease in the order of the multiphoton transition between the ground and the first excited electronic states of a molecule. We should also note that W_D slightly increases in the frequency range $\hbar\omega \leq 0.2$ eV. Since, for homonuclear systems, electromagnetic transitions are forbidden within the same term in the dipole approximation, the population of these states should occur through multiphoton transitions via excited terms. However, for $\hbar\omega = 0.12$ eV, the number of photons coupling two lower terms of a molecule with an equilibrium distance between the nuclei is on the order of 30. Such a high nonlinearity order of multiphoton excitation and dissociation processes indicates that we should employ an alternative approach to describe transitions between electronic terms in a molecule in the presence of a low-frequency field.
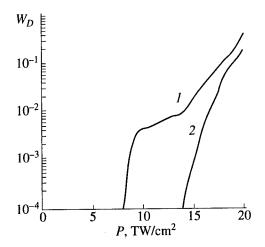

Fig. 2. Dissociation probabilities for (*1*) H_2^+ and (2) D_2^+ molecular systems as functions of radiation intensity for $\hbar\omega = 0.12$ eV.

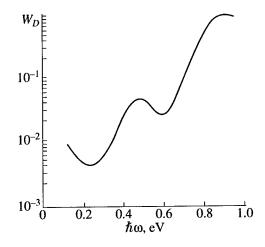Fig. 3. Dissociation probability for an H_2^+ molecule as a function of the quantum energy of the electromagnetic field for $P = 1.4 \times 10^{13}$ W/cm^2.

4.2. The Quasi-Static Model of Dissociation of Molecules in an IR Field

We should note at the outset that the expansion of the wave function $\Psi(x, R, t)$ of a molecular system in a set of molecular terms unperturbed by the field is not the only possible method of simplifying the general problem (8). From the mathematical point of view, we can perform such an expansion using any complete orthonormalized set of functions. The choice of the basis set of functions is dictated by mathematical convenience and physical expediency. A concept of field-dressed states [10] is preferable for the description of a molecule in intense fields within the optical frequency range. This concept permits one to successfully account for various specific features of above-threshold dissociation observed in experiments [11–13].

In a low-frequency IR radiation field, the perturbation of electronic terms of a molecule can be described within the framework of the quasi-static approximation, which implies that the frequency of the laser field is small as compared with the characteristic frequency of electronic motion in a molecule [9].

Indeed, for an H_2^+ molecular system in the presence of an external field, the frequency of electronic motion is determined by the inverse of the time τ_e characterizing the flow of the electron density from one nucleus to another and back in the process of variation of the field in the electromagnetic wave. Provided that

$$\tau_e \ll T = 2\pi/\omega, \qquad (15)$$

we can assume that the state of an electron is determined by the instantaneous strength of the electric field in the wave and is governed by the solution to the stationary Schrödinger equation

$$[H_e - d_e\varepsilon(t)\cos\omega t]\varphi_n^{(\varepsilon)}(x, R, t)$$
$$= E_n^{(\varepsilon)}(R, t)\varphi_n^{(\varepsilon)}(x, R, t), \qquad (16)$$

where H_e is the electron Hamiltonian of the molecule.

The solution of equation (16) is represented by a set of states $\{\varphi_n^{(\varepsilon)}(x, R, t)\}$ and the corresponding set of energies $\{E_n^{(\varepsilon)}(R, t)\}$, which parametrically depend not only on the nuclear coordinate but also on time.

Thus, we found quasi-stationary states $\varphi_n^{(\varepsilon)}(x, R, t)$. We will assume that the electric field in the wave is sufficiently weak, so that the decay time of the state is large as compared with the pulse duration. In the case under consideration, this condition is satisfied, because we can neglect the ionization of a molecule.

The total wave function of the system $\Psi(x, R, t)$ can be expanded in the set (16):

$$\Psi(x, R, t) = \sum_i \alpha_i^{(\varepsilon)}(R, t)\varphi_i^{(\varepsilon)}(x, R, t), \qquad (17)$$

where $\alpha_i^{(\varepsilon)}(R, t)$ is the nuclear wave function of a molecule that belongs to the ith term restructured by the slowly varying field $\varepsilon(t)\cos\omega t$. Substituting expansion (17) into equation (8) and using the Born–Oppenheimer adiabatic approximation, we can derive the following set of equations for the functions $\alpha_i^{(\varepsilon)}(R, t)$:

$$i\hbar\frac{\partial\alpha_i^{(\varepsilon)}}{\partial t} + i\hbar\sum_n \alpha_n^{(\varepsilon)}\left\langle \varphi_i^{(\varepsilon)}\left|\frac{\partial\varphi_n^{(\varepsilon)}}{\partial t}\right.\right\rangle$$
$$= \left[-\frac{\hbar^2}{2\mu}\frac{\partial^2}{\partial R^2} + V_{\text{eff}}^{(i)}(R, t)\right]\alpha_i^{(\varepsilon)}. \qquad (18)$$

Here, $V_{\text{eff}}^{(i)}(R, t) = e^2/R + E_i^{(\varepsilon)}(R, t)$ is the electronic term of a molecule distorted by the low-frequency field.

Thus, we derived a set of equations that describe the motion of a nuclear wave packet in an effective potential modified by a slowly varying electric wave field. The second term on the left-hand side of (18) describes field-induced transitions between the modified terms.

In calculating the lower modified molecular term in the presence of fields with moderate strengths, we can neglect the mixing of all the states of the electron Hamiltonian of a molecule except for the two lower states. In a quasi-static field, the energies of these states are given by [14]

$$E_{1,2}^{(\varepsilon)}(R, t) = \frac{1}{2}(E_1(R) + E_2(R))$$
$$\mp \sqrt{(\Delta E(R)/2)^2 + |W_{12}(R, t)|^2}, \qquad (19)$$

where $\Delta E(R) = E_2(R) - E_1(R)$, $W_{12} = d_{12}(R)\varepsilon(t)\cos\omega t$, and $E_1(R)$ and $E_2(R)$ are the energies of the electronic states of the molecule in the absence of the field.

Then, taking into account that $\langle\varphi_i^{(\varepsilon)}|\partial\varphi_i^{(\varepsilon)}/\partial t\rangle = 0$ and using (18), we derive a set of two equations for nuclear functions that belong to two terms modified in the low-frequency field:

$$i\hbar\frac{\partial\alpha_1^{(\varepsilon)}}{\partial t} + i\hbar Q_{12}\alpha_2^{(\varepsilon)}$$
$$= \left[-\frac{\hbar^2}{2\mu}\frac{\partial^2}{\partial R^2} + V_{\text{eff}}^{(1)}(R, t)\right]\alpha_1^{(\varepsilon)}(R, t),$$
$$\qquad (20)$$
$$i\hbar\frac{\partial\alpha_2^{(\varepsilon)}}{\partial t} - i\hbar Q_{12}\alpha_1^{(\varepsilon)}$$
$$= \left[-\frac{\hbar^2}{2\mu}\frac{\partial^2}{\partial R^2} + V_{\text{eff}}^{(2)}(R, t)\right]\alpha_2^{(\varepsilon)}(R, t).$$

The quantity

$$Q_{12} = \left\langle\varphi_1^{(\varepsilon)}(R, t)\left|\frac{\partial\varphi_2^{(\varepsilon)}}{\partial t}\right.\right\rangle = -\left\langle\varphi_2^{(\varepsilon)}(R, t)\left|\frac{\partial\varphi_1^{(\varepsilon)}}{\partial t}\right.\right\rangle \qquad (21)$$

determines the probability of transition from one term to another under the action of a laser field.

To find the complete set of terms $V_{\text{eff}}^{(i)}(R, t)$, we should solve (16) for different moments of time t. The characteristic behavior of two lower terms distorted by the field of an electromagnetic wave is illustrated in Fig. 4.

The adjustment of the electron function in accordance with the instantaneous strength of the wave field leads to the repulsion of nuclei during both half-cycles of the optical field [15, 16]. Physically, this repulsion can be accounted for by the fact that, in the case of adiabatically slow variation of the electric wave field, the electron density has enough time to flow from one nuclear center to the other within a half-cycle of the optical field. Taking into account that the probability of electron tunneling through the internal potential barrier

arising in the case when the distance between the nuclei is large is

$$W_T \sim \Delta E / \hbar,$$

condition (15) can be rewritten as

$$\Delta E(R) \gg \hbar\omega, \qquad (22)$$

In other words, the quantum energy should be less than the minimum separation between the terms. If condition (22) is not satisfied, field variation cannot be considered as adiabatically slow, and an electron has no time to tunnel from one center to the other. In such a situation transitions between the field-modified terms may occur, and the force that pushes the nuclei apart from each other vanishes upon the averaging over the optical cycle [15, 16].

Calculation of the quantity Q_{12} with the use of explicit formulas for the electron wave functions $\varphi_1^{(e)}(R, t)$ and $\varphi_2^{(e)}(R, t)$ performed in [9] with allowance for the smooth variation in the amplitude of the wave field, $|\dot\varepsilon| \ll \omega\varepsilon$, yields

$$Q_{12}(R, t) = -\frac{1}{2}\frac{\Delta E(R)/2}{(\Delta E(R)/2)^2 + |W_{12}(R, t)|^2} \qquad (23)$$

$$\times |d_{12}(R)|\omega\varepsilon(t)\sin\omega t.$$

In the case of weak fields and moderate R,

$$\Delta E(R) \gg |d_{12}(R)|\varepsilon, \qquad (24)$$

the probability of transitions between the modified terms is low,

$$Q_{12}(R, t) = -\frac{|d_{12}(R)|\varepsilon(t)}{\Delta E(R)}\omega\sin\omega t, \qquad (25)$$

and the dynamics of nuclear motion can be described within the framework of the model of a single modified term. The condition when transitions between the modified terms can be ignored was determined in [9]. If inequality (24) holds true, then this condition is written as

$$\hbar\omega \ll \hbar\Omega\frac{\Delta E(R)}{|d_{12}(R)|\varepsilon}. \qquad (26)$$

Here, $\hbar\Omega$ is the vibrational quantum of a molecule. For CO_2-laser radiation with $P \sim 10^{13}$ W/cm^2, this condition is satisfied up to $P \approx 5$ A.

For large R, two lower electronic terms of a molecule in the absence of an external field are always degenerate. In this case, the quantity Q_{12} infinitely increases at the moments of time determined by the condition $\cos\omega t = 0$ even in weak fields. Indeed, introducing the notation
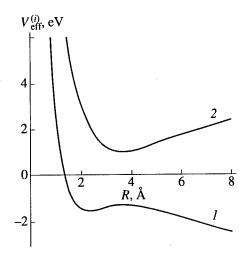
$$\xi = |d_{12}|\varepsilon\cos\omega t$$

Fig. 4. The structure of two lower electronic terms in an H_2^+ molecule in the presence of the field of an electromagnetic wave: (*1*) the ground term and (*2*) the first excited term.

and taking into account that

$$\lim_{\alpha \to 0}\frac{\alpha}{\alpha^2 + \xi^2} = \pi\delta(\xi),$$

we find from (23) that

$$\lim_{R \to \infty} Q_{12}(R, t) = \frac{\pi}{2}\delta(\xi)\frac{d\xi}{dt}. \qquad (27)$$

Therefore, the approximation of a single modified term is insufficient for the description of nuclear motion for large R. However, for CO_2-laser radiation, transitions between modified terms are significant only for such values of R that correspond to virtually noninteracting H and H^+, which implies that, if condition (26) is satisfied, then the dissociation probability can be calculated without allowance for transitions between modified terms.

Approximation where nonadiabatic transitions, i.e., summands responsible for term mixing in (20), are neglected is an analogue of the Born–Oppenheimer approximation, which makes it possible to decouple equations for nuclear motion in the absence of the external field. The main advantage of the considered approach is that it provides an opportunity to replace a set of equations for nuclear wave functions (13) by a single equation.

At the same time, in calculating the energy spectra of protons emerging from dissociation within the framework of the quasi-static model, we should take into account nonadiabatic transitions between modified terms. Indeed, due to transitions between the terms, which occur within each half-cycle of the field at the moments of time when $\varepsilon(t) = 0$, the system may reside with equal probabilities in each of the terms for large R, so that the force that pushes the nuclei apart from each
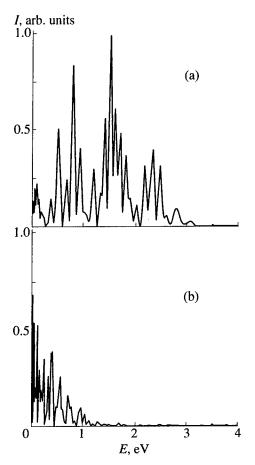
Fig. 5. Energy spectra of protons emerging from the dissociation of H_2^+ for $\hbar\omega = 0.12$ eV and $P = 1.8 \times 10^{13}$ W/cm^2: (a) approximation of a single modified term and (b) simulation with allowance for transitions between two lower modified terms.

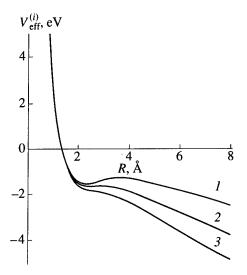other vanishes upon time averaging. However, within the framework of the model of a single term, the average force acting between the protons differs from zero for any R, which substantially distorts the energy spectra of dissociation fragments. This effect is illustrated by Fig. 5, which presents the spectra of protons calculated for $\hbar\omega = 0.12$ eV and $P = 1.8 \times 10^{13}$ W/cm^2 within the framework of approximation of a single modified term (Fig. 5a) and with allowance for transitions between two lower modified terms (Fig. 5b).

As mentioned above, the dependence of the dissociation probability on the radiation intensity for the system under study can be understood within the framework of approximation of a single modified term. Figure 6 presents the results of calculations for the ground electronic term of a molecule in the field of an electromagnetic wave performed with the use of (19) for different radiation intensities $P = c\varepsilon_0^2/8\pi$. In the range of relatively low radiation intensities, $P \le 9 \times 10^{12}$ W/cm^2, the curve $V_{\text{eff}}^{(1)}(R, t)$ features an area of classical finite motion, which indicates that quasi-stationary vibrational states of a molecule may exist in the radiation field. These states decay due to the tunneling through the potential barrier. If intensities $P \approx 1.0 \times 10^{13}$ W/cm^2 are reached within a certain part of the optical cycle, the potential barrier vanishes, and the curve $V_{\text{eff}}^{(1)}(R, t)$ features a plateau (curve 2), i.e., an area where the force acting between the nuclei, $F = -\partial V_{\text{eff}}^{(1)}/\partial R$, is approximately equal to zero. With the further growth in radiation intensity, the plateau vanishes (curve 3), which gives rise to the appearance of the repulsion force within the entire range of internuclear distances R.
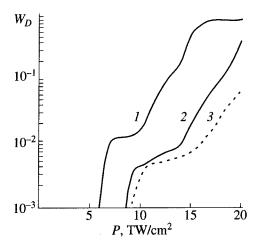

Fig. 6. The ground term of an H_2^+ molecule distorted by the field of an electromagnetic wave with an intensity of (1) 5.0×10^{12}, (2) 1.2×10^{13}, and (3) 2×10^{13} W/cm^2. The presented data correspond to the amplitude value of the electric field in the wave.

Fig. 7. Dissociation probability of H_2^+ (1, 3) in the ground ($v = 0$) and (2) vibrationally excited ($v = 1$) states as a function of the intensity of laser radiation: (1, 2) approximation of four terms and (3) simulation within the framework of the quasi-static approximation.

Figure 7 shows the dissociation probability for H_2^+ calculated as a function of radiation intensity within the framework of the considered quasi-static model with allowance for four terms. As can be seen from the presented plots, in the range of intensities $P \leq 1.5 \times 10^{13}$ W/cm^2, these curves qualitatively agree with each other. The proposed quasi-static model allows us to account for the main specific features of the $W_D(P)$ dependence. Specifically, in the range of intensities $P \leq 10^{13}$ W/cm^2, an H_2^+ molecule dissociates due to the tunneling of the nuclear wave packet through the potential barrier (see curve 1 in Fig. 6). The probability of this process drastically increases with the growth in the radiation intensity. Within the range of intensities $P \sim 1.0–1.5 \times 10^{13}$ W/cm^2, the nuclear wave packet falls within the plateau in the $V_{eff}^{(1)}(R)$ curve, and the dissociation probability is a weak function of radiation intensity. With the further growth in the radiation intensity, the dissociation probability increases again due to the growth in the repulsion force $F = -\partial V_{eff}^{(1)} / \partial R$ during the laser pulse.

If an H_2^+ molecule resides in an excited vibrational state at the initial moment of time, then one can expect that tunneling will occur in the range of lower radiation intensities. The role of plateau in the $V_{eff}^{(1)}(R)$ curve will also diminish due to the broadening of the nuclear wave packet. These specific features of the $W_D(P)$ dependence were revealed in calculations carried out for the vibrational state $v = 1$ (see curve 2 in Fig. 7).

The considered quasi-static model also permits us to understand the specific features of the $W_D(\hbar\omega)$ dependence for H_2^+ in the range of low frequencies ($\hbar\omega \geq 0.12$ eV). Specifically, the increase in the oscillation frequency of the potential $V_{eff}^{(1)}(R, t)$ with the growth in the quantum energy $\hbar\omega$ reduces the time interval within which the nuclear wave packet stays in the area of infinite motion and, as a consequence, lowers the dissociation probability. Thus, the lowering of the frequency of the driving field increases the dissociation probability of the system under study.

As the radiation frequency increases above $\hbar\omega \sim 0.25$ eV, which corresponds to the minimum in the $W_D(\hbar\omega)$ curve, the condition (26) of applicability of the quasi-static approximation is violated, and the considered model becomes inapplicable.

At the same time, in the case of D_2^+, the quasi-static model that takes into account a single electronic state of a molecule does not provide agreement with the results of exact simulations because of a slower motion of nuclei in this molecule and the violation of the condition (26) of applicability of the quasi-static approximation.

5. CONCLUSION

In this paper, we have considered the dissociation of molecular hydrogen ions in an intense IR laser field. The results of calculations carried out within the framework of the approximation of n terms have been compared with the results of exact numerical two-body simulation. The dependences of the dissociation probability on the intensity and frequency of laser radiation are determined. A quasi-static model of dissociation is considered. It is demonstrated that, in the range of low frequencies, this model provides a physically adequate description of the interaction between a laser wave field and a molecular system and allows one to understand the specific features of the dependence of the dissociation probability on the intensity and frequency of laser radiation.

REFERENCES

1. Delone, N.B. and Krainov, V.P., 1993, *Multiphoton Processes in Atoms* (Heidelberg: Springer-Verlag).
2. Volkova, E.A. and Popov, A.M., 1995, *Laser Phys.*, **5**, 1065.
3. Giusti-Suzor, A., Mies, F.H., DiMauro, L.F., *et al.*, 1995, *J. Phys. B*, **28**, 309.
4. Chelkowski, S., Zuo, T., Atabek, O., and Bandrauk, A.D., 1995, *Phys. Rev. A*, **52**, 2977.
5. Kulander, K.C., Mies, F.H., and Schafer, K.J., 1996, *Phys. Rev. A*, **53**, 2562.
6. Volkova, E.A., Popov, A.M., and Tikhonova, O.V., 1996, *JETP*, **83**, 889.
7. Il'inskii, Yu.A. and Keldysh, L.V., 1989, *Interaction of Electromagnetic Radiation with Matter* (Moscow: Mosk. Gos. Univ.) (in Russian).
8. Popov, A.M., Tikhonova, O.V., and Volkova, E.A., 1997, *Laser Phys.*, **7**, 843.
9. Volkova, E.A., Popov, A.M., and Tikhonova, O.V., 1998, *JETP*, no. 1.
10. Fedorov, M.V., Kudrevatova, O.V., Makarov, V.P., and Samokhin, A.A., 1975, *Opt. Commun.*, **13**, 293.
11. Zavriyev, A., Bucksbaum, P.H., Muller, H.G., and Schumacher, D.W., 1990, *Phys. Rev. A*, **42**, 5500.
12. Zavriyev, A., Bucksbaum, P.H., Squier, J., and Saline, F., 1993, *Phys. Rev. Lett.*, **70**, 1077.
13. Rottke, H., Ludwig, J., and Sandner, W., 1996, *Phys. Rev. A*, **54**, 2224.
14. Landau, L.D. and Lifshitz, E.M., 1974, *Quantum Mechanics* (Moscow: Nauka) (in Russian).
15. Dietrich, P., Ivanov, M.Yu., Ilkov, F.A., and Corkum, P.B., 1996, *Phys. Rev. Lett.*, **77**, 4150.
16. Krainov, V.P. and Sukharev, M.E., 1997, *Laser Phys.*, **7**, 803.

The Role of Electrons in Laser-Induced Explosion of Diatomic Molecules and Small Clusters

M. Brewczyk

Filia Uniwersytetu Warszawskiego, ul. Lipowa 41, Białystok, 15-424 Poland
e-mail: brewczyk@cksr.ac.bialystok.pl
Received August 30, 1997

Abstract—To investigate the role of electrons during the Coulomb explosion of few atoms systems exposed to the strong subpicosecond laser field, we have developed hydrodynamic time-dependent Thomas–Fermi model. The electron gas is assumed to obey the hydrodynamic equations of motion whereas the nuclei are moving classically. We solve the equations of our model both for diatomic molecules and small linear atomic clusters. Assuming that the linear system can rapidly get aligned along the linearly polarized laser field, we restrict the motion of the electrons to the one direction–the axis of the molecule or cluster. For diatomic molecules we identify the mechanism underlying the so-called kinetic energy defect (energies of the dissociating fragments are lower in comparison to those obtained from the simple Coulomb explosion picture). For small clusters we find qualitatively new phenomena not present in the case of molecules. Hot electrons are generated in the cluster via inverse bremsstrahlung effect, their energy is transferred to the ions through the scattering on the outermost layer of atoms which leads to the disassembly of the cluster.

1. INTRODUCTION

Recent experiments on clusters exposed to the strong laser field [1–8] have revealed a new phenomena qualitatively different from those encountered for diatomic molecules. The emission of intense X-ray radiation from "hollow" atoms [1] has been observed, as well as production of highly charged ions [1–6], generation of hot electrons [5, 8] and atomic ions [4, 5] or the effect of nonuniform energy distribution among the same charge state ions [5]. The different response of diatomic molecules and clusters is caused by the presence of collective phenomena. They play an important role in many-atom systems like clusters. Some of them have been recently recognized in experiment. For example, in experiments with large clusters (>1000 atoms) [2] the effect of heating electrons by photoabsorption during the electron–ion collisions has been found to be very efficient. The energy of hot electrons is then transferred to the ions leading to the explosion of clusters and production of atomic ions with energy up to 1 MeV [5].

At the same time, experiments with diatomic molecules show the kinetic energy of atomic fragments below 100 eV [9–11]. In this case, the fragments energy are consistent with a simple Coulomb explosion, however at internuclear distances larger by 20–50% than the equilibrium separation. This observation led to several tentative explanations [10, 12, 13]. The "stabilization" mechanism has been proposed in [10] whereas the "electron localization" followed by enhanced ionization of molecular ion at some critical distance has been suggested in [12]. Our calculations do not support any of those ideas. Instead, we find rather that the escaping ions are decelerated by electronic charge remaining in the space between ions [13].

The post-explosion screening effect leads to the values of kinetic energy defect in agreement with experiment [10]. However, for clusters yet another mechanism is present. The electrons are heated in early stages of cluster explosion when the density of cluster ions is high. The energy of hot electrons is transferred to the ions. So, the cluster explosion is governed by the competition of both deceleration and acceleration of the ions by the electrons. It is discussed in Section 3.

2. BASICS OF THE MODEL

The hydrodynamic time-dependent Thomas–Fermi model is based on the assumption that the oscillations of the electron cloud in multiatom system can be described as a motion of a fluid characterized by the mass density $\rho(\mathbf{r}, t)$ and velocity field $\mathbf{v}(\mathbf{r}, t)$ which obey the following equations [14]:

$$\frac{\partial \rho(\mathbf{r}, t)}{\partial t} + \nabla \cdot [\rho(\mathbf{r}, t)\mathbf{v}(\mathbf{r}, t)] = 0,$$

$$\frac{\partial \mathbf{v}(\mathbf{r}, t)}{\partial t} + [\mathbf{v}(\mathbf{r}, t) \cdot \nabla]\mathbf{v}(\mathbf{r}, t) \quad (1)$$

$$= -\frac{1}{\rho(\mathbf{r}, t)}\nabla P(\mathbf{r}, t) + \frac{e}{m}\nabla\Phi(\mathbf{r}, t).$$

First of them is the continuity equation, it expresses the conservation of mass. The second one is a classical equation of motion for an infinitesimal element of fluid. Since we deal with the electrons we consider, besides the usual force originated from the gradient of the pressure, the electric force due to all nuclei, the laser field and all electrons treated in mean-field approximation.
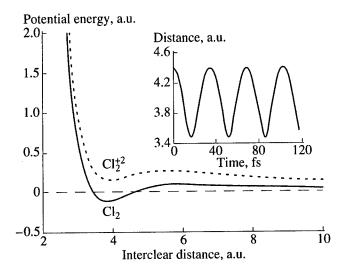
Potential energy, a.u.

Fig. 1. Potential energy curves for Cl_2 and Cl_2^{+2}, as computed with the parameters $A = 0.3$, $b = 1.22$, $c = 1.65$ a.u. Inset: Internuclear distance as a function of time for free oscillations of Cl_2 for small internuclear excursions away from an equilibrium separation.

To solve a set of equations (1) it is necessary to know the constitutive relation between the pressure and the density. A first approximation to this relation was derived by Thomas and Fermi [15]. Electrons are considered as a locally uniform noninteracting gas at zero temperature, then from Fermi–Dirac statistics the following equation appears: $P(\mathbf{r}) = \frac{1}{5}(3\pi^2)^{2/3}\frac{\hbar^2}{m^{8/3}}\rho^{5/3}(\mathbf{r})$.

The Pauli exclusion principle is the only quantum contribution to this model.

Since we assume the linear system is getting rapidly aligned with the electric field of a linearly polarized strong laser field [16, 17], we confine the motion of the electrons to one direction—along the polarization vector. So, we actually solve a one-dimensional version of equations (1):

$$\frac{\partial\rho(x)}{\partial t} + \frac{\partial}{\partial x}[\rho(x)v(x)] = 0$$

$$\frac{\partial v(x)}{\partial t} + v(x)\frac{\partial v(x)}{\partial x} = -\frac{1}{\rho(x)}\frac{\partial}{\partial x}P(x) + \frac{e}{m}\frac{\partial}{\partial x}\Phi(x). \tag{2}$$

However, we found that the three-dimensional semi-classical relation between the pressure and density does not work well in one dimension. Experimentation with possible forms for energy of one-dimensional gas, justified by Hohenberg–Kohn theorem [18], led us to the following constitutive equation: $P(x) = A\rho^2(x)$. The value of constant A turns out to be independent of the atomic number and is about 0.3 in atomic units. This value yields reasonable stationery properties of a model molecule such as binding energies and equilibrium separations.

The electric potential is calculated from the integral formula (instead of Poisson equation):

$$\Phi(x, t) = \sum_{i=1}^{N}\frac{Ze}{\{b^2 + [x - x_i(t)]^2\}^{1/2}}$$

$$-\frac{e}{m}\int_{-\infty}^{\infty}\frac{\rho(x', t)}{[c^2 + (x - x')^2]^{1/2}}dx' + eE(t)x, \tag{3}$$

where $x_i(t)$, $i = 1, ..., N$ are positions of the nuclei, b and c are smoothing parameters necessary to eliminate

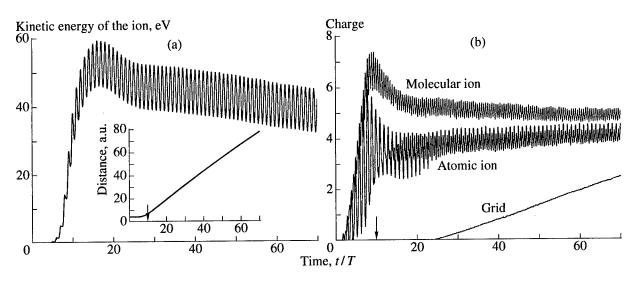Kinetic energy of the ion, eV

Fig. 2. Evolution of the molecular features for a peak intensity of 1.3×10^{16} W/cm^2 and the wavelength equal to 610 nm with the field ramped to maximum intensity in 10 optical periods, as marked by the arrow. (a) Kinetic energy of the atomic ion fragments vs. time; inset shows internuclear distance vs. time. Note that Coulomb explosion begins near the peak intensity; deceleration of the fragments sets in around $t = 20$ optical periods. (b) Distribution of net electrical charge (includes both nuclear and electronic components). Grid: net charge of the system on our spatial grid, which is contained in a box of length 200 a.u.

singularity at coinciding points which is common for one-dimensional problems [19]. External laser field is treated in dipole approximation. Again, parameters b and c are taken to produce reasonable static structure. It can be shown [20] that $A = (e/m)^2 \ln(c/b)$. Since $A = 0.3$ a.u. it means that there is only one free parameter in the model just like in well known one-electron calculations [19].

Figure 1 shows Born–Oppenheimer curves for chlorine molecule, calculated from static version of (2) [20] with parameters: $b = 1.22$ a.u., $c = 1.65$ a.u. which yields $R_e = 3.8$ a.u. and $D = 0.11$ a.u. We checked also the vibrational motion of the molecule when the external field is not present. The inset in Fig. 1 shows the free

oscillations of the internuclear distance with period equal to 34 fs.

3. LASER-INDUCED EXPLOSION OF MOLECULES AND CLUSTERS

To investigate the effects of an intense subpicosecond laser pulse on many-atom systems, we start with chlorine molecule [10]. The laser pulse of wavelength equal to 610 nm is turned on with a $\sin^2(\pi t/2\tau)$ ramp. We consider short pulses with ramp time $\tau = 10$ optical periods (20 fs).

Figures 2 summarize the dynamics of the system for a peak pulse intensity $I = 1.3 \times 10^{16}$ W/cm^2. First, Fig. 2a shows the Coulomb explosion of a molecule. It starts soon after the intensity is high enough to strip off loosely bound electrons. The kinetic energy of the atomic fragments increases rapidly (within a few optical periods) up to the value of about 120 eV consistent with the energy of the simple Coulomb explosion of channel (4, 4) at the equilibrium separation and simultaneously higher than observed in experiment [10]. However, as we can see in Fig. 2a, the energy of the fragments is decreasing after about 20 optical periods.

Figure 2b explains what happens. We plot the "atomic ion" and "molecular ion" charges as a function of time, where the "atomic charge" value is the charge within 3 a.u. of either ion and molecular ion is the sum of two atomic ions charges and the charge between them. Since the final charge of each ion is +4 and for a "molecule" it is +5 than there is a negative charge of three units in the space between ions. These electrons screen the mutual repulsion of the ions leading to the kinetic energy defect of about 20 eV [10]. Thus the deceleration of the Coulomb explosion caused by the
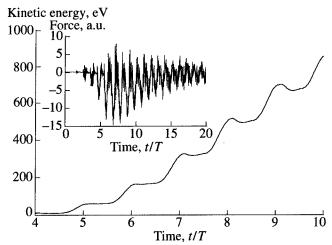
Fig. 3. Maximum kinetic energy of the electron fluid vs. time for Xe$_{12}$ and Xe$_2$ for a peak intensity of 1.4×10^{15} W/cm^2 and the wavelength equal to 800 nm. Electron heating is more effective in the larger cluster.
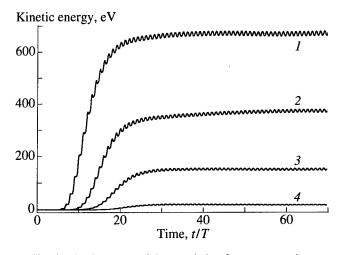
Fig. 4. Kinetic energy of the atomic ion fragments vs. time for Xe$_8$ irradiated at $I = 1.4 \times 10^{15}$ W/cm^2, $\lambda = 800$ nm. The energies are those of ions moving to the left; to each of these there corresponds a similar ion moving to the right. Note the stepwise character of the explosion, with ions being launched from the extremities of the cluster, the first to leave being most energetic.

Fig. 5. Time dependence of the kinetic energy of (main figure, in eV), and the total force acting on (inset, in a.u.), the outermost ion of a Xe$_{12}$ cluster for laser intensity of 5.6×10^{15} W/cm^2. Note the discrete jumps in energies near integral multiples of the optical period.
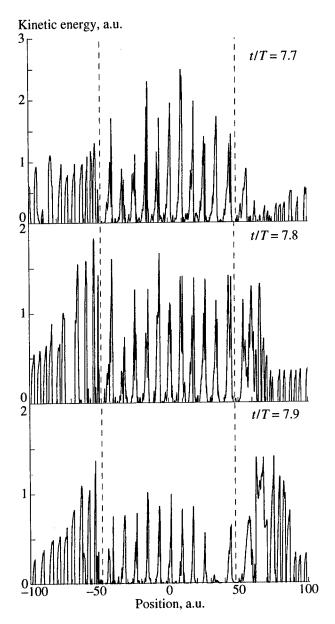
Kinetic energy, a.u.

Fig. 6. Distribution of kinetic energy of the electron fluid in the case of Fig. 5 at times of (a) 7.7, (b) 7.8, and (c) 7.9 of optical period. Positions of the outermost ions are marked by the vertical dashed lines. Note that when the electrons scatter on the "left" outermost ion, simultaneously hot electrons go out to the right from the cluster to scatter, in the next half of laser period, on the "right" ion.

Fig. 7. Final kinetic energy of the most energetic ion vs. number of atoms in the cluster: (a) the time-dependent Thomas–Fermi model of the present paper; (b) simplified Coulomb explosion model, i.e., instant removal of electronic charge. Laser parameters are the same as for Fig. 4. Note the huge increase of the kinetic energy over that obtained for the diatomic system. Inset: Demonstration of the crucial role of the electrons during the initial explosion of the Xe_{10}.

electronic charge kept in the space between ions is an underlying mechanism for kinetic energy defect.

For cluster, however, the situation changes dramatically [21]. Figure 3 compares the maximum electron energy for Xe_{12} and Xe_2 clusters for peak laser intensity of 1.4×10^{15} W/cm² and wavelength of 800 nm. The energies of electrons are much higher in the case of 12-atom cluster. This electron heating occurs in the early stage of explosion (<30 optical periods) when the density of the ions is still high. We interpret this as an effect of photoabsorption during the electron–ion collisions (inverse bremsstrahlung).

The energy of hot electrons is transferred to the ions. This mechanism is particularly efficient for the outer ions. Figure 4 shows the energies of four ions ejected in left (or right) direction by explosion of Xe_8 cluster. We see that the explosion is not instantaneous nor uniform. The ions are fired one by one with those ejected first being more energetic. So, as opposed to the explosion of diatomic molecules, for clusters we have a wide spectrum of kinetic energies for the same charge state ions. Such an observation has been reported recently [5]. The curves representing more energetic ions in Fig. 4 do not exhibit the decreasing part characteristic for diatomics (Fig. 2a). It means that the ion heating mechanism dominates the screening effect present for molecules, only for most inner ions the screening is still important.

The details of how the energy of the hot electrons is transferred to the ions are explained in Figs. 5 and 6. Figure 5 is a closer inspection of the kinetic energy of the most energetic ion (left one) but for peak intensity 5.6×10^{15} W/cm² (the inset shows the force acting on it). It is seen that the energy of the ion increases in a stepwise character by approximately 100 eV in a half of optical period. The mechanism of this tremendous acceleration can be recognized in Fig. 6 which shows the snapshots of spatial distribution of electron kinetic energy (the positions of outermost ions are marked by dashed lines). It is seen that hot electrons travel through and out of cluster to the right. When the field changes its direction, these electrons will be forced to scatter on the outermost "right" ion just like they scatter on the "left" outermost ion at times 7.7–7.9 optical periods (Fig. 6) leading to the huge increase of the energy of the

"left" ion (Fig. 5). This is the way how the cluster is disrupted.

Finally, Fig. 7 reveals another aspect of the role of electrons in course of laser-induced explosion of many-atom systems. We compare the results of our model with the simple Coulomb explosion model, in which six electrons (since the final charge states of the ions in our calculations is +6 for $I = 1.4 \times 10^{15}$ W/cm^2) are suddenly stripped off every Xe atom. From the main figure we see that in both cases the final energies of most energetic ions are comparable but the way how the energy is gained differs significantly. For "real" clusters the hot electrons are able to move the ions to their final states in an extremely efficient way. At the same time a simple model drives as a very slow process.

4. CONCLUSIONS

By using the hydrodynamic time-dependent Thomas–Fermi model we identify various mechanisms present during the Coulomb explosion of multiatom systems. We find that for diatomic molecules a post-explosion screening effect is dominant and responsible for kinetic energy defect. For clusters, however, the generation of hot electrons is much more important. The consequence of this is an efficient transfer of energy to the ions by the scattering of electrons on the outermost ions which leads to the stepwise explosion of clusters.

ACKNOWLEDGMENTS

REFERENCES

1. McPherson, A., Thompson, B.D., Borisov, A.B., et al. 1994, Nature, 370, 631; McPherson, A., Luk, T.S., Thompson, B.D., et al., 1994, Phys. Rev. Lett., 72, 1810.

2. Ditmire, T., Donnelly, T., Falcone, R.W., and Perry, M.D., 1995, Phys. Rev. Lett., 75, 3122.

3. Snyder, E.M., Buzza, S.A., and Castleman, A.W., 1996, Phys. Rev. Lett., 77, 3347.

4. Lezius, M., Dobosz, S., Normand, D., and Schmidt, M., 1997, J. Phys. B (in press).

5. Ditmire, T., Tisch, J.W.G., Springate, E., et al., 1997, Nature, 386, 54.

6. Ditmire, T., Tisch, J.W.G., Springate, E., et al., 1997, Phys. Rev. Lett., 78, 2732.

7. Donnelly, T., Ditmire, T., Neuman, K., et al., 1996, Phys. Rev. Lett., 76, 2472.

8. Shao, Y.L., Ditmire, T., Tisch, J.W.G., et al., 1996, Phys. Rev. Lett., 77, 3343.

9. Codling, K. and Frasinski, L.J., 1993, J. Phys. B, 26, 783.

10. Schmidt, M., Normand, D., and Cornaggia, C., 1994, Phys. Rev. A, 50, 5037.

11. Schmidt, M., D'Oliveira, P., Meynadier, P., et al., 1995, J. Nonlinear Opt. Phys. Materials, 4, 817.

12. Seideman, T., Ivanov, M.Yu., and Corkum, P.B., 1995, Phys. Rev. Lett., 75, 2819.

13. Brewczyk, M., Rzążewski, K., and Clark, C.W., 1997, Phys. Rev. Lett., 78, 191.

14. Ball, J.A., Wheeler, J.A., and Fireman, E.L., 1973, Rev. Mod. Phys., 45, 333.

15. Parr, R.G. and Yang, W., 1989, Density-Functional Theory of Atoms and Molecules (Oxford: Oxford Univ. Press).

16. Bucksbaum, P.H., Zavriyev, A., Muller, H.G., and Schumacher, D.W., 1990, Phys. Rev. Lett., 64, 1883.

17. Kulander, K.C., Mies, F.H., and Schafer, K.J., 1996, Phys. Rev. A, 53, 2562.

18. Hohenberg, P. and Kohn, W., 1964, Phys. Rev., 136, B864.

19. Javanainen, J., Eberly, J.H., and Su, Q., 1988, Phys. Rev. A, 38, 3430; Su, Q., Eberly, J.H., and Javanainen, J., 1990, Phys. Rev. Lett., 64, 862.

20. Brewczyk, M., Rzążewski, K., and Clark, C.W., to be published.

21. Brewczyk, M., Clark, C.W., Lewenstein, M., and Rzążewski, K., to be published.

Intense Field Photoelectron Emission, and High Harmonic Generation From Crystal Surfaces and Quantum-Wells

F. H. M. Faisal*, J. Z. Kamiński**, and S. S. M. Soliman***

* Fakultät für Physik, Universitä Bielefeld, Bielefeld 1, 33615 Germany
e-mail: ffaisal@physik.uni-bielefeld.de
** Institute of Theoretical Physics, Warsaw University, Hoża 69, Warszawa, 00-681 Poland
*** Physics Department, Faculty of Science, El-Minia University, El-Minia, Egypt
Received September 1, 1997

Abstract—In this paper we present a Floquet–Bloch analysis of photoemission of electrons and high harmonic generation from a crystal surface subjected to intense laser fields. We also investigate harmonic generation from single and double quantum-well structures by direct numerical solution of the associated time-dependent Schrödinger equation. The results of simulations of the photoelectron emission spectra show a whole set of new phenomena including above-threshold surface-emission bands of photoelectrons separated exactly by the photon energy, and *modulation* of the envelope of the spectrum. Simulation of the emission spectrum of high harmonics from an electron beam reflected from the surface in the presence of a laser beam at grazing incidence show a sequence of emission "hills" associated with strong enhancements of the high-harmonic signals. The results of photoemission and high harmonic generation spectra are interpreted in terms of modification of the band-structure of the crystal by the laser field. Finally, efficient harmonic generation from quantum-well structures are shown to be possible; it is suggested that this can provide a source of generating coherent radiation in far-infrared, at as yet unavailable wavelengths.

1. INTRODUCTION

Photoelectron emission of high currents (e.g., [1]) and spectrum of high-harmonic radiation (e.g., [2]), from a crystal surface subjected to intense laser fields have recently been the objects of vigorous investigation. They are motivated both by the desire to understand the behavior of crystals and surfaces in intense laser fields as well as by the need to obtain pulses of high electron currents of very short durations and/or high harmonic radiations with high efficiency. In particular, it had been found that the interaction of short laser pulses with metal surfaces generates nanosecond or picosecond pulses of highly directional electron beams [3, 4]. It is expected that such electron sources can find applications in electron beam lithography and high resolution electron microscopy [5], as well as in free-electron laser devices [6]. Also, a number of experiments have been carried out recently for high-harmonic generation from solid targets [2], in the intensity range between 10^9 and 10^{17} W/cm^2. Such coherent sources of radiation can have application in many domains of atomic, molecular, and solid state physics. Theoretical studies of high harmonic generation in condensed matter media are also initiated recently [7–12].

Nonlinear interaction of laser pulses with crystal surfaces have been analyzed in the past often within some version of the free-electron Sommerfeld model [13]. For the usual one-photon processes, the free-electron model is of some significance, but in the case of multiphoton processes such models appear to fail, e.g., to give many orders of magnitude higher currents

observed experimentally [3, 4] or the high emission probability of harmonics observed [2].

2. FLOQUET–BLOCH THEORY AND EXPRESSIONS FOR PHOTOELECTRON EMISSION AND HIGH HARMONIC GENERATION SPECTRA

We have recently developed a fully nonperturbative Floquet–Bloch theory [11, 12] of interaction of intense laser fields with periodic (or crystalline) electronic structures. In this paper we present results of Floquet–Bloch analysis of above-threshold surface-emission of photoelectrons and production of high harmonics by reflecting an electron beam of moderate energy from a crystal surface, subjected to an intense laser field.
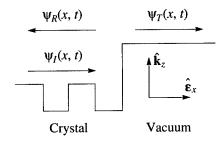

Fig. 1. A schematic description of a crystal with its surface State of an electron inside the crystal and that in the vacuum are indicated. The laser field is assumed to propagate parallel to the surface, along $\hat{k}_z$, with the polarization vector perpendicular to it, along $\hat{\varepsilon}_x$.

In Fig. 1, we show schematically the basic model of the surface and the alignment of the laser field. The laser field is assumed to be propagating parallel to the surface, $\hat{k}_z$, with the polarization vector perpendicular to it, $\hat{\epsilon}_z$. An electron initially in an occupied band-state $\psi_I(x, t)$ inside the crystal (and driven by the laser field) is shown to move toward the surface on the right hand side. After reaching the surface it is either reflected or transmitted with wavefunctions $\psi_R(x, t)$ or $\psi_T(x, t)$, respectively. (We note that in the case of the generation of high harmonics by reflecting an electron beam, the incident state has to be taken to approach the surface from the right but is not shown here explicitly). In the presence of an intense laser field these states can be most conveniently described by the associated Floquet–Bloch states [12] having definite expectation values of the momenta. The Floquet–Bloch states are generalizations [12] of the usual Bloch states in the absence of the laser field. They are of the form (in atomic units) [19, 20]:

$$\psi_{\beta k}(x, t) = e^{-iE_\beta(k)t} e^{ikx} \phi_{\beta k}(x, t), \qquad (1)$$

where $\beta = 1, 2, 3, \ldots$ is the band index, $E_\beta(k)$ is the Floquet–Bloch eigenenergy, $\phi_{\beta k}(x, t)$ is a periodic functions of both x and t with periods $2\pi/l$ and $2\pi/\omega$, respectively.

The associated field modified band structure can be represented either in terms of the "mean energy spectrum," obtained from the expectation value of the energy operator in the Floquet–Bloch state or in terms of the Floquet–Bloch quasienergy spectrum. The most significant properties of these spectra is the appearance of minigaps at specific k-values for which avoided crossings between the Floquet replicas can take place due to the fulfillment of a (multiphoton interband) resonance condition, to be discussed below.

The crystal wave function including the surface may be constructed conveniently making use of the Floquet–Bloch wave functions. Thus, the reflected wavefunction, $\psi_R(x, t)$, for example, can be given by a linear combination of the Floquet–Bloch states having negative expectation values of momenta and the corresponding "closed-channel" states [14]. Similarly, the transmitted wavefunction in the vacuum, $\psi_T(x, t)$, is given by a linear combination of the well-known Volkov states with positive momenta, e.g. [15], and the corresponding closed-channel states that decrease exponentially in the vacuum, away from the surface. The condition of continuity of the total wave function propagating in the crystal and in the vacuum, as well as its space derivative at the surface (for all time t) allows one to determine the desired transmission probability, $P_T(\beta, k; v)$, where (β, k) denote the initial band index and the Bloch momentum, respectively, and v denotes the final velocity of the photoelectron in the vacuum.

The transmission probabilities, P_T, permit us to define [16] the photoelectron spectrum, $\dfrac{dS(v)}{dv}$,

$$\frac{dS(v)}{dv} = \sum_{\beta, k} \frac{m_e v v_\beta(k)}{4k_F |E'_\beta(k)|} P_T(\beta, k; v), \qquad (2)$$

where the summation is over all initially occupied Floquet–Bloch states with positive momenta that fulfill the energy conservation condition

$$E = \frac{1}{2} m_e v^2 = E_\beta(k) \bmod \omega. \qquad (3)$$

$v_\beta(k)$ is the expectation value of the velocity of the electron in the initial states (β, k), m_e is the electron mass, k_F is the Fermi momentum, and $1/|E'_\beta(k)|$ is the density of the occupied initial states. Thus, the current emitted per unit surface area is given by

$$i = en \int_0^\infty \frac{dS(v)}{dv} dv, \qquad (4)$$

where e is the charge of the electron and n is the density of conduction electrons.

The high harmonic emission spectra of interest are obtained from the Fourier transform of the expectation value of the current density. The expression for the rate of emission at the frequency Ω then takes the form [12]

$$\frac{dW}{d\Omega} = \frac{2}{3} \alpha^3 \sum_{N \in Z} \delta(\Omega - N\omega) N^2 \omega^2 |\mathscr{I}_N(E_i)|^2, \qquad (5)$$

where $\mathscr{I}_N(E_i)$ is the Nth Fourier component of the current, α is the fine structure constant and E_i is the energy of incident electrons. The expectation value of the current operator consists of two terms. Outside the crystal it is calculated with a wavefunction that is a sum of the incoming Volkov wave of energy E_i and the Volkov waves reflected from the surface, with all possible positive energies $E_i + n\omega$. Inside the crystal the expectation value of the current operator is determined by the wavefunction which is a sum of all possible Floquet–Bloch states propagating from the surface into the crystal.

3. BAND STRUCTURE IN INTENSE FIELD

For the numerical simulations to be discussed below, we have used the parameters of the crystal potential such that a Fermi energy of 5.53 eV and a work function of 5.1 eV, corresponding to that of gold, are reproduced by the model [12]. We shall not go here in the details of the method of computation of the Floquet–Bloch band-structure and their general symmetry properties but refer the reader to our previous work [12], for the details.

In Fig. 2 we show the mean energy spectrum for a Nd : YAG laser of frequency $\omega = 1.169$ eV and intensity $I = 3 \times 10^{-5}$ a.u. $(1.053 \times 10^{12}$ W/cm$^2)$. The most interesting features seen in Fig. 2 are the rather sharp modifications of the band structure near a multiphoton resonance between a pair of bands. As we shall see below such interband resonances predominantly determine the above-threshold surface-emission spectrum, nigh harmonics spectrum, as well as the energy-spectrum of electrons reflected from the surface.

In Fig. 3 we show the unperturbed band structure (left panel) and compare them with the principal branch of the Floquet–Bloch bands associated with it (in the presence of the field). Notice in particular the appearance of a number of mini-gaps in the field modified band structure in this figure; they are due to avoided crossings between the Floquet replicas occurring at an interval of the photon energy. Physically they correspond to the influence of multiphoton resonances between pairs of bands of the "crystal + field" system. Another quantity that also characterizes the field modified band structure is the expectation value of the energy operator in the Floquet–Bloch states (or the mean energy spectrum), shown in Fig. 2 above. It shows also the influence of multiphoton resonances on the mean energy of the system by modifying the mean energy spectrum strongly for those quasi-momenta, k, which satisfy the resonance condition.

4. PHOTOELECTRON EMISSION SPECTRUM

In Fig. 4 we present the photoelectron emission spectrum, simulated for the case of interaction of the surface with a Nd : YAG laser at a wavelength $\lambda = 1064$ nm, and an intensity $I = 5 \times 10^9$ W/cm^2. The prominent feature of the spectrum seen here is the appearance of a whole sequence of individual energy-bands of the photoelectrons, marked by strips (white strips) of "zero current," the edges of which are separated exactly by the photon energy (1.169 eV). These bands, in the present case of surface photoemission, are direct analogs of the above-threshold ionization (ATI) peaks, well-known in the case of atomic ionization (e.g. [17, 18]). Note that the individual members of such "above-threshold surface-emission (ATSE)" spectra also exhibit sharp lines of high electron currents that are reminiscent of the sharp atomic resonance lines which are known to characterize the individual atomic ATI peaks [18]. We have found that in the present case they arise from intermediate miltiphoton resonances between pairs of Floquet–Bloch bands of the crystal. It can be seen from Fig. 4 that in the low energy part of the spectrum (up to about 4 eV), the envelope of the ATSE spectrum decreases linearly (in logarithmic scale). This is consistent with the usual power-law behavior (with respect to the photon order) expected from the perturbation theory. However, for larger energies (e.g., between 5 up to 9 eV) we observe formation of a broad bump in the envelope of the spectrum. This effect becomes more prominent
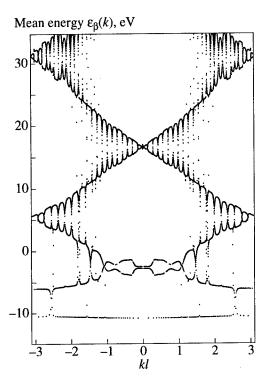
Mean energy $\varepsilon_\beta(k)$, eV

Fig. 2. The single valued spectrum of the mean band energy $\mathscr{E}_\beta(k)$ (in eV) for the laser intensity 1.053×10^{12} W/cm^2 at $\omega = 1.169$ eV.
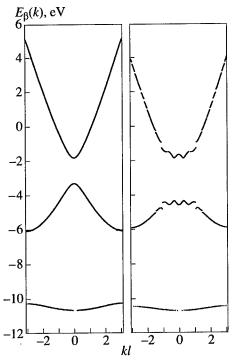
$E_\beta(k)$, eV

Fig. 3. On the left-hand side we present the field free band structure for the one-dimensional crystal. The dots appearing in the band structure in this (and in the subsequent) figures are due to limited density of points in the computations; they may be connected smoothly by interpolation, if desired. This band structure is compared on the right-hand side with the principal branches of the Floquet–Bloch bands in the presence of the field.

with increasing intensity and the envelope of the ATSE spectrum becomes characterized by a modulation due to the appearance of broad minima and maxima. Such modulations can be seen clearly in the ATSE spectrum in Fig. 5 which is obtained for a higher intensity $I = 3.51 \times 10^{11}$ W/cm^2. This is clearly a nonperturbative phenomenon which we attribute to the existence of energy-gaps in the band-structure of the crystal. Thus, a comparison of the positions of the modulation min-
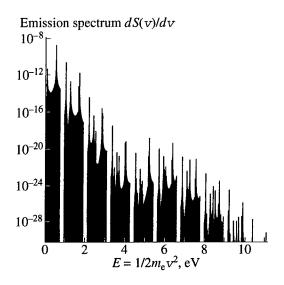
ima in these spectra with the calculated position of the band-gaps show that the former occur exactly and only in the vicinity of the latter. We also find that such modulations of the ATSE spectra require merely the existence of band-gaps of the crystal and is independent of whether the unperturbed crystal is a metal, as discussed here, or a semiconductor or an insulator. The modulation effect, therefore, is a universal phenomenon that should be observable in all above-threshold surface-emission spectra, independent of the conduction properties of the unperturbed surface.

Fig. 4. Calculated "above-threshold surface-emission (ATSE)" spectrum for the Nd : YAG laser frequency, $\omega = 1.169$ eV, at an intensity $I = 5 \times 10^9$ W/cm^2. Note the presence of a sequence of energy-bands separated exactly by the photon energy. Observe also the sharp resonance-like lines of high currents in the individual emission-bands and the hint of a broad maximum of the envelope between 5 to 9 eV.

5. HIGH-HARMONIC GENERATION FROM A CRYSTAL SURFACE

In the following sequence of figures we present the results of simulation of the high harmonic generation spectra, W, in terms of the squared Fourier components of the current, $|\mathcal{I}_N(E)|^2$, multiplied by the factor $\frac{2}{3}\alpha^3 N^2\omega^2$ [cf. (5)]. For the sake of concreteness we assume that crystal electrons interact with the laser field in the first 20 layers (of the order of the skin-depth for gold) of the surface.

Figure 6 shows the calculated spectrum at the intensity $I = 2 \times 10^{-5}$ a.u. $(7.02 \times 10^{11}$ W/cm$^2)$ for the case of electrons incident perpendicularly on the surface from the vacuum with energy $E_i = 25.8$ eV. Note that both odd and even harmonics are generated in the present system, as one expects from the lack of inversion symmetry. Already for such a moderate intensity we observe the formation of a bump in the spectrum for up to $N \approx 17$ which is due to a strong interband resonant transition in the crystal and the interference between the corresponding Floquet–Bloch states as well as between the Volkov states in the vacuum. For higher N we observe the appearance of plateaus (well-known in
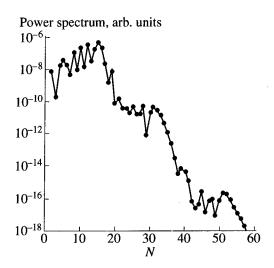

Fig. 5. The same as in Fig. 4 but for a higher intensity $I = 3.51 \times 10^{11}$ W/cm^2. Notice a broad minimum and a maximum at the envelope of the spectrum indicating a modulation of the envelope of the spectrum as a function of the energy.

Fig. 6. The harmonic spectrum generated by a beam of electrons of energy 25.8 eV impinging on the gold surface.

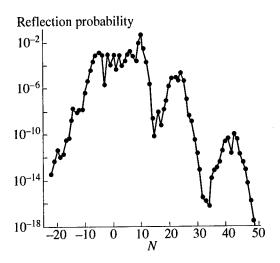**Fig. 7.** The reflection probabilities of electrons of energy 25.8 eV reflected from the gold surface.

Fig. 8. The harmonic spectrum generated by a beam of electrons of energy 22.3 eV impinging on the gold surface.

atomic physics) extending up to $N \approx 32$ in the case of the first plateau, and up to $N \approx 52$ for the second one. The resonant origin of these structures is clearly seen in Fig. 7 presenting the reflection probabilities of impinging electrons. We see that each plateau can be related to a resonant peak in the reflection probability spectrum and the bump in the harmonic spectrum is associated to the inelastic reflection process with the absorption of 10 laser photons. The first structure in the harmonic spectrum that extends up to $N = 17$ is due to both resonant transitions and interference of states of energies between $E_i - 7\omega$ and $E_i + 10\omega$. The origin of the remaining two plateaus can be explained in a similar way.

In view of the resonance coupling mechanism between the band of the incident electrons and the empty bands, one expects that the high harmonic spectra may be also controlled by suitably tuning the energy of the incident electrons. In Fig. 8 we show the spectra calculated for the incident electron energy $E_i = 22.3$ eV. At this energy and $I = 2 \times 10^{-5}$ a.u. $(7.02 \times 10^{11}$ W/cm^2) there appear now two well-separated hills in the harmonic spectrum which are followed by a second-and a third plateau; this is in contrast to the appearance of the bump in the corresponding case of Fig. 6. The explanation of such a difference can again be provided by the analysis of the reflection probabilities presented in Fig. 9. The first hill is due to the resonant transitions between the states with energies ranging from $E_i - 9\omega$ to $E_i + 5\omega$ with the very narrow and well-separated peak for $E_i - 9\omega$ in the spectrum of reflection probabilities. The appearance of the second hill in the harmonic spectrum is caused by the second (very narrow) well-separated resonant peak for energy $E_i + 14\omega$. The remaining two plateaus seen in Fig. 8 are, as in the previous case, due to broad resonant peaks in the spectrum of reflection probabilities centered around energies $E_i + 24\omega$ and $E_i + 47\omega$, respectively.
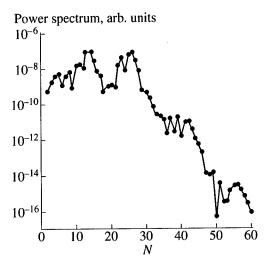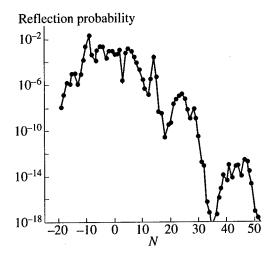

Fig. 9. The reflection probabilities of electrons of energy 22.3 eV reflected from the gold surface.

We may end this section by observing that the multiphoton resonant coupling creates a large amplitude for the corresponding Fourier component in the Floquet–Bloch state. This in its turn leads to large amplitudes in the current density oscillating at various difference frequencies associated with the product of the resonant- and the non-resonant Fourier amplitudes. These oscillations are then radiated into the higher harmonic modes with large signals constituting the "hills."

6. HARMONIC GENERATION FROM QUANTUM-WELLS

Quantum-well structures can nowadays be fabricated in the laboratory [21]. They provide a kind of "macroscopic atoms" and it is of interest, therefore, to investigate how these structures may be used to generate harmonics of incident laser fields, particularly in the far-infrared frequencies.
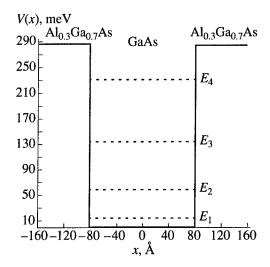
$V(x)$, meV

Fig. 10. Potential energy of an $Al_{0.3}Ga_{0.7}As/GaAs$ single quantum-well with width 160 Å and height 287 meV. The bound state energies (in meV) are: $E_1 = 15.13$, $E_2 = 60.41$, $E_3 = 134.55$, and $E_4 = 232.101$.
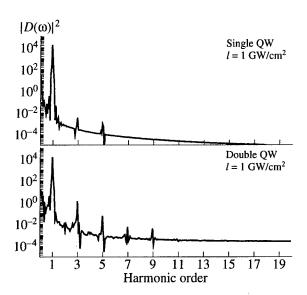

Fig. 12. High harmonic generation power spectrum for the single and the double QW structures at a CO_2 laser field wavelength $\lambda = 10640$ nm and with intensity $I = 1$ GW/cm^2.

$V(x)$, meV

Fig. 11. Potential energy of an $Al_{0.3}Ga_{0.7}As/GaAs/Al_{0.3}Ga_{0.7}As$ double quantum-well with individual well-width 60 Å, barrier-width 40 Å, well-depth 287 meV, and barrier-height 287 meV. The bound state energies (in meV) are: $E_1 = 62.57$, $E_2 = 66.80$, $E_3 = 229.98$, and $E_4 = 252.78$.

Fig. 13. The same as in Fig. 12, but for a larger intensity $I = 5$ GW/cm^2.

In Figs. 10 and 11 we show, respectively, a single- and a double-well structure with comparable characteristic dimensions. Note that unlike the model potentials used often with unrealistic infinite walls, these wells have finite heights which can lead not only to excitation but also to propagation of the electrons in the continuum above them.

The harmonic generation spectra in this case are obtained by Fourier transform of the dipole expectation value computed from the simulated total time-dependent wave function of the system interacting with the f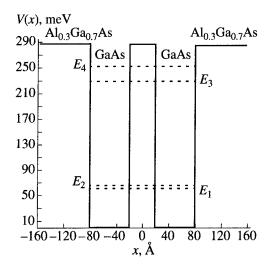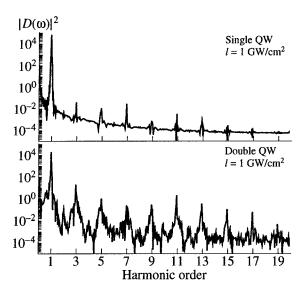ield, and evolving from their respective unperturbed ground states. For the purpose of simulations we have used a typical CO_2 laser frequency, $\omega = 0.117$ eV, at selected intensities in the region of GW/cm^2.

In Figs. 12 and 13 we show the calculated harmonic generation spectra for the single-well and compare them with that obtained from the double-well of comparable total extension. It is seen that at a given intensity the double well structure permits a stronger signal for the corresponding harmonic than that for the single well-structure. Moreover the number of harmonics of significant emission intensity are also, in general, greater for the double quantum-well than for the single

quantum-well. These results show that quantum-well structures could be used to generate harmonics of infrared radiation quite efficiently, and preferably from a double-well of comparable total dimension than a corresponding single-well. Also, as expected, the number of high harmonics generated is found to increase significantly with increasing incident intensity.

7. CONCLUSION

To conclude, we have presented a Floquet–Bloch analysis of interaction of intense Nd : YAG laser light with an ideal crystal surface, and direct simulations of the time-dependent Schrödinger wavefunctions for quantum-well structures interacting with intense CO_2 laser fields. Numerical simulations of the photoelectron spectrum, corresponding to a model gold surface subjected to the Nd : YAG laser field, reveal a sequence of "above-threshold surface-emission (ATSE)" *bands* of photoelectrons, that is a direct analog of the so-called above-threshold-ionization (ATI) spectrum, well-known in atomic physics. Thus, the edges of the present ATSE bands, are found to be separated exactly by the energy of the laser photon; the individual bands are further characterized by sharp lines of high currents that are analogous to the so-called atomic resonances that are known to appear inside an ATI peak. At high intensities, the envelope of the ATSE spectrum is found to be *modulated* by broad minima and maxima as a function of emission energy.

High harmonic generation in the presence of an electron beam incident perpendicular to the surface in the presence of an intense laser field (that is propagating parallel to the surface with its polarization vector parallel to the electron beam) is investigated. It is found that the harmonic radiation spectrum is characterized by the presence of "resonance hills" which arise from the intermediate multiphoton interband resonances between pairs of Floquet–Bloch bands in the presence of the field. The efficiency of generation of high harmonics is particularly high for the harmonics appearing on the "hills."

Finally, harmonic generation, in the infrared region, from single and double quantum-well structures are investigated. It is found that a double quantum-well of the same overall dimension, is more efficient for the purpose than the corresponding single quantum-well. This is expected to provide an efficient source of coherent radiation in the far-infrared region of spectra.

ACKNOWLEDGMENTS

REFERENCES

1. Fujimoto, J.G., Liu, J.M., Ippen, E.P., and Bloembergen, N., 1984, *Phys. Rev. Lett.*, **53**, 1837; Charalambidis, D., Hontzopoulos, E., Fotakis, C., *et al.*, 1989, *J. Appl. Phys.*, **65**, 2843; Girardeau-Montaut, J.P. and Girardeau-Montaut, C., 1989, *J. Appl. Phys.*, **65**, 2889; Farkas, Gy. and Tóth, Cs., 1993, *Opt. Eng.*, **32**, 2469; Falke, M. and Hippler, R., 1994, *Appl. Phys. A*, **59**, 537.

2. Farkas, Gy., Tóth, Cs., Moustaizis, S.D., *et al.*, 1992, *Phys. Rev. A*, **46**, R3605; von der Linde, D., Engers, T., Janke, G., *et al.*, 1995, *Phys. Rev. A*, **52**, R25; Kohlweyer, S., Tsakiris, G.D., Wahlstrom, C.-G., *et al.*, 1995, *Opt. Commun.*, **117**, 431.

3. Moustaizis, S.D., Tatarakis, M., Doukas, A.G., and Fotakis, C., 1991, *Appl. Phys. Lett.*, **58**, 194; Moustaizis, S.D., Tatarakis, M., Kalpouzos, C., and Fotakis, C., 1992, *Appl. Phys. Lett.*, **60**, 1939.

4. Agostini, P., private communication.

5. Lee, C.H., 1984, *Appl. Phys. Lett.*, **44**, 565.

6. Fraser, J.S., Sheffield, R.L., and Gray, F.R., 1986, *Nucl. Instrum. Methods Phys. Res., Sect. A*, **250**, 71.

7. Plaja, L. and Roso-Franco, L., 1992, *Phys. Rev. B*, **45**, 8334.

8. Huller, S. and Meyer-ter-Vehn, J., 1993, *Phys. Rev. A*, **48**, 3906.

9. Kamiński, J.Z., 1994, *J. Phys. C*, **6**, 1577.

10. Misra, A. and Gersten, J.I., 1992, *Phys. Rev. B*, **45**, 8665; Varró, S. and Ehlotzky, F., 1994, *Phys. Rev. A*, **49**, 3106; 1995, *J. Phys. B*, **28**, 121; Kálmán, P. and Brabec, T., 1995, *Phys. Rev. A*, **52**, R12.

11. Faisal, F.H.M. and Kamiński, J.Z., 1996, *Phys. Rev. A*, **54**, R1769.

12. Faisal, F.H.M. and Kamiński, J.Z., 1997, *Phys. Rev. A*, **56**, 748.

13. Smith, R.L., 1962, *Phys. Rev.*, **128**, 2225; Bunkin, F.V. and Fedorov, M.V., 1965, *Zh. Eksp. Teor. Fiz.*, **48**, 1341 [1965, *Sov. Phys. JETP*, **21**, 896]; Misra, A. and Gersten, J.I., 1991, *Phys. Rev. B*, **43**, 1883; Daniele, R., Ferrante, F., Fiordilino, E., and Varró, S., 1992, *J. Opt. Soc. Am. B*, **9**, 1916; Fiordilino, E., Daniele, R., and Ferrante, G., 1994, *ibid. B*, **11**, 1462.

14. They are associated with states that acquire a negative imaginary part of the Bloch momentum, k, in the presence of the field (see [12] for details and the method of computation).

15. Faisal, F.H.M., 1987, Theory of Multiphoton Processes (New York: Plenum).

16. Faisal, F.H.M. and Kamiński, J.Z. (unpublished).

17. Agostini, P., Fabre, F., Mainfray, G., *et al.*, 1979, *Phys. Rev. Lett.*, **42**, 1127; Kruit, P., Kimman, J., and van der Wiel, M.J., 1981, *J. Phys. B*, **14**, L597.

18. Freeman, R.R., Bucksbaum, P.H., Milchberg, H., *et al.*, 1987, *Phys. Rev. Lett.*, **59**, 1092.

19. Faisal, F.H.M. and Genieser, R., 1989, *Phys. Lett. A*, **141**, 297.

20. Kamiński, J.Z., 1993, *Acta Phys. Pol., A*, **83**, 495.

21. See, e.g., 1990, *Science and Engineering of One- and Zero-Dimensional Semiconductors*, Beaumont, S.P. and Torres, C.M.S., Eds. (New York: Plenum); 1990, *Physics of Quantum Electron Devices*, Capasso, F., Ed. (Berlin: Springer).

Down-Conversion IR FEL: Nonlinear Theory

I. V. Smetanin

P.N. Lebedev Physical Institute, Russian Academy of Sciences, Leninskii pr. 53, Moscow, 117924 Russia
e-mail: smetanin@neur.lpi.msk.su
Received October 8, 1997

Abstract—The unconventional scheme of an optical undulator IR free-electron laser which realizes the Doppler conversion of frequency down is investigated. Analytical nonperturbative theory of this down-conversion FEL in the nonlinear strong-signal low-gain Compton regime is developed. Electromagnetic field distribution and electron beam evolution inside the interaction region are investigated and FEL saturation intensity is determined.

One of the actual aspects in the theory of interaction of high-power laser radiation with free electrons is the problem of an optical undulator free-electron laser (FEL). Optical undulator FEL is considered now as a promising coherent and rather compact X-ray source. In the IR spectral domain, the new unconventional "down-conversion" scheme of the optical undulator FEL is suggested [1, 2]. In this paper, we develop the nonlinear strong-signal kinetic theory of the down-conversion FEL in the low-gain Compton regime.

Conventional FEL schemes are based on stimulated scattering by relativistic electron beam (REB) of a counterpropagating electromagnetic pumping wave (see Fig. 1a). As a result of the Doppler conversion of pumping frequency "up," an amplification of the signal wave occurs at the wavelength ($\gamma \gg 1$)

$$\lambda_s \approx \lambda_i / 4\gamma^2, \tag{1}$$

where $\gamma = (1 - \beta_z^2)^{-1/2}$ is the "longitudinal" relativistic factor, $c\beta_z$ is the electron velocity along the beams propagation direction, and λ_i is the pump wavelength (in the case of a static undulator with λ_w the period for equivalent wave is $\lambda_i = 2\lambda_w$). According to relation (1), conventional IR FELs, which operate usually at undulator periods $\lambda_w = 2$–10 cm, must be driven by high-energy (tens and hundreds MeV) electron beams being, therefore, high-cost large devices of rather low gain (the gain of an FEL scales as $\sim\gamma^{-3}$). To overcome these disadvantages a number of alternative FEL concepts are now under development. One of the possible alternatives is the optical undulator IR FEL which is based on the Doppler conversion of pumping wave frequency down.
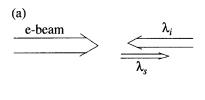
In the "down-conversion" FEL the high-power electromagnetic pumping wave and the REB penetrate in the same direction (Fig. 1b). The signal amplified is then counterpropagating and its wavelength is determined by reversed to (1) relation ($\gamma \gg 1$):

$$\lambda_s \approx 4\gamma^2\lambda_i. \tag{2}$$

Assuming high-power Nd-laser ($\lambda_i = 1.06$ μm) radiation as a pump and $\gamma \approx 5$, we have $\lambda_s \approx 100$ μm. Thus, that it is possible to cover all the IR spectral domain using low-voltage high-current electron accelerators is the unquestionable advantage of the scheme, which can result in relatively compact low-cost device.

In fact, the scheme in question is based on the symmetry of stimulated emission and absorption processes in the scattering of pumping wave by an electron beam. Relations (1) and (2) result from the condition of resonant interaction between the REB and the wave of ponderomotive potential, formed by the pump and signal waves. An amplification of high-frequency field component is attained when the electron velocity some exceeds the resonance one. In the reversed situation, when electrons are slightly breaking away from ponderomotive wave, an absorption of high-frequency and an amplification of low-frequency field components arise. In the latter case the energy stored in high-frequency pumping wave is distributed between the beam electrons and low-frequency signal.

Linear theory of the down-conversion IR FEL in the low-gain Compton regime was given in [2]. It was found that this scheme has some specific features which are quite different from those of conventional FELs. As a result of lasing, in the down-conversion FEL the beam electrons have to be accelerated instead of decelerating in the conventional devices, because the
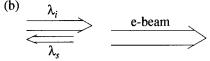

Fig. 1. The interaction geometry in (a) up-conversion and (b) down-conversion FEL.

energy of pumping wave is shared between the amplified signal wave and the electron beam. It was found that the beam quality restrictions are substantially less severe than that in conventional FELs. Due to all mentioned advantages, the down-conversion FEL looks like rather promising IR source.

In this paper we develop the nonperturbative strong-signal nonlinear theory of the down-conversion FEL in the low-gain Compton regime. We will use the well-known procedure which allows us to treat FEL dynamics in terms of quasi-Bloch equations [3]. We consider the 1D problem which corresponds to the collinear interaction geometry and small transverse beam emittance. A homogeneous REB is propagating along the positive z-axis direction at a velocity $c\beta_z$. Neglecting the influence of REB self-induced fields and harmonic generation effects, the electromagnetic field potential is the superposition of pumping (i) and signal (s) wave potentials,

$$\mathbf{A} = \mathbf{A}_i + \mathbf{A}_s. \qquad (3)$$

For definiteness sake, we choose pump and signal to be the plain waves of circular polarization:

$$
\begin{aligned}
\mathbf{A}_i(z, t) &= \mathbf{e}_- A_i(z)\exp\{i(\omega_i t - k_i z)\} + \text{c.c.},\\
\mathbf{A}_s(z, t) &= \mathbf{e}_- A_s(z)\exp\{i(\omega_s t + k_s z)\} + \text{c.c.}
\end{aligned}
\qquad (4)
$$

Here the wave amplitudes are slowly varying functions, $(k_{i,s} A_{i,s})^{-1} dA_{i,s}/dz \ll 1$.

We consider the quasi-steady-state problem, so that the pulse durations of beam current τ_b, pump τ_p, and signal τ_s are assumed to be large compared to the electron time of flight,

$$\tau_b, \tau_p, \tau_s \gg L/c\beta_z, \qquad (5)$$

where L is the length of the interaction region (i.e., the length of the optical undulator).

Under assumptions indicated above the dynamics of electrons is described by the one-dimensional kinetic equation [3, 4]

$$\frac{\partial f}{\partial t} + \frac{p}{m\gamma}\frac{\partial f}{\partial z} = \frac{e^2}{m\gamma}\frac{\partial}{\partial z}(A^2/2)\frac{\partial f}{\partial p}. \qquad (6)$$

Here $f(z, p, t)$ is the REB distribution function, $p = m\gamma c\beta_z$ is the longitudinal dynamical momentum of an electron (in the reasonable optical fields the shift in electron mass is insignificant, $\delta m/m \sim e^2 A^2/m^2 c^4 \ll 1$). It is assumed that the boundary condition for equation (6) is the steady-state momentum distribution at the entrance of undulator,

$$f(z = 0, p, t) = F_0(p). \qquad (7)$$

We will use the resonance approximation, containing in (6) only the terms corresponding to the synchronism of electrons and ponderomotive wave,

$$\beta_z \approx \omega/ck, \qquad (8)$$

where $\omega = \omega_i - \omega_s$ and $k = k_i + k_s$ are the frequency and the wavenumber of the ponderomotive wave, respectively.

Kinetic equation (6) should be solved jointly with the wave equation

$$
\begin{aligned}
\frac{\partial^2 A}{\partial z^2} + \frac{\partial^2 A}{c^2 \partial t^2} &= -\frac{4\pi}{c}j_{tr},\\
j_{tr} &= \frac{n_e e^2}{mc}\int f(z, p, t)A\frac{dp}{\gamma},
\end{aligned}
\qquad (9)
$$

describing the evolution of the signal and pump waves. Here, n_e is the density of electrons in the beam, and the following relation for transverse electron velocity, $v_{tr} = eA/(m\gamma c)$, is assumed, which is valid when the beam transverse emittance is small enough.

It is easy to show that material equations and wave equations can be solved separately under the condition

$$\frac{1}{A_{i,s}}\frac{\partial A_{i,s}}{\partial z} \ll \frac{1}{f_1}\frac{\partial f_1}{\partial z}, \qquad (10)$$

i.e., the gain in wave amplitudes is much slower than the growth rate of the oscillating part of the distribution function. As we neglect the higher harmonic generation, we seek the solution to (6) in the form of the sum of steady-state and oscillating at the frequency of the ponderomotive potential components ($\phi = \omega t - kz$):

$$
\begin{aligned}
&f(z, p, t)\\
&= f_0(z, p) + f_1(z, p)\exp(i\phi) + f_1^* \exp(-i\phi).
\end{aligned}
\qquad (11)
$$

Here and below the asterisk denotes the sign of complex conjugation. After substitution of (11) in the kinetic equation (6), the latter can be reduced by the well-known procedure to the system of quasi-Bloch equations [3]:

$$\frac{\partial f_0}{\partial z} = -\frac{ke^2}{pc^2}\frac{\partial R_1}{\partial p},$$

$$\frac{\partial R_1}{\partial z} + \mu R_2 = -2\frac{ke^2}{pc^2}|A_i|^2|A_s|^2\frac{\partial f_0}{\partial p}, \qquad (12)$$

$$\frac{\partial R_2}{\partial z} - \mu R_1 = 0.$$

Here the new functions, $iR_1 = A_i^* A_s f_1 - A_i A_s^* f_1^*$ and $R_2 = A_i^* A_s f_1 - A_i A_s^* f_1^*$, are introduced, and $\mu = m\gamma\omega/pc - k$ is the parameter of detuning of an electron from exact resonance with the ponderomotive wave. By analogy with the conventional Bloch equations, the functions f_0, $R_{1,2}$ can be regarded as the functions of medium excitation and imaginary and real parts of medium polarization, respectively. The natural boundary conditions to equations (12), corresponding to (7), are $(z = 0)$

$$f_0 = F_0(p), \quad R_1 = R_2 = 0. \tag{13}$$

The wave equation (9) is then reduced to the following form:

$$\frac{\partial |A_s|^2}{\partial z} = -\frac{2\pi n_e e^2}{mc^2 k_s} \int R_1 \frac{dp}{\gamma},$$

$$\frac{\partial |A_i|^2}{\partial z} = -\frac{2\pi n_e e^2}{mc^2 k_i} \int R_1 \frac{dp}{\gamma}. \tag{14}$$

One can see that the pump wave amplitude decreases much slower than the signal amplitude, $\partial |A_i|^2/\partial z \approx (4\gamma^2)^{-1}\partial |A_s|^2/\partial z$. Note also that equations (14) lead immediately to the photon number conservation law, which is natural for Compton scattering,

$$\frac{1}{\hbar\omega_i}\frac{\partial I_i}{\partial z} = \frac{1}{\hbar\omega_s}\frac{\partial I_s}{\partial z}, \tag{15}$$

where $I_{i,s}$ are the pump and signal intensities, respectively.

In the small-signal approximation, the stationary part of the electron distribution function remains constant in the lowest order of perturbation theory, $f_0(p, z) \approx F_0(p)$. It is easy to find the power gain coefficient [2], which is, of course, of the same form as that for the up-conversion FEL [4], but the relation between wavenumbers $k_{i,s}$ is determined by (2) rather than (1),

$$\alpha = \frac{1}{I_s}\frac{\partial I_s}{\partial z}$$

$$= \frac{4\pi^2 r_0^2 mn_e L}{k_i k_s c} I_i \int dp F(p_z) \frac{d}{dp}\left\{\frac{1}{\gamma p}\left(\frac{\sin\eta}{\eta}\right)^2\right\}. \tag{16}$$

Here $r_0 = e^2/mc^2$ is the classical radius of an electron, $\eta = \mu L/2$ is the parameter of detuning from resonance. The formal analogy of (16) with the corresponding result of [4] for up-conversion FEL scheme is caused by the symmetry of stimulated energy exchange discussed above.

The maximum gain is in the regime of dominant homogeneous broadening of line, which can be realized when the initial energy spread $\Delta\gamma/\gamma$ and the mean angle spread due to the beam emittance $\langle\Delta\Theta^2\rangle$ of beam electrons satisfy the inequality, as it follows just from analysis of the integrand in (16) [2],

$$\frac{\langle\Delta\Theta^2\rangle}{2}, \quad \frac{\Delta\gamma}{\gamma} < \frac{4\gamma^2}{2N}, \tag{17}$$

where $N = L/\lambda_i$ is an effective number of periods of the optical undulator. The optimum oscillation conditions are at the detuning parameter $\eta \approx \pi/2$, and we have for the gain per pass

$$G = \alpha L \approx \frac{128 r_0^2 n_e L^3}{\pi} \frac{I_i}{mc^2 \gamma^3 \omega_i}. \tag{18}$$

It is worth of emphasizing that the beam quality restrictions in the down-conversion FEL (17) are not so drastic as in the up-conversion scheme, $\Delta\gamma/\gamma < 1/2N$. It is rather crucial advantage of the scheme under discussion: it becomes possible to use undulators with larger number of periods (compared to up-conversion devices), which results in higher gain, $G \sim N^3$.

Let us consider the strong-signal nonlinear operation regime, when, with an increase in signal amplitude, perturbations of the electron distribution function become large and should be accounted exactly. Under condition (10), one can derive from (12) the following equation for the function R_1 in dimensionless variables $x = z/l$, $y = \mu l$:

$$\frac{\partial^2 R_1}{\partial x^2} + y^2 R_1 = 4\frac{\partial^2 R_1}{\partial y^2}. \tag{19}$$

Here the characteristic length $l = 2^{1/4}\gamma^2\beta(a_i a_s)^{-1/2}k^{-1}$ and normalized amplitudes $a_{i,s} = e|A_{i,s}|/mc^2$ are introduced. This equation can be solved by separation of variables, and y-dependent eigenfunctions are the functions of parabolic cylinder (Weber functions) [5]. It is convenient to represent solution to (19) in the form

$$R_1 = \sum_{n=0}^{\infty} B_n \exp\left(-\frac{y^2}{4}\right) H_n\left(\frac{y}{\sqrt{2}}\right) \sin(\lambda_n x), \tag{20}$$

where the eigenvalues are $\lambda_n^2 = 4(n + 1/2)$. Here $H_n(u)$ are the Hermite polynomials generated by the function $\exp(-u^2)$ [5], the boundary conditions (13), $R_1 = 0$ at $x = 0$, are taken into account.

Coefficients B_n can be determined using the second equation in the system (12), considered at the point $x = 0$. For definiteness, we assume the Gaussian distribution

function of beam electrons entering the interaction region,

$$F_0(p) = \frac{1}{\sqrt{2\pi}\sigma_0}\exp\left(-\frac{(p-p_0)^2}{2\sigma_0^2}\right). \qquad (21)$$

Using the Meler formula [5]

$$\sum_{n=0}^{\infty}\frac{1}{n!}\left(\frac{z}{2}\right)^n H_n(x)H_n(y)$$

$$= \frac{1}{\sqrt{1-z^2}}\exp\left\{\frac{2xyz - (x^2+y^2)z^2}{1-z^2}\right\},$$

we find

$$B_n = \frac{2|A_i||A_s|}{\sqrt{\pi}}\frac{\sigma}{\sigma_0 2^n n! \lambda_n}$$

$$\times \exp\left[-\frac{y_0^2}{4(1+\sigma^2)}\right](1+\sigma^2)^{-1/2}\left(\frac{1-\sigma^2}{1+\sigma^2}\right)^{\frac{n-1}{2}}$$

$$\times\left\{\frac{1}{2}\left(\frac{1-\sigma^2}{1+\sigma^2}\right)H_{n+1}\left(\frac{y_0}{\sqrt{2(1-\sigma^4)}}\right)\right.$$

$$\left. -nH_{n-1}\left(\frac{y_0}{\sqrt{2(1-\sigma^4)}}\right)\right\}, \qquad (22)$$

where the introduced parameters are $y_0 = \mu(p_0)l$, and $\sigma = \sigma_0 kl(\sqrt{2}\,\gamma^2 p_0)^{-1}$ is the normalized momentum spread of electrons in the beam.

The growth rate of signal amplitude is guided by (14), which, after substitution of the solution (20), (22), becomes of the following form:

$$\frac{\partial a_s}{\partial z} = \frac{\sqrt{2}\pi n_e e^2}{mc^2 k_s \gamma}a_i\exp\left[-\frac{y_0^2}{4(1+\sigma^2)}\right](1+\sigma^2)^{-1/2}$$

$$\times\sum_{n=0}^{\infty}\frac{1}{2^{2n}n!}\left(\frac{1-\sigma^2}{1+\sigma^2}\right)^n H_{2n+1}\left(\frac{y_0}{\sqrt{2(1-\sigma^4)}}\right) \qquad (23)$$

$$\times\left[\frac{\sin\lambda_{2n}x}{\lambda_{2n}} - \frac{\sin\lambda_{2n+2}x}{\lambda_{2n+2}}\right].$$

The exponential gain function $\alpha(z)$, $\alpha = a_s^{-1}\partial a_s/\partial z$, calculated according to (23) at different signal amplitudes, is represented in Fig. 2. Calculations are made in the case of pumping by high-power Nd-laser radiation, $\lambda_i = 1.06$ μm, $I_i = 10^{14}$ W/cm^2, FEL is driven by high-current REB with the current density of 5 kA/cm^2 (the
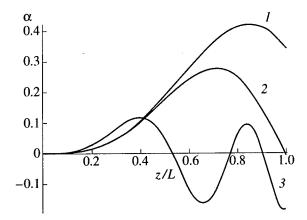

Fig. 2. The exponential gain $\alpha(z) = a_s^{-1}\partial a_s/\partial z$ at different signal intensities: (1) $I_s = 3.3 \times 10^4$ W/cm^2; (2) $I_s = 8 \times 10^4$ W/cm^2; and (3) saturation, $I_s = 3.3 \times 10^5$ W/cm^2. The pump intensity is $I_i = 10^{14}$ W/cm^2 ($\lambda_i = 1.06$ μm); the electron beam parameters are $n_e = 10^{12}$ cm^{-3}, $\gamma = 3.3$, $\sigma = 0.2$; initial beam detuning is $\mu(p_0)L = \pi$.

corresponding electron density is $n_e = 10^{12}$ cm^{-3}), $\gamma = 3.3$, and for the normalized momentum spread $\sigma = 0.2$. The wavelength of signal amplified is then $\lambda_s \approx 40$ μm, according to relation (2). Also, the optimum injection condition $\eta = \pi/2$ is assumed, which corresponds to the maximum linear gain per pass, $G \approx 0.5$. When the signal is rather small, i.e., the characteristic length l exceeds optical undulator length L, the amplitude growth rate is a monotonically increasing function of the coordinate z. With an increase in amplitude, even the lowest space modes in (23) begin oscillate, resulting in a decrease in the signal growth rate. In saturation, $\alpha(z)$ exhibits fast oscillations of sign and has rather low amplitude.

To determine the saturation intensity, one should integrate (23). This procedure becomes very easy if we assume that the parameters y_0 and σ are constant. Really, one can estimate using the data in Fig. 2 that maximum variations in a_s do not exceed a few percent in the regime close to saturation. Thus, one can write

$$a_s(0) - a_s(x) = \frac{2\sqrt{2}\pi n_e e^2}{mc^2 k_s\gamma}a_i l\exp\left[-\frac{y_0^2}{4(1+\sigma^2)}\right]$$

$$\times(1+\sigma^2)^{-1/2}\sum_{n=0}^{\infty}\frac{1}{2^{2n}n!}\left(\frac{1-\sigma^2}{1+\sigma^2}\right)^n \qquad (24)$$

$$\times H_{2n+1}\left(\frac{y_0}{\sqrt{2(1-\sigma^4)}}\right)\left[\frac{\sin^2(\lambda_{2n}x/2)}{\lambda_{2n}^2} - \frac{\sin^2(\lambda_{2n+2}x/2)}{\lambda_{2n+2}^2}\right].$$

Thus, we derived an analytical formula which describes the distribution of signal amplitude within the undulator in the strong-signal nonlinear FEL oscillation
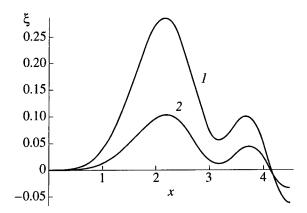
Fig. 3. The normalized signal amplitude, $\xi = (a_s(0) - a_s(x))/a_s(0)$ for different detunings $y_0 = \mu(p_0)l$, (1) $y_0 = 1$ and (2) 0.75, as a function of the dimensionless coordinate $x = z/l$. The pump intensity is $I_i = 10^{14}$ W/cm² ($\lambda_i = 1.06$ μm); the electron beam parameters are $n_e = 10^{12}$ cm^{-3}, $\gamma = 3.3$, $\sigma = 0.2$.
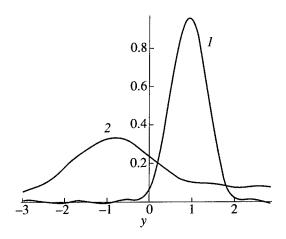

Fig. 4. The evolution of the electron beam normalized distribution function $\sqrt{2\pi}\,\sigma_0 f_0$, $y = \mu(p)l$, in the undulator, for the parameters $I_i = 10^{14}$ W/cm² ($\lambda_i = 1.06$ μm), $I_s = 0.1$ MW/cm², $n_e = 10^{12}$ cm^{-3}, and $\gamma = 3.3$, $\sigma = 0.3$; initial beam detuning is $\mu(p_0)L = \pi$: (1) initial distribution, $z = 0$; (2) exit distribution, $z = L = 2$ cm.

regime. Examples of this distribution are shown in Fig. 3 at two different values of initial beam detunings from the exact resonance with the ponderomotive wave. Beam and pump conditions are chosen the same as those used in Fig. 2. There is a characteristic point in Fig. 3 where $A_s(0) - A_s(x)$ becomes equal to zero, $x \approx 4.2$. We have found that this is a universal value which is constant in a rather wide range of beam detunings and energy spreads y_0, σ. It is easy to understand that it is the point that corresponds to saturation at given undulator length L (or, on the other hand, it determines the saturation length at given signal intensity),

$$L \approx 4.2l = 4.2\frac{2^{1/4}\gamma^2\beta}{k\sqrt{a_i a_s}}. \qquad (25)$$

Really, it is an equilibrium point: if the signal amplitude slightly exceeds the value determined by this relation, $x > 4.2$ at the undulator edge and, according to Fig. 3, we have that the total per pass absorption exceeds amplification of the signal wave, resulting in a decrease in the signal amplitude, and, consequently, in the value of x. In the opposite case $x < 4.2$, we have an amplification of the signal and an increase in x, respectively. Note, this point corresponds to the "absolute" saturation regime: in reality, however, since every FEL oscillator has definite losses (the mirror reflectivity $R < 100\%$, for example) the saturation emerges at lesser signal intensities, when the gain compensates the roundtrip losses.

At the above conditions ($\gamma = 3.3$, $I_i = 10^{14}$ W/cm², $\lambda_i = 1.06$ μm), assuming the undulator length $L \sim 2$ cm, we find from (25) that the saturation intensity is $I_s \approx 3.3 \times 10^5$ W/cm².

It is interesting to note that this value is close to the estimate from the condition of complete beam trapping by the ponderomotive wave [2]: saturation occurs when the electron energy spread $\Delta\gamma^*$ caused by lasing gives the spread in detuning parameter of the order of line bandwidth $\Delta\mu L/2 \sim \pi$,

$$I_s = \frac{1}{4}m\gamma c^3\beta^3 n_e(NG)^{-1}, \qquad (26)$$

and, with the above parameters, we find that this value is $\approx 2.5 \times 10^5$ W/cm², if we use the above-estimated value of small-signal gain per pass $G = 0.5$.

It is easy to understand, just considering an elementary Compton scattering event, that as a result of lasing in the down-conversion FEL beam electrons become accelerated, instead of deceleration in conventional up-conversion schemes: the energy of the absorbed pump mode quantum $\hbar\omega_i$ is shared between the emitted $\hbar\omega_s$ quantum and the electron. Also, the electron beam energy spread enhances. To describe these processes, we integrate the first equation in the system (12) using solution (20), (22) and find for the steady-state component of the distribution function

$$f_0(x, p) = F_0(p) - \frac{4}{\sqrt{\pi}\sigma_0}\frac{\sigma}{}\exp\left\{-\frac{y^2}{4} - \frac{y_0^2}{4(1 + \sigma^2)}\right\}$$

$$\times \sum_{n=0}^{\infty}\frac{1}{2^n n!}\left(\frac{1 - \sigma^2}{1 + \sigma^2}\right)^{\frac{n-1}{2}}\left[\frac{1}{2}\left(\frac{1 - \sigma^2}{1 + \sigma^2}\right)\right.$$

$$\times H_{n+1}\left(\frac{y_0}{\sqrt{2(1 - \sigma^4)}}\right) - nH_{n-1}\left(\frac{y_0}{\sqrt{2(1 - \sigma^4)}}\right)\right] \qquad (27)$$

$$\times \left[\frac{1}{2}H_{n+1}\left(\frac{y}{\sqrt{2}}\right) - nH_{n-1}\left(\frac{y}{\sqrt{2}}\right)\right]\frac{\sin^2(\lambda_n x/2)}{\lambda_n^2}.$$

Note that the dimensionless detuning y depends on the momentum of an electron as $y = \mu l \approx (kl/\gamma^2)(p_s - p)/p_s$, where p_s is the momentum, which corresponds to the exact synchronism between an electron and the ponderomotive wave. The distribution functions at the entrance (1) and at the exit (2) of the undulator are represented in Fig. 4. Beam and pump parameters are chosen the same as in above calculations, $\sigma = 0.3$; also, the optimum with respect to linear gain condition, $\mu(p_0)L = \pi$, is assumed. In these calculations, the signal intensity is ~1/4 of saturation intensity, i.e., $I_s = 8 \times 10^4$ W/cm². One can see that the characteristic energy spread, i.e., the characteristic width of the distribution function, increases in ~3 times due to lasing processes. The maximum point for the exit distribution is $y \approx -1$, i.e., electrons become accelerated ($\Delta y \approx -2$) in the down-conversion FEL, and the mean energy gain per electron is $\delta\gamma/\gamma \sim 2\gamma^2/kl \sim 0.3\%$.

In conclusion, we developed in this paper the strong-signal nonlinear nonperturbative theory of the down-conversion optical-undulator IR FEL. We derived analytical formulas describing evolution of the field amplitude and the electron beam distribution function inside the interaction region. The FEL saturation intensity is determined.

ACKNOWLEDGMENTS

REFERENCES

1. Gover, A., 1983, *Opt. Commun.*, **45**, 281.
2. Smetanin, I.V., 1994, *Zh. Eksp. Teor. Fiz.*, **106**, 1588 [1994, *JETP*, **79**, 856].
3. Hopf, F.A., Meystre, P., Scully, M.O., and Louisell, W.H., 1976, *Phys. Rev. Lett.*, **37**, 1342.
4. Hopf, F.A., Meystre, P., Scully, M.O., and Louisell, W.H., 1976, *Opt. Commun.*, **18**, 413.
5. Bateman, H. and Erdelyi, A., 1953, *Higher Transcendental Functions* (McGraw-Hill), vol. 2.

Studies of Nonlinear QED in High Energy Electron–Laser Collisions

Th. Kotseroglou

Stanford Linear Accelerator Center, Stanford, CA, 94309 USA

Based on results obtained by the E-144 Collaboration
C. Bamber, S. C. Berridge*****, S. J. Boege**, W. M. Bugg*****, C. Bulal*, D. L. Burke****, R. C. Field****,
G. Horton-Smith****, T. Koffas**, T. Kotseroglou**, ****, K. T. McDonald*, A. C. Melissinos**,
D. D. Meyerhofer**, ***, E. J. Prebys*, W. Ragg**, D. A. Reis**, K. Shmakov*****, J. E. Spencer****,
D. Walz,**** and A. W. Weidemann*******

* Joseph Henry Laboratories, Princeton University, Princeton, NJ, 08544 USA
** Dept. of Physics and Astronomy, University of Rochester, Rochester, NY, 14627 USA
*** Dept. of Mechanical Engineering, University of Rochester, Rochester, NY, 14627 USA
**** Stanford Linear Accelerator Center, Stanford University, Stanford, CA, 94309 USA
***** Dept. of Physics and Astronomy, University of Tennessee, Knoxville, TN, 37996 USA
e-mail: theo@slac.stanford.edu

Abstract—We discuss results obtained at the Stanford Linear Accelerator Center in the interaction of 46.6 GeV electrons crossing through the focus of a terawatt laser at $\lambda = 527$ nm. Under those circumstances the field seen in the electron rest frame approaches the critical field of QED. Multiphoton Compton scattering with the absorption of as many as 4 photons from the laser field as well as e^+e^- pair production in the collision of a high energy γ with several laser photons were observed. This is the first evidence for strong QED interactions and the data agree with the theoretical predictions. Furthermore this is the first observation of inelastic light-by-light scattering involving only real photons.

Progress in laser technology has made possible the creation of intense electromagnetic fields in the laboratory, which in turn has opened up the science of nonlinear optics. However these fields are several orders of magnitude weaker than the critical field of QED at which vacuum polarization effects become important: The critical field [1] was introduced sixty years ago and is defined such that in one electron Compton wavelength $\lambda_c = \hbar/mc$ an electron gains energy equal to its rest mass

$$E_c = \frac{m^2 c^3}{e\hbar} = 1.3 \times 10^{16} \text{ V/cm} \qquad (1)$$

with m, e the mass and charge of the electron.

To reach the critical field we take advantage of the high energy electron beam at the Final Focus Test Beam (FFTB) [2] at the Stanford Linear Accelerator Center (SLAC). The electrons have energy $\mathscr{E} = 46.6$ GeV and thus a Lorentz factor $\gamma = \mathscr{E}/mc^2 = 9.1 \times 10^4$. When these electrons traverse the focus of the laser they see in their rest frame an electric field

$$E^* = 2\gamma E, \qquad (2)$$

where E is the laboratory field. This is equivalent to an increase of the laser intensity by a factor of ~10^{10}. We used a Nd : glass laser system [3] operating at 0.5 Hz and which delivered at the second harmonic ($\lambda = 527$ nm) as

much as 1 J of energy in 1.6 ps, focussed to 25 mm^2. This corresponds to an intensity $I = 2.5 \times 10^{18}$ W/cm^2 and thus to an electric field (root mean square value) at the focus

$$E_{\text{rms}} = \sqrt{Z_0 I} = 3 \times 10^{10} \text{ V/cm}, \qquad (3)$$

where Z_0 is the vacuum impedance. According to (2) the field in the rest frame reaches $E^* = 5.6 \times 10^{15}$ V/cm, nearly half the critical value. This is the first experiment ever to have explored QED in this regime [4, 5].

To describe QED in the strong field region two dimensionless invariants are introduced. The first is

$$\eta^2 = \frac{e^2 |\langle A_\mu A^\mu \rangle|}{m^2}, \qquad (4)$$

where A_μ is the 4-vector potential of the incident field. In a given reference frame η can be expressed in terms of the rms electric field and the frequency of the wave ω as

$$\eta = \frac{e E_{\text{rmc}}}{\omega mc}. \qquad (5)$$

The parameter η is classical, since it does not contain $\hbar$. As $\omega \longrightarrow 0$ approaches unity, multiphoton effects become prominent in the interaction of electrons with the field. Note that η diverges as $\omega \longrightarrow 0$.

The second invariant is formed as $\sqrt{\langle (F_{\mu\nu}p^\nu)^2 \rangle}/mc$ where $F_{\mu\nu}$ is the field tensor and p^ν the 4-momentum of the incident electron. We then define

$$\Upsilon = \frac{E^*}{E_c} = 2\gamma\frac{eE\hbar}{m^2c^3}, \qquad (6)$$

Υ is a measure of the c.m. energy available in the collision (in units of the electron mass) multiplied by the multiphoton parameter η. When Υ approaches unity vacuum polarization effects become prominent and spontaneous pair production takes place. This effect has long been predicted and is referred to as the "sparking" or "break-down" of the vacuum [6]. Note that Υ is independent of the frequency and thus can be defined for a static field as well. The effect of the Lorentz boost of the electric field is clearly apparent in the definition of Υ.

Here we report on the measurement of multiphoton Compton scattering [4, 7]

$$e^- + n\omega \longrightarrow e^{-1} + \gamma, \qquad (7)$$

where n is the number of absorbed laser photons, and on pair production in multiphoton light-by-light scattering [5, 8]

$$\gamma + n\omega \longrightarrow e^+e^-. \qquad (8)$$

While reactions (7) and (8) are related by crossing symmetry, experimentally they are quite different: high energy electrons are directly available in the incident beam whereas the high energy γ's needed for reaction (8) to proceed are produced by Compton backscattering as indicated by (7). These high energy γ's must interact within the laser focus to produce the e^+e^- pair. Furthermore while reaction (7) can proceed for any value of $n \geq 1$, in this experiment, reaction (8) can only proceed for $n \geq 4$; this is because $\hbar\omega = 2.35$ eV and the maximum γ-ray energy (for $n = 1$) is $E_\gamma = 29$ GeV. Pair production by a virtual photon, i.e. the trident process

$$e^- + n\omega \longrightarrow e^{-1} + e^+e^-, \qquad (9)$$

has a much lower probability for occurring under the conditions of our experiment than the two-step process of (7) followed by (8).

We refer to reaction (7) as Compton scattering because in the electron rest frame the laser photon energy is of the same order as the electron mass and the electron undergoes significant recoil. The geometry of the experiment is shown in Fig. 1, where the laser beam crosses the electron beam at an angle $\alpha = 17°$ and the (back)scattered photon angle θ is measured from the electron direction.

We use units where $\hbar = c = 1$ and where appropriate, make approximations due to the large value of $\gamma = \mathscr{E}/m$ with $\mathscr{E}$ the electron energy. The kinematical variables are defined as
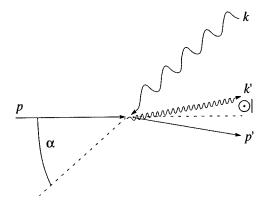
$$p^\mu, p'^\mu$$
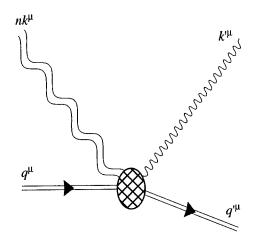

Fig. 1. The scattering geometry.

Fig. 2. Representation of nonlinear Compton scattering: an electron in a strong field (represented by the double line) absorbs a number of photons and emits a high energy γ.

4-momentum of the electron before and after scattering. These take the values $(\mathscr{E}, \vec{p})$, $(\mathscr{E}', \vec{p}')$ in the laboratory frame.

$$k^\mu, k'^\mu$$

4-momentum of a photon before scattering and of the scattered photon. These take the values $(\omega, \vec{k})$ and $(\omega', \vec{k}')$ in the laboratory frame.

The scattering process is expressed by

$$p^\mu + nk^\mu = p'^\mu + k'^\mu. \qquad (10)$$

Here n is the number of absorbed photons. The effective mass of the electron in the strong field is taken into account by replacing p^μ by q^μ (and $p'^\mu \longrightarrow q'^\mu$),

$$q^\mu = p^\mu + \frac{\eta^2 m}{2(kp)}k^\mu. \qquad (11)$$

This is illustrated in the diagram of Fig. 2 where the double lines indicate that the electron is not free but interacting with the field and the incoming wavy lines indicate the number of photons absorbed from the field.

The laboratory energy of the scattered photon is given by

$$\omega' = (2n\gamma^2\omega(1 + \beta\cos\alpha))/\Big(2\gamma^2(1 - \beta\cos\theta)$$

$$+ \Big[\frac{2n\omega\gamma}{m} + \frac{\eta^2}{1 + \beta\cos\alpha}\Big][1 + \cos(\theta - \alpha)]\Big).$$

$$(12)$$

For $\gamma = 1$, $\beta = 0$ and $n = 1$, $\eta^2 = 0$, (12) reduces to the familiar Compton condition.

At high incident electron energies the backscattered γ-rays are emitted at angles of order $(1/\gamma)$ and therefore we express the differential cross section as a function of the γ-ray energy. By introducing the invariants

$$x = \frac{2p'k}{m^2}, \quad y = 1 - \frac{p'k}{pk}, \tag{13}$$

which in the laboratory frame take the values

$$x \simeq \frac{2\omega E}{m^2}(1 + \cos\alpha), \quad y \simeq \frac{\omega'}{E}, \tag{14}$$

the Klein–Nishina single photon cross section [9] can be written in the invariant form

$$\frac{d\sigma}{dy} = \frac{2\pi r_0^2}{x}$$

$$\times \Big[(1 - y) + \frac{1}{(1 - y)} - \frac{4y}{x(1 - y)} + \frac{4y^2}{x^2(1 - y^2)}\Big]. \tag{15}$$

where $r_0 = e^2/m = 2.82 \times 10^{-13}$ cm is the classical electron radius. Integration of (15) yields the total Compton
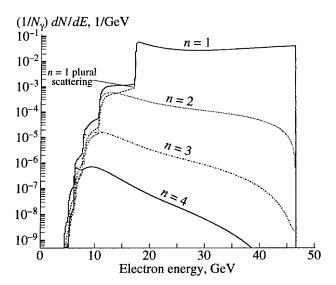
(1/N_γ) dN/dE, 1/GeV

Fig. 3. Recoil electron rates for linear, nonlinear and plural Compton scattering for incident green light ($\lambda = 527$ nm) and standard laser and electron beam parameters for this experiment. The cross section from [11] for circularly polarized light was used in the simulation. The solid line is the sum of all possible processes. The $n = 2$, $n = 3$, and $n = 4$ processes are shown separately as well.

cross section as a function of collision (cm) energy

$$\sigma_c = \frac{2\pi r_0^2}{x}$$

$$\times \Big[\Big(1 - \frac{4}{x} - \frac{8}{x^2}\Big)\ln(1 + x) + \frac{1}{2} + \frac{8}{x} - \frac{1}{2(1 + x)^2}\Big]. \tag{16}$$

The transition probability for reactions (7) and (8) has been calculated in [10, 11]. The incident wave is treated classically and the modified electron wavefunctions are used to obtain the Born amplitude for the emission (or absorption) of the high energy γ-ray. For circularly polarized incident photons the results can be expressed as a cross section in closed form

$$\frac{d\sigma}{dy} = \sum_{n=1}^{\infty} \frac{d\sigma_n}{dy} = \sum_{n=1}^{\infty} \frac{2\pi r_0^2}{u_1}\Big\{-\frac{4}{\eta^2}J_n^2(z)$$

$$+ \Big(2 + \frac{u^2}{1 + u}\Big)[J_{n-1}^2(z) + J_{n+1}^2(z) - 2J_n^2(z)]\Big\}, \tag{17}$$

where the following notation has been introduced

$$u = \frac{kk'}{kq'} \quad u_1 = \frac{2kq}{m^2} \quad u_n = nu_1$$

and

$$z = [2\eta\sqrt{u(u_n - u)}]/([u_1\sqrt{1 + \eta^2}],) \tag{18}$$

$J_n(z)$ are ordinary Bessel functions of order n. As $\eta^2 \longrightarrow 0$ only the $n = 1$ term contributes and (17) reduces to the Klein–Nishina cross section (15). To obtain results that can be compared with experiment it is essential to account for the variation of η^2 throughout the region of the laser focus either by numerical integration or by a Monte Carlo technique. Therefore the theoretical predictions of (17) are compared with our experimental results in terms of the rate of scatters rather than cross section.

The laboratory energy of the scattered electron can be found from (12) and has its minimal value when the laser photon backscatters. This gives rise to a kinematic edge which depends on the number of absorbed photons and the effective mass of the electron

$$\mathscr{E}_{edge}(n, \eta) = \frac{\mathscr{E}}{1 + nx/(1 + \eta^2)}.$$

For green laser light ($\lambda = 527$ nm) and 46.6 GeV electrons the kinematic edges are given below (for $\eta^2 = 0$)

$$n = 1 \quad \mathscr{E}_e > 17.6 \text{ GeV},$$

$$n = 2 \quad \mathscr{E}_e > 10.8 \text{ GeV},$$

$$n = 3 \quad \mathscr{E}_e > 7.8 \text{ GeV},$$

$$n = 4 \quad \mathscr{E}_e > 6.1 \text{ GeV}.$$

By observing electrons with momenta beyond (lower than) the n-photon kinematic edge one identifies events corresponding to the absorption of at least $n + 1$ photons. Since the cross section for absorption of n
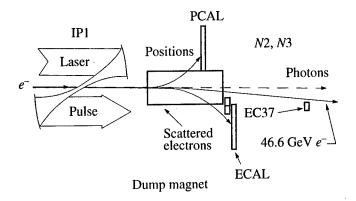
Fig. 4. Schematic layout of the experiment.

photons varies as η^{2n} and in this experiment $\eta \sim 0.3$ the different multiphoton orders can be distinguished. This is shown in Fig. 3 which gives the expected electron yield as a function of scattered electron momentum for the conditions of this experiment for $\eta = 0.25$ [laser wavelength 527 nm, laser energy 400 mJ, effective focal area 30 μm^2 and pulsewidth (FWHM) 2 ps].

There is one complication in this argument in that an electron can appear below the nth kinematic edge if it undergoes $n + 1$ separate scatterings in the laser focus. We refer to this process as "plural scattering" and it has exactly the same kinematics as the multiphoton process of the same order. The simulation indicates that for our experimental configuration the rate of plural scattering is 3–10 times lower than for the corresponding multiphoton process. This problem does not arise when forward γ-rays are observed with energy exceeding the corresponding kinematic edge.

A schematic layout of the experiment is shown in Fig. 4. The laser beam was focused onto the electron beam by an off-axis parabolic mirror of 30 cm focal length with a 17° crossing angle at the interaction point, IP1, 10 m downstream of the FFTB Final Focus.

The laser was a 1.5 ps, 527 nm, 500 mJ chirped-pulse-amplified Nd : glass terawatt system with a relatively high repetition rate of 0.5 Hz achieved by a final laser amplifier with slab geometry [3]. The laser-oscillator mode locker was synchronized to the 476 MHz drive of the SLAC linac klystrons with an observed jitter between the laser and linac pulses of 2 ps (rms) [12]. The spatial and temporal overlap of the electron and laser beams was optimized by observing the Compton scattering rate in the electron calorimeter (ECAL) detector during horizontal, vertical, and time scans of one beam across the other.

The electron beam parameters were varied during the course of the experiments. Typically the beam was operated at 10–30 Hz with an energy of 46.6 GeV and emittances $\mathscr{E}_x = 3 \times 10^{-10}$ m-rad and $\mathscr{E}_y = 3 \times 10^{-11}$ m-rad. The beam was tuned to a focus with $\sigma_x = 25$ μm and $\sigma_y = 35$ μm at the laser–electron interaction point. The electron bunch length was expanded to 7 ps (rms)
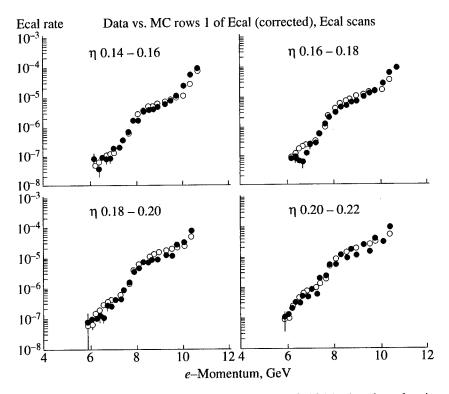

Fig. 5. The scattered electron rate normalized to the total Compton rate $(1/N_\gamma)(dN/dE)$ is plotted as a function of electron momentum, for 46.6 GeV incident electrons and $\lambda = 527$ nm. The solid dots are the data and the open circles are the prediction of the simulation. Data are shown for eight different laser intensities.
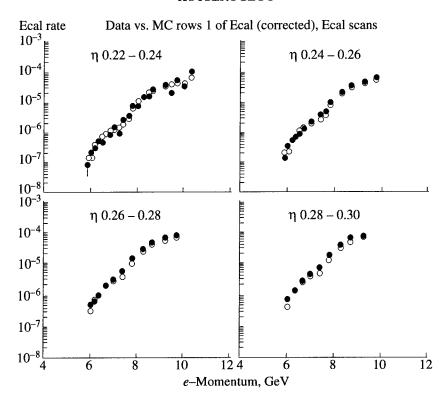
Ecal rate   Data vs. MC rows 1 of Ecal (corrected), Ecal scans

e–Momentum, GeV

Fig. 6. As in Fig. 5 but for higher laser intensities.

to minimize the effect of the time jitter between the laser and electron pulses. Typical bunches contained 7×10^9 electrons. However, since the electron beam was significantly larger than the laser focal area only a small
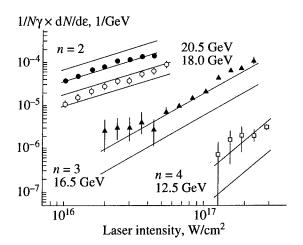

Laser intensity, W/cm^2

Fig. 7. The scattered electron rate normalized to the total Compton rate $(1/N_\gamma)(dN/dE)$ plotted as a function of laser intensity at fixed electron momentum. The incident electron energy was 46.6 GeV and the laser wavelength λ = 1054 nm (IR). The solid and open circles are data for two photon absorption; the triangles are for the n = 3 process and the open squares for the n = 4. The simulation for each process is shown as bands representing the 30% uncertainty in the laser energy and the 10% uncertainty in the measurement of the gamma flux. The slope of the bands is characteristic of the order of the nonlinear process.

fraction of the electrons crossed through the peak field region.

A string of permanent magnets after the collision point deflected the electron beam downwards by 20 mrad. Electrons and positrons of momenta less than 20 GeV were deflected by the magnets into two Si-W calorimeters (ECAL and PCAL) as shown in Fig. 4. The calorimeters measured electromagnetic shower energies with resolution $\sigma_E/E \approx 25\%/\sqrt{E[\text{GeV}]}$ and determined the position of isolated showers with resolution of 2 mm.

Momentum spectra of the scattered electrons are shown in Figs. 5 and 6 for incident linearly polarized green light at different laser intensities. To reduce the uncertainties in the overlap in space and time between the electron beam and the laser pulse the data are normalized by the total flux of forward γ's. The forward γ's are due mainly to n = 1 scattering and were measured by a Cerenkov monitor. Typically there were 10^7 high energy γ's per pulse. The solid circles are the data and the open circles the simulation, showing good agreement over several decades. The data shown begin beyond the n = 2 kinematic edge and span the n = 3 and n = 4 region.

A systematic study of Compton scattering was carried out for both IR and Green and the results are summarized in Figs. 7 and 8 where the normalized electron yield is shown at fixed momentum as a function of laser intensity for the two incident wavelengths. The data exhibit the exponential dependence on laser intensity
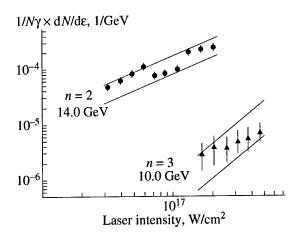
Fig. 8. As in Fig. 7 but for laser wavelength $\lambda = 527$ nm (green). Data are shown for two and three photon absorption.

Fig. 9. Layout of CCD spectrometer for measuring forward γ's.

$(1/N_\gamma)(dN/dE) \propto I^{(n-1)}$ expected for nonlinear processes. The shaded area represents the results of the simulation when the uncertainty in the laser intensity is taken into account. While the agreement is reasonable for $n = 2$, the $n = 3$ and $n = 4$ data have larger errors and show more scatter as well as deviating from the simulation. This is due to the difficulty in measuring these low rates in the presence of the background created from the high rate of recoil electrons due to lower n Compton scattering.

To measure the spectrum of the forward γ's a thin converter was placed in the $0°$ line and the electrons and positrons were momentum analyzed by a spectrometer with CCD read out planes as shown in Fig. 10. In view of the high rate no attempt was made to reconstruct the γ's but the electron or positron spectrum reflect the spectrum of the parent γ's. Preliminary results are shown in Fig. 11, and are well matched by the simulation. The $n = 1$ kinematic edge can be seen, as well as events arising from $n = 2$ scattering.

We now turn to positron production. As already mentioned, a high energy y produced by backscattering (7), rescatters within the laser focus to produce the pair (8). Thus the minimum number of photons absorbed from the field in order to produce a pair is $n = 5$ and this suppresses the event rate. At the same time positrons produced by the electron beam scraping upstream of the interaction region contribute in the background.

This background is reduced by careful tuning of the electron beam. The positron spectrum is symmetric around $E_y/2 \sim 14$ GeV and extends by ± 10 GeV on either side. The accompanying electron could not be identified because of the much larger number of Compton electrons scattered into the same momentum range.

Positrons were detected in the positron calorimeter (PCAL) and identified by comparing the momentum deduced from the impact point to the energy recorded by the calorimeter. The response of the PCAL to positrons originating at the interaction point was studied by inserting a wire into the electron beam at the
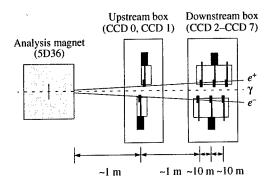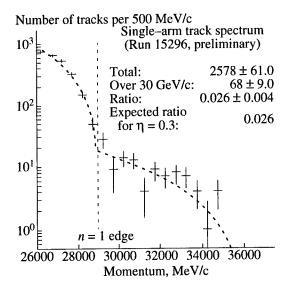

Fig. 10. Momentum spectrum of converted electrons from the forward γ's as measured by the CCD spectrometer.

location of the laser focus to produce e^+e^- pairs. These data were used to develop an algorithm to group contiguous PCAL cells containing energy deposits into "clusters" representing positron candidates. The clusters were characterized by their position in the horizontal (X_{pos}) and vertical (Y_{pos}) direction and by the total energy deposited E_{clu}. The vertical position gives the momentum P_{clu} and in Figs. 11a and 11b we show the ratio E_{clu}/P_{clu} vs. Y_{pos} and X_{pos} vs. Y_{pos}. Only clusters within the signal regions bounded by the solid lines were accepted.

To measure the background rate data were taken when the laser was off. Figure 12a shows the observed yield for laser-on positrons and laser-off positrons (shaded area) as a function of momentum. The laser-off rates have been normalized to the same number of triggers as the laser-on events. In Fig. 12b the subtracted momentum spectrum is shown and compared with the expected distribution. A total of 106 ± 14 positrons were found after all cuts were imposed. The signal-to-noise ratio increases and the comparison with the theoretical

spectrum improves, when only data corresponding to high laser intensity are selected as in Figs. 12c and 12d.

Because of the highly nonlinear nature of this process, fluctuations in the laser intensity have a dramatic effect on the e^+e^- rate. Deducing the laser intensity for each shot from measurements of the laser energy, pulse width and focal spot area is not sufficiently precise.
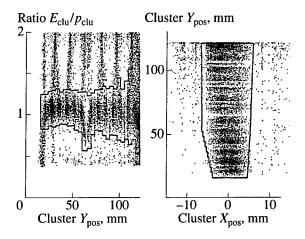

Fig. 11. Cluster densities from positrons produced by a wire inserted at IP1. The solid line shows the signal region for positron candidates. (a) Ratio of cluster energy to momentum vs. vertical impact position above the lower edge of PCAL. The low ratios at the center of PCAL are caused by a 1.5-mm-wide inactive gap. (b) Cluster position in PCAL.
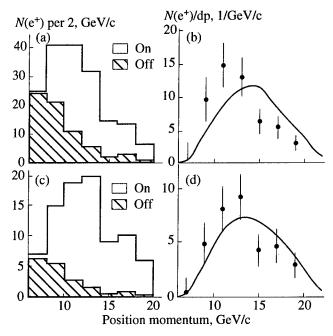

Fig. 12. (a) Number of positron candidates vs. momentum for laser-on pulses and for laser-off pulses scaled to the number of laser-on pulses. (b) Spectrum of signal positrons obtained by subtracting the laser-off from the laser-on distribution. The curve shows the expected momentum spectrum from the model calculation. (c) and (d) are the same as (a) and (b) but for higher laser intensity ($\eta > 0.216$).

Instead we used two fixed monitors which measured $n = 2$ and $n = 3$ recoil electrons. For $\eta \ll 1$ these rates are related to the $n = 1$ rate through

$$N_2 = k_2 N_1 \eta^2 \quad N_3 = k_3 N_1 \eta^4,$$

with k_2, k_3 fixed constants which can be determined from the simulation of the experiment. Thus the ratio of any two of the three rates N_1, N_2, N_3 determines the laser intensity η^2. We used all three rates in a self-consistent way resulting in an 11% error in the determination of η.

In Fig. 13 we show the yield (R_{e^+}) of positrons/laser shot as a function of η. The line is a power law fit and gives $R_{e^+} \propto \eta^{2n}$ with $n = 5.1 \pm 0.2$ (stat) ± 0.5 (syst). Namely the positron production rate varies as the fifth power of the laser intensity as expected for multiphoton reactions involving five photons (for $\eta^2 \ll 1$). The detailed simulation shows that on the average six photons are absorbed from the laser field but that the exponent n for the two-step process varies only slightly with η and has a mean value $n = 5.3$ in our range of η. The two points at the lowest values of η while statistically consistent with the fit, indicate the presence of background at the level of 2×10^{-3} positrons/laser shot.

The two-step process of reaction (7) followed by reaction (8) can be calculated exactly [11]. For reaction (9) there exists no complete theoretical calculation and we have used instead Weiszäcker–Williams approximation for the virtual photon flux of the incident electron and then treated it as real photons scattering according to (8). The results are shown in Fig. 14 where we plot the positron yield normalized by the total number of forward Comptons. This procedure reduces significantly the uncertainties due to fluctuations in the spatial and temporal overlap of the electron and laser beams. The results of the simulation for the two-step process corrected for reconstruction efficiency (0.93)
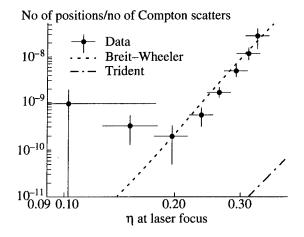

Fig. 13. Dependence of the positron rate per laser shot on the laser field-strength parameter η. The line shows a power law fit to the data. The shaded distribution is the 95% confidence limit on the residual background from showers of lost beam particles after subtracting the laser-off positron rate.
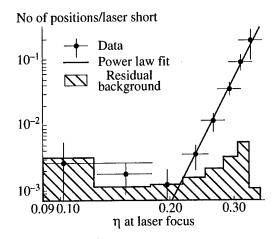
No of positions/laser short

Fig. 14. Dependence of the positron rate on the laser field-strength parameters η when the rate is normalized to the number of Compton scatters inferred from the EC37 monitor. The solid line is the prediction based on the numerical integration of the two-step Breit–Wheeler process, (4) followed by (2). The dashed line represents the simulation for the one-step trident process (3).

and overlap correction (0.88) are shown by the solid line. The agreement with the data both in slope and absolute value is remarkably good. The dashed line represents the contribution from the direct (trident) process calculated as discussed above. It's contribution is negligible as compared to the two-step process.

It is also interesting to consider the pair production process classically as occurring from the spontaneous breakdown of the vacuum rather than from photon-photon scattering. In this case we can treat the incident field as static since the wavelength as seen in the electron rest frame is longer than the electron Compton wavelength

$$\frac{1}{\gamma}\frac{\lambda}{2\pi} \simeq 10^{-10} \text{ cm} \simeq 2.5\lambda_c,$$

with the Compton wavelength representing the range in which the e^+e^- pair is produced. For a static field the rate of pair production can be calculated as a tunneling process [1, 6] with the result

$$R_{e^+e^-} \propto e^{-\pi/\Upsilon}. \tag{20}$$

This expression is compared to the data in Fig. 15 where the positron rate/shot is fitted to an exponential of the form $\exp(-\alpha/\Upsilon)$. Using the rms electric field in the definition of (6) one finds $\alpha = 2.34 \pm 0.13 \pm 0.4$ with $\chi^2 = 1.1/\text{DF}$. However since the incident field was linearly polarized, using the peak value of the field would give an exponent $\alpha_{\text{peak}} = 3.3$ close to the prediction of the classical calculation for a static field. The simulation indicates that as Υ approaches unity (20) ceases to be valid for a time-dependent field.

The results reported are the first observation of QED in strong fields. They are found to be in agreement with the theoretical prediction. They also represent the first observation of inelastic light-by-light scattering involv-
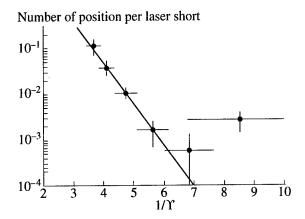

Fig. 15. Number of positrons per laser shot as a function of $1/\Upsilon$. The solid line is a fit to the data of the form $R_{e^+e^-} \propto \exp(-\alpha/\Upsilon)$ and yields $\alpha = 2.3.4 \pm 0.13 \pm 0.4$.

ing only real photons, and can be interpreted as a demonstration of the breakdown of the vacuum by a strong electromagnetic field. The interesting issue of the effective mass of the produced pairs could not be addressed in this experiment.

ACKNOWLEDGMENTS

REFERENCES

1. Heisenberg, W. and Euler, H., 1936, *Zeits. f. Phys.*, **98**, 718; see also Sauter, F., 1931, *Zeits. f. Phys.*, **69**, 742.
2. Balakin, V. *et al.*, 1995, *Phys. Rev. Lett.*, **74**, 2479.
3. Bamber, C. *et al.*, 1997, *Laser Phys.*, **7**, 135.
4. Bula, C. *et al.*, 1996, *Phys. Rev. Lett.*, **76**, 3116.
5. Burke, D.L. *et al.*, 1997, *Phys. Rev. Lett.* (in press).
6. Greiner, W. and Reinhardt, J., 1992, *Quantum Electrodynamics* (Berlin: Springer), p. 285.
7. Kotseroglou, Th., 1996, *Ph.D. Thesis* (Univ. Rochester), UR-1459.
8. Electron-positron production in photon–photon scattering was first calculated by Breit, G. and Wheeler, J.A., 1934, *Phys. Rev.*, **46**, 1087.
9. Klein, O. and Nishina, Y., 1929, *Zeits. f. Phys.*, **52**, 853.
10. Nikishov, A.I. and Ritus, V.I., 1964, *Sov. Phys. JETP*, **19**, 529, 1191; 1965, **20**, 757; see also Reiss, H.R., 1962, *J. Math. Phys.*, **3**, 59.
11. Narozhny, N.B. *et al.*, 1965, *Sov. Phys. JETP*, **20**, 622.
12. Kotseroglou, Th. *et al.*, 1996, *Nucl. Instrum. Methods Phys. Res., Sect. A*, **383**, 309.

Laser-Modified Electron Velocity Distributions and Harmonic Generation in a Homogeneous Plasma

G. Ferrante, P. I. Porshnev*, S. A. Uryupin**, and M. Zarcone

Istituto Nazionale di Fisica della Materia and Dipartimento di Energetica ed Applicazioni di Fisica, Viale delle Scienze, Palermo, 90128 Italy

* *Physics Department, Byelorussia State University, F. Skorina av. 4, Minsk, 220050 Byelorussia*
** *P. N. Lebedev Physical Institute, Leninsky pr. 53, Moscow, 117924 Russia*

Received October 20, 1997

Abstract—The kinetic equation of the electron velocity distribution function (EDF) of a dense, fully ionized, two component plasma interacting with a strong, linearly polarized, high frequency laser field is solved by a two-dimensional (2D) procedure in a wide range of the problem parameters. The time evolution of an initially isotropic EDF is investigated in a time interval of hundreds of the external field cycles. For fields of intermediate strength, a plasma dominated by electron-ion collisions acquires an oblate EDF (i.e., elongated along the external field polarization), which slowly evolves towards an isotropic shape. For stronger fields, instead, the plasma acquires a prolate EDF (i.e., elongated along the poles, perpendicular to the external field polarization), which is found to evolve to an oblate shape before tending towards isotropization. In the case of very strong fields, full isotropization for the considered dense plasma model is expected to require thousands of fields cycles. For the same dense plasma model, high order harmonic generation is investigated within the same kinetic equation, basing on nonlinear field dependence of the high-frequency conductivity. To the aim of developing an analytical theory of harmonic generation, the kinetic equation is solved within the small-anisotropy approximation. The cases are considered when the plasma, embedded in the field, possesses an anisotropic, two-temperature EDF (a bi-Maxwellian), and when possesses a Maxwellian EDF, formed by the dominant role of the electron-electron collisions. Different harmonic spectra are reported, showing an interesting interplay among efficiency of generation, symmetry of the EDF, heating process and external field polarization direction.

1. INTRODUCTION

In this Report we address two related aspects of strong-field laser–plasma interaction; namely (1) the question of how the electron velocities are modified in a plasma interacting with a strong laser field, and (2) that of the basic characteristics of high-order harmonics generated in such a plasma, due to the nonlinear field-dependence of the high-frequency conductivity.

Concerning the first question, it is expected that a plasma interacting with a strong laser field will exhibit an electron velocity distribution function (EDF) generally differing from a Maxwellian. In fact, depending on the duration of the interaction, laser polarization, importance of the different types of collisions and mechanisms of interaction, etc. the electron parallel and perpendicular (with respect to the field polarization) degrees of freedom may be heated by the field *on the average* in a different way. As a result, the plasma electrons may exhibit on the average higher velocities in a given direction than in others. With reference to the velocity space, the corresponding EDF during the interaction will be no more isotropic (as the Maxwellian is), but will exhibit some kind of anisotropy. Further, depending on electron–laser interaction duration and on different collisions responsible for relaxation, an anisotropic EDF is generally expected to relax more or less slowly towards a Maxwellian or some other isotropic distribution. Considering that during the laser

plasma interaction, the plasma electron velocities may be substantially altered, it is evident that many plasma processes and characteristics too may result altered. Due to its basic relevance, the question of the EDF shape in a strong laser field has been addressed by several authors both theoretically [1–13] and experimentally [14–18]. Further, interesting plasma physics aspects of the kind considered here are currently investigated within the context of tunnel ionization of gases [19–21].

Below we report new results on the evolution of the EDF of a fully ionized, classical plasma, interacting with a linearly polarized intense laser field.

Concerning the harmonic generation we investigate some aspects of this nonlinear process in a dense fully ionized plasma, and relate the characteristics of the harmonic spectra to the EDF shapes and to the different stages of their time evolution.

2. PLASMA MODEL AND PROCESS PARAMETERS

The calculations and results reported below are obtained within a "standard" dense plasma model. In fact, we use the model of a two-component, nonrelativistic, fully ionized homogeneous classical plasma, where electron–ion (e–i) and electron–electron (e–e) collisions control the shape of the EDF. When the

unbalanced ion charge Z is large, the e–e collisions may be neglected. As a condition to neglect e–e collision, we use

$$\left(\frac{v_E}{v_T}\right)^2 \gg \frac{3}{Z} \qquad (1)$$

with $v_E = eE_L/m\omega$ the amplitude of the quiver electron velocity and $v_T = \sqrt{T_e/m}$ the thermal electron velocity. No plasma instability is taken into consideration. The most pertinent to the present calculation is the Weibel instability [22], which is briefly discussed below, after presentation of the numerical results.

A key physical parameter in our calculation is the ratio

$$R(t) = \frac{v_E}{v_T(t)} \qquad (2)$$

with v_E and v_T defined above. In (2), we explicitly express the fact that due to laser heating through collisions, the thermal velocity evolves with time, and with it the ratio $R(t)$ too. Because of it, we introduce also the initial thermal velocity $v_T(0)$ and the initial ratio

$$R(0) = \frac{v_E}{v_T(0)}. \qquad (3)$$

Significant alteration (anisotropy) in the EDF shape is expected when R_0 is appreciably larger than one.

An other important parameter is the ratio

$$\delta = \frac{\nu(v)}{2\omega} \qquad (4)$$

with $\nu(v)$ the electron–ion collision frequency given below and ω the laser frequency. Below we will consider only cases when $\delta \ll 1$; in other words we are considering a high-frequency external field and/or a weakly collisional plasma.

3. SHAPES OF THE ELECTRON VELOCITY DISTRIBUTION FUNCTION AND THEIR EVOLUTION

Here we report a specific contribution to the analysis of the EDF behavior and evolution without the limitation of the small-anisotropy assumption. The emphasis is on the changes of the EDF shape with time. We address the case of a uniform fully ionized plasma with a value of the ion charge Z that allows us to disregard e–e collisions. As a distinctive feature of our calculations is the purpose of accounting for an arbitrary degree of anisotropy in the shape of the EDF, we solve a two dimensional (2D) partial differential equation. It is done using a modified version of the alternating direct method. The evolution of the EDF in a uniform,

fully ionized plasma dominated by Coulomb collisions is described by the equation [23]

$$\left\{\frac{\partial}{\partial t} + \frac{e}{m}E_L\cos(\omega t)\frac{\partial}{\partial \mathbf{v}}\right\}f(\mathbf{v}, t) = I_{ei} + I_{ee}, \qquad (5)$$

where

$$I_{ei} = \frac{\partial}{\partial v_j}D_{jl}(\mathbf{v}, t)\frac{\partial f(\mathbf{v}, t)}{\partial v_l}, \qquad (6)$$

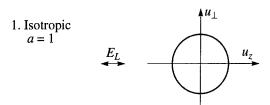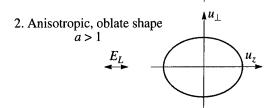$$D_{jl}(\mathbf{u}, t) = \frac{1}{2}\nu(v)[v^2\delta_{jl} - v_j v_l], \qquad (7)$$

and

$$I_{ee} = \frac{1}{2N_e}\frac{\partial}{\partial v_j}\int d\mathbf{v}\nu_{ee}(|\mathbf{v} - \mathbf{v}'|)[(\mathbf{v} - \mathbf{v}')^2\delta_{jl}$$

$$- (\mathbf{v}_j - \mathbf{v}_j')(\mathbf{v}_l - \mathbf{v}_l')]\left[\frac{\partial}{\partial v_l} - \frac{\partial}{\partial v_l'}\right]f(\mathbf{v}, t)f(\mathbf{v}', t), \qquad (8)$$

where v_j is the jth component of the electron velocity, $\nu(v) = 4\pi Ze^4N_e\ln\Lambda/(m^2v^3)$, the electron–ion collision frequency $\nu_{ee} = \nu(v)/Z$ the electron–electron collision frequency, N_e the electron density, and $\ln\Lambda$ is the Coulomb logarithm which in the present work is taken in the modified form suggested by Silin [23] suited to deal with interactions between plasmas and fast oscillating fields. δ_{ij} is the Kronecker delta symbol. The laser field is assumed to be monochromatic and linearly polarized along the z direction with the cosine form [see (5)]. In some cases from (5), using the spherical harmonic expansion and averaging over the field period, a well-known equation for the isotropic part of the EDF is obtained. Here, intending to study the plasma properties without any assumption about the angular dependence of the distribution function, we must solve (5) directly. We cannot average over the field period since we do not know in advance the "fast" time dependence of the distribution function. It is only under the small-anisotropy assumption that the anisotropic part of the EDF oscillates together with the field, thus allowing the isotropic part to be averaged over the period and the "slow" time dependence extracted. This simplified procedure will be used below, when treating harmonic generation. In the case under consideration here, averaging over the field period is possible only after solving (5). As suggested by the symmetry of the problem, the natural coordinate system for our case is cylindrical. Moreover, in view of the numerical modeling to be developed below, it is convenient to define the following equation to remove the velocity gradient of the distribution function:

$$\mathbf{u} = \mathbf{v} + \mathbf{v}_E\sin\omega t, \qquad (9)$$

where $\mathbf{v}$ and $\mathbf{u}$ are, respectively, the electron velocity in the rest frame, and in a reference frame oscillating with the same frequency as the external field. Assuming that

EDF shapes   The laser electric field E
                         is polarized along z

1. Isotropic
   $a = 1$

E_L u_z

2. Anisotropic, oblate shape
   $a > 1$

E_L u_z

2. Anisotropic, prolate shape
   $a < 1$

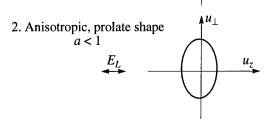E_L u_z

Fig. 1. Schematic representation of the shapes the EDF exhibits in the oscillating frame as a result of the interaction with a strong laser field. The quantity $a(t)$ is defined in (11).

the condition (1) is fulfilled and neglecting e–e collisions, in the coordinates ($u_\perp$, u_z), with u_z and $u_\perp$ being, respectively, the velocity component parallel and perpendicular to the direction of the external field polarization, equation (5) becomes

$$u_\perp \frac{\partial\varphi}{\partial t'} = \frac{\partial}{\partial u_\perp}\left[\frac{\delta u_\perp u_t}{(u_\perp^2 + u_t^2)^{\frac{3}{2}}}\left(u_t\frac{\partial\varphi}{\partial t_\perp} - \frac{\partial\varphi}{\partial u_z}\right)\right]$$

$$+ \frac{\partial}{\partial u_z}\left[\frac{\delta u_\perp^2}{(u_\perp^2 + u_t^2)^{\frac{3}{2}}}\left(u_\perp\frac{\partial\varphi}{\partial t_z} - u_t\frac{\partial\varphi}{\partial u_\perp}\right)\right], \quad (10)$$

where $\varphi(\mathbf{u}, t) = f(\mathbf{u} + \mathbf{v}\sin t, t)$, $t' = t$. Equation (10) has been made dimensionless: the velocity components are taken in unit of v_e, time in unit of ω^{-1}, besides $u_t = u_z + \sin t'$.

The results of numerical modeling will be given through the values of the quantity

$$a(t) = \sqrt{\frac{2\bar{u}_z^2(t)}{\bar{u}_\perp^2(t)}}, \quad (11)$$

where

$$\bar{u}_x^2(t) = \frac{\int \bar{u}_x^2(t)\varphi(\mathbf{u}, t)d^3u}{\int \varphi(\mathbf{u}, t)d^3u}, \quad (x = z, \perp). \quad (12)$$
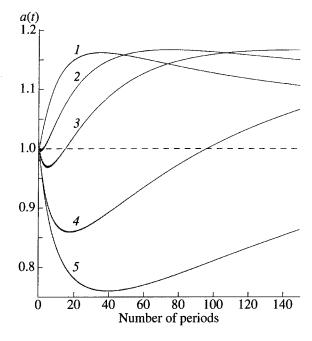

Fig. 2. Evolution of the quantity $a(t)$, formula (11), vs. the number of field periods for different initial value of the ratio $R_0 = v_E/v_T(0)$, with v_E and v_T being, respectively, the peak quiver velocity and the thermal velocity. $a(t)$ is a measure of the anisotropy (in the velocity space) of the electron velocity distribution function (EDF); $a(t) = 1$ corresponds to an isotropic EDF; $a(t) > 1$, to an oblate EDF, i.e., elongated in direction of the electric field polarization; $a(t) < 1$, to a prolate EDF, i.e., elongated perpendicularly to the electric field polarization. To the curves *1–5* correspond, respectively, the values $R_0 = 3.2$, 4.1, 5.0, 7.4 and 10.3. For brevity we omit the single values of all the process parameters entering to form v_E, $v_T(0)$ and δ, (4). In all the cases considered, their choice obey the limitations under which the kinetic equation is solved.

The quantity $a(t)$ is a direct measure of the degree of anisotropy exhibited by the plasma EDF. If the EDF is isotropic (in the velocity space) and, accordingly, on the average the absolute values of the velocities in all direction are equal, we have that $2\bar{u}_z^2(t) = \bar{u}_\perp^2(t)$ and $a(t) = 1$. If the EDF is prolate, i.e., elongated in the direction perpendicular to the laser electric field polarization we have that $2\bar{u}_z^2(t) < \bar{u}_\perp^2(t)$. Thus values $a(t) < 1$ are a measure of anisotropy of the EDF having prolate shape. Conversely, values $a(t) > 1$ are a measure of anisotropy of oblate shape, i.e., the EDF is elongated in the direction parallel to the laser electric field polarization (see also Fig. 1).

Of course, there are other equivalent ways to measure the EDF's anisotropy (see below). The particular choice of $a(t)$ as a measuring quantity stems from the circumstance that $a(t)$ results in a natural way in a recently proposed procedure aimed at obtaining approximate analytical EDF in the case of relatively strong anisotropy [8].

Selected calculations of $a(t)$ as function of the number of field periods are reported in Fig. 2, for different initial values R_0 of the ratio $R(t)$, equation (2).

As a rule, below the results are presented for chosen initial values of particular characteristic parameters of the process, like, for instance, the ratio R and δ. These parameters, in their turn are defined through several plasma and external field parameters, which may be numerically combined in many ways to give a desired value of R and δ. In presenting the numerical results, only the dependency on the most significant and cumulative parameter will be given, omitting to list the values of the lumped parameters. In the largest part of the calculations however, the plasma density is $N_e = 8 \times 10^{20}$ cm^{-3}, δ is equal to $10^{-3} \times 10^{-4}$, the laser frequency $\omega = 1.82 \times 10^{15}$ s^{-1}.

Figure 2 shows that for R_0 up to values slightly larger than 4, an initially isotropic EDF [$a(t = 0) = 1$] first rapidly (in few tens of periods) evolves towards an oblate shape, and then slowly relaxes to a smaller degree of anisotropy, but still keeping the oblate shape. The larger the initial value R_0, the longer times are required to pass through the stages of deformation and relaxation. For initial values R_0 appreciably larger than 4, $a(t)$ exhibit a completely different behavior: now, an initially isotropic EDF, first, rapidly evolves towards a prolate shape; then, under the action of laser heating and collisions, changes to an oblate shape; finally, reaches the maximum degree of deformation in the latter shape, entering a stage of slow relaxation toward a less oblate shape. Again, the larger the initial value R_0, the longer time intervals are required to pass through the different stages of evolution. Here we must note that 2D calculations are computer time consuming, and our calculations follow the evolution of the EDF only up to about 150 periods. Accordingly, in some of the reported cases our calculations do not allow us to follow exhaustively all the stages of evolution. However, we believe that the overall physical picture, as it comes out from the reported results is sufficient clear and self-explanatory. On the other hand, our results may well be considered representative of the electron plasma behavior when interacting with very short laser pulses.

We observe also that while the different curves when $a(t)$ is greater than 1 (oblate shape) do not exceed the value of $a = 1.17$, the curves of the prolate shape do not show to be limited from below. It is a clear indication that the longitudinal and parallel effective collision frequency undergo, under the action of the external field, different changes, depending on the field intensity. The same holds true for the heating of the longitudinal and parallel degrees of freedom. We now discuss briefly the Weibel instability in relation to our calculation.

From the theory of plasma instabilities is known that in all cases when the mean kinetic energy in some direction exceeds the energy in a perpendicular direction, an aperiodic electromagnetic instability is able to

develop, which is just the Weibel instability [22]. In principle, it applies to our case too, where we have a laser forming an evolving anisotropic velocity distribution. However, it is not immediate to answer the question to which extent the Weibel instability may interfere and alter the picture given here concerning the EDF shape evolution. The existing plasma instability analysis deal, as a rule, with rather different physical situations (counterstreaming beams, inhomogeneous plasmas, collisionless plasma, very strong anisotropies, very long times of interaction and so on), and are of no particular use to our case, which, instead would require a separate, detailed investigation. However, considering that in our case the collisions are rather a efficient relaxation mechanism; that the plasma is dense and the times of evolution small; that the Weibel instability ultimately must act to reduce the anisotropy as do the collisions; and that the EDF degree of anisotropy in our case is never very high, we expect that this instability, if present, does not play any significant role in the reported relaxation picture of the EDF, and on this basis is here ignored. By the way, the Weibel instability in the context of powerful laser–plasma interaction is considered by one of the present authors in a separate Report presented in this Conference [24]. Besides, in the different context of plasmas produced by tunneling ionization, the role of the Weibel instability has been considered recently in [19] and found to be important for EDF isotropization (a much less dense plasma without collisions, however, and much longer 'observation' times were considered).

4. HARMONIC GENERATION

Now we address the high harmonics generation in a plasma acted upon by an intense laser field. The plasma model is the same of that outlined in Section 2. For useful summaries and discussions of the several issues characteristic of the physics of harmonic generation see [25–31].

A dense plasma as a nonlinear medium where to observe high order harmonic generation has been considered in the early eighties [32, 33] and recently [34, 35].

Among the different physical mechanisms able to lead to harmonic generation in a dense plasma, a well-known one is the nonlinear field-dependence of the high-frequency conductivity in a strong e.m. field.

Silin first seems to have addressed the item of harmonic generation considering the just quoted mechanism [36]. Under the condition $R \gg 1$, and assuming the initial EDF to be a Maxwellian, Silin predicted effective odd-harmonics generation with linearly polarized fields. Very recently, this same physical process has been revisited by the present authors [37], basing on the consideration that there is now a lot of evidence, both theoretical [1–13, 19, 20] and experimental [14–19], that in a plasma embedded in a strong laser field, the

EDF may significantly differs from a Maxwellian (as shown, by the way, in Section 3).

Below we report on the harmonic generation in a dense plasma taking into account plasma electron heating due to inverse bremsstrahlung absorption of an intense high-frequency electromagnetic wave, using the information of the numerical modelling on the EDF shapes of the previous section. However, instead of carrying out a further numerical modelling of the harmonic generation process, we take advantage of the information of the previous section and of analytical results obtained previously by one of the present authors [4], to develop an almost completely analytical theory, up to simple formulas which well approximate the harmonic spectrum. In particular, below, we consider two cases, which exploit two different physical situations: (A) the case, when the nonstationary EDF acquires a prolate shape, i.e., elongated perpendicular to the laser electric-field direction. Analytical derivations [4] show that such a prolate shape is bi-Maxwellian (anisotropic, two-temperature) in the first stages of the laser-plasma interaction. Furthermore, results of numerical modelling, not reported here [38], show that in the later stages of its evolution, a prolate EDF is still well approximated by a bi-Maxwellian. Accordingly, for this case, we calculate harmonic spectra using a bi-Maxwellian EDF. (B) the case, when due to the high intensity of the laser field the e–i collisions are considerably weakened, while the e–e ones remain unaffected by the field. When the e–e collisions becomes dominant, their randomizing effect yields a Maxwellian. Below, we calculate harmonic spectra for this case too. In both cases, $R_0 \gg 1$.

The starting point is the expression yielding the electron current density **j**:

$$\frac{\partial}{\partial t}\mathbf{j} = \frac{\omega_{Le}^2}{4\pi}\mathbf{E}_L\cos\omega t + e\int d\mathbf{u}\,\mathbf{u}\frac{\partial}{\partial t}\varphi(\mathbf{u}, t), \qquad (13)$$

defined by the EDF function $\varphi(\mathbf{u}, t)$, solution of the kinetic equation (10), with the e–e collision term accounted for. In (13) ω_{Le} is the Langmuir frequency of the electrons and the physical quantities appearing in (10) and (13) have their usual dimensions and units. Similarly to the previous section, we assume that the frequency ω is much larger than the effective electron collision frequency, but the kinetic equation is now solved following the procedure suited for small anisotropy. The distribution function is written in the form $\varphi = \bar{\varphi} + \delta\varphi$. $\bar{\varphi}$ is the averaged over the field period large part of the EDF,

$$\bar{\varphi} = \frac{\omega}{2\pi}\int_0^{2\pi/\omega} dt\varphi(\mathbf{u}, t), \qquad (14)$$

which changes slowly with time. $\delta\varphi$ is a rapidly oscillating small addendum, $|\delta\varphi| \ll \bar{\varphi}$.

Case A

If the intermediate intensity conditions

$$Zv_T \gg v_E \gg v_T \qquad (15)$$

hold, an anisotropic two-temperature EDF results having the form of the bi-Maxwellian [4]

$$\bar{F} = \frac{Nm\sqrt{m}}{2\pi\sqrt{2\pi}T_\perp\sqrt{T_z}}\exp\left(-\frac{mu_\perp^2}{2T_\perp} - \frac{mu_z^2}{2T_z}\right), \qquad (16)$$

with T_z and $T_\perp$ duly defined longitudinal and transverse effective temperatures. Under the conditions (15) and for the times for which (16) holds, T_z and $T_\perp$ increase linearly with time

$$T_z(t) = mv_T^2(0) + \frac{2}{\pi}mv_E^2\mathbf{v}(v_E)t, \qquad (17)$$

$$T_\perp(t) = mv_T^2(0) + \frac{2}{\pi}mv_E^2\mathbf{v}(v_E)t\ln\left[\frac{v_E}{v_T(0)}\right]. \qquad (18)$$

As $v_E \gg v_T(0)$, from (17) and (18) we see that for $t > 0$, $T_\perp > T_z$; in other words, the field modified EDF acquires a prolate shape, i.e., elongated towards the poles, perpendicularly to the electric field direction. Here, it is appropriate to mention that the EDF is valid, by derivation, only for very short times, but the numerical modelling shows [38] that instead it is approximately valid for all the stage in which the prolate shape is maintained. Now the solution given by (16)–(18) is used to determine the current density from (13). After same algebra, for the current density along the z-axis j we obtain the expression

$$\frac{\partial}{\partial t}j = \frac{\omega_{Le}^2}{4\pi}\mathbf{E}_L\cos\omega t - env_E^3\mathbf{v}(v_E)\left(\frac{m}{T_\perp}\right)^{3/2}\int_0^\infty dy\int_{-1}^1 dx\,x^2$$

$$\times\left[v_E\sin\omega t + ixy\frac{(T_z - T_\perp)}{\sqrt{mT_\perp}}\right] \qquad (19)$$

$$\times\exp\left[-\frac{y^2}{2} + ixy\sqrt{\frac{m}{T_\perp}}v_E\sin\omega t\right].$$

This result is now written in the form of an expansion over the harmonics of high-frequency field

$$\frac{\partial}{\partial t}j = \frac{\omega_{Le}^2}{4\pi}\mathbf{E}_L\cos\omega t$$

$$-\omega\sum_{n=0}^\infty (2n + 1)\sigma_n\mathbf{E}_L\sin[(2n + 1)\omega t], \qquad (20)$$

where σ_n is the conductivity at the frequency $(2n + 1)\omega$. It has the form

$$\sigma_n = \frac{\omega_{Le}^2}{\omega^2}\sqrt{\frac{2}{\pi}}\frac{Ze^4 N\Lambda}{\sqrt{mT_\perp}T_\perp(2n + 1)}$$

$$\times \int_0^1 dx x^2 \left[1 - x^2\left(\frac{T_z}{T_\perp} - 1\right)\right]\exp\left(-\frac{mx^2}{4T_\perp}v_E^2\right) \quad (21)$$

$$\times \left\{I_n\left(\frac{mx^2}{4T_\perp}v_E^2\right) - I_{n+1}\left(\frac{mx^2}{4T_\perp}v_E^2\right)\right\},$$

where $I_n(z)$ is the modified Bessel function.

We now use the derived expression for the high-frequency current, (20) and (21), to investigate the generation of high-order harmonics of the radiation field and some of their characteristics. From Maxwell's equations and from (20) is readily seen that the generated harmonics are polarized along the z axis and propagate in the (xy) plane. It is, thus, natural to write the field of the $(2n + 1)$th harmonic in the form

$$\mathbf{E}_n(\mathbf{r}, t) = \text{Re}\{\mathbf{E}_n\exp[i(2n + 1)(\mathbf{kr} - \omega t)]\}, \quad (22)$$

where $\mathbf{k} \cdot \mathbf{r} = 0$, $\mathbf{E}_n = (0, 0, E_n)$, $n = 0, 1, 2, ...$ Then, taking into account the dispersion equation for the fundamental wave $\omega^2 = \omega_{Le}^2 + k^2 c^2$ and (20), from Maxwell's equations we get

$$\frac{\mathbf{E}_n}{\mathbf{E}_L} = -\frac{i\pi\omega\sigma_n(2n + 1)}{\omega_{Le}^2 n(n + 1)}, \quad n = 1, 2, ... \quad (23)$$

Using the definition $I_n = cE_n^2/8\pi$, the ratio of the radiation intensities at the frequencies $(2n + 1)\omega$ and ω is found in the form

$$\frac{I_n}{I_L} = J_n\left[\frac{\nu(v_E)}{\omega}\right]^2, \quad (24)$$

with

$$J_n = \frac{2}{\pi}\left\{\frac{1}{n(n + 1)}\int_0^{\varepsilon_\perp} dz\sqrt{z}\right.$$

$$\times \left[1 + \frac{z}{\varepsilon_\perp}(1 - \Delta)\right]\exp(-z)[I_n(z) - I_{n+1}(z)]\right\}^2 . \quad (25)$$

The quantities $\varepsilon_\perp$ and Δ appearing in (25) are defined as

$$\varepsilon_\perp = \frac{\varepsilon_0}{(1 + \tau\ln 4\varepsilon_0)}, \quad (26)$$

$$\Delta = \frac{(1 + 2\tau)}{(1 + \tau\ln 4\varepsilon_0)} \quad (27)$$

with

$$\varepsilon_0 = \frac{v_E^2}{4v_T^2(0)}, \quad (28)$$

and

$$\tau = \left(\frac{4\varepsilon_0}{\pi}\right)\nu(v_E)t. \quad (29)$$

$\varepsilon_\perp$ is basically the ratio of the quiver kinetic energy to the average transverse kinetic energy, while Δ is a measure of the degree of anisotropy of the field-modified EDF, and corresponds to the ratio of the longitudinal temperature T_z to the transverse one $T_\perp$. From their definitions and (17) and (18), it is apparent that $\varepsilon_\perp$ and Δ are decreasing functions of time; $\varepsilon_\perp$ decreases thanks to the heating due to inverse bremsstrahlung; Δ decreases because, according to (17) and (18), in the early stages of interaction in the given regime, the field energy flows preferentially into the transverse degrees of freedom. The decrease of Δ means that the degree of anisotropy of the prolate EDF is increasing. Obviously, for the behavior of $\varepsilon_\perp$ and Δ hold true the same considerations given above after (17) and (18). In the limit $2\varepsilon_\perp \gg n^2$ (25) becomes approximately

$$J_n = \left[\frac{(2n + 1)}{2\pi n(n + 1)}\left(\ln\frac{2\varepsilon_\perp}{n^2} + 1 - \Delta\right)\right]^2, \quad (30)$$

showing that the intensity of harmonics of relatively low orders depends weakly on both transverse and longitudinal effective temperatures.

Case B

If the plasma is acted upon by a very intense laser field, such that $v_E \gg v_T$ and $v_E \gg Zv_T$ hold, the e–e collisions dominate over the e–i ones, and the resulting EDF is found to be approximately Maxwellian [4] (in the oscillating coordinate system).

The expressions pertinent to this case are readily obtained from those of the previous case, taking into account that for an isotropic EDF $T_z = T_\perp = 1$, $\Delta = 1$ and $\varepsilon_\perp$ changes into ε given by

$$\varepsilon = \frac{\varepsilon_0}{\left[1 + \frac{2}{3}\tau(\ln 4\varepsilon_0 + 1)\right]}, \quad (31)$$

having the meaning of the ratio of quiver kinetic energy to the average full electron kinetic energy.

Using $\Delta = 1$ and ε, equation (25) allows us to investigate as well the high-order harmonics generation in a plasma with a Maxwellian EDF.

5. HARMONIC SPECTRA

Equations (24)–(31) are now used to calculate the harmonics spectra under different physical conditions.

Maxwellian EDF

In Fig. 3 we report the results of calculations of the intensity of the harmonic spectrum for four initial values of the parameter ε, (31), namely 400, 100, 25, and 4. Considering the physical meaning of ε and that it is a decreasing function of time, the four spectra reported in Fig. 1 may be looked at in two equivalent ways: either as spectra corresponding to different initial ε (as they, actually, are), or as shapes of the same spectrum, recorded at different times, related to the values of ε. Thus, the spectra reported in Fig. 3 considered together account as well for their time evolution. The initial value $\varepsilon_0 = 400$ is equivalent to $R(0) = 40$ (curve *1*), while the initial value $\varepsilon_0 = 100$ of curve 2 to $R(0) = 20$. Considering that the initial temperature double in a
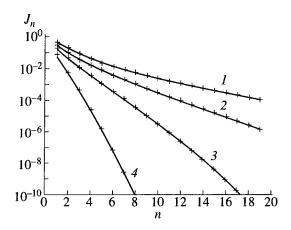
Fig. 3. The intensity J_n of the harmonics $(2n + 1)\omega$ for a plasma with Maxwellian electron distribution for 4 different initial values of the parameter ε, (31). The series of data, forming the four spectra may be viewed also as shape of the same spectra, recorded at different times, ε being a decreasing function of time. ε = 400 (curve *1*); 100 (curve 2); 25 (curve *3*); 4 (curve *4*). The lines intersecting the data are meant to help visualization.
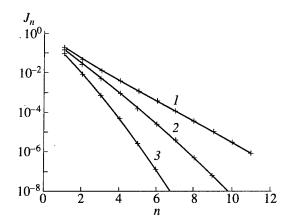
time approximately equal to $\tau_d = [\nu(v_E)\varepsilon_0 \ln 4\varepsilon_0]^{-1}$, the spectrum 2 corresponds to the evolution of the spectrum *1* after a time during which the electron temperature has increased four times. Similarly, the spectra *3* and *4* correspond to the increase of temperature, respectively, of 8 and 20 times as compared to that of the spectrum *1*.

Bi-Maxwellian EDF

Figure 4 reports calculations similar to those of Fig. 3 for the following sets of parameters: $\varepsilon_\perp = 25$, $\Delta = 1$ (curve *1*); $\varepsilon_\perp = 10$, $\Delta = 0.66$ (curve 2); $\varepsilon_\perp = 4$, $\Delta = 0.525$ (curve *3*). As before the three reported spectra may be viewed as a given spectrum in three subsequent stages of its time evolution. The harmonics spectrum for the anisotropic heating is found to exhibit sensible differences as compared with that of isotropic heating. In particular, in the stage of anisotropic heating (when the energy flows preferentially from the field to the transverse degrees of freedom of the plasma electrons) a sizable inhibition of the high-order harmonics is found as compared to the case of isotropic heating. This effect is shown also in Fig. 5, where harmonics spectra corresponding to isotropic and anisotropic heating are compared, the other physical conditions being largely the same: $\varepsilon_\perp = 4$, $\Delta = 0.525$ (curve 2, bi-Maxwellian EDF); $\varepsilon = 5.26$, $\Delta = 1$ (curve *1*, Maxwellian EDF).

6. CONCLUDING REMARKS

We have reported on 2D calculation concerning the EDF in a completely ionized, homogeneous plasma in the presence of a strong high frequency laser field. The basic result is that the EDF is, in general, no more isotropic if the electron–ion collision are dominant. The EDF becomes elongated along the laser electric field direction in the case of fields of intermediate strength, and is found to relax slowly towards an isotropic shape.
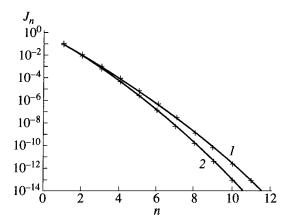

Fig. 4. The harmonics intensity J_n vs. *n* for a plasma with a two-temperature electron distribution function. $\varepsilon_\perp = 25$, $\Delta = 1$ (curve *1*); $\varepsilon_\perp = 10$, $\Delta = 0.66$ (curve 2); $\varepsilon_\perp = 4$, $\Delta = 0.52$ (curve *3*).

Fig. 5. The harmonic intensity J_n vs. *n* for the same time moment τ and two different electron velocity distributions: Maxwellian distribution with ε = 5.26, $\Delta = 1$ (curve *1*); bi-Maxwellian distribution with $\varepsilon_\perp = 4$, and $\Delta = 0.52$ (curve 2).

(a) Oblate EDF

$u_z \parallel E_L$

Laser energy → $u_\parallel$ parallel degrees of freedom → Harmonic generation

$u_\perp$ perpendicular degrees of freedom

(b) Prolate EDF

$u_z \parallel E_L$

Laser energy → $u_\parallel$ parallel degrees of freedom → Harmonic generation
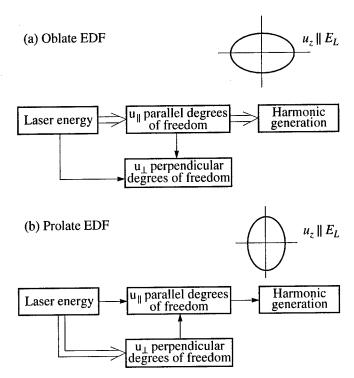
$u_\perp$ perpendicular degrees of freedom

Fig. 6. Schematic representation of the laser energy flow during the laser–plasma interaction, in the cases when an initially isotropic electron distribution function (EDF) evolves towards an oblate shape (a), or towards a prolate shape (b). The double arrow indicates a relatively more efficient process of harmonic generation and of heating of selected electron degrees of freedom. The energy flow pathways are controlled by the collisions. The case of an EDF remaining isotropic is expected to be intermediate with respect to cases A and B, because the laser heats in the same way parallel and perpendicular degrees of freedom.

For stronger fields, the EDF becomes elongated along the poles, perpendicular to the electric field direction. Then evolves towards an oblate shape, and from the latter towards isotropization. The key to understand the overall behavior of the EDF is the mechanism of electron–ion collisions. Characterizing such collisions by means of an effective collision frequency, we have that for fields of intermediate-strength the "parallel" collision frequency is larger than the "perpendicular" one. As a result the electron parallel degrees of freedom are heated more efficiently, and an EDF elongated along the electric field results. The opposite takes place for stronger fields, because the parallel collision frequency suffers a drastic reduction. The further EDF evolution is bound to the overall electron heating and transfer of energy among parallel and perpendicular degrees of freedom through collisions.

We have also calculated harmonics spectra under the conditions of isotropic and anisotropic heating, and found that the emitted harmonics are remarkably intense.

In the case of isotropic heating, the increase of electron temperature with time reduces the intensity of

high-order harmonics; thus the harmonics spectrum becomes increasingly poorer of high-order harmonics. In the case of anisotropic heating, which is very likely to take place in real experimental conditions, we have found that generation of high-order harmonics is significantly inhibited by the circumstance that, during the radiation–plasma interaction, the energy from the field flows preferentially into the electron degrees of freedom perpendicular to the radiation electric field direction, which is the same of the generated harmonics. We believe that the dependence of harmonics spectra on the heating characteristics be a general property of harmonic generation in a plasma, when the dominating mechanism is the inverse bremsstrahlung absorption. However, we expect that this property may manifest itself and act in different and even opposite ways, than those considered by us (initial stage of a strong anisotropic regime of prolate type) to be the only one (see, Fig. 6).

ACKNOWLEDGMENTS

REFERENCES

1. Langdon, A.B., 1980, *Phys. Rev. Lett.*, **44**, 575.
2. Balescu, R., 1982, *J. Plasma Phys.*, **27**, 553.
3. Jones, R.D. and Lee, K., 1982, *Phys. Fluids*, **25**, 2307.
4. Chichkov, B.N., Shumsky, S.A., and Uryupin, S.A., 1992, *Phys. Rev. E*, **45**, 7475.
5. Porshnev, P.I., Ferrante, G., and Zarcone, M., 1993, *Phys. Rev. E*, **48**, 2081.
6. Jorna, S. and Wood, L., 1987, *Phys. Rev. A*, **36**, 397.
7. Porshnev, P., Bivona, S., and Ferrante, G., 1994, *Phys. Rev. E*, **50**, 3943.
8. Porshnev, P., Khanevich, E., Bivona, S., and Ferrante, G., 1996, *Phys. Rev. E*, **53**, 1100.
9. Pulsifer, P.E. and. Whitney, K.G., 1994, *Phys. Rev. E*, **50**, 4926.
10. Town, R.P.J., Bell, A.R., and Rose, S.J., 1995, *Phys. Rev. Lett.*, **74**, 924.
11. Deck, D., 1987, *Laser and Particle Beams*, **5**, 49.
12. Ferrante, G., and Porshnev, P.I., 1996, Quasi-Steady States of Ionized Media in Intense Laser Fields, *Super Intense Laser Atoms Physics*, Muller, H.G. and Fedorov, M.V., Eds. (Klewer).
13. Daniele, R., Ferrante, G., Morales, F., and Porshnev, P.I., 1996, *Laser Phys.*, **6**, 553.

14. Amendt, P., Eder, D.C., and Wilks, S.C., 1991, *Phys. Rev. Lett.*, **66**, 2589.

15. Mohideen, V. *et al.*, 1993, *Phys. Rev. Lett.*, **71**, 509.

16. Mevel, E. *et al.*, 1993, *Phys. Rev. Lett.*, **70**, 406.

17. Glover, T.E. *et al.*, 1995, *Phys. Rev. Lett.*, **75**, 445.

18. Donnely, T.D., Lee, R.W., and Falcone, R.W., 1995, *Phys. Rev. A*, **51**, R2691.

19. Leemans, W.P. *et al.*, 1992, *Phys. Rev. A*, **46**, 1091 and references therein.

20. Goreslavsky, S.P. and Popruzhenko, S.V., 1997, *Laser Phys.*, **3**, 700.

21. Chichkov, B.N. *et al.*, 1995, *Phys. Rev. A*, **52**, 1629 and references therein.

22. Weibel, E.S., 1959, *Phys. Rev. Lett.*, **2**, 83.

23. Silin, V.P., 1960, *Zh. Eksp. Teor. Fiz.*, **38**, 1771 [1960, *Sov. Phys. JETP*, **11**, 1277]; 1964, *Zh. Eksp. Teor. Fiz.*, **47**, 2254 [1965, *Sov. Phys. JETP*, **20**, 1510].

24. Uryupin, S.A., Romanov, A. Yu., and Silin, V.P., Anomalies at Powerful Radiation Interaction with Plasma, This Conference.

25. Mc Pherson, A. *et al.*, 1987, *J. Opt. Soc. Am. B*, **4**, 595.

26. Ferray, M. *et al.*, 1988, *J. Phys. B*, **21**, L31.

27. Sarukura, N. *et al.*, 1991, *Phys. Rev. A*, **43**, 1669.

28. Kubodera, S. *et al.*, 1993, *Phys. Rev. A*, **48**, 4576.

29. Akiyama, Y. *et al.*, 1992, *Phys. Rev. Lett.*, **69**, 2176.

30. Balcou, Ph. *et al.*, 1992, *J. Phys. B*, **25**, 4467.

31. Lewenstein, M. *et al.*, 1994, *Phys. Rev. A*, **49**, 2117.

32. Carman, R.L., Rhodes, C.K., and Benjamin, R.F., 1981, *Phys. Rev. A*, **24**, 2649.

33. Bezzerides, B., Jones, R.D., and Forslund, D.W., 1982, *Phys. Rev. Lett.*, **49**, 202.

34. Von der Linde, D., Schulz, H., Engers, T., and Schüler, H., 1992, *IEEE J. Quantum Electron.*, **28**, 2388.

35. Kohlweyer, S. *et al.*, 1995, *Opt. Commun.*, **117**, 431.

36. Silin, V.P., 1965, *Sov. Phys. JETP*, **20**, 1510.

37. Ferrante, G., Uryupin, S.A., Zarcone, M., and Porshnev, P.I., 1997, *J. Opt. Soc. Am. B*, **14**, 1716.

38. Porshnev, P.I., Ferrante, G., and Zarcone, M., Harmonic Generation in a Plasma by a 2D Solution of the Kinetic Equation (to be published).

Theory of Line Broadening in a Quantum Cyclotron Resonance due to Neutral Impurities

S. P. Andreev*, A. S. Andreev**, and Yu. A. Gurvich**

*Moscow State Engineering Physics Institute (Technical University), Kashirskoe sh. 31, Moscow, 115409 Russia
**Moscow Pedagogical State University, Malaya Pirogovskaya ul. 29, Moscow, 119435 Russia
e-mail: sergeand@theor.mephi.msk.ru
Received September 2, 1997

Abstract—We present the results of our recent theoretical investigations [1, 2] on quantum cyclotron resonance ($T \ll \hbar\omega_H$, $\Delta\omega \ll \omega_H$, T is the temperature, $\omega_H \equiv eH/m^*c$ is the cyclotron frequency, $\Delta\omega \equiv \omega - \omega_H$ is the frequency detuning, m^* is the effective mass, and ω is the frequency of the electric field) in semiconductors with an isotropic energy spectrum of charge carriers scattered by small-size centers with a small radius $r_c^2 \ll l^2 \equiv c\hbar/eH$, where l is the magnetic length. The proposed approach does not imply the use of perturbation theory in the interaction of carriers with scatterers. It is demonstrated that the contour of the absorption line in quantum cyclotron resonance (QCR) is described by a universal formula of τ-approximation, which is applicable for any frequency detuning, temperature, and magnetic field strength that meet the QCR conditions. The developed theory allowed us to eliminate significant discrepancies that have existed for a long time between theoretical predictions and the results of experiments on QCR due to neutral impurities with the use of FIR lasers with discharge (H_2O and D_2O lasers, 220–119 μm) pumping as sources of electromagnetic waves. Theoretical temperature–field and concentration dependences for the QCR line half-width $\delta\omega(T, H, N)$ (N is the concentration of impurities) obtained in this paper for the scattering due to small-size neutral donors are compared with the relevant experimental data.

1. Cyclotron resonance (CR) in semiconductors is a powerful tool that allows one to obtain the data concerning the parameters of semiconductors, including the effective mass of charge carriers, dispersion relations, the type and the concentration of defects, interaction potential, etc. All the data on these parameters are extracted from the experimental results processed in accordance with the temperature–field and concentration dependence of the CR absorption curve. This curve becomes especially well defined at low temperatures ($T \ll \hbar\omega_H$), in the domain of quantum cyclotron resonance (QCR), where phonon mechanisms of scattering are strongly suppressed. In weakly compensated semiconductors, the scattering of carriers due to ionized impurities is also suppressed under these conditions (because of the low concentration of such impurities). In such a situation, the interaction of charge carriers with neutral defects plays the main role.

Until the publication of our papers [1, 2], it was possible to theoretically investigate QCR for any mechanisms of electron–hole scattering only within the framework of the Born approximation (BA). This approximation provides a good agreement between theoretical predictions and experimental data in the case of phonons and ionized impurities. The Erginsoy formula (EF) [4] is successfully used for the description of the scattering of electrons by neutral impurities in semiconductors in nonquantizing magnetic fields. In particular, the EF permits a correct estimation of the CR line half-width $\delta\omega$ [5]. The problem of QCR

description remained unsolved for several years. Attempts to adapt the EF to QCR within the framework of BA! were not successful—the calculated quantity $\delta\omega$ was greater than the measured line half-width by more than an order of magnitude and displayed a qualitatively different dependence on H and T (see [3] and Figs. 1, 2).

We have solved (see [1, 2]) a set of kinetic integrodifferential QCR equations for a translation-invariant Wigner density matrix and a single-center correlator in the case when electrons are scattered by neutral centers with a potential U and radius r_c meeting the inequalities

$$\text{(a)} \ |U| \ll \hbar^2/m^* r_c^2, \quad \text{(b)} \ r_c^2 \ll l^2 \qquad (1)$$

without using perturbation theory in the interaction of charge carriers with scattering centers. The derived solution makes it possible to describe the absorption QCR line with a universal formula of τ-approximation (8)–(10), which is valid for any T, $\Delta\omega$, and H under QCR conditions. We revealed a change in the dependence $\delta\omega(H, T)$ within the range where the values of H and T correspond to the resonant scattering of an electron from magnetic-impurity (MI) states and the half-width of the QCR line reaches its maximum.

2. Suppose that a gas of noninteracting electrons is placed in a uniform quantizing magnetic field $H \| z$ and a resonant electric field $E(t) = E \exp\{i(\omega - i\delta)t\}$, $E \perp H$, $\delta = +0$, in the presence of the potential of chaotically distributed impurities. Assuming that the concentration
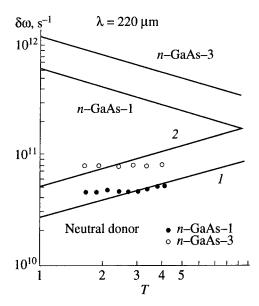
ANDREEV *et al.*

Fig. 1. Temperature dependence of the half-width of the QCR line in *n*–GaAs for $H = 3.5 \times 10^4$ G. The concentration of neutral donors N is (*1*) 7.5×10^{14} and (2) 15×10^{14} cm^{-3}. Lines *1* and 2 represent the results of calculations performed with the use of formula (12). The dots and the circles correspond to the results of experiments carried out in [3]. Two upper curves show the results of calculations in accordance with the EF [3].

Fig. 2. The half-width of the QCR line in *n*–GaAs as a function of the magnetic field for $T = 4.2$ K and (*1*) $N = 7.5 \times 10^{14}$ and (2) 15×10^{14} cm^{-3}. Lines *1* and 2 represent the results of calculations performed with the use of formula (12). The dots and the circles correspond to the results of experiments carried out in [3]. Two upper curves show the results of calculations in accordance with the EF [3].

of impurities N is small, we can write the following equation for the density matrix $\rho(1, 2, \{R_i\}, t)$ in the coordinate representation:

$$i\hbar\dot{\rho}(1, 2, \{\mathbf{R}_i\}, t) = \left\{ \hat{H}_1 - \hat{H}_2^* + e\mathbf{E}(t)(\mathbf{r}_1 - \mathbf{r}_2) \right.$$

$$\left. + \sum_i [U(\mathbf{r}_1 - \mathbf{R}_i) - U(\mathbf{r}_2 - \mathbf{R}_i)] \right\} \rho(1, 2, \{\mathbf{R}_i\}, t), \quad (2)$$

$$\hat{H}_{1,2} \equiv \hat{H}(1, 2), \quad 1, 2 \equiv \mathbf{r}_{1,2},$$

$$\hat{H} = p_z^2/2m_\parallel + 1/2m_\perp(\mathbf{p}_\perp + e/c\mathbf{A}(\mathbf{r}, t))^2,$$

where $\hat{H}$ is the Hamiltonian of an electron in the uniform magnetic field, $\mathbf{A}$ is the vector potential of the magnetic field, and $\mathbf{R}_i$ is the radius vector of the ith scattering center. Applying a standard technique, we can use this equation to derive a closed set of equations for the single-electron density matrix $\rho(1, 2, t)$ averaged over the arrangement of scatterers in the coordinate representation and a single-center correlator $g(1, 2, \mathbf{R}, t)$,

$$\rho(1, 2, t) \equiv V^{-N_s} \int \prod_i d^3\mathbf{R}_i \rho(1, 2, \{\mathbf{R}_i\}, t),$$

$$g(1, 2, \mathbf{R}, t) \equiv \rho(1, 2, \mathbf{R}, t) - \rho(1, 2, t)$$

(V is the volume, N_s is the number of scattering centers, and $\rho(1, 2, \mathbf{R}, t)$ is the density matrix averaged over the
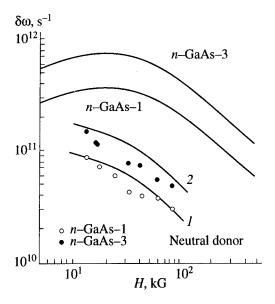
arrangement of all the centers except for one),

$$i\hbar\dot{\rho}(1, 2, t) = [\hat{H}_1 - \hat{H}_2^* + e\mathbf{E}(t)(\mathbf{r}_1 - \mathbf{r}_2)]\rho(1, 2, t)$$

$$+ N\int d\mathbf{R}[U(\mathbf{r}_1 - \mathbf{R}) - U(\mathbf{r}_2 - \mathbf{R})]g(1, 2, \mathbf{R}, t), \quad (3)$$

$$i\hbar\dot{g}(1, 2, \mathbf{R}, t) = [\hat{H}_1 - \hat{H}_2^* + e\mathbf{E}(t)(\mathbf{r}_1 - \mathbf{r}_2)]$$

$$\times g(1, 2, \mathbf{R}, t) + [U(\mathbf{r}_1 - \mathbf{R}) - U(\mathbf{r}_2 - \mathbf{R})]\rho(1, 2, t).$$

The function ρ does not feature translation invariance and can be represented as a product of the translation-invariant density matrix $\tilde{\rho}(\mathbf{r}_1 - \mathbf{r}_2, t)$ and a phase factor $\exp\{i\Phi(\mathbf{r}_1, \mathbf{r}_2)\}$, which is determined by the gauge of the vector potential of the magnetic field [6].

Next, we will use the translation-invariant density matrix $F(\mathbf{k}, z, t)$ in the mixed representation,

$$F(\mathbf{k}, z, t) = d^2\boldsymbol{\chi}\exp(i\mathbf{k}\boldsymbol{\chi})\tilde{\rho}(\boldsymbol{\chi}, z, t),$$

$$\mathbf{r}_2 - \mathbf{r}_1 \equiv \{\boldsymbol{\chi}, z\}, \quad \boldsymbol{\chi} \perp \mathbf{H}. \quad (4)$$

Analogously, we introduce a single-center correlator in the mixed representation ($z_{1,2} - R_z \equiv z_{1,2}^-$):

$$G(\mathbf{s}_1, \mathbf{s}_2, z_1^-, z_2^-, t) = (2\pi)^{-4}$$

$$\times \int d^2\boldsymbol{\rho}_1 d^2\boldsymbol{\rho}_2 e^{-i(\mathbf{s}_1\boldsymbol{\rho}_1 + \mathbf{s}_2\boldsymbol{\rho}_2)}\tilde{g}(\boldsymbol{\rho}_1, \boldsymbol{\rho}_2, z_1^-, z_2^-, t)e^{il^2[\mathbf{s}_2, \mathbf{s}_1]_H},$$

$$\tilde{g}(\mathbf{r}_1 - \mathbf{R}, \mathbf{r}_2 - \mathbf{R}, t) \quad (5)$$

$$= \exp\{-i\Phi(\mathbf{r}_1, \mathbf{r}_2)\}g(\mathbf{r}_1, \mathbf{r}_2, \mathbf{R}, t).$$

Definition (4) implies that the kinematic momentum $\hbar k = p + e/c \cdot A$ is chosen as a variable, which makes the problem under study translation-invariant [6] and radically simplifies calculations. In contrast to [6], we perform Fourier transformation in (4) only in transverse variables, which allows us, upon the separation of transverse and longitudinal variables in the set of equations for F and G, to employ the functions of longitudinal (along H) motion of the single-center problem in the coordinate representation. We linearize the set of equations for $F(k, z, t)$ and $G(s_1, s_2, z_1 - R_z, z_2 - R_z, t)$ in E assuming that $F = F^0 + F^1$ and $G = G^0 + G^1$, where $F^1, G^1 \sim E$.

In the absence of impurities, the function $F^0(k, z)$ in a quantizing field H was derived in [6]:[1]

$$F^0(k, z) = \pi^{-1} n_e l^2 \exp(-k^2 l^2) \Phi(z), \qquad (6)$$

where n_e is the concentration of electrons and $\Phi(z)$ is the one-dimensional equilibrium density matrix. In the presence of impurities, $F^0(k, z)$ varies due to transitions of electrons to upper Landau bands stimulated by impurities. However, if the coupling of Landau levels due to a single center (1a) is weak and the concentration of centers is low, the dependence $F^0(k, z)$ remains unchanged. Then, keeping only the terms that correspond to the resonant approximation, we find the function F^1:

$$F^1(k, z) = -(e n_e E / \pi \hbar) e^{-i\phi} k \exp(-k^2 l^2) f(z). \qquad (7)$$

Now, it is convenient to employ the momentum representation: $\Phi(z) \Rightarrow \Phi(p)$ and $f(z) \Rightarrow f(p)$. Then, we can solve the integral equation for the function $f(p)$ in the case of small-size centers (1a) with a small radius (1b) (see [1, 2]):

$$f(\varepsilon) = \frac{1}{\hbar} \frac{\Phi(\varepsilon)}{\Delta\omega + \eta(\varepsilon, \Delta\omega) - i\tau^{-1}(\varepsilon, \Delta\omega)}, \qquad (8)$$

$$\eta - i\tau^{-1} = \frac{2\pi N l^2}{\hbar} \sqrt{2m^*}$$

$$\times \int_0^\infty \frac{d\varepsilon_1}{\sqrt{\varepsilon_1}} |T_{p_1}(p)|^2 [(\varepsilon_1 - \varepsilon_+ + i\delta)^{-1} - (\varepsilon_1 - \varepsilon_- - i\delta)^{-1}], \qquad (9)$$

where $\varepsilon_\pm = \varepsilon \pm \hbar\Delta\omega$; $\hat{H}\chi_p = \varepsilon\chi_p$; $T_{p_1} \equiv \int_{-\infty}^{+\infty} d\xi U(\xi) \times \chi_{p_1}(\xi) \exp(ip\xi/\hbar)$ are the matrix elements of the operator of scattering in the presence of the potential $U(z)$; $\{\chi_p\}$ is the set of the wave functions of the continuous spectrum of the Hamiltonian $\hat{H} = \hat{H}_0 + U(z)$, $\hat{H} = p_z^2/2m^*$ and $U(z) = l^{-2}\int_0^\infty \rho d\rho U(\rho, z)$ is the one-

[1] We restrict our consideration to the case of nondegenerate electrons.

dimensional potential of the impurity averaged over the transverse motion of an electron in the magnetic field; and $\varepsilon = p^2/2m^*$ is the energy of the longitudinal motion of an electron.

Absorption is proportional to the integral

$$Q(\Delta\omega, H, T) = \int_0^\infty \frac{d\varepsilon}{\sqrt{\varepsilon}} \text{Im} f(\varepsilon). \qquad (10)$$

As it follows from (8)–(10), provided that inequalities (1) are satisfied, the QCR line is described by a universal formula of τ-approximation, and the inverse of the relaxation time of the current τ^{-1} and the frequency shift η are determined by the operator of single-center scattering $\hat{T}$ and the frequency detuning $\Delta\omega$.

Setting $\Delta\omega = 0$ in (9) and replacing χ_p by plane waves, we arrive at BA expressions [7, 8].

3. In the case of small-size impurities ($U \ll \hbar^2/m^* r_c^2$), there are no bound electron states due to impurities when $H = 0$. A nonzero magnetic field gives rise to a spectrum of magnetic-impurity states [9] classified in accordance with the momentum projection m. This spectrum converges to the continuum as $\sim(r_c/l)^{4m}$. The depth ε_H of the ground level with $m = 0$ beneath the bottom of the Landau band (0, 1) defines the energy of a weakly bound electron state in a one-dimensional potential $U(z)$ ($\varepsilon_H = -\frac{\alpha^2}{2}\hbar\omega_H$ and $\alpha \equiv f_B/l$, where f_B is the Born amplitude of scattering of an electron by a potential $U(r)$) [1]. This depth also determines the matrix elements of the scattering operator: $|T_{p_1}(p)|^2 = \hbar\varepsilon_H/\pi m^* D(\varepsilon)$, where $D(\varepsilon) = (1 + \varepsilon_H/\varepsilon)^{-1}$ is the transmission coefficient of an electron with energy ε through one-dimensional potential $U(z)$. Evaluating integrals in (9), we can easily find the parameters of the QCR line: $\gamma_T \equiv \varepsilon_H/T$ and $\delta \equiv \hbar/T\tau_0 \ll 1$, $\tau_0^{-1} = 2\tau^{-1}(\varepsilon = \varepsilon_H, \Delta\omega = 0) = 4\pi\hbar N|f_B|/m^*$. The dimensionless frequency detuning $x = \Delta\omega\tau_0$ is employed as a natural argument of function (10).

The chain of equations for F and g was decoupled in such a manner (see [1, 2]) that the longitudinal electron energy is defined with an accuracy up to $\varepsilon/T \sim \delta_T \equiv \hbar/\tau_0 T \ll 1$. Therefore, in the vicinity of the resonance, we can set $\Delta\omega = 0$ in (9).

For zero frequency detuning, we have $\eta(\Delta\omega = 0) = 0$, and the inverse of the relaxation time of the current is proportional to the product of the density of initial electron states in the lower Landau band and the coefficient of transmission of an electron through the relevant one-dimensional potential. Replacing the electron energy in $\tau(\varepsilon, \Delta\omega = 0)$ by thermal energy, we obtain an estimate for the half-width of the QCR line as a
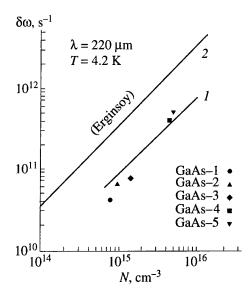
Fig. 3. The half-width of the QCR line in n–GaAs as a function of the concentration of small-size neutral donors for $H = 3.5 \times 10^4$ G in accordance with (1) formula (12) and (2) the EF [3]. The dots, triangles, squares, and rhombi represent the results of experiments carried out in [3].
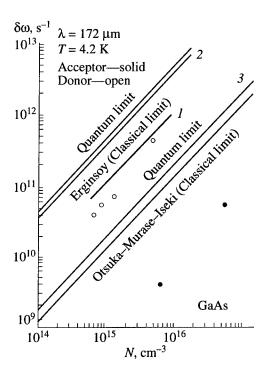

Fig. 4. The half-width of the QCR line in n–GaAs as a function of the concentration of small-size neutral donors for $H = 4.5 \times 10^4$ G (1) in accordance with formula (12), (2) according to the EF for the scattering of electrons by neutral donors (in the classical limit), and (3) calculated by Otsuka *et al.* [3] for the scattering of electrons by neutral acceptors. The circles represent the results of experiments carried out in [3] for the scattering of electrons by neutral donors.

function of temperature and the strength of the magnetic field:

$$\delta\omega(H, T) \sim \tau_0^{-1}\gamma_T^{1/2}D(\gamma_T). \qquad (11)$$

It can be seen that $\delta\omega$ is proportional to the product of the density of initial electron states $\sim\gamma_T^{1/2}$ and the coefficient $D(\gamma_T)$ of transmission of an electron through the relevant one-dimensional potential. Within the range of high temperatures ($\gamma_T \ll 1$, the BA domain), the half-width of the QCR line is $\delta\omega \sim H/T^{1/2}$. Within the range where $\gamma_T \gg 1$, we have $\delta\omega \sim T^{1/2}/H$. Hence, within the range of temperatures and strengths of the magnetic field corresponding to the resonant scattering of an electron from MI states ($\gamma_T \sim 1$), the QCR line half-width $\delta\omega$ changes its behavior as a function of H and T. For $T = \varepsilon_H$, i.e., in the case of resonant scattering, $\delta\omega$ reaches its maximum, $\delta\omega^{\max} = 1/2\tau_0^{-1}$. Setting $D = 1$ in (11), we obtain the result that coincides with the BA prediction [7, 8]. Since the transmission coefficient satisfies the inequality $D(\gamma_T) < 1$ and increases with a growth in T, it is obvious that, for any T, the BA gives an overestimated value for $\delta\omega$, and the discrepancy between the results of exact analysis and Born approximation increases with a decrease in temperature.

4. The data on QCR in n–GaAs for $T = 1.7$–4.2 K, $H = (1$–$8) \times 10^4$ G, and N (neutral donors) = $(7.5$–$100) \times 10^{14}$ cm^{-3} have been presented in [3]. According to [3], we have $r_c = 10^{-6}$ cm, so that inequality (1b) is satisfied for virtually all H: $r_c^2/l^2 = 0.1$–1.2. The quantity $|U|m^*r_c^2/\hbar^2$ can be estimated in the following manner. Under conditions of experiments described in [3], the spin of a donor electron is parallel to the spin of an electron involved in scattering (triplet scattering). For triplet scattering, we have $U < 0$. However, bound states are absent when $H = 0$ [10]; i.e., $|U|m^*r_c^2/\hbar^2 \ll 1$. (In singlet scattering, a bound state exists in the form of a D^--center [11].) Consequently, we can assume that condition (1a) is satisfied.

Calculations with the use of the Born amplitude f_B predict the values of $\delta\omega$ that differ from the relevant results of measurements by a factor no greater than two. As shown in [9, 12], when we abandon the approximation of weak coupling, we should replace f_B by the exact scattering amplitude f. For triplet scattering, we have $f = f_t = 1.768r_c$ [10]. Using this relationship, we can apply (11) to obtain the following estimate for $\delta\omega$:

$$\delta\omega = 5.77 \times 10^{-8}HN\sqrt{1/T}$$
$$\times (1 + 3.8 \times 10^{-8}H^2 \times 1/T)^{-1}\text{s}^{-1}. \qquad (12)$$

We employed (12) to calculate the dependences $\delta\omega(H, T, N)$. The results of these calculations agreed well with the experimental data. We also used r_c as a fitting

parameter by setting a correspondence between $\delta\omega$ and a definite point in one of the experimental curves from [3]. This procedure also provided a satisfactory agreement between $\delta\omega_{exp}(H, T, N)$ and $\delta\omega_{theor}(H, T, N)$ (see Figs. 1–4).

REFERENCES

1. Andreev, A.S., Andreev, S.P., Gurvich, Yu.A., and Podlivaev, I.F., 1996, *Laser Phys.*, **6**, 1214.

2. Andreev, A.S., Andreev, S.P., and Gurvich, Yu.A., 1997, *Laser Phys.*, **7**, 488.

3. Kobori, H., Ohyama, T., and Otsuka, E., 1990, *J. Phys. Soc. Jpn.*, **59**, 2171.

4. Gantmakher, V.F. and Levinson, I.B., 1984, *The Scattering of Current Carriers in Metals and Semiconductors* (Moscow: Nauka) (in Russian).

5. Blagosklonskaya, L.E., Gershenzon, E.M., Ladyzhinskii, Yu.P., and Popova, A.P., 1969, *Fiz. Tverd. Tela*, **11**, 2967.

6. Levinson, I.B., 1969, *Zh. Eksp. Teor. Fiz.*, **57**, 660.

7. Gurvich, Yu.A., 1974, *Zh. Eksp. Teor. Fiz.*, **66**, 667.

8. Kawabata, A., 1967, *J. Phys. Soc. Jpn.*, **23**, 999.

9. Andreev, S.P., 1984, *Usp. Fiz. Nauk*, **143**, 213.

10. Drukarev, G.F., 1978, *Collisions of Electrons with Atoms and Molecules* (Moscow: Nauka) (in Russian).

11. Gershenzon, E.M., Mel'nikov, A.P., and Rabinovich, R.I., 1985, *Modern Problems in Condensed Matter Sciences*, **10**, 483.

12. Skobov, V.G., 1959, *Zh. Eksp. Teor. Fiz.*, **37**, 1467.

Polarization Effects in Two-Photon Free–Free Transitions in Laser-Assisted Electron–Hydrogen Collisions

A. Cionga and G. Buică

Institute for Space Sciences, P.O. Box MG-36, Bucharest-Măgurele, Bucharest, R-76900 Romania
e-mail: acionga@venus.ifa.ro
Received September 28, 1997

Abstract—Two-photon free–free transitions in elastic laser-assisted electron–hydrogen collisions are studied in the domain of high scattering energies and low or moderate field intensities, in the third order of perturbation theory, taking into account all the involved Feynman diagrams. Based on the analytical expressions of the transition amplitudes, the differential cross sections for two-photon absorption/emission are computed at impact energy $E_i = 100$ eV. The effect of field polarizations on the angular distribution and on the frequency dependence of the differential cross section is analyzed.

1. INTRODUCTION

Recently, a series of experimental [1] and theoretical [2] works have been devoted to the study of free–free transitions in laser-assisted elastic electron–atom collisions at low scattering energies.

It is the aim of this work to investigate free–free transitions in a different regime, that of high scattering energies and low or moderate field intensities such that the use of perturbation theory might provide a sensible description of the process. We focus our attention on the study of free–free transitions that involve the absorption/emission of two *different* photons by the compound projectile–target system in an external radiation field. The target is the hydrogen atom in the ground state. The process can be formally represented by

$$H(E_{1s}) + e^-(\mathbf{k}_i, E_i)$$
$$\pm [\gamma(\boldsymbol{\varepsilon}_1, \omega_1) + \gamma(\boldsymbol{\varepsilon}_2, \omega_2)] \longrightarrow H(E_{1s}) + e^-(\mathbf{k}_f, E_f), \quad (1)$$

where $E_{i(f)}$, $\mathbf{k}_{i(f)}$ are the initial (final) energy and momentum of the projectile; ω_j, $\boldsymbol{\varepsilon}_j$ denote the frequency and the polarization vector of the photon j ($j = 1, 2$). The upper sign corresponds to the absorption of both photons, the lower one corresponds to their stimulated emission.

The process (1) has been previously investigated for two *identical* photons. Kracke *et al.* [3] have studied the differential cross section of two-photon free–free transitions at high scattering energies (50–500 eV) for photon energies below the ionization threshold of hydrogen ($\omega < 20$ eV). They have used in their work the lowest order perturbation theory, taken into account all the involved Feynman diagrams. For strong fields, the laser–particle interaction must be treated beyond the perturbation theory. In this context, Dörr *et al.* [4] developed the Born–Floquet theory, in which both laser–projectile and laser-target interactions are treated exactly. This approach is valid in the domain of high

scattering energies since it involves the first Born approximation to treat the projectile–target interaction. We refer to this paper for a comprehensive analysis of other previous works.

In Section 2 we present the formalism we have used to evaluate transition matrix elements for two-photon absorption/emission: the projectile–target interaction as well as the interaction between the electrons and the electromagnetic field have been treated perturbatively. We have evaluated the analytic expressions of the corresponding transition amplitudes in the third order of perturbation theory, including the twenty-four Feynman diagrams. The third section is devoted to the discussion of the numerical results. We report here our results concerning the influence of the state of polarization of the two photons on the differential cross section of the scattered electron. We claim that this effect is significant in the domain in which the dressing of the target is important: at small scattering angles in general and, in particular, close to atomic resonances.

2. BASIC EQUATIONS

The time evolution of the electron–hydrogen system in the presence of an electromagnetic field described by the vector potential

$$\mathcal{A}(t) = \boldsymbol{\varepsilon}_1 A_{01} \cos(\omega_1 t) + \boldsymbol{\varepsilon}_2 A_{02} \cos(\omega_2 t), \quad (2)$$

is governed by the Hamiltonian

$$\mathcal{H} = \frac{\mathbf{p}^2}{2} - \frac{1}{r} + \frac{\mathbf{P}^2}{2} + \frac{1}{|\mathbf{r} - \mathbf{R}|} - \frac{1}{R} + \frac{1}{c}[\mathbf{p} + \mathbf{P}]\mathcal{A}(t)$$
$$\equiv H_0 + V + W(t), \quad (3)$$

where $\mathbf{r}$, $\mathbf{p}$ are the position and momentum operator of the bound (atomic) electron and $\mathbf{R}$, $\mathbf{P}$ are the position and momentum operator of the free (projectile) electron. $V \equiv -R^{-1} + |\mathbf{r} - \mathbf{R}|^{-1}$ denotes the e–H interaction in

the direct channel and $W(t) \equiv c^{-1}[\mathbf{p} + \mathbf{P}]\mathcal{A}(t)$ denotes the interaction of the charge particles with the field, treated in the velocity gauge, using the dipole approximation. The $\mathcal{A}^2$-term was eliminated through a unitary transformation.

In the *first nonvanishing order* of the perturbation theory, the S-matrix elements corresponding to two-photon processes are given by

$$S^{(2)} = -\int\limits_{-\infty}^{+\infty} dt_1 \int\limits_{-\infty}^{t_1} dt_2 \langle \chi_f^- | \tilde{W}(t_1) \tilde{W}(t_2) | \chi_i^+ \rangle, \qquad (4)$$

where $\tilde{W}(t) = e^{iH_0 t} W(t) e^{-iH_0 t}$. In the previous equation $|\chi_i^+\rangle$ and $|\chi_f^-\rangle$ describe the initial and final states of the colliding system (electron–atom)

$$|\chi_i^+\rangle = |\Psi_i\rangle + G^+(\mathcal{E}_i)V|\Psi_i\rangle, \qquad (5)$$

$$|\chi_f^-\rangle = |\Psi_f\rangle + G^-(\mathcal{E}_f)V|\Psi_f\rangle, \qquad (6)$$

where

$$G^\pm(\mathcal{E}) = [\mathcal{E} - H_0 - V \pm i\delta] \qquad (7)$$

and δ a positive infinitesimal number. $|\Psi_{i,f}\rangle$ are the asymptotic states corresponding to the colliding system in the absence of the interaction V

$$|\Psi_i\rangle = |\psi_{1s}\rangle|K_i\rangle, \qquad (8)$$

$$|\Psi_f\rangle = |\psi_{1s}\rangle|K_f\rangle. \qquad (9)$$

Here $|\psi_{1s}\rangle$ denotes the ground state of a hydrogen atom and $|K_{i,f}\rangle$ are plane waves. The initial and final energies of the electron–atom system are

$$\mathcal{E}_i = E_{1s} + \frac{k_i^2}{2}, \qquad (10)$$

$$\mathcal{E}_f = E_{1s} + \frac{k_f^2}{2} \pm (\omega_1 + \omega_2). \qquad (11)$$

The transition-matrix element involving two *different* photons, both absorbed or emitted, is given by

$$T^{(2)} = \frac{1}{4}(1 + \mathcal{P}_{12})\langle \chi_f^- | \mathbf{A}_1 \cdot (\mathbf{p} + \mathbf{P}) \qquad (12)$$
$$\times G^+(\mathcal{E}_i \pm \omega_2)\mathbf{A}_2 \cdot (\mathbf{p} + \mathbf{P})|\chi_i^+\rangle,$$

where $\mathcal{P}_{12}$ is the permutation operator between the vector potentials $\mathbf{A}_j = \varepsilon_j A_{0j}$ ($j = 1, 2$), which describe the two components of the field (2). In (12) the upper sign corresponds to absorption, the lower one to stimulated emission. It is possible to write this matrix element as the sum of three terms, each of them connected with

specific Feynman diagrams, as we shall discuss later in this section. These terms are

—*the electronic term*

$$T_P = \frac{1}{4}(1 + \mathcal{P}_{12})\langle \chi_f^- | \mathbf{A}_1 \cdot \mathbf{P} G^+(\mathcal{E}_i \pm \omega_2)\mathbf{A}_2 \cdot \mathbf{P} |\chi_i^+\rangle, \qquad (13)$$

—*the mixed term*

$$T_M = \frac{1}{4}(1 + \mathcal{P}_{12})(1 + \mathcal{P}_{\mathbf{pP}})\langle \chi_f^- | \mathbf{A}_1 \cdot \mathbf{p} G^+ \qquad (14)$$
$$\times (\mathcal{E}_i \pm \omega_2)\mathbf{A}_2 \cdot \mathbf{P} |\chi_i^+\rangle,$$

where $\mathcal{P}_{\mathbf{pP}}$ is the permutation operator between $\mathbf{p}$ and $\mathbf{P}$, and

—*the atomic term*

$$T_A = \frac{1}{4}(1 + \mathcal{P}_{12})\langle \chi_f^- | \mathbf{A}_1 \cdot \mathbf{p} G^+(\mathcal{E}_i \pm \omega_2)\mathbf{A}_2 \cdot \mathbf{p} |\chi_i^+\rangle. \qquad (15)$$

Since we restrict ourselves to the domain of high scattering energies, we use the first Born approximation to treat electron-atom scattering, which implies

$$|\chi_i^+\rangle \simeq |\Psi_i\rangle + G_0^+(\mathcal{E}_i)V|\Psi_i\rangle, \qquad (16)$$

$$|\chi_f^-\rangle \simeq |\Psi_f\rangle + G_0^-(\mathcal{E}_f)V|\Psi_f\rangle, \qquad (17)$$

where

$$G_0^\pm(\mathcal{E}) = [\mathcal{E} - H_0 \pm i\delta]^{-1}. \qquad (18)$$

In this way, the evaluation of the transition matrix element is made in the third order of perturbation theory: the second order in the electric field and the first order in the scattering potential, V.

2.1. Electronic Term

The electronic term is connected to six Feynman diagrams in which only the projectile exchanges two different photons with the field (2). Only three of these diagrams are represented in Fig. 1a, the other three are obtained by interchanging ω_1 and ω_2.

In the standard way, after integration over the projectile coordinates, the electronic term in (13) may be written as

$$T_P = \frac{\sqrt{I_1 I_2}}{4\omega_1^2 \omega_2^2}(\varepsilon_1 \cdot \mathbf{q})(\varepsilon_2 \cdot \mathbf{q})\langle \psi_{1s} | F(\mathbf{q}) | \psi_{1s} \rangle, \qquad (19)$$

where I_j is the intensity of the component j of the field (2), $\mathbf{q}$ is the momentum transfer of the projectile and $F(\mathbf{q})$ is the form factor operator

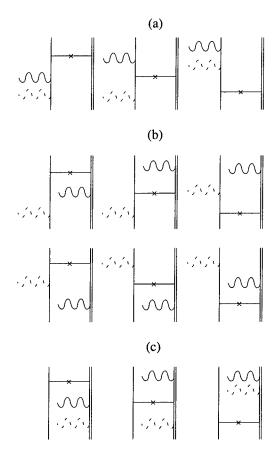$$F(\mathbf{q}) = \frac{1}{2\pi^2 q^2}[\exp(i\mathbf{q} \cdot \mathbf{r}) - 1].$$

(a)

(b)

(c)

Fig. 1. Feynman diagrams for two-photon processes in laser-assisted electron–atom scattering: (a) electronic diagrams, (b) mixed diagrams, and (c) atomic diagrams. The projectile is represented by a single line, the bound electron by a double line.

We remind that this is the only term which gives contributions to the weak field intensity limit of Bunkin–Fedorov formula [5]. That approach describes the target by a potential and neglects the atomic dressing. In order to take into account the atomic dressing we include in our calculation the other eighteen Feynman diagrams, corresponding to the mixed and atomic terms.

2.2. Mixed Term

The mixed term is connected to twelve Feynman diagrams, in which each electron (free and bound) absorbs/emits one photon from each component of the field (2). Only six diagrams are represented in Fig. 1b, the other six are obtained again by interchanging ω_1 and ω_2.

In order to evaluate the mixed term we took advantage of the analytic form of the vectors

$$|\mathbf{w}_{100}(\Omega)\rangle = -G_C(\Omega)\mathbf{p}|\psi_{1s}\rangle,$$

which were previously studied in [6]. Here $G_C(\Omega)$ is the Coulomb Green function. After integration over the pro-

jectile coordinates, the mixed term in (14) is written as

$$T_M = \mp\frac{\sqrt{I_1 I_2}}{4\omega_1\omega_2}\left\{\frac{\boldsymbol{\varepsilon}_2\cdot\mathbf{q}}{\omega_2}[\langle\psi_{1s}|F(\mathbf{q})|\boldsymbol{\varepsilon}_1\cdot\mathbf{w}_{100}(\Omega_1^{\pm})\rangle\right.$$

$$+\langle\boldsymbol{\varepsilon}_1\cdot\mathbf{w}_{100}(\Omega_1^{\mp})|F(\mathbf{q})|\psi_{1s}\rangle]$$

$$+\frac{\boldsymbol{\varepsilon}_1\cdot\mathbf{q}}{\omega_1}[\langle\psi_{1s}|F(\mathbf{q})|\boldsymbol{\varepsilon}_2\cdot\mathbf{w}_{100}(\Omega_2^{\pm})\rangle \quad (20)$$

$$\left.+\langle\boldsymbol{\varepsilon}_2\cdot\mathbf{w}_{100}(\Omega_2^{\mp})|F(\mathbf{q})|\psi_{1s}\rangle]\right\},$$

where the parameters $\Omega_{1,2}^{\pm}$ are given by

$$\Omega_{1,2}^{\pm} = E_{1s}\pm\omega_{1,2}.$$

In (20) the upper signs correspond to absorption and the lower ones correspond to stimulated emission of both photons.

The atomic matrix elements in (20), which appear also in one photon processes, have been evaluated analytically [7]. Based on this result it is possible to write down the general structure of the mixed term as

$$T_M = \sqrt{I_1 I_2}(\boldsymbol{\varepsilon}_1\cdot\mathbf{q})(\boldsymbol{\varepsilon}_2\cdot\mathbf{q})\mathcal{T}_M(\omega_1,\omega_2;q), \quad (21)$$

where the radial part, $\mathcal{T}_M(\omega_1,\omega_2;q)$, is expressed in terms of hypergeometric functions.

2.3. Atomic Term

The atomic term is connected to six Feynman diagrams in which two different photons are exchanged between the bound electron and the field (2). Only three diagrams are represented in Fig. 1c, the other three are obtained by interchanging ω_1 and ω_2.

Our analytic formula for the atomic term is computed using the tensors

$$|\omega_{ij,100}(\Omega',\Omega)\rangle = G_C(\Omega')p_i G_C(\Omega)p_j|\psi_{1s}\rangle,$$

studied in [8]. After integration over the coordinates of the projectile, the atomic term in (15) is written as

$$T_A = \frac{\sqrt{I_1 I_2}}{4\omega_1\omega_2}\sum_{j,l=1}^{3}\varepsilon_{1j}\varepsilon_{2l}$$

$$\times[\langle w_{j,100}(\Omega_1^{\mp})|F(\mathbf{q})|w_{l,100}(\Omega_2^{\pm})\rangle$$

$$+\langle w_{l,100}(\Omega_2^{\mp})|F(\mathbf{q})|w_{j,100}(\Omega_1^{\pm})\rangle$$

$$+\langle\psi_{1s}|F(\mathbf{q})|w_{jl,100}(\Omega'^{\pm},\Omega_2^{\pm})\rangle \quad (22)$$

$$+\langle\psi_{1s}|F(\mathbf{q})|w_{lj,100}(\Omega'^{\pm},\Omega_1^{\pm})\rangle$$

$$+\langle w_{lj,100}(\Omega'^{\mp},\Omega_1^{\mp})|F(\mathbf{q})|\psi_{1s}\rangle$$

$$+\langle w_{jl,100}(\Omega'^{\mp},\Omega_2^{\mp})|F(\mathbf{q})|\psi_{1s}\rangle].$$

Here the parameter Ω' takes the values

$$\Omega'^{\pm} = E_{1s} \pm (\omega_1 + \omega_2)$$

and $\Omega^{\pm}_{1,2}$ were defined above. In (22) the upper signs correspond to absorption and the lower ones correspond to emission of two different photons.

We have evaluated analytically the atomic matrix element in (22); based on this results one can write the general structure of the atomic term as

$$T_A = \sqrt{I_1 I_2}[(\boldsymbol{\varepsilon}_1 \cdot \mathbf{q})(\boldsymbol{\varepsilon}_2 \cdot \mathbf{q})\mathcal{T}'_{sd}(\omega_1, \omega_2; q)$$

$$+ (\boldsymbol{\varepsilon}_1 \cdot \boldsymbol{\varepsilon}_2)\mathcal{T}''_{sd}(\omega_1, \omega_2; q)], \quad (23)$$

where the radial parts, $\mathcal{T}'_{sd}(\omega_1, \omega_2; q)$ and $\mathcal{T}''_{sd}(\omega_1, \omega_2; q)$, are expressed as series of hypergeometric functions [9].

For the sake of simplicity, the equations (19)–(23) have been written using linear polarizations. We point out that for photon emission, one must take the complex conjugate of the polarization vector.

Finally, the differential cross section for the absorption/emission of two different photons in laser-assisted elastic electron–hydrogen collisions can be written as

$$\frac{d\sigma}{d\Omega} = (2\pi)^4 \frac{k_f}{k_i}|T_P + T_M + T_A|^2, \quad (24)$$

where the electronic, mixed, and atom structure given in (19), (21) and (23).

3. RESULTS

We have computed the differential cross section for two-photon free–free transitions in laser-assisted elastic electron–hydrogen collisions at scattering energy $E_i = 100$ eV. We have chosen to report here the case of two laser sources having the same frequency, $\omega_1 = \omega_2 \equiv \omega$, but different polarizations. The investigated photon energies are smaller than the ionization energy of hydrogen. The results are valid for low and moderate field intensities, bellow 10^{10} W/cm². In all the cases that we have studied the initial momentum of the projectile, $\mathbf{k}_i$, defines the Oz-axis.

We discuss here the effect of the state of polarization of the photons on the frequency dependence of the differential cross section and on the azimuthal angular distribution of the scattered electrons, for scattering angles in the domain where target dressing effects are important. In general, this domain corresponds to small scattering angles, as it has been pointed out by Kracke et al. [3], who studied the monochromatic case.

3.1. Frequency Dependence

In Fig. 2 we present the differential cross section for two-photon absorption in (24), normalized with respect to the field intensities, $I_1 I_2$, as a function of the photon frequency, in the range $0 < \omega < 6.8$ eV. The scattering angle, $\theta = 5°$, is in the domain where the dressing
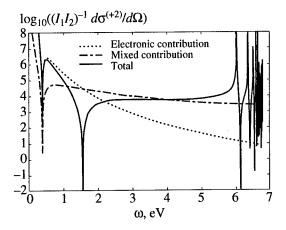
$\log_{10}((I_1 I_2)^{-1} d\sigma^{(+2)}/d\Omega)$

Fig. 2. The differential cross section for two-photon absorption, normalized with respect to field intensities $I_1 I_2$, as a function of the frequency of the photons. I_1, I_2 and $d\sigma^{(+2)}/d\Omega$ are in a.u. The energy of the projectile is $E_i = 100$ eV; $\mathbf{k}_i||Oz$ and the scattering angle is $\theta = 5°$. The polarization vectors are linear: $\boldsymbol{\varepsilon}_1||Oz$ and $\boldsymbol{\varepsilon}_2||Ox$. Solid line represents the differential cross section in (24), dotted line the electronic contribution and dot–dashed line the mixed contribution.

effects are important. Our calculations were performed for linear polarizations. We have chosen $\boldsymbol{\varepsilon}_1||Oz$ and $\boldsymbol{\varepsilon}_2 \perp \boldsymbol{\varepsilon}_1$, the polarization vectors defining the scattering plane.

The differential cross section (solid line) exhibits a series of resonances, located between 6 and 6.8 eV. These resonances occur at photon frequencies such that $2\omega = |E_{1s}|(1 - 1/n^2)$ for $n > 2$, where n is the principal quantum number. They correspond to poles in the radial integrals $\mathcal{T}'_{sd}$ and $\mathcal{T}''_{sd}$ which appear in the atomic term. The resonance corresponding to $n = 2$, i.e., $\omega = 5$ eV, does not exist for orthogonal polarization: the connected pole appears in (23) only in the radial integral $\mathcal{T}''_{sd}$, which multiplies the scalar product $\boldsymbol{\varepsilon}_1 \cdot \boldsymbol{\varepsilon}_2$, which vanishes. To emphasize the origin of these resonances we have plotted also in Fig. 2 the electronic (dotted) and mixed (dot–dashed) contributions, which were calculated when only T_P and T_M, respectively, were taken into account in (24).

We believe that this series of resonances is particularly interesting from the experimental point of view. Indeed, two-photon processes may be easier to detect at photon energies close to one of these resonances because they do not correspond to resonances of the lower order processes, namely one-photon absorption/emission.

A second series of resonances, not shown in Fig. 2, is located between 10 and 13.6 eV. They occur for photon frequencies such that $\omega = |E_{1s}|(1 - 1/n^2)$, where $n \geq 2$. This time the resonances correspond to poles which exist in three radial integrals: $\mathcal{T}_{M}$, $\mathcal{T}'_{sd}$, and $\mathcal{T}''_{sd}$.
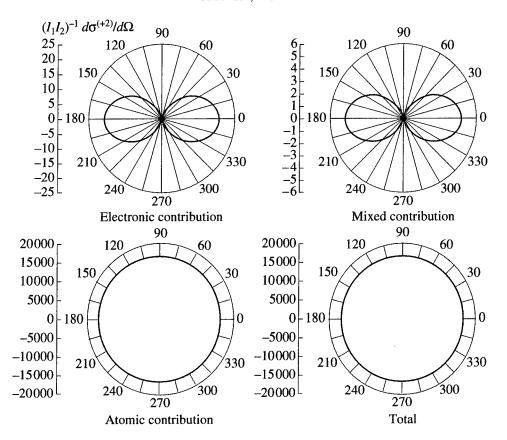
Fig. 3. The differential cross section for two-photon absorption, normalized with respect to field intensities $I_1 I_2$, as a function of the azimuthal angle ϕ. $I_1 I_2$ and $d\sigma^{(+2)}/d\Omega$ are in a.u. The energy of the projectile is $E_i = 100$ eV, $\mathbf{k}_i \| Oz$ and the scattering angle is $\theta = 20°$. The frequency of the photons is $\omega = 5$ eV, $\boldsymbol{\varepsilon}_1 = \mathbf{e}_z$, and $\boldsymbol{\varepsilon}_2 = (\mathbf{e}_z + i\mathbf{e}_x)/\sqrt{2}$. The electronic, mixed, and atomic contributions are also plotted in the same conditions as the differential cross section.

In Fig. 2 the differential cross section (solid line) has also a series of minima. The first minimum is due to the fact that, in this geometry, the differential cross section in (24) is proportional to $|(\boldsymbol{\varepsilon}_1 \cdot \mathbf{q})|^2 = |\mathbf{k}_i - k_f \cos\theta|^2$, which is vanishing at $\theta = 5°$. The other minima are due to interferences between the electronic, mixed, and atomic terms.

3.2. Azimuthal Angular Distribution

We have found out that the azimuthal angular distributions of the scattered electrons are significantly modified in the case of complex polarization vectors if virtual transitions to continuum are energetically allowed, i.e., $2\omega > |E_{1s}|$. To illustrate this remark we discuss two distinct cases. In the first case the photon frequency corresponds to KrF laser, $\omega = 5$ eV. One has $2\omega < |E_{1s}|$ and the radial integrals $\mathcal{T}_{\mathcal{M}}$, $\mathcal{T}_{\mathcal{A}}'$ and $\mathcal{T}_{\mathcal{A}}''$ are real. On the contrary, in the second case, when the frequency of the photons corresponds to the second harmonic of KrF, one has $2\omega > |E_{1s}|$ and the corresponding radial integrals are complex. Each of these frequencies corresponds to atomic resonances. For each of these frequencies, we present the differential cross section of two-photon absorption at a fixed scattering angle, $\theta = 20°$, as a func-

tion of the azimuthal angle ϕ. Two different choices of the polarization vectors were investigated.

1. $\boldsymbol{\varepsilon}_1 = \mathbf{e}_z$ and $\boldsymbol{\varepsilon}_2 = (\mathbf{e}_z + i\mathbf{e}_x)/\sqrt{2}$

In this case one laser beam, which direction defines the Ox axis, is linearly polarized with the polarization vector parallel to the initial momentum of the projectile, $\boldsymbol{\varepsilon}_1 \| Oz$. The other laser beam, of the same frequency, defines the Oy-axis and is circularly polarized,

$$\boldsymbol{\varepsilon}_2 \equiv (\mathbf{e}_z + i\mathbf{e}_x)/\sqrt{2}.$$

For this choice of polarizations the electronic and the mixed terms in (19, 21) have the same ϕ-dependence, namely of the form $\alpha(\alpha + i\beta\cos\phi)$. As a consequence, the electronic and the mixed contribution to the differential cross section are symmetric with respect to the reflection in the planes xOz and yOz for both frequencies, $\omega = 5$ eV in Fig. 3 and $\omega = 10$ eV in Fig. 4.

The atomic term (23) has a different ϕ-dependence, given by

$$T_A \sim \mathcal{T}_{\mathcal{A}}'' + \alpha^2 \mathcal{T}_{\mathcal{A}}' + i\alpha\beta\mathcal{T}_{\mathcal{A}}' \cos\phi. \qquad (25)$$

The atomic contribution has the above mentioned reflection properties only in Fig. 3, where $\omega = 5$ eV.
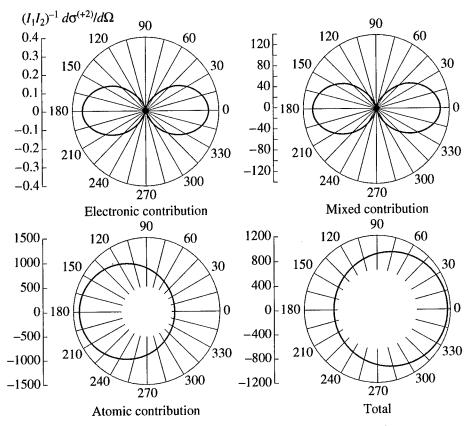
$(I_1 I_2)^{-1} d\sigma^{(+2)}/d\Omega$

Electronic contribution

Mixed contribution

Atomic contribution

Total

Fig. 4. Same as Fig. 3, but $\omega = 10$ eV.

$(I_1 I_2)^{-1} d\sigma^{(+2)}/d\Omega$
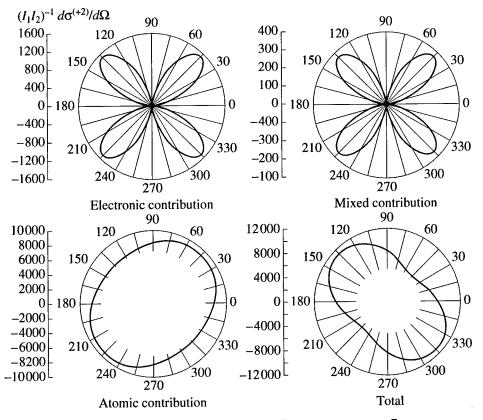
Electronic contribution

Mixed contribution

Atomic contribution

Total

Fig. 5. Same as Fig. 3, but $\varepsilon_1 \equiv (e_z + ie_x)/\sqrt{2}$ and $\varepsilon_2 \equiv (e_y + ie_z)/\sqrt{2}$.
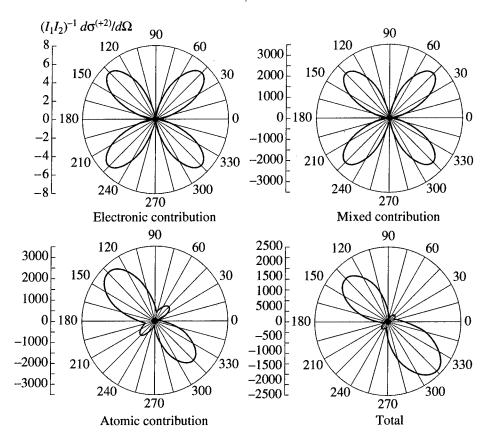
Fig. 6. Same as Fig. 5, but $\omega = 10$ eV.

In Fig. 4, where $\omega = 10$ eV, the atomic contribution has only one symmetry plane. Indeed, $\phi \longrightarrow -\phi$ is a symmetry operation for the quantity in (25), therefore xOz is a symmetry plane. yOz is no more a symmetry plane because both $\mathcal{T}'_{sA}$ and $\mathcal{T}''_{sA}$ are complex and the modulus square of the quantity in (25) is not symmetric to the change $\phi = \pi/2 - \xi \longrightarrow \pi/2 + \xi$.

At small scattering angles in general and in particular close to resonances, where the dressing effects are important, there are interferences between the atomic and the mixed contributions. They impose the ϕ-dependence of the differential cross section (24), given by

$$\frac{d\sigma}{d\Omega} \sim \left| \mathcal{T}''_{sA} + \alpha^2 \mathcal{T}_1 + i\alpha\beta \mathcal{T}_1 \cos\phi \right|^2, \quad (26)$$

where $\mathcal{T}_1 = \mathcal{T}_{\mathcal{P}} + \mathcal{T}_{\mathcal{M}} + \mathcal{T}'_{sA}$ and $\mathcal{T}_{\mathcal{P}}$ is the radial part of the electronic term (19). In particular, only $\mathcal{T}''_{sA}$ has a pole when $\omega = 5$ eV, therefore the atomic contribution in Fig. 3 is almost ϕ-independent (a circle) and it is dominant in the differential cross section. The situation is different in Fig. 4 because three radial integrals, $\mathcal{T}_{\mathcal{M}}$, $\mathcal{T}'_{sA}$ and $\mathcal{T}''_{sA}$, have poles when $\omega' = 10$ eV.

At large scattering angles the electronic term is dominant and it imposes the angular distribution of the differential cross section.

We note also that the change from right to left circular polarization implies a simultaneous change of the sign of the last term in (25)–(26), which is equivalent to a rotation by π of the curves in Figs. 3 and 4. This rotation is visible in the angular distributions only if the radial integrals have complex values, i.e., when $2\omega > |E_{1s}|$.

2. $\varepsilon_1 = (\mathbf{e}_z + i\mathbf{e}_x)/\sqrt{2}$ and $\varepsilon_2 = (\mathbf{e}_y + i\mathbf{e}_z)/\sqrt{2}$

In this second case both polarization vectors are right circularly polarized. The direction of the first laser beam defines the Oy-axis, the other one the Ox-axis.

The electronic and the mixed terms have again the same ϕ-dependence, given by

$$\alpha\beta(\sin\phi - \cos\phi) + i(\alpha^2 + \beta^2 \sin\phi\cos\phi).$$

For both frequencies, $\omega_1 = 5$ eV in Fig. 5 and $\omega_2 = 10$ eV in Fig. 6, the first ($\omega = \pi/4$) and the second ($\phi = 3\pi/4$) bisector of the angle xOy are symmetry axes of the electronic and the mixed contributions to the differential cross section.

The atomic term (23) has a different ϕ-dependence, namely

$$T_A \sim \alpha\beta \mathcal{T}'_{sA} (\sin\phi - \cos\phi)$$

$$+ i(\mathcal{T}''_{sA} + \alpha^2 \mathcal{T}'_{sA} + \beta^2 \mathcal{T}'_{sA} \sin\phi\cos\phi). \quad (27)$$

The atomic contribution has the two previous symmetry axes only when $\omega = 5$ eV (Fig. 5); when $\omega = 10$ eV the atomic part has only one symmetry axis: along the second bisector (Fig. 6). Since the atomic term is always important for the chosen value of θ, it will determine the symmetry properties of the differential cross section.

The study of two photons with left circular polarizations implies the change of the general sign in the second line of (27). The corresponding curves are rotated by π around the Oz-axis. Due to the number of symmetry axis, this rotation is relevant only for the atomic contribution and the differential cross section in Fig. 6, where $2\omega > |E_{1s}|$.

4. CONCLUSIONS

Our investigations show that the differential cross sections for two-photon free–free transitions are strongly influenced by the state of polarization of the two photons in the domain where the dressing effects are important, that means for small scattering angles and in the vicinity of atomic resonances.

When at least one polarization vector is complex, one mirror symmetry is broken in the azimuthal angular distribution of the scattered electron if the virtual transitions to continuum of the bound electron are energetically allowed, i.e., $2\omega > |E_1|$. We have shown also that the differential cross sections of two-photon free–free transitions are sensible with respect to the helicity of the polarization vectors. These effects are present only

if the atomic diagrams (Fig. 1c) are included in the calculation.

REFERENCES

1. Wallbank, B. and Holmes, J.K., 1994, *J. Phys. B*, **27**, 1221; 1994, *J. Phys. B*, **27**, 5405.
2. Cionga, A., Dimou, L., and Faisal, F.H.M., 1997, *J. Phys. B*, **30**, L361; see also the references herein.
3. Kracke, G., Briggs, J.S., Dubois, A., et al., 1994, *J. Phys. B*, **27**, 3241.
4. Dörr, M., Joachain, C.J., Potvliege, R.M., and Vučić, S., 1994, *Phys. Rev. A*, **49**, 4852.
5. Bunkin F.V. and Fedorov, M.V., 1965, *Zh. Eksp. Teor. Fiz.*, **49**, 1215 [1966, *Sov. Phys. JETP*, **22**, 884].
6. Florescu, V. and Marian, T., 1986, *Phys. Rev. A*, **34**, 4641.
7. Cionga, A. and Florescu, V., 1992, *Phys. Rev. A*, **45**, 5282.
8. Florescu, V., Halasz, A., and Marinescu, M., 1993, *Phys. Rev. A*, **47**, 394.
9. Cionga, A. and Buică, G., to be published.

Nonlinear Processes in Liquid Water under Infrared Laser Radiation Resonant for H₂O Molecules

Yu. A. Bykovskii, D. V. Klotchkov, V. B. Oshurko, and A. A. Chistyakov

Moscow Engineering Physics Institute, Kashirskoe sh. 31, Moscow, 115409 Russia

Received September 5, 1997

Abstract—Molecules of liquid water are excited in the range of OH-stretch vibrations by intense nanosecond laser pulses. Nonmonotonous dependence of water absorption magnitude on radiation intensity at 3.36 μm wavelength has been observed. Raman OH-stretching spectra from water under infrared laser radiation are registered. Nonthermal band-shape changes of Raman spectrum are detected in the case of resonant excitation of water molecules with 3.36 mm wavelength radiation. Nonequilibrium distribution of excitation between strongly hydrogen-bonded and essentially free H₂O molecules is proposed for experimental results explanation.

1. INTRODUCTION

Water continues to be one of the most extensively studied molecular systems because of its importance in chemical and biological processes. But its multiplicity of structures due to intermolecular hydrogen bonds leads to significant problems in understanding of chemical and physical mechanisms of molecular processes (intermolecular interactions) in liquid water. Also the chemical structures of the water associates are difficult to determine because of the complexity of interaction of water molecules. So, water is generally known to possess a number of unique physical properties, such as anomalous behaviors of thermodynamical, electrical, and other parameters under different temperatures and pressures [1]. Also, water demonstrates unexpected nonlinear optical properties.

The effect of absorption saturation of water in OH-stretch vibration region at rather low intensities (~10^6 W/cm^2) has been recently discovered [2] and interpreted as a result of hydrogen-bond rupture which leads to high-frequency shift of inhomogeneously broadened absorption band. This interpretation is passed of a model, which postulates that wide OH-stretch band of liquid water arises from the superposition of absorption bonds of two spectroscopically distinguishable classes of molecules. The first is strongly hydrogen-bonded in structures (clusters of different sizes) [3, 4]. A low-frequency region of inhomogeneously broadened OH-stretch absorption band corresponds for those molecules, because the strong intermolecular coupling results in a lowering of their OH-stretch frequency [5]. The second is thought to be weakly bonded or essentially free. This class of molecules forms high-frequency region of inhomogeneously broadened OH-stretch absorption band.

The character of nonlinear photoprocesses can also depend on the excitation region. The effect of absorption saturation of water, described in [2], has been observed in the range of 2.79–2.94 μm infrared radiation wavelengths. This excitation region (3580–3400 cm^{-1}) corresponds to weakly hydrogen-bonded water molecules. The character of chemical bonding and molecular interactions of strongly hydrogen-bonded water molecules can greatly differ from the case of non-hydrogen-bonded molecules. Therefore, the experiments on vibrational excitation of water with infrared radiation of >3 μm wavelengths (corresponding to hydrogen-bonded molecules) are necessary for description of water properties in optical region corresponding to strongly hydrogen-bonded H₂O molecules. The comparison of such experiments with previously executed [2] can disclose the influence of water structures on its optical properties.

This paper investigates the relation between the absorption of liquid water in OH-stretch absorption band region and infrared pulse (8 ns) laser radiation intensity. Also we test the band-shape changes of Raman spectra from water in the OH-stretching region due to resonance excitation of H₂O molecules with infrared laser radiation (2.73 and 3.36 μm wavelengths).

2. EXPERIMENTAL

The experiments on the resonant excitation of water molecules have been carried out by the use of the infrared Optical Parametric Oscillator (OPO), with pulse duration of ~8 ns and pulse energy up to 5 mJ. This device has been made of LiNbO₃ nonlinear crystal and single-cavity scheme [6]. The tuning waverange of LiNbO₃-based OPO is 2.4–4.0 μm (4100–2500 cm^{-1}). The IR spectrum of liquid water displays a wide absorption band at 3000–3800 cm^{-1}. So, IR pulse is tuned to this frequency position by the choice of the angle between the crystal and the pumping beam axis. Radiation of YAG : Nd³⁺ pulsed laser (λ = 1.064 μm, τ_p = 10 ns) has been used for OPO pumping.

The principle installation of absorption experiments is demonstrated in Fig. 1. All absorption measurements were made under ambient conditions. The thickness of the sample was about 10^{-3} cm. Two channels were used for water absorption registration. We changed the radiation intensity on the sample with Ge filters (N_1). The total number of Ge filters (N) in the first channel was constant. As a result, the radiation intensity on the photodetector (PhD$_1$) was also constant and independent of the radiation intensity on the sample. The number of filters in the second channel was chosen to guarantee the same radiation intensities on both photodetectors. Identical photodetectors in both channels provide the coincidence of photosensitivities. Therefore, there is no influence of pulse energy instability on the absorption data registered. Any change of ratio between signals in two channels was determined by the corresponding change of absorption coefficient of water sample.

The second harmonic of YAG : Nd^{3+} laser ($\lambda = 532$ nm, $\tau_p = 8$ ns) was used to excite the Raman spectrum of water sample. Water specimen initially at 300 K and atmospheric pressure was contained in quartz cell. Raman-scattered light, exiting from the a quartz cell, was collected at 90° to the axis of exciting beam with three-lens quartz condensor. The condensor formed an image of the excitation region of the sample on the slit of a monochromator. The Raman scattering signals were registered with a photomultiplier. Digitized electric signals were collected and recorded by a computer. Two channels were used for Raman spectra registration. The first one has been described above. The second channel is necessary to test exciting pulse energy. The Raman scattering measurements were carried out in the temperature range of 300–350 K. In experiments on registration of Raman scattering from water, excited by IR laser radiation, the beam convergence of IR and 532 nm wavelengths radiation in the same region of the sample was realized. Raman-scattered light was collected only from IR-excited region of water sample.

In all experiments we have used dust-free double-destilled water. Great care was taken with regard to water purity.

3. RESULTS AND DISCUSSION

Figure 2 shows the dependence of the water absorption magnitude on the radiation intensity of 3.36 μm (curve 1) and 2.73 μm (curve 2) wavelengths, respectively. The wavelengths were chosen on the base of coincidence of absorption coefficients in low-frequency and high-frequency regions of inhomogeneously broadened OH-stretch absorption band of water. By this choice we provide the coincidence of thermodynamical conditions in the sample under different wavelengths radiation. The figure demonstrates a nonmonotonous dependence of the water absorption magnitude on radiation intensity at 3.36 μm wavelength, whereas the corresponding dependence appears
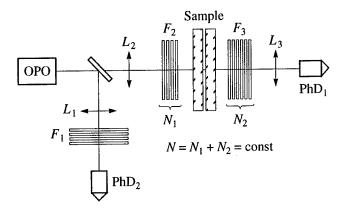

Fig. 1. Principle installation of absorption experiments: L_1, L_2, L_3, quartz lenses; F_1, F_2, F_3, banks of Ge filters; PhD$_1$, PhD$_2$, photodetectors; OPO, Optical Parametric Oscillator.
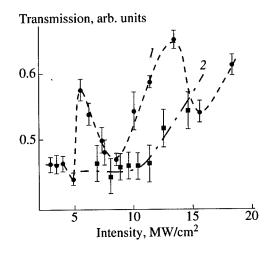

Fig. 2. Dependence of the water absorption magnitude on the IR radiation intensity. The dashed curve corresponds to water absorption at 3.36 μm wavelength. The dash–dotted curve corresponds to water absorption at 2.73 μm wavelength.

to be monotonous at 2.73 μm wavelength under the same thermodynamical conditions. (Nonmonotonous dependencies of water absorption magnitude on radiation intensity at other wavelengths corresponding to the low-frequency region of the absorption bond of water have been detected. These results will be published separately.) It should be noted that absorption at 3.36 μm wavelength corresponds to the hydrogen-bonded molecules (clusters). So, we can suppose (see Fig. 2) that nonmonotonous character of absorption is determined by dissociation of hydrogen bonds mostly in water clusters. But this is true only for thermodynamically nonequilibrium distribution of excitation between clusters and "free" water molecules throughout laser pulse duration (8 ns). It is known that the rate of vibrational relaxation can depend on the type of structure (clusters or "free molecules"), that incorporates the selectively excited molecule [7, 8]. It therefore can be expected
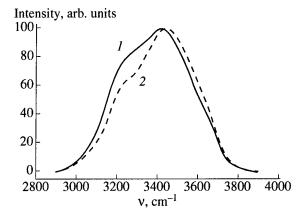
Intensity, arb. units

Fig. 3. Comparison of spontaneous Raman spectra of OH-stretch band of liquid water for $T = 300$ and 350 K. The solid curve is the spectrum of water at a temperature of 300 K. The dashed curve is the spectrum of water at a temperature of 350 K.
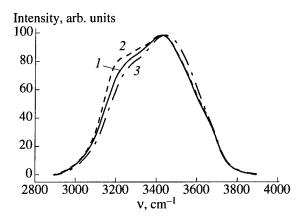
Intensity, arb. units

Fig. 4. Comparison of spontaneous Raman spectra of OH-stretch band of liquid water for normal and infrared excitation conditions. The solid curve is the spectrum of water at $T = 300$ K. The dashed and dash–dotted curves are the spectra of water under the action of laser IR radiation with 3.36 and 2.73 μm wavelengths, respectively.

that hydrogen bond dissociation should proceed differently in various types of water structures.

To test this hypothesis a number of experiments has been made to register the Raman OH-stretching spectra from water under infrared radiation of ~5 MW/cm² intensity with the same (2.73 and 3.36 μm) wavelengths. It is known that Raman spectra from liquid water are greatly dependent on temperature. The scattering intensity drops with temperature rise at wavelengths, corresponding to strongly hydrogen-bonded molecules and rises in the area of "free" water [9]. This effect can be easily explained by the processes of hydrogen bond rupture wising temperatures. We also report the experiments on Raman scattering spectra registration versus temperature of water. The results fully correspond to the known ones. Figure 3 shows the

Raman OH-stretching spectra from water at 300 (*1*) and 350 K (*2*), respectively. The heating $\Delta T = 50$ K (between 1 and 2) is chosen on the base of the maximum heating temperature under laser infrared radiation pulse.

Raman spectra of liquid water under the action of 3.36 (curve *2*) and 2.73 μm (curve *3*) wavelengths radiation are presented in Fig. 4. The exciting radiation intensities were the same (~5 MW/cm²) for both wavelengths. Comparison of these results with the Raman spectrum of water under the ambient conditions (curve *1*) shows that Raman scattering signal from water under the action of 3.36 μm wavelength radiation rises only in the spectral region corresponding to strongly hydrogen-bonded molecules (i.e., molecules incorporated in clusters). The increase of Raman scattering signal was observed at frequencies that are considerably shifted from exciting radiation wavelength. On the other hand, as Fig. 4 shows, the Raman spectrum of water under the action of 2.73 μm wavelength radiation ("free" water molecules excitation) appears to be generally similar to the corresponding spectrum in the case of thermodynamically equivalent equilibrium heating (Fig. 3). Thus, the nature of band-shape changes of Raman spectrum of water is fundamentally different in the cases of resonant excitation of "free" and hydrogen-bonded water molecules. But, as has been mentioned above, the thermodynamic conditions are the same for both 2.73 and 3.36 μm wavelengths excitation. Hence, the band-shape changes of Raman spectrum of liquid water under the action of 3.36 μm radiation are nonthermal and determined only by the choice of exciting radiation wavelength, resonant for hydrogen-bonded H_2O molecules.

So, the observed results should be better interpreted in terms of hydrogen bond dissociation in water clusters of different types. Therefore, the cluster dissociation products can enable the Raman signal rise at frequencies shifted relative to the frequencies of exciting radiation. Furthermore, as the exciting radiation grows, the equilibrium in the source cluster/products system can shift, which may cause the effect shown in Fig. 2.

4. CONCLUSIONS

Thus, in this paper the effect of nonmonotonous water absorption in low-frequency region of inhomogeneously broadened OH-stretch absorption band has been found. Also the rise of intensity of Raman scattering from water under the influence of pulse infrared laser radiation has been observed. The experiments show that these phenomena can be interpreted in terms of nonequilibrium distribution of excitation between clusters and "free molecules."

ACKNOWLEDGMENTS

REFERENCES

1. Aysenberg, D. and Kautsman, B., 1975, *Structure and Properties of Water* (Leningrad) (in Russian).

2. Vodopyanov, K.L., 1990, *Zh. Eksp. Teor. Fiz.*, **97/1**, 205.

3. Lee, C., Chen, H., and Fitzgerald, G., 1995, *J. Chem. Phys.*, **102**, 1266.

4. Aleshkevich, V.A., Baranov, A.N., and Saletsky, A.M., *Proc. SPIE*, **2965**, 97.

5. Holmes, N.C., Nellis, W.J., and Graham, W.B., 1985, *Phys. Rev. Lett.*, **55**, 2433.

6. Bahirkin, Yu.A., Bykovskii, Yu.A., Chistyakov, A.A., *et al.*, 1991, *Kristallografiya*, **36**, 1226.

7. Bahirkin, Yu.A., Bykovskii, Yu.A., Chistyakov, A.A., *et al.* 1991, *Zh. Eksp. Teor. Fiz.*, **99**, 1739.

8. Barinov, A.V., Bahirkin, Yu.A., Bykovskii, Yu.A., *et al.*, 1993, *JETP Lett.*, **58**, 23.

9. Walrafen, G.E., Fisher, M.A., Hokmabadi, M.S., and Yang, W.H., 1986, *J. Chem. Phys.*, **85**(12).

Er : YAG Laser in Dentistry

H. Jelínková*, T. Dostálová**, K. Hamal*, O. Krejsa**, J. Kubelka***, and S. Procházka***

* Czech Technical University, Faculty of Nuclear Sciences and Physical Engineering,
Břehová 7, Prague 1, 115 19 Czech Republic
e-mail: hjelin@troja.fjfi.cvut.cz
** The Institute of Dental Research, Vinohradská 48, Prague 2, 120 60 Czech Republic
e-mail: vuspraha@mbox.vol.cz
*** Preciosa-Crytur, Přepeřská 1447, Turnov, 511 19 Czech Republic
e-mail: pro@crytur.preciosa.cz
Received August 8, 1997

Abstract—Pulsed Er : YAG laser system has been found to be an effective instrument for drilling hard dental tissue. This article summarizes the results which were obtained with the constructed Er : YAG dental laser system whose radiation interacts with the hard dental tissue. Different tests with this system were made *in vitro*. The shapes of the prepared cavities were studied either by using varying laser energies (from 70 to 500 mJ) for a constant number of pulses or varying number of pulses (from one to thirty) for constant laser energy. Also the tests with the cutting speed were made. It was recognized that the preparation with the laser radiation is a little slower than with a classical technique. Besides the study of higher energy effect, the low–energy Er : YAG laser radiation was used for laser etching and conditioning. It was proved that the energy about 100 mJ is sufficient for tooth tissue conditioning. The measured share bond strength of the composite restoration with the tooth tissue treated by laser radiation is comparable with the strength which is needed for the example when the tissue was prepared by classical chemical treatment.

1. INTRODUCTION

The early dental laser research began in 1963 [1] which was a little later than in some other fields of medicine, for example, ophthalmology or dermatology. It was due to the fact that the first dental research was based on the ruby laser whose wavelength is not suitable for dental treatment [2]. Through the years many other lasers were investigated with better or worst results but for the practice only Er : YAG laser was chosen. The mid-infrared radiation of this laser showed the remarkable ablation effect in hard dental tissue [3] and the solid–state Er : YAG laser has reasonable compactness and reliability.

Since 1988, when the first publication [4] on enamel and dentine ablation by Er : YAG laser radiation appeared, the number of investigations using the laser as a dental tool has been steadily increasing. Most of the published papers concentrate on *in vitro* studies of cavity preparation, measurements of temperature increase, microscopical analysis and studies of the cooling effect. But, nevertheless, some questions of the primary parameters of laser preparation and application of it are still to be clarified. The aim of the first part of our study was to evaluate the depth and diameter of the prepared cavity as against the laser exposure, number of pulses, and type of hard tissue and further to compare the speed of the laser preparation to have a possibility to define the differences between the classical and the laser drilling effect.

In the second part of our study the other applications of Er : YAG laser radiation interacting with tooth's tissue—the etching of the enamel and Er : YAG laser surface conditioning where investigated. This procedure could be used for the preparation of tooth tissue before the restoration compensation is bonding to it. The attachment of composite resin to the etched surface is achieved by application of a low–viscosity liquid resin or intermediate bonding agent, which flows into the micropores created by etching. These tags achieve a mechanical bond on polymerization. The disadvantage of using acid for etching of the enamel and dentine are the removal of the enamel surface layer, variability in etched depth, contamination of the etched surface with water and oil, damage of the etched pattern by over-rigorous rubbing, inadequate washing or drying affecting of bond strength [5]. For that reason dentists would like to find an alternative procedure for preparing of the enamel surface. One of the effective methods may be to pretreat the enamel by laser radiation. According to the literature, various types of lasers were used, namely, ruby laser [6], CO_2 laser [7], Nd : YAG laser [8], and Er : YAG laser [9, 10]. Therefore the aim of the second part of this study was to compare the topography of Er : YAG–laser- and acid-etched enamel surfaces and to measure the shear bond strength for both types of treatment and examine the effect of Er : YAG laser and acid conditioning to the bond of composite resin to and dental tissues.

2. GENERATION OF Er : YAG LASER RADIATION

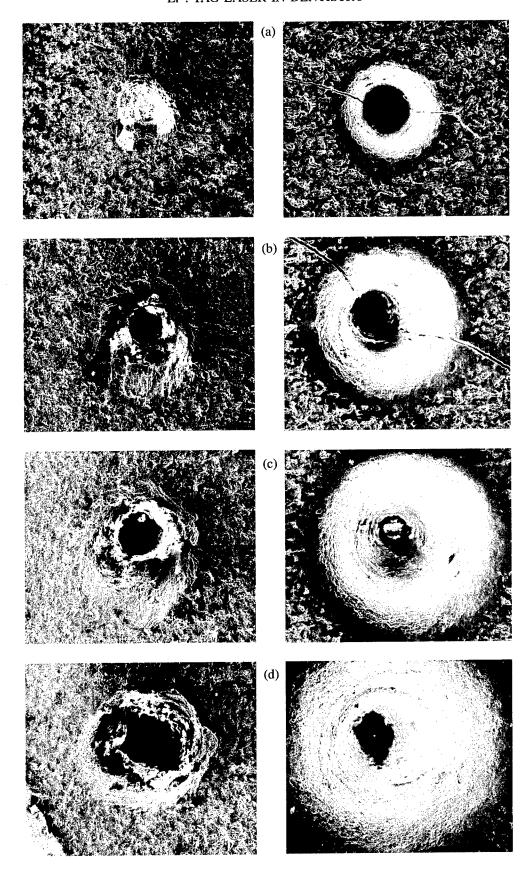Our experiment was based on the *in vitro* interaction of the Er : YAG laser radiation with the hard dental

Fig. 1. Dependence of the prepared hole depths in the enamel and dentin on the laser radiation energy for a constant number of applied pulses; energy (a) 90, (b) 190, (c) 300, and (d) 400 mJ; 10 pulses; rep. rate 1 Hz (magnification 100×).

tissues. For that reason the Er : YAG drilling laser system was constructed. The system had a laser head with an articulated arm, water cooler, and power supply with automatic control. The laser head consisted of an Er : YAG crystal with a diameter of 4 mm and length of 100 mm placed along with a xenon flashlamp into the pumping cavity (LMI 1620). The resonator enabled us to generate the output energy up to 700 mJ in a free running (long–pulse mode) regime. The length of the generated pulses was measured to be 200 μs. By the articulated arm formed by eight mirrors ($R = 100\%$ for $\lambda = 2.94$ μm, $R = 80\%$ for $\lambda = 0.63$ μm, angle of incidence 90°) the radiation was incited on the investigated place and focused by the CaF_2 lens ($f = 55$ mm) placed inside the dental tip on the tested samples of the tooth's tissue. In a previous study [11–14] it was proved that during laser exposure the tissue has to be cooled to prevent carbonization of the surrounding part of it. For that reason fine water mist (water–50 ml/min with the pressure of 0.2 MPa, air pressure of 0.3 MPa) was used. Therefore during the experiment along with the articulated arm, the water and air were focused at the same place as laser radiation.

3. EXPERIMENTAL ARRANGEMENT AND RESULTS

3.1. Shape and Depth of Prepared Tooth's Cavity

To examine the dependence of prepared cavity shape and depth on laser radiation energy fifteen flat surfaces of teeth along with three samples of ivory (all samples cut into the longitudinal section to have the thickness from 3 to 5 mm and polished to have two parallel surfaces) were gradually irradiated (a) by five different energies from 70 to 500 mJ (ten pulses for each energy), (b) one to thirty pulses were used for the exposure with a constant energy. In both cases a repetition rate was 1 or 2 Hz.

With the exposure of 10 pulses with the energy from 70 to 500 mJ, the depth of the generated holes increased from 0.14 up to 0.9 mm in the enamel, and from 0.55 up to 1.51 mm in the dentine (Fig. 1). It was seen that some saturation effect appeared for the energy about 400 mJ in the enamel and 300 mJ in the dentine. The change of the diameter of holes in the enamel was from

0.08 up to 0.52 mm and in the dentine from 0.18 up to 0.52 mm.

The dependence of the hole depth prepared in the enamel and dentine by different numbers of pulses (from 2 up to 20, for 300 mJ input laser energy) is shown on Fig. 2. The depth of the generated holes increased from 0.2 mm (2 pulses) up to 0.6 mm (20 pulses) in the enamel and 0.4 mm (2 pulses) up to 1.5 mm (20 pulses) in the dentine. The saturation effect appears when more than 10 pulses were used for the preparation. The corresponding change of the hole diameters in the dentine was from 0.17 mm (2 pulses) up to 0.39 mm (20 pulses).

The measured depth of holes prepared in the sample of ivory was from 0.42 mm (1 pulse/115 mJ of input energy) up to 2.5 mm (30 pulses/410 mJ of input energy). Also for ivory, in comparison with the tooth tissue much more homogeneous material, some saturation effect appeared around the energy 300 mJ/10 pulses.

3.2. Comparison of Preparation Speed

To define the differences between the classical and the laser drilling effects 30 samples of extracted human teeth were cut by both drilling machine it is by the Er : YAG laser and by the classical driller (Sirona M1, Siemens). The cut was made transversally, 5 to 7 mm from the occlusal surface of the crown. Two laser energies, 344 and 578 mJ, with the repetition rate of 3 Hz, were used and the number of pulses required for cutting was observed. The time of preparation was measured for both the laser and classical drilling machine.

To evaluate the circumference and area of sections, a CCD camera Mitsubishi (Japan) and computer analyzing system Sigma Scan and Sigma Scan Pro (USA) were used. A JEOL and TESCAN scanning electron microscopes (JEOL Superprobe 733, TESCAN Brno 92) were applied to observe the surface structure of the sections—roughness of the cut area. Also, the element analysis of the cut surface was executed by TESCAN. The results from tooth cross sections measurements are summarized in the table. The circumference and area of the sections were similar for both the Er : YAG laser and classical drilling machine. For the laser treatment no differences were found between energies 344 and 578 mJ (also here the saturation effect was proved) and thus the results are presented in one group only. However,

Evaluation of preparation speed: classical and laser drilling machine

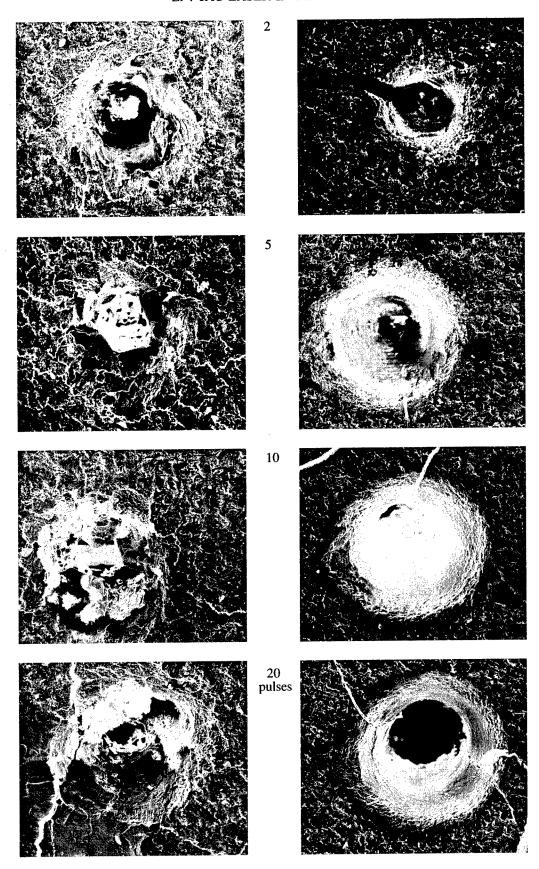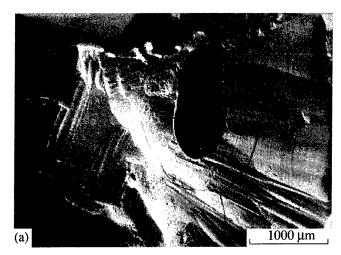|	Laser drilling system		Classical drilling machine	
	mean	SE	mean	SE
Circumference of section [mm]	20.26	0.77	25.02	2.04
Area of section [mm^2]	28.61	2.05	43.02	6.98
Number of pulses	465.0	34.2	–	–
Preparation time [s]	155.0	11.4	28.4	3.20
Time [s/mm^2]	5.42	0.64	0.66	0.11

Fig. 2. Dependence of the hole depth prepared in the enamel and dentine by different numbers of pulses (from 2 up to 20) for a constant input laser energy 300 mJ (magnification 150×).
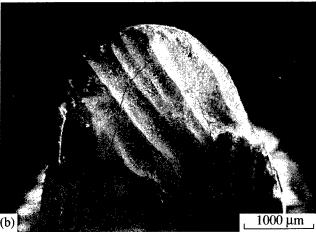
Fig. 3. Tooth crown decapitation surface (a) after cutting tissue by the classical driller (Sirona M1, Siemens) and (b) after laser ablation by Er : YAG laser driller.
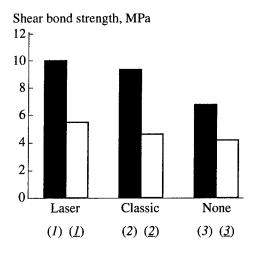

Fig. 4. Shear bond strength of the composite restoration with the tooth tissue. Summary of results (1–3) without and (1–3) with thermocycling (1000 cycles, from 10 to 37°C in water). Preliminary treatment of the tooth surface by: (Laser) Er : YAG laser radiation, (Classic) classical treatment by acid etching and (none) natural surface of tooth without conditioning.

significant differences were observed between the time of preparation. It was 155 s when the Er : YAG laser was used and 28.4 s for the classical drilling machine. If relating the time of preparation to the area of the cut surface, the time of preparation per 1 mm² was 5.42 s for the former and 0.66 s for the latter system. It is seen that the laser treatment is eight times slower than the classical preparation technique.

When the cut surfaces roughness was compared, no great differences were found. From Figs. 3a and 3b it follows that the surface roughness is similar. Only with the classical drilling system the structure is sharper in comparison with a smoother surface cut by laser ablation. There were no differences between distribution of the elements, especially calcium and phosphorus.

3.3. Laser Radiation Conditioning of Tooth Tissue

For this experiment 30 freshly extracted healthy human teeth—molars—caries– and restorations-free were used. Enamel and dentine cross sections (from 2 to 3 mm from pulp chamber—X-ray control, Trophy, France) were cut with low speed saw (Isomet, AB Buehler, Chicago, USA). The enamel and dentine surfaces were further prepared with strip grinder (AB Buehler, Chicago, USA) by abrasive strips (the finest 600 grit). The smear layer was removed in EDTA (pH 7.4, 0.5 M).

Ten flat surfaces of teeth were irradiated by the Er : YAG laser (100 mJ/2 Hz). Surfaces of every sample were covered by laser pulses aimed one beside other. The surface of other ten molars was prepared with steel burs (round ISO 014, Maillefer, Swisse, cylinder square ISO 012, Maillefer, Swisse) in the classical handpiece. The samples were etched for 60 s with 35% phosphoric acid (Esticid Gel, Kuker, Germany). Ten remaining teeth were not treated and stayed flat with natural surfaces only. When all 30 samples of tooth tissues were prepared, the composite resin filling (Charisma, Kulza, Germany) was applied on every surface. The cleaning and conditioning of dentine with Denthesive cleaner (40 s) was performed. Dentine bonding with Denthesive A + B mixture was applied to the dentine surface and base lining (15 s). The cavity was sealed with Adhesive bond which was placed on the enamel and dentin surface and polymerized with a Translux light unit (20 s). Then the composite restoration was built up and cured with the Translux and finished with discs/silicone polishers.

All samples were stored in saline solution with the temperature 37°C. First group (15 teeth, five from every group) was tested after 24 hr. Second group (15 teeth, five from every group) was submit to thermocycling (1000 cycles, temperature 37°C and 10°C, dwell 20 s). Tested retentive strength was measured using a universal tester L + R Alvetron (AB Lorentzen, Wettre, Sweden). Load was applied at a cross–head speed of 0.5 cm/min until the restoration was separated from the tooth. The significant differences between the experi-

mental and control groups were calculated by Student's test at probability $P = 0.05$.

The retentive strengths of composite restoration with teeth are presented on Fig. 4. The shear bond strength of composite resin for the Er : YAG laser radiation ablation and etching was 9.96 MPa (SE–0.93) (Fig. 4, *1*), while for the classical drilling and acid etching it was 9.33 MPa (SE–0.52) (Fig. 4, *2*). A significant difference was measured for the natural flat surface of tooth samples without any conditioning of surface. In this case the shear bond strength was 6.74 MPa (SE–0.78) (Fig. 4, *3*).

Changes of temperature (specially increase from 10°C to 37°C and back to 10°C, dwell 20s, 1000 cycles) have direct influence on the retentive effect of composite resin restoration. After thermocycling in water the retentive strengths declined to 5.52 MPa (SE–0.51) for laser etching (Fig. 4, (*1*)), to 4.62 MPa (SE–0.37) for acid conditioning (Fig. 4, (*2*)), and to 4.19 MPa (SE–0.81) for natural flat surface (Fig. 4, (*3*)). The decline for the last case is significant. From the results follows that the methods of the tooth tissue primary treatment by the classical (chemical) or by the Er : YAG laser method are comparable. Only a little better results were found for the laser conditioning.

4. CONCLUSIONS

This studies summarize the results of the interaction of Er : YAG laser radiation with the hard dental tissues. It has been demonstrated that the higher energy (more than 200 mJ) of Er : YAG laser radiation might drill very well defined holes into the enamel and dentine. With proper cooling, the holes are clean without considerable damage of the adjacent hard substances and without dentine carbonization. For an effective ablation process there exist an optimum energy and dose of number of pulses. The chosen parameters for laser treatment are pulse energy from 300 up to 400 mJ and pulse repetition rate from 2 to 3 Hz when the enamel has to be prepared, and 250 mJ applied with 2 Hz for dentine preparation. In this case also the time of preparation is acceptable and admitting that the laser preparation is painless, from the point of view of the patient the prolonged time of preparation is acceptable.

The energy below 200 mJ is sufficient for the tooth tissue conditioning. The measured share bond strength of the composite restoration with the tooth tissue is approximately the same value for the classical and laser radiation pretreatment but using a laser radiation it is possible to decrease a bad influence of that primary treatment on the surrounding tissue as could exists when the classical chemical treatment is used.

As a conclusion it is possible to that the Er : YAG laser radiation can be safely used for the hard tissue preparation and also for the tissue conditioning.

ACKNOWLEDGMENTS

REFERENCES

1. Stern, R.H. and Sognnaes, R.F., 1964, *J. Dent. Res.*, **43**, Abstract 307, 873.
2. Gordon, T.E., 1967, *J. Am. Dent. Assoc.*, **74**, 398.
3. Jelinkova, H. *et al.*, 1994, *Proc. of CLEO/EUROPE-EQEC, Medical and Biological Appl.*, 62.
4. Hibst, R., Keller, U., and Steiner, R., 1988, *Laser in Medicine and Surgery*, **4**, 163.
5. Jamjoul, H., Pearson, G.J., and McDonald, A.V., 1995, *Lasers Med. Sci.*, **10**, 1, 37.
6. Vahl, J. and Pfefferkorn, G., 1967, *Dtsch. Zahnarztl Z.*, **22**, 2, 386.
7. Ferreira, J.M. *et al.*, 1989, *Arch. Oral. Biol.*, **34**, 7, 551.
8. Myers, T.D., 1990, *Proc. SPIE*, **1200**, 425.
9. Lukač, M. *et al.*, 1993, *Proc. SPIE*, **1880**, 169.
10. Schilke, R. and Geurtsen, W., 1994, *Dtsch. Zahnarztl Z.*, **49**, 160.
11. Hibst, R. and Keller, U., 1990, *Proc. SPIE*, **1200**, 379.
12. Burkes, E.J., Hoke, J., Gomes, E., and Wolbarsht, M., 1992, *J. Prosthet. Dent.*, **67**, 847.
13. Paghdiwala, A.F., Vaidyanathan, T.K., and Paghdiwala, M.F., 1993, *Scanning Microscopy International*, **7**, 3, 989.
14. Dostálová, T. *et al.*, 1993, *Proc. SPIE*, **2080**, 51.

Laser–Deposited Hydroxyapatite Films on Dental Implants—Biological Evaluation *in vivo*

T. Dostálová*, M. Jelínek**, L. Himmlová*, and Ch. Grivas***

* *Institute of Dental Research, Vinohradská 48, Prague 2, 120 60 Czech Republic*

** *Institute of Physics, Czech Academy of Sciences, Na Slovance 2, Prague 8, 18040 Czech Republic*

*** *FORTHIESL, P.O. Box 1527, Heraclion, Crete, 711 10 Greece*

Received August 8, 1997

Abstract—Aim of the study was to evaluate the osseointegration of the hydroxylapatite–coated titanium implants. Thin films of biocompatible ceramic were fabricated by KrF excimer pulsed laser deposition (PLD) on real dental cylindrical implants. For *in-vivo* investigation the minipigs were used. The implants were placed into the lower jaw. For analyses a standardized radiography, microradiography, and transmission and fluorescent microscopy were used. The level of osseointegration of the host bone were observed and the percentage of bone/implant contact was determined.

1. INTRODUCTION

For orthopedic and dental prostheses the metal or metal alloy implants are used. One of the major causes of failure of such implants is corrosion [1–4]. Some metal implants can support the creation of tumors [5], or assault of lungs [6]. The best known biocompatible material—hydroxyapatite (HA)—has a low tensile strength [7], is brittle and suffer from fatigue [8]. With the goal to ensure the best and stable connection of implant with the surrounding bone or tissue, the metal implants are covered with thin films of biocompatible ceramic. Coated implants connect advantages of good mechanical properties of metal with convenient chemical and biological properties of coating.

Various criteria for success of dental implants have been published [9]. Whether the implant is blade or root form, criteria for success include the use of standardized radiography procedures in a longitudinal evaluation. Standardized radiographic evaluation of peri-implant bone tissue may allow one to recognize potentially failing implants [10].

Failure of implants has been related to the surgical technology, occlusal overloading, and microorganism-related inflammation of tissues [11]. One of the most important factors of failure could be the implant itself (biomaterial failure) or remaining tissues adherence to the implant. Lemons [12] suggested that biomaterials and biomechanical properties directly influence the tissue interface response.

This study was designed to quantify and compare the host response following placement of commercially pure cylindrical-shaped titanium implants and titanium implants coated with PLD–created hydroxylapatite films. Technique employed to evaluate tissue responses includes standardized radiography and microradiography.

In this work, our experiences with pulsed laser deposition of HA thin films on dental cylindrical implants and results of physical and *in vivo* analyses are presented and discussed.

2. MATERIALS AND METHODS

2.1. HA Film Deposition

Coming out from our experiences with deposition, physical (XRD, morphology, adhesion, stoichiometry, microhardness), and *in vitro* biological characterization (T-lymphocytes proliferation, fibroblasts, macrophages, metabolic activity) of HA layers created by PLD [13–16], we have decided to cover real dental implants with HA layer in Ar–water vapor atmosphere at substrate temperature (T_S) round 500°C. In such deposition conditions the films exhibit good adhesion to the implant material and favorable biocompatible properties. Ratio of gas flows was 12 sccm/10 sccm (Ar/water vapors). The flows were measured with Aalborg GFM 1700 mass flowmeters.

Real dental implants were fabricated from pure titanium material (VNI-Medico Dent, Brno, Czech Republic), with sand blasted surface, length of 13 mm, diameter of 3.3 mm. On the bottom part of implants was a slit and in the upper part there was a hole with an internal screw (see Fig. 1). The HA target was 25 mm in diameter. It was rotated during the deposition and was replaced for a new one for each HA implant deposition. Targets were made of dry HA powder (supplied by MERCK, Darmstadt, Germany), pressed and sintered in oxygen atmosphere. Energy density of KrF excimer laser beam (Lambda Physik LPX 200, Goettingen, Germany) on HA target was 3 J cm^{-2}.

Special ceramic holder was screwed into the implant for deposition process. It made possible to rotate and decline the implant during deposition and substrate heating and to cover the whole implant surface. Substrate was heated with CO_2 laser (Synrad-Model 57-1-28W). The Gaussian beam from the CO_2 laser was expanded using a ZnSe diverging lens and passed through a copper reflective beam homogenizer, to obtain rectangular shape of CO_2 laser beam having cross section of dental implant (see Fig. 2). The chosen T_S was adjusted by tun-
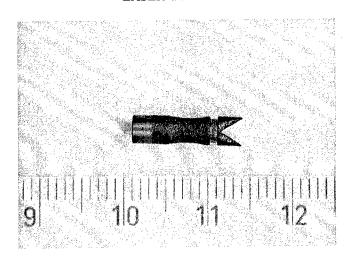
Fig. 1. Real implant shape.

Fig. 2. Apparatus for deposition of HA layers onto real dental implants: (*1*) KrF laser beam, (*2*) ZnSe focusing lens, (*3*) ZnSe window, (*4*) ZnSe diverging lens, (*5*) CO_2 laser beam, (*6*) plasma plume, (*7*) dental implant, (*8*) ceramic holder, (*9*) cooper homogenizer, (*10*) HA target, (*11*) vacuum gauge, (*12*) Ar/water vapor input).

Fig. 3. XRD spectra of deposited HA layer.

ing of CO_2 laser power output. The implant temperature was checked by Ni–NiCr thermocouple.

The thickness of PLD–created hydroxylapatite layer was about 1 μm. Beside of cylindrical implants the flat titanium substrates were also covered with HA layer at the same conditions as dental ones. The flat specimens were used for checking of films physical properties.

2.2. In vivo Experiment

Three minipigs, 2 years old, weight 40 kg in average were used in this investigation. Ten weeks before implantation all lower premolars were extracted. After healing process, 16 coated cylindrical implants and 2 noncoated, control, pure titanium implants, were inserted into both halves of lower jaw due to manufacturer's direction and healed without loading for 16 weeks. In the end of the healing period a Calcein (DCAF) (Merck, Darmstadt, Germany) was injected into experimental animals. Five days after fluorochrome label administration, the experimental animals were sacrificed and blocks of bone with implants were soaked into Schaffer's solution for fixing. Then the specimens were embedded into the methyl-methacrylate resin (Merck, Darmstadt, Germany).

2.3. Analyses

After sufficient fixing, the bone blocks were removed from solution, photographed and radio-graphed (Trophy, Paris, France). The position of implants was controlled on X–ray photos. The radio-grams were viewed using a CCD camera (Mitsubishi, Tokyo, Japan). A computer software system (Sigma Scan and Sigma Scan Pro, Jandel, Erkrath, Germany) was used to analyze and calculate a percentage of osseointegration. The significant differences between experimental and control groups were calculated by Student's t-test at a probability $P = 0.05$.

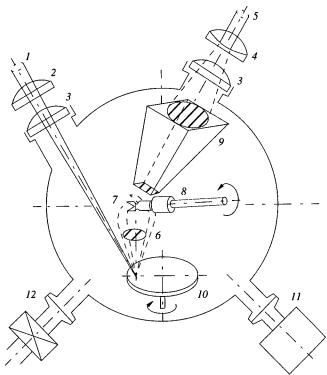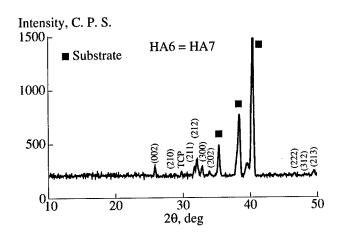Microscopical sections were cut using a diamond saw blade and grinded (both Buehler, Lake Bluff, Illi-

nois, USA) with a water as a coolant to a thickness about 100 μm. From this sections the microradiograms were made (Cabinet X-ray system, Hewlett Packard, Mc Minnville, Oregon, USA).

After that the sections were grinded down to a thickness about 70 μm for microscopy. Ground sections were colored by Giemsa's method with Azure-eosin methyl-blue for hematology (Merck, Darmstadt, Germany)

Fig. 4. Newly formed bone is present around all the implant. In the middle part of implant is visible a narrow gap between metal body and bone.

Fig. 5. All implant is embedded in dense bone. In the narrow middle part of implant is visible a leak between metal and bone.

and observed in transmitted and fluorescent light using a microscope Nikon Microphot FXA (Nikon, Tokyo, Japan).

3. RESULTS

3.1. Physical Properties

Flat titanium substrates, covered with HA layers at the same conditions as the cylindrical ones, exhibited the same gold- yellow and shiny surface as HA coating on cylindrical implants. It is rough indication that the film properties of both shapes of substrate are to be the same. Film surface is smooth with very limited number of droplets. The responsible XRD spectra are in Fig. 3. We see that only HA oriented peaks with a small additional amount of tricalciumphosphate phase are present. HA film is partly amorphized.

3.2. Standardized Radiography and Microradiography

The implants were evaluated quantitatively and qualitatively. The area of bone in long–axis cross section were measured. The ratios of bone-implant were

checked. The percentage of bone/implant contact was determined and the level of osseointegration of the host bone was evaluated.

Presence of newly formed bone around all implant was confirmed. Implants holds firmly in bone and we could say that implants were after 16 weeks osseointegrated (Figs. 4 and 5).

The data for the percentage of bone/implant contact of each of experimental and control sample are presented in the table.

The area of implant in long-axis cross section was in the range from 25.32 to 28.13 mm for pure titanium implant (average 27.10 mm, SE–0.90) and from 21.08 to 36.72 mm (average 29.94 mm, SE–1.34) for coated implant. The area of osseointegration was determined in the range from 18.47 to 22.21 mm (average 20.53 mm, SE–1.10) for pure titanium implant and from 15.39 to 29.86 mm (average 23.27 mm, SE–1.28) for coated implant.

The percentage of osseointegration created from 73.0% to 78.9% (average 75.7%, SE–1.7) for pure titanium implants and from 70.4% to 85.8% (average 77.3%, SE–1.3).

Quantitative analysis of osseointegration in experiment *in vivo* on minipigs (unloaded integration, healing period 16 weeks)

	Area of implant (mm)	Area of osse-oinegration (mm)	Percentage of osseoi-negratio (%)		Area of implant (mm)	Area of osse-oinegration (mm)	Percentage of osseoi-negratio (%)
Ti6Al4V	25.32	18.47	73.0	HA coated	34.90	28.79	82.5
Ti6Al4V	28.13	22.21	78.9	HA coated	34.67	27.55	79.4
Ti6Al4V	27.86	20.92	75.1	HA coated	36.72	29.86	81.3
Average	27.10	20.53	75.7	HA coated	29.87	23.06	77.2
SE	0.90	1.10	1.7	HA coated	25.37	19.06	75.1
HA coated	23.84	16.79	70.4	HA coated	27.26	22.52	82.6
HA coated	21.08	15.39	73.0	HA coated	32.76	28.11	85.8
HA coated	22.92	16.27	71.0	HA coated	31.31	25.28	80.7
HA coated	34.49	24.81	71.9	Average	29.94	23.27	77.3
HA coated	30.93	22.83	73.8	SE	1.34	1.28	1.3
HA coated	33.06	25.52	77.2				

No statistical difference between various implants and in the bone contact between control pure titanium implants and implants with the hydroxylapatite film was found.

3.3. Transmission Microscopy

Surrounded bone is without any marks of irritation and inflammation (Fig. 6). It is possible to detect the new bone formation, new osteons, and the resorption line with old bone. In the border of implant and newly formed bone the osteoblasts are seen. Close to implant cover the foreign body cells are observed, but very rarely. By laser-deposited coat the layer of fibrous connective tissue was seen only seldom. By control group (titanium implant without cover) the fibrous connective tissue was seen between implant and newly formed bone [17].

3.4. Fluorescent Microscopy

Active bone formation (light fluorescent label) was seen both in the neck and in the bottom of the implant, surrounded osteons and braid the fibrous connective tissue on the implant [17].

4. DISCUSSION

The resorption of alveolar bone subsequent to tooth loss has been a considerable issue in prosthodontics for as long as dentists have endeavored to restore missing intraoral structures. The establishment of a predictable implant technique that can provide a long–lasting prosthetic foundation has created new or different consideration for replacement of missing tissues [18]. The accurate assembly of implant components and precision of fit of the prosthesis to the implant is absolutely essential for the long–term survival of dental implants and the

preservation of the supporting bone. Percussion, visual observation and specially conventional radiographs are the methods most frequently used to evaluate accurate assembly of implants components [19]. The percentage of the osseointegration could be measured quantitatively
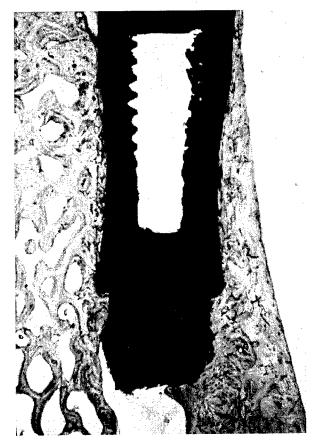

Fig. 6. Bone surrounding coated implant is without irritation and inflammation.

(percent of osseointegration) and qualitatively (evaluation of surrounding tissues). The success rate for all our implants was more than 70% in this case—unloaded osseointegration. These values are in accord with value of 40 to 80% previously reported in literature [10, 20]. Partial osseointegration depends on the type of implants and time of insertion [20, 21]. In our study the osseointegration of the laser–deposited films was shown in all cases. The degree of unloaded osseointegration was more than 70%. At the light microscope level, no fibrous tissue interposition was evident. The active bone formation is visible [17]. All created films were adherent.

5. CONCLUSION

Commercially used materials for implants are metals. Unfortunately, metals and metal alloys, mechanically highly resistant are directly connected with problems of corrosion [1]. From literature [2, 22] it is known, that toxicity of vanadium and the association of aluminum (both contained in Ti6AL4V alloy) can be connected with various neurological disorders [6, 23]. Ceramic materials are chemically inert, but some of them can be dissolved and they are fragile [10]. These problems were solved with methods where a metal substrate is coated with a bioceramic material. Commonly used coating material is a hydroxylapatite. The protection is based on the high adhesion of hydroxylapatite layer to the titanium substrate [24].

After 16 weeks, all implants hold firmly in the bone. At the light microscope level it was evident, that at coated implants no irritation and inflammation was visible and fibrous tissue interposition was observed only seldom. The active bone formation and presence of foreign body cells were seen in both, covered and control cases.

From our study it is apparent that our method using KrF laser for covering hydroxylapatite films is able to prepare the new type of adherent coating for each implant and that this coating is compatible with process of osseointegration.

6. ACKNOWLEDGMENTS

REFERENCES

1. Reclau, R. and Mayer, J.M., 1994, *J. Dent.*, **22**, 159.
2. Thompson, A., Law, F.C., and Rushton, N., 1991, *Biomaterials*, **12**, 37.
3. Cotell, C.M., 1993, *Appl. Surf. Sci.*, **69**, 140.
4. Williams, D.F., 1994, *J. Mater. Sci.: Materials in Medicine*, **5**, 303.
5. Gillespte, W.J., Frampton, C.M.A., Henderson, R.J., and Rvan, P.M., 1988, *J. Bone Joint Surg. B*, **70**, 539.
6. Schliephake, H., Reiss, G., Urban, R., *et al.*, 1993, *Int. J. Oral Maxilofac. Implants*, **8**, 5, 502.
7. de Groot, K., 1983, *Ceramics in Surgery* (Amsterdam: Elsevier), 79.
8. de Putter, C., de Lange, G.L., de Groot, K., and Sillevis Smitt, P.A.E., 1984, *Biomaterials and Biomechanics* (Amsterdam: Elsevier), p. 439.
9. Albrektsson, T. and Sennerby, L., 1991, *J. Clin. Periodontol.*, **18**, 474.
10. Basquill, P.J., Steflik, D.E., Brennan, W.A., *et al.*, 1994, *J. Periodontol.*, **65**(9), 872.
11. Steflik, D.E., Parr, G.R., Singh, B.B., *et al.*, 1994, *J. Oral Implantol.*, **20**, 1, 8.
12. Lemons, J.E., 1988, *J. Dent. Educ.*, **52**, 748.
13. Jelínek, M., Olšan, V., Jastrabík, L., *et al.*, 1995, *Thin Solid Films*, **257**, 1, 125.
14. Dostálová, T., Himmlová, L., Jelínek, M., and Bártová, J., 1995, *Cells and Materials*, **5**, 3, 255.
15. Jelínek, M., Dostálová, T., Fotakis, C., *et al.*, 1996, *Int. J. Laser Phys.*, **5**, 143.
16. Jelínek, M, Jastrabík, L., Grivas, C., *et al.*, 1996, *Int. Conf. Laser Methods for Biological and Environmental Applications (ALT 96), Heraklion Crete, Greece, Book of Abstracts*, p. 4.
17. Dostálová, T., Jelínek, M., Himmlová, L., and Grivas, Ch., 1997, *Cells and Materials* (in press).
18. Albora, P., 1997, *J. Prosth. Dent.*, **77**, 5, 492.
19. May, K.B., Edge, M.J., Russel, M.M., *et al.*, 1997, *J. Prosth. Dent.*, **77**, 5, 497.
20. Lew, D., Marino, A.A., Startzell, J.M., and Keller, J.C., 1994, *J. Oral Maxillofac. Surg.*, **52**(9), 952; discussion 959.
21. Varrer, K., Karring, T., and Gotfredsen, K., 1993, *J. Periodontol.*, **64**, 1, 29.
22. Narayan, J., Fan, W.D., Narayan, R.J., *et al.*, 1994, *Mater. Sci. Eng. B*, **25**, 5.
23. Schliephake, H., Neukam, F.W., Hutmacher, D., and Wustenfeld, H., 1995, *J. Oral Maxillofac. Surg.*, **53**(1), 46; discussion 52.
24. Oguchi, 1994, *Year-book for Oral Implantology'94* (Berlin: Quintessenz).

Specific Vibrational Relaxation in Protein Macromolecules Under Resonant Infrared Laser Excitation

V. B. Oshurko, A. A. Chistyakov, A. B. Karpiouk, and D. V. Klotchkov

Moscow State Engineering Physics Institute, Kashirskoe sh. 31, Moscow, 115409, Russia
e-mail: avb@phsearch.msk.ru
Received September 2, 1997

Abstract—The effect of spatially selective thermal dissociation under infrared laser excitation, found in cellulose nitrate macromolecules, leads to the conclusion that the rate and the way of vibrational relaxation might be dependent on the spatial (conformational) structure of a macromolecule. In the present work, this conclusion has been experimentally and theoretically tested for protein (albumin) macromolecules. High-power tunable infrared parametric oscillator (5000–2500 cm^{-1}) and anti-stokes Raman spectroscopy method have been used in experiments. It was shown that changes in anti-Stokes spectra of protein, caused by infrared laser excitation cannot be explained by an equilibrium heating. The model of vibrational relaxation in a macromolecule with complex topology has been proposed.

In complex molecules (like biopolymers) the rates of vibrational relaxation are known to be extremely high, and the typical times of such relaxation are generally in picosecond or subpicosecond range. Therefore, it is difficult to expect any specific role of vibrational excitation in biologic functions in biopolymers. In spite of that, it was shown recently in some works [1–3] that the effect of the spatial topology of supermolecular structure on the rate vibrational relaxation may be sometimes essential [1]. In works [2, 3] the effect of spatial selectivity has been found experimentally. The essence of this effect is in conservation of excitation energy in spatial nonuniformities of a macromolecule. Then nonequilibrium vibrational excitation distribution occurs to be delayed up to a time, which is sufficient even for reaction of selective dissociation (not less than 20 ns in these experiments) [3]. That is why one has to expect similar phenomena in protein macromolecules, which are known to have a very complex spatial organization [4].

The purpose of the present work was the experimental study of the possibility of conservation of the nonequilibrium excitation distribution for times exceeding the time of vibrational relaxation.

MODELING CALCULATIONS

In order to test the possibility of existence of relatively long-lived nonequilibrium distributions of excitation in a spatially nonuniform macromolecules of protein (for example, the delayed cooling of protein secondary structure elements-α-helices, sheets, etc.) the modeling simulations have been carried out. To perform these simulations, we conveniently use a model proposed in [5]. Following [5], we will consider a quasi-one-dimensional structure consisting of separate units or cells (which corresponds to a linear polymer). We assume that these cells are involved in energy

exchange with each other and the surroundings. Then, the state of each cell (monomer) can be described by a nonequilibrium time-dependent distribution function $f(e, t)$, which can be interpreted as the population of an energy level (here, e is the energy level and t is the time). Integrating this function over all energies from 0 to E_{dis} (the activation energy of dissociation), we can find the so-called vibrational temperature for a separate monomer $V_i(t)$:

$$V(t) = \int_0^{E_{dis}} f(e, t)de.$$

It therefore will be correct to compare this temperature with the temperatures of other monomers [5]. The main assumption that limits the application of this model is as follows: let us assume that the quantum energy of elementary excitation is much lower than the total energy corresponding to vibrational excitation of each monomer. This approximation is justified for complex molecule, in particular, for polymers, where the spectrum of higher energy states is virtually continuous (above the lowest excited state). This approximation is even more reasonable for the case when vibrational temperature is close to the dissociation threshold. In this situation, in accordance with [5], vibrational relaxation can be considered as a diffusion process in the energy space, and the corresponding kinetic equations can be reduced to appropriate diffusion equations (of the form $df_i/dt = -dJ_i/de$, where J_i is the flow of the excitation energy for a given ith monomer).

Let us consider a process of vibrational relaxation for a specific model of a linear polymer that consisted of 20 monomer units where links with numbers from 7 to 16 form structures like α-helix (1) and sheet (2) stabilized by hydrogen bonds, as it is shown in Figs. 1a and 1b We assume that each covalent and each hydrogen
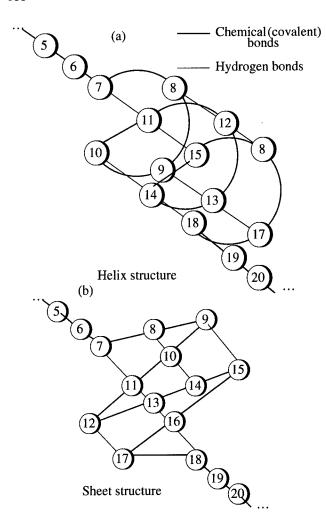
Fig. 1. Schematic diagram of covalent and hydrogen bonds in modeling structures: (a) helix-like structure, (b) sheet-like structure.
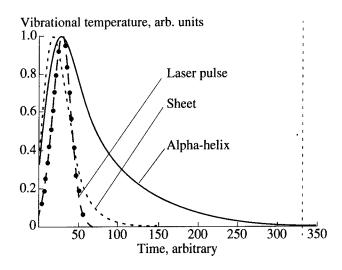

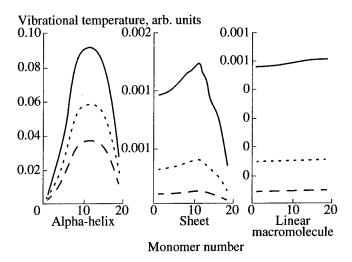**Fig. 2.** Temperature dynamics in monomer cell no. 11 under laser excitation in helix, sheet, and linear structures.

Fig. 3. Temperature distributions over all the monomers at different instants after laser excitation (helix, sheet, and linear).

bond provides channels for the flow of the excitation energy for a given unit, as well as channels for energy relaxation. We will define the probability of energy exchange through a given channel for a given link (per unit time) as the characteristic rate of intramolecular vibrational relaxation (the time of vibrational relaxation is estimated as approximately ~1 ps for covalent bonds and approximately ~10 ps for hydrogen bonds). We will also take into account the relaxation channel that corresponds to the relaxation of the monomer energy to the environment (~10 ps). Then, performing the transformations analogous to those described in [5] we derive the equation that describes the dynamics of the vibrational temperature for the ith monomer,

$$\frac{dV_i}{dt} = A_i(V_{i-1} - 2V_i + V_i)$$

$$+ \sum_k b_k V_k - \sum_n b_n V_i + c_i V_i + J_i(t),$$

where V_i is the vibrational temperature of the ith monomer, A_i is the rate of relaxation of the monomer energy through the channel of covalent bonds (thus, the first term describes relaxation due to covalent bonds that couple a monomer with the nearest neighbors with numbers $i + 1$ and $i - 1$), J_i is the flow of external excitation for a given monomer (a laser pulse), the index n is referred to all the neighbors coupled with the considered monomer by hydrogen bonds in accordance with Fig. 1, and the corresponding term describes the excitation flow from to these neighbors. The index k, which is also determined for each monomer in accordance with Fig. 1, takes the values of indices of all the neighbors coupled with the monomer under consideration by hydrogen bonds. The term that involves this index describes the relaxation flow from the ith unit to neigh-

boring units. Finally, $c_i V_i$ describes relaxation to the surroundings.

Figures 2 and 3 display the solutions to this system of equations obtained with the use of fourth-order Runge–Kutta method for polymers that contain helix and sheet structure shown in Fig. 1a and for a linear polymer that does not contain such structures [the third and fourth terms in equations (1) are set equal to zero]. The excitation laser pulse has been chosen of Gaussian form (Fig. 2) with a duration of 1 ns.

Results of calculations are shown in Fig. 2 (temperature dynamics of 11th monomer in different structures) and Fig. 3 (temperature distributions over monomers along the chain after laser pulse in different structures). As can be concluded from these pictures, the dynamics of vibrational temperature for linear polymer is to be coincident with the shape of laser pulse. But for the sheet structure the temperature relaxation occurred to be delayed for hundreds of picoseconds, whereas this delay for α-helix may be up to several nanoseconds, despite of picosecond rates of relaxation. Obviously, these surprising results must be tested experimentally. The attempt of experimental test of these conclusions is given below.

EXPERIMENTAL

Traditionally, vibrational excitations in proteins were studied in the spectral region of deformational vibrations ($\lambda \sim 6$–10 μm). This region looks to be not enough informative for our purposes, because spectra of deformational vibrational states in proteins are still difficult for interpretation. Also they are sufficiently dependent on conformational states of macromolecules and give no reasons to expect any spatially-selective excitation. Therefore, for our purposes the range of the frequencies of stretch vibrations ($\lambda = 2.0$–4.0 μm) looks to be more convenient.

As to selective excitation in this region, for example, OH chemical groups are present only in 5 from 20 aminoacids, whereas CH-groups are contained in all of aminoacids, and, consequently, one can expect the spatially various primary distribution of excitation energy at exposure with corresponding frequencies (resonant to CH or OH).

For the spectrally selective excitation of different vibrational states of protein macromolecules in present work the tunable pulsed infrared parametrical oscillator (OPO) (wavelengths from 2.0 to 4.0 μm) has been used. OPO was made on lithium niobium crystal according to a single-resonator noncollinear scheme. The radiation of pulsed (duration 10 ns, repetition rate 10 Hz) neodymium laser has been used as OPO pump. For the registration of vibrationally excited states the method of anti-Stokes Raman scattering was used [the wavelength of scattered radiation was 532 nm (10 ns), the spectral range of registration was 4000–2500 cm^{-1}]. This method has been chosen as the most sensitive to a
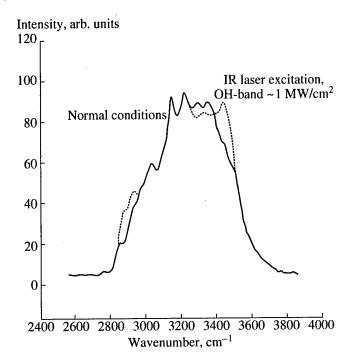
Fig. 4. Anti-Stokes Raman scattering spectra of solid *Albuminium Humanoserum* at normal conditions and under OH-resonant laser excitation.

vibrational states populations. The liophilly dried *Albuminum Humanoserum* powder ("Serva," Heidelberg, purified), mechanically pressed into samples of 1 mm thickness, was used as a sample.

RESULTS AND DISCUSSION

The spectra of anti-Stokes Raman scattering of albumin samples at normal conditions (1) and at the exposure of infrared laser pulse (2), resonant to OH-stretching vibrations (wavelength of 3.1 μm, intensity of ~2.5 MW/cm^2, and pulse duration of 10 ns) are shown in Fig. 4. The spectrum of proteins is obviously formed as a collection of the contributions of each aminoacid contained in a protein macromolecule. As can be seen from this figure, the action of infrared radiation results in the growth of intensity of the anti-Stokes scattering signal in the region of 3200–3500 cm^{-1} (hydrogen-bounded OH groups) and 2800–3000 cm^{-1} (CH groups in aromatic and unsaturated hydrocarbonic fragments), whereas the intensity at the rest part of spectrum does not change, or decreases.

These changes in spectra may be dealed with an equilibrium thermal heating under IR radiation. In order to compare these changes with the results of heating the maximal possible temperature of laser heating may be easily estimated as [3]

$$\Delta T \approx \frac{K_{abs} q \tau_p}{C \rho} \approx 10 \text{ K},$$
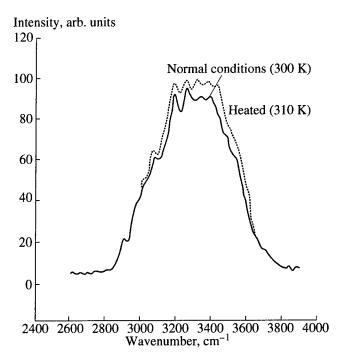
Intensity, arb. units

Fig. 5. Anti-Stokes Raman scattering spectra of solid *Albuminium Humanoserum* at 300 and 310 K.

where K_{abs} is the absorption coefficient; q is the laser pulse intensity; τ_p is the pulse duration; C and ρ are the heat capacity and density, respectively.

In Fig. 5 the spectra of anti-Stokes Raman scattering of albumin sample at temperatures 300 (*2*) and 310 K (*1*) are presented. It is easy to see that the changes in spectra at the exposure of OPO radiation and equivalent stationary heating are qualitatively different.

This difference can be attributed to three factors: (a) formation of quasi-stationary population of vibrational level during the time of laser pulse; (b) difference in dynamics of heating and cooling in the case of infrared laser action and at stationary heating; ($\hat{a}$) the existence of thermodynamical nonequilibrium vibrational temperature distribution along macromolecules due to the presence of spatial nonuniformities (α-helices, β-sheets, etc.). However, direct estimates of population display

that at known rates of excitation and relaxation the population of excited level does not exceeds the share of $\sim 10^{-8}$ from all absorptive groups. Hence, this reason, evidently cannot explain the observed effect. On the other hand, the formation of quasi-stationary population on the level close to 3.1 μm (~ 3400 cm^{-1}) anyway could not explain the increasing of the signal about 3000 cm^{-1}. Difference in dynamics heating and cooling neither gives satisfactory explanation. It is easy to show, that because of high heat capacity of protein, heating and cooling dynamics occurs to be rather slow ($\gg 10$ ns) and, thereby, close to that in the case of stationary heating. Hereto in this instance there is no mechanism that could qualitatively explain the changes in spectra in Fig. 2.

But possibly the observed effect (Fig. 4) deals with a different heating of nonuniformities other than secondary structure elements (such as macroscopic nonuniformities) in a polycrystalline sample? Obviously, in order to provide the effect in Fig. 4, there must be a chemical difference between differently heated macroscopic elements. But the sample is chemically homogeneous. Hence, the effect in Fig. 4 most likely deals with delayed cooling of secondary structural elements as described above rather than other elements.

Thus, in the present work the principal possibility of the conservation of nonequilibrium vibrational temperature distribution at proteins structural elements (for a time exceeding the times of vibrational relaxation) has been shown both theoretically and experimentally.

REFERENCES

1. Schofield, S.A., Wyatt, R.E., and Wolynes, P.G., 1996, *J. Phys. Chem.*, **8**.

2. Bakhirkin, Yu.A., Bykovsky, Yu.A., and Chistyakov, A.A., 1991, *Zh. Eksp. Teor. Fiz.*, **99**, 1739.

3. Bakhirkin, Yu.A., Bykovsky, Yu.A., Oshurko, V.B., and Chistyakov, A.A., 1996, *Laser Phys.*, **6**, 690.

4. Yu, K. and Dill, K., 1995, *Proc. Natl. Acad. Sci. USA*, **92**, 146.

5. Oraevskii, A.N. and Pleshanov, P.G., 1978, *Kvantovaya Elektron.*, **5**, 2243.

Photodynamic Therapy in Ocular Vascular Disease[1]

U. Schmidt-Erfurth*, R. Birngruber**, and T. Hasan***

* *University Eye Hospital Lübeck, Lübeck, D-23538, Germany*
** *Medizinisches Laserzentrum Lübeck, Lübeck, D-23562 Germany*
*** *Wellman Laboratories of Photomedicine, Massachusetts General Hospital,*
Harvard Medical School, Boston, MA 02114 USA
e-mail: BGB@mll.mu-luebeck.de
Received August 6, 1997

Abstract—Photodynamic therapy (PDT) is a novel therapeutical approach which is noninvasive and potentially selective for neoplastic pathologies. Association of photosensitizers with low density lipoprotein (LDL) leads to direct targeting of the treated lesions with enhanced efficiency and selectivity. LDL-mediated PDT is particularly useful in the treatment of neovascular structures since LDL receptors are abundantly expressed on vascular endothelial cells. To evaluate the potential of selective photodynamic vasoocclusion in ocular neovascular disease, a sequence of experiments was designed: efficiency of the LDL-carrier was tested *in vitro*, and the system was then transferred to an *in vivo* model demonstrating a vascularized neoplasm. Occlusion was successfully performed in experimentally-induced neovascularization in the cornea, while selective photothrombosis of subretinal vasculature revealed lack of collateral damage. The experimental results were used to establish a first clinical trial for the use of PDT in *age-related macular degeneration*, one of the leading causes for blindness.

1. INTRODUCTION

Photodynamic therapy (PDT) was first evaluated as a potential diagnostic and therapeutic tool about 25 years ago. Lipson [1] used the photodynamic approach for the detection and treatment of skin metastasis in lung cancer. Diamond [2] studied the phototoxic effect in experimental cerebral tumors. It was the group of Dougherty [3] who succeeded based on their extensive experimental work to introduce photodynamic therapy into the clinical spectrum of modalities used in modern cancer treatment.

The concept of PDT is based on the combination of two mechanisms: the accumulation of a light-activitable chromophore within pathologic tissue and the induction of a chemical reaction by light absorption. The photodynamic process requires the presence of a sensitizer, oxygen, and light of a wavelength absorbed by the sensitizer used [3]. The treatment modality is easily applicable: a sensitizer is administered either topically or intravenously. The dye is distributed within the organism with a more or less preferential uptake and retention by neoplastic tissue. A spatially confined exposure to monochromatic light leads to the generation of cytotoxic species, such as singlet oxygen followed by irreversible cell destruction [4]. Based on the biomicroscopic and histologic observations in the treatment of tumors, it became soon evident that vascular effects play a major role in the transmission of the photodynamic effect. Castellani found a transitory interruption of the blood flow within photosensitized tissue of the frog tongue and rat mesentery [5]. Accordingly,

a distribution ratio of the sensitizer haematoporphyrin of 5 : 1 between vascular stroma and tumor cells was documented [6]. Transparent observation chambers enabled Star to visualize alterations in the microcirculation of sensitized rat mammary tumors as well as within normal tissue [7]. Hence, the photodynamic approach should provide an appropriate treatment for vascularized tumors and, in addition, for lesions composed exclusively of neovascular structures.

Since PDT is dependant on the interaction of light and tissue, the accessibility of the lesion to laser light is a major concern. PDT is therefore mostly used for the treatment of internal or external surface lesions such as skin, lung, gastrointestinal and bladder tumors [3]. The eye with its specific anatomy potentially benefits most from a laser-mediated treatment. The transparent media-like cornea, aqueous humor, lens, and vitreous allow an unlimited penetration of light without significant losses due to scatter or absorption. This condition also facilitates a precise localization and controlled treatment of the lesion. The therapeutical effect can easily be evaluated by clinical examination, photography, and angiography. Ocular pathologies are mostly small, in the range of a few millimeters, so that reduced transmission of light into deeper layers is not a problem. Furthermore, the noninvasive nature of PDT makes it a particularly appropriate approach in sites where the preservation of the sensitive structures adjacent to the lesion exclude excisional surgery if function and maintenance of the organ should be achieved.

Due to these inherent advantages of PDT in the eye, clinical trials were performed early in the development of the new modality. However, the results were
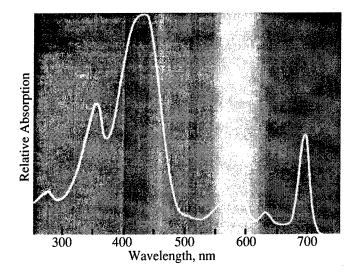
Fig. 1. Absorption spectrum of benzoporphyrin derivative.
The peak at 692 nm is used for photosensitization.

Fig. 2. Schematic drawing of the LDL metabolism. Endothelial cells express the apo B/E receptor that leads to endocytosis of LDL via coated pits and vesicles to endosomes and then to lysosomes where the apoB is degraded and the cholesterol is used in the cell.

disappointing [8–10]. Intraocular tumors regressed only incompletely and physiological structures were significantly altered. Briefly, the selectivity of the treatment was not satisfactory. The selectivity of PDT is defined by the nature of the sensitizer used. Haematoporphyrin (HPD) and its purified form Photofrin, for years the only sensitizers available for the clinical use, exhibit an intensive nonspecific tissue localization. Retention within the skin is responsible for an intensive and prolonged cutaneous photosensitivity for as long as six weeks [11]. Other disadvantages of HPD include its composition of a mixture of different porphyrins which is unstable, dependant on storage and temperature of the drug [12] and the inconsistent cellular localization of the various chemical subtypes [3]. Many investigators have focussed on the development of chromophores, second generation sensitizers, with improved properties. Among them are phthalocyanines, chlorins and benzoporphyrin derivatives. Phthalocyanine offers a uniform molecular composition, efficient phototoxicity [13], and a somewhat preferential accumulation within neoplastic tissue [14]. However, it is not approved for clinical trials. Chlorins provide a better tissue penetration by absorbing at a higher wavelength the HPD [15] and less skin sensitivity [16].

Chlorins are easily coupled to carrier molecules which would increase the concentration of sensitizer within the neoplastic tissue [17].

Benzoporphyrin (BPD) has been shown to provide a tenfold increased phototoxicity *in vitro* compared to HPD [18] and a significantly increased production of the cytotoxic species singlet oxygen [19]. The absorption characteristics of this compound demonstrate an absorption peak at 690 nm offering appropriate tissue transmission (Fig. 1). In contrast to HPD light exposure
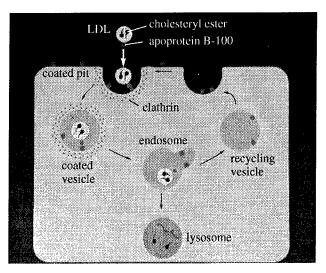
after 24 h induced only a minimal skin reaction [18]. Clinical experience with BPD is already available since it has been used in first clinical trials for the treatment of psoriasis and basal cell carcinomas [20]. Since sensitizers *per se* do not exhibit any reliable selectivity, several attempts have been made to combine sensitizers with carrier systems which mediate a selective targeting of neoplastic cells. Monoclonal antibodies (Mab) seem to provide an optimal selectivity. *In vitro*, low concentrations of Mab-bound HPD effectively inactivated leukemia cells [21]. Chlorin e6 coupled to Mabs was effective against bladder carcinoma cells [22] and ovarian carcinoma cells [23]. However, *in vivo*, Mabs have difficulties to pass the vascular barrier and are rapidly cleared by the reticuloendothelial system. The increased binding of sensitizers to plasmaproteins within the vascular system provided evidence for an important role of lipoproteins for the biodistribution [24]. Most of the dye molecules have been found to be associated with plasma-derived low-density lipoproteins (LDL) shortly after intravenous administration [25]. LDL is subsequently bound to membrane receptors and endocytosed within vesicles, coated pits [26] (Fig. 2). Accordingly, LDL-associated sensitizer is bound, internalized and intracellularly incorporated into enzymatically active lysosomes-several factors increasing the efficiency of PDT. Since proliferating cells express increased numbers of LDL receptors [27], LDL might be used as endogenous carrier to target tumor as well as endothelial cells. Liposomes have been shown to effectively deliver sensitizers to plasma LDL [25]. BPD, a lipophilic compound, is delivered in a liposomal formulation to provide solubility and is therefore an appropriate molecule to benefit from the endogenous LDL carrier system. We have evaluated the potential of

BPD-mediated PDT for a selective treatment of intraocular vascularized pathologies. Experiments described in the following article were started in the *in vitro* system, continued *in vivo* in the animal model and then transferred to the *application in a pilot clinical trial*.

2. *In vitro* EVALUATION OF THE LDL CARRIER SYSTEM

Retinoblastomas are intraocular tumors which develop during early childhood. Their histologic nature as nonpigmented and intensively vascularized lesions make them particularly attractive for PDT. Established therapeutical methods are external beam or plaque radiotherapy with serious complications such as the induction of secondary cancers, retinopathy with blindness, facial bone deformities, and central nervous system defects [28]. A selective, targeted photochemotherapy would be a preferable approach. Sery has shown photosensitivity of human retinoblastoma cell lines using HPD and white light [29], while other authors demonstrated that the tumor response *in vivo* was restricted to 33% [30]. Complexing of sensitizer with LDL demonstrated enhanced photodynamic activity compared to the use of sensitizer (PS) alone [25]. As a more reliable modality of PS carrier association we [31] used covalent chemical binding to LDL molecules. The PS-LDL system was tested regarding binding to the membrane receptor and uptake by the neoplastic cells as well as phototoxic efficiency.

Method: Y79 human retinoblastoma cells were grown in dishes coated with poly-D-lysine until cultures were subconfluent. Human LDL was prepared from human plasma. Ce6 was used as sensitizer because of its chemical properties for binding. For covalent coupling ce6 was activated with 1-ethyl-3-carbodiimide (EDAC) followed by addition of LDL. Cells were incubated at 37° and 2°C for up to 24 h and then lyzed. Ce6 from the lysate was determined by spectrofluorimetry. Competitive binding was analyzed by addition of free LDL in excess after 4 h. To determine the phototoxic effects cultures were incubated for 2 h in 4 nmol of Ce6, Ce6-LDL and a mixture of free Ce6 and LDL. Irradiation was performed using 660 nm at 50 mW/cm^2 and a fluence of 10 J/cm^2. Cell kill was documented by an MTT assay and colorimetric evaluation. The method was described in detail in Schmidt-Erfurth *et al.* [31].

Results: Optimal binding efficiency was achieved at a Ce6 : LDL ratio of 50 : 1, while higher amounts of Ce6 reduced the receptor affinity of the compound. Binding of the sensitizer to LDL reproducibly increased the uptake by a factor of 4–5. Using the PS-LDL conjugate binding was increased at 2°C due to receptor recognition *alone, since active uptake mechanisms are blocked at this temperature level*. At 37°C, *a temperature allowing physiological metabolism*, binding followed by active internalization of the compound into the neoplastic cells *led to the highest conjugate*

binding. Addition of free LDL induced a decrease in sensitizer uptake as a consequence of receptor competition. Furthermore, uptake showed saturation after 2 h. Increased uptake of the conjugates directly translated into enhanced phototoxicity: A cell kill of 80% was obtained using Ce6-LDL at parameters which did not alter cell functions using unbound sensitizer.

Conclusion: The role of LDL for PDT using lipoprotein associated sensitizers was evaluated in a controlled *in vitro* system. Sensitizer-LDL conjugates were bound and taken up by neoplastic cells at significantly higher rates than sensitizer with no carrier interaction. Saturation and effective competition indicated direct binding to the receptors on the cell membrane. Targeting led to increased phototoxic efficiency. Hence, human LDL may be used as an endogenous carrier system in combination with sensitizers which bind to plasma LDL. It offers the advantage of an autologous protein that does not induce any side-effects as a foreign body reaction or the formation of auto-antibodies as seen with the use of Mabs. LDL is known to possess high affinity receptors on proliferating cells [32] due to their higher demand of cholesterol for the synthesis of membrane lipids [33]. Association of sensitizers with LDL should not only enhance the uptake of the chromophore, but also lead to an increased selectivity. PDT induces vascular occlusion with subsequent hypoxia. Lack of oxygen, however, eliminates photodynamic effects [34]. It might be essential to transfer sensitizer to tumor cells and target them directly. Zhou has shown that timing of the PDT strongly influences the site of sensitizer localization, i.e., the site of the phototoxic damage [35]. The first barrier to pass *in vivo* is the vascular endothelium which also expresses LDL receptors [36]. LDL binds to the endothelial cell and is then transcytosed to the tumor cells and associated macrophages [37]. The time interval between administration and irradiation might, therefore, be crucial to select the appropriate target, i.e., microvasculature or neoplastic cells themselves.

3. PHOTODYNAMIC EFFECTS IN A VASCULARIZED TUMOR MODEL *in vivo*

The number of models for intraocular neoplastic lesions which are vascularized is limited. *Experimental* retinoblastomas are not successfully implanted into the *retinal and choroidal layers* and are usually rejected as soon as the implant gets access to the host vasculature. The established model is the amelanotic Greene melanoma [38]. It is derived from hamster tissue and exhibits a continuos proliferation with ingrowth of a dense microvascular network when implanted into the rabbit eye. Choroidal melanomas represent by far the most common *primary* intraocular malignancy in *adult* humans [39]. Radiotherapy commonly used in affected eyes leads to visual loss and intensive damage to physiological structures leading to enucleation in a high percentage of treated patients [40]. PDT using HPD was
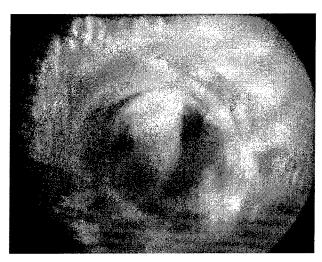
Fig. 3. Choroidal tumor 1 h after BPD-PDT. Superficial hemorrhage and increased edema in an otherwise intact tumor nodula characterize the early stage after PDT.
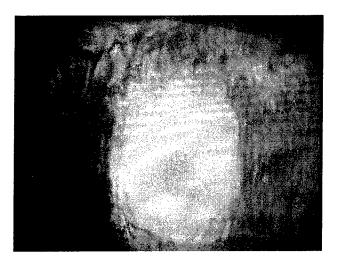

Fig. 4. Regression of a treated choroidal tumor. Two weeks after PDT an avascular area covered with lipids and macrophages is seen.
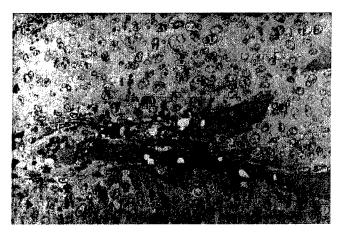

Fig. 5. Histology of a treated melanoma. The tumor neovasculature is filled with thrombi, endothelial cells are attenuated. Remaining cells are markedly altered, while tumor cells appear intact.

performed by several centers unsuccessfully [8–10]. Most tumors demonstrated partial, superficial necrosis with recurrence after a short interval. Nonselective effects caused severe side-effects such as neovascular glaucoma, iritis and hemorrhage *following photodynamic treatment of affected eyes* [41, 42]. The reports indicated that PDT had a potential benefit which was limited by lack of efficiency and selectivity.

Experimental choroidal melanomas were used [43] to evaluate the effects of PDT with LDL-mediated BPD *in vivo*.

Method: Fragments of a Greene melanoma were implanted into the *supra*choroidal space of the eye in New Zealand white rabbits so that the final tumor was located *in the subretinal space beneath the retina*. Tumors 3–4-mm diameters in size were treated. Benzoporphyrin derivative monoacid was complexed with human LDL by incubation at 38°C for 30 min at a BPD : LDL ratio of 1 : 2.5 mg. Intravenous administration of BPD-LDL at a dose of 2 mg/kg was followed by photosensitization at 692 nm and an irradiance of 150 mW. Photodynamic effects were documented by photography, angiography, and LM- and EM-histology. For details see Schmidt-Erfurth *et al.* [43].

Results: After PDT at 100 J/cm^2 all treated tumors responded with complete regression. Ophthalmoscopically the neoplasm showed increased edema shortly after PDT with no change in gross appearance (Fig. 3) and then progressively shrank with continous blanching (Fig. 4). A small, avascular nodule was seen after one week, a localized lipid deposit was left after four weeks. Complete vascular thrombosis was detected angiographically as soon as one hour after PDT. Tumors did not recanalize during follow-up. In early light microscopy thrombosis was seen throughout the entire lesion (Fig. 5). Endothelial cells were swollen and markedly reduced in number, tumor cells appeared unchanged. 24 h after PDT all lesions exhibited homogenous necrosis of both compartments. Resorption by macrophages finally leaves an area with granulomatous inflammation and multinucleated giant cells. EM microscopy of endothelial cells revealed clumped nuclear chromatin, vacuolization and multiple breaks of the cytoplasmic membrane with protrusion of plasma and organelles. Tumor cells predominantly demonstrated alterations of the mitochondrial and nuclear ultrastructure. *Tumors in control eyes showed continuous growth leading to hemorrhage and complete retinal detachments*.

Conclusion: Since HPD-PDT was ineffective and nonselective clinically, efficiency and selectivity have to be both enhanced. BPD absorbs at a higher wavelength than HPD providing better effects in deeper layers. It offers superior toxicity [44] and localized better in neoplastic than in physiologic tissue in a rhabdomyosarcoma model *in vivo* [45]. The radiant exposure necessary for experimental tumor regression using HPD was therefore higher (540 J/cm^2) than the correspond-
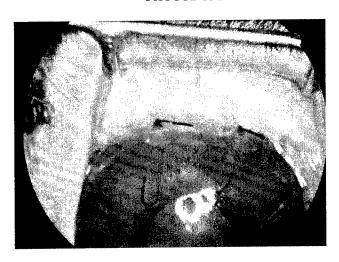
Fig. 6. Experimental corneal neovascularization after PDT. Sensitized areas appear cyanotic, but continous (right and left of the sutures). The central area shows the untreated control.

Fig. 7. Angiography after BPD-PDT. Dark areas delineate the irradiated sites where hypofluorescence indicates vascular occlusion.

ing light dose required with BPD (100 J/cm^2) [46]. The predominant feature of BPD-PDT was endothelial damage with subsequent thrombosis. Particularly the disruption of endothelial membranes supports the hypothesis of a direct targeting of endothelial cells via LDL carriers. Proliferating endothelium exhibits an increased LDL receptor expression [47]. Direct binding to tumor neovasculature should further enhance the uptake of sensitizer as well as the selectivity of the method. A separation of vascular and tumoricidal effects is not possible in the experimental setting used. Both cell systems, endothelial cells and tumor cells, are possible targets of LDL-mediated photochemotherapy. In addition, endothelial cells demonstrate an increased sensitivity for PDT [48] and an overwhelming vascular effect will mask direct tumor cell toxicity. Damage to normal tissue, particularly physiological intraocular vasculature was not seen in our experiments possibly due to an increased selectivity for neovasculature compared to resting endothelium and suggests an application of this modality for the treatment of purely neovascular lesions.

4. PHOTODYNAMIC OCCLUSION OF OCULAR VASCULATURE

Ocular neovascular disease represents the leading cause for blindness in developed countries, most prominent among them macular degeneration and diabetic retinopathy [49]. Damage to intraocular structures is significant because of the invasive neovascular growth and related scaring as well as by the mostly invasive therapeutical attempts, e.g., mechanical surgery and laser photocoagulation to eliminate neovascularization embedded within sensitive physiological tissue mainly retina. An approach that avoids any additional alteration would maintain visual function. The concept of PDT provides a dual selectivity by a tight spatial con-
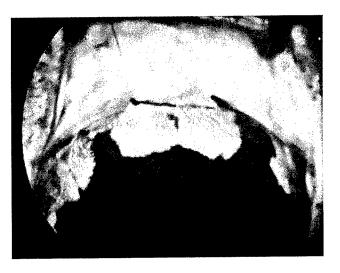
finement of the photoactivating irradiation beam and a selectivity within the treated area which is dependant on the sensitizer distribution. Two *in vivo* models were used [50] to evaluate the vasoocclusive potential of LDL-mediated BPD-PDT: Neovascularization induced in the rabbit cornea which consist of an easily accessible monolayerlike neovascular net within a transparent matrix. This setup allows one to assess vasoocclusive efficiency in an isolated purely neovascular structure. *In additional experimental series, photodynamic occlusion of the choriocapillary layer directly beneath intact retina was performed to document vascular selectivity with maintenance of extravascular structures such as the sensitive neural retina.*

Methods: Corneal neovascularization was induced in Dutch-belted rabbits by introducing ophthalmic silk sutures radially into the corneal stroma as done in corneal transplant surgery in humans. Dense neovascular nets arise from the corneal margins and cover about 3 mm of the corneal periphery after ten days. Normal choriocapillary of the same rabbit species was treated with BPD-PDT. BPD was precomplexed with LDL or used in a liposomal preparation. A drug dose of 2 mg/kg was administered, irradiation after three hours was performed at 692 nm, 100 mW/cm^2 and exposures ranging from 5 to 100 J/cm^2. Vascular occlusion and damage to adjacent tissue was monitored by clinical examination, angiography and light and electron microscopy. Experiments are described in detail in [50].

Results: When PDT was performed one hour following BPD administration in corneal neovascularization, first effects started at 5 J/cm^2 with focal areas of capillary nonperfusion. At 10 J/cm^2 most sites were thrombosed completely, reproducible and homogenous occlusion was obtained with application of 25 J/cm^2 and higher. Vascular integrity was maintained clinically, occluded areas could be recognized by their
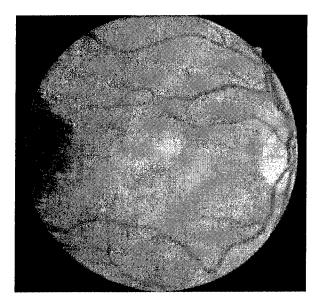
Fig. 8. Choroidal neovascularization in an eye before PDT. The central macular area exhibits edema and the faint outlines of subretinal vessels.

Fig. 9. CNV shown in Fig. 8 one week after PDT. Retinal transparency is preserved, edema is reduced, discrete subretinal hemorrhage is seen.

cyanotic appearance (Fig. 6). Angiography revealed immediate and complete vasoocclusion (Fig. 7). Histologically vessels were filled with erythrocyte and platelet aggregates. Damage to endothelial cells included discontinuity of luminal cytoplasmic membranes, vacuolization of mitochondria and endoplasmatic reticulum and clumping of nuclear chromatin. No difference either in the required dosage, clinical or histological features was found between PDT using LDL-complexed BPD or the liposomal preparation of BPD.

PDT in the choriocapillary model provided comparable results: At 10 J/cm^2 occlusion of choriocapillaries was achieved, while capillaries and larger vessels were affected at exposures of 50 J/cm^2 and above. In the 10 J/cm^2 group all retinal layers overlying the occluded area remained intact including photoreceptors in immediate vicinity to thrombosed vessels. At the higher light dose photoreceptors were focally altered at 50 J/cm^2, only intensive exposure at 100 J/cm^2 led to retinal destruction. However, the retinal pigment epithelial layer (RPE) was regularly disturbed.

Conclusion: BPD-PDT was shown to be an appropriate system for reproducible occlusion of *ocular vasculature. Occlusion was demonstrated in experimental models such as corneal neovascularization and choriocapillaries in the rabbit eye.* Damage was strictly confined to vascular structures and no signs of phototoxicity were found extravascularly neither in the corneal nor in the subretinal model. Thrombosis was induced by an intraluminal mechanism which is consistent with endothelial membrane targeting via the LDL pathway. Other PDT-induced factors such as secretion of clotting factors [51] possibly enhance the intravascular efficiency and lack of nonvascular destruction.
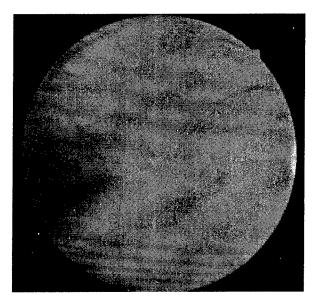
A second goal of this study was the evaluation of the liposomal preparation of BPD since this modality has to be used in patients. Identical results of LDL and liposomal systems suggest an identical localization of BPD with both delivery systems. Redistribution of BPD from liposomes to LDL within the blood system is the most important feature of BPD-related selectivity [52]. Association of the lipophilic compound with lipoproteins also reduces extravascular leakage with subsequent collateral damage [53]. Phototoxic destruction of RPE cells appears to be the consequence of LDL-targeting since RPE cells are known to carry LDL receptors [54]. The RPE layer usually recovered within a few weeks [55].

5. CLINICAL TRIAL FOR THE TREATMENT OF CHOROIDAL NEOVASCULARIZANON USING BPD-PDT

Subretinal neovascularization in age-related macular degeneration (AMD) causes a progressive and irreversible loss of visual acuity. *AMD is, among diabetes and glaucoma,* responsible for most cases of legal blindness in Europe and North America [49]. The prognosis of the disease is extremely poor as there is no safe and efficient treatment available. Conventional laser photocoagulation induces a nonselective thermal necrosis of all layers within the treated area and a significant collateral destruction. Particularly if the neovasculature is located in the sensitive center of the retina laser-treated patients experience an additional visual loss. Lipoprotein-mediated PDT was shown to provide confined intravascular thrombosis in the rabbit as well as a primate model of choroidal neovascularization [56]. Based on these encouraging results a first
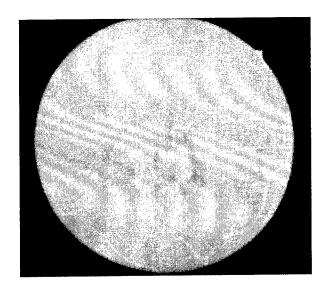
Fig. 10. Angiography of a CNV lesion before PDT. The central hyperfluorescent area indicates the presence of a classic neovascularization.

Fig. 11. Angiography one week following BPD-PDT. The sensitized area does not exhibit any hyperfluorescence consistent with complete occlusion of CNV. Note the preservation of retinal vessels overlying the occluded region.

clinical trial phase I/II was started to evaluate the effect of BPD-PDT in patients suffering from choroidal neovascularization (CNV) in the center of the retina, the subfoveal are. *It is a multicenter trial meeting strict IRB guidelines in the United States as well as in Europe.*

The trial is still ongoing and results have to be considered as preliminary.

Methods: Liposomal BPD is delivered intravenously at a drug dose of 6 mg/m² or 12 mg/m². Light exposures of 50, 75, 100, and 150 J/cm² were applied. Photosensitization at 692 nm and 600 mW/cm² was performed 15–30 min after administration of BPD. Retinal function was documented by visual acuity testing and focal testing of the central visual field by microperimetry. Vascular occlusion was analyzed by angiography. Data were summarized in [57,58].

Results: No clinically significant destruction of retinal structures was found ophthalmoscopically (Figs. 8 and 9). Angiographically classic and occult CNV was delineated by hyperfluorescence (Fig. 10). After BPD-PDT the treated lesions characteristically demonstrated closure of classic CNV at one week indicated by hypofluorescence (Fig. 11). At four weeks partial reperfusion could be seen dependant on the treatment parameters used. PDT did not cause any additional defects of the central visual field. In the group with optimal results defects even decreased in size in 80% of the patients. The visual acuity remained stable.

Conclusion: In a pilot study, selective occlusion was achieved in the majority of patients. Simultaneously visual acuity was maintained and the visual field was not compromised in contrast to the results obtained with laser photocoagulation in this type of lesion. Appropriate treatment regimens and the long-term
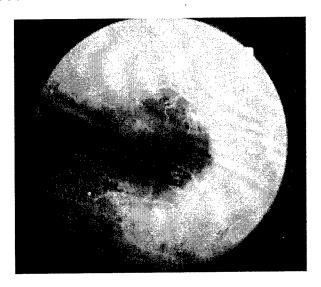
prognosis are currently being investigated in a subsequent phase II/III of the clinical trial.

REFERENCES

1. Lipson, R.L., Baldes, E.J., and Olsen, A.M., 1964, *Dis. Chest*, **46**, 676.
2. Diamond, I., Granelli, S.G., McDonagh, A.F., *et al.*, 1972, *Lancet*, 1175.
3. Dougherty, T.J., Potter, W., and Belnier, D., 1989, Photodynamic Therapy for the Treatment of Cancer: Current Status and Advances, *Photodynamic Therapy of Neoplastic Disease*, Kessel, D., Ed. (Boca Raton, FL: CRC).
4. Weishaupt, K., Gomer, C.J., and Dougherty, T., 1976, *Cancer Res.*, **36**, 2326.
5. Castellani, A., Pace, G.P., and Concioli, M., 1963, *J. Pathol. Bacteriol.*, **86**, 99.
6. Bugelski, P.J., Porter, C.W., and Dougherty, T.J., 1981, *Cancer Res.*, **41**, 4060.
7. Star, W.M., Marijnissen, J.P.A., van den Berg-Blok, A., and Reinhold, H.S., 1986, *Cancer Res.*, **46**, 2532.
8. Bruce, R.A.,Jr., 1987, *Photochem. Photobiol.*, **46**, 919.
9. Tse, D.T., Dutton, J.J., Weingeist, T.A., *et al.*, 1989, *Arch. Ophthalmology*, **102**, 833.
10. Murphree, A.L., Cote, M., and Gomer, C.J., 1987, *Photochem. Photobiol.*, **46**, 919.
11. Zahler, G.L., Poh, M., Fitz, P., *et al.*, 1977, *Arch. Dermatol.*, **116**, 1392.
12. Byrne, C.J., Marshal, L.V., and Ward, A.D., 1987, *Photochem. Photobiol.*, **46**, 575.
13. Kimel, S., Tromberg, B.J., Roberts, W.G., and Berns, M.W., 1989, *Photochem. Photobiol.*, **50**, 175.
14. Glassberg, E., Lewandowski, L., Lask, G., and Vitto, J., 1990, *J. Invest. Dermatol.*, **94**, 604.
15. Roberts, W.G., Shiau, Y., Nelson, J.S., *et al.*, 1988, *J. Nat. Cancer Inst.*, **80**, 330.

16. Nelson, J.S., Roberts, W.G., and Berns, M.W., 1987, *Cancer Res.*, **47**, 4681.

17. Bachor, R., Shea, C.R., Gillies, R., and Hasan, T., 1991, *Proc. Nat. Acad. Sci.*, **88**, 1580.

18. Richter, A.M., Cerruti-Sola, S., Sternberg, E., *et al.*, 1990, *J. Photochem. Photobiol. B*, **5**, 231.

19. Aveline, B., Hasan, T., and Redmond, R.W., 1994, *Photochem. and Photobiol.*, **59**, 328.

20. Lui, H., Kollias, N., Wimberly, J., *et al.*, 1993, *Laser Dermatol. Plast. Surg., SPIE B*, **1876**, 37.

21. Mew, D., Lum, V., Wat, C.K., *et al.*, 1985, *Cancer Res.*, **45**, 4380.

22. Hasan, T., 1993, in *Proc. SPIE*, **1203**, 1136.

23. Goff, B.A., Bamberg, M., and Hasan, T., 1991, "Photoimmunotherapy of human ovarian carcinoma cells ex vivo," *Cancer Res.*, **51**, 4762–4767.

24. Barel, A., Jori, G., Perrien, A., *et al.*, 1986, *Cancer Lett.*, **32**, 145.

25. Jori, G., Beltramini, M., Reddi, E., *et al.*, 1984, *Cancer Lett.*, **24**, 291.

26. Goldstein, J.L., Anderson, R.G.W., and Brown, M.S., 1979, *Nature*, **179**, 679.

27. Gal, D., McDonald, P.C., Porter, J.C., and Simpson, E.R., 1981, *Int. J. Cancer*, **28**, 315.

28. Shields, C.L., Shields, J.A., and de Poner, P., 1993, *Ophthalmol.*, **100**, 216.

29. Sery, T.W., 1979, *Cancer Res.*, **39**, 96.

30. Winther, J., 1989, *J. Cancer Res. Clin. Oncol.*, **115**, 73.

31. Schmidt-Erfurth, U., Diddens, H., Birngruber, R., and Hasan, T., 1996, *Br. J. Cancer.*

32. Vitols, S., Gahrton, G., Bjorkhol, M., and Peterson, C., 1985, *Lancet*, **2**, 1150.

33. Rudling, M.J., Angeli, B., Peterson, C.O., and Collins, V.P., 1990, *Cancer Res.*, **50**, 483.

34. Henderson, B.W. and Fingar, V.H., 1989, *Photochem. Photobiol.*, **49**, 299.

35. Zhou, C., Milanesi, C., and Jori, G., 1988, *Photochem. Photobiol.*, **48**, 487.

36. Simionescu, N. and Simionescu, M., 1991, *Targeted Diagn. Ther.*, **5**, 45.

37. Hamblin, M.R. and Newman, E.L., 1994, *J. Photochem. Photobiol. B*, **26**, 147.

38. Greene, H.S.N., 1958, *Cancer Res.*, **18**, 422.

39. Zimmerman, L.E. and McLean, I.W., 1979, *Am. J. Ophthalmol.*, **87**, 741.

40. Lommatzsch, P.K., 1986, *Br. J. Ophthalmol.* **70**, 844.

41. Sery, T.W., Shields, J.A., Augsburger, J.J., and Shah, H.G., 1987, *Ophthalmic Surg.*, **18**, 413–418.

42. Lewis, R.A., Tse, D.T., Phelps, C.D., and Weingeist, T.A., 1984, *Arch. Ophthalmol.*, **102**, 839.

43. Schmidt-Erfurth, U., Bauman, W., Gragoudas, E., 1994, *Ophthalmol.*, **101**, 89.

44. Richter, A.M., Kelly, B., Chow, J., *et al.*, 1987, *J. Nat. Cancer Inst.*, **79**, 1320.

45. Richter, A.M., Cerruti-Sola, S., Sternberg, E., 1990, potent *J. Photochem. Photobiol. B*, **5**, 231.

46. Sery, T.W. and Dougherty, T.J., 1984, *Curr. Eye Res.*, **3**, 519.

47. Vlodavsky, I., Fielding, P.E., Fielding, C.J., and Gospodarowicz, D., 1978, *Proc. Nat. Acad. Sci.*, **75**, 356.

48. Gomer, C.J., Rucker, N., and Murphree, A.L., 1988, *Cancer Res.*, **48**, 4539.

49. Hyman, L.G., Lilienfeld, A.M., Ferris, F.L., and Fine, S.L., 1983, *Am. J. Epidemiol.*, **118**, 213.

50. Schmidt-Erfurth, U., Hasan, T., Gragoudas, E., *et al.*, 1994, *Ophthalmol.*, **101**, 1953.

51. Fingar, V.H., Wieman, T.J., and Doak, K.W., 1990, *Cancer Res.*, **50**, 2599.

52. Allison, B.A., Watertield, E., Richter, A.M., and Levy, J.G., 1991, *Photochem. Photobiol.*, **54**, 709.

53. Okunaka, T., Eckhauser, M.C., and Kato, H., 1992, *Lasers Surg. Med.*, **12**, 98.

54. Hayes, K.C., Lindsay, S., Stephan, Z.F., and Brecker, D., 1989, *Invest. Ophthalmol. Vis. Sci.*, **30**, 225.

55. Matsumoto, M., Miki, T., Obana, A., *et al.*, 1993, *Lasers and Light in Ophthalmol.*, **5**, 157.

56. Husain, D., Miller, J.W., Michaud, N., *et al.*, 1996, *Invest. Ophthalmol. Vis. Sci.*, **37**, S223.

57. Schmidt-Erfurth, U., Miller, J.W., Sickenberg, M., *et al.*, 1996, *Invest. Ophthalmol. Vis. Sci.*, **37**, S122.

58. Miller, J.W., Schmidt-Erfurth, U., Sickenberg, M., *et al.*, 1996, *Invest. Ophthalmol. Vis. Sci.*, **37**, S223.

Development of Diode-Pumped Solid-State Laser and Its Application to Laser Fusion and Industry

S. Nakai*, Y. Izawa*, M. Nakatsuka*, M. Yamanaka*, Y. Kozaki*, T. Jitsuno*, T. Kanabe*,
N. Miyanaga*, E. Yoshida*, K. Tsubakimoto*, H. Kiriyama*, H. Matsui*, T. Yamanaka*,
S. Motokoshi**, H. Furukawa**, C. Yamanaka**, T. Sasaki***, Y. Mori***,
H. Kan****, and T. Hiruma****

* *Institute of Laser Engineering, Osaka University, 2-6 Yamada-oka, Suita, Osaka, 565 Japan*
e-mail: nakai@ile.osaka-u.ac jp
** *Institute for Laser Technology, 2-6 Yamada-oka, Suita, Osaka, 565 Japan*
*** *Faculty of Engineering, Osaka University, 2-1 Yamada-oka, Suita, Osaka, 565 Japan*
**** *Hamamatsu Photonics K.K., 5000 Hirakuchi, Hamakita, Shizuoka, 434 Japan*
Received August 8, 1997

Abstract—The goal of Inertial Fusion Energy (IFE) development is to prove that fusion energy can be available as electric power source. Recent progress of laser fusion research and relevant technologies enable us to examine technical and economical feasibility, and to plan the realistic strategy to the commercial power plant. The most important key issue for IFE is the driver technology. The development of the laser fusion driver is opening new industrial technologies based on the photon processes and is attracting attention in wide industrial fields.

1. INTRODUCTION

Laser fusion is one of the most feasible approaches in the fusion energy development [1]. The most important key technology of laser fusion is the reactor driver. Laser-diode-pumped solid-state laser (DPSSL) is expected to be industrial power laser and also to be feasible candidate for the driver of laser fusion power plant.

The technical and economical feasibility of DPSSL for laser fusion driver have been investigated through a conceptual design study of a laser fusion power plant KOYO. A small-scale disk-type DPSSL system, which contains all key elements for a driver, was constructed, and the performance was investigated to show the feasibility of DPSSL for fusion driver.

A new conceptual design of a DPSSL for laser fusion driver has been developed. Zigzag path slab amplifier is adopted because of its advantage that the laser beam does not pass through the cooling media, which enables the use of flowing water having high cooling capability.

A novel LD-pumped Nd : YAG laser with eight-pass amplifier architecture has been developed to achieve high average output power with high efficiency and good beam quality. The thermal birefringence in the Nd : YAG slab was compensated by introducing a 90-degree quartz rotator at symmetric position of the path.

High-power laser diode is one of the key elements of DPSSL. The development and improvement of laser diode and its stacking technique are being proceeded with attentions on efficiency, frequency control, and suppression of chirping, life, and manufacturing cost. The performance characteristics are satisfactory for laser pumping. The cost reduction is the future technical issue which is most important figure for the application to laser fusion driver. Frequency conversion of output laser beam is being investigated and developed especially for high-repetition operation.

The industrial applications of high-power laser are progressing with the development of DPSSL with the feature of high efficiency and low photon cost. Cooperative programs with industry are also proceeded to enhance the spin off of power laser development on the way to achieve a giant laser system of high average power (MW) with high efficiency (>10%) and good beam quality for laser fusion driver.

2. LASER FUSION POWER PLANT KOYO

The design study of the laser fusion power plant KOYO has been conducted as a joint program of universities, national laboratories, and industries in Japan and also with international collaborations [2]. Following to the conceptual design study, the most critical key technologies which may affect the technical and economical feasibility of the commercial power plant KOYO have been examined, and the research and development on important issues have been performed. Figure 1 shows the KOYO power plant and the reaction chamber.

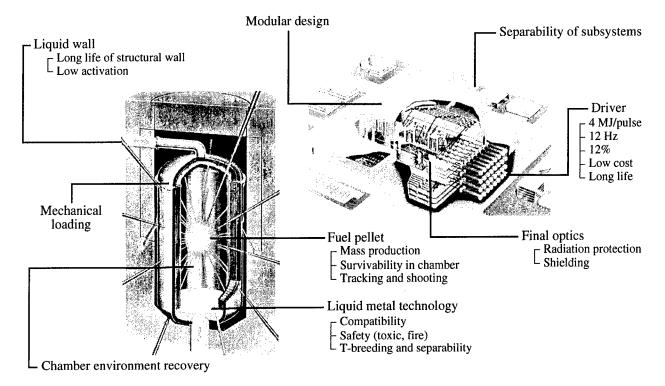The design concept of KOYO is based on (i) the use of gain scaling of direct drive implosion taking into

Modular design   Separability of subsystems

Liquid wall
  ┌ Long life of structural wall
  └ Low activation

                                                                  Driver
                                                                    ┌ 4 MJ/pulse
                                                                    ├ 12 Hz
                                                                    ├ 12%
                                                                    ├ Low cost
                                                                    └ Long life

Mechanical
loading

                                          Fuel pellet   Final optics
                                            ┌ Mass production   ┌ Radiation protection
                                            ├ Survivability in chamber   └ Shielding
                                            └ Tracking and shooting

                                          Liquid metal technology
                                            ┌ Compatibility
                                            ├ Safety (toxic, fire)
                                            └ T-breeding and separability

  └ Chamber environment recovery

Fig. 1. KOYO Power Plant and the reaction chamber.

account the tolerable nonuniformity of fuel pellet and irradiation intensity, (ii) the use of high-efficiency diode-pumped solid-state laser (DPSSL) as the fusion driver, (iii) protection of structural wall from microexplosion by liquid metal which flows down in woven

Table 1. Major parameters of the laser fusion modular power plant KOYO

Plant Power Balance		
Fusion Power	Pf	7200 MWth
Thermal Power	Pt	7920 MWth
Gross Electric Power	Pe	3406 MWe
Net Electric Power	Pn	2840 MWe
Reactor Module Thermal Power	Pct	1980 MWth
Reactor Module Number	n	4
Driver		
Laser Energy	E_L	4 MJ
Laser Wavelength		0.35 μm
Beam Number		32
Laser Repetition Rate	r_L	12 Hz
Laser Efficiency	η_D	12%
Reactor		
Micro Explosion Output/Shot		600 MJ
Reactor Pulse Repetition Rate	r_C	3 Hz
Tritum Breeding Ratio		1.1
Reactor Radius (at First Wall)		4.0 m
Reactor Radius (at Vessel Steel)		5.45 m

SiC tube, and (iv) modular power plant where multireaction chambers are driven by one driver laser.

The major parameters of KOYO are shown in Table 1. The driver of KOYO is the DPSSL whose efficiency and repetition rate are 12% and 12 Hz, which drives four reaction chambers with 3 Hz. The laser energy is 4 MJ per pulse at wavelength of 0.35 μm. The number of beams is 32 to achieve the required uniformity of irradiation. The moderate modular output of 1980 MW thermal (MWt), 850 MW electric (MWe), and the conservative pulse rate of 3 Hz are chosen to satisfy the condition of reactor chamber restoration.

Economic modeling and parametric system studies have been carried out to assess the sensitivity of the above design point to key physics and engineering parameters and uncertainties of assumptions, and to find the most attractive design point.

3. DRIVER DEVELOPMENT FOR LASER FUSION POWER PLANT

3.1. Requirement to Fusion Driver

The requirement to a fusion driver for commercial power plant is given by the knowledge on implosion physics and technical and economical feasibility study through a conceptual design as seen in the preceding sections. The specifications of a laser driver are (1) energy (~ MJ/pulse), (2) intensity (10^{14}–10^{15} W/cm² on target), (3) pulse shape (tailored in 20–40 ns pulse), (4) wavelength (0.5–0.3 μm), (5) spatial uniformity of irradiation (<1%), (6) efficiency (~10%), (7) repetitive
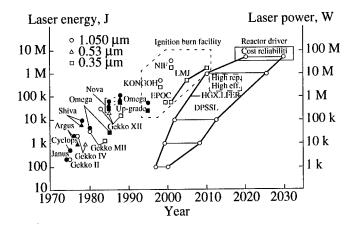
Fig. 2. Glass laser system for implosion and DPSSL development in the world.

Fig. 3. Output intensity and electrical to optical conversion efficiency versus current with the two-dimensional 0.8-μm AlGaAs LD array.
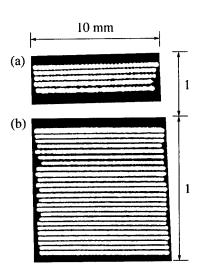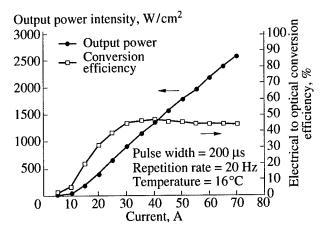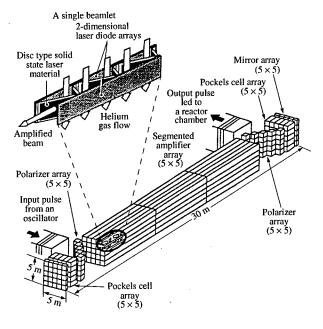

Fig. 4. 2.5-kW/cm^2 two-dimensional 0.8-μm AlGaAs LD arrays near-field laser output pattern of (a) 5 bars with 33 laser junctions per bar, (b) 25 bars with 66 junctions per bar.

Fig. 5. A conceptual main segmented amplifier of 200 kJ output energy per pulse at 1054 nm, consisting of 25 single segmented amplifiers in a 5 × 5 array. These amplifiers are surface-pumped using AlGaAs LD arrays.

operation (~10 Hz), (8) cost (capital and operational cost, including life and maintainability), (9) reliability or availability [1].

In the above specifications, items (1) to (5) are required for the research phase of high gain demonstration. These specifications are well achieved by the flashlamp-pumped glass-laser technology. Items (6) to (9) are required of a driver for a laser fusion power plant. New solid-state laser technology which had technical breakthrough of laser diode pumping gives us feasible prospect toward the power plant driver. Figure 2 shows the progress of flushlamp-pumped glass laser

and the expected growth of Diode-Pumped Solid-State Laser (DPSSL).

3.2. Laser Diode Development

High-power AlGaAs laser diode (LD) which satisfies the required specifications for pumping Nd-doped solid-state laser materials has been successfully developed [3]. Spectral control of LD to match the laser materials and reduction of frequency chirping of LD within the absorption line width of the materials have been achieved. Two-dimensional quasi-cw LD array of high power intensity (2.5 kW/cm^2), high electrical to optical
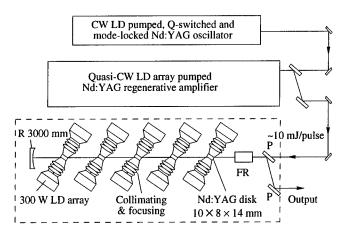
Fig. 6. The experimental set up of an LD array surface-pumped Nd : YAG disk amplifier system: P, thin film polarizer; FR, Faraday rotator.


Fig. 7. Energy extraction efficiency measured as a function of incident LD pump energy. Theoretical curves (solid line) without thermal birefringence loss and (dotted line) with the loss are shown.

conversion efficiency (50%), long life ($>4 \times 10^9$ shots) has been achieved as shown in Fig. 3.

The uniformity of output power on the 2-D LD array is sufficiently high enough for the construction of a large-scale system of KOYO driver as shown in Fig. 4.

Since 2.5-kW LD array has 1×1 cm aperture, as seen in Fig. 4b, a 1 MW LD array can be stacked in 10×40 cm aperture to pump the Nd : glass disk. To collimate the LD output beam, a microlens array can be directly attached to each LD bar.

High power, 0.9-μm InGaAs quasi-cw LD array of an electrical to optical conversion efficiency as high as 60% has also been developed for pumping the Yb-doped laser materials such as Yb : glass and Yb : S-FAP.

3.3. Diode-Pumped Solid-State Laser System

Technical and economical feasibility of diode-pumped solid-state laser (DPSSL) driver for the fusion reactor such as KOYO is examined. Nd-doped solid-state laser materials with lasing wavelength at 1 μm are selected. Using a conceptual designing technique [4], a prototype-model driver is designed, which has the specifications for a reactor driver of an output of 4 MJ per pulse at the wavelength of 351 nm, overall efficiency of 12%, and a repetition rate of 12 Hz.

The DPSSL system for KOYO is composed of 32 beams. An example of the set up of the main amplifier in one beam line is schematically shown in Fig. 5. To achieve 12% overall efficiency at 351 nm for the system, a regenerative amplifier as preamplifier and a multipass saturation amplifier as main amplifier will be adopted. The Nd : glass (HAP4) disks in $1.5 \times 30 \times 55$ cm are pumped by 1.3-kW/cm^2 AlGaAs LD array and cooled by helium gas from both sides.

A small-scale DPSSL system [5] which has all the elemental components for the large-scale system (Fig. 6) has been constructed, with a high pumping density of 3 kW/cm^2, to investigate the technical problems of
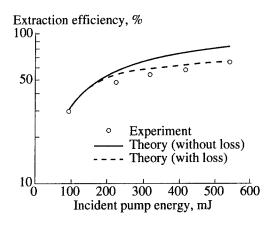
high-repetition operation with good beam quality and high efficiency. They are thermal lens effect and thermally induced birefringence effect in the LD surface pumped disk, energy extraction efficiency by saturation amplification, and cooling technique of laser disks. The net extraction efficiency of 65% was achieved by taking into account the thermally induced birefringence loss of 11%, as shown in Fig. 7. It was demonstrated in the experiment on Nd : glass (HAP4) rod laser that the thermally induced birefringence loss of about 10% has been compensated down to 1% by using a 90-degree quartz rotator between two identical LD-pumped Nd : glass rods [6]. This compensation technique can be useful for the DPSSL driver.

The overall efficiency and that of each elementary process in the small-scale DPSSL have been experimentally examined and compared with the values which are designed in the reactor driver for KOYO. It seems to be a reasonable goal to achieve 12% of driver efficiency even for the large system of 4 MJ/pulse.

For optimization of different concepts of amplifiers, a zigzag path slab amplifier has been designed and prototype module development has been started. Zig-Zag path slab has an advantage that the laser beam does not pass through the cooling medium as it propagates by means of total internal reflections. Therefore, the slab can be cooled on both sides with flowing water having high cooling capability.

For the laser gain medium, we have adopted the glass host which can be manufactured in large size with good optical quality. The HAP4 glass has the appropriate material parameters [4] for designing a high-power and repetitively operating laser system. The slab dimensions were determined under the several operational constraints such as thermal shock fracture, optical damage, parasitic oscillation, total gain, and so on. The cost optimization was also considered.

Figure 8 shows the schematic design of a driver module. It consists of 15 beams. Each beam is ampli-
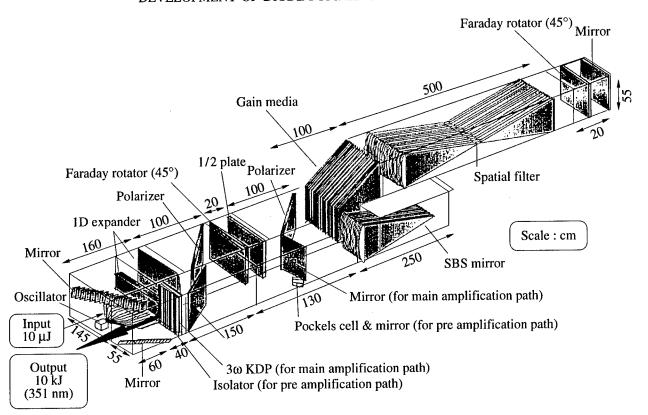
Fig. 8. A blue 10-kJ module consists of 15 beamlets. Each of preamplification path and main amplification path passes four times in gain media.

fied from 10 µJ input energy to 700 J of blue output energy giving 10 kJ total output energy of a module. Thermal effects such as focusing and birefringence are compensated by using SBS mirror and a 45-degree Faraday rotator.

4. DEVELOPMENT OF INDUSTRIAL DPSSL WITH HIGH BEAM QUALITY

A new laser-diode (LD) pumped eight-pass Nd : YAG zigzag slab amplifier architecture is proposed, and the energy extraction performance has been experimentally investigated. High energy extraction efficiency of up to 71% has been achieved with thermal birefringence compensation.

Figure 9 shows the schematic set up of the system. The eight-pass amplifier consists of a Nd : YAG slab, a permanent magnet Faraday rotator, thin film polarizers, high-reflection mirrors of M_1–M_5, a 90-degree quartz rotator, and a quarter-wave plate. The input laser pulse to the amplifier, which is 2 mm in diameter and p-polarized to the polarizer P_1, can pass through the amplifier slab for eight times. The pulse is finally extracted by polarizer P_1.

The amplifier module consists of a Nd : YAG zigzag slab side-pumped by a 30 × 1.2 mm LD arrays (emission wavelength around 807 nm) on each side. Each LD array of 36 mm² operates at a peak power of 900 W for a duration of 200 µs at 50 Hz repetition rate synchro-
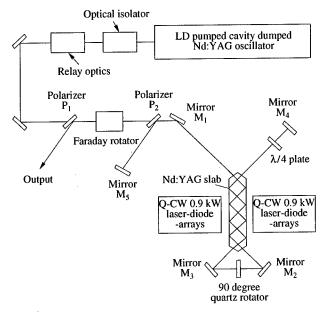
Fig. 9. Schematic setup of laser-diode-pumped novel eight pass slab amplifier geometry.

nized with the oscillator. The LD arrays were placed close to the slab and the output was directly coupled into the slab without any coupling optics.

The energy of output laser pulse E_{out} was measured as a function of small-signal gain, G_0, with thermal
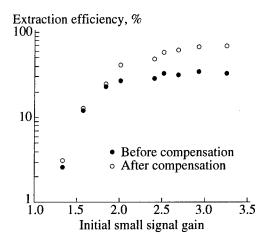
Fig. 10. Energy extraction efficiency as a function of initial small-signal gain.
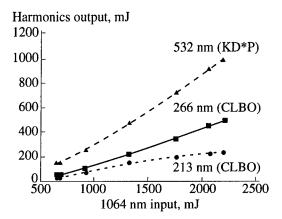
Fig. 11. Fourth- and fifth-harmonic generation of Nd : YAG laser by CLBO.

birefringence compensation (i.e., without a 90-degree quartz rotator) and with compensation (with insertion of a 90-degree quartz rotator). The small-signal gain was varied from 1.33 to 3.25 by changing the LD array output peak power.

Figure 10 shows the extraction efficiency as a function of small-signal gain. It is seen in Fig. 10 that the extraction efficiency increased with birefringence compensation especially at higher G_0 values. A maximum extraction efficiency of up to 71% for the laser mode volume was obtained at G_0 of 3.25.

A higher power laser system with high efficiency and high beam quality is under construction, which will deliver 100 W of average power of 8-ns pulse with a repetition rate of 50 Hz.

5. NEW NONLINEAR OPTICAL CRYSTAL $CsLiB_6O_{10}$

For applying to the laser driver with repetitive operation, much effort has been spent on developing the borate series as new nonlinear optical (NLO) materials because of their higher NLO susceptibility and lower temperature sensitivity in the phase-matching (PM) condition than KDP. Recently, a new NLO crystal, cesium lithium borate, $CsLiB_6O_{10}$ (CLBO), has been discovered [7], which exhibits excellent NLO properties and simplicity in growth.

Table 2 shows values of angular, spectral, and temperature bandwidths and walk-off angle for various frequency conversion process in CLBO. For comparison, values of KDP and BBO calculated from the refractive index data are shown. For second- and third-harmonic generation (SHG and THG), CLBO shows relatively smaller values of angular and spectral bandwidths compared to a KDP crystal with the same thickness. On the other hand, due to the 2.5 times larger d_{eff} of CLBO with respect to KDP, the same nonlinearity can be obtained with a thinner CLBO crystal. This means that increased values for angular, spectral, and temperature bandwidths of CLBO compared to KDP can be obtained. For example, the temperature bandwidth of CLBO with a thickness of 0.4 cm becomes 108°C for SHG, which is over 5 times larger than that of 1-cm-thick KDP crystal ($\Delta T = 19.1$°C), leading to the higher stability for frequency conversion of high average power laser output.

Table 2. Nonlinear optical properties of CLBO compared with those of KDP and BBO

| Wavelength, nm	Crystal	PM angle θ, deg	Calculated d_{eff}, pm/V	$\Delta\theta l$, mrad cm	$\Delta\lambda l$, nm cm	ΔTl, °C cm	Walk-off angle, deg	Damage threshold, GW/cm²
1064 + 1064 = 532	CLBO (Type-II)	42.3	0.95	1.7	5.6	43.1	1.78	26
	KDP (Type-II)	59	0.38	3.4	11.5	19.1		~20
	BBO	22.8	2.06	0.92	2.1	37.1	3.20	13.5
1064 + 532 = 355	CLBO (Type-II)	48.5	0.94	0.82	0.84	21.3	2.10	
	KDP (Type-II)	58	0.38	1.06	0.95			
532 + 532 = 266	CLBO	61.6	0.84	0.49	0.13	8.3	1.83	
	KDP	78	0.51	1.7	0.13	1.2		
	BBO	47.5	1.32	0.17	0.07	4.5	4.80	
1064 + 266 = 213	CLBO	67.3	0.87	0.42	0.16	5.1	1.69	
	BBO	51.1	1.26	0.11	0.08	3.1	5.34	
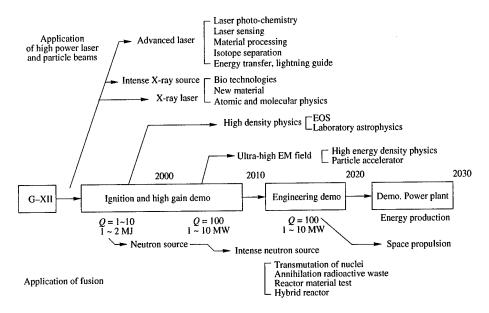
Fig. 12. Application and spin-off of ICF.

It is also demonstrated that fourth and fifth harmonics can be generated easily with a relatively high conversion efficiency as shown in Fig. 11.

6. APPLICATION OF HIGH-POWER LASER

The most important and basic key issue for a laser fusion power plant is the advanced high-power laser as a driver. The precision and high-power laser technology could open a new field in sciences and industrial technologies. Some examples of spin off and application of high-power laser and ICF technologies are summarized in Fig. 12 along with the strategic development of laser fusion toward achievement of power plant.

For the industrial application, the overall cost of laser light (COL) or photon cost is the key parameter. The COL (¥/kW h) may be analyzed as follows.

$$COL = \left(\frac{aS_L}{\tau R_{op}} + C_{LM} + \frac{P_L}{\eta_d}COE\right)/P_L, \qquad (1)$$

where S_L is the laser system capital cost, τ is the redemption duration, a/τ is the rate of capital redemption, R_{op} is the operational rate or availability, C_{LM} is the maintenance cost, P_L is the laser output power, η_d is the laser efficiency, and COE (¥/kW h) is the cost of electricity. Putting the specific figures for KOYO driver into (1), the COL is estimated to be less than 200 ¥/kWh.

The cost limitation of a laser fusion power plant to be economically acceptable and competitive to other electricity sources is given by

$$COL \cdot P_L + \frac{aS_R}{\tau R_{op}} + C_{RM} \leq COEP_E, \qquad (2)$$

where $P_E = P_L Q \eta_g$ is the electrical output; S_R and C_{RM} are the reactor system capital cost and maintenance cost, respectively; and Q and η_g are the energy gain and electric generation efficiency. The right-hand term is the sales income of electricity. It is expected that $Q = 100$ and $\eta_g = 40\%$; therefore, the absolute upper limit of COL is given by $40 \times COE$, that is, 400 ¥/kWh in Japan, ignoring S_R and C_{RM} terms.

The above discussion on the COL is based on the expected and assumed figures of cost and technical evaluation. It is our goal of development to realize a laser fusion power plant. An advanced laser with this value of COL, together with the features of compactness, durability, and easy maintenance, will provide us powerful and effective tools for new industrial technology. It could be a revolution of not only manufacturing also in wide areas such as architecture, civil engineering, mining, and heavy industry.

REFERENCES

1. 1995, Energy from Inertial Fusion (Vienna: IAEA).
2. Mima, K. et al., 1992, IAEA-CN-56/G-2-3 (Würzburg); Mima, K. et al., 1994, IAEA-CN-60/F-1 (Seville); Nakai, S. et al., 1996, IAEA-CN-64/G1-3 (Montreal).
3. Kan, H. et al., 1995, Review of Laser Engineering (in Japanese), **23**, 41.
4. Naito, K. et al., 1992, Jpn. J. Appl. Phys., **31**, 259.
5. Ohmi, M. et al., 1996, AIP Conf. Proc. (American Inst. Phys.), **369** Part 2, 836.
6. Kiriyama, H. et al., 1996, Opt. Rev., **3**, 14.
7. Mori, Y. et al., 1995, Appl. Phys. Lett., **67**, 1818.

Mn³⁺: Fundamental Spectroscopy and Excited-State Absorption

S. Kueck, S. Hartung, S. Hurling, and K. Petermann

Institut für Laser-Physik, Universität Hamburg, Jungiusstrasse 9a, Hamburg, 20355 Germany
e-mail: kueck@physnet.uni-hamburg.de
Received August 18, 1997

Abstract—Mn³⁺-doped garnet crystals were spectroscopically investigated with respect to the realization of a new solid-state laser emitting in the red to near-infrared spectral range. The room temperature absorption and emission spectra are dominated by the spin-allowed broad-band transitions between the Jahn–Teller split quintet states, i.e., the ^5E ground state and the $^5T_2$ excited-state. The whole spectral region of the emission is covered by strong excited state absorption transitions arising from the $^1T_2$ level, which is energetically lower than the $^5T_2$ level. Both energy levels are thermally coupled. Due to this strong excited-state absorption, laser oscillation will be unlikely in Mn³⁺-doped garnets.

INTRODUCTION

Since the development of the $Ti^{3+} : Al_2O_3$ laser (tunable in the 700–1000 nm range) [1, 2] much research has been done on tunable solid-state lasers for shorter wavelengths. However, none of them has been successful yet, mostly because of strong excited-state absorption at the pump or laser wavelength. Tunable solid-state lasers in the spectral region between 600 and 700 nm are useful for a variety of applications, e.g., display technology, medicine, and spectroscopy. The Mn³⁺ ion seems to be an interesting candidate for an active laser center for this spectral region, because its emission covers the entire wavelength region between 550 and 1300 nm [3, 4]. The crystal field splitting of the Mn³⁺ energy levels is described (in cubic approximation) by the Tanabe–Sugano diagram for the d^4 electron configuration [5] (see Fig. 1). Although for a d^4 electron system a large number of energy levels exists, only two of them are quintet states, i.e., the ^5E ground state and $^5T_2$ excited state. Many excited-state absorption transitions from the $^5T_2$ into higher lying levels are expected, but all of these transitions are spin-forbidden, i.e., the excited-state absorption cross section is much smaller than the emission cross section of the $^5T_2 \longrightarrow {}^5E$ transition. However, in this paper it will be shown, that excited-state transitions from the energetically lower metastable $^1T_2$ level prevent laser action in Mn³⁺-doped garnets.

The Jahn–Teller effect [6] can strongly influence the optical spectra of transition metal ion doped materials. The absorption spectra of the Mn³⁺ ion in octahedral coordination reveal a strong Jahn–Teller distortion in the ^5E ground state [4, 7, 8, 9]. In [4] the influence of the Jahn–Teller distortion and the thermalization of different energy levels on the emission characteristic was investigated in detail; here, we focus on the basic spectroscopy and on the influence of the excited-state absorption.

CRYSTAL GROWTH

All crystals under investigation were Mn-doped garnets, that are $Y_3Al_5O_{12}$ (YAG), $Y_3Ga_5O_{12}$ (YGG), $Gd_3Ga_5O_{12}$ (GGG), $Y_3Sc_2Ga_3O_{12}$ (YSGG), and $Gd_3Sc_2Ga_3O_{12}$ (GSGG). Garnets are cubic crystals with
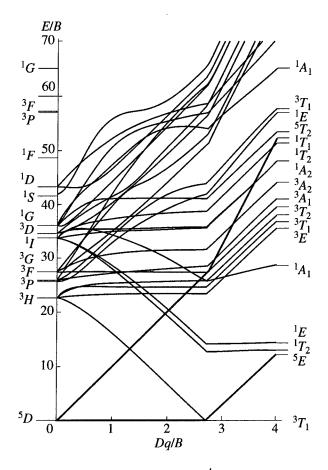

Fig. 1. Tanabe–Sugano diagram for a d^4 electron configuration in octahedral symmetry.

space group $Ia3d$ (O_h^{10} in Schoenfliess notation) [10]. The stoichiometric formula is $\{C\}_3[A]_2(D)_3O_{12}$, where C, A, D denote lattice sites with dodecahedral, octahedral, and tetrahedral coordination, respectively, and with site symmetries D_2, C_{3i}, and S_4, respectively. The crystals were grown in our institute by the Czochralski method using an iridium crucible and RF heating.

The total manganese concentrations in the crystals were determined for YSGG and YGG with atomic emission spectroscopy to be 5.2×10^{15} cm^{-3} and 2.5×10^{18} cm^{-3}, respectively. These concentrations have to be considered as upper limits for the Mn^{3+}-ion concentration, as well as the manganese distribution coefficients of 0.12 and 0.07 for YSGG and YGG, respectively. These distribution coefficients are rather low, although the ionic radii of manganese and the constituent lattice ions are quite similar [r(Sc^{3+}) = 75 pm, r(Ga^{3+}) = 62 pm, r(Mn^{2+}) = 83 pm, r(Mn^{3+}) = 65 pm, r(Mn^{4+}) = 54 pm] [11].

SPECTROSCOPIC METHODS AND EXPERIMENTAL SETUPS

The room-temperature absorption spectra were measured with a CARY 2400 spectrophotometer. The fluorescence measurements were performed under argon-ion laser excitation at 514.5 nm. The emission was detected with a photomultiplier with S1 characteristic or a cooled InSb detector, which was placed behind a 0.5-m spectrometer. The spectral resolutions were 1.6 nm between 500 and 1000 nm and 3.2 nm between 1000 nm and 1500 nm. Appropriate optical filters were used to block scattered light of the excitation beam and to avoid second-order effects. The lifetime measurements were carried out under excitation with a Q-switched, frequency-doubled Nd:YAG laser operating at 532 nm with a pulse length of 10 ns. The excited-state absorption measurements were performed with a pump- and probe technique in the continuous-wave regime. The double modulation technique with two lock-in amplifiers was used, described in detail in [12, 13]. Both the difference in the transmitted intensities in the pumped and unpumped case ($I_p - I_u$) as well as the transmitted intensity ($I \approx I_p \approx I_u$) through the crystal were measured simultaneously. It can be shown that the following equation holds [13]:

$$\frac{I_p(\lambda) - I_u(\lambda)}{I_p(\lambda)} \propto \sigma_{GSA}(\lambda) + \sigma_{ESA}(\lambda). \quad (1)$$

Here, σ_{GSA}, σ_{SE} and σ_{ESA} are the ground-state absorption, stimulated emission, and excited-state absorption cross section, respectively. Pump and probe beams were provided by an argon-ion laser operating at 514.5 nm and a broadband tungsten lamp, respectively. The transmitted intensities were measured with a Si detector or a cooled InSb detector, which was placed behind a 0.5-m spectrometer. The spectral resolution was 3.2 nm for the entire spectral range between 500 and 2000 nm. For the
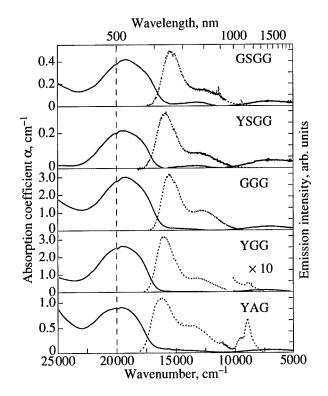
Fig. 2. Room-temperature absorption (full lines) and emission spectra (broken lines) of Mn^{3+}-doped garnets. The dashed line indicates the position of the Fano antiresonance.

12 K spectra, the crystals were placed in a closed-cycle He cryostat. In this case, the resolution was 1 nm in the whole spectral range.

RESULTS AND DISCUSSION

Absorption

In Fig. 2 the room-temperature absorption spectra of the investigated crystals are shown. They are dominated by a strong broad band around 500 nm, which is assigned to the interconfigurational transition between the two Jahn–Teller split quintet levels, i.e., the ^5E ground state and the $^5T_2$ excited state. The Jahn–Teller splitting of both energy levels (especially of the ground state) causes the large bandwidth of ≈ 4000 cm^{-1} in all investigated crystals. As expected from the Tanabe–Sugano diagram (see Fig. 1), a shift of this band to shorter wavelengths is observed with increasing crystal field strength. On the short-wavelength side of this main absorption band a characteristic feature is observed, which is attributed to a Fano-antiresonance effect [14] between the ^3E and the $^5T_2$ levels (see also Fig. 2). The energetic position of this feature (dashed line) is independent of the host crystal, i.e., of the crystal field strength. This antiresonance effect is caused by the mixing between spin–orbit components of these levels and happens at the crossing of a spin-forbidden, crystal field independent term with a spin-allowed, crystal field dependent term [15]. With this antiresonance
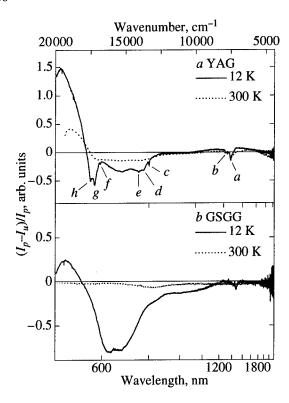
Wavenumber, cm^{-1}

Fig. 3. $(I_p - I_u)/I_p$ spectra of Mn^{3+} : YAG (a) and Mn^{3+} : GSGG (b) at 300 K and 12 K.

the ratio between the crystal field strength Dq and the Racah parameter B was roughly estimated to be $Dq/B \approx 2.3$.

The infrared absorption band centered around 1400 nm is assigned to a transition between the two Jahn–Teller split components of the ^5E ground state. The band shape is nearly Gaussian, which is a hint for a transition with a large Stokes shift. The bandwidths of 3200 to 3900 cm^{-1} of this transition are caused by a strong Jahn–Teller effect of the ^5E ground state. For Mn^{3+} in acidic and aqueous solutions similar bands were observed by Davis *et al.* [9]. A clear relation between the crystal field strength and the energetic position of this band is not found and also not expected, because the energetic difference between the two Jahn–Teller split components of the ^5E level is determined by

Table 1. Jahn–Teller stabilization energies of the Mn^{3+} ^5E, $^5T_2$, and $^1T_2$ levels, $\Delta E(^5T_2 - {}^1T_2)$, and quantum efficiency η in the investigated garnet crystals

Crystal		GSGG	YSGG	GGG	YGG	YAG
$\Delta E_{JT}(^5E)$	[cm^{-1}]	1838	2014	1823	1885	1800
$\Delta E_{JT}(^5T_2)$	[cm^{-1}]	366	347	348	308	301
$\Delta E_{JT}(^1T_2)$	[cm^{-1}]	178	210	163	167	189
ΔE	[cm^{-1}]	351	900	900	1030	1290
η (300 K)	[%]	<0.05	<0.05	<0.05	0.4	1

the Jahn–Teller stabilization energy. This energy is not necessarily correlated to the crystal field strength, but to the local site symmetry. The Jahn–Teller stabilization energies $\Delta E_{JT}(^5E)$ are listed in Table 1; their calculation from spectroscopic data were performed in detail in [4]. The values are between 1800 cm^{-1} for YAG and 2014 cm^{-1} for YSGG.

Emission

The room-temperature emission spectra are also shown in Fig. 2. They consist of two broad bands in the visible spectral range with maxima around 630 and 800 nm. These bands are due to the transitions between the thermally populated $^5T_2$ excited state and the two components of the Jahn–Teller split ^5E ground state. The spin-forbidden emission bands from the $^1T_2$ level are only observed at low temperatures, when the population of the $^5T_2$ level is small. The emission bands exhibit a blue shift with increasing crystal field strength as expected from the Tanabe–Sugano diagram and from the absorption spectra. The band shapes are Gaussian with bandwidths of about 1420 and 3300 cm^{-1}. The Jahn–Teller energies $\Delta E_{JT}(^5T_2)$ are between 300 and 366 cm^{-1} (see Table 1). The low-temperature emission spectra of the Mn^{3+} ion were also analyzed in detail in [4]. They consist of spin-forbidden transitions from the energetically lower lying $^1T_2$ energy level. The $^5T_2$ level is not populated at these temperatures and, therefore, no emission from this level is observed. The energetic distance ΔE between the $^1T_2$ and the $^5T_2$ was determined from the temperature dependence of the lifetime, the results are also listed in Table 1.

A third emission transition is observed at room temperature in the infrared spectral region around 1150 nm for Mn^{3+} : YAG and barely for Mn^{3+} : YGG. At lower temperatures, this transition is also observed in all of the other investigated crystals. This band is assigned to the transition between the $^1T_2$ and $^3T_1$ levels. As expected from the Tanabe–Sugano diagram (Fig. 1), the energetic position of this band is nearly independent of the crystal field strength, i.e., the host crystal, because both levels have nearly the same crystal field dependence. Furthermore, they exhibit a smaller bandwidth. For elevated temperatures the intensity of this spin-forbidden transition drops below the detection limit for GGG, YSGG, and GSGG due to the nonradiative quenching process. The room temperature emission lifetime is between 1.1 ms for Mn^{3+} : Y$_3$Al$_5$O$_{12}$ and <0.5 μs for Mn^{3+} : Gd$_3$Sc$_2$Ga$_3$O$_{12}$. A detailed analysis of the temperature dependence of the lifetimes was performed in [4] and revealed a strong host crystal dependent quenching process between the involved energy levels. The quantum efficiencies at room temperature are between 100% for YAG and < 5% for GGG, YSGG, and GSGG (see Table 1).

Excited-State Absorption

The $(I_p - I_u)/I_p$-spectra of the Mn^{3+}-doped garnets were measured at room temperature and at 12 K.

The results for Mn^{3+} : YAG and Mn^{3+} : GSGG (these crystals represent the host materials with the highest and the lowest crystal field) are shown in Fig. 3. They reveal strong excited-state absorption covering the whole region of the Mn^{3+} emission, so that laser oscillation is prohibited at any temperature. For YAG with a high energetic distance of about 2000 cm^{-1} between the $^1T_2$ and $^5T_2$ level only the singlet level is occupied at low temperatures. Some sharp features are observed, which are transitions into higher singlet levels. An exact assignment of all observed transitions is difficult, because of the large number of final states and the Jahn–Teller splitting of some of these levels. However, some peaks were assigned with the help of the Tanabe–Sugano diagram (Fig. 1).

The peak (a) around 1335 nm (7490 cm^{-1}) is assigned to the transition between the $^1T_2$ and the $^1A_1$ level. This assignment is rather straightforward, because no other singlet level is present at this energetic distance. The sharp features (c), (f), and (g) at 752 nm (13304 cm^{-1}), 633 nm (15787 cm^{-1}, and 582 nm (17194 cm^{-1}), respectively, are probably due to transitions from the $^1T_2$ level to the nearly degenerate $^1T_2(^1I)$ and $^1A_2(^1I)$ levels, to the $^1T_1(^1I)$ level, and to the $^1E(^1G)$ level, respectively. Peak (c) with a bandwidth of only 39 cm^{-1} seems to be a zero-phonon transition, for the peaks (a), (f), and (g) with bandwidths of 86, 52, and 148 cm^{-1}, respectively, the assignment to zero-phonon lines is uncertain. The peaks (b), (d), and (h) at 1285 nm (7792 cm^{-1}), 735 nm (13605 cm^{-1}), and 572 nm (17492 cm^{-1}), respectively, could be attributed to a phonon sideband structure, because all have the same energetic distance of 300 cm^{-1} from the peaks (a), (c), and (g). Peak (e) at 712 nm (14051 cm^{-1}) cannot be accounted for; probably this is a second phonon sideband structure of peak (c). The data of the observed structures are summarized in Table 2.

At higher temperatures the sharp features disappear due to the thermal occupation of higher vibronic levels. Furthermore, the $^1T_2$ population drops and, therefore, the strengths of the excited-state absorption transitions. The $^5T_2$ level becomes higher populated; however, no higher quintet level exists and therefore, all excited-state transitions are spin-forbidden with smaller intensities. Ground-state absorption bleaching is observed for Mn^{3+} : YAG in the visible around 500 nm and in the infrared spectral range around 1200 nm, according to the transitions $^5E \longrightarrow {}^5T_2$ and $^5E \longrightarrow {}^5E$. For Mn^{3+} : GSGG the low-temperature $(I_p - I_u)/I_p$ spectrum looks very similar to the room-temperature Mn^{3+} : YAG spectrum, because the thermal population of the $^1T_2$ and $^5T_2$ levels are comparable in both cases. At elevated temperatures, the signal is almost diminished, because due to the short lifetime only a small excited-state population is reached.

SUMMARY AND OUTLOOK

Mn^{3+}-doped garnet crystals were spectroscopically investigated with respect to the realization of new laser

Table 2. Summary of the observed structures in the Mn^{3+}: YAG $(I_p - I_u)/I_p$ spectrum at 12 K

Peak	Wave-length [nm]	Energy [cm^{-1}]	Bandwidth [cm^{-1}]	Transition $^1T_2(^1I) \longrightarrow$
a	1335	7490	86	$^1A_1$
b	1285	7792		Phonon
c	752	13304	39	$^1T_2(^1I)$, $^1A_2(^1I)$
d	735	13605		Phonon
e	712	14051		
f	633	15787	52	$^1T_1(^1I)$
g	582	17194	148	$^1E(^1G)$
h	572	17492	118	Phonon

materials in the red to near-infrared spectral range. However, strong excited-state absorption due to singlet–singlet transitions overlaps the spectral regions of emission; therefore, laser oscillation is not expected in these materials, even at low temperatures. Until now, no host crystal is known, for which the $^5T_2$ level is the lowest metastable level. This would reduce the excited-state absorption, because from the $^5T_2$ only spin-forbidden transitions to higher lying levels exist. On the other hand, the strong quenching process between the energetically close levels has to be considered, so that low phonon hosts should be preferred, e.g., fluorides and chlorides.

REFERENCES

1. Moulton, P.F., 1982, *Opt. News*, **8**, 9.
2. Moulton, P.F., 1986, *J. Opt. Soc. Am. B*, **3**, 125.
3. Petermann K. and Huber, G., 1984, *J. Lumin.*, **31&32**, 71.
4. Kueck, S., Hartung, S., Hurling, S., *et al.*, accepted for publication in *Phys. Rev. B*.
5. Tanabe, Y. and Sugano, S., 1954, *J. Phys. Soc. Jpn.*, **9**, 753.
6. Jahn, H.A. and Teller, E., 1937, *Proc. Roy. Soc. A*, **161**, 220.
7. McClure, D.S., 1962, *J. Chem. Phys.*, **36**, 2757.
8. Dingle, R., 1962, *Mol. Spectrosc.*, **9**, 426.
9. Davis, T.S., Fackler, J.P., and Weber, M.J., 1968, *Inorg. Chem.*, **7**, 1994.
10. Menzer, G., 1928, *Z. Kristallogr.*, **69**, 300.
11. Kaminskii, A.A., 1981, *Laser Crystals* (Berlin: Springer).
12. Zemon, S., Lambert, G., Miniscalco, W.J., *et al.*, 1991, *Proc. SPIE*, **1373**, 21.
13. Koetke, J. and Huber, G., 1995, *Appl. Phys. B*, **61**, 151.
14. Fano, U., 1961, *Phys. Rev.*, **124**, 1866.
15. Sturge, M.D. and Guggenheim, H.J., 1970, *Phys. Rev. B*, **2**, 2459.

Room-Temperature Continuous-Wave Upconversion-Pumped Laser Emission in Ho, Yb : KYF$_4$ at 756, 1070, and 1390 nm

P. E.-A. Möbert*, A. Diening*, E. Heumann*, G. Huber*, and B. H. T. Chai**

* *Institut für Laser-Physik, Universität Hamburg, Jungiusstraße 9a, Hamburg, D-20355 Germany*
e-mail: moebert@physnet.uni-hamburg.de
** *Center for Research and Education in Optics and Lasers (CREOL), University of Central Florida,*
Orlando, FL 32816 USA
Received August 5, 1997

Abstract—We report room-temperature continuous-wave laser operation in Ho(0.5%), Yb(5%) : KYF$_4$ on the $^5S_2 \longrightarrow {}^5I_7$ transition at 756 nm, on the $^5S_2 \longrightarrow {}^5I_6$ transition around 1070 nm, and on the $^5S_2 \longrightarrow {}^5I_5$ transition at 1390 nm. Room-temperature absorption and fluorescence spectra are presented. An upconversion pumping mechanism was employed to populate the upper laser level $^5S_2$ of holmium. In first experiments a Ti : sapphire laser was used as pump source. Laser operation around 1070 nm and at 1390 nm was also obtained by laser diode excitation. The maximum achieved laser output power under laser diode pumping was 5 mW at 1070 nm and 1 mW at 1390 nm.

INTRODUCTION

Upconversion pumping is a possible excitation method to realize laser transitions from higher lying energy levels in rare-earth-doped solid-state materials. Ytterbium-sensitized upconversion energy transfer is particularly attractive for this purpose due to ytterbium's broad absorption band and the availability of high-power InGaAs laser diodes for excitation. There have been realized plenty of laser transitions in different rare-earth ions such as praseodymium, thulium, and erbium by means of energy transfer and upconversion mechanisms through ytterbium codoping [1–3].

Holmium is a well-known activator ion in solid-state materials for laser operation in the eyesafe 2-μm spectral region for LIDAR atmospheric wind measurements and laser radar applications [4, 5]. In contrast to laser operation in the 2-μm spectral range, laser transitions originating from the upper lying energy level $^5S_2$ in holmium are favorable in fluoride-based glasses, crystals, and fibers due to their lower phonon energies. However, there have been realized other different laser transitions in holmium-doped laser materials at room temperature: Pulsed operation in the 3 μm spectral range was demonstrated in Cr^{3+} : Yb^{3+} : Ho^{3+} : YSGG, continuous-wave running at 1390 nm was obtained in Ho^{3+}: YLF, and lasing at 753 and 553 nm was achieved in a holmium-doped fluorozirconate fiber by upconversion pumping [6–8]. Upconversion fluorescence and laser operation near 550 nm at 77 K in different Ho, Yb-doped fluoride crystals have already been investigated [9, 10]. This paper presents the spectroscopic and laser characteristics on the $^5S_2 \longrightarrow {}^5I_7$ transition at 756 nm, on the $^5S_2 \longrightarrow {}^5I_6$ transition around 1070 nm, and on the $^5S_2 \longrightarrow {}^5I_5$ transition at 1390 nm in ytterbium-sensitized holmium-doped potassium yttrium fluoride (KYF) using an Yb^{3+}–Ho^{3+} upconversion pumping

scheme to populate the upper laser level $^5S_2$ of holmium. Room-temperature continuous-wave laser operation at 756, 1070, and 1390 nm was attained by Ti : sapphire laser excitation. The 1070- and 1390-nm transitions were also realized by laser diode pumping.

UPCONVERSION PUMPING MECHANISM

The schematic illustration of the ytterbium and holmium energy level schemes, shown in Fig. 1, describes the excitation mechanism. In a first step, ytterbium is excited into the $^2F_{5/2}$ level by absorption of pump photons near 970 nm. A nonradiative energy transfer from ytterbium to holmium leads to the excitation of the holmium $^5I_6$ level. Subsequently, the indicated upconversion process $(^2F_{5/2}, {}^5I_6) \longrightarrow (^2F_{7/2}, {}^5S_2)$ between ytterbium and holmium efficiently populates the upper laser
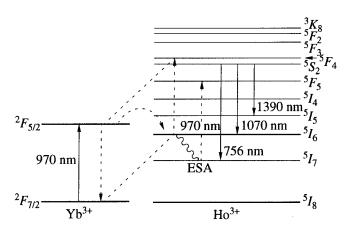

Fig. 1. Energy level diagram for the Yb^{3+} and Ho^{3+} ion showing the upconversion pumping mechanism employed to populate the upper laser level.
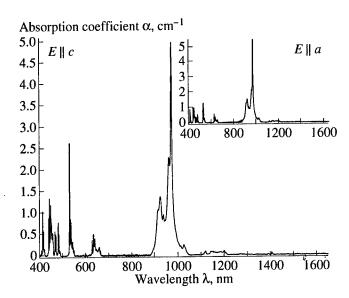
Absorption coefficient α, cm⁻¹

Fig. 2. Polarized room-temperature absorption spectra of Ho(1%), Yb(10%) : KYF₄.

level $^5S_2$ of holmium. The laser emission, as indicated in Fig. 1, takes place at 756 nm, around 1070 nm, and at 1390 nm.

CRYSTAL AND SPECTROSCOPIC DATA

The crystals investigated were grown at the CREOL crystal growth facility using a modified Czochralski technique. The uniaxial potassium yttrium fluoride crystal has a trigonal lattice (space-group C_3^2 Schönfließ). The Ho^{3+} and Yb^{3+} ions are substituting the Y^{3+} ions occupying six inequivalent lattice sites with lowest site symmetry C_1 [11]. The composition of the studied crystals was $K_1Y_{0.945}Ho_{0.005}Yb_{0.05}F_4$ and $K_1Y_{0.89}Ho_{0.01}Yb_{0.1}F_4$.

The room-temperature absorption and fluorescence spectra are depicted in Figs. 2–4. The absorption spectra in π- (parallel to the crystal c-axis) and σ-polarization (parallel to the crystal a-axis) were detected with a Perkin–Elmer spectrophotometer (resolution below 850 nm about 1 nm, above 850 nm about 2 nm). The polarized room-temperature fluorescence spectra were measured in the visible (resolution 0.32 nm) using a silicon diode and in the infrared spectral region (resolution 3.2 nm) using an InSb detector at 77 K, respectively. Excitation was accomplished by dint of a 4-W fiber-coupled (core diameter 100 μm) laser diode with a center wavelength at 970 nm. The spectra were calibrated with a spectrum of a tungsten halogen lamp at 2473 K. Clearly recognizable are the inhomogenous broadened absorption and fluorescence bands due to the inequivalent lattice sites occupied by Ho^{3+} and Yb^{3+} ions. However, the fluorescence spectra around 1390 nm were not detectable because of a too weak signal.

The fluorescence lifetimes τ of the different energy levels were determined using a frequency-tripled
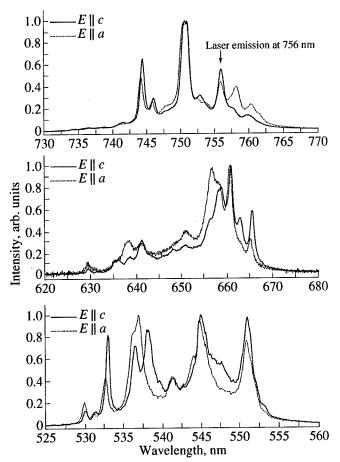
Fig. 3. Polarized room-temperature fluorescence spectra of Ho(1%), Yb(10%) : KYF₄ around 540, 660, and 750 nm; the realized laser transition is indicated.

flashlamp-pumped Nd : YAG laser ($\lambda = 355$ nm, $E \approx 100$ mJ, $\Delta t = 10$ ns)-pumped optical parametric oscillator for excitation at 537 and 970 nm, respectively, and a S_1 photomultiplier tube at 233 K for detection. The data are summarized in the table. A significant shortening of the holmium upper laser level lifetime $^5S_2$ was observed from 180 μs under direct excitation of holmium at 537 nm to 50 μs under ytterbium excitation at 970 nm. A possible reason for this behavior is an ytterbium–holmium upconversion process ($^2F_{5/2}$, $^5S_2$) ⟶ ($^2F_{7/2}$, $^5G_5$) resulting in a population of higher lying holmium energy levels and just being present under

The measured fluorescence lifetimes of ytterbium and holmium under 537-nm and 970-nm excitation, respectively

Rare-earth ion	Fluorescence lifetime τ			
	Yb^{3+}	Ho^{3+}		
Energy level	$^2F_{5/2}$	$^5I_7$	$^5I_6$	$^5S_2$
Excitation @ 537 nm	1.55 ms	19.9 ms	3 ms	180 μs
Excitation @ 970 nm	1.1 ms	18.3 ms	3.7 ms	50 μs
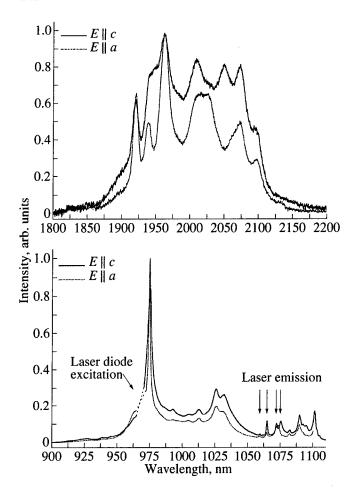
Fig. 4. Polarized room temperature fluorescence spectra of Ho(1%), Yb(10%) : KYF$_4$ around 1 and 2 μm; the realized laser transitions are indicated.

ytterbium excitation. The longer lifetime of the $^5I_6$ level under 970-nm excitation is not yet understood and is possibly due to some measurement errors.

EXPERIMENTAL RESULTS

The uncoated 4-mm-long Ho(0.5%),Yb(5%) : KYF$_4$ crystal was placed inside a nearly concentric cavity (radii of mirrors R = –50 mm) in the experimental setup using the Ti : sapphire laser as pump source. The input mirror was high reflecting at the laser wavelength and high transmitting for the pump wavelength around 970 nm in all sets of mirrors for each of the realized laser wavelengths (756, 1070, and 1390 nm). Each output coupler was high reflecting at the laser wavelength, the transmission of the pump wavelength was larger than 90%. An argon-ion laser-pumped titanium-sapphire laser was used as pump source. The maximum used pump output power was up to 1100 mW at 970 nm. The wavelength of the pump radiation was tunable by a three-plate birefringent Brewster filter, and the focusing of the pump beam was accomplished by a f = 50 mm focal length lens.

Two 1-W laser diodes coupled by a polarizing beam splitter were used in the laser diode-pumped experiments. The pump beams were combined and focused by an f = 20 mm focal length AR-coated lens after collimation. The maximum available pump power was 1.5 W at 970 nm. The nearly hemispherical laser cavity consisted of a plane input mirror and an R = –50 mm output coupler. The Ho(0.5%), Yb(5%):KYF$_4$ crystal was placed inside the cavity near to the plane input mirror. The set of mirrors for the 1390 nm transition was

λ_{laser}	λ_{pump}	P_{thr}	$T_{o/c}$	η_s		λ_{laser}	λ_{pump}	P_{thr}	$T_{o/c}$	η_s
■ 1390 nm	970 nm	234 mW	HR	3.1%	◆	1070 nm	971 nm	411 mW	HR	1.8%
△ 756 nm	974 nm	96 mW	HR	1.0%	◇	1070 nm	971 nm	630 mW	2.4%	3.2%
◆ 1070 nm	969 nm	234 mW	HR	0.7%	■	1390 nm	971 nm	734 mW	HR	0.2%
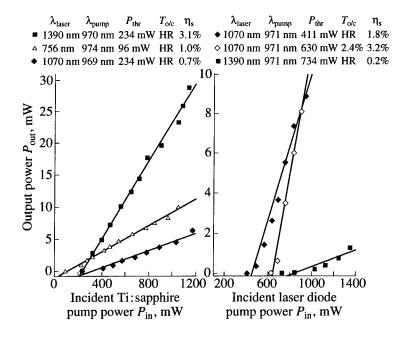
Fig. 5. The 756-, 1070-, and 1390-nm laser output power of Ho(0.5%), Yb(5%) : KYF$_4$ as a function of the total incident Ti : sapphire (left-hand side) and laser diode (right-hand side) pump power, respectively.

the same as in the Ti : sapphire setup. The input mirror transmission at 970 nm was 60% for the 1070-nm transition, and a second experiment was performed using an output mirror with 2.4% output coupling at 1070 nm instead of the HR output mirror.

The laser wavelengths were determined by a 0.25-m SPEX-spectrometer with a resolution of 0.9 nm. The pump laser output was mechanically chopped in all experiments to reduce the thermal load on the crystal (duty cycle of 50%). The crystal itself was mounted on a water-cooled copper heat sink for efficient cooling. However, it was not possible to use the Ho(1%), Yb(10%) : KYF_4 for laser experiments due to the poor mechanical properties and the low thermal conductivity of KYF_4, resulting therefore in the cracking of the crystal at a relatively low input power level.

With the 4-mm-long Ho(0.5%), Yb(5%) : KYF_4 crystal, we achieved a laser output power of up to 10 mW at 756 nm, up to 6.5 mW at 1070 nm, and up to 29 mW at 1390 nm with the Ti : sapphire laser as pump source. Using the laser diodes for excitation, we obtained a laser output power of more than 8 mW at 1070 nm and more than 1 mW at 1390 nm. An output coupling of 2.4% for the 1070-nm laser resulted in an increased laser threshold power and almost the same maximum laser output power, which was only limited by the maximum available laser diode pump power. The slope efficiency of 3.2% was the highest for all investigated laser transitions no matter which pump source used. The absorbed pump power was measured to be about 65% of the incident pump light. However, laser oscillation at 756 nm was not possible under laser diode excitation. The laser output power versus the total incident pump power for all investigated laser transitions is shown in Fig. 5. As already mentioned above, a possible explanation for these relatively low efficiencies is an ytterbium-holmium upconversion process $(^2F_{5/2}, {}^5S_2) \longrightarrow (^2F_{7/2}, {}^5G_5)$, which populates the higher lying holmium energy levels. This quenching of the holmium upper laser level $^5S_2$ results in a reduced laser output power for all the examined laser transitions.

CONCLUSIONS

In conclusion, lasing on three transitions in Ho, Yb : KYF_4 has been demonstrated. Utilizing an upconversion pumping scheme between ytterbium and holmium to excite the upper laser level, room-temperature continuous-wave laser emission in Ho(0.5%), Yb(5%) : KYF_4 at 756 nm, around 1070 nm, and at 1390 nm has been obtained to our knowledge for the first time. 756-nm laser operation was possible under Ti : sapphire laser excitation with a maximum laser output power of 10 mW and a slope efficiency of 1%. The maximum attained slope efficiency for the diode-pumped 1070-nm laser was 3.2% resulting in a maximum laser output power of more than 8 mW. The maximum output power achieved at 1390 nm was 29 mW at 1100 mW of incident Ti : sapphire pump power at 970 nm with a slope efficiency of 3.1%. Improvements to further enhance the efficiency of the upconversion-pumped laser transitions are possible by optimizing the Yb^{3+}–Ho^{3+} concentration ratio in KYF_4.

REFERENCES

1. Sandrock, T., Heumann, E., Huber, G., and Chai, B.H.T., 1996, *OSA TOPS on ASSL*, **1**, 550.
2. Thrash, R.J. and Johnson, L.F., 1994, *J. Opt. Soc. Am. B*, **11**, 881.
3. Möbert, P.E.-A., Heumann, E., Huber, G., and Chai, B.H.T., 1997, *Opt. Lett.* (in press).
4. Nabors, C.D., Ochoa, J., Fan, T.Y., *et al.*, 1995, *IEEE J. Quantum Electron.*, **31**, 1603.
5. Rustad, G. and Stenersen, K., 1996, *IEEE J. Quantum Electron.*, **32**, 1645.
6. Umyskov, A.F., Zavartsev, Y.D., Zagumennyi, A.I., *et al.*, 1996, *Quantum Electron.*, **26**, 563.
7. Podkolozina, I.G., Tkachuk, A.M., Fedorov, V.A., Feofilov, P.P., 1976, *Opt. Spectrosc.*, **40**, 196.
8. Allain, J.Y., Monerie, M., and Poignant, H., 1990, *Electron. Lett.*, **26**, 261.
9. Zhang, X.X., Bass, M., Chai, B.H.T., and Peale, R.E., 1993, *OSA Proc. on ASSL*, **22**, 1.
10. Zhang, X.X., Hong, P., Bass, M., and Chai, B.H.T., 1993, *Appl. Phys. Lett.*, **63**, 2606.
11. Le Fur, Y., Khaidukov, N.M., and Aleonard, S., 1992, *Acta Cryst. C*, **48**, 978.

Diode-Pumped cw Lasing of Yb, Ho : KYF$_4$ in the 3 μm Spectral Range in Comparison to Er : KYF$_4$

A. Diening*, P. E.-A. Möbert*, E. Heumann*, G. Huber*, and B. H. T. Chai**

Institut für Laser-Physik, Universität Hamburg, Jungiusstr. 9a, Hamburg, D-20355 Germany
e-mail: diening@physnet.uni-hamburg.de
** *Center for Research and Education in Optics and Lasers, CREOL, University of Central Florida, Orlando, Florida, USA*
Received August 5, 1997

Abstract—We present diode-pumped cw lasing at room temperature of Yb^{3+}-codoped Ho : KYF$_4$ on the transition $^5I_6 \longrightarrow {}^5I_7$ in bulk material. Laser experiments with Ti : Al$_2$O$_3$ and diode excitation at 970 nm were performed. The pump energy is absorbed by Yb^{3+} and then transferred to the upper laser level $^5I_6$ in Ho^{3+}. In a second step, the lower laser level $^5I_7$ is depopulated by an upconversion process $(^2F_{5/2}, {}^5I_7) \longrightarrow (^2F_{7/2}, {}^5F_5)$ and by excited-state absorption (ESA) at the pump wavelength. The observed laser wavelength was 2.84 μm. Under Ti : Al$_2$O$_3$-pumping, a slope efficiency of 1% with respect to incident power and a maximum output power of 11 mW could be achieved. With laser diodes as pump sources the slope efficiency was reduced to 0.3% with a maximum output power of 2.5 mW. These diode-pumped laser results are compared with the 3 μm laser in Er : KYF$_4$ under the same experimental conditions. In addition, spectroscopical data are presented for both systems.

INTRODUCTION

Lasers in the 3 μm spectral range are used mainly in medical applications due to the high absorption of liquid water around this wavelength. In most cases the Er^{3+} laser on the $^4I_{11/2} \longrightarrow {}^4I_{13/2}$ transition is used for these applications. Diode-pumped erbium 3 μm lasers in various host materials show high slope efficiencies and cw output powers [1].

Another possibility to produce 3 μm radiation is the $^5I_6 \longrightarrow {}^5I_7$ transition of Ho^{3+}. Pulsed lasing under flashlamp excitation in bulk material [2] and cw-pumped at 640 nm in fibers [3] was already demonstrated for this transition. Flashlamp-pumped experiments with ytterbium codoping revealed very low thresholds.

THEORETICAL EXPLANATION OF CW LASING IN Er^{3+}- AND Yb^{3+},Ho^{3+}-DOPED SYSTEMS

The energy level scheme of Er^{3+} and Yb^{3+},Ho^{3+} is shown in Fig. 1. In Er^{3+} lasing occurs on the $^4I_{11/2} \longrightarrow {}^4I_{13/2}$ transition. The upper laser level is directly pumped by 970 nm laser diodes. Normally, cw lasing should be impossible due to the self-terminating character of this transition. But for high erbium concentrations (>10%), the lifetime of the lower laser level is quenched by a strong upconversion process $(^4I_{13/2}, {}^4I_{13/2} \longrightarrow {}^4I_{9/2}, {}^4I_{15/2})$. This process depopulates not only the lower laser level but also recycles one Er^{3+} ion back to the upper laser level. Another upconversion process from the upper laser level reduces the lasing efficiency and leads to a population of the $^4S_{3/2}$ multiplet which allows lasing at 551 nm [4].

In singly Ho^{3+}-doped crystals the situation is similar, but the strong upconversion process from the lower laser level does not exist and the upper laser level cannot be directly pumped by laser diodes. These problems can be avoided by ytterbium codoping. In a first step Yb^{3+} absorbs a pump photon at 970 nm and then transfers its energy to the upper laser level in Ho^{3+}. A second excited ytterbium ion can then exchange its energy with a Ho^{3+}-ion either in the $^5I_6$ or the $^5I_7$ multiplet. In the first case, population is excited from the upper laser level $^5I_6$ to the $^5S_2$ level, which allows several laser transitions from this level. In the second case one ion from the lower laser level is recycled to the upper one. But from the lifetime measurements it can be seen
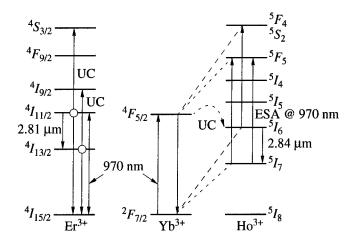
Fig. 1. Energy level scheme of Er^{3+} and Yb^{3+},Ho^{3+} (UC, upconversion process: ESA, excited-state absorption).
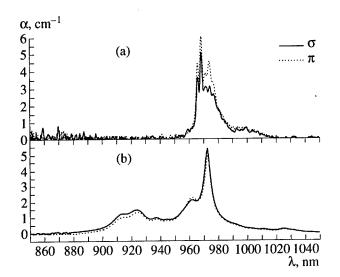
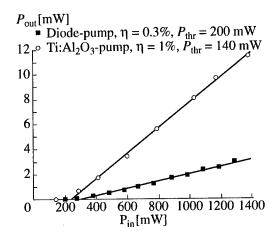**Fig. 2.** Absorption coefficient of (a) Er(20%) : KYF$_4$ and (b) Yb(10%),Ho(1%) : KYF$_4$.

Fig. 3. Fluorescence spectrum of Yb(5%),Ho(0.5%) : KYF$_4$ in the 3 μm region.

Fig. 4. Input-output characteristics of the 3 μm laser in Yb(5%),Ho(0.5%) : KYF$_4$ under Ti : Al$_2$O$_3$ and diode excitation.
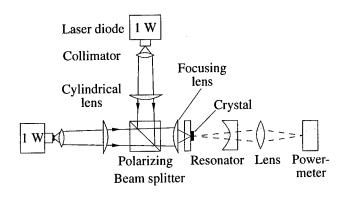
Fig. 5. Setup for laser diode-pumped experiments.

(Table 1) that this process is not very strong. The depopulation of the lower laser level is mainly done by a strong excited-state absorption from the $^5I_7$ level at the pump wavelength [5]. Due to the long lifetime of the $^6I_7$ level in KYF$_4$, these processes are efficient enough to avoid lasing on the 2.1 μm ground-state transition.

SPECTROSCOPIC INVESTIGATIONS

The absorption coefficients obtained for Er^{3+}- and Yb^{3+}, Ho^{3+}-doped KYF$_4$ around 970 nm are shown in Fig. 2.

Both systems show nearly polarization-independent strong absorption from the ground state to the $^4I_{11/2}$ and

Table 1. Lifetimes of the metastable energy levels in Yb(5%), Ho(0.5%) : KYF$_4$

Level	Lifetime under excitation at 537 nm (Ho^{3+})	Lifetime under excitation at 970 nm (Yb^{3+})
$^5S_2$(Ho^{3+})	180 μs	50 μs
$^5I_6$(Ho^{3+})	3 ms	3.7 ms
$^5I_7$(Ho^{3+})	19.9 ms	18.3 ms
$^5F_{5/2}$(Ho^{3+})	1.55 ms	1.1 ms

Table 2. Lifetimes of the metastable energy levels in Er(20%) : KYF$_4$

Level	Lifetime under excitation at 537 nm
$^4S_{3/2}$	13 μs
$^4F_{9/2}$	90 μs
$^4I_{9/2}$	9 μs
$^4I_{11/2}$	9 ms
$^4I_{13/2}$	17.5 ms

P_{out}[mW]

$\eta = 7.5\%$
$P_{thr} = 60$ mW

P_{in}[mW]
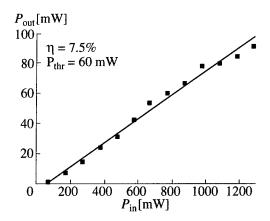
Fig. 6. Laser output power versus input power of the 3 μm laser in Er(20%) : KYF_4 under diode excitation.

the $^2F_{5/2}$ multiplet, respectively. At this wavelength, InGaAs laser diodes are available for pumping.

The fluorescence spectrum of Yb, Ho: KYF_4 at 3 μm shows a strong peak at the observed laser wavelength of 2.84 μm with polarization parallel to the *a*-axis (σ-polarization).

The emission lifetimes of the investigated crystals are listed in Tables 1 and 2. For both systems an excita-

Table 3. Stark levels in Er(20%) : KYF_4

Multiplet	Level	Energy, cm^{-1}
$^4I_{11/2}$	6	10352
	5	10328
	4	10289
	3	10267
	2	10252
	1	10235
$^4I_{13/2}$	7	6790
	6	6745
	5	6682
	4	6597
	3	6565
	2	6538
	1	6505
$^4I_{15/2}$	8	366
	7	290
	6	186
	5	106
	4	62
	3	15
	2	6
	1	0

tion wavelength of 537 nm was used. For the Yb^{3+}-codoped system, these measurements were also performed under ytterbium excitation at 970 nm.

It can be seen that the lower laser level is bottlenecked for both ions due to the longer lifetimes of the lower laser levels. The lifetime ratio for Er^{3+} ($\approx 1 : 2$) is better than for Ho^{3+} ($\approx 1 : 6$). In addition, under ytterbium excitation the lower laser level in Yb, Ho: KYF_4 is quenched due to the $Yb^{3+} \longrightarrow Ho^{3+}$ upconversion process. Also the lifetime of the $^5S_2$ level is reduced, which could be caused by another upconversion process to higher energy levels. The ESA at 970 nm can be neglected for these measurements due to the shortness of the pump pulses of 10 ns.

In measurements at 10 K, the Stark levels of the lower multiplets in Er : KYF_4 were determined. The results are shown in Table 3. For the Stark levels of the $^4I_{15/2}$ a clear identification was not possible, due to many equidistant lines in the fluorescence and absorption spectra.

LASER EXPERIMENTS

For Yb, Ho: KYF_4 laser experiments under Ti : Al_2O_3 excitation were performed. The crystal was mounted on a Peltier element inside a spherical resonator. The resonator was 100 mm long and both mirrors had an output coupling of 0.2% at the laser wavelength. With this setup a maximum output power of 11.5 mW at an input power of nearly 1.4 W could be achieved (Fig. 4). The laser threshold was 140 mW, and the slope efficiency was 1% with respect to incident pump power. It turned out that the output power could be raised when the crystal was slightly heated. This effect could be caused by better energy resonance due to the thermal population of the involved Stark levels.

Laser diode-pumped cw lasing could be achieved with the same crystal in the setup shown in Fig. 5. Two polarization-coupled 1 W laser diodes were focused into a hemispherical resonator with the crystal close to the plane mirror. Under these conditions, the lasing threshold was increased to 200 mW and the slope efficiency was decreased to 0.3% resulting in nearly 3 mW of maximum output power.

In this setup laser experiments with Er : KYF_4 were also performed. This crystal showed a laser threshold of 60 mW and a slope efficiency of 7.5% with respect to incident pump power. The maximum output power was 90 mW (Fig. 6).

SUMMARY

In summary, we have demonstrated cw diode-pumped lasing on the $^5I_6 \longrightarrow {}^5I_7$ transition in holmium-doped bulk material, to our knowledge for the first time. The self-terminating character of this transition can be avoided by energy transfer between Yb^{3+} and Ho^{3+} and ESA from the lower laser level.

The results were compared with an Er^{3+}-laser in the same host material, which turned out to be the more useful system due to the lower laser threshold and higher slope efficiency.

In spectroscopic investigations, the polarization-dependent absorption and emission measurements for both systems in KYF$_4$ were performed. The lifetimes of all metastable energy levels in Er^{3+} and Yb^{3+},Ho^{3+} were determined. Via absorption and fluorescence measurements at 10 K the Stark level splitting of Er^{3+} in KYF$_4$ was determinated.

REFERENCES

1. Jensen, T., Diening, A., Chai, B.H.T., and Huber, G., 1995, *CLEO*, vol. 15, Postdeadline paper CPD 29.

2. Umyskov, A.F., Zavartsev, Y.D., Zagumennyi, A.I., *et al.*, 1992, *J. Quantum Electron.*, **29**, 771.

3. Wetenkamp, L., 1990, *Electron. Lett.*, **26**, 883.

4. Heine, F., Heumann, E., Möbert, P., *et al.*, 1995, *OSA Proceedings on Advanced Solid State Lasers 2*, **24**, 74.

5. Diening, A., Dicks, B.-M., Heumann, E., *et al.*,1997, *OSA TOPS*, **10**, 202.

The Influence of Anisotropy of Nonlinear Absorption in a Cr^{4+} : YAG Passive Q Switch upon the Polarization State of a Neodymium Laser

N. N. Il'ichev, A. V. Kir'yanov, E. S. Gulyamova, and P. P. Pashinin

General Physics Institute, Russian Academy of Sciences, ul. Vavilova 38, Moscow, 117942 Russia
e-mail: ilichev@kapella.gpi.ru
Received September 2, 1997

Abstract—The polarization state of a solid-state neodymium laser with a Cr^{4+} : YAG passive Q switch and a partial polarizer is investigated. It is demonstrated that polarization properties of radiation are determined by the anisotropy of nonlinear absorption induced in the Cr^{4+} : YAG passive Q switch. The results of calculations agree well with the experimental data.

1. INTRODUCTION

In [1], we experimentally investigated polarization characteristics of Nd, Cr : GSGG and Nd : YAG lasers with passive Q switching of the cavity by means of a Cr^{4+} : YAG switch. It was demonstrated that, if the laser cavity includes a polarizer, the energy of the giant pulse and the polarization state of laser radiation depend on the angle of the passive Q switch (with respect to the cavity axis), the spatial arrangement of the switch relative to the waist of the cavity, and the type of the polarizer.

It was shown that a cavity with a partial polarizer produces elliptically polarized radiation. The orientation of the principal axis of the polarization ellipse (polarization azimuth) and the ellipticity degree of the laser beam produced by such a system depend on the angle of the Cr^{4+} : YAG passive Q switch (with a period of 90°). These dependences were associated with self-induced anisotropy arising in the Cr^{4+} : YAG passive Q switch at a certain stage of the development of a giant pulse when absorption saturation is switched on. The characteristic feature of this effect is that the azimuth of the polarization of radiation produced in such a system follows the orientation of phototropic Cr^{4+} centers relative to the plane of minimum linear cavity losses determined by the orientation of the partial polarizer.

The purpose of this study is to develop a model of a neodymium laser with a Cr^{4+} : YAG passive Q switch and partial polarizer and to compare the predictions of this model with the experimental data.

2. THEORY

In accordance with currently existing concepts, Cr^{4+} phototropic centers in YAG crystals are considered as groups of linearly absorbing dipoles [2, 3] oriented along three orthogonal directions (along the principal crystallographic axes of YAG). As is well known [3–6], the propagation of high-power resonant radiation in a

crystal medium with distinguished orientations of dipole moments of resonant transitions is accompanied by the appearance of self-induced anisotropy of saturable absorption. Specifically, this effect was observed in experiments on intracavity probing of a Cr^{4+} : YAG crystal by high-power radiation with the wavelength $\lambda = 1.06$ μm [2, 6]. Self-induced anisotropy of saturable absorption should influence also (see [1]) the output characteristics (the lasing energy and polarization state) of a neodymium laser with a Cr^{4+} : YAG passive Q switch when the switch is bleached (absorption is saturated) by a lasing pulse that passes many times through a medium of Cr^{4+} phototropic centers.

We will assume that the laser cavity includes an active element (an isotropic neodymium-containing material), a Cr^{4+} : YAG passive Q switch, and a partial polarizer. Suppose that the optical axis of the cavity coincides with the orientation of one of three orthogonal groups of Cr^{4+} centers (e.g., the [100]-axis, which perpendicular to the plane of Fig. 1). Then, the other two groups of Cr^{4+} centers (the X_s [010] and Y_s [001] directions) lie in the plane of Fig. 1. Let the directions corresponding to minimum and maximum losses of the partial polarizer be defined as X_p and Y_p, respectively. Transmission in these directions will be denoted as T_{X_p}
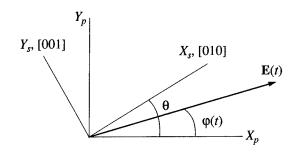
Fig. 1. The scheme of calculation of the polarization state of a neodymium laser with a Cr^{4+} : YAG passive Q switch.

and T_{yp}. The orientation of the principal axis of the polarization ellipse will be described by a vector $\mathbf{E}$.

Suppose that the active medium and the mirrors have no influence on the polarization state of the laser, which is determined only by the linear (partial polarizer) and nonlinear (Cr^{4+} : YAG passive Q switch) amplitude anisotropy of the cavity. Let anisotropic nonsaturable (linear) losses be continuously distributed along the length of the switch, similar to the distribution of nonsaturable losses due to Cr^{4+} phototropic centers. Then, the polarization of the medium can be written as a sum of three components: $\mathbf{P} = \mathbf{P}_0 + \mathbf{P}_1 + \mathbf{P}_2$, where $\mathbf{P}_0$ is the polarization of the YAG material, $\mathbf{P}_1$ is the polarization related to Cr^{4+} phototropic centers, and $\mathbf{P}_2$ is the fictitious polarization that corresponds to the contribution of the partial polarizer.

We will assume that the polarization state of laser radiation being generated corresponds to the eigenstate of the cavity with all intracavity elements at each moment of time. Then, the condition

$$\det \left| \frac{\omega^2}{c^2}\hat{\varepsilon} - K^2\hat{I} \right| = 0, \tag{1}$$

should be satisfied, where ω is the frequency of the laser transition, c is the speed of light, K is the wave number, and $\hat{\varepsilon} = \hat{I} + 4\pi\hat{\chi}$ is the dielectric permittivity tensor for the considered composite medium ($\hat{\chi}$ is the susceptibility tensor, $\mathbf{P} = \hat{\chi}\mathbf{E}$, and $\hat{I}$ is the identity matrix). Writing each of the components $\mathbf{P}_i$ of the polarization of the medium in the system of coordinates related to the partial polarizer (see Fig. 1), we find that

$$\hat{\varepsilon} = \left| \begin{array}{cc} \varepsilon_0 + 4\pi(\chi_{11} + \chi_{pX}) & 4\pi\chi_{12} \\ 4\pi\chi_{12} & \varepsilon_0 + 4\pi(\chi_{22} + \chi_{pY}) \end{array} \right|, \tag{2}$$

where ε_0 is the dielectric constant of pure YAG (without impurities), χ_{ij} is the polarizability corresponding to Cr^{4+} impurity centers, and χ_{pX} and χ_{pY} are the polarizabilities corresponding to the partial polarizer.

Taking (2) into account, we can demonstrate that (1) is reduced to the equation

$$\det \left| \begin{array}{cc} 2ia - \Delta & 2ic \\ 2ic & 2ib - \Delta \end{array} \right| = 0, \tag{3}$$

where

$$a = \frac{\ln(1/T)}{4l}\left(\cos^2\varphi\frac{n_{sX}}{n_{s0}} + \sin^2\varphi\frac{n_{sY}}{n_{s0}} + \frac{\alpha_{pX}}{2\ln(1/T)} \right),$$

$$b = \frac{\ln(1/T)}{4l}\left(\sin^2\varphi\frac{n_{sX}}{n_{s0}} + \cos^2\varphi\frac{n_{sY}}{n_{s0}} + \frac{\alpha_{pY}}{2\ln(1/T)} \right), \tag{4}$$

$$c = \frac{\ln(1/T)}{4l}\cos\varphi\sin\varphi\left(\frac{n_{sX}}{n_{s0}} - \frac{n_{sY}}{n_{s0}} \right).$$

Here, α_{pX} and α_{pY} are the magnitudes of linear losses in the medium along the X- and Y-directions (the contribution of the partial polarizer), respectively; T is the initial transmission coefficient, which is determined by totally saturable losses (Cr^{4+} centers); l is the length of the Q switch; and $n_{sX}(t)$ and $n_{sY}(t)$ are the populations of Cr^{4+} centers oriented along the [010] and [001] axes in the ground state during the build-up of the giant pulse, $n_{sX}(t = 0) = n_{s0}$.

Formula (3) involves an additive $\Delta = K - K_0$ to the wave number $K_0 = \omega\sqrt{\varepsilon_0}/c$, $|\Delta| \ll |K_0|$. If we assume that the polarization eigenstate ensuring minimum losses is implemented in the laser, then we can find the corresponding values of the electric vector $\mathbf{E}$.

Since $\Delta_{max} = i(a + b) + \sqrt{(a - b)^2 + 4c^2}$, we find that

$$\tan\varphi \equiv \frac{E_Y}{E_X} = \frac{a - b + \sqrt{(a - b)^2 + 4c^2}}{2c}$$

$$= \frac{\sqrt{1 + \gamma^2} - 1}{\gamma}, \tag{5}$$

where

$$\gamma = \frac{2c}{a - b} = \frac{\delta n\sin(2\theta)}{\delta n\cos(2\theta) - g}. \tag{6}$$

In the last expression, we have introduced the following notations:

$$\delta n = \frac{1}{n_{s0}}(n_{sX} - n_{sY}),$$

$$g = \frac{1}{2\ln(1/T)}(\alpha_{pX} - \alpha_{pY}). \tag{7}$$

We can demonstrate that $\tan(2\varphi) = \gamma$, so that

$$\tan(2\varphi) = \frac{\delta n\sin(2\theta)}{\delta n\cos(2\theta) - g}. \tag{8}$$

In expression (8), we need to find the population difference $\delta n(t)$ for two orthogonal groups of Cr^{4+} centers in the ground state, which arises during the build-up of the giant pulse.

As mentioned above, Cr^{4+} centers interact with the field as linear absorbing dipoles. Therefore, the evolution of the ground-state populations of these centers is governed by the equations

$$\frac{dn_{sX}}{dt} = -n_{sX}\sigma_s\cos^2(\theta - \varphi(t))J_s(t),$$

$$\frac{dn_{sY}}{dt} = -n_{sY}\sigma_s\sin^2(\theta - \varphi(t))J_s(t), \tag{9}$$

where σ_s is the cross section of transitions in Cr^{4+} centers at the wavelength $\lambda = 1.06$ μm and $J_s(t)$ is the total intensity of counterpropagating waves at the point where the switch is located.

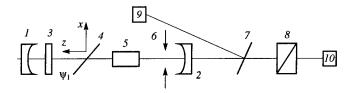**Fig. 2.** The scheme of measurement of the polarization state of a neodymium laser with a Cr^{4+} : YAG passive Q switch: (*1, 2*) cavity mirrors, (*3*) Cr^{4+} : YAG passive Q switch, (*4*) partial polarizer, (*5*) active element, (*6*) diaphragm, (*7*) beam splitter, (*8*) Glan prism, (*9, 10*) integrating photodiodes.

Let us denote the relative lasing energy density emitted by the moment of time t in the cavity at the point where the passive Q switch is located as (see [4])

$$X = \sigma_s \int_{-\infty}^{t} J_s(t')dt' \tag{10}$$

and introduce the following notations:

$$C = \sigma_s \int_{-\infty}^{t} \cos[2\varphi(t')]J_s(t')dt' = \int_{0}^{X} \cos(2\varphi)dX,$$

$$S = \sigma_s \int_{-\infty}^{t} \sin[2\varphi(t')]J_s(t')dt' = \int_{0}^{X} \sin(2\varphi)dX. \tag{11}$$

Then, we can write

$$\delta n(X)$$
$$= -2\exp\left(-\frac{X}{2}\right)\sinh\left(\frac{1}{2}C\cos(2\theta) + \frac{1}{2}S\sin(2\theta)\right). \tag{12}$$

As it follows from (11),

$$\frac{dC}{dX} = \cos(2\varphi); \quad \frac{dS}{dX} = \sin(2\varphi), \tag{13}$$

and (8) yields

$$\frac{dC}{dX} = \frac{g - \delta n\cos(2\theta)}{\sqrt{(\delta n)^2 + g^2 - 2\delta ng\cos(2\theta)}}, \tag{14}$$

$$\frac{dS}{dX} = -\frac{\delta n\sin(2\theta)}{\sqrt{(\delta n)^2 + g^2 - 2\delta ng\cos(2\theta)}}. \tag{15}$$

Thus, the polarization state of the giant pulse being generated, i.e., the polarization azimuth φ and the ellipticity parameter D, is described by

$$\varphi = \frac{1}{2}\arctan\left(\frac{S}{C}\right),$$
$$D = \frac{\sqrt{C^2 + S^2}}{X}, \tag{16}$$

To find C and S, we should solve the set of equations (12), (14), and (15).

3. COMPARISON WITH THE EXPERIMENTAL DATA

Let us assess the polarization state of a passively Q-switched neodymium laser with a Cr^{4+} YAG Q switch based on the known parameters of the passive switch and the partial polarizer. Experimental investigations of polarization characteristics of such a laser, which have been carried out earlier [1], make it possible to compare experimental data with the results of calculations performed with the use of formulas (12) and (14)–(16).

Experiments were devoted, in particular, to studying the polarization state of a Nd : YAG laser with a Cr^{4+} YAG passive Q switch and a partial polarizer—a glass plate mounted at a certain angle ψ_1 with respect to the optical axis of the cavity (see Fig. 2). The Cr^{4+} YAG passive Q switch in these experiments was oriented in the same manner as it was assumed in calculations.

Using the Glan prism placed outside the cavity, we assessed the polarization state of the giant pulse being generated as a function of the angle (with respect to the optical axis of the cavity) and spatial coordinates (relative to the waist) of the intracavity Cr^{4+} YAG passive Q switch. To estimate the azimuth of the polarization of laser radiation being generated, we determined the angle ψ corresponding to the maximum signal from a photodiode placed behind the Glan prism. The ellipticity degree of the polarization was estimated as the ratio of the minimum and maximum signals from the photodiode.

The procedure of measurements is illustrated by Fig. 2. The signal from the photodiode (*10*) is proportional to the energy of the pulse,

$$\mathcal{E} \sim \int_{-\infty}^{t} \cos^2(\psi - \varphi(t'))J_{out}(t')dt'$$
$$\sim \frac{X(t)}{2} + \frac{1}{2}\cos(2\psi)C + \frac{1}{2}\sin(2\psi)S,$$

where the parameters C and S are defined in accordance with (14) and (15) and ψ corresponds to the maximum transmission of the Glan prism.

Equating $d\mathcal{E}/d\psi = 0$, we find that the angle corresponding to the maximum (minimum) signal from the photodiode (polarization azimuth) is given by

$$\varphi^{exp} = \frac{1}{2}\arctan\left(\frac{S}{C}\right),$$

and the ellipticity degree is

$$D^{exp} = \frac{\sqrt{C^2 + S^2}}{X}.$$
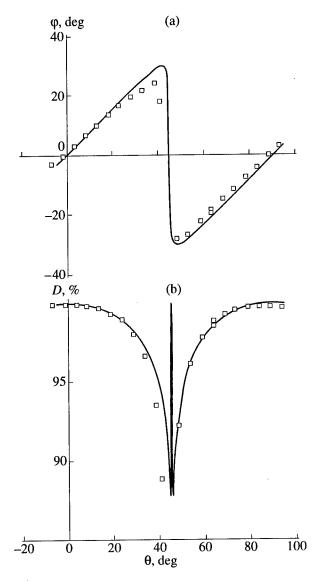
Fig. 3. (a) The rotation angle φ of the polarization plane and (b) the ellipticity parameter D as functions of the rotation angle θ of the Cr^{4+} : YAG passive Q switch in a laser with a Nd : YAG active element: (dots) experimental data and (curves) results of calculations. The initial and final transmission coefficients of the Cr^{4+} : YAG passive Q switch were 30 and 88%, respectively; the partial polarizer was placed at an angle $\psi_1 = 35°$; and the relative energy density in the passive Q switch was $X = 1.3$.

In other words, polarization characteristics are defined exactly as in the calculations performed above.

Figure 3 presents the experimental data along with the corresponding theoretical dependences for the polarization states of the laser under consideration. The energy density of laser radiation in the passive switch normalized to the saturation energy density (X) was used as the fitting parameter in these calculations.

As can be seen from the presented plots, the theoretical predictions agree well with the experimental data. We should only discuss in greater detail the behavior of the parameter D near $\theta = 45°$. As can be seen from the plots, the theory predicts that the $D(\theta)$ curve should display a narrow maximum near this point [corresponding to a sharp change in $\varphi(\theta)$]. However, the angle θ was varied with a rather large step in this experiment, so that it was impossible to observe this singularity.

4. CONCLUSION

We have proposed a model for calculating the polarization state of a neodymium laser with a Cr^{4+} : YAG passive Q switch and a partial polarizer. The performed calculations have demonstrated that the polarization state of a laser (the polarization azimuth and the ellipticity parameter) depends on both the orientation of the Cr^{4+} : YAG passive Q switch (nonlinear polarizer) in the cavity and the parameters of the partial linear polarizer. The results of calculations agree well with the data of experiments devoted to the investigation of polarization characteristics of a Nd : YAG laser with a Cr^{4+} : YAG passive Q switch and a glass plate employed as a partial polarizer.

The proposed model makes it possible to take into account the contribution of nonlinear-optical polarization effects in the development of lasers with crystal passive Q switches based on tetravalent chromium.

REFERENCES

1. Il'ichev, N.N., Kir'yanov, A.V., Gulyamova, E.S., and Pashinin, P.P., 1997, *Sov. J. Quantum Electron.*, **27**, 298.
2. Il'ichev, N.N., Kir'yanov, A.V., Pashinin, P.P., and Shpuga, S.M., 1994, *JETP*, **78**, 768.
3. Eilers, H., Hoffman, K.R., Dennis, W.M., *et al.*, 1992, *Appl. Phys. Lett.*, **61**, 2958.
4. Il'ichev, N.N., Kir'yanov, A.V., Malyutin, *et al.*, 1993, *Laser Phys.*, **3**, 182.
5. Dykman, M.I. and Tarasov, G.G., 1977, *Sov. Phys. JETP*, **45**, 1181.
6. Il'ichev, N.N., Kir'yanov, A.V., Pashinin, P.P., *et al.*, 1994, *Sov. J. Quantum Electron.*, **24**, 771.

Diode-Pumped Solid-State Lasers in the kW Range

Th. Brand, B. Ozygus, and H. Weber

Optical Institute, TU Berlin, Strasse des 17 Juni 135, Berlin, D-10623 Germany
e-mail: weber@physik.tu-berlin.de
Received August 22, 1997

Abstract—Experimental results on Nd-YAG-rod lasers with output power up to 1.6 kW are reported in detail. The scaling laws for output power and beam parameter product are discussed. A review on the present state of solid-state lasers with respect to output power and beam parameter product is given.

INTRODUCTION

Lamp-pumped solid-state lasers of more than 6 kW cw-output power are available and used in automotive industry. The main advantages compared with CO_2 lasers are the shorter wavelength (1.06 μm) and the beam transportation by flexible fibers (400–600 μm core diameter). But there are severe disadvantages as low efficiency ($\eta_{plug} \approx 3.5\%$), low beam quality ($D\theta/4 >$ 25 mm mrad at 750 W per module), and limited lifetime of the lamp ($\approx$1000 h). These shortcomings can be overcome by replacing the gas discharges by laser diodes.

DIODE-PUMPING CONFIGURATIONS

Many configurations were investigated in the recent years, using very sophisticated arrangements [1]. The most successful setups for high average power are:

Yb-YAG discs, pumped by fiber-coupled diodes [2]

Nd-YAG-rods, pumped transversely by fiber-coupled diodes [3];

Nd-YAG-rods, pumped directly by diode stacks [4].

This configuration is the only one which can be scaled to 5 kW or more and delivers 2 kW at the time being. It was investigated in detail, and the results will be presented here.

Diode arrays with output power of 30 W/cm at $\lambda =$ 0.809 μm can be assembled to microchannel cooled stacks of various dimensions with many kW total power and power densities of 150 W/cm². Higher power densities are on the way. The electrical/optical efficiency is above 40%. These systems are available commercially. An example is shown in Fig. 1. The wavelength shift due to the temperature rise with increasing electrical current is about $\Delta\lambda = 0.3$ nm/K, but does not strongly influence the YAG-laser output in the configuration under investigation.
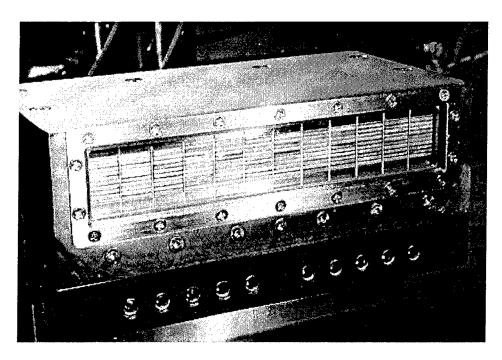
Fig. 1. Stacked array with 3.5 kW output power (DILAS, Mainz-Germany).

Reflector Microchannel cooled stack Diodes

Rod Flow tube
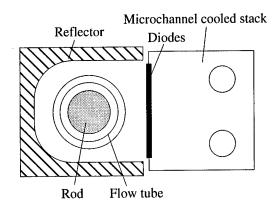
Fig. 2. Laser cavity with rod and resonator.

Mirror Rod D_f Mirror

l

d d

L

Fig. 3. The symmetric plane/plane cavity.

The stack is cooled with 50 l/min at a pressure of 4–5 × 10⁵ Pa. To avoid damage of the diodes due to dust particles, the system is mounted inside a box, the front side protected with a glass plate.

LASER SYSTEM

A Nd-YAG rod (5 × 177 mm), inside a ceramic cavity, water cooled was used. The stack is directly mounted asymmetrically at one side of the cavity as shown in Fig. 2.

For all experiments a symmetric plane–plane resonator was used as plotted in Fig. 3. The resonator length was varied between $L = 0.4$ m and $L = 1$ m. L is related to d, the distance between the principal planes of the laser rod and the mirrors, by

$$L = 2d + l[1 - 1/n], \qquad (1)$$

where l is the geometrical length of the rod and n its refractive index.

The reflectivity of the output mirror was 80%. The laser output power P_{out} vs. the optical power of the diodes P_{opt} for different resonator lengths L is shown in Fig. 4. The beam parameter product BP, defined by full waist diameter D times full far-field divergence θ divided by 4

$$BP = \frac{D\theta}{4}$$

depends on the resonator length and the pumping power. One example is given in Fig. 5 using the second moment definition and the 86% power content value according ISO [5].

INTERPRETATION OF THE RESULTS

The theoretical relation between pumping power P_{opt}, output power P_{out}, and the beam parameter product BP is outlined in Fig. 6.

Output power P_{out}/W

5mm × 7" Nd:YAG Stab(L514)
Resonator symm. plan/plan R=80%

- 30cm
- 40cm
- 50cm
- 60cm
- 70cm
- 80cm
- 90cm
- 100cm

Radial pol.

Azimuthal pol.

Optical pumping power P_{out}/W

Fig. 4. Output power P_{out} vs. pumping power P_{opt} for different resonator lengths L. Nd-YAG rod, 5 mm × 178 mm, $R_{out} = 0.8$.

Beam parameter product BP/mm mrad

Second moment

86.5% power content value

Output power P_{out}/W
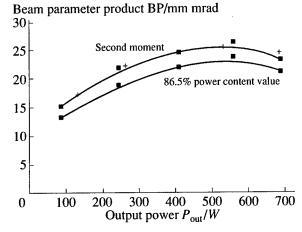
Fig. 5. Beam parameter product BP vs. pumping power P_{opt} for $L = 0.5$ m and a 6.3 mm × 17.8 mm Nd-YAG rod.

For the symmetric plane/plane resonator holds [6–8]

$$BP = (BP)_{max}\sqrt{D_f d(2 - D_f d)}, \qquad (2)$$

$$(BP)_{max} = R^2/2d, \qquad (3)$$

where D_f is the refractive power of the laser rod, depending on the internal heating power, and R is the
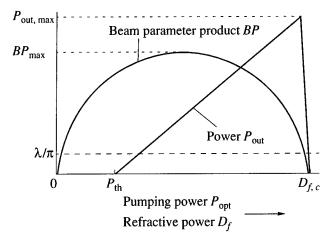
Fig. 6. Theoretical relation between beam parameter product *BP*, output power P_{out} and pumping power P_{opt}. The refractive power D_f of the rod is proportional to the pumping power P_{opt}.

rod radius. The above equations hold for $BP \geq \lambda/\pi$, which sets upper and lower limits for $D_f d$. The resonator becomes unstable and the output power zero at the upper limit $D_{f,c} \approx 2/d$. The refractive power is related to the optical pumping power. Approximately holds [8]

$$D_f \approx \beta \frac{P_{opt}}{\pi R^2},\tag{4}$$

with β the thermal lensing coefficient. The laser output power P_{out} is proportional to the pumping power:

$$P_{out} = \eta_s(P_{opt} - P_{th}),\tag{5}$$

with η_s the slope efficiency. The differential increase of the refractive power per output power is

$$\frac{\delta D_f}{\delta P_{out}} = \frac{\beta}{\eta_s \pi R^2} = \frac{\gamma}{\pi R^2}, \quad \gamma = \frac{\beta}{\eta_s}.\tag{6}$$

The maximum output power of the system is obtained near the critical refractive power $D_{f,c} \approx 2/d$. Neglecting the threshold power, which is allowed for high pumping power levels, the above equations deliver

$$P_{out,\,max} \approx \frac{2\pi R^2}{\gamma}\frac{}{d}.\tag{7}$$

From (3)–(7) a very simple relation is obtained, which relates the maximum values of the output power and the beam parameter product as shown in Fig. 6 [8]:

$$\frac{(BP)_{max}}{P_{out,\,max}} = \frac{\beta}{4\pi\eta_s} = \Gamma.\tag{8}$$

This relation holds for any symmetric resonator. For asymmetric systems [8] Γ has to be replaced by $\Gamma/2$ and $P_{out,max}$ by $\Delta P_{out} = P_{out,max} - P_{out,min}$ which is the range of stable operation of the particular resonator. If a very low beam parameter product is desired, the stable range of operation becomes very narrow.

The relevant parameters β, γ, Γ can be determined by using the above relations. It has to be considered that these equations are rough approximations predicting the trend but not precise numbers. The results are compiled in the table. It has to be considered that due to thermally induced birefringence the radially and azimuthally polarized beams suffer different refractive powers $D_{f,r}$ and $D_{f,\phi}$, which differ by about 10%. The system becomes first unstable for the radial polarization and then for the azimuthal one as can be seen in Fig. 4.

It is difficult to compare with lamp-pumped systems, because other dopings and rod dimensions are used. But roughly holds:

• the total efficiency (electrical/optical) is higher by a factor of 2–2.5, assuming 5% for lamp-pumped systems;

• the thermal lensing coefficient of lamp-pumped systems is about $\gamma = 0.4$ mm/kW, which is about 30% higher than for diode pumping;

Results of different diode-pumped Nd-YAG systems. (LMTB: this paper, ILT: Institut fur Lasertechnik, Aachen)

	LMTB		ILT
Rod radius R, mm	2.5	3.2	2.5
Slope efficiency (optical/optical) η_s [%]	23	32	32
Total efficiency (optical/optical) η_t [%]	18	30	28
Overall efficiency (electrical/optical) η [%]	≈ 8.1	13.5	11.2
Refractive power (radial)			
D_f/P_{opt}, m^{-1}/kW	3	2.5	4.3
$\delta D_f/\delta P_{out}$, m^{-1}/kW	16	14.3	15.6
Lensing coefficient β, mm/kW	0.06	0.057	0.069
Differential lensing coefficient γ, mm/kW	0.33	0.29	0.31
Beam parameter product per maximum output power Γ, mm mrad/kW	20	21	20
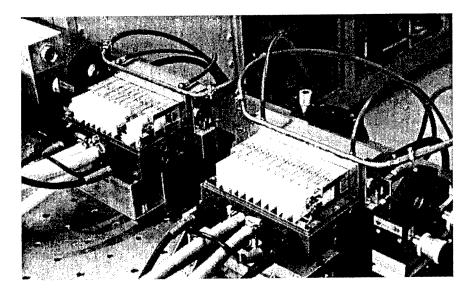
Fig. 7. The two-rod system. Pumped with 7.2 kW optical power. Two stacks with 12 arrays each.
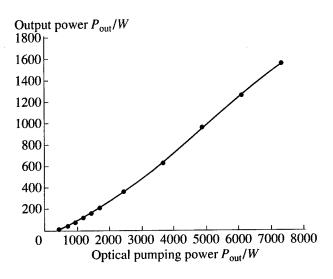
Fig. 8. Output power vs. optical pumping power for a two-rod system.

• from this can be concluded, that the thermal load is about 30% lower. The maximum pumping power can be higher, and it is possible to extract more output power per cm rod. With the here discussed system 1100 W were produced with a 7″ rod.

Fig. 9. The water-cooled disc laser.

SCALING

If the pumping light distribution inside the rod is homogeneous a parabolic lens profile is produced. Then the beam quality is not changed, if several cavities inside or outside the resonator are used to increase the output power. An example is shown in Fig. 7. Two rods deliver nearly 2 kW power. A scaling to 5 kW or more with a 30% better beam quality compared with lamp-pumped systems can be realized.

OTHER CONFIGURATIONS

The diode-pumped Yt-YAG disc laser is the most advanced configuration, promising high output power at low beam parameter products. The Cu-heat-sink cooled disc will be discussed elsewhere [2]. Another configuration is the water- cooled disc as shown in Fig. 8. First experiments deliver about 10 W from a 2 × 10-mm disc. Scaling to higher output power is possible. The direct water cooling is very effective and distortions of the laser beam by the water were not observed up to now.
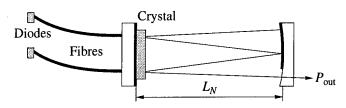
Fig. 10. The multipath laser.
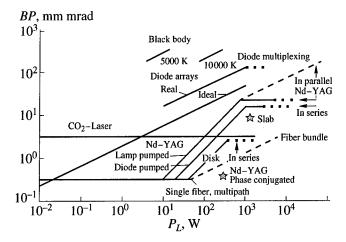
Fig. 11. Beam parameter product BP vs. output power P_{out} for various systems.

Another interesting system is the multipath laser as shown in Fig. 10. At distinct resonator lengths L_N, given by

$$g_1 g_2 = \cos^2 \frac{\pi}{N} \quad N = 1, 2, \ldots,$$

with g_i the resonator g-parameters, the beam reproduces itself after N bounces. At the reflection points the beam is pumped by fiber-coupled diodes. The beam diameter is adapted to the fiber produced gain profiles and ensures high efficiency and fundamental mode operation. The output power increases proportional to the number of pumped reflection points. Two dimensional multipath systems were realized with 10 reflection points [9]. With only two diodes of 12 W each an output power of 12 W at M2 = 1.5 was produced. Scaling to near 100 W seems possible.

CONCLUSIONS

In Fig. 11 an up-dated survey [10] is given on realized or scaled systems. The values of output power are plotted vs. the beam parameter products. For most systems the upper limit for the output power is given by the

thermal load and cannot be increased. Higher output power can be obtained by coupling several modules. There are two possibilities: coherent and incoherent coupling.

Coherent coupling: The multirod system is the best known example, but the same holds for the multipath laser. In these cases the output power increases proportional to the number N of modules, the beam parameter product remains constant and is equal to the BP of the single system. In the diagram this situation is indicated by horizontal solid lines. The upper limit is given by technical problems (stability, alignment) and finally by the damage of the crystals.

Incoherent coupling: examples are fiber bundles or Nd-YAG lasers in parallel. In this case the output power increases also proportional to the number of coupled systems, but the beam parameter product increases proportional to the square root of the number N of modules. These systems are indicated by the rising broken lines.

Which of these systems will fulfill the industrial standards is open. Besides the here discussed parameters industry has additional demands as

- reliability;
- stability (mode structure, pointing, power);
- no sophisticated technology;
- costs (investment, running);

REFERENCES

1. Peuser, P. and Schmitt, N.P., 1995, *Diodengepumpte Festkorperlaser* (Berlin: Springer).
2. Giesen, A. *et al.*, 1964, *Appl. Phys. B*, **58**, 365.
3. Golla, D. *et al.*, 1996, *Opt. Lett.*, **21**, 210.
4. Brand, T., 1965, *Opt. Lett.*, **20**, 1776.
5. DIN EN ISO 11146.
6. Kortz, H.P. *et al.*, 1981, *Appl. Opt.*, **20**, 4124.
7. Weber, H., 1997, *Solid State Lasers, Handbook of the European Laser Academy* (London: Chapman & Hall), chapter 4.
8. Hodgson, N. and Weber, H., 1997, *Optical Resonators*, (London: Springer).
9. Hauck, R.J., 1997, *Spektrales Verhalten von Multipath-Ringoszillatoren*, Diploma thesis (Berlin: Optical Institute, Technical University).
10. Weber, H. *et al.*, 1986, *Proc. SPIE*, **650**, 92.

Dynamic Gratings in the Cr⁴⁺: GSGG Saturable Absorber

G. A. Bufetova, D. A. Nikolaev, V. B. Tsvetkov, and I. A. Shcherbakov

General Physics Institute, Russian Academy of Sciences, ul. Vavilova 38, Moscow, 117942 Russia
e-mail: bufetova@tsvet.gpi.ru
Received September 4, 1997

Abstract—Passive GSGG: Cr⁴⁺ Q-switch placed in a loop scheme of laser resonator enables one to achieve more effective laser operation. In this case internal resonator beams are crossed under certain angle inside the shutter volume and form dynamic volume periodic gratings. Refraction modulations in these gratings lead to a realization of the phase conjugation by degenerate four-wave mixing. High efficiency of the phase conjugation one permits to reduce the lasing threshold and to improve the output laser characteristics. In our experiments dynamic gratings in GSGG: Cr⁴⁺ shutter were studied in the laser with Nd³⁺: YAG rod ($\lambda = 1.06$ μm). The interference picture, arising due to the interference of resonator beams, may be fixed for the certain period in Cr-doped crystal by thermal or "resonance" mechanism. The thermal mechanism is connected with a change of refractive index of a crystal under local temperature increase. The "resonance" mechanism is caused by a change of refractive index due to absorption saturation at lasing wavelength. Computer simulations were fulfilled for estimation of parameters and time dependence of these gratings. According to our simulation the magnitude of "resonance" gratings achieves its maximum faster than laser pulse does, and the magnitude of the thermal gratings merely coincides in its time development with the development of the laser spike. It was found that for "resonance" gratings the peaks of interference picture are in phase with maximums of refractive index, the same is true for thermal mechanism too. The change of refractive index for both types of induced gratings approaches the value of 10^{-6}, which corresponds to reflection coefficient of about ~0.1–0.2%. The correlation between the maximum value of the magnitude of the thermal and "resonance" gratings depends on the reflection coefficient R of the output coupler.

INTRODUCTION

During the last ten years, crystals with garnet structure, doped with Cr ions, have been widely investigated and used as passive shutters. Passive Cr⁴⁺: GSGG Q-switch placed in a loop scheme of laser resonator enables one to achieve more effective laser operation. In this case internal resonator beams are crossed under certain angles inside the shutter volume and form an interference picture which is "recorded" as dynamic spatial periodic gratings. Refraction modulations in these gratings lead to a realization of the phase conjugation by degenerate four-wave mixing. High efficiency of the phase conjugation (more than 0.9) permits one to reduce the lasing threshold and to improve the output laser characteristics.

To improve a laser scheme by using these gratings it is necessary to estimate parameters of the gratings and their time dependence. Two different mechanisms cause the "record" of interference picture. The first one ("resonant" grating) occurs due to the change of the refraction index as a result of absorption saturation. Absorption bands of Cr⁴⁺ are changed in absorption spectra under the action of a saturating beam. The value of saturation is different in the max and min of interference picture. The second mechanism (thermal grating) is connected with the dependence of the refractive index on the temperature, because the local temperature in spatial gratings changes from max to min. But what is the difference between these two types of gratings in the amplitude, in the time of development, and in sign (do they add or subtract)?

To answer these questions we used the laser scheme in which the writing waves are internal and the signal wave is output wave for the laser. Both types of grating were formed in two perpendicular directions, which coincide with bisectors of the crossing beams. In this scheme it is possible in experiment to separate the signal, which is reflected from induced gratings, and in computer simulations, to neglect the influence of the reflected beam on the lasing.

Dynamical gratings were formed in the volume of the Cr⁴⁺: GSGG shutter, placed in the loop resonator, with Nd³⁺: YAI O₃ used as an active rod with $\lambda = 1.06$ μm (Fig. 1).

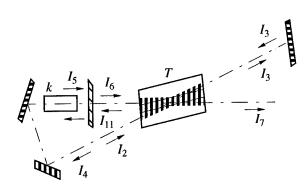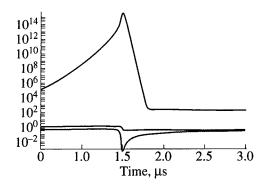**Fig. 1.** Laser experiment scheme.

Fig. 2. Photon density q, population inversion N_2, and absorption of a shutter ζ as functions of time.

Interaction of the beams 2, 3, 6 results in the formation of the space modulated picture of the radiation intensity distribution in the shutter. The values of the beams intensities are connected by the following ratios:

$$I_1 = \frac{I_7}{T}\frac{R}{1-R} = I,$$

$$I_2 = kI,$$

$$I_3 = kTI,$$

$$I_4 = kT^2I,$$

$$I_5 = k^2T^2I,$$

$$I_6 = k^2T^2(1-R)I,$$

$$I_7 = k^2T^3(1-R)I,$$

$$k = \frac{1}{T\sqrt{R}}.$$

The interference picture in the shutter can be calculated using these ratios between the amplitudes of the waves. To determine the time development of this picture it is necessary to solve the system of the rate equations for photon density and population inversions in the active rod and in the shutter. The approach taken in the model involves the assumption that the lasing parameters are determined by average intensity in the resonator, but cross-coordinate dependencies in the resonator are neglected and the pumping is assumed constant. Saturable shutter is taken as a two-level scheme. The following notation and data were used:

$n_t = 1.3 \times 10^{21}$ cm^{-3}, total dopant concentration in the active rod;

n_{2-} cm^{-3}, upper laser level population;

n_g, ground state population;

q, cavity photon density (cm^{-3});

$L = 100$ cm, resonator length;

$n_0 = 1.8$, refraction index of laser crystal;

$l = 5$ cm, laser rod length;

$n_{02} = 1.9$, index of refraction of the shutter;

$L_1 = L + (n_0 - 1)l + (n_{02} - 1)l_2$, optical length of the resonator;

$l_2 = 3.7$ cm, shutter length;

$\tau = 2.3 \times 10^{-4}$ s, decay time of the upper laser level of the active rod;

$2\tau_r = 2L_1/c$, the round-trip time;

I, laser light intensity within the resonator;

$\sigma_e = 3.5 \times 10^{-19}$ cm^2, laser emission cross section;

$\sigma_a = 3.5 \times 10^{-18}$ cm^2, shutter absorption cross section;

$T = 0.7$, transmission of the shutter in saturated condition; $T = 0.29$, initial transmission;

k, gain coefficient of the laser medium;

$T_{1a} = 1.3 \times 10^{-6}$ s, decay time of the upper absorber state in shutter;

$\tau_p = 1.5 \times 10^{-4}$ s, pumping pulse duration;

$\eta = 0.05$, pumping efficiency;

$E = 50$ J, pumping energy;

$\hbar\omega_p = 2.4 \times 10^{-19}$ J, quantum energy of pumping radiation;

$V = \pi \times 0.39 \times 5/4$ cm^3 pumping volume of active rod;

$Q = E\eta/(\hbar\omega V \tau_p) = W$, pumping rate;

$\chi = 0.024$ cm^2/s, thermal conductivity of garnet;

$c_m = 0.53$ J/(g deg), specific heat of garnet;

$\rho = 0.46$ cm^3, density of garnet;

$\alpha = 0.11$ cm^{-1}, absorption coefficient of the shutter in saturated condition;

$$\frac{d}{dT}q = qN_2(\gamma + \zeta_0) - q(\gamma + \zeta), \qquad (1)$$

$$\frac{d}{dT}N_2 = W\frac{\tau_r}{n_{20}} - qc\sigma_e N_2\tau_r - \frac{N_2\tau_r}{\tau}, \qquad (2)$$

$$\frac{d}{dT}\zeta = -2\zeta\sigma_a c\tau_r q + (\zeta_0 - \zeta)\frac{\tau_r}{T_{1a}}, \qquad (3)$$

γ is the magnitude of losses which does not depend on photons flow; ζ is the magnitude of losses in the shutter, which depends on photons flow, and ζ_0 is its initial value.

For normalization of rate equations the following designations were used:

$$I = \frac{qc\hbar\omega}{2},$$

$$\tau_r = \frac{L_1}{c}, \quad T = \frac{t}{\tau_r}.$$

For the steady-state case of lasing, $dI/dt = 0$; hence, $n_2 = (\gamma + \zeta)/(\sigma_e l) = n_{20}$, i.e.,

$$n_{20} = \frac{\gamma + \zeta_0}{\sigma_e l}.$$

The threshold value of the population inversion was chosen as a unit of inversion (normalized value). So, the initial value $N_2 = n_2/n_{20}$ is about unit.

The rate equations system was computed for different values of output coupler reflection R.

Photon density q, population inversion N_2 and the absorption of a shutter ($\zeta = \sigma_a N_a$, N_a is the population inversion in the shutter) as a function of time are shown below in log scale (Fig. 2).

THE THERMAL GRATING AMPLITUDE

The amplitude of thermal gratings is proportional to the magnitude of the space modulated absorbed energy, which in turn is proportional to the intensity distribution in the interference picture. The formation of this grating is caused by the local change of the refraction index due to the heat generation in the shutter volume (in the volume of beams crossing).

The change of refraction index is proportional to absorbed energy Q and it is connected with light intensity I by the following ratios:

$$Q = c_m \rho \Delta t^0, \quad Q = 4\alpha I \tau.$$

In this equation one may multiply max value of I by pulse duration I, or integrated τ by t.

$$\Delta t^0 = \frac{4\alpha I e^{-\alpha l}\tau}{c_m \rho},$$

$$\Delta n = \frac{\partial n}{\partial t}\Delta t,$$

$$Q = 4\alpha e^{-0.5\alpha l}\sqrt{(1-R)}\sqrt{R}\frac{qc\hbar\omega}{2}\tau.$$

It should be taken into consideration that the thermal gratings of short period could be smoothed during the laser pulse due to the thermal conductivity. The period of grating written by beams crossing under $86°$ is about $\Lambda = 3 \times 10^{-5}$ cm, and its relaxation time ($\Lambda^2/\chi \sim 8$ ns) is less than the pulse duration 50–80 ns.

THE ESTIMATION OF RESONANT GRATING AMPLITUDE

The resonant gratings are formed as a result of a change of the shutter refraction index due to saturation of absorption bands (near 1 μm) of Cr^{4+} ions. The change in spectra under saturation absorption enables us to evaluate Δn, the change of the refractive index. Different local values of saturation in interference picture corresponds to a modulation of induced gratings.
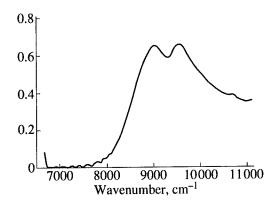
Fig. 3. Absorption coefficient of saturable shutter as a function of frequency.

In the max of the interference picture the space photon density and the population inversion are higher than the average ones. The absorption saturation in max is reached earlier than in min and than in the shutter as a whole. It is possible to estimate the time dependence of the local inversion population by introducing the additional equation to the system. This one differs from the equation for the average inversion by the coefficient at the photon density, which is equal to the ratio between local and average photon density in interference picture. If the degree of saturation differs in max and min, then the corresponding refractive index differs too.

From the most general properties of function $\varepsilon(\omega)$, real and imaginary parts of dielectric constant are related by the equation

$$\varepsilon_1(\omega) - 1 = \frac{2}{\pi}\int_0^\infty \frac{x\varepsilon_2}{x^2 - \omega^2}dx. \tag{4}$$

After substitution of the oscillator force

$$f(\omega) = \frac{m}{2\pi^2 e^2}\omega\varepsilon_2(\omega),$$

$$\int_0^\pi f(\omega)d\omega = N,$$

and taking into account the relation between f and σ_a,

$$\sigma_a(\omega) = \frac{\pi e^2}{mc}fG(\omega)$$

($G(\omega)$ is the spectral shape of the line and f a is the maximum value of oscillator force), it is possible to receive the final expression

$$\varepsilon_1(\omega) - 1 = -4c\int_0^\infty \frac{N_0\sigma_a(x)}{\omega^2 - x^2}dx, \tag{5}$$

$$N_0\sigma_a(x) = \alpha(x).$$

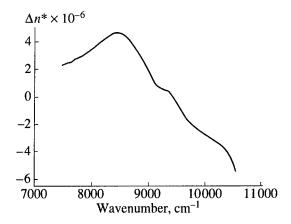The experimental value of absorption coefficient as a function of frequency is shown in Fig. 3.

$\Delta n^* \times 10^{-6}$

Fig. 4. The change of refraction index Δn of Cr^{4+}: GSGG under absorption saturation as a function of frequency.
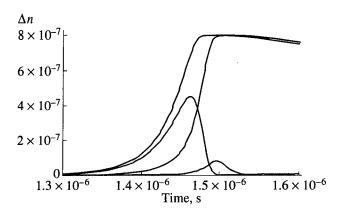
Δn

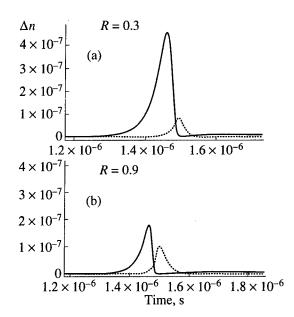**Fig. 5.** The temporal development of resonant and thermal gratings (linear scale).

Fig. 6. The temporal development of resonant and thermal gratings (linear scale) for different reflection coefficients of the output coupler R.

Precisely this function is integrated in equation for $\varepsilon_1(\omega)$.

$$\Delta\varepsilon_1(\omega) - 1 \tag{6}$$
$$= -2c\left[\int_{-\omega+\Delta}^{\infty}\frac{\alpha(x)}{\omega^2 - x^2}dx + \int_{\infty}^{\omega-\Delta}\frac{\alpha(x)}{\omega^2 - x^2}dx + 2\Delta\frac{d}{dx}\frac{\alpha(\omega)}{(\omega + x)}\right].$$

Under saturation of the crystal the absorption band $\omega 1 - \omega 2$ disappears. To find its contribution to the refractive index of unsaturated shutter, it is sufficient to integrate an isolated band near 1 μm,

$$\Delta\varepsilon_1(\omega) - 1 \tag{7}$$
$$= -2c\left[\int_{-\omega+\Delta}^{\omega 2}\frac{\alpha(x)}{\omega^2 - x^2}dx + \int_{\omega 1}^{\omega-\Delta}\frac{\alpha(x)}{\omega^2 - x^2}dx + 2\Delta\frac{d}{dx}\frac{\alpha(\omega)}{(\omega + x)}\right].$$

For frequency $\omega = 9250$ cm^{-1} the value of this expression is positive (Fig. 4). It means that, if this band disappears in the spectrum, i.e., at saturation of absorption, the refraction index increases.

Consequently, thermal and resonant gratings both have maximum refraction index in maximum of absorption.

Function $\Delta\varepsilon(\omega)$ enables us to determine the maximum value of Δn, which corresponds to complete absorption saturation. It means the transition of maximum number of particles to the upper level of the shutter crystal.

During the absorption process the shape of the absorption line does not change. For any moment the aforesaid $\Delta\varepsilon$ (and, consequently, for Δn) and $\sigma(\omega)$ relation is true, but in different stages of pulse development the number of absorbed particles is different. The value of this addition to ε is proportional to the number of absorbed particles (k is the coefficient of proportionality here).

$$\Delta n(t) = k\int_0^{\infty}\frac{N(t)\sigma_a(x)}{\omega^2 - x^2}dx,$$

$$\Delta n(t) = \Delta n_{max}\frac{N(t)}{N_{max}}, \quad \Delta n(t) = \Delta n_{max}\frac{\alpha(t)}{\alpha_{max}}.$$

By solving the system of differential rate equations we obtain the values of the inverse population N_2 in the active element and the population in the saturable shutter N_a as functions of time. By using the equations for the average values of N_a, we determine its local value in min and max of interference picture in the shutter. It is obvious that in peaks of interference picture the shutter refraction index begins to grow and reaches the constant value earlier than in minimum. Later the refraction index in min increases and then reaches the same constant value too (Fig. 5). Therefore, the "resonant"

Pulse magnitude, arb. units
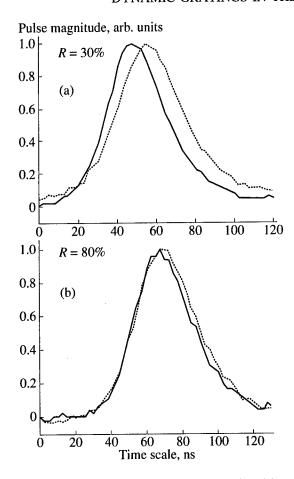
Fig. 7. Experimental data for reflected signal time delay.

laser pulse does, and the magnitude of the thermal gratings merely coincides in its time development with the development of the laser spike. It was found that for "resonant" gratings the peaks of interference picture are in phase with maximums of refractive index; the same is true for the thermal mechanism too. The change of refractive index for both types of induced gratings approaches the value of 10^{-6}, which corresponds to reflection coefficient of about ~0.2%. The correlation between the maximum value of the magnitude of the thermal and "resonance" gratings depends on the reflection coefficient R of the output coupler (Fig. 6). If R is small, the amplitude of the "resonant" grating is greater than the thermal one. It was observed in the experiment that the signal reflected from the induced gratings had the time shift with respect to the laser spike for $R = 0.3$, while for $R = 0.8$ the time shift was equal to 0 (Fig. 7). Good agreement between calculated and experimental parameters verifies the validity of the model used and it enables us to apply the model for the optimization of similar laser schemes.

ACKNOWLEDGMENTS

(connected with saturable absorption) grating disappears before the laser pulse will reach its peak value, while the thermal grating reaches its maximum at the end of the laser pulse, because the heating of the crystal continues through the whole pulse duration.

According to our simulation, the magnitude of "resonance" gratings achieves its maximum faster than

REFERENCES

1. Eilers, H., Hoffman, K.R., Dennis, W.M., *et al.*, 1992, *Appl. Phys. Lett.*, **61**, 2958.
2. Brignon, A. and Huignard, J.-P., 1994, *Opt. Commun.*, **110**, 717.
3. Bufetova, G.A., Klimov, I.V., Nikolaev, D.A., *et al.*, 1995, *Quantum Electron.*, **22**, 791.
4. Il'ichev, N.N., Kir'yanov, A.V., Pashinin, P.P., and Shpuga, S.M., 1994, *JETP*, **78**, 7698.
5. Bufetova, G.A., Klimov, I.V., Nikolaev, D.A., *et al.*, 1995, *Technical Digest of 8th Laser Optical Conf.* (St. Petersburg, Russia), vol. 2, p. 245.

PHYSICS OF SOLID STATE

LASERS

Control of the Nd-Laser Output by Cr-Doped Q-Switches

I. V. Klimov, I. A. Shcherbakov, and V. B. Tsvetkov

General Physics Institute, Russian Academy of Sciences, ul. Vavilova 38, Moscow, 117942 Russia
e-mail: tsvetkov@lazkr2.gpi.ru
Received September 4, 1997

Abstract—Results of experimental investigations on controlling lasing characteristics of Nd lasers (pulse width, energy and repetition rate of giant pulses, and polarization properties) with passive Q-switches based on Cr^{4+}-doped crystals are presented. The studies were performed with both a flashlamp and laser-diode-pumped lasers. The possibility of this nonconventional use of passive Q-switches stems from the intrinsic properties of Cr^{4+}-doped crystals. The dipole moments of active centers in cubic hosts are oriented along the [001]-axes. Therefore, the processes of absorption saturation and the magnitude of residual losses display orientational dependence on the angle between the polarization plane and the crystal axes of the passive Q-switch. This paper presents the results of the study of passive Q-switches that bleach during giant-pulse lasing in a Nd laser. We have demonstrated the possibility to control laser parameters by the rotation of a preliminarily oriented Cr^{4+}-doped crystal around the optical axis of the laser cavity. With a stabilized pumping power, the energy, the pulse width, and the repetition rate of giant pulses can be changed within an order of magnitude as functions of the angular orientation of the Q-switch.

1. INTRODUCTION

The method of passive Q-switching of a laser cavity is widely used in laser technology due to its simplicity and efficiency. In recent years, an increasing interest has been expressed in the application of passive Q-switches in 1-μm neodymium lasers, which is associated with the appearance of a new class of saturable absorbers—crystals doped with Cr^{4+} ions (e.g., see [1]). Due to a combination of the high stability of phototropic centers, sufficiently high thermal conductivity of the host, and the well-developed growth technology, this class of passive Q-switches is very attractive for various applications.

Earlier studies have revealed the effect of polarization anisotropy in absorption saturation in Cr^{4+}-doped optically isotropic crystals [2, 3]. It was demonstrated that the propagation of 1-μm radiation in an optically isotropic crystal of yttrium aluminum garnet gives rise to the self-induced nonlinear absorption anisotropy in the range of absorption saturation. This effect was investigated in Cr^{4+} : YAG crystals and other garnet hosts (YSGG, GSGG, etc.) [2–4] for both short probing pulses (when the pulse duration is much shorter than the lifetime of the excited state of a Cr^{4+} ion) and virtually continuous-wave excitation. It was demonstrated [2, 5] that the highest accuracy of the description of this effect can be achieved within the framework of the model of linearly absorbing dipoles oriented along the principal crystallographic axes of the host (there are three possible orientations of dipoles in garnet crystals).

However, the induced anisotropy virtually vanishes when probing radiation has a high energy density, i.e., in the range of total absorption saturation. Nevertheless, experiments have demonstrated that the characteristic of a neodymium laser depend on the angular orientation of a Cr^{4+}-doped passive Q-switch [6, 7].

The purpose of this work is to experimentally investigate the bleaching of a Cr^{4+}-doped passive Q-switch in a cavity of a neodymium laser and the possibility to control the lasing parameters (pulse width, the energy and repetition rate of giant pulses, and polarization properties) of such a system only by the rotation of the Q-switch around the optical axis of the cavity.

2. EXPERIMENTAL

Experiments were carried out both with flashlamp pumping and under conditions when the active element was pumped with a diode laser. Figure 1 displays a diagram of the experimental setup for studying the bleach-
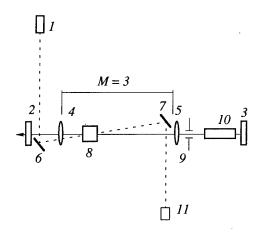

Fig. 1. Diagram of an experiment on measuring the bleaching of a passive Q-switch with the use of an external probing source: (*1*) source of probing radiation (diode-pumped cw Nd : YAG laser), (*2*) output coupler of the cavity, (*3*) rear mirror of the cavity, (*4, 5*) telescope, (*6, 7*) 45° totally reflecting mirrors, (*8*) passive Q-switch (Cr^{4+} : YSGG), (*9*) diaphragm, (*10*) active element, and (*11*) photodiode.
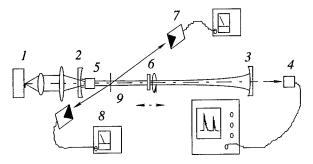
ing of a Q-switch during giant-pulse generation (in the case of flashlamp pumping). As an active element, we employed a Nd : YAG crystal ($\varnothing$6.3 × 90 mm). A diaphragm 1.5 mm in diameter was used to ensure lasing in the TEM$_{00}$ mode. The reflection coefficient of the output coupler was $R = 60\%$. To investigate the influence of radiation intensity inside the cavity on the bleaching of the Q-switch, we employed a telescope with a magnification $M = 3$. The switch in such a scheme can be placed virtually at any point inside the telescope. As passive Q-switches, we studied Cr^{4+} YSGG crystals with initial (unsaturated) transmission coefficients of 30, 50, 62, and 80%. The length of Q-switches was varied within the range of 5–7 mm. The bleaching of Q-switches during lasing was measured with the use of a probing beam. As a source of the probing beam, we employed a diode-pumped Nd : YAG laser. The size of the probing beam was limited at ~0.8 mm with a specially designed diaphragm. The maximum angle between the probing beam and the cavity axis in the crystal of the Q-switch did not exceed 2°, which ensured sufficient overlapping of the probing and intracavity beams. The total cavity length was 90 cm.

Measurements performed with the use of a probing beam allowed us to obtain interesting data concerning the time dynamics of bleaching in the switch in the process of lasing. However, the data concerning the real magnitude of bleaching obtained with this approach may be characterized by considerable errors, because the interference of electromagnetic waves inside the cavity leads to a nonuniform bleaching of the switch. We can improve the accuracy of experimental data in the case under study by measuring the transmission of the switch with a split intracavity beam (in Fig. 2, this technique is illustrated for a diode-pumped laser). Placing a switch at various points along the cavity axis, we observed variations in the power density of intracavity radiation in the material of the switch (similar to a flashlamp-pumped system with a telescope). An analogous scheme was employed for a flashlamp-pumped laser. These experiments demonstrated that the results of measurements performed with the use of two different methods fall within the limits of experimental errors.

In experiments with diode pumping, we employed Nd : YAG, Nd : YAlO$_3$, and Nd : GdVO$_4$ active elements. As a passive Q-switch, we used Cr^{4+} : YAG crystals with initial transmission coefficients varying from 90 to 98% and a thickness of 0.4–1 mm.

We also measured the output characteristics of neodymium lasers based on anisotropic crystals as functions of the angular orientation of the switch crystal in the cavity.

As mentioned above, Cr^{4+} active centers form three orthogonal groups of dipoles oriented along the principal crystallographic axes of the host with a garnet structure. All the crystals of Q-switches employed in experiments were cut out of slabs and mounted in the cavity in such a manner that one of the principal crystallographic axes was parallel to the optical axis of the cav-

Fig. 2. Diagram of the setup for studying the influence of the relation of the intensities in the Q-switch and in the active element on the dependences of lasing parameters on the angular orientation of the Q-switch: (*1*) pumping diode laser, (*2, 3*) cavity mirrors ($R_{2,3} = 99.9\%$, $r_2 = 50$ mm, and $r_1 = 200$ mm), (*4*) photodiode, (*5*) active element, (*6*) passive Q-switch (Cr^{4+} : YAG, $T_0 = 91\%$), (*7, 8*) power meters, and (*9*) beam splitter.
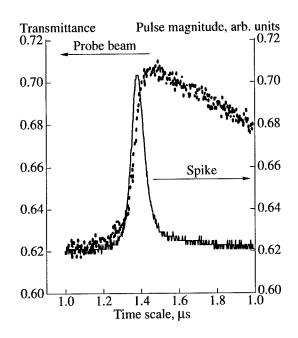
Fig. 3. A giant pulse of a neodymium laser and the time dynamics of bleaching in a Cr^{4+}-doped Q-switch.

ity. In this case, two other axes lay in the perpendicular plane. Thus, the rotation of a Q-switch around the optical axis of the laser cavity changed the orientation of the switch axes relative to the polarization plane of radiation produced by the active element. In such a situation, the transmission of a switch with incompletely saturated absorption should also change.

3. EXPERIMENTAL RESULTS

3.1. A Flashlamp-Pumped Neodymium Laser

To understand the physical mechanism behind lasing in a laser with a passive Q-switch, we should know how the Q-switch is bleached. Using the scheme shown
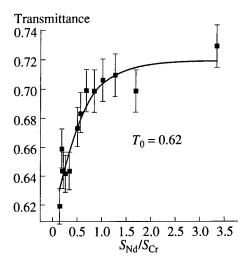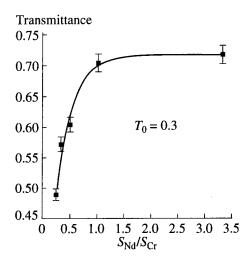
Fig. 4. Bleaching of the Q-switch as a function of the intensity of intracavity radiation; S_{Cr}/S_{Nd} is the ratio of the area of the cross section of the intracavity beam in the Q-switch to the area of the cross section of the intracavity beam in the active element; $T_0 = 62\%$.

Fig. 5. Bleaching of the Q-switch as a function of the intensity of intracavity radiation; S_{Cr}/S_{Nd} is the ratio of the area of the cross section of the intracavity beam in the Q-switch to the area of the cross section of the intracavity beam in the active element; $T_0 = 30\%$.

in Fig. 1, we measured the curves that represent the bleaching of the Q-switch simultaneously with the observation of giant-pulse radiation (Fig. 3). In this experiment, we employed a Q-switch with an initial transmission coefficient of 62%. The transmission of the Q-switch displays fast bleaching and slow relaxation to the initial state with a characteristic time equal to the lifetime of the excited state of Cr^{4+} ions in the crystal of the switch. As can be seen from the presented dependence, the characteristic time of bleaching noticeably differs from the characteristic time of the increase in the photon density in the cavity (giant-pulse radiation). At the initial stage, the bleaching of the Q-switch is faster than the increase in radiation intensity. Next, at the stage of lasing, radiation intensity grows much faster, and the giant pulse is generated with an incompletely bleached switch. In the case under study, the maximum transmission coefficient of an open Q-switch was ~71%, although the measurement of the characteristics of this switch in accordance with a standard technique of absorption saturation measurement gave the maximum transmission coefficient equal to 85%.

Analysis of the set of kinetic equations governing a passively Q-switched laser has demonstrated (e.g., [8]) that the ratio of the decrease rate of losses in the cavity under conditions when the Q-switch is bleached to the decrease rate of the gain in the active element under conditions of pulse generation is an important parameter that characterizes the process of lasing. This parameter can be written in the following form [9]:

$$\gamma = \frac{\sigma_a S_g}{\sigma_g S_a} > 1, \tag{1}$$

where σ_a and σ_g are the cross sections of absorption and radiation emission in the Q-switch and the active ele-

ment, respectively, and S_a and S_g are the areas of the cross section of the laser beam in the Q-switch and the active element, respectively. For $\gamma \gg 1$, the criterion is rigorously satisfied, and small changes in the relation between the areas of the cross section of the beam in the Q-switch and the active element do not exert a considerable influence on parameters of radiation being produced. In this case, the filter is bleached virtually instantaneously, i.e., much faster than the inversion in the active medium decreases. For the majority of neodymium lasers, this parameter falls within the interval $1 < \gamma \leq 10$ (in the case when the areas of the cross section of the beam in the active medium and in the Q-switch are equal to each other), i.e., Q-switching is relatively slow and the complete bleaching of the absorber may be unattainable.

To test this conclusion, we measured the transmission of the Q-switch during the generation of a laser pulse (the experimental scheme is shown in Fig. 1) for various power densities in the Q-switch. The absorber in these experiments was placed at different points along the axis of the telescope. Thus, we were able to vary the S_a/S_g ratio.

Figures 4 and 5 display the measured dependences of the transmission of a saturated Q-switch on the ratio of the areas of the cross section of the beam in the active medium and in the absorber in the process of lasing. The maximum contrast (the ratio of the saturated transmission coefficient to the initial transmission coefficient) was achieved with a dense ($T_0 = 30\%$) Q-switch. However, for all the studied Q-switches, the maximum transmission was 72%, which is much less than the transmission $T_{max} \approx 85\%$ achieved in intracavity experiments. The maximum energy density inside the cavity was as high as ~750 mJ/cm^2.

Thus, we can assert that passive Q-switches based on Cr^{4+}-doped crystals are not bleached during the generation of a laser pulse up to the maximum transmission coefficient. Therefore, the magnitude of residual losses should depend on the relative orientation of the crystallographic axes of the Q-switch and polarization of laser radiation.

We experimentally studied the dependence of the output laser energy on the angular orientation of the Q-switch in a cavity with a length of 90 cm. In these experiments, we employed a $\varnothing 6.3 \times 90$-mm $Nd : YAlO_3$-crystal active element oriented in such a manner that the polarization of laser radiation in the free-running mode lay in the vertical plane. To measure the transmission of the Q-switch, we split the laser beam inside the cavity (using a scheme similar to that presented in Fig. 2).

The results of measurements presented in Fig. 6 demonstrate a close correlation between the bleaching peaks of the Q-switch and the maxima of the output laser energy. The pumping energy was fixed in these measurements, and the energy of laser radiation was varied only by the rotation of the $Cr^{4+} : YSGG$-crystal Q-switch around the cavity axis. The minimum magnitude of residual losses in the Q-switch and the maximum output energy were achieved when one of the crystallographic axes of the switch crystal was parallel to the polarization plane of laser radiation defined by the active element. Laser radiation was linearly polarized in all the cases (the ellipticity coefficient was less than 1/100). The polarization plane of laser radiation coincided with the vertical plane with a high accuracy. Analogous results can be obtained when an optically isotropic active medium and an intracavity polarizer are employed (e.g., see [7]).

3.2. Diode-Laser-Pumped Neodymium Lasers

Based on the results presented above, we can assume that much better results can be obtained by using continuous-wave diode-laser pumping, because, in the case of diode lasers, the pumping rate would be much lower, the pumping power would not considerably exceed the lasing threshold, and the stability of pumping would be much higher.

Figure 7 presents the results of measurements performed with the use of the following experimental scheme. A 0.4-mm-thick $Cr^{4+} : YAG$ crystal with [001] orientation and initial transmission of 0.91 was placed inside a plane–concave cavity (the cavity length was 24 mm) of a $Nd : GdVO_4$ laser. The $Cr^{4+} : YAG$ crystal had an antireflection coating for 1.06-μm radiation. The entrance face of the $Nd : GdVO_4$ crystal (with a length of 2 mm) had a reflection coating for 1.06-μm radiation and served as a rear cavity mirror, which was used to couple pumping radiation of an SDL-2462 diode laser (with a maximum power of 1 W) into the laser cavity in the longitudinal geometry. The other face of the active element had an antireflection coating for 1.06-μm laser radiation. The output coupler of the cav-
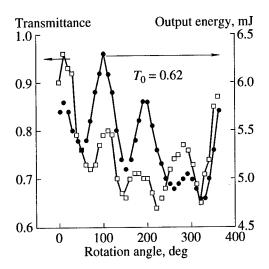
Fig. 6. Lasing energy and transmission of the Q-switch as functions of the angular orientation of the Q-switch in the laser cavity. The initial transmission of the Q-switch is $T_0 = 62\%$.
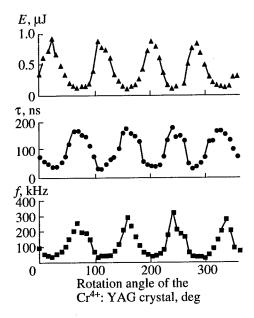
Fig. 7. Dependences of the lasing parameters of the $Nd : GdVO_4$ laser on the angular orientation of the Q-switch.

ity had a reflection coefficient of 93% and a curvature radius of 200 mm. A passive laser Q-switch was mounted on a table that could rotate by an angle of 360° around the optical axis of the cavity. The measurements were performed with a power of continuous-wave pumping of ~500 mW. Rotating the passive Q-switch around the optical axis of the cavity, we measured the output power, the repetition rate, and the duration of a single pulse. The results of measurements are shown in Fig. 7.

The presented plots demonstrate that all the radiation parameters depend on the rotation angle of the passive Q-switch. For example, the pulse duration (FWHM) ranged from 30 to 170 ns, while the minimum

and maximum values of the power of a single pulse, defined as E_p/t_p, differed from each other by more than two orders of magnitude. We should emphasize that the highest stability of pulse amplitude and repetition rate was achieved when the orientation of the Q-switch corresponded to the maximum energy and the minimum duration. The orientation of the polarization plane of output radiation remained unchanged regardless of the rotation angle of the Q-switch and was completely determined by the orientation of the Nd : $GdVO_4$ crystal.

For active media with smaller radiation emission cross sections, where higher energy densities were achieved inside the cavity, the angular dependences
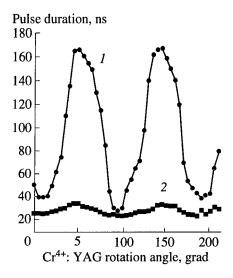
Fig. 8. Comparison of the dependences of the laser pulse duration on the angular orientation of the Q-switch for (*1*) Nd : $GdVO_4$ and (*2*) Nd : $YAlO_3$ lasers.
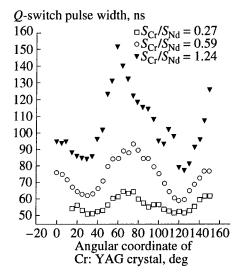
Fig. 9. Dependences of the laser pulse duration on the angular orientation of the Q-switch for different ratios of the beam areas in the Cr^{4+} : YAG Q-switch and Nd : $YAlO_3$ active element.

of the parameters of laser radiation become less clearly pronounced (Fig. 8). We experimentally studied a 5-mm Nd : $YAlO_3$-crystal active element. The effective radiation emission cross section for Nd ions in this host is 2.5 times lower than that for the $GdVO_4$ host, which decreases the contrast of the angular dependences.

Simultaneously, we investigated the influence of the power density of intracavity radiation inside the Q-switch on the angular dependences of the lasing parameters. For this purpose, we moved the crystal of the Q-switch along the optical axis of the cavity with a variable beam diameter (Fig. 2). Figure 9 displays temporal characteristics of laser radiation measured with the use of a broadband photodiode (2.5 GHz). As can be seen from these plots, the decrease in the power density in the Q-switch (the increase in the $\dfrac{S_{Cr}}{S_{Nd}}$ ratio) increases both the mean pulse duration and the contrast of its angular dependence. Because of the decrease in the energy density in the Q-switch with the growth in the S_{Cr}/S_{Nd} ratio, the residual absorption in the Q-switch increases, which lowers the total power of laser radiation (Fig. 10). Note that, even with $S_{Cr}/S_{Nd} = 1$, one can observe a considerable decrease in the contrast of the Q-switch and, correspondingly, in the output laser power relative to the maximum attainable parameters.

The comparison of angular dependences corresponding to the rotation of a Q-switch inside a laser cavity with the curves characterizing the bleaching of Q-switches outside a laser cavity allowed us to infer that the maximum energy and the minimum pulse duration can be achieved when a Q-switch is oriented in such a manner that the polarization plane of radiation in the cavity coincides with one of the axes of a Cr^{4+} : YAG crystal, and, vice versa, laser radiation has the worst parameters (the minimum energy and the maximum pulse duration) when the polarization plane of laser radiation makes an angle of 45° with one of the crystal axes.
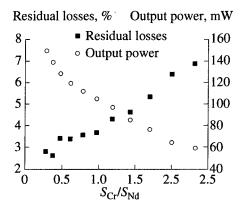
Fig. 10. The output lasing power of the Nd : $YAlO_3$ laser and the residual absorption in the Cr^{4+} : YAG Q-switch as functions of the ratio of the beam areas in the Q-switch and the active element.

4. CONCLUSION

Thus, the results presented in this paper clearly demonstrate that the angular orientation of a Cr^{4+}-crystal Q-switch is one of the key factors for passively Q-switched neodymium lasers with polarized radiation. Rotating a Q-switch around the optical axis of the cavity and varying the energy density of intracavity radiation inside the Q-switch, one can readily change the lasing parameters of such a system within a broad range. Such effects are especially well pronounced in diode-pumped neodymium lasers based on anisotropic crystals.

ACKNOWLEDGMENTS

REFERENCES

1. Denisov, A.L., Zharikov, E.V., Zavartsev, Yu.D., *et al.*, 1991, *Izv. Akad. Nauk SSSR, Ser. Fiz.*, **55**, 239.

2. Eilers, H., Hoffman, K.R., Dennis, W.M., *et al.*, 1992, *Appl. Phys. Lett.*, **61**, 2958.

3. Il'ichev, N.N., Kir'yanov, A.V., Pashinin, P.P., *et al.*, 1994, *Sov. J. Quantum Electron.*, **24**, 771.

4. Rusanov, S.Ya., Nikolaev, D.A., Shcherbakov, I.A., *et al.*, 1996, *Technical Digest of CLEO/Europe Conf.* (Hamburg), CFD5, p. 329.

5. Il'ichev, N.N., Kir'yanov, A.V., Pashinin, P.P., and Shpuga, S.M., 1994, *Zh. Eksp. Teor. Fiz.*, **105**, 1426.

6. Klimov, I.V., Tsvetkov, V.B., Shcherbakov, I.A., *et al.*, 1996, *OSA TOPS on Advanced Solid-State Lasers*, Pain, S.A. and Pollock, C., Eds., vol. 1, p. 438.

7. Il'ichev, N.N., Kir'yanov, A.V., Gulyamova, E.S., and Pashinin, P.P., 1997, *OSA TOPS on Advanced Solid-State Lasers*, Pollock, C.R. and Rosenberg, W.R., Eds., vol. 10, p. 137.

8. Siegman, A.E., 1986, *Lasers* (California: Univ. Science Books).

9. Kuo, Y.K., Chen, W., Spariosu, K., *et al.*, 1994, *Appl. Opt.*, **33**, 6348.

Competition of Axial Modes in a Double-Mode Nd³⁺ : YAG Laser with Semiconductor Pumping

R. A. Karle-Shananin, V. N. Petrovskiy, D. I. Soloviev, and I. V. Yevseyev

Department of Quantum Electronics, Moscow State Engineering Physics Institute (Technical University), Kashirskoe sh. 31, Moscow, 115409 Russia

e-mail: quan_el@orc.ru

Received September 30, 1997

Abstract—The competition of axial modes with mutually orthogonal polarizations in an Nd³⁺ : YAG laser is studied theoretically and experimentally. An Nd³⁺ : YAG laser capable of generating two axial modes with mutually orthogonal polarizations was developed and implemented for the experimental investigation of axial-mode competition. A linear phase-anisotropic cavity was employed to implement the double-mode regime. Investigations of this laser have demonstrated that the intermode separation falls within the range from 30 MHz to 9 GHz, and the maximum area of double-mode lasing is $c/2L \approx 9$ GHz. The signal-to-noise ratio for the intermode-beat signal is no less than 30 dB. For the theoretical analysis of such a laser, we derived differential equations that describe the competition of orthogonally polarized modes, including competition due to spatial inversion hole burning. Comparison of theoretical predictions with experimental results allowed us to provide a detailed description of the competition of axial modes with mutually orthogonal polarizations in an Nd³⁺ : YAG laser.

1. INTRODUCTION

The studies on the development of double-mode lasers have started more than 30 years ago with the pioneering paper by V. Evtuhov and A.E. Siegman [1]. The authors of this paper developed and implemented a double-mode ruby laser, where lasing occurred only in two axial modes with circular polarizations. However, Evtuhov and Siegman did not provide a detailed investigation of specific features of double-mode lasing, which is, apparently, due to the complexity of the theoretical description of lasing even for a single-mode ruby laser. Therefore, within the next over 30 years, double-mode lasing has been investigated only for gas lasers, where it is much easier to provide a detailed theoretical description than in the case of solid-state lasers.

The papers by W.E. Lamb [2] provided a significant contribution to the theoretical description of double-mode lasing in gas lasers. However, these studies ignored the degeneracy of resonant levels, which does not permit one to apply this approach to the investigation of double-mode lasing with different mode polarizations. In the meanwhile, double-mode lasers with orthogonally polarized modes have proved to be convenient for various applications.

Our research group provided the main contribution to the subsequent investigation of double-mode lasing in gas lasers. At the first stage, detailed theoretical and experimental studies of double-mode gas lasers with atomic active media have been carried out. Double-mode He–Ne lasers using various transitions have been developed and implemented. A consistent theory of a double-mode laser with a working transition between energy levels of an atomic gas has been devised under the supervision of Professor V.M. Yermachenko.

Subsequent investigations of our group have been concentrated on gas systems where a molecular gas is used as an active medium. Such a double-mode CO_2 laser has been developed by our research group in 1985 [3]. We performed a detailed theoretical and experimental investigation of the specific features of double mode lasing in this system. The developed methods for controlling mode coupling allowed us to implement double-mode lasing within an area on the order of the separation between unsplit modes.

Note that gas lasers usually have large dimensions, high energy consumption, and a short service lifetime. In addition, such lasers require high-voltage sources. Solid-state lasers with longitudinal diode-laser pumping are free of these drawbacks. Such single-mode solid-state lasers have been created less than five years ago.

The advent of single-mode solid-state lasers with longitudinal diode-laser pumping has stimulated research into double-mode solid-state lasers. The development of a double-mode Nd³⁺ : YAG minilaser has started virtually simultaneously in the United States and Russia [4, 5]. In contrast to our approach, which implied that double-mode lasing is implemented with the use of a phase-anisotropic cavity, the other research groups have employed the photoelasticity effect. The main drawback of the latter technique is associated with the low ratio of the intermode-beat signal to the level of noise due to technical difficulties that arise when a uniform field of elastic stress should be induced in an active crystal.

In this paper, we report the development and implementation of an Nd³⁺ : YAG minilaser (with the cavity length $L = 17$ cm) that generates two axial modes with mutually orthogonal polarizations (a double-mode

laser). The intermode-beat frequencies can be continuously tuned in this laser.

Properties of radiation produced by the developed laser have been studied theoretically and experimentally. For the theoretical analysis of such a laser, we derived equations that describe double-mode lasing in a solid-state laser with orthogonally polarized modes.

The performed investigations have shown that the intermode separation for the developed laser falls within the range from 30 MHz to 9 GHz, and the maximum area of double-mode lasing is $c/2L \approx 9$ GHz. The signal-to-noise ratio for the intermode-beat signal is no less than 30 dB, which cannot be achieved with any other laser in the world.

2. A DOUBLE-MODE Nd³⁺ YAG LASER

For the experimental investigation of the competition of axial modes, we developed and implemented a double-mode Nd³⁺ : YAG laser with diode-laser pumping (Fig. 1). For this purpose, we used a continuous-wave Nd³⁺ : YAG laser with an isotropic cavity. As an active element (5), we employed a crystal with a diameter of 5 mm and the length of 5 mm with plane ends antireflection-coated for 1.06-μm radiation. Longitudinal pumping was implemented with the use of a standard diode laser (1) with a power of 120 mW. Pumping laser radiation was focused by a three-lens objective (3) with 2× magnification into the volume of the active element. The characteristic size of the spot of pumping radiation within the length of the active element (≈300 μm) was close to the waist diameter of the zeroth-order laser mode. To match the maximum in the spectrum of pumping radiation with the absorption line of the active element near λ = 0.809 μm, we varied the temperature of the laser diode by means of a thermoelectric cooler. The temperature was automatically maintained near the maximum of the pumping radiation spectrum with an accuracy up to 0.01°C.

The laser cavity was formed by two mirrors with interference coatings. The inner dichroic mirror, which was used to couple pumping radiation into the laser cavity, was virtually totally reflecting for Nd³⁺ : YAG laser radiation ($\rho_{1.06} \geq 99.9\%$) and sufficiently transparent for pumping radiation ($\rho_{0.809} = 90\%$). The curvature radius of this mirror was $R \approx 20$ mm. The outer mirror had the reflection coefficient $\rho_{1.06} = 98\%$ for $\lambda = 1.06$ μm and $R = 1.5$ m. The inner mirror was pasted onto the end of the active element. The output cavity mirror was mounted on a piezotransducer, which allowed the mirror to move progressively within an interval of $\pm 3/2\lambda$ around its nonperturbed position. To scan laser modes through the contour of the gain line during experiments, we applied a sinusoidal voltage to the piezotransducer.

To eliminate higher order transverse modes, we introduced a diaphragm 0.5 mm in diameter into the
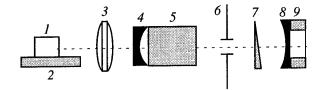
Fig. 1. A double-mode Nd³⁺ : YAG laser with longitudinal diode-laser pumping: (1) pumping diode laser, (2) thermoelectric cooler, (3) focusing objective, (4) inner cavity mirror, (5) Nd³⁺ : YAG active element, (6) diaphragm 0.5 mm in diameter, (7) phase-anisotropic wedge ($\alpha \approx 1°$), (8) output mirror of the cavity, and (9) piezoceramic element.

laser cavity near the end of the active element and chose the cavity length in such a manner that the cavity operated near the boundary of the stability regime. The cavity length was $L = 17$ mm, which corresponded to the frequency separation between longitudinal modes $c/2L \approx 8.8$ GHz.

The excess of the gain above losses $\eta = \alpha/T$ (the ratio of the gain α to the magnitude of losses T) in the laser was chosen so that the active part of the gain line contour (the region where the gain was higher than the magnitude of losses) approximately corresponded to the frequency separation between the longitudinal cavity modes. To measure the excess of the gain above losses, we deliberately implemented a single-mode regime of lasing in the Nd³⁺ : YAG laser. As is well known, for lasers with a homogeneously broadened gain line (Nd³⁺ : YAG lasers belong to this class of lasers), the ratio η in the single-mode regime of lasing can be expressed in terms of the line width Γ and the width Δv of the active part of the gain line contour,

$$\eta = \left(\frac{\Delta v}{\Gamma}\right)^2 + 1. \tag{1}$$

The regime of double-mode lasing was implemented with the use of an intracavity phase-anisotropic element. In such a scheme, each axial mode of an initially isotropic cavity was split into two modes with different frequencies and mutually orthogonal polarizations. As a phase-anisotropic element, we used an optical wedge made of crystalline quartz. We were able to continuously adjust the frequency separation between the split modes by varying the position of the wedge in the direction perpendicular to the optical axis of the cavity.

Depending on the frequencies of the modes within the gain line contour, a laser of such a configuration always generated only two linear modes with mutually orthogonal polarizations and the intermode separation equal to either $\omega_{12} = \omega_1 - \omega_2$ or $\omega_{23} = c/2L - \omega_{12}$ (Fig. 2).

A diagram of the experimental setup for studying the competition of axial modes in a double-mode
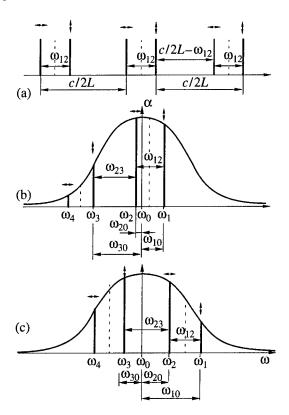
Fig. 2. Arrangement of laser modes within the contour of the gain line: (a) the spectrum of modes for a phase-anisotropic cavity, (b) modes with frequencies ω_1 and ω_2 are involved in lasing, and (c) modes with frequencies ω_2 and ω_3 are involved in lasing; $\omega_{12} = \omega_1 - \omega_2$, $\omega_{23} = \omega_2 - \omega_3 = c/2L - \omega_{12}$, and $\omega_{20} = \omega_2 - \omega_0$.

Fig. 3. Diagram of the experimental setup for studying the competition of axial modes.

Nd^{3+} : YAG laser is shown in Fig. 3. To control the spectral composition of radiation, we used Fabry–Perot scanning interferometers with (1) the free-dispersion range $c/2L_0 \approx 30$ GHz (L_0 is the length of the interferometer) and the resolution $\Delta\nu \approx 3$ GHz, which made it possible to determine the entire spectrum of modes, and (2) the free-dispersion range $c/2L \approx 7$ GHz and the resolution $\Delta\nu \approx 1$ GHz, which allowed us to study the spectrum in greater detail (Fig. 3 shows only one of the Fabry–Perot interferometers). To determine the polarizations of the laser modes, we placed a polarizer in front of each interferometer. Optical decoupling was used to reduce the influence of backreflection.

In studying laser characteristics, we employed a semitransparent mirror to divide laser radiation into two beams with approximately equal powers. A polarizer oriented along the direction of polarization in each of the modes and a photodetector were placed in each of the channels. To measure the intermode separation ω_{12}, we employed the third channel of the system, where laser radiation passed through a polarizer oriented at an angle of 45° with respect to the polarization directions in separate modes. Emerging radiation was detected by a photodiode with a bandwidth of 700 MHz.
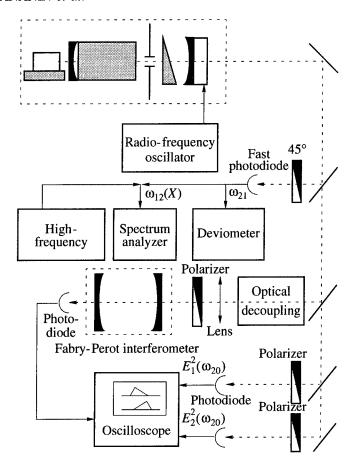
The output signal of the photodiode was fed to a spectrum analyzer, which detected the signal of intermode beats with frequencies from ≈ 0 to 700 MHz. To observe the signal of intermode beats within the frequency range from 700 MHz up to 1.5 GHz by means of the spectrum analyzer, we mixed the signal of intermode beats with a signal of an external radio-frequency oscillator (the oscillator frequency was 800 MHz) on a photodiode (see Fig. 3). Finally, to determine intermode separations with frequencies higher than 1.5 GHz, we used a method of a calibrated birefringent wedge (Fig. 4). This method can be described as follows. The phase-anisotropic wedge introduces phase shifts for each of the orthogonally polarized modes inside the cavity. These shifts determine the frequencies of these modes. Since the intermode-beat signal is a periodic function of the difference of phase shifts for the modes with mutually orthogonal polarizations, the wedge was designed in such a manner that it had two points along its length where the frequencies of intermode beats were equal to each other (we have chosen the points where $\omega_{12} = 0.5$ GHz, which allowed us to detect the intermode-beat signal using a spectrum analyzer). Since ω_{12} is a linear function of the displacement of the wedge (this fact was verified experimentally), we grad-

uated the linear displacement of the wedge on a frequency scale.

3. BASIC RELATIONS

For the theoretical investigation of the developed laser, we derived differential equations that describe the competition of orthogonally polarized modes, including competition due to spatial inversion hole burning. To obtain these equations, we employed the Lamb approach, which implies the classical description of the electromagnetic field and quantum-mechanical description of the active medium.

In the case of double-mode lasing, the field $\varepsilon(z, t)$ can be written in the form

$$\varepsilon(z, t) = \mathbf{e}_1(t)E_1(t)\sin(k_1 z)\cos(\omega_1 t) \\ + \mathbf{e}_2 E_2 \sin(k_2 z)\cos(\omega_2 t), \tag{2}$$

where $\mathbf{e}_{1,2}$ are the unit polarization vectors of the fields corresponding to the laser modes [for the modes with mutually orthogonal polarizations, we have $(\mathbf{e}_1 \cdot \mathbf{e}_2) = 0$], $E_{1,2}(t)$ are the slowly varying amplitudes of the modes, $\omega_{1,2}$ are the frequencies of the laser modes being generated, $k_{1,2} = \omega_{1,2}/c$, c is the speed of light, $0 \leq z \leq L$, and L is the cavity length.

The amplitudes $E_{1,2}(t)$ and the mode frequencies $\omega_{1,2}$ can be determined from the Maxwell equations

$$\dot{E}_i + \frac{\Delta\Omega_i}{2}E_i = 2\pi\omega_i \mathrm{Im}\left[\frac{2}{L}\int(\mathbf{e}_i\mathbf{D}(z, t))\sin(k_i z)dz\right], \tag{3}$$

$$E_i(\omega_i - \Omega_i)$$

$$= -2\pi\omega_i \mathrm{Re}\left[\frac{2}{L}\int(\mathbf{e}_i\mathbf{D}(z, t))\sin(k_i z)dz\right]. \tag{4}$$

Here, $\Delta\Omega_i$ is the cavity band; Ω_i are the eigenfrequencies of the cavity; and $\mathbf{D}_i(z, t)$ are the slowly varying parts of the polarizability of the active medium $\mathbf{P}_i(z, t)$,

$$\mathbf{P}_i(z, t) = \frac{1}{2}\sum_i \mathbf{D}_i(z, t)\exp(i\omega_i t) + \text{c.c.} \tag{5}$$

The polarizability of the active medium can be found from the equations

$$\frac{\partial^2 \mathbf{P}}{\partial t^2} + 2\Gamma\frac{\partial \mathbf{P}}{\partial t} + \omega_0^2 \mathbf{P} = -\frac{2\omega_0 d^2}{\hbar}\varepsilon N, \tag{6}$$

$$\frac{\partial N}{\partial t} = \gamma(N_e - N) + \frac{1}{\hbar\omega_0}\varepsilon\frac{\partial \mathbf{P}}{\partial t}. \tag{7}$$

Here, $N(z, t)$ is the population inversion, N_e is the population inversion determined by pumping in the case
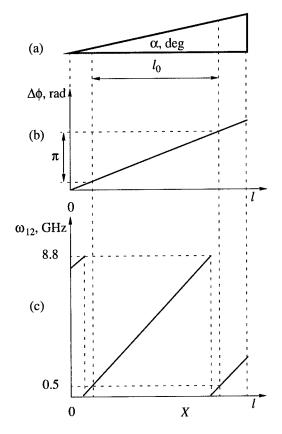
Fig. 4. The method for the calibration of a birefringent wedge.

when $\varepsilon = 0$, Γ is the homogeneous half-width of the spectral line, γ is the inverse lifetime of a particle in the upper level, and ω_0 is the central frequency of the working transition.

Analyzing equations (6) and (7), we will assume that atoms are at rest. If the saturation of the active medium is weak, we can expand the polarizability and the population inversion as power series in the field:

$$\mathbf{P} = \mathbf{P}^{(1)} + \mathbf{P}^{(3)}, \quad N = N_e + N^{(2)}, \tag{8}$$

where $P^{(1)} \sim E_i$, $P^{(3)} \sim E_i^3$, and $N^{(2)} \sim E_i^2$.

Substituting (8) into (6) and (7) and taking relation (5) into account, we find that

$$\dot{D}_i^{(1)} + (\Gamma + i\omega_{i0})D_i^{(1)} = i\frac{\omega_0 d^2}{\hbar\omega_i}N_e E_i \sin(k_i z), \tag{9}$$

$$\frac{\partial N^{(2)}}{\partial t} = -\gamma N^{(2)} - \frac{d^2}{4\hbar^2}N_e$$

$$\times \sum_{i,k} E_i E_k \sin(k_i z)\left[\frac{\exp(i\omega_{ik}t)}{\Gamma + i\omega_{ik}} + \text{c.c.}\right], \tag{10}$$

where $\omega_{i0} = \omega_i - \omega_0$, $\omega_{ik} = \omega_i - \omega_k$, and d is the dipole moment of the working transition.

The condition

$$\Gamma \gg \Delta\Omega, \tag{11}$$

which is satisfied in the solid-state laser, implies that the variation rate of the polarizability in the active medium is much higher than the variation rate of the field amplitude in the cavity. Thus, the field amplitude E_i can be considered to be constant; i.e.,

$$D_i^{(1)} = i\frac{\omega_0 d^2}{\hbar\omega_i} N_e \frac{E_i \sin(k_i z)}{\Gamma + i\omega_{i0}}. \tag{12}$$

Substituting (12) into (10) and solving the resulting equation with respect to $N^{(2)}$, we derive

$$N^{(2)}(z, t) = \sum_{i,j} (A_i \exp(i\omega_{ij}t) + \text{c.c.}),$$

$$A_{ij}(z, t) = -\frac{d^2}{4\hbar^2} N_e \sin(k_i z) \sin(k_j z) \tag{13}$$

$$\times \int_0^t e^{-\gamma\tau} E_i(t-\tau) E_j(t-\tau) \frac{\exp(-i\omega_{ij}\tau)}{\Gamma + i\omega_{ij}} d\tau.$$

Using a similar procedure, we can find $D_i^{(3)}$:

$$D_i^{(3)} = i\frac{\omega_0 d^2}{\hbar\omega_i} \frac{\sum_j E_j \sin(k_{jk}z)(A_{ij} + A_{ij}^*)}{\Gamma + i\omega_{i0}}. \tag{14}$$

Substituting (14) and (12) into equations (3) and (4) and integrating in the spatial coordinate z, we derive

$$\frac{dE_i}{dt} = \frac{\Delta\Omega_i}{2} E_i \left[\alpha_i - \beta_i\gamma \int_0^t e^{-\gamma\tau} \frac{d^2 E_i^2(t-\tau)}{4h^2\gamma\Gamma} d\tau \right.$$
$$\left. - \theta_{ij}\gamma \int_0^t e^{-\gamma\tau} \frac{d^2 E_i^2(t-\tau) E_j^2(t-\tau)}{4h^2\gamma\Gamma} d\tau \right], \tag{15}$$

$$\omega_i - \Omega_i = \frac{\Delta\Omega_i}{2} \left[\sigma_i + \rho_i\gamma \int_0^t e^{-\gamma\tau} \frac{d^2 E_i^2(t-\tau)}{4\hbar^2\gamma\Gamma} d\tau \right.$$
$$\left. + \tau_{ij}\gamma \int_0^t e^{-\gamma\tau} \frac{d^2 E_i^2(t-\tau) E_j^2(t-\tau)}{4h^2\gamma\Gamma} d\tau \right] \tag{15'}$$

$(i, j = 1, 2; i \neq j)$, where the coefficients are introduced in accordance with conventional Lamb definitions:

α_i is the gain for the ith mode,

$$\alpha_i = \eta\frac{\Gamma^2}{\omega_{i0}^2 + \Gamma^2} - 1,$$

β_i is the coefficient of saturation due to the field of the considered mode,

$$\beta_i = \frac{3}{4}\eta\frac{\Gamma^4}{(\omega_{i0}^2 + \Gamma^2)^2};$$

θ_{ij} is the coefficient of cross-saturation due to the field of the other mode,

$$\theta_{ij} = 1 + \frac{1}{2}\cos\left(\frac{\omega_{ij}l}{c} + 2\delta\right)\frac{\sin\left(\frac{\omega_{ij}l}{c}\right)}{\frac{\omega_{ij}l}{c}}$$

$$\times \eta\frac{\Gamma^4}{(\omega_{i0}^2 + \Gamma^2)(\omega_{j0}^2 + \Gamma^2)};$$

σ_i is the coefficient that describes the pulling of the mode to the center of the gain line,

$$\sigma_i = -\eta\frac{\omega_{i0}\gamma}{\omega_{i0}^2 + \Gamma^2};$$

ρ_i is the coefficient that describes the repulsion from the center due to the field of the considered mode,

$$\rho_i = \frac{3}{4}\eta\frac{\omega_{i0}\Gamma^3}{(\omega_{i0}^2 + \Gamma^2)^2};$$

τ_{ij} is the coefficient that describes the repulsion from the center due to the field of the other mode,

$$\tau_{ij} = 1 + \frac{1}{2}\cos\left(\frac{\omega_{ij}l}{c} + 2\delta\right)\frac{\sin\left(\frac{\omega_{ij}l}{c}\right)}{\frac{\omega_{ij}l}{c}}$$

$$\times \eta\frac{\omega_{i0}\Gamma^3}{(\omega_{i0}^2 + \Gamma^2)(\omega_{j0}^2 + \Gamma^2)};$$

η is the excess of the gain over losses,

$$\eta = \frac{4\pi\omega_0 d^2}{\hbar\Gamma\Delta\Omega}\frac{l}{L}N_e;$$

and l is the length of the active medium.

To derive equations (15), we have introduced dimensionless functions

$$I_i(t) = \frac{d^2 E_i^2(t)}{4\hbar^2\gamma\Gamma}$$

and

$$n_{ij} = \gamma\int_0^t e^{-\gamma\tau}\sqrt{I_i(t-\tau)I_j(t-\tau)}d\tau$$

and dimensionless time $t' = \sigma t$.
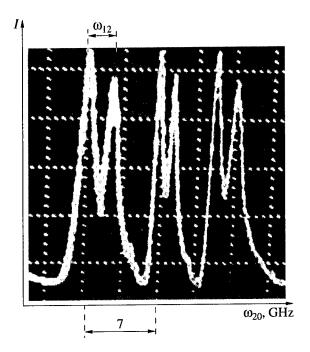
Fig. 5. Oscilloscope trace of the spectrum of modes for the double-mode Nd³⁺ : YAG laser with ω_{12} = 3 GHz.

Fig. 6. The signal of intermode beats $E_1 E_2$ for ω_{12} = 0.5 GHz.

The set of equations (15) with time-dependent ω_{i0} describes the scanning of the modes along the contour of the gain line. For a homogeneously broadened transition line, the set of equations under study can be considerably simplified in the limiting case of adiabatically slow scanning:

$$\frac{dI_i}{dt} = I_i(\alpha_i - \beta_i n_{ii} - \theta_{ij} n_{ij}), \qquad (16)$$

$$\frac{dn_{ij}}{dt} = -\gamma n_{ij} - \gamma \sqrt{I_i I_j}. \qquad (17)$$

The set of equations (16) and (17) was solved numerically. The results of these simulations are presented in the following section.

4. THE RESULTS OF STUDYING MODE COMPETITION IN A DOUBLE-MODE Nd³⁺ : YAG LASER

The measurement of the field distribution in the plane transverse with respect to the optical axis of the cavity demonstrated that radiation is concentrated in a single beam with nearly Gaussian distribution. This finding indicates that, first, the birefringent wedge does not divide the fields in the laser modes in the transverse direction, and, second, higher order transverse modes are reliably suppressed.

Figure 5 displays the spectrum of laser modes measured with the use of a Fabry–Perot interferometer ($c/2L$ ≈ 7 GHz). This spectrum features three recurring mode structures with a frequency separation ω_{20} ≈ 7 GHz.

Each of these structures has two components. Experimental studies have demonstrated that these components have mutually orthogonal polarizations, and the frequency separation between these components is equal to the intermode separation ω_{12} (the frequency separation between the components measured in units of $c/2L$ was compared with the frequency of intermode beats measured with the use of a spectrum analyzer for sufficiently small intermode separations).

Figure 6 presents the oscilloscope trace of the signal of intermode beats, i.e., the frequency dependence of the beat intensity $E_1 E_2$ ($E_{1,2}$ are the field strengths in the generated laser modes). The oscilloscope trace shown in Fig. 6 corresponds to ω_{12} = 0.5 GHz. The ratio of the signal of intermode beats to noise is higher than 30 dB, and the width of the beat marker at half maximum is about 10 kHz. The investigation of the spectrum of the intermode-beat signal has demonstrated that parameters of this signal remain unchanged within the entire range where ω_{12} was measured. Spectral investigations of the intermode-beat signal also indicate that higher order transverse modes are reliably suppressed.

Figure 7 displays a typical dependence of the mode intensities $E_{1,2}^2$ on the detuning $\omega_{20} = \omega_2 - \omega_0$ of the mode frequency ω_2 from the center of the gain line (the frequency ω_0). Depending on the frequencies of the modes, we were able to generate either two modes (E_1^2 and E_2^2) with the intermode separation ω_{12} (the AB section) or two modes (E_2^2 and E_3^2) with the intermode
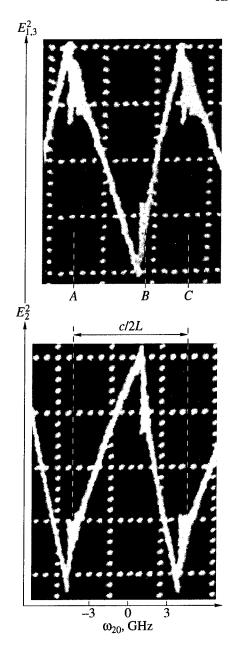
Fig. 7. Experimental dependences of the intensities of the modes $E^2_{1,2,3}$ on the detuning ω_{20} for $\omega_{12} \approx 3$ GHz.
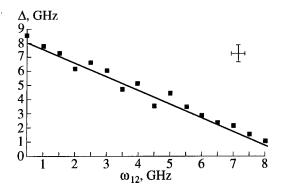

Fig. 8. Experimental dependence of the width Δ of the range of double-mode lasing on the intermode separation ω_{12} for $\eta \approx 1.0001$.
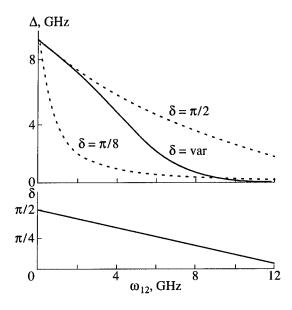

Fig. 9. Calculated dependence $\Delta(\omega_{12})$ for $\eta \approx 1.08$.

interval $\omega_{23} = c/2L - \omega_{12}$ (the BC section). In this figure, $\omega_{12} = 3$ GHz and $\omega_{23} \approx 6$ GHz. The order in which lasing is switched from one pair of modes to another was determined by the proximity of the corresponding pair of modes to the symmetric arrangement and their closeness to the center of the gain line. To clarify this point, we additionally introduce the average frequency $\omega' = (\omega_1 + \omega_2)/2$ for the modes with frequencies ω_1 and ω_2 and the average frequency $\omega'' = (\omega_2 + \omega_3)/2$ for the modes with frequencies ω_2 and ω_3. Then, the quantities $|\omega' - \omega_0|$ and $|\omega'' - \omega_0|$ determine the proximity of the modes to the symmetric arrangement and their close-

ness to the center of the gain line. Specifically, if $|\omega' - \omega_0| \ll |\omega'' - \omega_0|$, then the modes with frequencies ω_1 and ω_2 are involved in lasing, whereas, for $|\omega' - \omega_0| \gg |\omega'' - \omega_0|$, lasing occurs in modes with frequencies ω_2 and ω_3.

The switching of lasing from one pair of modes to another has an oscillatory character (point B in Fig. 7). Similarly to thoroughly studied analogous regimes in double-mode CO_2 lasers [6], oscillations revealed in mode scanning are associated with inertial properties of the active medium, i.e., with a time lag between the change in the population of the working levels and variations in the strength of the electromagnetic field in the cavity.

Double-mode lasing was implemented within the range of intermode separations 5 MHz $\leq \omega_{12} \leq 8.8$ GHz. The lower bound of this range is related to the residual anisotropy of the active medium, whereas the upper

bound is determined by the frequency separation between the modes that do not experience splitting. Figure 8 displays the width Δ of the range of double-mode lasing, i.e., the frequency region where lasing simultaneously occurs in both modes, as a function of ω_{12}. We should note that, for small values of the inter-mode separation, the width Δ of the range where double-mode lasing occurs may be rather large and even comparable with the separation $c/2L$ between the modes that do not undergo splitting. Such large values of Δ indicate the weakness of intermode coupling for axial modes with mutually orthogonal polarizations in an Nd³⁺ : YAG laser for small intermode separations. Note that the widths of the range of double-mode lasing achieved in the Nd³⁺ : YAG laser are at least an order of magnitude greater than the values of Δ for double-mode lasers developed earlier.

Figure 9 displays the calculated dependence $\Delta(\omega_{12})$. To clarify the results presented in this figure, we should note that the displacement of the phase-anisotropic wedge in experiments changed both the intermode separation and the longitudinal spatial shift δ between the nodes and the loops of standing electromagnetic waves. Therefore, we took into account in calculations that δ changes with a variation of ω_{12} (the solid line). The dashed lines represent the dependences $\Delta(\omega_{12})$ calculated for fixed values of the longitudinal shift δ. As can be seen from these results, δ plays a significant role in the formation of the dependence $\Delta(\omega_{12})$, and the effective values of δ fall within the range $\pi/8 \le \delta \le \pi/2$. Note that the dependence $\Delta(\omega_{12})$ calculated for various δ agrees well with the relevant experimental dependence, which confirms that the employed theoretical approach is correct.

To elucidate the character of competition between axial modes with mutually orthogonal polarizations in an Nd³⁺ : YAG laser, we calculated the degree of intermode coupling S for the modes symmetrically arranged within the gain line contour,

$$S = \frac{\beta_0 - \theta_0}{\beta_0 + \theta_0}, \qquad (18)$$

as a function of the intermode separation ω_{12} (β_0 and θ_0 are the Lamb coefficients for the modes symmetrically arranged within the gain line contour; $S = 0$ for strongly coupled modes, and $S = 1$ when mode coupling is absent). The results of these calculations are presented in Fig. 10. In calculating the dependence $S(\omega_{12})$, we took into account the variation in the longitudinal shift δ. As can be seen from the presented results, the intermode coupling is rather weak for small ω_{12}, which confirms our conclusions based on the experimental data. However, the intermode coupling becomes stronger with the growth of the intermode separation due to the increase in δ with the growth of ω_{12}.

Figure 11 presents the measured dependence of Δ on the excess η of the gain above losses. As can be seen
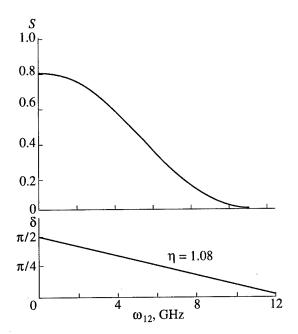
Fig. 10. The degree of intermode coupling S calculated for orthogonally polarized modes of the Nd³⁺ : YAG laser as a function of the intermode separation ω_{12}.
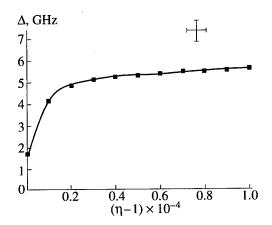
Fig. 11. Experimental dependence of the width Δ of the range of double-mode lasing on the excess η of the gain over losses.

from this plot, for $\eta - 1 \le 5 \times 10^{-4}$, the dependence $\Delta(\eta)$ steeply increases, whereas, for large η, the growth of this dependence slows down. At the same time, the active part of the gain line contour Δv, as can be seen from formula (1), increases with the growth in η as $\Delta v(\eta) = \Gamma\sqrt{\eta - 1}$, where Γ is the homogeneous width of the gain line. Comparison of the experimental dependences $\Delta(\eta)$ and $\Delta v(\eta)$ demonstrated that, within the accuracy of measurement errors, these dependences coincide with each other. Such a situation can be implemented only in the case when the coupling between the axial modes with mutually orthogonal polarizations in an Nd³⁺ : YAG laser is sufficiently weak. For a cavity

with a constant length, the possibility of increasing Δ is mainly associated with the increase in the active part of the gain line contour.

It is of interest to investigate the dependence $\Delta(\eta)$ for large η. Figure 12 shows the dependence $\Delta(\eta)$ calculated for $\omega_{12} = 4$ GHz and $\delta = \pi/4$. The dashed line displays the linear dependence. As can be seen from the presented data, for small η, the dependence under study can be considered as linear, which implies that the influence of the longitudinal spatial shift becomes significant only for sufficiently large η.
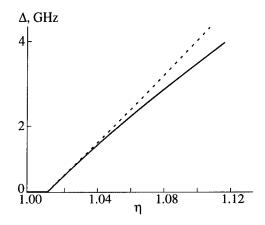
Fig. 12. Calculated dependence $\Delta(\eta)$ for $\omega_{12} \approx 4$ GHz and $\delta = \pi/4$.
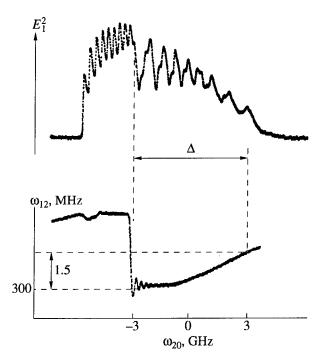
Fig. 13. Experimental dependence of the intermode-beat frequency ω_{12} on the arrangement of laser modes within the contour of the gain line, ω_{20}.

An important specific feature of a double-mode laser is that such a laser makes it possible to transfer an information signal through both mode intensities and the intermode-beat frequency. Therefore, it is of interest to investigate the dependence of the intermode-beat frequency on the arrangement of the modes scanned within the contour of the gain line. Figure 13 presents the measured dependence of the intermode-beat frequency ω_{12} on the arrangement of the modes position within the contour of the gain line, ω_{20}. As can be seen from this dependence, the deviation of the intermode-beat frequency, which is defined as $D = \omega_{12}^{max} - \omega_{12}^{min}$, does not exceed 1.5 MHz if the modes remain within the range Δ. To account for such a small (as compared with ω_{12}) value of D, we will consider the calculated dependence of the additive to the intermode-beat frequency, $\delta\omega_{12} = \omega_{12} - \Omega_{12}$, on the arrangement of the modes scanned within the contour of the gain line, Ω_{20}, in units of the cavity band $\Delta\Omega$ (Fig. 14), where $\Omega_{20} = \Omega_2 - \Omega_0$, Ω_2 is the frequency of the second cavity mode within the contour of the gain line, and $\Omega_0 = \omega_0$ is the frequency that corresponds to the center of the spectral line. As is clear from the presented results, the intermode-beat frequency is virtually independent of Ω_{20}. Indeed, it can be seen from the plot that the coefficients $\sigma_1 - \sigma_2$ that characterize the pulling of the modes toward the center of the gain line are compensated for by the coefficients of mode repulsion from the center due to the field of the considered mode, $\rho_1 E_1^2 - \rho_2 E_2^2$, and the field of the other mode, $\tau_{12} E_2^2 - \tau_{21} E_1^2$. Thus, the effects of pulling toward the center of the gain line and repulsion from the center cancel each other out, which explains the
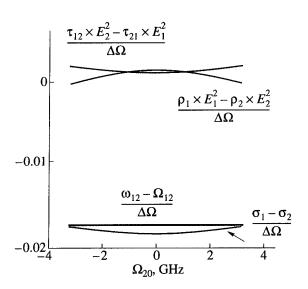
Fig. 14. Calculated dependence of the additive to the intermode-beat frequency, $\delta\omega_{12} = \omega_{12} - \Omega_{12}$, on the arrangement of the modes within the contour of the gain line, Ω_{20}, in units of the cavity band $\Delta\Omega$ for $\Omega_{12} = 300$ MHz.

small deviation of the intermode-beat frequency observed in experiments.

Note that the small deviation of the intermode-beat frequency provides an opportunity to transfer an information signal contained in this frequency virtually without nonlinear distortions, which is extremely important for numerous technological applications of double-mode Nd^{3+} : YAG lasers, such as laser communication and ranging.

In conclusion, let us consider the possibility of expanding the range of intermode separations $\Delta(\omega_{12})$. As mentioned above, the lower bound of the $\Delta\omega_{12}$ range is determined by the residual phase anisotropy of the active element. One can lower this quantity only with a careful choice of the active element. The upper bound of the $\Delta\omega_{12}$ range is determined by the cavity length and can be considerably increased if we decrease the sizes of the active element and arrange intracavity elements in a more compact manner.

5. CONCLUSION

In conclusion, we will summarize the main results of this work.

(1) A double-mode Nd^{3+} : YAG laser with a phase-anisotropic cavity has been developed and implemented.

(2) The basic relations for a double-mode solid-state laser with orthogonally polarized modes and an inertial active medium have been derived.

(3) The competition of axial modes with mutually orthogonal polarizations in an Nd^{3+} : YAG laser has been studied experimentally and theoretically.

6. ACKNOWLEDGMENTS

REFERENCES

1. Evtuhov, V. and Siegman, A.E., 1964, *Appl. Opt.*, **4**, 142.

2. Lamb, W.E., 1964, *Phys. Rev. A*, **149**, 1468.

3. Yermachenko, V.M., Petrovskiy, V.N., Protsenko, E.D., *et al.*, 1985, *Kvantovaya Elektron.*, **12**, 571.

4. Owioung, A. and Esherick, P., 1987, *Opt. Lett.*, **12**, 999.

5. Nanii, O.E. and Paleev, M.R., 1993, *Kvantovaya Elektron.*, **20**, 761.

6. Bakaev, D.S., Yermachenko, V.M., Kurochkin, V.Yu., *et al.*, 1988, *Kvantovaya Elektron.*, **15**, 37.

Characteristics of a Diode-Pumped Q-Switched Nd : YAG Laser, with Continuously Variable Output Pulsewidth 20–100 ns

E. Georgiou and V. Ladopoulos

Institute of Electronic Structure and Laser, Foundation for Research and Technology–Hellas (FO.R.T.H.), P.O. Box 1527, Heraklio, Crete, GR-71110 Greece
e-mail: geostrat@iesl.forth.gr
Received September 05, 1997

Abstract—The characteristics of a variable-pulsewidth Q-switched diode-pumped Nd : YAG laser developed at FORTH are reported. The laser is electro-optically Q-switched, and emits polarized output ($\lambda = 1.06$ μm) with almost Gaussian transverse beam profile. The output pulsewidth of the laser can be continuously varied in the 20–100 ns regime, with pulse energy in the 1.5–3.5 mJ range. By frequency doubling with KTP, variable output pulsewidths in the same ns regime were also obtained at $\lambda = 532$ nm.

1. INTRODUCTION

In the last decade, diode pumping has become a mainstream technique for solid-state laser optical excitation, due to a combination of favorable parameters, including high efficiency, reliability, output stability, compactness, long operational lifetime, easy maintenance, low-voltage power supply, etc. [1]. There already exists a large variety of diode-pumped systems developed, differing in pumping geometry (transversely-pumped vs. collinearly-pumped), pump pulse duration (cw-pumped vs. quasi-cw pumped), output pulsewidth (continuous wave, Q-switched, mode-locked), beam mode structure (single-mode vs. multi-mode), method of pulse modulation (passive vs. active Q-switching or modelocking), and geometry of the laser-active crystal (rod vs. slab). Despite their obvious advantages, the higher cost of diode-pumped lasers better justifies their use in critical applications, where conventional flashlamp-pumped systems may be less suitable.

In this paper we report on a Q-switched Nd : YAG laser transversely pumped by laser diode arrays, with output pulsewidth adjustable in the 20–100 ns range. This system exploits diode pumping for reduced thermal lensing of the laser-active material, and a laser cavity design with mode characteristics relatively insensitive to resonator length variations. Apart from adjustable pulse duration, this laser offers all the advantages of the diode-pumped technology plus a combination of interesting features, including multimillijoule output (with true TEM$_{00}$ option), better than 1% pulse-to-pulse energy stability, active Q-switching, simple and efficient design, direct pump coupling, small size, and low cost.

2. BASIC DIODE-PUMPED LASER SETUP

A schematic arrangement of our diode-pumped Q-switched laser setup is shown in Fig. 1. The laser res-

onator consists of one dielectric flat output coupler (O.C.) and a concave dielectric high reflector (H.R.) with long radius of curvature $r = 20$ m. This particular choice of cavity mirror curvatures was based on considerations presented in Section 4. The laser crystal was a 2-mm dia. × 20-mm long plane/parallel-cut Nd : Ya$_3$Al$_5$O$_{12}$ rod (1.1 at. % nominal doping level) with finely ground cylindrical surface and polished A/R coated end faces. The rod was mounted in a matched gold-plated copper "pump chamber", having a cylindrical trough of equal diameter (2 mm), with a slotted side opening to accept pump radiation. This chamber served both as a conductive cooling block for the laser rod, and as a diffuse back-reflector for the unabsorbed pump radiation. The rod and reflector dimensions and surface finish were selected in order to homogenize as much as possible the pump radiation distribution over the whole
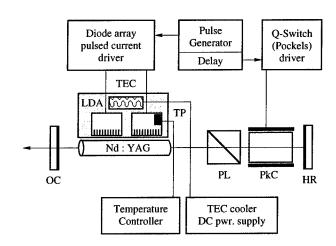

Fig. 1. Schematic block diagram of basic diode-pumped Q-switched laser system, including optical and electronic parts: Nd : YAG = laser crystal rod, LDA = laser diode array, PkC = Pockels cell, PL = Polarizer, TEC = thermoelectric cooler/heater, TP = temperature probe, OC = output coupler mirror, HR = highly reflective mirror.

rod volume, instead of relying on pump light concentration in certain crystal areas, as is customary with the majority of other diode-pumped laser designs (including slab lasers). This approach is justified by the design goals for single transverse mode operation and insensitivity of laser gain to changes in the resonator length, as it will be further discussed later.

The laser rod is transversely pumped by two single-bar quasi-continuous-wave (QCW) diode laser arrays, optically parallel, connected electrically in series, each delivering approximately 55 W of optical pump power at λ = 807-nm in long-pulse (200 μs) operating mode. The combination of pump length and maximum duty factor specifications limits the repetition rate of our laser to 100 Hz max. A pulsed current-source driver developed at FORTH served as the semiconductor-laser electrical power supply, delivering square 70-A × 200 μs current pulses to the pump diode arrays. The pump laser diodes were conductively heat-sunk to a temperature-stabilized (±0.1 K) aluminum mounting block. Laser-diode wavelength tuning in a limited range (±4 nm) was possible by cooling (or heating) the mounting block with a solid-state thermoelectric cooler (TEC), via a PID-type temperature controller.

For efficient and reliable Q-switched operation with high pulse-to-pulse energy stability, low pulse-timing jitter and long operational lifetime [1], an electro-optic LiNbO$_3$ Pockels cell was employed in λ/4 configuration in conjunction with an air-spaced high damage threshold and low loss calcite-prism Glan polarizer, A/R coated for 1.06 μm. The Pockels cell High Voltage driver (Fig. 1) switches off the $V_{\lambda/4}$ voltage with a fast fall time (<20 ns), to restore the resonator Q and allow laser giant pulse emission.

3. LASER OUTPUT ENERGY AND BEAM QUALITY

The laser output energy was measured as a function of input optical pump energy incident on the Nd : YAG rod, for several values of output coupler (O.C.) reflectivity ranging from 40% to 95%, in various modes of operation.

In free-running (long-pulse mode) operation, Nd : YAG laser output energy measurements were performed at an L = 12.5 cm resonator length (Fig. 2), which represents the shortest possible cavity with mirrors and rod alone, and is characterized by the lowest diffractive losses. The Fig. 2 plots show that free-running operation yields output pulse energy up to 6.5 mJ for incident optical pump energy of 22.5 mJ, while optical slope efficiency up to n_{opt} = 40.9% can be obtained. A Findlay–Clay analysis [2] run on the Fig. 2 threshold data allows the determination of the internal round-trip resonator losses, including parasitic absorption, scattering and diffraction on the laser rod. Thus, Fig. 3 shows a plot of the threshold optical pump energy versus the

Free-running laser operation, L = 12.5 cm
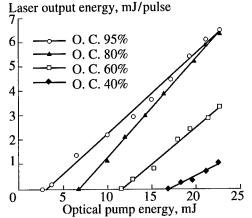
Fig. 2. Laser output pulse energy in free-running (long pulse) operation vs. optical input pump energy, for several output coupler (O.C.) mirror reflectivities. Optical slope efficiencies, determined form the linear data fits, are n_{opt} = 0.33 for $R_{O.C.}$ = 95%, n_{opt} = 0.41 for $R_{O.C.}$ = 80%, n_{opt} = 0.31 for $R_{O.C.}$ = 60%, and n_{opt} = 0.18 for $R_{O.C.}$ = 40%.
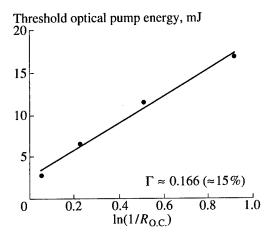
Fig. 3. Findlay–Clay analysis on the Fig. 2 threshold data plotted vs. the negative logarithm of output coupler reflectivity. The derived intracavity roundtrip loss (logarithmic) value is Γ = 0.166, corresponding to a roundtrip fractional photon loss approx. 15%.

natural logarithm of the corresponding inverse output coupler reflectivities. The slope of the linear data fit, along with the extrapolated threshold value for $\ln(1/R_{O.C.})$ = 0, yield a logarithmic internal round-trip loss Γ = 0.166, corresponding to a fractional photon loss value approximately 15%. Within experimental error (±2%) these losses can be attributed mainly to diffraction from the thin Nd : YAG rod employed, based on a calculation of the TEM$_{00}$ gaussian distribution transmission through a 2-mm circular aperture.

In electro-optically Q-switched operation with LiNbO$_3$ Pockels cell, the output pulse energy as a function of input optical pump energy is plotted in Fig. 4

Q-switched laser operation, $L = 27.5$ cm
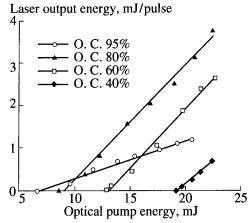
Laser output energy, mJ/pulse

Fig. 4. Laser output energy in multimode Q-switched operation vs. optical input pump energy, for several output coupler (O.C.) mirror reflectivities.

for various values of output coupler reflectivity ranging from $R_{O.C.} = 40\%$ to $R_{O.C.} = 95\%$ at a cavity length $L = 27.5$ cm. Here, output pulse energies up to 3.8 mJ can be obtained for 22.5 mJ incident optical pump energy by using a $R_{O.C.} = 80\%$ output coupler mirror, while an optical slope efficiency $n_{opt} = 27.5\%$ is derived from the corresponding linear data fit. The pulse-to-pulse energy stability is within $\pm 1\%$ when a laser-head cover is employed to provide some atmospheric isolation from dust and air drafts.

In multimode Q-switched laser operation the output beam exhibits a smooth, slightly elliptical, symmetrical profile, without any irregular "hot spots." Visual observation (with the aid of an infrared viewer) of the beam profile, enlarged on a white screen with a diverging lens, revealed that the output consisted mostly of a TEM_{00} mode component, with pulse-to-pulse minor "transverse mode hopping" effects, as some fraction of the output pulse energy was transferred to TEM_{01}. To achieve true TEM_{00} operation, a circular aperture with diameter slightly smaller that the calculated fundamental mode waist was inserted in the cavity near the output coupler mirror. For a cavity length $L = 27.5$ cm, the necessary aperture diameter was < 1.4 mm, while for cavities longer than 50 cm the 2-mm laser rod aperture alone was sufficient to guarantee TEM_{00} operation. Maximum obtained TEM_{00} output pulse energy is 1.6 mJ at $L = 27.5$ cm, while the optical slope efficiency is now limited to 13% due to the increased diffraction losses. To determine quantitatively the relevant beam parameters (spot size, quality factor and divergence angle), we measured the intensity distribution across the beam profile by scanning a 50-μm slit at various distances z from the laser output mirror. Following Siegman's approach [3] we determined a full divergence angle $2\theta = 1.5$ mrad and an excellent beam quality factor $M^2 = 1.1 \pm 0.1$ which demonstrates true TEM_{00} operation.

4. Q-SWITCHED VARIABLE PULSE WIDTH LASER

An analytical expression for the pulse duration τ_p of a fast-Q-switched laser (with fixed Q risetime) has been given by Degnan [4]:

$$\tau_p = \frac{2L}{\Gamma c} \frac{\ln z}{z - \left(\frac{z-1}{\ln z}\right)\left[1 + \ln\left(\frac{z \ln z}{z-1}\right)\right]}, \quad (1)$$

where L is the resonator optical length,[2] $\Gamma = \Gamma_{int} + \ln(1/R_{O.C.})$ is the roundtrip logarithmic total resonator loss consisting of an internal loss term Γ_{int} (absorption, diffraction, scattering) and an output coupling loss term $\ln(1/R_{O.C.})$, c is the speed of light, while the dimensionless parameter z is defined as

$$z = 2g_0 l/\Gamma, \quad (2)$$

where l is the active medium (rod) length, and g_0 the laser small-signal gain.

Thus, the output pulse duration of a Q-switched laser can be varied by changing any of the following parameters: output coupler reflectivity, laser small-signal gain (or, equivalently, pump energy), resonator internal losses, or, resonator length. However, these methods should not be considered equally efficient in practice, either in terms of convenience, or in the sense of affecting simultaneously other pulse parameters, apart from pulse duration. More specifically, changes in the output coupling values are usually "discontinuous" in practice, thus yielding only discrete values of pulsewidth, while they also affect severely the output pulse energy (compare Fig. 4 data). Pulse energy is also severely affected by changes of the laser gain g_0 or internal resonator loss Γ_{int}, while either of these methods may also affect the pulse shape (risetime/falltime ratio) [5]. Changes in the resonator length L may affect its stability; the same holds true for changes in the pump energy, which may cause strong thermal lensing effects [1]. Finally, all the above-mentioned methods can in principle affect the transverse mode structure of the laser beam [1], which may be undesirable for certain applications. Therefore, the design of a variable-pulsewidth laser system should take into account and eliminate such undesirable "side effects" on other pulse parameters, as much as possible.

Expression (1) can be simply rewritten as

$$\tau_p = kL, \quad (3)$$

where the constant of proportionality k is a rather complicated function of the small-signal gain g_0 and loss Γ through the parameter z. Thus, it is seen that the simplest method of varying the Q-switched laser pulse duration is by changing the resonator length L, which should yield a linearly proportional variation in the output pulsewidth, if the gain and loss that determine k in

[2] For all practical purposes, in the following we will consider L approximately equal to the physical resonator length L'.

(3) are held constant. For this scheme to work, the main concern is resonator stability throughout the whole range of cavity lengths L_{min} to L_{max}. Simultaneously, to achieve insensitivity of output pulse energy to these cavity length changes, the resonator should be designed so that the mode diameter inside the laser rod (which effectively determines the laser gain and the rod diffractive losses) does not depend heavily on L. Additionally, if insensitivity of beam quality to cavity length is also desired, the laser should be made to operate always at the fundamental transverse mode TEM_{00}.

This is exactly the approach we used for the practical realization of the diode-pumped variable pulsewidth laser system reported here: we employed a resonator where the output coupler mirror can be moved back and forth to vary the cavity length L, while the other optical parts stay fixed (Fig. 5). For this purpose the O.C. mirror mount was mounted on a sliding stage which could be re-positioned along a standard quality optical rail (by OWIS) and locked in place. In practice the precision of this commercial rail (mounted on an optical breadboard table) proved sufficient to maintain lasing action at all cavity lengths, while only a minimal O.C. mirror-mount readjustment was needed to peak-up the laser output power, following any resonator length change. In our prototype system, to reduce variation of other pulse parameters and simultaneously maintain resonator stability over a wide ratio L_{max}/L_{min} of cavity lengths, we employed a plano-concave resonator with H.R. radius of curvature $r = 20$ m much longer than the maximum resonator length ($r \gg L_{max}$). Furthermore, to encourage TEM_{00} operation with good efficiency, a thin 2-mm laser rod was used, matched to the calculated fundamental transverse mode diameter. For such resonator and rod combination Fig. 6a shows how the TEM_{00} mode cross sectional area (thick line) and the diffractive losses (thin line) vary, as the resonator length is increased from 0 to 20 m. As is evident, apart from the last region ($L > 16$ m) where the mode area starts diverging, there is a large range of resonator lengths where the mode cross section varies very slowly. However, the diffractive losses are prohibitively high for the most part of this L range, except for small L. Therefore, in practice it is possible to work within a shorter range, e.g., 0.2 m $< L < 1$ m, where both the mode diameter (Fig. 6b, thick line) varies slowly and the diffractive losses (thin line) stay within manageable levels.

Apart from resonator design considerations, it should be stressed that the diode-pumping technique is advantageous for the operation of such a variable-pulsewidth laser system. The excellent pump spectral matching and high efficiency characteristics of diode pumping result in reduced thermal lensing "perturbations" of the cavity [1], and help to maintain resonator stability for all cavity lengths L. Furthermore, diode pumping is characterized by low pump-pulse energy fluctuation (pump jitter), which in turn translates to low
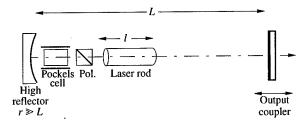
Fig. 5. Q-switched laser variable pulsewidth scheme, by changing the resonator length L.
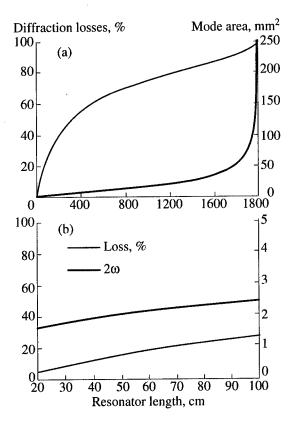
Fig. 6. (a) Fundamental transverse mode cross section with $r = 20$-m concave H.R. (thick line), and cavity diffractive losses for 2-mm diameter laser rod (thin line), in the 0–20 m range of resonator lengths L. (b) Fundamental transverse mode diameter (thick line), and diffractive losses (thin line), "zoomed" in the 0.2–1 m range. Mode diameter 2ω, mm.

pulse-to-pulse gain variation, and therefore in very low pulsewidth fluctuation according to (1).

The experimentally measured Q-switched $\lambda = 1.06$-μm pulse durations (FWHM) vs. the resonator length are presented in the graph of Fig. 7, showing that output pulsewidths in the range 22–90 ns can be obtained in linear relationship to the cavity length from 25 to 85 cm (which was the maximum available resonator length in our setup, and at present is the only limitation for extending the laser pulsewidth range beyond 100 ns, as it will be further discussed below). Two sets of data points and the related linear fits are shown in the Fig. 7 plot: one corresponding to multimode operation
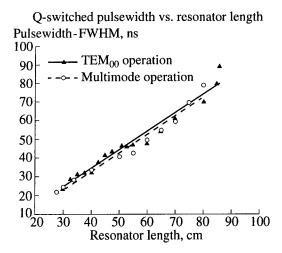
Q-switched pulsewidth vs. resonator length

Pulsewidth-FWHM, ns

Fig. 7. Measured Q-switched diode-pumped laser output pulse duration vs. resonator length L. Slopes of linear data fits are both equal to 0.98 ns/cm.

Pulse energy vs. cavity length
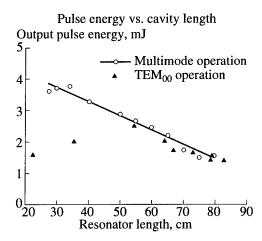
Output pulse energy, mJ

Fig. 8. Measured Q-switched output pulse energies at different resonator lengths L. In the case of single transverse mode operation (triangles), intracavity apertures have been used at $L \le 50$ cm.

(circles) and another corresponding to single transverse mode (triangles). A rather surprising result evident from these Fig. 7 data is the fact that, within experimental error, practically identical pulsewidths were obtained both in TEM_{00} and in multimode laser operation, despite the large differences in gain, loss, mode structure, and output pulse energies. The same equality applies to the corresponding "pulse stretching rates" (slopes of the linear data fits), both equal to 0.98 ns/cm. This effect implies that, by using a thicker Nd : YAG rod, a more efficient variable-pulsewidth laser could be developed in the future, where the output pulse energy will be less dependent on cavity length; such a system may be useful in applications where beam profile is not a critical issue.

Typical output pulse energies obtained in variable-pulsewidth operation of our diode-pumped laser system

are shown in Fig. 8, where two measurement sets of pulse energy vs. resonator length are included, one for multimode (circles) and another for TEM_{00} operation (triangles). In multimode operation the measured output energies range approximately from 1.5 mJ to 3.5 mJ, where the observed decrease of pulse energy vs. L results from the increasing diffractive losses as a function of resonator length due to the thin laser rod employed (Fig. 6), a situation that represents a trade-off . between beam quality and energy efficiency. However, if pure TEM_{00} operation is selected with intracavity apertures at $L \le 50$ cm as previously mentioned, the variation of output energy with resonator length L is considerably reduced (Fig. 8). Furthermore, to compensate for any energy variations vs. L, the gain of the laser can be correspondingly adjusted by reducing the pump diode drive current at short cavity lengths.

To extend the Q-switched pulsewidth range covered by this diode-pumped laser, a larger ratio of cavity lengths L_{max}/L_{min} could be employed. In our present setup, optical and mechanical component size constraints and optical table space limit the physically possible resonator lengths from approximately 22 to 85 cm. However, following mechanical construction improvements, the pulsewidth range of the present system should be extended well above 100 ns. Another interesting possibility is the generation of variable duration pulses at other wavelengths via frequency upconversion and mixing in non-linear optical crystals. For example, by using an intracavity KTP doubling crystal and a dichroic output coupler with reflectivity $R = 100\%$ at the 1.06 μm fundamental and transmissivity $T > 80\%$ in the visible, pure 532-nm laser pulses with adjustable duration from 35 to 116 ns were obtained in a similar fashion. The longer 532-nm pulse durations obtained with intracavity frequency upconversion (compared to the 1.06 μm results) are attributed to the additional laser-cavity loss introduced by the doubling crystal. Other possibilities include the use of extracavity doubling to produce shorter green pulse durations, and/or frequency tripling/quadrupling for variable pulsewidth operation in the ultraviolet spectrum (355 and 266 nm). These experiments are currently in progress, and will be reported in a future article.

5. APPLICATIONS

The diode-pumped Q-switched laser with continuously variable pulse duration capability in the ns regime is a useful tool for studies in several research areas in nonlinear optics and laser-matter interactions, as it provides the possibility of performing experiments in a wide pulsewidth range, in a continuous fashion, with multimillijoule pulse energies, using a single laser system. Typically, such experiments to date required the use of several different lasers having dissimilar optical characteristics [1], or modification of the laser pump input to obtain different output pulsewidths [4], however, these schemes may also affect pulse energy,

beam mode structure, etc. To our knowledge, no comparable previous system has covered the 20–100 ns range, important for the study of a variety of optical phenomena in the ns time scale.

In *nonlinear optics*, thanks to the separate adjustment of pulse energy and duration, this laser system is ideal for distinguishing fluence-dependent (i.e., population-dependent) optical effects in the ns regime from intensity-dependent ones. As an example, the present system has been used in our lab for studying the nonlinear optical behavior of fullerene (C_{60}) solutions; in this case the variable pulsewidth capability in the green (532 nm) was applied to probe the intensity-dependent absorbance and index of refraction of C_{60} by the "z-scan" technique [6].

In *laser–matter interaction* studies, the system described here should prove useful for investigating ns laser-pulse duration effects on the ablation efficiency, plume formation, heat diffusion, etc., as well as for testing various ablation and laser-plasma model mechanisms thought to evolve in the ns time scale [7]. In laser processing of materials there exist already potential applications in studies and optimization of pulsewidth effects in surface micromodulation of magnetic recording media [8]. Finally, this system is well suited for optical damage-threshold measurements, since energy or pulse duration (i.e., peak power) can be independently varied to obtain simultaneously the desired optical intensity/fluence combinations in a wide pulsewidth range. For the latter application, the constant pulse

shape and the true Gaussian beam profile are also significant advantages.

6. CONCLUSION

A diode-pumped electro-optically Q-switched laser with output pulse energies in the 1.5–3.5 mJ regime and pulse duration in the range 20–100 ns, continuously variable by a factor $\tau_{max}/\tau_{min} \approx 5$, has been demonstrated and characterized. This system provides almost independent adjustments of pulse duration and energy, and has the capability of variable ns-pulsewidth operation in the infrared, visible, or ultraviolet spectrum.

REFERENCES

1. Koechner, W., 1996, *Solid-State Laser Engineering* 4th ed. (Berlin: Springer).
2. Findlay, D. and Clay, R.A., 1966, *Phys. Lett.*, **20**, 277.
3. Siegman, A.E., 1993, in *Solid-State Lasers: New Developments and Applications*, Inguscio, M. and Wallenstein, R., Eds. (New York: Plenum).
4. Degnan, J.J., 1989, *IEEE J. Quantum Electron.*, **25**, 214.
5. Wagner, W.G. and Lengyel, B.A., 1963, *J. Appl. Phys.*, **34**, 2040.
6. Koudoumas, E., Couris, S., and Georgiou, E., to be published.
7. Walters, C.T., Barnes, R.H., and Beverly, R.E. III, 1978, *J. Appl. Phys.*, **49**, 2937.
8. Baumgart, P. *et al.*, 1995, *IEEE Trans. Magn.*, **31**, 2946.

Solid-State Laser with a Saturable Absorber Models for the Tunable Passive Loss Modulation and Mode-Locking Regimes

L. A. Kotomtseva

B. I. Stepanov Institute of Physics, National Academy of Sciences of Belarus, pr. F. Skaryna 70, Minsk, 220072 Belarus
e-mail: kotomts@dragon.bas-net.by
Received August 3, 1997

Abstract—Theoretical models for consideration of the solid-state chip lasers with a saturable absorber for the passive loss modulation and for the passive mode-locking behavior are proposed. Steady states for the set of longitudinal modes and areas of parameters for their existence are given. Models for the computer simulations of the single-mode passive loss modulation and for the passive mode locking taking into account the detunings between resonant frequencies of the active medium and absorber are discussed.

1. INTRODUCTION

New active media for the solid-state lasers open wide prospects for stable precisely tunable sources of coherent light. Saturable absorbers are placed inside the cavity for Q-switching and passive mode locking to get intensive short single pulses of nanosecond durations or permanent pulsations of radiation of microsecond, nanosecond, or picosecond scale in time. Some models of theoretical consideration of a laser with a saturable absorber (LSA) with the detunings of the resonant frequencies of the transition in an active medium w_a, absorber w_b, and the cavity w_c taking into account various spectral widths of the gain g_a and absorption g_b lines are proposed.

2. BASIC SYSTEMS OF EQUATIONS

The basic equations are written for the complex amplitudes of field e_i, polarizations p_i, and inversions of populations k_i of an active medium ($i = a$) and absorber ($i = b$) for the running wave in a ring laser with a saturable absorber [1, 2]:

$$\frac{\partial e_i}{\partial t} + \frac{\partial e_i}{\partial x} = -ia p_i - b_i e_i,$$

$$\frac{\partial p_i}{\partial t} + g_i p_i = ig_i k_i e_i - i\delta_i p_i, \qquad (1)$$

$$\frac{\partial k_i}{\partial t} = d_i(q_i - k_i + i(e_i^* p_i - p_i^* e_i)/2).$$

Here b_i are the distributed losses, a is the constant for the interaction of field with substance, q_i is the nonsaturated gain ($q_a > 0$) or absorption ($q_b < 0$), and the values $k_{a,b}$ are normalized to the loss of laser. Decay rates of populations d_i and of polarization g_i are written in units of the decay rate of the populations in the active medium. Time t is normalized to the time of the decay of populations in the active medium, and space coordinate x is normalized to the distance which light passes during the time of the decay of populations in an active medium. Amplitudes of field $e_{a,b}$ are normalized to the amplitude of saturation of the corresponding medium $e_{i\,sat}$. Ratio of the intensities of saturations $s = |e_{asat}|^2/|e_{bsat}|^2 = |\mu_b|^2 d_a g_a/(d_b g_b|\mu_a|^2)$, where $|\mu_i|^2$ are the squares of moduli of the matrix elements of the dipole moments of the transition. Detunings of the frequency of light w from the resonant frequencies of the active medium w_a, absorber w_b, and cavity w_c are taken into consideration through the values $\delta_{a,b} = w - w_{a,b}$ and $\delta_c = w - w_c$. Frequencies and rates of relaxation are written in units of rate of relaxation of populations of an active medium and value $d_a = 1$.

The boundary conditions taking into account the lengths of an active medium l_a, of absorber l_b, and optical length of the cavity L for the light passage through media from the active medium to the absorber look in the following way:

$$e_a(0, t)$$
$$= Re_b(x_c, t - t_1)\exp[-i\delta_c L - i \times 2\pi n]/\sqrt{s}, \qquad (2)$$
$$e_b(x_b, t) = \sqrt{s}e_a(l_a, t - t_2).$$

Amplitude $e_a(0, t)$ of the field is written at the entrance into the active medium at $x = 0$ at moment t after reflection on mirrors with amplitude reflectivity R and after exit out of an absorber at $x = x_c$ at moment $t - t_1$ with addition into phase its change due to detuning $-\delta_c L$ at point $x = L$ (which coincides with $x = 0$) and $-i \times 2\pi n$ with n being an integer number, for the resonant frequency of the cavity w_c. The second equality expresses the field coming into the absorber at $x = x_b$ (it is evident that $x_c - x_b = l_b$) at the moment t through the field, which exits out of an active medium $x = l_a$ at the moment of time $t - t_2$. It is supposed that mirrors do not change the phase of light. For our notations the length of the cavity L is equal to the round-trip time T.

For the microchip solid-state laser the decay rate of polarization g_a is some orders higher than the decay rate of populations d_a and approximation of the polarization following the field is valid and we can introduce

$$p_a = ik_a(1 - i\Delta_a)/(1 + \Delta_a^2) \qquad (3)$$

for polarization p_a into equations for the amplitude of the field and for the inversion of populations of active medium. For the case when a saturable absorber has more narrow spectral line than the active medium, $g_b < g_a$, and the rate of relaxation of polarization for it remains important, we obtain such a system of equations:

$$\frac{\partial e_a}{\partial t} + \frac{\partial e_a}{\partial x} = ak_a e_a/(1 + \Delta_a^2) - b_a e_a,$$

$$\frac{\partial k_a}{\partial t} = d_a(q_a - k_a - k_a e_a e_a^*/(1 + \Delta_a^2)).$$

$$\frac{\partial e_b}{\partial t} + \frac{\partial e_b}{\partial x} = -iap_b - b_b e_b, \qquad (4)$$

$$\frac{\partial p_b}{\partial t} + g_b p_b = ig_b k_b e_b - i\delta_b p_b,$$

$$\frac{\partial k_b}{\partial t} = d_b(q_b - k_b + i(e_b^* p_b - p_b^* e_b)/2).$$

A similar system of equations has been considered for the resonant case conditions for the passive mode locking in a YAG laser with a saturable absorber [1, 3], where the importance of the rate of relaxation of polarization in the active medium for the passive mode locking has been shown with an assumption that expression (3) is valid for a saturable absorber.

For both active and passive medium under assumption (3) the basic system of equations can be written as

$$\frac{\partial e_i}{\partial x} + \frac{\partial e_i}{\partial t} = ak_i e_i/(1 + \Delta_i^2) - b_i e_i,$$

$$\frac{\partial k_i}{\partial t} = d_i[q_i - k_i - k_i e_i e_i^*/(1 + \Delta_i^2)]. \qquad (5)$$

Such systems of equations can be used for description of LSA as distributed systems and can describe passive mode locking due to the presence of some longitudinal modes taking into account the detunings between resonant frequencies of the active medium, absorber, and the cavity, and some results have been given in [4].

For processes much slower than the time of the round trip of light in the cavity, equations for the field can be approximated over this time and systems of ordinary differential equations can be used to consider passive loss modulation in LSA. For the parameters with important role of the decay rates of polarizations in

both media the next system of equations can be used instead of the system (1):

$$\dot{e} = -\alpha e - i\delta_c e - i\alpha p_a - i\alpha_b p_b,$$

$$\dot{p}_i = ig_i k_i e_i - i\delta_i p_i - g_i p_i, \qquad (6)$$

$$\dot{k}_i = d_i[q_i - k_i + i(e_i^* p_i - e_i p_i^*)].$$

Here, $\alpha = al_a/T$, $\alpha_b = al_b/T$, and field e is the same for both media. For the parameters of active medium with relation (3) valid for the active medium the next equation for the field must be used for a single-mode system instead of equations for the field in the system (4):

$$\dot{e} = -\alpha e - i\delta_c e + \alpha g_a k_a e/(g_a + i\delta_a) - i\alpha_b p_b. \qquad (7)$$

And the most usable for the solid-state lasers system of equations for LSA which takes into account the detunings of both media and cavity is the next one:

$$\dot{e} = -\alpha e - i\delta_c e + \alpha g_a k_a e/(g_a + i\delta_a)$$

$$+ \alpha_b k_b g_b e/(g_b + i\delta_b),$$

$$\dot{k}_{ai} = d_a(q_a - k_a - k_a ee^*/(1 + \Delta_a^2)), \qquad (8)$$

$$\dot{k}_{bi} = d_b(q_b - k_b - k_b see^*/(1 + \Delta_b^2)).$$

Here,

$$\Delta a = (w_{st} - w_a)/g_a, \quad \Delta_b = (w_{st} - w_b)/g_b. \qquad (9)$$

This system can be rewritten for the intensity $u = ee^*$ and for the phase of field $f = \arctan(\mathrm{Im}(e)/\mathrm{Re}(e))$ and permits one to determine the shift of the laser frequency.

3. STEADY STATES FOR THE SYSTEMS

Steady state of all these systems with constant in time intensity and definite frequency may be written in the next way for the intensity of light in active medium $u = |e_{ast}|^2$ and frequency $x = w_{st} - w_c$ in the steady states:

$$q_a l_a(1 + \Delta_b^2 + su)(1 + \Delta_a^2)$$

$$+ q_b l_b(1 + \Delta_a^2 + u)(1 + \Delta_b^2)$$

$$= (1 + \Delta_b^2 + su)(1 + \Delta_a^2 + u),$$

$$(x + 2\pi j/L)(1 + \Delta_a^2 + u)(1 + \Delta_b^2 + su)$$

$$+ aq_a l_a \Delta_a(1 + \Delta_b^2 + su]/L$$

$$+ aq_b l_b \Delta_b(1 + \Delta_a^2 + u)/L = 0. \qquad (10)$$

Detailed consideration shows us that the steady state depends on relative detunings between the transition frequencies in the active medium and the absorber and the cavity. These expressions are solutions of the concentrated LSA for the systems (6)–(8) for $j = 0$. The presence of member $2\pi j/L$ with integer number $j = 0$, $\pm 1, \pm 2, \dots$, which appears from the boundary conditions
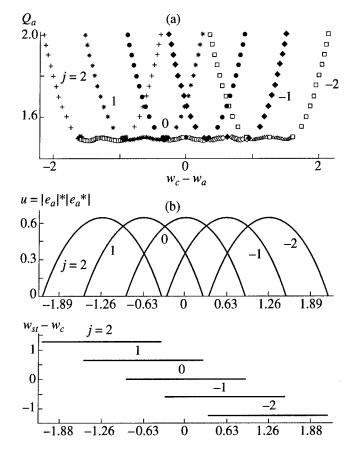
Fig. 1. (a) Boundaries of the areas of the steady states existence for $j = 2, 1, 0, -1, -2$ in the $(w_c - w_a, Q_a = q_a l_a)$ plane for $\alpha = 0.0005$, $q_b l_b = -0.5$, $g = 0.5$, and $L = 0.3$ cm. (b) Steady states intensities u and frequencies $w_{st} - w_c$ for the longitudinal modes with $j = 2, 1, 0, -1, -2$ at $\alpha = 0.05$, $q_a l_a = 2$, $q_b l_b = -0.5$, $g = 0.5$, $s = 2$, and $L = 3$ cm.

in the extended LSA, permits us to consider steady states for the set of longitudinal modes.

A trivial steady state with zero intensity and nonsaturated gain q_a and nonsaturated absorption q_b exists for any parameters of our system.

For the microchip lasers, the next values of parameters can be taken into account. It is known [5, 6] that the typical time of decay of populations is $\tau_s \sim 100–300$ μs and the spectral width of the gain in laser is $\Delta\lambda \sim 0.5–2$ nm for the lengths of wave of light in the area near 1000 till 1320 nm. In accordance with it we take the decay rate of inversion of populations $D_a \sim 8000–20000$ s^{-1} and the spectral width of gain corresponding to $\Gamma_a \sim 10^{11}–10^{13}$ s^{-1}. The length of an active medium is $\sim 100–300$ μm, and the length of the cavity is not less than such values and may be higher. Some kinds of glass doped with neodymium ions and dyes embedded into a solid-state matrix and some crystals can be used as saturable absorber. That is why for absorber we can take D_b of the same order as for the active medium or some orders higher. We take these values for our estimations

and give the limits of existence of the steady states and the intensities and frequencies for the definite modes.

Areas of the existence of the steady state for the longitudinal mode with definite number are given in Fig. 1a for the cavity with mirrors reflectivity $R^2 = 0.99$ and the length of the cavity of 0.3 cm. The steady state with nonzero intensity is inside the boundaries in the plane of detuning $\delta_{ca} = w_c - w_a$ and nonsaturated gain in the active medium $Q_a = q_a l_a$ for longitudinal modes with numbers $j = 0, \pm 1, \pm 2$ for the symmetric case $\delta_{ab} = w_a - w_b = 0$ with equal resonant frequencies of an active medium and absorber. It is seen that practically at any point where steady state exists at least two or three longitudinal neighbor modes can have nonzero intensity. So in the resonant case for $w_c = w_a$, the central mode $j = 0$ exists over the value $Q_a \geq 1.487$. For $Q_a \geq 1.68$, two neighbor modes with $j = 1$ and $j = -1$ can have nonzero intensity at this frequency and coexist with the central mode. At values $Q_a \geq 2.3$, modes with numbers $j = \pm 2$ can exist for the same frequency and we can speak about the coexistence of the steady intensities for five longitudinal modes. The same can be seen for tuning to each longitudinal mode with the other number $j = \pm 1, \pm 2$.

In articles [7–11] three types of the steady states of single-mode LSA have been described and for our system of equations for the case $\delta_c = 0$ in a single-mode laser [12] various steady states and reciprocal action of dispersions of active medium and absorber have been presented. Detailed examples for the intensity and frequency of the steady state as functions of the detuning for the symmetrical case $\delta_{ab} = 0$ are given in Fig. 1b for parameters corresponding to the microchip laser. Intensity in the active medium $u = |e_a|^2$ and frequency of the steady state $w_{st} - w_c$ versus detuning of the cavity $w_c - w_a$ for five longitudinal modes with $j = -2, -1, 0, 1, 2$ are presented for the length of the cavity of 3 cm for nonsaturated gain $Q_a = 2$ and nonsaturated absorption $q_b l_b = -0.5$. It is seen that for the definite frequency intervals of tuning $w_c - w_a$ two or three steady states with nonzero intensity for neighbor modes coexist.

Stability of these steady states can be considered in the typical way for the linearized system for small deviations from the steady states.

4. NUMERICAL SIMULATIONS

Results of numerical experiment for some parameters of the single-mode LSA on the basis of the system (8) are given in Fig. 2. To show the action of detunings we give the results for the intensity in an active medium $u = ee^*$ and for the shift of the frequency of light df/dt ($f = \arctan(\mathrm{Im}(e_a)/\mathrm{Re}(e_a))$). We can see changes in the amplitude and frequency depending on detunings δ_a and δ_b. Computer simulations have been done for the beginning conditions in the vicinity of the trivial steady state for the amplitude of light much less than the amplitude of saturation of active or passive medium and for the beginning gain higher than the nonsaturated
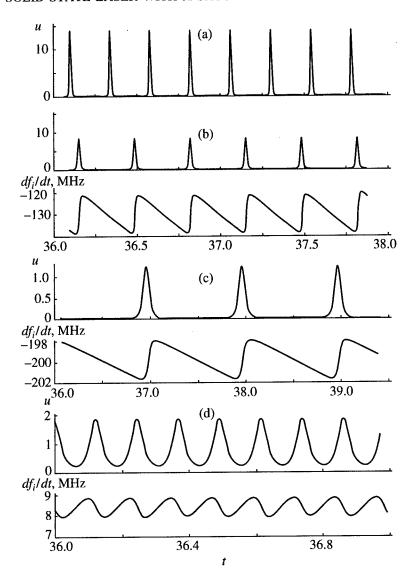
Fig. 2. Changes in time of intensity u and deviations of frequency df/dt of the field (a) for the resonant case $\delta_a = \delta_b = \delta_c = 0$, for equal detunings of the active medium and absorber (b) $\delta_a = \delta_b = 0.5$ and (c),0.8 and (d) for the detuning of an absorber $\delta_b = 0.3$ at $\alpha = 0.05$, $d_a = 1$, $d_b = 2$, $Q_a = 2$, $q_b l_b = -0.3$, $Td_a = 10^{-5}$, and $s = 2$.

loss in LSA. Comparison of results for the resonant case, given in Fig. 2a, with the detuned simultaneously active medium and absorber in Figs. 2b and 2c shows us not only changes in intensities and periods of pulsations but also deviations of the frequency of light in limits of MHz in single-mode pulsations for passive loss modulation behavior. Figure 2d gives us practically sinusoidal pulsations for the detuned absorber with hesitations of the frequency.

Numerical simulations for the distributed LSA give us steady state with constant intensity u for very short cavity at all detunings. For higher lengths of the cavity, various kinds of passive mode locking take place. Behavior of the phase f_a and change of frequency df_a/dt depends on detunings in accordance with the kind of dispersion in the gain medium or absorber and shows

change of the direction of phase deviation (and consequently of the sign of the shift of the frequency of light df_a/dt) on the sign of detunings.

5. CONCLUSION

Theoretical models proposed in this article for consideration of a laser with a saturable absorber permit us to describe a set of single-mode steady solutions for the longitudinal modes and to see their multistabilities as inside one separate mode and between coexisting neighbor modes. Computer simulation of the laser dynamics shows us a detailed explanation of the phase and frequency behavior for various detunings in an active medium or an absorber. Further investigation of both the steady states and their instabilities and nonlinear dynamics of this system for arbitrary detunings is

supposed to be continued. Results of this work can be useful for description of the simultaneous action of the dispersions of an active medium and absorber as in a single-mode so in multimode laser with a set of longitudinal modes.

ACKNOWLEDGMENTS

REFERENCES

1. Samson, A.M., Kotomtseva, L.A., and Loiko, N.A., 1990, *Self-Sustained Oscillations in Lasers* (Minsk: Nauka i Tekhnika) (in Russian).

2. Kotomtseva, L.A., Samson, A.M., and Turovets, S.I., 1996, *High Power Lasers-Science and Engineering*, Kossowsky, R. *et al.*, Eds. (Kluwer Academic), p. 125.

3. Demchuk, M.I., Kotomtseva, L.A., Loiko, N.A., *et al.*, 1985, *J. Appl. Spectrosc.*, **43**, 1328.

4. Kotomtseva, L.A. and Samson, A.M., 1994, *Proc. Int. Conf. Tunable Solid State Lasers*, Voitovich, A.P. *et al.*, Eds. (Minsk: Inst. of Physics), p. 98.

5. Matthews, D.G., Boon, J.R., Conray, R.S., and Sinclair, B.D., 1996, *J. Mod. Opt.*, **43**, 1079.

6. Beier, B., Meyn, J.-P., Knappe, R., *et al.*, 1994, *Appl. Phys. B*, **58**, 381.

7. Dembinski, S.T., Kossakowski, A., Peplowski, *et al.*, 1978, *Phys. Lett. A*, **68**, 20.

8. Mandel, P., 1980, *Phys. Rev. A*, **21**, 2020.

9. Mrugala, F. and Peplowski, P., 1980, *Z. Phys. B*, **38**, 359.

10. Erneux, T. and Mandel, P., 1981, *Z. Phys. B*, **44**, 353; 365; Erneux, T. and Mandel, P., 1984, *Phys. Rev. A*, **30**, 1893; 1902.

11. Chyba, D.E., Abraham, N.B., and Albano, A.M., 1987, *Phys. Rev. A*, **35**, 2936.

12. Kotomtseva, L.A. and Samson, A.M., 1995, *J. Appl. Spectrosc.*, **62**, 99.

Cobalt Disilicide-Induced Crystallization of Amorphous Silicon under XeCl Excimer Laser Irradiation

S. Luby*, E. Majkova*, M. Jergel*, E. D'Anna**, A. Luches**, M. Martino**, P. Mengucci***, G. Majni***, and E. Dobrocka****

* *Institute of Physics, Slovak Academy of Sciences, Bratislava, 84228 Slovak Republic*
e-mail: majkova@savba.sk
** *Department of Physics, Department of Physics, Univ. Lecce, Lecce, 73100 Italy*
*** *Department of Materials and Earth Sciences, Univ. Ancona, Ancona, 60131 Italy*
**** *Faculty of Mathematics and Physics, Comenius Univ., Bratislava, 84215 Slovak Republic*
Received August 8, 1997

Abstract—Amorphous silicon (a-Si), 100 and 200 nm thick, was vacuum-evaporated onto oxidized Si wafers covered by Co layers 0.5, 1, and 3 nm thick. A-Si was crystallized by XeCl excimer laser beam in high-energy regime from 0.26 to 0.50 J cm^{-2}. A-Si films were irradiated by 1, 10, or 100 laser pulses directed to the same site. The samples were analyzed by X-ray diffraction (XRD) and grazing incidence XRD. With 3-nm-thick Co layers, the formation of CoSi$_2$ was determined. This underlayer improved the crystallization of a-Si considerably. The 200-nm-thick film was crystallized in the whole thickness even after the first laser pulse of the energy density corresponding to the complete melting of a-Si. Without CoSi$_2$ the same result was obtained only with higher number of pulses.

1. INTRODUCTION

In the last years there has been an increasing interest in the use of large grain polycrystalline silicon (poly Si) in semiconductor devices and circuits [1, 2]. Often poly-Si films were prepared by solid-phase crystallization or by laser-induced melting and resolidification of amorphous silicon (a-Si). If silicon is chemical-vapor-deposited, especially by plasma-enhanced CVD process, it contains hydrogen (a-Si:H). Here, difficulties arise due to the rapid release of the hydrogen under melting [2, 3].

In solid-phase crystallization, the nucleation starts at the silicon substrate interface as a rule, revealing a strongly heterogeneous process [4]. Liquid-phase laser crystallization is more complex. Homogeneous nucleation in the supercooled bulk competes with interface-induced heterogeneous nucleation. Depending on the energy density of laser beam, i.e., low/high energy density regime, liquid Si/solid Si, liquid Si/solid substrate, or even liquid substrate/solid substrate interfaces should be considered in the crystallization process [5, 6].

Various methods were used to improve the Si crystallinity on amorphous substrates like glass, oxidized Si, or plastic substrates. Some of them are following: (1) Sulphurization of the SiO$_2$ surface of the substrate [7] which might compensate for defects which otherwise preclude the Si atoms to reach the position of thermal equilibrium. (2) Metal induced crystallization of a-Si using metals which form eutectics or silicides with Si. Metals are deposited onto the a-Si surface as a rule. The crystallization is induced by the diffusion of metal into silicon, changing Si–Si bonding, and reducing the activation energy for nucleation [8]. Results with Al and Pd are in [8, 9] and [10], respectively. (3) Local epitaxial

growth of poly-Si layer on ZnS continuous underlayer [11] or furnace crystallization of a-Si:H with NiSi$_2$ overlayer [12]. In both cases the lattice mismatch between nucleous layer and crystalline Si is only 0.4%. (4) Crystallization or recrystallization of silicon using ultrathin island-like and nucleation-enhancing seeding layer like Pd [13] or self-seeding layer of Si [14, 15]. Seeds are created also on the surface of a-Si by local laser crystallization [16].

Some of the above-cited works employed laser melting and resolidification [15, 16]. However, metal ultrathin-islands-like or continuous nucleation-inducing layers were not used in combination with laser processing up to now, as far as we know. In this paper such a study is performed using cobalt layers at the interface between the oxidized silicon substrate and a-Si. Co was applied because of good lattice match of CoSi$_2$ (CaF$_2$ structure) with silicon (1.2%) and a lot of informations on the formation of above-mentioned silicide [17]. Moreover, Co and SiO$_2$ are perfectly stable in contact with each other [17] and CoSi$_2$ and Si X-ray diffraction maxima do not overlap, like for NiSi$_2$ [12].

It is evident that the depth of melting of a-Si under our laser irradiation will be crucial parameter. Therefore, the simulation of the melting process is unavoidable.

2. EXPERIMENTAL PROCEDURES

Co layers d_{Co} = 0.5, 1, and 3 nm thick, were deposited onto oxidized Si(100) substrates with SiO$_2$ thickness d_{ox} = 300 nm. The thinnest Co layer is assumed to be discontinuous, the most thick one to be continuous (cf. [18, 19]). A-Si films of thickness d_{Si} = 100 and

200 nm were deposited onto Co layers. Also, samples without Co were prepared for comparison. Hence, eight various types of structures were studied. Both Co and a-Si were electron-beam evaporated in a vacuum of 2×10^{-7} Pa in order to avoid the problem with hydrogen in silicon.

The relatively low thickness of SiO_2 was chosen according to our previous results [6]: It was shown that a-Si on the thinner oxide crystallizes better because of the larger temperature gradient in the Si melt prior to solidification.

The samples were processed with XeCl laser (Lambda Physik LPX 315i with beam homogenizer) in a vacuum of 10^{-3} Pa. Laser beam energy densities $F = 0.26, 0.31,$ and 0.36 J cm^{-2} and number of laser pulses $N = 10$ and 100 were used for samples with $d_{Si} = 100$ nm, $F = 0.40, 0.45,$ and 0.50 J cm^{-2}, and $N = 1$ and 10 were

used for $d_{Si} = 200$ nm according to our previous results [6]. The laser pulse duration was 30 ns. Hence, 48 various experimental irradiations were performed. The repetition rate of the successive laser pulses directed to the same irradiation spot was ≤50 Hz. Under these conditions the irradiation could be considered as a sequence of thermally independent pulses [20].

The samples were analyzed by X-ray diffraction (XRD) and grazing incidence XRD (GI XRD) using Cu$K\alpha$ radiation. The grazing angles (α) of X-rays were $\alpha = 0.5°, 1°,$ and $5°$. Under these conditions the X-rays are diffracted from the depth ≤1.2 μm for $\alpha = 0.5°$ and $1°$, and from ≈ 6 μm for $\alpha = 5°$, as calculated from decrease of the relative intensity of X-rays to 1/e. Therefore, at lower α crystallized silicon, SiO_2 underlayer and interface with substrate are analyzed, at $\alpha = 5°$, the substrate can influence the spectra considerably.

The temperature time and depth profiles in the samples were calculated using procedures for ns laser irradiations based on a finite-difference scheme [20].

3. CALCULATION OF THE TEMPERATURE EVOLUTION

Since the direct measurements of temperature under pulsed excimer laser irradiation is complicated due to the fast heating and cooling cycles, numerical computations were performed for a-Si on SiO_2 and a-Si/Co$3nm$/SiO_2 structures. Here, Co is assumed to be continuous. Some results are shown in Fig. 1. In Tables 1–3, all results are summarized. Our calculations are valid only for the first laser pulse during which the crystallization starts.

From Tables 1–3, it follows that a-Si layer ($T_m^{Si} = 1485$ K) melts at all irradiations. Co layer ($T_m^{Co} = 1768$ K) melts at $F = 0.31$ and 0.36 J cm^{-2} for $d_{Si} = 100$ nm, and at $F = 0.5$ J cm^{-2} for $d_{Si} = 200$ nm. This can be seen also from

Table 1. Summary of the results of temperature calculations for energy density $F = 0.260$ and 0.400 J cm^{-2}. T_{max}^{Si} is maximum surface temperature (of Si), T_{max}^{Co} is the maximum temperature of Co layer, ΔZ_{mmax} is the maximum depth of melting of the irradiated structures, and Δt_{max}^{Si} is the melting duration of Si film

d_{Co}	d_{Si}	$F = 0.260$ J cm^{-2}			
[nm]	[nm]	T_{max}^{Si} [K]	T_{max}^{Co} [K]	ΔZ_{mmax} [nm]	Δt_{max}^{Si} [ns]
0	100	1540	–	100	94
3	100	1500	1470	100	94
		$F = 0.400$ J cm^{-2}			
0	200	1550	–	200	268
3	200	1520	1425	200	268

Table 2. Summary of the results of temperature calculations for energy density $F = 0.310$ and 0.450 J cm^{-2}. T_{max}^{Si} is maximum surface temperature (of Si), T_{max}^{Co} is the maximum temperature of Co layer, ΔZ_{mmax} is the maximum depth of melting of the irradiated structures and Δt_{max}^{Si} is the melting duration of Si film

d_{Co}	d_{Si}	$F = 0.310$ J cm^{-2}			
[nm]	[nm]	T_{max}^{Si} [K]	T_{max}^{Co} [K]	ΔZ_{mmax} [nm]	Δt_{max}^{Si} [ns]
0	100	1870	–	100	116
3	100	1810	1780	103	113
		$F = 0.450$ J cm^{-2}			
0	200	1800	–	200	296
3	200	1755	1640	200	297

Table 3. Summary of the results of temperature calculations for energy density $F = 0.360$ and 0.500 J cm^{-2}. T_{max}^{Si} is maximum surface temperature (of Si), T_{max}^{Co} is the maximum temperature of Co layer, ΔZ_{mmax} is the maximum depth of melting of the irradiated structures, and Δt_{max}^{Si} is the melting duration of Si film

d_{Co}	d_{Si}	$F = 0.360$ J cm^{-2}			
[nm]	[nm]	T_{max}^{Si} [K]	T_{max}^{Co} [K]	ΔZ_{mmax} [nm]	Δt_{max}^{Si} [ns]
0	100	2270	–	112	140
3	100	2160	2130	110	139
		$F = 0.500$ J cm^{-2}			
0	200	2050	–	200	318
3	200	200	1870	203	318

the depth of melting values. However, for 0.31 J cm^{-2} the time of melting of Co is very short (a few nanoseconds only). The time of melting of Si in structures with $d_{Si} = 200$ nm is 2.3–2.9 times higher than in structures with $d_{Si} = 100$ nm.

The temperature gradient in the molten Si can be calculated for structures with Co layers as ($T_{max}^{Si} - T_{max}^{Co}$)/$d_{Si}$ For $d_{Si} = 100$ nm we obtain 30×10^5 K cm^{-1} and for $d_{Si} = 200$ nm, $\approx 55 \times 10^5$ K cm^{-1}. These values are expected for SiO$_2$ layer with the chosen thickness [6]. The temperature gradient may drive the melt front and thus improve the grain growth conditions.

We are assuming the following to fulfill our experimental aim: (1) the underlying oxide should not be melted to avoid contamination of the crystallized Si by oxygen and the formation of substoichiometric SiO$_x$ ($x < 2$) with good wettability, which speeds up the nucleation of the Si yielding poor crystallinity [21]; (2) the a-Si should be melted completely or near completely in order to avoid the influence of the a-Si or explosively crystallized Si [5] sublayer on the crystallization. As follows from Tables 1–3, the irradiation conditions correspond to the high-energy regime to which it is necessary to get the melted zone contact with Co underlayer.

We can consider two influences of the Co underlayers: (a) a nucleation-enhancing seeding effect of discontinuous Co layer or Co silicide layer, if Co is reacted with silicon. This layer should not melt under laser irradiation. Such conditions are expected at $F = 0.26$ J cm^{-2} for $d_{Si} = 100$ nm, and at $F = 0.4$ J cm^{-2} and 0.45 J cm^{-2} for $d_{Si} = 200$ nm (Tables 1, 2); (b) local epitaxial growth of crystalline Si on continuous Co silicide underlayer formed at the interface with the substrate.

The higher melting duration and temperature gradient could also positively influence the crystallization.

4. RESULTS AND DISCUSSION

X-ray diffraction was used for the fast checking of the crystalline state of irradiated samples which were later studied by GI XRD in detail, and for the calculations of the grain size of the samples from the broadening of the diffraction peaks. GI XRD measurements showed that as in our previous work [6] strong 111, 220, and 311 and sometimes weak 400, 331, and 511 Si peaks were detected in irradiated samples (Figs. 2–7). The 111 and 220 peaks are strongly correlated, i.e., they appear together and with approximately the same intensity. With some exceptions, the peak 311 is intense and broad, which is attributed to Si substrate and the presence of residual stress in the films. The spectra recorded at 5° show broad peak at $2\theta \approx 86°$, close to 422 peak of Si, which can be due to both silicon oxide and crystalline silicon. At $2\theta \approx 22°$, broad maxima of SiO$_2$ are observed, with the highest intensity at the
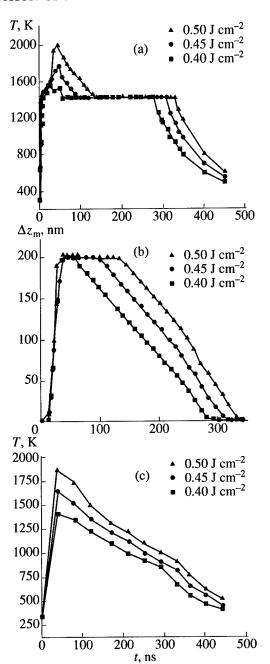
Fig. 1. Results of the calculations of the a-Si (200 nm)/Co(3 nm)/SiO$_2$ (300 nm)/Si-substrate structure at 0.40, 0.45, and 0.50 J cm^{-2}: (a) surface temperature vs. time, (b) depth of melting vs. time, and (c) Co layer temperature vs. time.

grazing angle of 1°, corresponding to the optimum diffraction depth for SiO$_2$.

In our samples with Co underlayers 0.5 and 1 nm thick, no Co peaks (of cubic or hexagonal structure) were found, probably due to the amorphous structure of Co. In samples with Co underlayer 3 nm thick, a slight hint of the poorly developed Co phase was detected.

In samples with Co layer 3 nm thick, a weak 220 peak of fcc CoSi$_2$ is observed ($2\theta = 47.92°$) after irradiation.

Intensity, arb. units
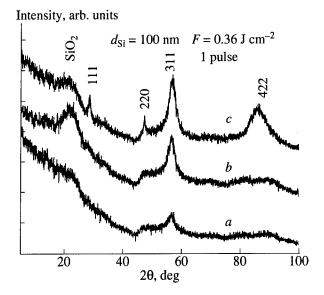
Fig. 2. GI XRD spectra of a-Si 100-nm-thick without Co underlayer irradiated at the energy density of 0.36 J cm^{-2} by 1 laser pulse: (a) grazing angle 0.5°, (b) grazing angle 1°, and (c) grazing angle 5°.

It appeared even after the first laser pulse at all energy densities, corresponding to the melting of both a-Si and Co, but also only to the melting of a-Si. No other silicide phases like CoSi, Co$_2$Si were detected. The silicide phases appear in various time sequences in solid-state reactions of amorphous or crystalline Co with silicon [17, 22]. In our samples, CoSi$_2$ is formed via melting, mutual dissolution, and resolidification of Si and Co. The Si less-rich phases are not observed because there is much more Si than is required for the formation of the final CoSi$_2$ phase. The formation of CoSi$_2$ cannot be

excluded also for thinner Co layers, but obviously we are under the detection limit of our equipment.

From the comparison of crystallization of samples with d_{Si} = 100 nm (Fig. 2) and 200 nm (Figs. 3a, 4a), it follows that thicker a-Si crystallizes better. This may be due to the larger time of melting (Tables 1–3) and higher thermal gradient in the melt. In the further discussion we will limit ourselves to samples with a-Si 200 nm thick.

Some interesting features of the crystallization of a-Si without Co underlayer follow from Figs. 3a and 3b (F = 0.4 J cm^{-2}) and Figs. 4a and 4b (F = 0.5 J cm^{-2}). The results for F = 0.45 J cm^{-2} are similar. We can observe that in this case the crystallization seems to start from the interface with the substrate, as expected for the complete melting of a-Si, but after the first pulse it is not yet finished. Only after 10 pulses is silicon well crystallized near the surface to show spectra for the α = 0.5°.

It is known that laser-crystallized Si films often show stratified structure with different crystallinity in various depths. This is typical for the low energy density regime with incomplete melting of Si [23, 24], where the explosively crystallized Si is melted and vertically regrown towards the surface of the film. But in our samples the grain size increases downwards. This can be explained by the competition of the formation of grains by homogeneous nucleation from a supercooled Si melt and by heterogeneous nucleation at the interface with the substrate. Both processes are expected in the high energy density conditions [5, 15]

The influence of CoSi$_2$ underlayer onto the crystallization of Si is revealed from the comparison of the spectra in Figs 3, 4 and those in Figs. 5, 6. It is evident that in both cases corresponding to two energy densities, viz., F = 0.4 and 0.5 J cm^{-2}, the Si layer growing

Intensity, arb. units
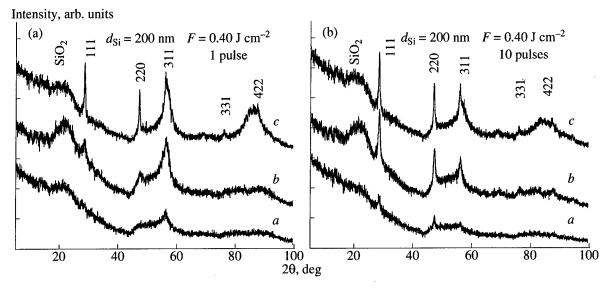
Fig. 3. GI XRD spectra [(a) grazing angle 0.5°, (b) grazing angle 1°, and (c) grazing angle 5°] of a-Si 200-nm-thick without Co underlayer irradiated at the energy density of 0.40 J cm^{-2} by (a) 1 laser pulse and (b) 10 laser pulses.

Intensity, arb. units
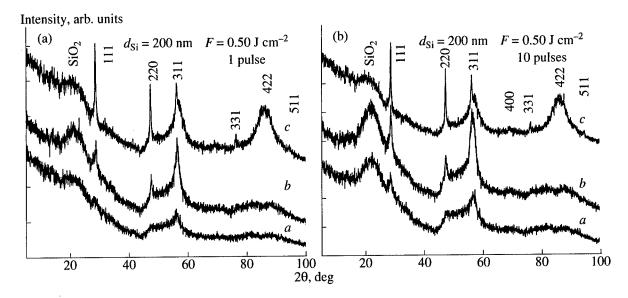
Fig. 4. GI XRD spectra [(a) grazing angle 0.5°, (b) grazing angle 1°, (c) grazing angle 5°] of a-Si 200-nm-thick without Co underlayer irradiated at the energy density of 0.50 J cm^{-2} by (a) 1 laser pulse and (b) 10 laser pulses.
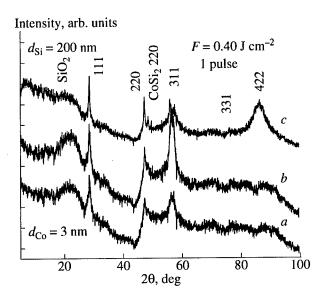
Fig. 5. GI XRD spectra [(a) grazing angle 0.5°, (b) grazing angle 1°, (c) grazing angle 5°] of a-Si 200-nm-thick with Co underlayer of 3 nm irradiated at the energy density of 0.40 J cm^{-2} by 1 laser pulse.
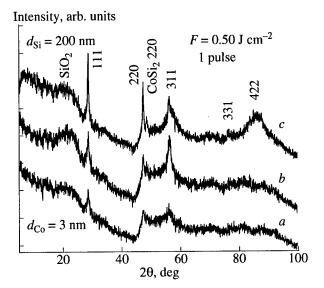
Fig. 6. GI XRD spectra [(a) grazing angle 0.5°, (b) grazing angle 1°, (c) grazing angle 5°] of a-Si 200-nm-thick with Co underlayer of 3 nm irradiated at the energy density of 0.50 J cm^{-2} by 1 laser pulse.

on CoSi$_2$ is completely crystallized up to the surface even after the first laser pulse. We assume that is proof of the improvement of the heterogeneous crystallization conditions at the interfaces which may approach the local epitaxial growth.

The effect of CoSi$_2$ was not confirmed for thinner Co layers which are expected to form CoSi$_2$ as well, but for a discontinuous one. For $F = 0.40$ J cm^{-2} and 1 pulse, the effect of Co underlayer is shown in Fig. 7. For Co layer thicknesses of 0.5 and 1 nm, the crystalline structure is even worse than for the corresponding sample

without Co underlayer. It cannot be excluded that the positive Co or CoSi$_2$ seeding effect could be proved by trimming the energy density of the laser beam into the narrow experimental window required for the critical near-complete melting regime. In papers [5, 15] the energy density was increased using 0.01 J cm^{-2} steps to find the appropriate value.

It is somewhat surprising that the 220 orientation of CoSi$_2$ did not create stronger 220 texture in Si films.

The average grain size calculated from the broadening of 111 and 220 X-ray peaks of the best crystallized

Intensity, arb. units
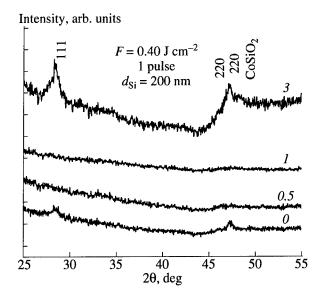
Fig. 7. GI XRD spectra (grazing angle 0.5°) of a-Si 200-nm-thick samples with Co underlayer 0, 0.5, 1, and 3 nm thick irradiated at the energy density of 0.40 J cm^{-2} by 1 laser pulse.

samples is about 20 nm. This is the lowest limit because the peaks are broadened also due to residual stress and defects in the films. The calculated grain size is two times larger than in our previous work [6], where $CoSi_2$ underlayer was not used, and is typical for the high energy density regime of a-Si crystallization

5. CONCLUSIONS

It has been shown that the XeCI laser crystallization of amorphous Si may be improved using 3-nm-thick Co underlayer. This transforms into $CoSi_2$ with 220 preferential orientation in the regime of complete melting of Si films corresponding to high energy density conditions. It is assumed that the crystal growth of Si on the surface of $CoSi_2$ is positively influenced by good lattice match of both layers. This way a-Si is crystallized in the whole thickness even after the first laser pulse. Without $CoSi_2$ underlayer, the surface of silicon was not fully crystallized, or 10 pulses were necessary to complete the crystallization.

ACKNOWLEDGMENTS

REFERENCES

1. Brotherton, S.D., 1995, *Semicond. Sci. Technol.*, **1**, 721.
2. Mei, P., Boyce, J.B., Hack, M., *et al.*, 1994, *Appl. Phys. Lett.*, **64**, 1132.
3. Sameshima, T. and Usai, S., 1993, *J. Appl. Phys.*, **74**, 6592.
4. Haji, L., Joubert, P., Stoemenos, J., and Economou, N.A., 1994, *J. Appl. Phys.*, **75**, 1994.
5. Im, J.S., Kim, H.J., and Thompson, M.O., 1993, *Appl. Phys. Lett.*, **63**, 1969.
6. Luby, S., Jergel, M., Majkova, E., *et al.*, 1996, *Phys. Status Solidi A*, **154**, 647.
7. Wang, K.C., Hwang, H.L., and Yew, T.R., 1994, *Appl. Phys. Lett.*, **64**, 1024.
8. Kim, J.H. and Lee, J.Y., 1996, *Jpn. J. Appl. Phys.*, **35**, 2052.
9. Masaki, Y., Ogato, T., Ogawa, H., and Jones, D.I., 1994, *J Appl. Phys.*, **76**, 5225.
10. Lee, S.W., Jeon, Y.C., and Joo, S.K., 1995, *Appl. Phys. Lett.*, **66**, 1671.
11. Matsumoto, T., Nagahiro, Y., Nasu, Y., *et al.*, 1994, *Appl. Phys. Lett.*, **65**, 1549.
12. Kawazu, Y., Kudo, H., Onari, S., and Arai, T., 1990, *Jpn. J. Appl. Phys.*, **29**, 2698.
13. Liu, G. and Fonash, S.J., 1993, *Appl. Phys. Lett.*, **62**, 2554.
14. Heath, J.R., Gates, S.M., and Chess, C.A., 1994, *Appl. Phys. Lett.*, **64**, 3569.
15. Giust, G.K. and Sigmon, T.W., 1997, *Appl. Phys. Lett.*, **70**, 767.
16. Toet, D., Koopmans, B., Santos, P.V., *et al.*, 1996, *Appl. Phys. Lett.*, **69**, 3719.
17. Maex, K., 1993, *Mater. Sci. Eng.*, **R11**, 53.
18. Kolb, E., Mulloy, M., Dupas, C., *et al.*, 1995, *J. Magn. Magn. Mater*, **148**, 315.
19. Kolb, E., Walker, M.J., Velu, E., *et al.*, 1996, *J. Magn. Magn. Mater*, **156**, 377.
20. D'Anna, E., Luby, S., Luches, A., *et al.*, 1993, *Appl. Phys. A*, **56**, 429.
21. Miyasaka, M., Itoh, W., Komatsu, T., *et al.*, 1994, *Jpn. J. Appl. Phys.*, **33**, 444.
22. Shim, J.Y., Park, S.W., and Baik, H.K., 1997, *Thin Solid Films*, **292**, 31.
23. Sands, D., Williams, G., and Key, P.H., 1997, *Semicond. Sci. Technol.*, **12**, 750.
24. Smith, P.M., Carey, P.G., and Sigmon, T.W., 1997, *Appl. Phys. Lett.*, **70**, 342.

Growth of Ti : Sapphire Thin Films by Pulsed Laser Deposition

J. Gonzalo, P. H. Key, and M. J. J. Schmidt

Department of Applied Physics, University of Hull, HU6 7RX UK
e-mail: p.h.key@apphys.hull.ac.uk
Received August 27, 1997

Abstract—A route to the growth of Ti : sapphire thin films is the pulsed laser ablation deposition technique. In this paper we describe a study of Ti : Al_2O_3 deposition on single crystal MgO substrates using ArF laser ablation of bulk target material in a low pressure oxygen environment. The matrix of processing parameters investigated was limited to laser fluences of 1 and 8 J cm^{-2}, oxygen pressures of 0.02 and 0.2 mbar and substrate temperatures of 300 and 1400 K. The films grown on high temperature substrates in low oxygen pressure exhibited the highest degree of crystallinity, the laser fluence having little effect under these conditions. XRD studies indicate that these films consist of a polycrystalline mosaic of α-Al_2O_3. Photoluminescence studies reveal that the films grown using the higher laser fluence have an emission intensity 10 times that of films grown at low fluence. The studies indicate the suitable combination of parameters for the effective growth of optically active thin films.

1. INTRODUCTION

The growth of laser-active thin film materials is of interest for the production of microlasers [1] based on waveguiding. These structures offer the possibility of incorporation into integrated opto-electronic systems. Suitable materials for these applications are Nd : YAG and Ti : Sapphire, the latter allowing tunable output in the ~0.68 to ~0.98 μm wavelength range [2].

A number approaches to the fabrication of such optically active thin film materials have been taken. These include established techniques such as liquid phase epitaxy [3], flame hydrolysis deposition [1], ion implantation [4], and MOCVD [5].

Pulsed laser deposition (PLD) is an alternative thin film growth method which has already seen much use in the production of High-T_C Superconductors and other crystalline and amorphous materials. The success and versatility of the technique is mainly due to the simplicity of the method and, using short pulse UV lasers, the essentially stoichiometric transfer of material from target to substrate. The deposition of materials for thin film micro-lasers by this technique has recently been reported [6, 7].

In this paper we report the results of experiments in the PLD of Ti^{3+} : Al_2O_3 thin films on single crystal MgO (100) substrates using an ArF excimer laser. The effect of laser fluence, ambient pressure, and substrate temperature on the film quality are discussed.

2. EXPERIMENTAL

The samples were prepared by PLD using an ArF Laser (wavelength: 193 nm, pulsewidth: ≈ 10 ns FWHM). The complete deposition system used has been described elsewhere [8, 9].

The MgO substrates were heated by a RF CO_2 laser via a second MgO backing plate, to ensure a good, uniform heat distribution. The front surface temperature of the substrate was determined by thermocouple and optical pyrometer and then calibrated against the output energy of the RF laser. Prior to the deposition process, each substrate was ultrasonically cleaned in methanol and deionized water

Temperature, pressure, and fluence were kept constant during each deposition run which typically consisted of 50000 pulses at the chosen fluence onto a rotating target of high purity bulk Ti : Sapphire (Ti concentration: 0.23 at. % of cations) in a dynamic oxygen pressure of 0.2 or 0.02 mbar.

The deposition conditions used for each sample is shown in the table, which shows sample identification number, #; substrate material, S; substrate temperature, T_S; laser fluence, F; and ambient oxygen pressure, P.

All films were analysed by Normal Incidence Reflectance (NIR), Photo Luminescence (PL), and X-Ray Diffraction (XRD). The morphology of some of the films was determined by Atomic Force Microscopy (AFM).

The NIR measurements were made on films deposited on Si substrates since the difference in refractive indices between MgO (n ~ 1.736) and Sapphire (n ~ 1.756) is too low to obtain reliable results. The reflectivity was subsequently modelled using a standard

List of samples

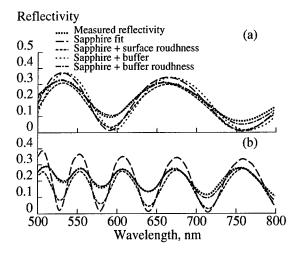| #	S	T_S, K	F, J cm^{-2}	P, mbar
3.08	Si	300	1.5	0.23
6.14	Si	1100	4.9	0.15
7.02	MgO	300	1.0	0.02
7.06	MgO	1400	1.11	0.02
7.10	MgO	1400	8.1	0.02
7.11	MgO	1400	8.5	0.20

Reflectivity

Fig. 1. Measured and modelled reflectivity of (a) sample #6.14 and (b) sample #3.08.

transfer matrix formulation [10] in conjunction with a purpose written optimisation routine [11].

PL measurements were performed at room temperature with excitation by the $\lambda = 514.5$ nm line of an Ar^+ ion laser (max. power ~250 mW). The PL intensity was measured using a single grating monochromator (spectral resolution 20 nm) and a photomultiplier (RCA 7210) as the detector system with standard lock-in technique. Further details of the experimental configuration can be found elsewhere [12].

XRD has been performed in a, computer controlled, Siemens D5000 XRD System, using Cu Kα Radiation. The standard XRD analysis employs a Θ/2Θ geometry.

In order to identify planes that are not parallel to the surface of the substrate/film system, detector scan geometry was also employed. In this scan geometry, the incident X-ray radiation is fixed in angle, while the detector scans the 2Θ range and can also been used to perform grazing incidence analyses of a surface, by using very low incident angles.

Rutherford Backscattering Spectroscopy (RBS) and Proton Induced X-ray Emission (PIXE) has been performed with protons of ~2 MeV.

3. RESULTS AND DISCUSSION

3.1. NIR

Normal Incidence Reflectance measurements, from 500 to 800 nm, were attempted on all samples. The low signal-to-noise ratio, however, gave unreliable results for deposited Ti : sapphire films on MgO. We, therefore, present here NIR results only for films deposited on Si substrates

It has then been attempted, to approximate the measured reflectivity curves by modelling the layer structure via transfer matrix formulation. In Fig. 1, the different models for two films are shown. The simple model consists of an appropriate thickness layer of Sapphire on a Si bulk substrate. Surface roughness is modelled by adding a mixed layer of air and sapphire. The modelling is completed by the inclusion of a few nm thin layer of SiO_2 between the silicon and the sapphire to account for substrate oxidation during the heating phase prior to deposition. The optimum fit between the original data and the model is achieved, by assuming the following layer structure [13]:
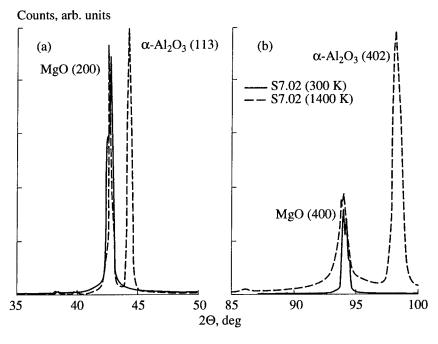
Fig. 2. XRD Patterns for samples #7.02 and #7.06.

#3.08:–Si (385 μm)–SiO$_2$ (47 nm)–Ti : Al$_2$O$_3$ (1.6 μm)–Ti : Al$_2$O$_3$/air(91 nm)

#6.14:–Si (385 μm)–SiO$_2$ (42 nm)–Ti : Al$_2$O$_3$ (0.68 μm)–Ti : Al$_2$O$_3$/air(70 nm)

The results are in good agreement with our estimates of thickness and refractive index of the deposited films.

3.2. XRD Analysis

3.2.1. Θ/2Θ geometry. Initial analysis was performed in standard Θ/2Θ geometry. Figure 2 shows the diffraction patterns of two different films, grown at 300 and 1400 K under low fluence (~1 J cm^{-2}) and low pressure (0.02 mbar) ablation conditions. The patterns show distinctive diffraction peaks which can be attributed to the main orientation, (100) and (400), of the MgO substrate crystal. The graphs have been normalised to these MgO peak-heights.

The film (#7.06) prepared on a high temperature substrate shows two additional peaks, which can be identified as the (113) and (402) reflections of α-Alumina [14]. Both reflections are very distinctive and are larger than the MgO peaks. As can be expected, both diffraction peaks are located very close to a MgO diffraction peak. This would indicate a preferred alignment of the film in respect to the substrate orientation. In addition to these main peaks other, smaller, Alumina peaks could be found. These would suggest a confirmation of the dominance of the α-phase in the film in comparison with the many other phases of Al$_2$O$_3$ [15], and indicate different orientations of crystallites, at a significantly lower number.

Comparing the intensities of the two major peaks with theoretical calculations [16], we find that in a powder pattern they should have a ratio of 50 : 1 between the (113) and the (402) peaks. In practice, we measured a ratio of about 15 : 1 or less, indicating a significant preference of orientation towards the (402) plane in comparison with the powder.

We therefore would expect to have a crystallite mosaic composing a large proportion of the film thickness. The results suggest that at least two different crystallite orientations exist, since both planes should be parallel to the surface. AFM imaging indicates that the size of crystallites is in the region of 1 μm.

The films grown on low temperature substrates (e.g., #7.02) show no features other than the MgO peaks and it can be assumed, therefore, that these films are amorphous.

3.2.2. Detector scan geometry. Figure 3 shows the spectrum of a film grown under conditions of high deposition temperature and fluence (#7.10). Again a number of diffraction peaks, attributable to α-Al$_2$O$_3$ planes; (300), (315) and (318) can be readily identified. These planes, observed in detector scan geometry, are not necessarily parallel.
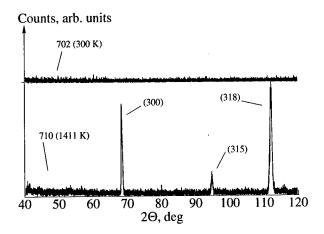
Fig. 3. Detector scan of films prepared at 300 and 1400 K.
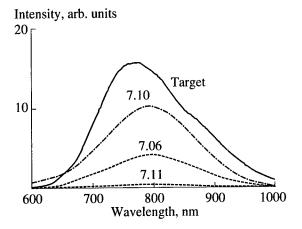
Fig. 4. Room temperature Photo Luminescence spectra of deposited Ti : Sapphire films. The PL spectrum of the Ti : Sapphire target is included as a reference.

Similar results have been seen from other films. In general, at low incident angles (2° and 3°), MgO peaks are suppressed and the film peaks can be examined. At 10°, however, the MgO substrate exhibits the most prominent features of the whole scan.

3.3. Photo Luminescence

The PL emission from the $^2E \longrightarrow {}^2T_2$ transition measured for Ti : Sapphire films grown under different experimental conditions is shown in Fig. 4. In all cases, the contribution of the substrate has been subtracted. The PL spectrum corresponding to the Ti : Sapphire target, measured with the same spectral resolution but lower pump power (10 mW) is included in the figure as a reference. The best PL response was obtained for films grown at high substrate temperature, low O$_2$ pressure and high fluence (#7.10). The PL emission consists of a broad band in the 600–1000 μm range, that is characteristic of bulk Ti : Sapphire. Nevertheless, the wavelength at which the PL emission becomes maximum
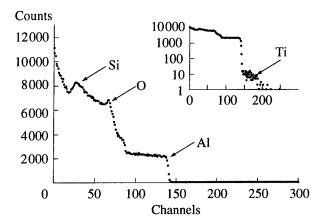
Fig. 5. RBS of sample #6.14. The inset shows the same spectrum on a logarithmic count scale.

(λ_M) is higher in the case of the film (793 nm) than in that of the target (775 nm), and in addition, the asymmetry of the emission band, observed for the target, disappears in the PL spectra of the films. In the case of Ti : Sapphire, the crystal field of the host material (Sapphire) produces the splitting of the degenerate ^2D ground state of the Ti^{3+} ions. The electronic transition that produces the luminescence taking place between two of them [2]. The observed change in the shape of the luminescence band and in the value of λ_M therefore suggests a modification in the crystal field, that could be produced by a modification of the local Ti^{3+} environment. The presence of defects, dislocations and/or stresses expected in crystalline films grown on substrates with different crystalline structure (as it is our case: Hexagonal sapphire on cubic MgO) could produce such a modification.

Films deposited at 300 K exhibit almost no photoluminescence and are not shown. Under these conditions the deposited films are amorphous, as was shown in Fig. 2, and the crystal field is inconsistent with an adequate splitting of levels leading to non-luminescent films.

To analyse the influence of the oxygen pressure on the PL emission, films were grown using the optimum temperature and fluence but at higher O_2 pressure (#7.11). In this case, the PL emission is also very small, but no significant change on the crystalline structure could be observed for these films. Absorption experiments in Ti : Sapphire have shown that the presence of Ti^{4+} ions produces a decrease in the intensity of the $^2T_2 \longrightarrow {}^2E$ absorption band [2], and consequently, a decrease of the PL emission. The oxidation of Ti^{3+} to Ti^{4+}, has been observed when annealing bulk Ti : Sapphire in an O_2 environment. Therefore, in our case the presence of a relatively high O_2 pressure when growing films at 1400 K may effectively induce the oxidation of Ti^{3+}, thus leading to the observed decrease of the PL emission [17, 18]. Similar results have been found in the case of Er : Al_2O_3 [19], although in this

case this behaviour was attributed to the deposition of less dense films at high O_2 pressures.

Finally the PL emission also decreases for films grown at lower fluences (#7.06). The dynamics of the species bombarding the growing film depends on the laser fluence and background pressure [20] and may be influential in terms of film structure. The films are certainly thinner (for the same number of laser pulses) than those deposited at high fluence and may be less dense. Furthermore, chemical reactions within the plume, e.g., $Ti^{3+} \longrightarrow Ti^{4+}$, may also be different. All of these factors may contribute to the observed decrease in PL emission.

3.4. Ion Beam Analysis

RBS results are shown in Fig. 5 and indicate a good stoichiometric transfer ratio for aluminium oxide, according to the tabulated backscattering yields [21]. Titanium can be shown to be present, although it is only visible on a logarithmic scale due to the low concentration

A PIXE measurement of the films, shows that they contain about 55–60% of the amount of titanium that is present in the bulk material. This appears to be independent of the substrate material or the substrate temperature.

4. CONCLUSIONS

A number of factors in the PLD process can affect the properties of the deposited films. In the case of Ti : Al_2O_3 for applications as an active laser medium, it is important that the α-phase of Al_2O_3 is deposited and that the substitutional cation is Ti^{3+}.

In terms of structure it is clear from the experimental evidence of both XRD and PL measurements that deposition onto a high temperature substrate (in our case 1400 K) is necessary to create the correct polytype. This is likely to be assisted by deposition onto a substrate which provides a good lattice match with the required film.

The influence of background gas pressure is more complex since it is linked to the laser fluence used. Whilst high fluences result in a higher ablation rate, they can also result in more energy being deposited into the plume of removed material. The ratio of this deposited energy to the background gas pressure is fundamental to the dynamics of the plume expansion and the possibility of gas phase chemistry occurring within it [20]. The evidence from the films deposited with low fluence and low pressure together with films deposited with high fluence and high pressure would indicate that both of these are unfavourable conditions for the deposition good quality films. In these cases, whilst the α-phase Al_2O_3 has been deposited, it appears that the plume chemistry has lead to the incorporation of Ti^{4+}, rather than Ti^{3+}, ions into the film.

It has been shown from a limited matrix of experimental parameters that the most favourable conditions for the PLD of Ti^{3+} : α-Al_2O_3 thin films for micro-laser applications include a high substrate temperature together with a high ratio of laser fluence to background gas pressure.

ACKNOWLEDGMENTS

REFERENCES

1. Kitigawa, T., Hattori, K., Hibino, Y., and Ohmori, Y., 1994, *J. Lightwave Technol.*, **12**, 436.

2. Moulton, P.F., 1986, *J. Opt. Soc. Am. B*, **3**, 125.

3. Grabmaier, J.H., Plattner, R.D., Mockel, P., and Kruhler, W.W., 1976, *J. Cryst. Growth*, **34**, 280.

4. Chandler, P.J., Field, S.J., Hanna, D.C., *et al.*, 1989, *Electron. Lett.*, **25**, 985.

5. Bai, G.R., Chang, H.L.M., and Forster, C.M., 1994, *Appl. Phys. Lett.*, **64**, 1777.

6. Ezaki, M., Obara, M., Kumagai, H., and Toyoda, K., 1996, *Appl. Phys. Lett.*, **69**, 2977.

7. Anderson, A.A., Eason, R.W., Jelinek, M., *et al.*, 1997, *Thin Solid Films*, **300**, 68.

8. Dyer, P.E., Greenough, R.D., Issa, A., and Key, P.H., 1990, *Appl. Phys. Lett.*, **57**, 186.

9. Dyer, P.E., Issa, A., Key, P.H., and Monk, P., 1990, *Supercond. Sci. Technol.*, **3**, 89.

10. Toussaere, E. and Zyss, J., 1993, *Thin Solid Films*, **234**, 432.

11. Attrill, K.J., 1986, *PhD Thesis* (Univ. Bradford).

12. Serna, R. and Afonso, C.N., 1996, *Appl. Phys. Lett.*, **69**, 1541.

13. Dyer, P.E., Gonzalo, J., Key, P.H., *et al.*, 1997, *Appl. Surf. Sci.*, **109/110**, 345.

14. X-Ray Powder Diffraction Card JCPDS #10-173 (Corundum).

15. X-Ray Powder Diffraction Cards JCPDS #s 26-31, 35-121 (Θ), 4-0875 (η), 10-414 (β), 23-1009 (Θ), 10-425 (γ), 4-0877 (δ), 4-878 (κ), 4-0880 (χ).

16. Data for calculations taken from: Ishizawa, Miyata, Minato, Marumo, and Iwai, 1980, *Acta Crystallogr., Sect. B*, **36**, 228.

17. Yamaga, Yoshida, Hara, Nodama, and Henderson, 1994, *J. Appl. Phys.*, **75**, 1111.

18. Sanchez, Strauss, Aggarwal, and Fahey, 1988, *IEEE J. Quantum Electron*, **24**, 995.

19. Sema, R., Afonso, C.N., Ballesteros, J.M., and Zschocke, A., 1997, *Appl. Surf. Sci.*, **109/110**, 524.

20. Dyer, P.E., Farrar, S.R., Issa, A., and Key, P.H., 1992, *Proc. E-MRS Summer School on "Laser Ablation of Electronic Materials; Basic Mechanisms and Applications,"* Fogarassy, E., Lazare, S., and Narayan, J., Eds. (Elsevier).

21. 1977, *Ion Beam Handbook for Materials Analysis*, Mayer, J.W. and Rimini, E., Eds. (Academic).

Study of Carbon Nitride Synthesis and Deposition by Reactive Laser Ablation of Graphite in Low-Pressure Nitrogen Atmosphere

M. L. De Giorgi*, G. Leggieri*, A. Luches*, A. Perrone*, A. Zocco*, J. Zemek**, M. Trchova***, G. Barucca****, and P. Mengucci****

* INFM and University of Lecce, Department of Physics, Lecce, 73100 Italy
E-mail: luches@le.infn.it
** Institute of Physics, Czech Academy of Sciences, Prague 6, 16200 Czech Republic
*** Faculty of Mathematics and Physics, Charles University, Prague 8, 18000 Czech Republic
**** INFM and University of Ancona, Department of Materials and Earth Sciences, Ancona, 61100 Italy
Received August 6, 1997

Abstract—Carbon nitride films were deposited on $\langle 111 \rangle$ Si substrates by XeCl laser ablation of graphite in low-pressure (1–50 Pa) N_2 atmosphere at fluences of 12 and 16 J/cm^2. Substrates were usually at room temperature. Some films were deposited on heated (250 or 500°C) substrates. Different diagnostic techniques (SEM, TEM, RBS, XPS, FTIR, XRD) were used to characterize the deposited films. Films resulted plane and well adherent to their substrates. N/C atomic ratios up to 0.7 were inferred from RBS measurements. Nitrogen content increases with increasing ambient pressure and laser fluence. XPS spectra of the N 1s peak indicate two different bonding states of nitrogen atoms, bound to sp^2-coordinated C atoms and to sp^3-coordinated C atoms. XRD and TEM analyses point to an oriented microcrystalline structure of the films. Heating of the substrates results in a lower nitrogen concentration with respect to films deposited at room temperature in otherwise identical experimental conditions. Optical emission studies of the laser plasma plume indicate a positive correlation between the emission intensity of the CN radicals in the plume and the nitrogen atom concentration in the films.

1. INTRODUCTION

The prediction of a covalently bound carbon nitride β-C_3N_4 phase [1], with characteristics comparable or better than those of diamond, stimulated numerous attempts (see e.g. [2–4]) to synthesize and deposit thin films of this material. After almost a decade of trials this material has not yet been synthesized in stoichiometric phase. Nowadays carbon nitride, with composition CN_x ($x < 1$) is being prepared in order to study its formation processes and film characteristics.

Laser reactive ablation is emerging as an attractive technique for the deposition of thin films of compound materials. In this technique a solid substrate collects the material ablated by the pulsed laser irradiation of an elemental target and reacted with a low-pressure ambient gas. At sufficiently high laser fluences, the energy of species in the plasma plume created by laser pulses is high enough to promote reactions also with molecules with very high binding energies, like molecular nitrogen.

In previous papers [4–6] we have reported some characteristics of CN_x films deposited by excimer laser ablation of graphite in N_2 or NH_3 atmospheres at the fluences of 3 and 6 J/cm^2. Since the N/C atomic ratio in the deposited films increased with increasing laser fluences, new deposition tests were performed at 12 and 16 J/cm^2 in N_2 ambient atmosphere. Ammonia, even if more reactive than molecular nitrogen was no more used to avoid N–H bonds. Generally, films were depos-

ited on ambient-temperature substrates. Some films were deposited on heated substrates (250 or 500°C), with the aim of increasing the reactivity of the deposited species.

2. EXPERIMENTAL APPARATUS

A XeCl ($\lambda = 308$ nm, $\tau_{FWHM} = 30$ ns) excimer laser (Lambda Physik LPX 315i) was used for the ablations. The laser beam was incident under an angle of 45° on the target, which was rotating at the frequency of 3 Hz to reduce drilling of the graphite target. Laser fluences were either 12 or 16 J/cm^2. Usually 1×10^4 laser pulses at the repetition rate of 10 Hz were used for each irra-

Thickness (t) and N/C atomic ratio of the deposited films as a function of N_2 pressure (p), laser fluence (F) and substrate temperature T: (1) $F = 12$ J/cm^2 and T = room temperature; (2) $F = 16$ J/cm^2 and T = room temperature; (3) $F = 16$ J/cm^2 and $T = 250$°C

p (Pa)	t (nm) (1)	N/C (1)	t (nm) (2)	N/C (2)	t (nm) (3)	N/C (3)
1	220	0.20	280	0.20	250	0.20
5	150	0.25	600	0.25	200	0.20
10	60	0.30	150	0.70	200	0.25
50	10	0.50	<10	?	180	0.25

diation series. N_2 pressure was set at 1, 5, 10, or 50 Pa. A continuous flow of gas was introduced into the reaction chamber to maintain a constant pressure during each irradiation series. The ablated materials were collected on $\langle 111 \rangle$ Si single crystals, placed at a distance $d = 40$ mm from the target. These substrates were usually at room temperature (~20°C). Some depositions were performed with substrates heated at 250 or 500°C. During the depositions, time-integrated optical emission spectra of the plasma plume produced by each laser pulse over the target were recorded in the range 300–550 nm.
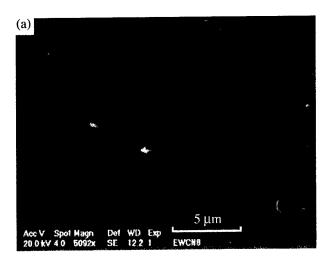
The deposited films were characterized with different diagnostic techniques. A Philips XL-20 scanning electron microscope (SEM) was used to study their surface morphology. Film thickness and composition were investigated by Rutherford backscattering spectrometry (RBS) with 2.2-MeV He⁺ ions. Chemical bonding of elements in surface region (~5 nm) were studied by angle-resolved X-ray induced photoelectron spectrometry (XPS) using Mg $K\alpha$ radiation at 20 eV pass energy (ADES-400, VG Scientific). Infrared measurements were carried out using a Nicolet IMPACT 400 Fourier-transform infrared (FTIR) spectrophotometer. An ambient-temperature deuterated triglicine sulfate detector was used in the wavelength range 400–4000 cm⁻¹. The crystalline structure of the films was investigated by X-ray diffraction (XRD) analysis and transmission electron microscopy (TEM).

3. EXPERIMENTAL RESULTS

The deposited films are always well adherent to their substrates. SEM investigations show that their surfaces are plane, without cracks or corrugations. Very few submicron droplets can be detected at very high magnification. Their typical dimensions are in the range 0.20–0.5 μm. Occasionally, larger irregular structures can be also observed on the deposited films (Fig. 1).

RBS analysis of the deposited films evidenced a quite high nitrogen incorporation. Thickness and N/C atomic ratios were deduced from RUMP [7] simulation of the experimental spectra (table). The thickness of the film deposited at $p = 50$ Pa and $F = 16$ J/cm² is too thin to allow a reasonable determination of the C/N ratio from the correspondent RBS spectrum. Nitrogen concentration into the films decreased when the collecting Si substrate was heated to 250°C, under otherwise identical experimental conditions. When increasing the temperature to 500°C, nitrogen concentration decreased to nondetectable levels. Typical RBS spectra are shown in Fig. 2.

Chemical bonding of elements in surface region (information depth ~5 nm) of the films were studied by XPS. An example of high resolution C 1s spectra is shown in Fig. 3. Maxima are peaked at binding energy of 285.0 eV. Peaks are broad and asymmetric at the
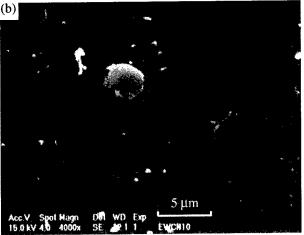
Fig. 1. SEM micrographs of the surface of the film deposited on $\langle 111 \rangle$ Si substrates at room temperature with $F = 16$ J/cm² and (a) $p = 1$ and (b) 10 Pa. The white mark corresponds to 5 μm.
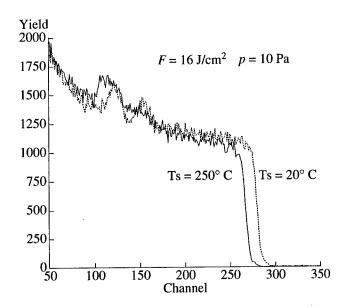
Fig. 2. RBS spectra of samples deposited at $F = 16$ J/cm², $p = 10$ Pa, and substrate temperature (open line) $T_s = 20$ and (solid line) 250°C.

higher binding energy side, indicating the presence of different types of bonds of carbon atoms, such as C–C, C–N and C–O bonds. High resolution N 1s spectra are presented in Fig. 4. These curves are almost symmetric and relatively broad (~3 eV). In agreement with recent literature data [5, 8], the N 1s spectra can be easily decomposed in two Gaussian curves having maxima at 398.7 ± 0.1 eV and 400.3 ± 0.1 eV, with an energy separation of 1.6 eV. It should be noted that the peak separations are the same for all the samples under study and that the corresponding peak area ratio is almost independent on the N_2 working pressure. This N 1s spectra decomposition indicates two different bonding states of nitrogen atoms with respect to carbon atoms. We ascribe the lower binding energy peak to N atoms bonded to C atoms in the sp^2 bonding state and the higher energy peak to N atoms bonded to C atoms in the sp^3 bonding state. This ascription is supported by recent quantum mechanical calculations [9] and with the N 1s spectra recorded from polycrystalline carbon nitride layers with a single dominating phase [10, 11]. It is also supported by FTIR spectra recorded from the same samples (see below). From XPS data it results that the surface layers are oxidized. Oxygen content is ~10%. It is higher in the samples deposited at the higher laser fluence and increases with increasing N_2 pressure,

Fig. 3. Typical C 1s high-resolution photoelectron spectra of CN_x layers prepared at $F = 16$ J/cm^2 and (*1*) $p = 5$, (*2*) 10, and (*3*) 50 Pa.
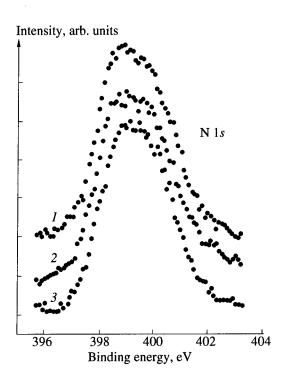
Fig. 4. Typical N 1s high-resolution photoelectron spectra of CN_x layers prepared at $F = 16$ J/cm^2 and (*1*) $p = 5$, (*2*) 10, and (*3*) 50 Pa.
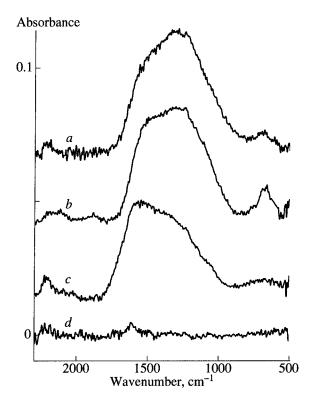
Fig. 5. FTIR absorbance spectra of samples deposited at $F = 16$ J/cm^2 and (a) $p = 1$, (b) 5, (c) 10, and (d) 50 Pa. The spectral features of Si wafers were removed. The spectra are displaced for clarity and baseline correction was made.

reaching the value of ~17% in the sample deposited at $F = 16$ J/cm^2 and $p = 50$ Pa.

Figure 5 shows the FTIR absorbance spectra of the films. The spectra are dominated by a broad asymmetric absorption band from 1000 to 1600 cm^{-1}, where stretching vibrations of both double and single C–N bonds are located [12]. The peak at about 2200 cm^{-1} is commonly attributed to a triple bonded C–N group. The low intensity broad band feature around 700 cm^{-1}, observed also by other authors [13], can be assigned to the out-of-plane bending mode in graphite-like domains.

The investigation on the crystalline structure of the films is quite complicated. Grazing-angle (0.5°–4°) XRD measurements do not show any appreciable crystalline structure of the deposited films, but XRD measurements performed in normal θ–2θ configuration have indicated a polycrystalline structure of the same films [14], which could be due to CN$_x$ phases, to a diamond phase and an N-doped diamond phase.

TEM analysis of the sample deposited at room temperature, $p = 1$ Pa and $F = 12$ J/cm^2 (Fig. 6) evidences the formation of monocrystals with an ellipsoidal basis. The major axis of the ellipses ranges between 2 and 15 μm, while the minor axis ranges between 1 and 5 μm. Electron diffraction studies indicate that the crystals, which seem to exhibit a diamond-like structure, grew almost epitaxially on the ⟨111⟩ Si substrate.

The optical emission spectra recorded during laser ablation of graphite in N$_2$ atmosphere are dominated by the bands of the C$_2$ Swan system and of the CN violet system [15]. Two main features come out from optical emission spectroscopy investigations. The first is that, at a fixed distance from the target, the intensity of the C$_2$ emission decreases and the intensity of the CN emission increases with increasing the ambient N$_2$ pressure. The second is that, at a fixed working pressure, the intensity of the C$_2$ emission decreases and the intensity of the CN emission increases with increasing the distance from the target.

4. DISCUSSION

The droplet density on the deposited films is quite low. They are always very small (<0.5 μm). Some quite large structures (Fig. 1) can be occasionally observed. They could be due to fragments expelled from the target. From RBS spectra it is observed that the N/C atomic ratios increase with ambient pressure and with laser fluence. The increasing with laser fluence is more evident if compared with our preceding depositions at $F = 3$ and 6 J/cm^2 [4, 6]. Oxygen contamination is always very low, since the oxygen peak can be hardly discriminated from the noise. It means that surface oxidation, observed during XPS analysis, is due to exposition to air.

The FTIR results indicate that the formed material is a combination of graphite and diamond-like C–C sp^2
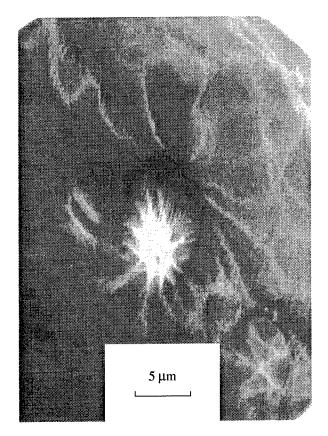
Fig. 6. TEM micrograph of a CN$_x$ layer prepared at $F = 12$ J/cm^2 and $p = 1$ Pa.

and sp^3 bondings. As demonstrated by Kaufman et al. [16], the main absorption band may be due to the D (disordered) and G (graphitic) Raman-active modes (at ~1360 cm^{-1} and ~1575 cm^{-1} for disordered C–C and crystalline C=C phases, respectively) which become IR active when nitrogen is incorporated in the sixfold carbon rings, producing an asymmetric dipole structure. A monotonic increase in the intensity ratio $I(G)/I(D)$ was observed as nitrogen pressure was increased. When trying to deconvolute the broad band into four Gaussian bands, it was found that the position of the maxima was different for different samples and that one could not distinguish between the single and double C–C and C–N bonds. It can only be concluded that the sp^2/sp^3 ratio of bonded carbon atoms is becoming larger with the rising N$_2$ pressure. It can thus be supposed that the relative amount of double bonds between C and N atoms becomes higher at higher N$_2$ pressures.

TEM results obtained for the sample deposited at $p = 1$ Pa and $F = 12$ J/cm^2 indicate that there is no contradiction between x-ray grazing-incidence data and the ones obtained in normal θ–2θ diffractometer method. In very well oriented crystallites or even single-crystal samples, it is possible to have no peaks on the x-ray grazing-incidence diagrams and, nevertheless, some peaks on the normal diffraction diagrams. The discrepancy between the two groups of diffraction

data can be considered as a proof for the formation of thin CN_x films with a very good orientation of the crystallites on the $\langle 111 \rangle$ Si substrate.

The increasing intensity of the CN emission of the plume is positively correlated to a higher nitrogen content in the deposited films. This fact suggests that the CN_x compound should be prevalently formed in gas phase. The lower concentration of nitrogen atoms in samples deposited on heated substrates could be due to desorption of volatile C–N compounds.

5. CONCLUSIONS

Carbon nitride films have been deposited on $\langle 111 \rangle$ Si substrates at room temperature by XeCl laser ablation of graphite targets in low-pressure N_2 atmosphere. N/C ratios up to 0.7 were inferred from RBS spectra. There are evidences of formation of quite large crystallites, which grow almost epitaxially on the substrate. The quality of the films increases with ambient N_2 pressure and with laser fluence. Heating of the substrates makes worse the quality of the deposited films. Reactive laser ablation was showed to be a promising technique for carbon nitride synthesis. Depositions have to be performed by using even higher laser fluences.

ACKNOWLEDGMENTS

REFERENCES

1. Liu, A.Y. and Cohen, M.L., 1989, *Science*, **245**, 841.
2. Bousetta, A., Lu, M., Bensaoula, A., and Schultz, A, 1994, *Appl. Phys. Lett.*, **65**, 696.
3. Zhang, Z.J., Fan, S., and Lieber, C.M., 1995, *Appl. Phys. Lett.*, **66**, 3582.
4. D'Anna, E., Luches, A., Perrone, A., *et al.*, 1996, *Appl. Surf. Sci.*, **106**, 126.
5. Zemek, J., Luches, A., Leggieri, G., *et al.*, 1995, *J. Electron Spectrosc. Relat. Phenom.*, **76**, 747.
6. Luches, A., Caricato, A.P., Leggieri, G., *et al.*, 1996, *Proc. SPIE*, **2789**, 293.
7. Doolittle, L.R., 1985, *Nuclear Instrum. Meth. B*, **9**, 344.
8. Ren, Z.M., Du, Y.C., Ying, Z.F., *et al.*, 1994, *Appl. Phys. Lett.*, **65**, 1361.
9. Sjostrom, H., Stafstrom, S., Boman, M., and Sundgren, J.E., 1995, *Phys. Rev. Lett.*, **75**, 1336.
10. Feng, J., Zheng, Y., and Xie, J, 1996, *Materials Lett.*, **27**, 219.
11. Chen, L.C., Yang, C.Y., Bhusari, D.M., *et al.*, 1996, *Diamond Relat. Mater.*, **5**, 514.
12. Novikov, N.V., Voronkin, M.A., Smekhnov, A.A., *et al.*, 1995, *Diamond Relat. Mater.*, **4**, 3900.
13. Kumar, S. and Tansley, T.L., 1995, *Thin Solid Films*, **256**, 44.
14. Caricato, A.P., Leggieri, G., Luches, A., *et al.*, 1997, *Thin Solid Films* (in press).\
15. Acquaviva, A., Caricato, A.P., De Giorgi, M.L., *et al.*, 1997, *Appl. Surf. Sci.*, **109/110**, 408.
16. Kaufman, J.H., Metin, S., and Saperstein, D.D., 1989, *Phys. Rev. B*, **39**, 39.

The Effect of Background Gas in Excimer Laser Ablation Deposition From SiC Targets

A. Contoret, D. Sands, and P. H. Key

Department of Applied Physics, University of Hull, Hull, HU6 7RX UK
e-mail: p.h.key@apphys.hull.ac.uk
Received August 27, 1997

Abstract—We have examined the laser ablation deposition (LAD) from a bonded SiC target in various ambients, including vacuum, propane, ethylene, and hydrogen at a maximum pressure of about 2 mbar. Films have been deposited onto both crystalline silicon and high quality quartz slides. Energy dispersive X-ray analysis (EDAX) and optical transmission measurements have been used to assess the effect of ambient gas on the film properties and scanning electron micrographs reveal important effects of the ambient gas on surface morphology. Annealing the films by relatively low power excimer laser irradiation following deposition causes the electrical conductivity to increase and the optical band-gap to reduce slightly.

1. INTRODUCTION

Interest in the semiconducting properties of SiC is increasing [1–3]. The material promises to find application in a range of high temperature semiconductor devices because of its combination of large band-gap and refractive properties. Polycrystalline SiC promises to be useful in a variety of thin film devices, including UV detectors. The most common deposition technique is chemical vapour deposition (CVD) but that has the disadvantage that relatively high substrate temperatures are required for the pyrolysis of the reacting gases. Plasma assisted CVD requires lower substrate temperatures but also causes the films to possess a high fraction of hydrogen, much like hydrogenated amorphous silicon [4]. In this paper we report results of experiments on the deposition of thin films by laser ablation of a bonded SiC rod in various ambient gases and show that the film properties depend crucially on the background gas.

2. EXPERIMENTAL

The laser ablation deposition system comprised a Lumonics TE 860-4 excimer laser emitting at 308 nm (XeCl) illuminating an aperture which is then imaged onto the SiC rod within the deposition chamber by means of a quartz lens. Neutral density filters served as attenuators to control the intensity of the incident radiation, which was approximately 2.5 J cm^{-2}.

The deposition chamber is shown in detail in Fig. 1. The SiC rod (10 mm diameter by 100 mm length, reaction bonded, from Goodfellow Cambridge Limited, UK) was mounted on a rotatable feed-through at the focal point of the lens at 45° to the normal, with the substrate mounted on a resistance heater on a similar feed-through directly opposite. The heater was capable of achieving continuous temperatures up to 450°C to an

accuracy of 2% and a thermocouple attached to the heater system was used to monitor the temperature. Typically the separation between the SiC rod and the substrate was 20 mm ± 2 mm.

Films were deposited in a variety of ambients; rough (low) vacuum, high vacuum, flowing argon, hydrogen, propane, and ethylene. Low vacuum conditions were achieved by pumping with a rotary vane pump only to a typical pressure of a few mbar. A 2 inch oil vapour diffusion pump attached to the system allowed high vacuum (base pressure 10^{-5} Torr). Typically the substrate was held at 400°C during the deposition and raised to 445°C for 30 min following deposition. This *in situ* post-deposition annealing was found to be essential to prevent
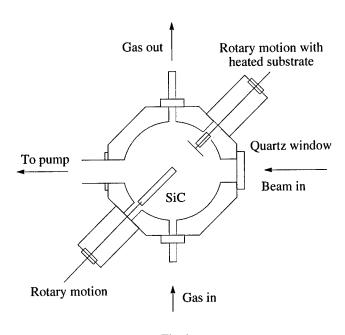
Fig. 1.
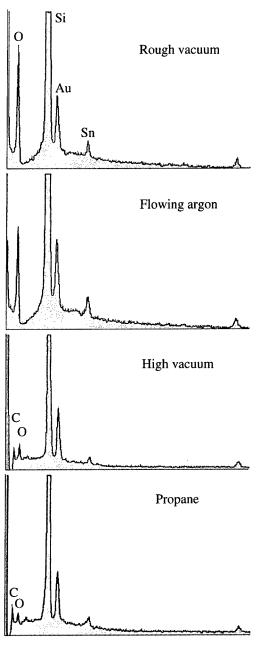
Fig. 2.

crazing of the film on exposure to atmosphere. The number of pulses incident on the SiC rod was typically in the range 2000–4000.

A number of films were annealed *ex situ* using the same excimer laser at a fluence of approximately 200 mJ cm⁻² (±20%).

3. RESULTS

The average growth rates under the conditions described in Section 2 are given in Table 1. The growth rate in rough vacuum is not given below but is identical to that in argon. Figure 2 shows typical EDAX measurements for four films deposited in low vacuum, with flowing argon, in high vacuum, and in propane gas onto single crystal silicon substrates. Silicon was chosen as the substrate in order to allow an assessment of the oxygen content of the films relative to the carbon. The high signal to the left of the spectrum represents a background edge and is a feature of the EDAX system. The gold signal arises from the conducting coating applied to the samples prior to the SEM measurements, and the signal labelled "Sn" appears to be an impurity within the film, possibly within the starting material.

A carbon signal should appear between the low energy edge and the large oxygen peak but there is virtually no carbon present until high vacuum is used. This is accompanied by a much reduced oxygen signal. For deposition in propane (bottom) the carbon signal is now larger than the oxygen signal. Deposition in hydrogen resulted in a similar spectrum to that obtained from propane, and deposition in ethylene showed a larger carbon signal relative to the oxygen signal.

Scanning electron micrographs of the surface of the four films illustrated in Fig. 2 show progressive variations in the surface morphology (Fig. 3).

The surface becomes progressively smoother as the carbon content increases, as judged by the EDAX of Fig. 3. However, it should be stressed that this degree of surface roughness is not visible to the naked eye and all films appear optically smooth.

Figure 4 shows the optical absorption coefficient plotted as a function of photon energy for three films in the as-grown state and after annealing with the excimer laser. The absorption coefficient has been calculated from optical transmission measurements made using a ATI Unicam Ltd. (Cambridge UK) UV3-200 spectrophotometer on films deposited on quartz substrates. The measured absorbance A is defined as

$$A = -\log_{10}\left(\frac{I}{I_0}\right), \qquad (1)$$

where I_0 is the incident intensity. This can be transformed to the absorption coefficient α using the relationship

$$2.3\frac{A}{d} = \alpha, \qquad (2)$$

Table 1. Growth rates for deposition in various ambients

	Argon	Propane	Hydrogen	Ethylene
Growth rate (nm/pulse)	0.045 ± 0.004	0.14 ± 0.01	0.17 ± 0.02	1.15 ± 0.1
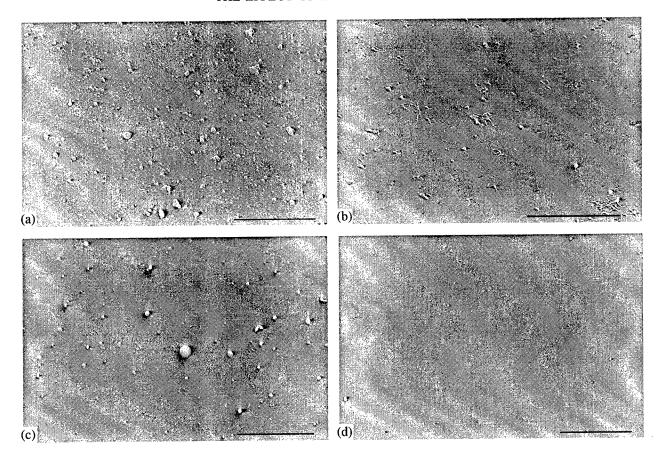
Fig. 3.

where d is the film thickness, measured here using a Dektak [3]ST surface profiler (Sloan Technical Division, Veeco Co. Inc., Santa Barbara, CA, USA). The absorption coefficients have a slight offset due to the reflectivity of the films. We have not independently measured this because the spectrophotometer is dedicated to transmission measurements, nor have we calculated it because we have not independently measured the refractive index. The effect is small though ($<10^3$ cm^{-1}) and not significant compared with absorption coefficients of the order of 10^4–10^5 cm^{-1}.

Films deposited in rough vacuum and in flowing argon were optically smooth and transparent, and were barely distinguishable from the quartz in their absorption characteristics. Coupled with the evidence from Fig. 2 we tentatively conclude that these films are predominantly silicon dioxide. Films deposited in high vacuum showed increased absorption in the UV and had a very slight brownish tint, consistent with a small amount of carbon indicated in Fig. 2. Films deposited in hydrogen and propane exhibited similar properties. Both were light brown in colour and showed a clearly distinguishable absorption tail stretching from approximately 350 to 480 nm. Films deposited in ethylene were much darker in colour and showed considerably increased absorption even out to 600 nm. Only the films deposited in these hydrogen containing ambients

exhibited sufficient absorption to merit particular attention. These films have also been annealed using the excimer laser in order to assess whether to the properties change upon heat treatment, as might be expected if the films contain hydrogen.

The absorption coefficient appears to be linear with photon energy but this is misleading because a plot of $\ln[\alpha]$ against photon energy reveals that the behavior
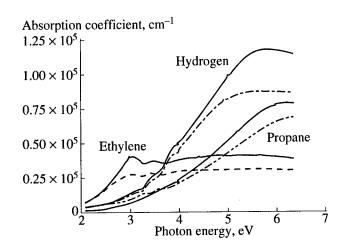
Fig. 4.

Table 2. Optical figure of merit for the films shown in Fig. 4. The data have been rounded to the first significant digit

	Hydrogen	Propane	Ethylene
As growth	3.0 eV	3.4 eV	2.1 eV
Laser annealed	2.9 eV	3.2 eV	1.9 eV

is in fact exponential, particularly over the lower range of absorption coefficients. This is the well known Urbach edge [5], the form of absorption edge most commonly found in amorphous semiconductors. The fact of the Urbach edge means that it is not possible to define with any certainty the optical gap for these films. Measurement of the absorption edge as a function of temperature in order to determine the "focal point" of the Urbach edge is the only certain means of ascribing a band-gap but these measurements are not within the scope of this paper. For convenience we extrapolate the linear part of the absorption curve down to the x-axis (allowing for the small offset due to reflectivity mentioned previously) and use that value of photon energy as a figure of merit for the films. We have made no attempt to relate this to optical band-gap, though the two quite probably are related. These results are summarised in Table 2.

There is clearly a small but significant reduction in this figure of merit consequent upon annealing. This is consistent with the observation that the films become darker. It is also evident that films deposited in hydrogen and propane are very similar in their properties, but films deposited in ethylene have a much lower band-gap.

Laser annealing of the films also greatly increases the electrical conductivity, the greatest effect being observed in the films deposited in ethylene. All the films are highly resistive as deposited ($>10^5–10^6$ Ω cm^{-1}) as measured using a crude four point probe arrangement. Upon annealing all films register an increase in conductivity of at least two orders of magnitude but for the films deposited in ethylene the resistivity lies in the range 1–10 Ω cm^{-1}, i.e., a good semiconductor.

4. DISCUSSION

SiC can be ablated with relative ease in all ambients, despite having a melting point in excess of 2700°C. However, the film properties depend crucially on the ambient gas. We believe the mechanism for this is ablation caused by the onset of sublimation at approximately 1700°C, dissociation of the SiC into Si and C, and the subsequent reaction of these with the ambient gas mediated by the ablation plume/plasma. Even if the surface temperature is sufficient to melt the SiC, there is evidence to suggest that SiC dissociates into its constituent elements [6]. However, we are not certain that melting has been achieved. Numerical calculations of excimer laser heating at 308 nm in 6H SiC [7], taking

into account the distributed heating arising from a relatively low absorption coefficient at 308 nm but assuming room temperature thermal properties throughout, indicate that at an incident fluence of 1.9 J cm^{-2} the surface temperature reaches only 1500°C, below even the sublimation point. Of course, a bonded rod such as that we have used is likely to contain different poly-types with their differing optical properties, so it is possible that inhomogeneous heating is occurring. This is an area of continuing investigations by us.

We are confident, however, that sublimation is important. Previous work on II–VI compound semiconductors, especially zinc sulphide [8] has shown that where the sublimation point lies significantly below the melting point, ablation can be dominated by purely thermal phenomena, and sublimation followed by dissociation is the dominant ablation mechanism. For SiC ablated in low vacuum and in flowing argon the deposited film properties are virtually indistinguishable from those of quartz, and the EDAX confirms that there is very little carbon present in the films. More than likely the carbon has reacted with residual oxygen to form gaseous CO_2 or CO and is subsequently pumped away while the silicon reacts to form SiO_2. In high vacuum, where less residual oxygen might be expected (residual oxygen might also be present in the argon cylinder) a greater concentration of C is found but there is still a significant amount of oxygen present. Deposition in hydrogen or propane leads to very similar films, from which it might be concluded that the dominant mechanism is the exclusion of oxygen rather than the addition of extra carbon. Finally deposition in ethylene yields a much higher growth rate, a greater carbon concentration, and a smaller optical band gap, which all imply that additional carbon is supplied from the ethylene. We are currently conducting experiments on deposition in methane to examine whether similar mechanisms are at work there, and also in nitrogen containing ambient to see whether silicon nitride can be deposited by exclusion of the carbon.

It is quite likely that all the films deposited in hydrogen containing ambients contain hydrogen themselves. We have not independently measured the hydrogen content of the films but infer its presence from both the expectation that hydrogen will be incorporated from the plume and the effect of laser annealing on the films. The changes induced by laser annealing are fully consistent with the evolution of hydrogen. Finally, the surface morphology of the films displays a very interesting dependence on the ambient gas. The smoothest surfaces are produced in the absence of residual oxygen, and at present we can offer no insight into the mechanisms at work. It is not clear, for example, whether the presence of oxygen leads to the formation of clusters within the plume or whether clusters are created during ablation and destroyed by reaction with the ambient gas.

5. CONCLUSION

We have demonstrated that optically smooth films can be deposited from SiC targets by LAD. The composition and properties can be varied simply by changing the ambient gas and this allows for the possibility of producing compositionally graded structures in a very simple and controllable manner.

REFERENCES

1. Weitzel, C.E., Palmour, J.W., Carter, C.H., *et. al.*, 1996, *IEEE Trans. Electron Devices*, **ED-43**, 1732.
2. Melloch, M.R. and Cooper, J.A., 1997, *MRS Bull.*, **22**(3), 42.
3. Cooper, J.A., 1997, *Materials Science Engineering B: Solid State Materials For Advanced Technology*, **44**(1–3), 38.
4. Giorgis, F., Pirri, C.F., Tresso, E., *et al.*, Rava, P., 1997, *Physica B*, **229**(3–4), 233.
5. Mott, N.F. and Davis, E.A., 1979, *Electronic Processes in Non-Crystalline Materials* (Oxford: Clarendon), p. 272.
6. Reitano, R., Baeri, P., and Marino, N., 1996, *Appl. Surf. Sci.*, **96–98**, 302–308.
7. Walton, C.D., Sands, D., and Key, P.H., Unpublished, University of Hull.
8. Cranton, W.M., Key, P.H., Sands, D., *et al.*, 1996, *Appl. Surf. Sci.*, **96–98**, 501.

Deposition of BCN Films by Laser Ablation

C. Popov*, B. Ivanov**, K. Masseli***, and V. Shanov**

* Central Laboratory of Photoprocesses "Academician Jordan Malinowski," Bulgarian Academy of Sciences,
Acad. Georgi Bontchev St., Bl. 109, Sofia, 1113 Bulgaria
** University of Chemical Technology and Metallurgy, Dept. of Semiconductors, 8 Kliment Ohridski St., Sofia, 1756 Bulgaria
*** University of Kassel, Institute of Technical Physics, 40 Heinrich-Plett St., Kassel, D-34109 Germany
e-mail: capopov@adm1.uctm.acad.bg
Received August 6, 1997

Abstract—Thin BCN films were deposited on monocrystalline silicon substrates by laser ablation at 510 nm using CuBr vapor laser. The target materials were synthesized from melamine and BCl_3 at 600 and 950°C, and the disks for laser irradiation were prepared by pressing the powders without binder. The focused laser beam scanned the targets with a speed of 4 μm/s. The element analysis by Auger electron spectroscopy (AES) showed that the layers were composed of B, C, and N with peaks at 177, 266, and 373 eV, respectively. A decrease of nitrogen content in the films compared to both starting materials was observed and the ratios of the main elements in the deposits were B : C : N = 3 : 9 : 2 and 6 : 2 : 1. Pulsed CuBr vapor laser irradiation probably caused partial destruction of the target material, accompanied by release of nitrogen-containing gas species. The formation of such species (N_2, NH_3, $(CN)_2$) was observed by quadrupole mass spectrometry during the deposition process. Fourier-transform infrared spectroscopy (FTIR) was used to derive structural information. The absorption bands at 1557, 1539, 1457, and 1436 cm^{-1} in IR spectrum of the films deposited from starting material synthesized at 600°C were attributed to the stretching vibration of the s-triazine ring. Therefore IR spectrum indicated that in the obtained layer the six-member (C_3N_3) rings remained undecomposed. The additional bands in the spectrum originated from the bridges between s-triazine rings, composing the layer. The IR spectrum of the films deposited from starting material synthesized at 950°C showed quite different pattern. The s-triazine rings were entirely decomposed above 620°C and the deposit was mixture of boron nitride and carbide (bands at 1404 and 1108 cm^{-1}). X-ray photoelectron spectroscopy (XPS) indicated that the atoms of all elements composing the films were in a wide variety of atomic arrangements and N–C, N–B and B–C bonds were established in the deposits. Electron diffraction (ED) showed that the films deposited from the starting material synthesized at 600°C had a layered graphite-like structure.

1. INTRODUCTION

Recently the interest in the materials of the ternary system containing boron, carbon, and nitrogen (BCN materials) has increased [1–13] since the properties of graphite-like BCN materials are expected to be hybrids of those of graphite and hexagonal boron nitride. For example, several types of semiconductors can be expected for these materials, depending on their composition and structure [1]. On the other hand, boron carbonitrides could be used as starting materials for the preparation of heterodiamond [2].

Thin films of BCN materials have been deposited by different techniques: chemical vapor deposition (CVD) using boron trichloride and ammonia as boron and nitrogen precursors, respectively, and methane [3, 4], acetylene [4–6] or propane [4] as carbon precursors; CVD from BCl_3 and acetonitrile [7–9] or acrylonitrile [10]; pyrolysis of borazine derivatives [11, 12] and amine boranes [13].

In this paper we report the deposition of thin BCN films by laser ablation using copper bromide vapor laser. This laser has a number of characteristics (wavelengths, repetition rate, and pulse width) which make it unique for applications in laser techniques. Our previous experience in laser processing with copper bromide vapor laser

showed substantial differences in processes mechanism compared to excimer lasers in case of polytetrafluoroethylene destruction [14] and to cw Ar⁺ laser in case of laser-induced chemical vapor deposition of Al from trimethylamine alane [15]. The target materials used in our experiments have been synthesized from melamine and BCl_3 at different temperatures. The s-triazine ring in melamine is rather stable (up to 620°C) [16] and the formation of layered materials, in which the s-triazine rings were preserved, has been reported [17, 18]. Melamine itself undergoes condensation with release of ammonia when heated above its melting point around 350°C and products with an increasing degree of condensation and composed of s-triazine rings bridged by NH groups were obtained in the temperature range of 350–620°C [19, 20]. In our case the condensation process proceeded in presence of BCl_3 and boron atoms were bound to nitrogen atoms of melamine condensates, giving in such way nitrogen-rich BCN materials.

2. EXPERIMENTAL

2.1. Target Materials

Nitrogen-rich BCN materials used as targets have been prepared by the reaction between melamine and

boron trichloride at different temperatures, as described previously [21]. The composition of the materials was dependent on the synthesis and annealing temperatures: $C_6N_{10.8-11}H_{9.4}B_{1.5-1.7}$ (for products synthesized and annealed at 400°C), $C_6N_{9.3-9.4}H_{3.8-3.9}B_{2.2-2.5}$ (for those synthesized at 400°C and annealed at 600°C) and $C_6N_{9.2}H_{3.6}B_{1.2-1.3}$ (for those synthesized and annealed at 600°C). FTIR and ^{13}C-nuclear magnetic resonance showed that the s-triazine rings from the melamine molecules were preserved in materials synthesized and annealed at 400 and 600°C. The sample obtained at 600°C had a graphite-like structure as suggested by X-ray and electron diffraction studies. The layers were composed of bridged s-triazine rings and the presence of bonds between boron, nitrogen and carbon atoms in the prepared materials was confirmed by XPS and FTIR. The s-triazine rings were decomposed in the materials synthesized or annealed at 950°C and the product obtained was a mixture of turbostratic boron nitride and boron carbide.

Two types of samples were used for the ablation experiments: samples synthesized and annealed at 600°C, and samples synthesized and annealed at 950°C. For ease these samples were named "yellow" and "grey" in correspondence with their color.

2.2. Experimental Procedure

The deposition of BCN thin films by laser ablation was carried out in vacuum chamber using the focused beam (20 µm) of copper bromide vapor laser with wavelengths of 510 and 578 nm (Laser Products Ltd.). The maximum laser output power was 5 W, the laser repetition rate 20 kHz and the pulse duration 60 ns. The target disks for laser irradiation (3 mm thick, 3 mm in diameter) were prepared by pressing the powders without binder. The disk of BCN material was placed on a holder in the chamber. The laser beam scanned the target with a speed of 4 µm/s. The films were deposited on monocrystalline silicon substrates (100) fixed on the holder, 12 mm apart from the target.

The changes in the gas phase during the ablation process were monitored *in situ* by a quadrupole mass spectrometer Leybold Inficon Quadrex-200. The elemental composition of the films was studied by Auger electron spectroscopy and chemical states by X-ray photoelectron spectroscopy on a VG ESCALAB II spectrometer. Infrared spectra were obtained on a spectrometer Bruker IFS 55. Electron diffraction data were collected using a transmission electron microscope Karl Zeiss EF 5.

3. RESULTS AND DISCUSSION

The element composition of the layers was studied by Auger electron spectroscopy (AES) and typical spectra for the two samples deposited from yellow and grey targets are presented in Fig. 1. As seen from this figure the both layers were composed of boron, carbon and nitrogen with peaks at 177, 266, and 373 eV, respectively. The peak
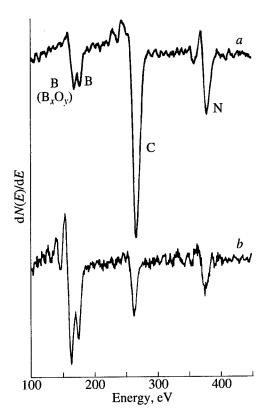
Fig. 1. Auger electron spectra of BCN films deposited by laser ablation: (a) from "yellow" target, (b) from "grey" target.

of oxidized boron can also been observed at 167 eV suggesting that the layers were oxidized after their exposure to the air prior the analyses. The element composition obtained by AES showed a ratio of the main elements in the deposits B : C : N = 3 : 9 : 2 (for the yellow target) and B : C : N = 6 : 2 : 1 (for the grey target). The compositions determined for the layers were compared to that of the target materials. Due to the high volatility of nitrogen with respect to the other elements of the target materials, growth of films with the same composition was a difficult task. It was found that the nitrogen content in the films deposited from the yellow targets has decreased while carbon and boron fractions were close to that in the target, and almost no changes were observed in the composition of the films deposited from the grey targets. This is an expected result having in mind the temperature for synthesis of the different target materials—600 and 950°C, respectively.

The ablation process was accompanied by *in situ* study of the gas phase composition by a quadrupole mass spectrometer. The mass spectrum of the gas products released during ablation of the yellow target is presented in Fig. 2. The most intensive peaks appeared at $m/z = 28, 17, 16, 14, 15, 52, 26$ corresponding to the formation of N_2^+, NH_3^+, NH_2^+, N^+, NH^+, $(CN)_2^+$, CN^+ species, respectively. We found that the main products from the laser ablation process were nitrogen N_2 with mass peaks at $m/z = 28$ (100%), 14 (5%), ammonia NH_3
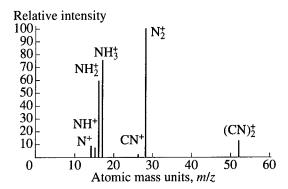
Relative intensity

Fig. 2. Mass spectrum of the gas products released during laser ablation of yellow target.

Relative transmission
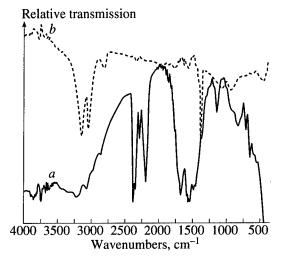
Fig. 3. IR spectra of BCN films deposited by laser ablation: (*a*) from yellow target, (*b*) from grey target.
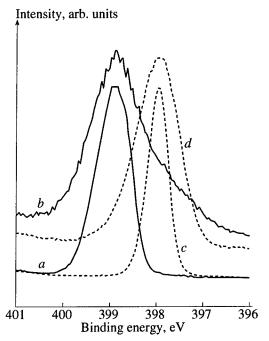
Intensity, arb. units

Fig. 4. XPS N_{1s} spectra: (*a*) melamine, (*b*) film deposited from yellow target, (*c*) h-BN, and (*d*) film deposited from grey target.

with mass peaks at $m/z = 17$ (100%), 16 (80%), 15 (8%), 14 (2%) and cyanogen $(CN)_2$ with mass peaks at $m/z = 52$ (100%), 26 (7%) [22, 23]. Probably CuBr vapor laser irradiation caused partial destruction of the target material, accompanied by release of nitrogen-containing gas species. Maya and coworkers have found that pyrolysis at 800°C of melamine, one of the starting materials for the synthesis of the target materials, resulted in formation of gas products: NH_3 (1.39 mol/mol melamine), N_2 (1.23 mol/mol) and HCN (0.97 mol/mol) [24]. The same gas products were detected in our case with the exception of HCN. This difference is probably due to the fact that greater part of hydrogen atoms from melamine molecules has been released in the form of NH_3 and HCl during the target materials synthesis. As a result of this, we observed formation of cyanogen $(CN)_2$ instead of hydrogen cyanide HCN. In contrast to the yellow target, no gas species were detected during ablation process from the grey target.

Fourier-transform infrared spectroscopy was used to derive structural information. The obtained IR spectra of the films were similar to that of the starting materials. The absorption bands at 1557, 1539, 1457 and 1436 cm^{-1} in IR spectrum (Fig. 3, curve *a*) of the films deposited from yellow target were attributed to the stretching vibration of the *s*-triazine ring [20]. Therefore IR spectrum indicated that in the obtained layer the six-member (C_3N_3) rings remained undecomposed. The additional bands at 3214 and 1650 cm^{-1} were attributed to N–H stretching and deformation vibrations, respectively, the bands at 1381 and 788 cm^{-1} could be assigned to B–N bonding and that at 1107 cm^{-1}, to C–B bonds. All these bands originated from the bridges between *s*-triazine rings, composing the layer. The IR spectrum of the films deposited from grey target showed quite different pattern. The *s*-triazine rings were entirely decomposed above 620°C and the deposit was mixture of boron nitride and carbide (bands at 1404 and 1108 cm^{-1}) (Fig. 3, curve *b*). The spectrum contained bands of hydrogen from the target material bonded to nitrogen (bands at 3143 and 3049 cm^{-1}) and to carbon (band at 2825 cm^{-1}).

The chemical states of the elements in the deposited layers were studied by XPS. The results for the composition of the films entirely supported the data obtained by AES. The shapes and positions of XPS peaks of the layers deposited from yellow and grey targets were compared to that of melamine (for N_{1s} and C_{1s}) and of h-BN (for N_{1s} and B_{1s}). The N_{1s} spectrum of the films deposited from yellow targets was broader compared to melamine (Fig. 4, curves *a* and *b*). The broadening suggested that the nitrogen atoms were in a wide variety of atomic environments. While the shoulder on the high-energy side of the peak was observed also for melamine (attributed to N–H), the shoulder on the low energy side indicated bonding with less electronegative atoms than carbon, i.e., with boron atoms. The N_{1s} peak of the films deposited from the grey targets was shifted
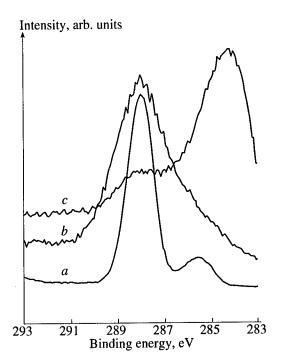
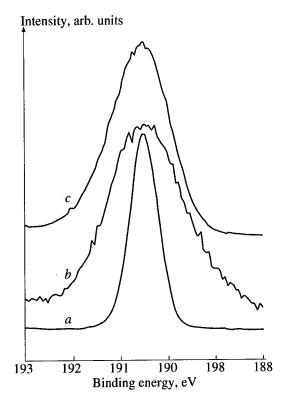Fig. 5. XPS C_{1s} spectra: (a) melamine, (b) film deposited from yellow target, and (c) film deposited from grey target.

Fig. 6. XPS B_{1s} spectra: (a) h-BN, (b) film deposited from yellow target, and (c) film deposited from grey target.

(–0.9 eV) due to the predominant N–B bonding (Fig. 4, curve d). The C_{1s} peak of the layers deposited from yellow targets had a shoulder at the low energy side due to bonds with boron atoms (Fig. 5, curve b). The shift in the C_{1s} peak position of films deposited from grey targets towards lower binding energy suggested that the predominant bonding was C–B [25] (Fig. 5, curve c). The weak peak at 287.6 eV was due to residual phase containing C–N bonds. The position of B_{1s} peak (190.4 eV) indicated that boron was bonded mainly to nitrogen in all samples (Fig. 6). The shoulder at the low energy side of the peaks supposed the formation of B–C bonds while that at the high energy side, the formation of B–O bonds due to the films oxidation.

The electron diffraction pattern taken using transmission electron microscopy from films deposited from yellow targets yielded fully developed rings although partial amorphisation was observed compared to the starting material. The interlayer spacing values calculated from ED pattern were 3.16, 2.03, and 1.58 Å and they coincided with those obtained for the target material. Such d-spacings are characteristic for (002), (101), and (004) reflections of turbostratic structure with disordered correlation between the planes. In such a way the ED showed that the deposited films had a graphite-like structure.

The results obtained by AES, FTIR, XPS, and ED showed that thin BCN films have been deposited by laser ablation using CuBr vapor laser. They layers had graphite-like structure and they were composed of bridged s-triazine rings.

4. CONCLUSIONS

Thin BCN films were deposited by laser ablation using CuBr vapor laser. The target were prepared from melamine and BCl_3 at 600 and 950°C. The films had different elemental composition depending on the starting materials. A decrease in nitrogen content was observed for the films deposited from target material synthesized at 600°C due to the formation of nitrogen containing gas products during ablation process. Although this change in composition, FTIR, XPS, and ED showed that the structure of the layers was similar to that of the target material—graphite-like with planes composed of bridged s-triazine rings. The films deposited from target material synthesized at 950°C had the same composition as the target. The s-triazine rings were entirely decomposed and the deposit was a mixture of boron nitride and carbide.

ACKNOWLEDGMENTS

REFERENCES

1. Kawaguchi, M. and Bartlett, N., 1994, Fluorine-Carbon and Fluoride-Carbon Materials: Chemistry, Physics,

and Applications, Nakajima, T., Ed. (New York: Marcel Dekker).

2. Bando, Y., Nakano, S., and Kurashima, K., 1996, J. Electron Microsc., **45**, 135.

3. Besmann, T.M., 1990, J. Am. Ceram. Soc., **73**, 2498.

4. Moore, A.W., Strong, S.L., Doll, G.L., et al., 1989, J. Appl. Phys., **65**, 5109.

5. Kaner, R.B., Kouvetakis, J., Warble, C.E., et al., 1987, Mat. Res. Bull., **22**, 399.

6. Saugnac, F., Teyssandier, F., and Marchand, A., 1992, J. Am. Ceram. Soc., **75**, 161.

7. Kouvetakis, J., Sasaki, T., Shen, C., et al., 1989, Synth. Metals, **34**, 1.

8. Morita, M., Hanada, T., Tsutsumi, H., et al., 1992, J. Electrochem. Soc., **139**, 1227.

9. Sasaki, T., Akaishi, M., Yamaoka, S., et al., 1993, Chem. Mater., **5**, 695.

10. Kawaguchi, M. and Kawashima, T., 1993, J. Chem. Soc., Chem. Commun., 1133.

11. Maya, L. and Harris, L.A., 1990, J. Am. Ceram. Soc., **73**, 1912.

12. Maya, L., 1988, J. Am. Ceram. Soc., **71**, 1104.

13. Riedel, R., Bill, J., and Passing, G., 1991, Adv. Mater., **3**, 551.

14. Ivanov, B., Popov, C., Lekova, M., et al., 1997, Appl. Surf. Sci., **108**, 297.

15. Popov, C., Ivanov, B., and Shanov, V., 1993, J. Phys. IV, **3**, 107.

16. Bann, B. and Miller, S.A., 1958, Chem. Rev., **58**, 131.

17. Kouvetakis, J., Bandari, A., Todd, M., et al., 1994, Chem. Mater., **6**, 811.

18. Kawaguchi, M. and Nozaki, K., 1995, Chem. Mater., **7**, 257.

19. May, H., 1959, J. Appl. Chem., **9**, 340.

20. Costa, L. and Camino, G., 1988, J. Thermal Anal., **34**, 423.

21. Popov, C., Saito, K., Yamamoto, K., et al., 1997, J. Mater. Sci. (in press).

22. Cornu, A. and Massot, R., 1975, Compilation of Mass Spectral Data (London: Heyden).

23. Stenhagen, E., Abrahamsson, S., and McLafferty, F.W., 1974, Registry of Mass Spectral Data (New York: John Wiley).

24. Maya, L., Cole, D.R., and Hagaman, E.W., 1991, J. Am. Ceram. Soc., **74**, 1686.

25. Moulder, J.F., Stickle, W.F., Sobol, P.E., and Bomben, K.D., 1992, Handbook of X-ray Photoelectron Spectroscopy, Chastain, J., Ed. (Minnesota: Perkin Elmer).

The Experience with Pulsed Laser Deposition of Nd : YAG and Nd : YAP Thin Films for Planar Laser Waveguides

J. Šonský*, M. Jelínek*, P. Hříbek**, J. Oswald*, L. Jastrabík*, V. Studnička*, C. Fotakis***, and C. Grivas***

* *Institute of Physics, Academy of Sciences of the Czech Republic, Na Slovance 2, Prague 8, 18040 Czech Republic*
** *Faculty of Nuclear Sciences and Physical Engineering, Czech Technical University, Department of Physical Electronics, V Holešovičkách 2, Prague 8, 18000 Czech Republic*
*** *Foundation for Research and Technology-Hellas, P.O. Box 1527, Heraklion, Crete, 71110 Greece*

Received August 8, 1997

Abstract—The thin films of YAG ($Y_3Al_5O_{12}$) and YAP ($YAlO_3$) doped with Nd were prepared by pulsed laser deposition on sapphire substrates of (0001) and ($1\bar{1}02$) orientations, and YAP substrate oriented as (001). The influence of the deposition parameters, i.e., the substrate temperature (T_S) and ambient O_2 pressure (p_O), on film properties including the structure, the morphology, the Al/Y ratio, the degree of incorporated Nd, and the refractive index was studied. The substrate temperature varied from 860°C to 1090°C and the O_2 pressure changed in the range from 8.5×10^{-3} Pa (vacuum) to 5.5 Pa. The experiments of amorphous films crystallization by thermal annealing in flowing Ar were carried out, and the change of structure and luminescence spectra are discussed. The film properties were characterized by XRD, SEM, electron microprobe, luminescence measurements, and mode spectroscopy.

1. INTRODUCTION

In recent years the laser amplifiers and laser generators in the form of thin planar waveguide film, channel waveguide or fiber have received great attention. Active devices combine the advantages of solid-state lasers and the waveguide medium. Thus, it allows one to create a miniature laser with high quality of output radiation, i.e., relatively narrow linewidth and large coherent length. Due to the waveguide geometry a high-energy confinement is available, which results in the large energy conversion efficiency along the full waveguide length. Especially in the active channel waveguide where the supported light mode is confined in both transversal directions, high gains and low threshold operations can be achieved [1]. They can also be easily coupled into the integrated optic systems and fibers.

YAG and YAP represent attractive laser host crystals with a narrow linewidth at wavelengths of 1064 and 1079 nm since laser action has been realized in Nd-doped YAG and YAP, respectively. The thin film for planar waveguide (PW) lasers has to be high epitaxial single-crystalline quality layer with minimum crystal defects and other scattering losses centers. For the film to act as a waveguide, the substrate must have a lower refractive index than that of the film. The substrate and film structure also have to correspond with the lattice mismatch smaller than 7%. Thus, the structural and refractive index requirements posed on the substrate strongly limited the substrate selection. YAG has cubic garnet structure ($a = 12.016$ Å) and refractive index of 1.816 at 633 nm [2], and YAP has orthorhombic perovskite structure ($a = 5.176$ Å, $b = 5.307$ Å, and $c = 7.355$ Å)

and refractive indices $n_\alpha = 1.929$, $n_\beta = 1.943$, and $n_\gamma = 1.952$ at 633 nm [2]. Although the other garnets and perovskites would be suitable substrates from structural point of view, their refractive indices exceed those of YAG or YAP [3]. So undoped YAG and YAP have been mainly used as substrates for preparation of Nd : YAG and Nd : YAP films. As it was demonstrated, the other promising substrate materials include especially sapphire [3] and MgO [4].

The broadly used technologies for creation of films for PW lasers including Nd-doped YAG and/or YAP layers, i.e., ion implantation [5], in-diffusion [6], and liquid-phase epitaxy [7], were enriched by pulsed laser deposition (PLD) very recently. Most importantly, PLD technique is able to reproduce the target stoichiometry onto the film and provides the epitaxial growing of thin films. Up to now the PW lasers of Nd : $Gd_3Ga_5O_{12}$ [8] and Ti : sapphire [9] were successfully grown by PLD; nevertheless, a variety of passive waveguide thin films were prepared. These include $LiNbO_3$ [10], $BaTiO_3$ [11], $KNbO_3$ [12], $LiTaO_3$ [13], etc. To our knowledge, the thin films of Nd : YAG have been prepared by PLD on various substrates such as Si (100), MgO (100), SGGG (111) (Zr- and Sc-doped $Gd_3Ga_5O_{12}$), and YAG (111) [4]; nevertheless, the waveguide effect has not been observed. In this study, we report the waveguide thin films of Nd : YAG and Nd : YAP prepared by PLD for the first time.

2. EXPERIMENTAL

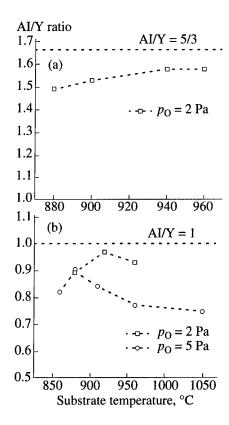The thin films of Nd : YAG and Nd : YAP were grown by PLD using KrF excimer laser (Lambda

Fig. 1. The substrate temperature dependence of Al/Y ratio for (a) Nd : YAG deposited films and (b) for Nd : YAP deposited films at different ambitient O_2 pressures p_O. The dashed lines represent bulk YAG and YAP crystal Al/Y ratio, respectively.
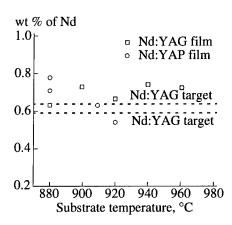

Fig. 2. The substrate temperature dependence of wt % of (square) Nd incorporated in grown Nd : YAG and (circle) Nd : YAP films. The dashed lines represent the wt % of Nd in Nd : YAG or Nd : YAP targets.

Physik LPX 200, $\lambda = 248$ nm, $\tau = 15$ ns, $f = 20$ Hz) with laser energy density of 3.1 J cm^{-2} on the target. We used monocrystalline YAG and YAP targets doped with 0.8 at. % of Nd and 0.74 at. % of Nd, respectively. The targets placed in the vacuum chamber were rotated during the deposition to keep the same condition for material ablation. The thin film of ablated target material

was grown on the substrate which was back-side heated by continuous 100-W CO_2 laser (Syndrad-model 57-1-28W, $\lambda = 10.6$ μm) with rf modulation to get the substrate temperature as high as 1000°C. The substrate temperature was measured by platinum–platinum–rhodium thermocouple. The substrate was placed into boron nitrid holder providing its homogenous heating and the target–substrate distance was 4 cm. We used sapphire substrates of (0001) and ($1\bar{1}02$) orientations for deposition of Nd : YAG films, and YAP (001) and sapphire (0001) substrates for deposition of Nd : YAP films. The substrate temperature T_S ranged from 860°C to 1090°C and the ambient O_2 pressure p_O in chamber pumped by turbomolecular pump varied from 8.5×10^{-3} to 5.5 Pa. The films of thickness of 6 μm were grown for 20 min and thicker films (thickness of 20 μm) of Nd : YAP on YAP (001) were grown for 100 min. To improve the crystalline quality of deposited films, the post-deposition annealing was carried out in flowing Ar at a set of temperatures from 1000 to 1400°C. The time of annealing was 5 and 10 h for 6 and 20 μm, thick films respectively.

The structure of films was analyzed by X-ray diffraction (XRD) measurements with a Bragg–Brentano powder diffractometer and Cu$K\alpha$ radiation. We observed the diffraction angle range from 15° to 65° in 2θ with a scanning step of 0.06° and exposition time per step of 2.5 s. The film stoichiometry was measured by electron microprobe analysis (JEOL JXA 733 superprobe) with microanalyzer KEVEX D-class V. Because the electron microprobe allows us to measure only the amount of heavy elements, the rates of Al, Y, and Nd in the films were measured. The film surface morphology was observed with scanning electron microscopy. The luminescence measurements of Nd^{3+} ions in prepared films were studied in the wavelength range from 1025 to 1125 nm with a scanning step of 0.25 nm at room temperature. The Nd^{3+} ions were excited by Ar^+ laser at 488 nm. The refractive index and the thickness of prepared films were measured by mode spectroscopy using the film-prism coupling. The mode spectroscopy, which is applicable only for the films acting as a waveguide, allows us to observed the waveguide effect. We have performed the measurements at wavelength of 632.8 nm for TE polarization using a He–Ne laser.

3. RESULTS AND DISCUSSION

Thin films of Nd : YAG and Nd : YAP have complicated composition even emphasized by the presence of Nd^{3+} doped ions. The ability of PLD to transform stoichiometrically the target composition into the film is related to the deposition parameters. The Al/Y ratio of Nd : YAG films is lower than the bulk YAG crystal ratio by 0.1 and slightly increases with T_S (in region of 880–960°C). The substrate temperature dependence of Al/Y ratio of Nd : YAG films prepared at $p_O = 2$ Pa is shown in Fig. 1a. In the case of Nd : YAP films, the Al/Y ratio
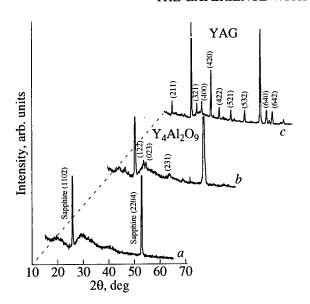
Fig. 3. The comparison of XRD patterns of Nd : YAG films grown at substrate temperatures of (a) 920°C, (b) 960°C, and (c) after thermal annealing in flowing Ar at 1300°C for 5 h.

Fig. 4. The comparison of XRD patterns of Nd : YAP films grown at following deposition parameters: (a) T_S = 920°C and p_O = 5 Pa, (b) T_S = 1050°C and p_O = 5 Pa, and (c) T_S = 1090°C and p_O = 8.5 × 10^{-3} Pa.

gets the best value at $T_S \approx$ 900°C dependently on p_O. The best value is lower than the bulk YAP crystal ratio by less than 0.1. With increasing and decreasing T_S (region of 860–1090°C) the Al/Y ratio decreases as it is shown in Fig. 1 (curve b) for p_O = 2 Pa and p_O = 5 Pa. All films appear to be slightly Al deficient. As concern of the amount of Nd, the wt % of Nd in prepared films is close to the target values and remains mainly independent on the deposition parameters. Figure 2 is a plot of the wt % of Nd in prepared films as a function of substrate temperature T_S.

The crystalline quality of prepared films varied with either deposition parameters and used substrate material. The XRD patterns of Nd : YAG films deposited on sapphire substrates at different substrate temperatures are shown in Fig. 3. Figure 3 (curve a) represents a film grown at T_S = 920°C which is completely amorphous with only the sapphire substrate peaks present. Figure 3 (curve b) shows that at T_S = 960°C a small amount of intermediate $Y_4Al_2O_9$ phase occurred. The Nd : YAG film has not been deposited at higher temperature. Subsequent thermal annealing of Nd : YAG films in flowing Ar caused the YAG crystallization at temperature of 1300°C or higher. Figure 3 (curve c) shows the XRD pattern of Nd : YAG film after thermal annealing at 1300°C which well corresponds with the polycrystalline YAG phase with micron-size grains. The YAG phase is produced through $Y_4Al_2O_9$ and YAP intermediate phases which are occurring at annealing temperatures of 1100°C and 1200°C, respectively. Nd : YAP films deposited at T_S below 1000°C on sapphire or YAP substrates were also completely amorphous or partly $Y_4Al_2O_9$ crystalline (Fig. 4 (curve a)). The growth of Nd : YAP films on YAP (001) substrate at T_S higher
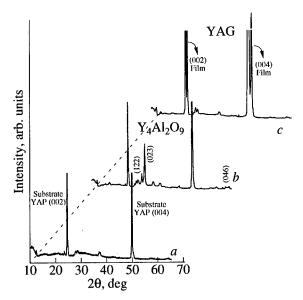
than 1000°C is strongly related to the O$_2$ pressure p_O. The epitaxial YAP film is grown on YAP (001) at T_S = 1090°C and p_O = 8.5 × 10^{-3} Pa as it is shown in Fig. 4 (curve b). The shift of lattice d-spacing of YAP (004) film peak by 0.047 Å is caused by high intrinsic strain between the film and the target. With increasing of ambient O$_2$ pressure, we assumed O$_2$ diffusion into the growing film has occurred, which results in the growth of textured oxygen-enriched $Y_4Al_2O_9$ phase in orientation of (023) as it is shown in Fig. 4 (curve c) for deposition at T_S = 1050°C and p_O = 5 Pa. The subsequent thermal annealing at temperatures below 1200°C did not change the crystalline quality.

The surface morphology of waveguide films deposited by PLD is negatively influenced by the presence of droplets which cause the additive losses of supported light mode. The presence of droplets can be eliminated by adjusting of deposition parameters. We have found that $T_S \approx$ 900°C and $p_O \approx$ 2 Pa are the deposition parameters regions leading to creation of high transparent quality films with minimum droplets on the surface. With increasing of p_O over 2 Pa the number of droplets increased as it is illustrated in Fig. 5. The films deposited at high temperature $T_S \approx$ 1100°C and under vacuum pressure $p_O \approx$ 10^{-3} Pa lose the transparency and include high number of droplets.

In the luminescence spectra (Fig. 6) of all deposited films, we observed $^4F_{3/2} \longrightarrow {}^4I_{11/2}$ transitions of Nd^{3+} ions in YAG or YAP in the region of 1.06 or 1.79 μm, respectively. Figure 6a shows the luminescence spectra of Nd^{3+} ions in typical Nd-doped amorphous YAP film grown at T_S below 1000°C The luminescence lines are inhomogeneously broadened due to different distribution of local sites of Nd^{3+} ions in amorphous film.
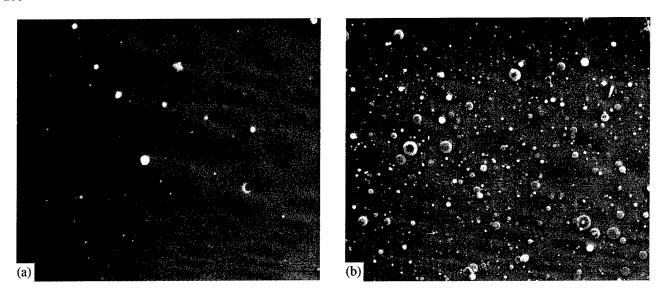
Fig. 5. The SEM pictures (magnification ×1000) of Nd : YAP films grown on YAP (001) at T_S = 880°C and two different p_O: (a) p_O = 2 Pa and (b) p_O = 5 Pa.
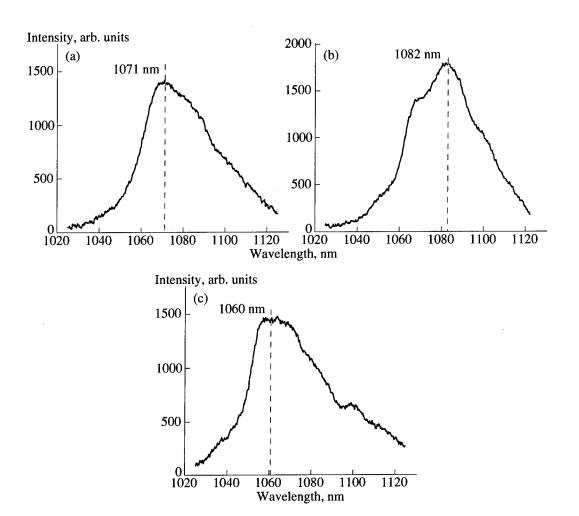

Fig. 6. The luminescence spectra of Nd : YAP films created on YAP (001) at following deposition parameters: (a) T_S = 920°C and p_O = 5 Pa, (b) T_S = 1090°C and p_O = 8.5 × 10^{-3} Pa, and (c) T_S = 1050°C and p_O = 5 Pa.
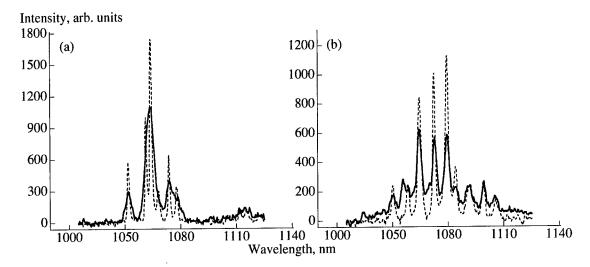
Fig. 7. The luminescence spectra of (a) Nd : YAG film and (b) Nd : YAP film after thermal annealing in flowing Ar at temperature of 1300°C and 1200°C, respectively, for 5 h. The dashed lines represent the luminescence spectra of Nd^{3+} ions in YAG and YAP bulk targets, respectively.

The luminescence spectra of Nd^{3+} ions in epitaxial crystalline Nd : YAP film grown at $T_S = 1090°C$ and $p_O = 8.5 \times 10^{-3}$ Pa on YAP (001) substrate are shown in Fig. 6b. We can observe only partial separation of luminescence lines, which indicates that the clystalline surrounding of N^{3+} ions is still not well defined, although XRD measurements proved the presence of epitaxial crystalline YAP (001) phase. For comparison, the luminescence spectra of Nd^{3+} ions in film grown at 1050°C and $p_O = 5$ Pa on YAP (001) substrate are presented in Fig. 6c. As we can see, the surrounding of Nd^{3+} ions defined by $Y_4Al_2O_9$ phase which is present in this film causes the significant shift of the maximum peaks toward to the lower wavelength region around 1.06 μm. Figure 7 shows the comparison of the luminescence spectra of Nd^{3+} ions in polycrystalline YAG and YAP films after thermal annealing at temperature of 1300°C and 1200°C, respectively. We can clearly observe the splitting of luminescence spectra into a set of separated lines. The dashed line in Fig. 7 corresponds with the luminescence spectra of Nd^{3+} ions in YAG or YAP target.

We observed a waveguide effect of all deposited films and they supported from 6 to 30 TE modes dependently on the film thickness. The refractive index of Nd : YAG films grown on sapphire substrates was 1.808 at wavelength 632.8 nm for TE modes. Due to the film amorphization this value is lower by 0.008 as compared to that of Nd : YAG bulk crystal. In the case of amorphous Nd : YAP film, the amorphization removes the birefringence and it is possible to use only single value of refractive index. Measured refractive index of Nd : YAP films deposited on sapphire substrates was 1.842 at wavelength of 632.8 nm for TE modes. The refractive index of films was not measured after thermal annealing because the annealing caused the crystallization into micron-size grains and the pres-

ence of numerous grain boundaries causes extremely high scattering of coupled mode. We can observe only the local waveguide effect.

4. CONCLUSION

We have created, for the first time, Nd-doped YAG and YAP waveguide thin films by PLD for use as a planar waveguide laser. The structure, stoichiometry, surface morphology, luminescence, and waveguide properties were studied in dependence on the substrate temperature and ambient O_2 pressure. As a substrate we used sapphire of (0001) and (1102) orientations and YAP (001). We have found very good stoichiometry transformation of Nd, Al, and Y from targets into films in the whole region of deposition parameters, i.e., T_S: 880–1090°C and p_O: 8.5×10^{-3}–5.5 Pa. In the case of deposition of Nd : YAP film, we have observed the best Al/Y ratio at $T_S = 900°C$ which slightly varied around this value dependently on the p_O. The number of droplets on the film surface also minimized as the film grown at $T_S \approx 900°C$ and $p_O \approx 2$ Pa. XRD measurements proved that the substrate temperatures T_S below 1000°C are not sufficient for creation of crystalline phase and the grown films are amorphous. Growth of Nd : YAP films on YAP (001) substrate at $T_S \approx 1100°C$ is strongly influenced by p_O, the epitaxial Nd : YAP film is grown at vacuum pressure of 10^{-3} Pa and textured oxygen enriched $Y_4Al_2O_9$ in orientation of (023) is formed at $p_O = 5$ Pa. The amorphous film crystallized into YAG or YAP after thermal annealing at temperature of 1300°C or 1200°C, respectively. The luminescence spectra of Nd^{3+} ions in amorphous films are broadened and the splitting into separated lines occurs after thermal annealing. All deposited films exhibited excellent waveguide effect.

The study showed that it is possible to create crystalline Nd-doped YAG or YAP films on sapphire substrate by PLD, although sapphire has a different crystal structure. It is necessary to use substrate temperatures of 1200°C and 1300°C to create YAG and YAP crystalline phase, respectively. The subsequent thermal annealing of deposited amorphous films is practically insufficient because it leads to creation of numerous micron-size grains which cause high scattering losses of coupled mode.

ACKNOWLEDGMENTS

REFERENCES

1. Gill, D.S., Eason, K.W., Mendiola, J., and Chandler, P.J., 1995, *Mater. Let*, **25**, 1.
2. Kaminskii, A.A., 1975, *Laser Crystals*, (Moscow: Nauka (in Russian)).
3. Grabmaier, J.G., Grabmaier, B.C., Kersten, R.Th., *et al.*, 1973, *Phys. Lett. A*, **43**, 219.
4. Ezaki, M., Kumagai, H., Kobayashi, K., *et al.*, 1995, *Jpn. J. Appl. Phys.*, **34**, 6838.
5. Chandler, P.J., Field, S.J, Hanna, D.C., *et al*, 1989, *Electron. Lett.*, **25**, 985.
6. Hickey, L.M.B., Anderson, A.A., and Wilkinson, J.S., 1997, *Europ. Conf Int. Opt.*, Paper PDC-1.
7. Hanna, D.C., Large, A.C., Shepherd, D.P., *et al.*, 1992, *Opt. Commun.*, **91**, 229.
8. Gill, D.S., Anderson, A.A., Eason, R.W., *et al.*, 1996, *Appl. Phys. Lett.*, **69**, 10.
9. Jelínek, M., Eason, R.W., Lančok, J, *et al.*, 1996, *Proc. SPIE*, **2888**, 51.
10. Haruna, M., Ishizuki, H., Tsutsumi, J., *et al.*, 1995, *Jpn. J. Appl. Phys.*, **34**, 6084.
11. Okada, T., Nakata, Y., Kaibara, H., and Meada, M., 1995, *Jpn. J. Appl. Phys.*, **34**, 1536.
12. Zaldo, C., Gill, D.S., Eason, R.W., *et al.*, 1994, *Appl. Phys. Lett.*, **64**, 502.
13. Xie, H., Hsu, W.Y, and Raj, R., 1995, *J. Appl. Phys.*, **77**, 3420.

Condensation of Vapor and Nanoclusters Formation within the Vapor Plume, Produced by ns-Laser Ablation of Si

B. S. Luk'yanchuk*, W. Marine**, and S. I. Anisimov***

* General Physics Institute, Russian Academy of Sciences, Moscow, 117942 Russia
e-mail: lukyanch@kapella.gpi.ru
** UMR CNRS 6631, Faculte des Sciences de Luminy, Marseille, 13288 France
e-mail: marine@gpec.univ-mrs.fr
*** L. D. Landau Institute for Theoretical Physics, Russian Academy of Sciences, Chernogolovka, 142432 Russia
e-mail: anisimov@landau.ac.ru
Received August 7, 1997

Abstract—The condensation within the expanding vapor plume produced by ns-laser ablation is discussed within the frame of Zeldovich and Raizer theory of condensation. The calculations have been done for the Si vapor. It is shown that the size of clusters formed during the condensation is very small because of fast expansion of the plume and quenching phenomena. The average cluster radius is calculated for different temperatures and densities of initial plume and it is typically of the order of few nanometers. The generalization of the theory is made for inhomogeneous plume where the rates of nucleation as well as condensation times are different for different parts of the plume. As a result, the distribution in cluster's size appears. Nevertheless, this distribution function is very sharp for the plume expanding in vacuum. For the clusters moving together with vapor one can distinguish three different waves propagating through the plume: (1) wave of saturation where the vapor becomes saturated, (2) supercooling wave where the highest supercooling is reached, and (3) the quenching wave. Parameters for these waves are calculated. The possibility of oscillation phenomena during condensation is discussed as well.

1. INTRODUCTION

The physics of nanoclusters should be attributed to one of the most intensively developing branches of modern physics. The nanoclusters occupy the intermediate position between the quantum objects (atom, molecules) and macroscopic objects, i.e., bulk materials. Thus, many properties of nanoclusters differ from both the quantum objects and bulk materials. This is of great practical and scientific interest [1–3]. The fast development of this scientific branch is caused by creation of reliable methods of cluster formation, including condensation of vapor during the fast expansion of pulsed laser ablation products. The latter method permits to generate clusters of any materials with sizes typically by order of 10–1000 Å [1–6].

There is an important problem related to control of cluster size distribution produced by laser ablation. In an ideal situation it is desirable to form monosize clusters. Nevertheless it is not possible to do so for principal reasons—clusters of different sizes are forming during the expansion of inhomogeneous plume. The recent paper [7] considers that the distribution function arises due to cluster coalescence caused by collisions between the clusters. Thus, the authors of [7] modeled the cluster growth on the basis of Lifshitz and Slyozov theory (see, e.g., [8]).

Meanwhile it is easy to estimate that for the typical conditions of nanosecond laser ablation of Si and evaporation in vacuum, the collisions between clusters are

very rare and coalescence is unimportant. We have also mentioned that a long duration stage of very slow cluster growth exists before the coalescence stage. During this stage the distribution function is "frozen" (see, e.g., [9])

Within the present paper we consider that coalescence is unimportant and discuss another effect related to the formation of distribution function due to the difference in condensation time in different parts of the plume. Roughly speaking, big clusters are formed within the center of the plume, while the smallest clusters are formed near the plume edge. For the theoretical analysis we used Zeldovich and Raizer (ZR) theory of condensation [10–12]. This theory refers to the initial stage of condensation process in contrast with Lifshitz and Slyozov theory which is applicable for the last stage of the condensation process (see, e.g., discussion in [8]).

An important part of the theory is the description of the nuclei production in oversaturated vapor. This description can be done on the basis of Zeldovich kinetic equation [10] which describes the production rate of overcritical nuclei (see also [8, 13]). Raizer [11] applied this kinetic equation (together with equation for the rate of droplet growth and the adiabatic equation in the condensation region) for the analysis of the problem of cosmic dust production during a collision (and further vaporization) of a large meteorite with the surface of a planet without an atmosphere. It was found that the degree of condensation, number of clusters and their size strongly depend on the velocity of the vapor expansion,

which, in turn, depends on the initial size of the vapor, evaporated mass, and internal energy. It was also shown in [11, 12] that condensation stops because of the quenching phenomenon.

Although ZR theory does not contain any fitting parameter, it is applicable (with small corrections) for the description of condensation within appreciably different conditions (it is sufficient to mention a tremendous difference, sixteen orders of magnitude, in evaporated mass of the meteorite discussed in [11] and typical evaporated mass in laser ablation experiments and also a large difference in many other parameters).

Applying the ZR theory, we introduce a few corrections related to the peculiarities of the vapor plume produced in laser ablation experiments. First, we discuss the cooling rate of vapor, which is several orders of magnitude higher than in [11, 12]. Thus, all the important events (formation of the condensation region, production of nuclei, etc.) occur during the nonlinear stage of expansion, while in [11] calculations have been done for the linear stage (inertial expansion). For this reason we discuss a more general description of the plume expansion.

Second, the nuclei produced in laser ablation plume have the size near the critical $r \approx r_k$. Thus, it is necessary to include the influence of curvature into the equation for the droplet growth. It was not very important in [11], where drops had a big size, $r \gg r_k$. We also made improvements in the procedure of the initial conditions calculation (initial condition for the droplet growth is not strictly defined within ZR theory).

The third correction refers to the estimation of the quenching time, $t = t_q$. In Raizer's paper the criterium $\theta q/T \approx 1$ was used for this estimation, where θ is supercooling, T is temperature, and q is the heat of vaporization (in Kelvin). The physical meaning of this criterium is a strong disturbance in thermodynamic "equilibrium" between the deposition and evaporation processes. We use another estimation which shows the moment of time when the collisions stop within the expanding vapor. This criterium yields approximately 2.5 times higher value of t_q, but it does not influence strongly the final size of condensed droplets (difference smaller than 10%). However, this difference can be easily detected experimentally (for example, with the help of time-of-flight mass spectrometry [14]).

Raizer's examination was developed for homogeneous plume. It can be applied also to inhomogeneous plume under the assumption that the condensed droplets are moving together with vapor. The latter permits one to estimate the distribution function of condensed particles, which is done in the present paper.

The paper is organized as follows: We discuss the gas dynamics of the plume expansion in Section 2 and the mentioned modifications introduced within ZR theory in Sections 3-5, where the main equations are formulated. Then we analyze Si-nanoclusters formation within Si-vapor plume produced in vacuum by ns-laser

ablation (Section 6). The main results of these studies are summarized in the conclusion (Section 7).

2. GAS DYNAMICS OF THE PLUME EXPANSION

Within the paper of Raizer [11] the simplified model of the spherical plume expansion was used, namely, the averaged vapor density was taken in the following form:

$$\rho(t) = \frac{3M}{4\pi R^3}, \quad R(t) = R_0 + ut, \tag{1}$$

where M is the total mass of the vapor, R_0 is initial radius of the plume, and $u = \sqrt{2E/M}$ = const is the velocity of expansion, related to initial internal energy E of the plume.

A more accurate description can be made on the basis of special solution of the gas dynamic equations (see, e.g., [15]), which yields the following law for isentropic expansion:

$$\left(\frac{R}{R_0}\right)^2 = \Psi(t) \equiv 1 + 2\frac{u_0}{R_0}t + \left[\left(\frac{u_0}{R_0}\right)^2 + \frac{16}{3}\frac{E}{MR_0^2}\right]t^2, \tag{2}$$

where u_0 is the initial velocity of the plume expansion. This solution holds for monoatomic gas with adiabatic exponent $\gamma = c_p/c_v = 5/3$. The general solution for arbitrary γ is given in the Appendix.

For the later stage of expansion from (2) follows the linear law (inertial expansion). The density, specific volume, pressure and temperature profiles within the plume are given by

$$\rho(t) = \rho_0(1 - \xi^2)^{3/2}\Psi(t)^{-3/2},$$
$$\rho_0 = \frac{8}{\pi^2}\frac{M}{R_0^3}, \tag{3}$$

$$V(t) = V_0(1 - \xi^2)^{-3/2}\Psi(t)^{3/2},$$
$$V_0 = \frac{\pi^2}{8}\frac{R_0^3}{M}, \tag{4}$$

$$P(t) = P_0(1 - \xi^2)^{5/2}\Psi(t)^{-5/2},$$
$$P_0 = \frac{128}{15\pi^2}\frac{E}{R_0^3}, \tag{5}$$

$$T(t) = T_0(1 - \xi^2)\Psi(t)^{-1}, \quad T_0 = \frac{\mu}{R_g}\frac{16}{15}\frac{E}{M}, \tag{6}$$

where $\xi = r/R(t)$ is the Lagrangian coordinate within the vapor ($0 \leq \xi \leq 1$), R_g is the gas constant, and μ is the atomic weight of the vapor.

We shall consider that small droplets of condensed vapor *move together with the vapor*. For this case the

condensation process can be discussed for each fixed Lagrangian coordinate ξ independently. Here, we assume that the condensation process does not change the expansion dynamics of the plume. For arbitrary value of ξ one can write the change of specific volume in the following form:

$$\frac{1}{V}\frac{dV}{dt} = \frac{3}{2}\frac{1}{\Psi}\frac{d\Psi}{dt}. \qquad (7)$$

This law will be used for further calculations.

3. THE SATURATION AND QUENCHING WAVES

The condensation process starts when the plume becomes saturated and stops when the plume starts to expand in collisionless (free-flight) regime. Within the inhomogeneous plume, saturation and free-flight regimes are reached for each point in different moments of time, i.e., saturation and quenching waves propagate through the expanding vapor.

Before the condensation starts, the expansion of the plume occurs along the Poisson adiabat $PV^\gamma = \mathrm{const}$. It is convenient to write this equation in $\{V, T\}$ coordinates, $TV^{\gamma-1} = \mathrm{const}$. Thus, for monoatomic gas

$$V = V_0\left[\frac{T}{T_0}\right]^{-3/2}. \qquad (8)$$

This expansion continues up to the moment when the Poisson adiabat intersects the saturated vapor adiabat given by Clapeyron–Klausius equation [16]

$$P = P_S\left(\frac{T_S}{T}\right)^{1/2}\exp\left[-\frac{q}{T}\right], \qquad (9)$$

where q is the heat of vaporization given in Kelvin, $T_S = 300$ K, P_S is preexponential factor. This equation in $\{V, T\}$ coordinates is given by

$$V = B\left(\frac{T}{T_S}\right)^{3/2}\exp\left[\frac{q}{T}\right], \qquad (10)$$

where $B = R_g T_S/\mu P_S$.

Condensation starts at the moment $t = t_c$ when the vapor is cooled up to the temperature $T = T_c$. This condensation temperature follows from (8) and (10). It is given by $T_c = q\Phi(a)$, where $\Phi(a)$ is the smaller root of the transcendental equation (the second, larger root, has no physical sense)

$$\Phi^{-3}\exp\left[-\frac{1}{\Phi}\right] = a, \quad a = \frac{B}{V_0}\left(\frac{q^2}{T_S T_0}\right)^{3/2}. \qquad (11)$$

Parameter a is typically small, $a \ll 1$. This permits us to write the approximate solution of (11) as

$$T_c \approx q\left\{\ln\left(\frac{1}{a}\right) + 3\ln\left[\ln\left(\frac{1}{a}\right) + 3\ln\ln\left(\frac{1}{a}\right)\right]\right\}^{-1}. \qquad (12)$$
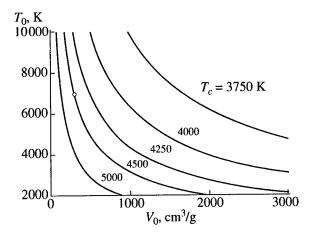
Fig. 1. Condensation isotherms T_c on the plane of parameters T_0, V_0.

It should be noted that T_c depends on initial parameters V_0 and T_0. At the same time it does not depend on Lagrangian coordinate ξ, i.e., we obtain the same condensation temperature for different parts of the given plume. This condensation temperature T_c is shown in Fig. 1. Parameters of silicon [17] which have been used in calculations are presented in Table 1.

The moment t_c when condensation starts, depends on Lagrange coordinate, i.e., the different parts of the plume start to condense at different moments. This moment of time can be found from the equation

$$\Psi(t_c) = \frac{T_0}{T_c}(1 - \xi^2). \qquad (13)$$

According to (13), the saturation wave propagates through the plume from its periphery to the center. The boundary of this wave $r = r_c(t)$ moves according to

$$\frac{r_c(t)}{R(t)} = \sqrt{1 - \frac{T_c}{T_0}\Psi(t)}. \qquad (14)$$

The plot of this function is shown in Fig. 2. For calculations we used parameters of vapor given in Table 2.

Table 1. Parameters of Si [17] which have been used in calculations

Parameter	Value
Density of condensed phase, ρ_c [g/cm^3]	2.4
Atomic weight, μ [g/mole]	28
Heat of vaporization, q [K]	50165
Normalization temperature, T_s [K]	300
Preexponential factor, P_s [atm]	6.72×10^6
B [cm^3/g]	1.31×10^{-4}
Surface tension, σ [erg/cm^2]	750
Cross section of collisions, σ_g [cm^2]	1.72×10^{-15}
Melting temperature, T_m [K]	1685
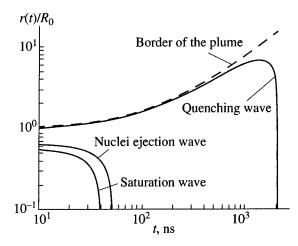
Fig. 2. Propagation of saturation, quenching, and "ejection" waves through the Si-vapor plume with parameters of vapor given in Table 2.

Value of u_0 was measured experimentally [18]. For these parameters $T_c = 4500$ K (the corresponding point is shown in Fig. 1). Propagation of saturation wave strongly depends on initial velocity of the plume expansion, u_0. For example, for $u_0 = 0$ saturation wave reaching point $r = 0$ (i.e., the whole plume becomes saturated) at the moment $t = 231$ ns while for $u_0 = 6 \times 10^5$ cm/s this time is 40 ns. Also, we note that for the profiles given by (3)–(6), part of the plume with $r > 0.6 R_0$ is situated within the region of saturation from the initial moment of time $t = 0$.

Now we should find the moment of time when the condensation will stop due to the so-called "quenching effect." It occurs because the collisions within the expanding vapor will stop at some stage of expansion (see more detail in [12]). A careful examination of this quenching effect needs the solution of Boltzmann kinetic equation.

We shall give the simplest estimation of this quenching time by a different way. Namely, to find the boundary $r = r_q(t)$ between the collision (hydrodynamic) and collisionless (free-flight) regions of the plume we use the criterium $l\nabla v = v_s$. Here, $l = 1/\sigma_g N = m/\sigma_g \rho(r)$ as the mean free path within the hydrodynamic region (σ_g is the cross section of collisions), and v_s is the velocity of sound at the given point. The mean-

ing of this criterium is rather simple. We consider that collisions exist until the neighbor particles (separated by l distance) may be connected by sound signal. Substituting the value of the hydrodynamic velocity gradient $\nabla v = \dot{R}/R = \frac{1}{2} \Psi^{-3/2} \dfrac{d\Psi}{dt}$ and sound velocity from

$$v_s(r) = \sqrt{\frac{5}{3}\frac{k_B T}{m}} = \sqrt{\frac{5}{3}\frac{k_B T_0}{m}}\Psi^{-1/2}\left(1 - \frac{r^2}{R^2}\right)^{1/2}, \quad (15)$$

we find the equation for the boundary of quenching wave

$$\frac{r_q}{R} = \sqrt{1 - \left(t_k \Psi \frac{d\Psi}{dt}\right)^2}^{1/2},$$

$$\text{where } t_k = \frac{m V_0}{2\sigma_g}\sqrt{\frac{3}{5}\frac{m}{k_B T_0}}. \quad (16)$$

It can be seen from (16) and (2) that at $u_0 = 0$ the collisionless region spreads from the outer part of the plume $r = R_0$ (at $t = 0$). With $u_0 > 0$, the outer part of the plume spreads from the beginning in free-flight regime. Finally, at $u_0 > u_k = R_0/2t_k$ the whole plume expands in collisionless regime. This critical velocity, u_k, is typically very high for developed ablation regime; however, it can be reached for subthreshold fluences when the evaporated mass M is extremely small. Our calculations show the strong influence of the initial velocity u_0 value on the quenching process. The whole plume becomes collisionless at $t = 5963$ ns with $u_0 = 0$ and at $t = 2071$ ns with $u_0 = 6 \times 10^5$ cm/s.

The propagation of the saturation and quenching waves through the plume is shown in Fig. 2. The picture is given in Euler's coordinates, the border of the expanding plume is shown in Fig. 2 as well. It can be seen from the figure that the linear stage of the plume expansion starts at around 700 ns; thus, all important events within the plume occur during the nonlinear stage of expansion.

The third wave shown in Fig. 2 refers to the trajectory where the maximum of supersaturation is reached. At this condition the nuclei are formed ("ejected" into the saturated vapor). The equation for this wave will be obtained further on [see (37)].

Table 2. Initial parameters of the plume which have been used in calculations

Initial parameters of the plume	Value
Initial temperature, T_0 [K]	7000
Initial specific volume, V_0 [cm³/g]	300
Initial size, R_0 [cm]	0.1
Initial pressure, P_0 [atm]	68.4
Initial velocity of expansion, u_0 [cm/s]	6×10^5

4. THERMODYNAMICS OF TWO-PHASE REGION

When the vapor becomes saturated and condensation starts, the matter within the plume is presented by two-phase system "condensed phase + vapor." One can denote the degree of condensation, x, as a ratio of the number density of molecules in the condensed phase to the total number density. If one supposes there is a thermodynamic equilibrium within the system, then the evolution of the system follows to equilibrium adiabat

of the "two-phase" region. This adiabate can be found from the equations ([11, 12])

$$[c_v(1-x) + c_l x]dT + \frac{R_g}{\mu}T(1-x)\frac{dV}{V}$$
$$= \left[\frac{R_g}{\mu}q - (c_l - c_v)T\right]dx \tag{17}$$

and

$$\frac{V}{(1-x)} = B\left(\frac{T}{T_S}\right)^{3/2}\exp\left[\frac{q}{T}\right]. \tag{18}$$

Equation (17) presents the energy balance for adiabatic process; here, c_v and c_l are the heat capacities of vapor (at constant volume) and liquid. For the problem under consideration one can put $c_v = 3R_g/2\mu$ and $c_l = 3R_g/\mu$. Equation (18) presents the saturation adiabat (10) where the specific volume of vapor is replaced by a specific volume of the original material. The system of equations should be solved together with initial condition

$$V|_{T=T_c} = V_c \equiv B\left(\frac{T_c}{T_S}\right)^{3/2}\exp\left[\frac{q}{T_c}\right] \tag{19}$$

$$\text{or } x|_{T=T_c} = 0.$$

It is convenient to exclude specific volume V from (17)–(19) and introduce the new variable $y = q/T$ ($y_c = q/T_c$) instead of temperature T. Then the problem under consideration is reduced to linear differential equation [19]

$$\frac{dx}{dy} + \frac{x}{y-1/2} = \frac{1-3/y}{y-1/2}, \quad x|_{y=y_c} = 0. \tag{20}$$

Integration of (20) yields the equilibrium degree of condensation within the vapor,

$$x_{eq} = \frac{2q}{2q-T}\left[\frac{T_c-T}{T_c} + 3\frac{T}{q}\ln\left(\frac{T}{T_c}\right)\right]. \tag{21}$$

One can find the adiabat of thermodynamically equilibrium two-phase system substituting (21) into (18),

$$V_{eq} = (1 - x_{eq}(T))B\left(\frac{T}{T_S}\right)^{3/2}\exp\left[\frac{q}{T}\right]. \tag{22}$$

We denote the temperature along the equilibrium adiabat as equilibrium temperature T_{eq}. If the specific volume changes versus time according to (4), then the variation of equilibrium temperature $T_{eq}(t)$ can be found from (22):

$$V_0\Psi^{\frac{3}{2}} = \left\{1 - \frac{2q}{2q-T_{eq}}\left[\frac{T_c-T_{eq}}{T_c} + 3\frac{T_{eq}}{q}\ln\left(\frac{T_{eq}}{T_c}\right)\right]\right\}$$
$$\times B\left(\frac{T_{eq}}{T_S}\right)^{3/2}\exp\left[\frac{q}{T_{eq}}\right]. \tag{23}$$

The variation of equilibrium degree of condensation is given by (21) where $x_{eq}(t) = x_{eq}[T_{eq}(t)]$. Using relation (7) one can rewrite the adiabatic equation (17) in the following form

$$(1+x)\frac{dT}{dt} + (1-x)\frac{T}{\Psi}\frac{d\Psi}{dt} = \left(\frac{2}{3}q - T\right)\frac{dx}{dt}, \tag{24}$$
$$T|_{t=t_c} = T_c.$$

It is easy to see that the functions $T_{eq}(t)$ and $x_{eq}(t)$ fulfill (24) automatically. Thus, for sufficiently slow expansion, when according to thermodynamics $x(t) \longrightarrow x_{eq}(t)$, the evolution of the system occurs near the equilibrium phase trajectory defined by (22). For a sufficiently fast expansion the phase trajectory can deviate from the equilibrium one. The similar phenomena can be seen quite often in nonequilibrium chemical kinetics [20].

One can see from (21) that at unrestricted vapor expansion, at the conditions close to equilibrium (i.e., when this expansion is realized rather slowly), the vapor should condense completely, $x_{eq}|_{T\to 0} \longrightarrow 1$. At the case of fast expansion, the complete condensation does not occur due to quenching effect, i.e., $x \longrightarrow x_q$, where $0 < x_q < 1$.

The formal solution of (24) with $x = x_q = \text{const}$ yields the "quenching adiabate"

$$V = V_q\left[\frac{T}{T_q}\right]^{-\frac{3}{2}\left(\frac{1+x_q}{1-x_q}\right)}, \tag{25}$$

which coincides with the Poisson adiabat with a renormalized adiabatic exponent. Thus, one can say that the quenching process goes along the Poisson quenching adiabat. However, this is rather formal, because the equation (24) is not valid to describe the collisionless vapor. It is more consequent to describe this effect in terms of "frozen temperature" T_q which corresponds to averaged kinetic energy of free-flight particles within the vapor.

In collisionless regime, the clusters cooling rate is mostly determined by radiation heat loss. This cooling is quite fast for small clusters. For this situation, discussed further in calculations, the time necessary for cooling of a 15-Å cluster from the quenching temperature $T_q = 2185$ K to the melting temperature T_m is $\Delta t \approx 370$ ns. It means that small clusters are deposited typically in solid-state phase.

The equilibrium temperature $T_{eq}(t)$ (23) and the temperature $T = T_p(t)$ (6) are shown in Fig. 3 together with calculated temperature $T(t)$.

5. KINETICS OF CONDENSATION

According to (2) and (6), the cooling rate at the condensation point is given by

$$\frac{dT}{dt}\Big|_{t=t_c} = -(1-\xi^2)\frac{2T_c^2}{T_0}\frac{u_0}{R_0}\left(1 + \frac{u_0 t_c}{R_0} + \frac{16}{3}\frac{Et_c}{MR_0 u_0}\right). \tag{26}$$

Temperature, T, K

Supercooling, θ

Degree of condensation, x
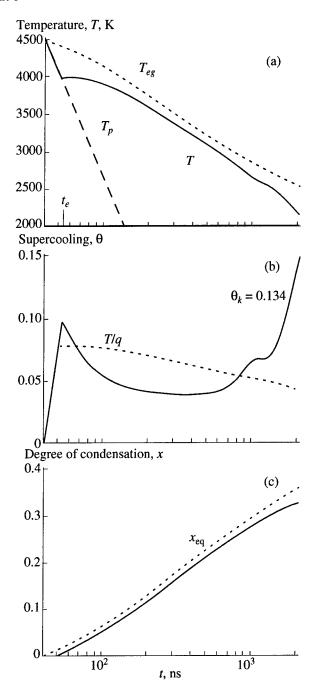
Fig. 3. Dynamics of the condensation process at adiabatic vapor expansion at $\xi = 0$. (a) Temperature $T(t)$ of Si vapor. Symbol T_P denotes the temperature along the Poisson adiabat (6), and T_{eq} is the equilibrium temperature from equation (23). (b) Supercooling $\theta = \theta(t)$ from calculations (solid line). The dotted curve presents dependence $\theta = T/q$ versus time. (c) Degree of condensation $x = x(t)$. Symbol x_{eq} denotes the equilibrium degree of condensation (21).

For the example shown in Fig. 3, this value is by order of 10^{11} K/s. It is evident that at such a high cooling rate vapor continues to expand during some time "by inertia" along the Poisson adiabat. As a result, vapor becomes oversaturated and the nucleation starts.

Later the supersaturation drops because of the formation of critical nuclei and their further growth. The change of oversaturation is caused by the interplay between the rate of cooling (due to work of vapor expansion) and rate of heating (due to latent heat of condensation).

The condensation kinetics is guiding by the value of supercooling (see, e.g., [12, 13]):

$$\theta = \frac{T_{eq} - T}{T_{eq}}. \tag{27}$$

We can write now the kinetic equations, assuming that for the given Lagrangian coordinate all the condensed clusters (nuclei) are of the same size.

Let us consider that each cluster consists of $g = g(t)$ atoms. We denote as $v = v(t)$ the number of condensation centers (per atom of vapor). Then the degree of condensation is given by

$$x(t) = v(t)g(t). \tag{28}$$

Correspondingly, the rate of condensation can be presented as

$$\frac{dx}{dt} = g\frac{dv}{dt} + v\frac{dg}{dt}, \quad x|_{t=t_c} = 0. \tag{29}$$

The first term in (29) describes the change of condensation due to the formation of nuclei, while the second one describes the change of condensation caused by cluster growth. Once again we emphasize that equations (28) and (29) are written for fixed Lagrangian coordinate.

The rate of nucleation can be described by solution of Zeldovich's kinetic equation [10]. The stationary solution of this equation (see, e.g., [8]) yields

$$\frac{dv}{dt} = k_v(1-x)(1-\xi^2)^{3/2}\Psi^{-3/2}\exp\left[-\frac{T_v}{T}\frac{1}{\theta^2}\right], \tag{30}$$

$$v|_{t=t_c} = 0,$$

where

$$k_v = \frac{\rho_0}{\rho_l}4\sqrt{\frac{2\sigma}{\pi m}}, \quad T_v = \frac{16\pi\sigma^3 m^2}{3k_B^3 q^2 \rho_l^2}. \tag{31}$$

Here, we use notation σ for the surface tension. Pre-exponential factor in (30) is proportional to density of vapor. The equation (30) differs from the Raizer equation by factor $(1-x)(1-\xi^2)^{3/2}\Psi^{-3/2}$.

Ions may play an important role at the condition of high supercooling $\theta > \theta_k$, where θ_k is critical supercooling for charged particles [11]. At $\theta > \theta_k$ the charged complexes of all sizes exhibit a tendency to grow without limit. For Si $\theta_k = 0.134$. At $\theta \longrightarrow 0$ the difference in nucleation of charged and uncharged particles disappears [11]. Thus, as a first approximation, one can neglect the influence of ionization onto the nucleation process (if θ is smaller and not very close to θ_k).

The equation for the growth of cluster can be written under the assumptions used in [11] that the growth of nuclei occurs in kinetically controlled regime, accommodation coefficient is equal to unity, and temperatures of gas and droplet are equal. Then

$$\frac{dg}{dt} = 4\pi r^2 (j_d - j_e), \tag{32}$$

where the flux of deposited atoms is given by $j_d = \frac{1}{4} n v_T$,

$n = \frac{\rho}{m}$ is the number density of atoms in gas, $v_T = \sqrt{\frac{8 k_B T}{\pi m}}$ is the arithmetic mean velocity (see, e.g., [21]).

The flux of evaporated atoms can be presented in the following form:

$$j_e = n_l v_l \exp\left[-\frac{q}{T}\left(1 - \frac{r_0}{r}\right)\right], \tag{33}$$

where v_l is preexponential factor in evaporation law, $n_l = \frac{\rho_l}{m}$ is the number density of atoms in condensed phase, term $\left(1 - \frac{r_0}{r}\right)$ takes into account the surface tension effect, $r_0 = \frac{2\sigma\omega}{k_B q}$, $\omega = m/\rho_l$ is volume per atom in liquid. The radius of critical nucleus is given by $r_k = r_0/\theta$. For nucleus of critical size, the balance of evaporated and deposited fluxes should take place. This condition permits us to exclude factor $n_l v_l$ within the equation for droplet growth, which is transformed to

$$\frac{dg}{dt} = \pi r^2 n v_T \left[1 - \exp\left(-\frac{q}{T}\theta\left(1 - \frac{r_k}{r}\right)\right)\right]. \tag{34}$$

This equation is different from the equation which has been used in [11] by general factor 1/4 (probably, misprinting) and factor $\left(1 - \frac{r_k}{r}\right)$, which describes the difference in evaporation from spherical and flat surfaces. This factor was not very important in [11], where drops had a big size $r \gg r_k$, but it is very important for the problem under discussion where sizes r and r_k are comparable.

Using $r = \left(\frac{3}{4\pi}\frac{mg}{\rho_l}\right)^{1/3}$ and formula (3) for the gas density we can rewrite (34) in the following form:

$$\frac{dg}{dt} = k_g g^{\frac{2}{3}} \sqrt{T}(1-x)(1-\xi^2)^{3/2}\Psi^{-3/2}$$
$$\times \left\{1 - \exp\left[-\frac{q}{T}(\theta - \alpha g^{-1/3})\right]\right\}, \quad g|_{t=t_s} = g_0, \tag{35}$$

where

$$k_g = \frac{\pi\rho_0}{m}\left(\frac{3}{4\pi\rho_l}\frac{m}{}\right)^{2/3}\sqrt{\frac{8k_B}{\pi m}}, \quad \alpha = \frac{2\sigma\omega}{k_B q}\left(\frac{4\pi}{3\omega}\right)^{1/3}. \tag{36}$$

The initial value of g_0 and "ejection time," t_e, should be found in a self-consistent way, using the assumption that cluster formation starts at the moment when supercooling reaches its maximum, and the smallest critical nuclei are ejected at this moment. Thus, $g_0 = g(t_e) = g_{min} = (\alpha/\theta_{max})^3 \gg 1$, where g_{min} is the number of atoms within the smallest critical nuclei. Remember that Zeldovich kinetic equation considered g as a continuous variable and applicable just for macroscopic description, i.e., $g \gg 1$.

To find time t_e we used the following procedure: During the initial stage, temperature T follows very close to Poisson adiabat $T = T_p(t)$, see (6), and one can put supercooling $\theta_p = 1 - T_p(t)/T_{eq}(t)$. Degree of condensation is also very small and one can neglect x within equation (24). The latter yields the moment t_e when the supercooling reaches extremum, $(d\theta/dt)|_{t=t_e} = 0$. This consideration yields the transcendental equation for t_e:

$$\frac{1}{T_{eq}}\frac{dT_{eq}}{dt} = -\frac{1}{\Psi}\frac{d\Psi}{dt} + \left[\frac{2}{3}\frac{q}{T_p} - 1\right]\left(\frac{\alpha}{\theta_p}\right)^3\frac{dv}{dt}. \tag{37}$$

The derivative dv/dt in (37) is taken along the Poisson adiabat, $T = T_p$. For the given example, this equation yields for the center of the plume $t_e = 52.6$ ns and $g_{min} \cong 16.5$ atoms. The plot of the function $r = r(t_e)$ is shown in Fig. 2. It corresponds to the propagation of the "nuclei ejection" wave.

It is also convenient to recalculate the other initial conditions to the moment t_e:

$$T|_{t=t_e} = T_p(t_e), \quad g_0 = g(t_e) = g_{min},$$

$$v|_{t=t_e} = v_0 = \int_{t_c}^{t_e} \frac{dv}{dt}\bigg|_{T=T_p(t)} dt, \tag{38}$$

and $x|_{t=t_e} = x_0 = g_0 v_0.$

Thus, for the description of the condensation process we use the system of four ordinary differential equations for four unknown functions $T(t)$, $x(t)$, $v(t)$, and $g(t)$ together with corresponding boundary conditions at the moment $t = t_e$.

6. NUMERICAL SIMULATION AND DISCUSSION

It should be noted that the "prehistory" of the system, for $t_c < t < t_s$, cannot be described well by the model. Calculations with initial condition $g_0 < g_{min}$ show the dissociation of subcritical nucleus, while at $g_0 > g_{min}$ it starts to grow. At the limit case $g_0 = g_{min}$ we observed that an effect of the numerical instability perturbations pushed the system either into the dissociation

Number of clusters, v
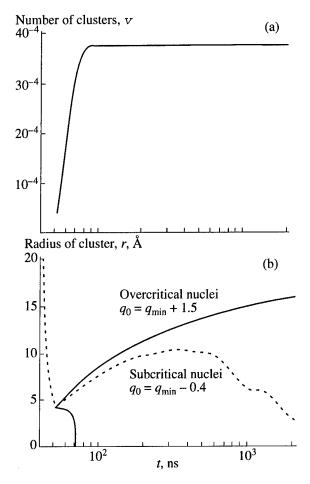
Fig. 4. Kinetics of condensation process at adiabatic vapor expansion. (a) Number of clusters $v(t)$ per atom of Si vapor. (b) Radius of growing cluster $r = r(t)$. Solid lines with $g_0 > g_{min}$ and $g_0 < g_{min}$ show the evolution of overcritical and subcritical nuclei, respectively. Symbol r_k denotes the critical radius for $g_0 > g_{min}$ (dotted line).

or condensation regions. In order to relieve these instabilities and taking into account that the Zeldovich equation describes the production of slightly overcritical nuclei, we use the following approximation: $g_0 = g_{min} + 1.5$, i.e., $g_0 = 18$ for $\xi = 0$.

The dynamics of the temperature $T(t)$, supercooling $\theta(t)$, and degree of condensation $x(t)$ from numerical solution of the system is presented in Fig. 3. Integration was done with the Mathematica software package [22]. The change of the temperature $T(t)$ (Fig. 3a) firstly follows along the Poisson adiabat, then after the start of nuclei formation it approaches the equilibrium temperature T_{eq}, and finally deviated from T_{eq} during the quenching. This behavior is typical for ZR theory.

Correspondingly, the supercooling (see Fig. 3b) reaches its first maximum at $t = t_e$, then it falls down, and finally increases up to the quenching time $t = t_q$. At the final stage of condensation, supercooling reaches the critical value θ_k, where condensation on ions becomes dominant. It does not influence strongly

the final size of the nuclei, because it takes place within the region $\theta q/T > 1$. For the given example, time t_R, which corresponds to $\theta q/T = 1$, is ≈ 830 ns. As it was mentioned above, this time $t = t_R$ was taken in [11] as an approximation of the end of condensation. Strictly speaking, for $\theta q/T > 1$ the kinetic equation of the droplet growth should be modified and the effects related to the difference in temperatures of the droplet and vapor should be taken into account. We have noted that this condition $\theta q/T > 1$ is also fulfilled at the initial stage of the process after a nuclei ejection. A careful examination of the case $\theta q/T > 1$ needs solving of Boltzmann equation. The stationary solution of the given problem was done in [23] but we did not find the general solution for the nonstationary situation.

Another important effect which can be seen in Fig. 3b is the oscillation in supercooling, which occurs at $t > 1000$ ns. This effect was not mentioned in [11], although the physics of this effect is rather simple. During the increase of supercooling, the rate of nuclei production and liberation of latent heat increase. At some conditions, the heat release may overcome cooling caused by the plume expansion. It leads to oscillation phenomena. These oscillations are very pronounced within some region of parameters T_0 and V_0 (for example, at $T_0 = 9000$ K and $V_0 = 300$ cm^3/g). If the amplitude of these oscillations is sufficiently high, then a new portion of nuclei is ejected during the condensation. Their further growth leads to the production of clusters of different size. A detailed discussion of these oscillation effects in condensation will be published elsewhere.

Change of the degree of condensation, x, versus time is shown in Fig. 3c. It is shifted to the lower value compared to equilibrium one, $x < x_{eq}$. Although the final value, $x = 0.33$, is close to those obtained in [11] for iron meteorite ($x = 0.4$), there is a large difference in the number and size of clusters due to a significant difference in cooling rates. These characteristics for Si vapor are shown in Fig. 4.

It can be seen from Fig. 4a that the number of clusters is practically a step-like function. Such behavior is in good agreement with the assumption that clusters within the vapor are practically of the same size (for the given Lagrangian coordinate). A cluster starts to grow from 18-atom nuclei and finally it contains approximately 880 atoms. For a comparison, the average number of atoms within the cluster which was found in [11] was $\approx 10^{10}$ atoms.

The radius of a growing cluster versus time is shown in Fig. 4b. From the figure we can see that a long stage of condensation occurs with $r \approx r_k$ where the effect of curvature is important. The final size of cluster for the given example is close to the minimal size of Si clusters (diameter 1–3 nm), obtained experimentally at low He background gas pressure [4]. The resulting size of the forming cluster depends on the initial parameters of the plume, its mass, volume, and temperature. The plots
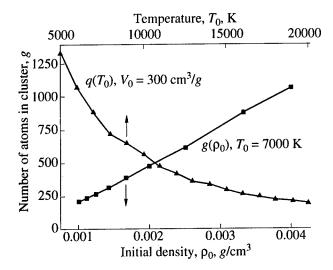
Fig. 5. Number of atoms within the cluster versus temperature (triangles, upper axis) and density (squares, bottom axis).

Fig. 6. The normalized distribution function $f(r)$. Normalization corresponds to $\int_0^\infty f(r)dr = 1$.

given in Fig. 5 illustrate dependencies of the cluster size versus the plume temperature and the specific volume. Although one can see from the calculations that the cluster size falls down with an increase of the temperature (at fixed specific volume), it is difficult to realize this experimentally, for example, by a variation of laser parameters. Indeed, the increase of laser fluence leads to an increase of T_0 but it leads simultaneously to a decrease of V_0, i.e., the compensation effect takes place. Thus, to investigate the optimal laser control of the cluster formation one should solve the laser ablation problem (to find parameters T_0, V_0, etc.) together with the hydrodynamic condensation problem.

In our calculations, we did not find any strong influence of the change of the surface tension, σ, on the rate of cluster formation (this effect was mentioned in [7]). From our point of view, the drastic change of the rate of the cluster growth is related not to the surface tension value by itself but to the above-mentioned sensitivity of the growth kinetics to the initial conditions (see Fig. 4b). We should emphasize that during the size evolution, nuclei should overcome the "narrow throat" of critical size near the maximum of oversaturation.

The calculations given above were made for the center of the plume, $\xi = 0$. The calculations were performed by the same way for arbitrary Lagrangian coordinate. This calculation shows that the cluster size moving along the Lagrangian coordinate from the plume center to the plume edge decreases while the number of clusters (per atom) increases. Thus, the degree of condensation from equation (28) varies slowly along ξ, but the decrease of the condensation also was obtained at the plume edge. To calculate dependencies $g(\xi)$ and $v(\xi)$ near the plume edge we use a smooth extrapolation of $g(\xi)$ and $v(\xi)$ by the best fitting cubic polynomial functions.
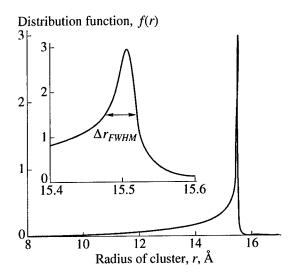
From $g(\xi)$ and $v(\xi)$ we plot the cluster size distribution function $f(r)$ (Fig. 6). The number of clusters produced within the interval $d\xi$ is given by

$$dN = 4\pi\frac{\rho_0 R_0^3}{m}(1-\xi^2)^{3/2}v(\xi)\xi^2 d\xi, \qquad (39)$$

and variation in their size is $dr = \frac{dr}{d\xi}d\xi$. Thus, the distribution function can be defined as

$$F(r) = -\frac{dN}{dr} = -\frac{32M}{\pi}\frac{v(\xi)\xi^2(1-\xi^2)^{3/2}}{m}\frac{}{dr/d\xi}. \qquad (40)$$

Here, $dr/d\xi < 0$; thus, $F(r)$ is positive. This distribution function has the usual meaning, $F(r)dr$ shows the probability to find clusters with sizes between r and $r + dr$. The distribution function $F(r)$ is normalized to the total number of clusters, N, produced during the condensation:

$$\int_0^\infty F(r)dr = N = \frac{32M}{\pi}\frac{1}{m}\int_0^1(1-\xi^2)^{3/2}v(\xi)\xi^2 d\xi. \qquad (41)$$

For the given example $N = 5 \times 10^{13}$ clusters. Instead of $F(r)$ we use the normalized distribution function, $f(r) = F(r)/N$. One can see from Fig. 6 that the obtained distribution function is extremely sharp. The half-width at half maximum of the distribution function is $\Delta(2r)_{FWHM} \approx 0.1$ Å.

We have to note that in most of the experimental works (e.g., [4, 6]) the distribution function of Si clusters shows a significant broadening. The high rate of Si clusters generation during these experiments was

observed during laser ablation of silicon into the background gas, which changes the expansion dynamics.

However, in our approach the distribution function also can be wider under the conditions when the pronounced oscillations in condensation take place or in the case of plume expansion into the surrounding media or in the case when the plume is asymmetrical (nonspherical). Analysis of these factors is out of the frame of the presented paper. We have only noted that the analysis of the asymmetrical 3D plume expansion can be done similarly to [24].

7. CONCLUSION

In this paper we discussed the peculiarities of fast condensation of vapor and nanocluster formation within the plume induced by pulsed laser ablation. The generalization of the Zeldovich-Raizer theory is done for inhomogeneous plume. The restrictions of the theory are discussed as well.

The calculations were made for Si-vapor plume produced at typical conditions of excimer ns-laser ablation. Results of the investigation can be summarized as follows:

(1) The typical cooling rate within the laser-produced plume is very high, by the order of 10^{11} K/s. Thus, the main events in the condensation process (formation of the condensation region, production of nuclei, clusters growth) occur during the nonlinear stage of the plume expansion. This stage was described by the particular solutions of gas dynamic equations. Important parameters guiding the expansion are initial plume size, total evaporated mass, internal energy, and initial velocity of expansion, u_0. In our calculations we used the experimental value $u_0 = 6 \times 10^5$ cm/s.

(2) Three waves propagate through the expanding plume: (a) wave of saturation; (b) supercooling wave, where the nuclei are ejected; and (c) the quenching wave, where the condensation stops. We found the basic equations for the propagation of these waves.

(3) At parameters used in calculations, clusters start to grow from 18 atoms (within the critical nuclei) to 880 atoms as final, which corresponds to cluster diameter ≈ 30 Å. The significant stage of the cluster growth occurs near the critical radius; thus, effects related to nuclei curvature are very important. We show that the size distribution function of clusters is extremely sharp. For the spherical plume which expands in vacuum the half-width at half maximum of the distribution function is $\Delta(2r)_{FWHM} \approx 0.1$ Å. The experimentally observed broadening of the size distribution function [4] is probably determined by the asymmetrical plume expansion.

The studies of the dependence of the cluster size versus the initial plume temperature and density show that for the fixed density of evaporated atoms, clusters become smaller at higher temperature T_0.

(4) We demonstrate the possibility of oscillation phenomena in condensation and we show that within some region of parameters these oscillations can produce clusters of different sizes.

APPENDIX

Special Solution of Gas Dynamic Equations

The spherical plume expansion is described by solution of gas dynamic equations

$$\frac{\partial \rho}{\partial t} + \frac{1}{r^2}\frac{\partial}{\partial r}(r^2 \rho v) = 0, \tag{A.1}$$

$$\frac{\partial v}{\partial t} + v\frac{\partial v}{\partial r} + \frac{1}{\rho}\frac{\partial P}{\partial r} = 0, \tag{A.2}$$

$$\frac{\partial P}{\partial t} + v\frac{\partial P}{\partial r} + \gamma P\frac{1}{r^2}\frac{\partial}{\partial r}(r^2 v) = 0, \tag{A.3}$$

where ρ, P, and v are density, pressure, and velocity within the vapor and $\gamma = c_p/c_v = \text{const}$ is the adiabatic exponent.

The self-similar isentropic solutions are sought in the following form (see, e.g., [15]):

$$v = r\frac{\dot{R}}{R}, \tag{A.4}$$

$$\rho = \frac{M}{I_1 R^3}\left[1 - \frac{r^2}{R^2}\right]^{\frac{1}{\gamma-1}}, \tag{A.5}$$

$$P = \frac{E}{I_2 R^3}\left(\frac{R_0}{R}\right)^{3(\gamma-1)}\left[1 - \frac{r^2}{R^2}\right]^{\frac{\gamma}{\gamma-1}}, \tag{A.6}$$

where normalization constants $I_1 = I_1(\gamma)$ and $I_2 = I_2(\gamma)$ are determined from the conditions of mass M and energy E conservation,

$$I_1 = \frac{\pi^{3/2}\Gamma\left(\dfrac{\gamma}{\gamma-1}\right)}{\Gamma\left(\dfrac{\gamma}{\gamma-1}+\dfrac{3}{2}\right)}, \quad I_2 = \frac{\pi^{3/2}}{\gamma-1}\frac{\Gamma\left(\dfrac{\gamma}{\gamma-1}+1\right)}{\Gamma\left(\dfrac{\gamma}{\gamma-1}+\dfrac{5}{2}\right)}, \tag{A.7}$$

where $\Gamma(x)$ is the gamma function [25].

Substituting distributions (A.4)–(A.6) into the set of gas dynamic equations, one can easily find that the continuity equation (A.1), as well as the entropy conservation equation (A.3), are fulfilled identically. The Euler's equation (A.3) is transformed into the ordinary differ-

ential equation which describes the motion law for expanding plume boundary,

$$\frac{d^2R}{dt^2} = (5\gamma - 3)\frac{E}{M}\frac{1}{R}\left(\frac{R_0}{R}\right)^{3(\gamma-1)},$$

(A.8)

$$R|_{t=0} = R_0, \quad \frac{dR}{dt}\bigg|_{t=0} = u_0.$$

The first integral of this equation is similar to energy conservation law in classical mechanics,

$$\left(\frac{dR}{dt}\right)^2 = u_0^2 + \frac{2}{3}\left(\frac{5\gamma-3}{\gamma-1}\right)\frac{E}{M}\left[1 - \left(\frac{R_0}{R}\right)^{3(\gamma-1)}\right].$$

(A.9)

The further integration of this equation yields the solution in the form of inverse function $t = t(R)$. This solution is represented through the hypergeometric function $_2F_1(a, b; c; z)$ [25], where parameters a, b, and c are

$$a = \frac{1}{2}, \quad b = -\frac{1}{3(\gamma-1)}, \quad c = 1 + b. \quad (A.10)$$

The final formula is given by

$$t^* = \left[u^{*2} + \frac{2}{3(\gamma-1)}\right]^{-\frac{1}{2}}$$

$$\times \left\{ R^*{}_2F_1\left[a, b; c; \frac{R^{*-3(\gamma-1)}}{1 + \frac{3}{2}(\gamma-1)u^{*2}}\right] \right.$$

(A.11)

$$\left. - {}_2F_1\left[a, b; c; \frac{1}{1 + \frac{3}{2}(\gamma-1)u^{*2}}\right] \right\}.$$

Here, we used the nondimension variables

$$t^* = \frac{t}{t_0}, \quad t_0 = R_0\sqrt{\frac{1}{5\gamma-3}\frac{M}{E}},$$

(A.12)

$$R^* = \frac{R}{R_0}, \quad u^* = \frac{u_0t_0}{R_0}.$$

This function $t^* = t^*(R^*)$ depends on two parameters: adiabatic exponent, γ, and initial velocity of the plume expansion, u^*. The behavior of this function is shown in Fig. 7.

It is easy to see directly from (A.9) that the velocity of expansion tends to constant $dR/dt \longrightarrow u_\infty$ for sufficiently extended time (inertial stage of expansion), where

$$u_\infty^2 = u_0^2 + \frac{2}{3}\frac{5\gamma-3}{\gamma-1}\frac{E}{M}.$$

(A.13)
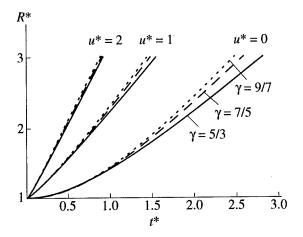
Fig. 7. Plots of dependencies $R^* = R^*(t^*)$ according to (A.11) for different values of parameters γ and u^*. Three curves with $\gamma = 5/3$ (solid), 7/5 (dash), and 9/7 (dots) are shown for three values of velocity $u^* = 0$, 1, and 2.

For the particular case $\gamma = 5/3$ from (A.11), a simple formula which has been used in calculations follows

$$\left(\frac{R}{R_0}\right)^2 = \Psi(t) \equiv 1 + 2\frac{u_0}{R_0}t$$

(A.14)

$$+ \left[\left(\frac{u_0}{R_0}\right)^2 + \frac{16}{3}\frac{E}{MR_0^2}\right]t^2.$$

REFERENCES

1. 1994, *Clusters of Atoms and Molecules*, Springer Series in Chemical Physics, vol. 52, Haberland, H. Ed. (Berlin: Springer).
2. Melinon, P., Paillard, V., Dupuis, V., *et al.*, 1995, *Int. J. Mod. Phys. B*, **9**, 339.
3. Smirnov, B.M., 1994, *Usp. Fiz. Nauk*, **164**, 1165; **164**, 665.
4. Marine, W., Movtchan, I., Simakine, A., *et al.*, 1996, *Mat. Res. Soc. Symp. Proc.*, Singh, R., Norton, D., Laude, L., *et al.*, Eds. (Pittsburgh) 397, 365.
5. van de Riet, E., Nillesen, C.J.C.M., and Dieleman, J., 1993, *J. Appl. Phys.*, **74**, 2008.
6. Yoshida, T., Takeyama, S., Yamada, Y., and Mutoh, K., 1996, *Appl. Phys. Lett.*, **68**, 1772.
7. Callies, G., Schittenhelm, H., Berger, P., and Hudel, H., 1997, *Abstracts of EUROMECH Colloquium 363 "Mechanics of Laser Ablation"* (Novosibirsk), 11.
8. Lifshitz, E.M. and Pitaevsky, L.P., 1979, *Physical Kinetics*, (Moscow: Nauka) (in Russian).
9. Bäuerle, D., 1996, *Laser Processing and Chemistry*, 2nd ed. (Berlin: Springer).
10. Zeldovich, Ya.B., 1942, *Sov. Phys. JETP*, **12**, 525.
11. Raizer, Yu.P., 1960, *Sov. Phys. JETP*, **37**, 1229.
12. Zeldovich, Ya.B. and Raizer, Yu.P., 1966, *Physics of Shock Waves and High-Temperature Hydrodynamic Phenomena*, (New York: Academic).

13. Frenkel, Ya.I., 1945, *Kinetic Theory of Liquids*, (Moscow: Acad. Sci.).

14. Ehbrecht, M., Ferkel, H., Holz, L., *et al.*, 1995, *J. Appl. Phys.*, **78**, 1.

15. Anisimov, S., Bäuerle, D., and Luk'yanchuk, B., 1993, *Phys. Rev. B*, **48**, 12076.

16. Landau, L.D. and Lifshitz, E.M., 1976, *Statistical Physics* (Moscow: Nauka) (in Russian) part 1.

17. 1972, *American Institute of Physics Handbook*, 3rd ed., Gray, D.E. Ed. (New York: McGraw-Hill).

18. Santis, M., Patrone, L., Luk'yanchuk, B., *et al.* to be published.

19. Anisimov, S.I. and Khokhlov, V.F., 1995, *Instabilities in Laser-Matter Interaction* (London: CRC).

20. Karlov, N.V., Kirichenko, N.A., and Luk'yanchuk, B.S., 1997, *Laser Thermochemistry: Fundamentals and Applications*, (Cambridge: Cambridge Interscience Press).

21. Hirschfelder, J.O., Curtiss, C.E., and Bird, R.B., 1967, *Molecular Theory of Gases and Liquids* (New York: John Willey & Sons).

22. Wolfram, S., 1991, *Mathematica* 2nd ed., (Addisson-Wesley).

23. Hubmer, G.B. and Titulaer, U.M., 1990, *J. Stat. Phys.*, **59**, 441; 1991, **63**, 203.

24. Anisimov, S., Luk'yanchuk, B., and Luches, A., 1996, *Appl. Surf. Sci.*, **96–98**, 24.

25. Gradshteyn, I.S. and Ryzhik, I.M., 1957, *Table of Integrals, Series, and Products* (New York: Academic).

Study of the Fabrication of the Channel Waveguide in Ti : Sapphire Layers

J. Lancok, M. Jelínek, J. Bulíř and P. Macháč*

Institute of Physics, Academy of Sciences of the Czech Republic, Na Slovance 2, 18040 Prague 8, Czech Republic
e-mail lancok@fzu.cz
* *Institute of Chemical Technology, Technická 5, Prague 6, 166 28 Czech Republic*
Received August 8, 1997

Abstract—The reactive ion etching (RIE) and the laser ablation by KrF excimer laser of Ti : sapphire have been investigated as a potential means for micropatterning thin deposited layers for preparation of the channel waveguide lasers. The RIE was performed in BCl_3 : He atmosphere. To obtain the high etching selectivity between sapphire and mask, the photoresist, SiO_2, tantalum, and platinum were used as masks. Dependencies of etched rate and etched selectivity between masks and sapphire on the reactor pressure, on the rf power and on the ratio BCl_3 : He were investigated. The maximum etch rate of Ti : sapphire and 11.9 nm/min together with etch selectivities between sapphire platinum equal to 3.87 and between sapphire and SiO_2 equal to 0.55 were achieved. The rib guides were fabricated from thin layers. The laser patterning of Ti : sapphire by using KrF excimer laser was also studied. To optimize the patterning process, the ablation threshold 1.36 J/cm^2 and absorption coefficient $\alpha = 1.81 \times 10^5$ cm^{-1} were determined. The etch rate and quality of the irradiated surface for KrF laser ablation of Ti : sapphire were examined.

1. INTRODUCTION

The planar waveguide laser configuration assures a good overlap between the pump and the emitted laser beams, leading to high slope efficiencies and decreasing of the threshold pump power. Because the laser threshold depends on the product of the vertical and horizontal spot sizes, a further order of magnitude reduction in threshold should be obtained in channel waveguides based on low loss thin films [1]. The channel waveguide laser can be also more easily coupled to fiber components than the planar waveguide laser [2]. After the creation of the Ti : sapphire layers by pulsed laser deposition (PLD) [3] the development of microchannel waveguides is next logical step. Many techniques can be used for preparation of channel waveguide such as Ti indiffusion [4–6], ion implantation [7, 8], proton exchange [9] and Ar^+ etching [10]. The one of the suitable way to fabricate the channel waveguide from waveguiding layer is to confine of the layer to stripes with width of order of several magnitude of wavelength. The roughness of channel surrounding walls cannot exceed the value of $\lambda/10$. It is essential for obtaining of low waveguiding losses in channel [11]. To minimize the propagation losses we have created the rib guide from waveguiding layer. The optimum channel width depends on the waveguide height, channel structure and boundaries quality, refractive index of waveguide and surroundings, and laser wavelength and mode structure. Roughness at waveguide boundaries can lead to the scattering losses. In narrow a waveguide, an enhancement of losses due to a given fabrication-induced edge roughness occurs as a waveguide dimensions are reduced [12]. The

smooth side walls are therefore very important. The optimum channel width can be calculated by various methods [12]. In the case of Nd : GGG [13] and Nd : YAG [14] the experimentally found optimum channel width for given layer parameters was in the range of 10–16 µm and 20 µm, respectively. These results confirm the observation of lower waveguide losses for the larger channel width as compared to theoretical calculations, and therefore better laser performance [13]. For example the channel waveguide laser Nd : YAG showed a threshold reduction of 20 times compared to a planar waveguide laser.

A lot of work has been well done on patterning mainly of the semiconductor materials by RIE method, but no attention was paid till now to the creation of microstructures on sapphire. In this paper we describe the studies of the preparation of rib guide with width about 20 µm on Ti : sapphire thin films by RIE and KrF laser patterning. Our results and experiences with creation of channel structures into the layers for channel lasers development are presented.

2. EXPERIMENTAL

The RIE experiments were performed in a CVD and RIE system of VacuTec with BCl_3 : He gas mixture. The plasma chamber consists of two aluminum electrodes of 30 cm diameter, which were separated by 2.2 cm and positioned in the center of the chamber. The rf (13.56 MHz) power density was set at values 0.225, 0.3375, and 0.45 W/cm^2, which are corresponding with total rf power 150, 225 and 300 W respectively. The process pressure was varied from 100 to

500 mTorr by changing of the pumping speed by means of a controllable valve. The BCl_3 flow rate was held constant at 15 (standard cubic centimeter per minute) and the flow of He was varied from 5 sccm to 120 sccm. For measurement of the etch rate the sample were patterned with positive photoresist. The etch rate was determined for platinum, SiO_2, tantalum and sapphire at different conditions. The stripes with thickness in order of 400 nm were made by using the platinum and SiO_2 masks.

The laser lithography has been made by KrF excimer laser (ELI-94) operating at the 248 nm wavelength and with pulse duration 25 ns. In order to obtain a well-defined fluence distribution on the spot, the output beam from the laser was passed through a rectangular aperture to select the central quasi-uniform section of the beam. A fused silica lens with focusing length 5 cm was then used to form an image of this aperture at the target plane. As a target, the Ti : sapphire crystal with 0.12 wt % concentration of Ti_2O_3 has been used.

The etch rate for both methods was measured by using alpha step (Tencor Alpha Step 500) to measure
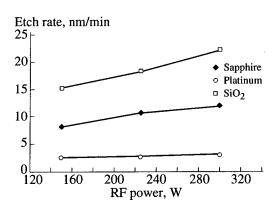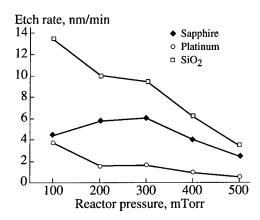
the depth of the etching or ablation, following exposure to a known etching time and number of pulses, respectively, with a resolution ±5 nm. The shape of the formation craters was also observed by microscope.

3. RESULTS

Figure 1 shows the dependencies of the etch rate on the rf power supplied to the BCl_3 : He plasma for various materials (sapphire, platinum and SiO_2). The etch rates of tantalum and photoresist were order of magnitude higher than etch rate of sapphire, and therefore they are not sufficient to be used as masks for patterning of the sapphire. The etch rate in the RIE process is determined by a combination of the chemical etching and ion-assisted etching. Chemical etching is a strong function of temperature, but its effect on the overall RIE process can be ignored [15]. The substrate temperature was held in the room temperature in our experiment. The etching rate linearly increases with increasing rf power with different slope for each materials. For this reason the highest selectivity of the etch rate sapphire–platinum = 3.87 (etch rate of sapphire divided by etch rate of platinum) can be obtained at rf power 300 W, while the selectivity of the etch rate sapphire–SiO_2 = 0.55 is approximately independent on rf power.

The effects of reactor pressure and helium flow rate on the etch rate have been also examined. As the BCl_3/He gas mixture pressure was increased, the etch rate of the platinum and SiO_2 always decreased, whereas the etch rate of the sapphire first increased and then decreased at pressure greater than about 300 mTorr (see Fig. 2). The increase of the etch rate in the lower pressure can be attributed to an increasing of concentration of ionized chlorine. But with further increasing pressure also change the electrical properties of the plasma, e.g. sheath potentials decrease with increasing pressure, and impact energy of chlorine ions bombarding the surface. These effects lead toward decreasing of the etch rate with increasing reactor pressure [15]. The best selec-

Fig. 1. Dependence of the etch rate on the rf power for sapphire, platinum, and SiO_2. The reactor pressure and gas flow rates were held on 300 mTorr and 15 sccm BCl_3/80 sccm He respectively.

Fig. 2. Dependence of the etch rate on the chamber pressure for sapphire, platinum, and SiO_2. The rf power, BCl_3 and He flow rates for etching were 150 W, 15 sccm, and 40 sccm, respectively.
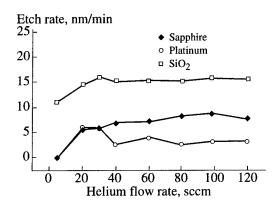
Fig. 3. Dependence of etch rate on the helium flow rate for platinum, sapphire, and SiO_2. The rf power, reactor pressure and BCl_3 flow rate for RIE etching were 150 W, 300 mTorr, and 15 sccm, respectively.

tivities sapphire–platinum = 4.1 and sapphire–SiO_2 = 0.7 have been obtained at pressure 500 mTorr, but, unfortunately, the etch rate of the sapphire in this pressure is very small, 2.45 nm/min. The more convenient condition should be at pressure 300 mTorr. The selectivity slightly decreases: sapphire–platinum = 3.68, sapphire–SiO_2 = 0.54, but the etch rate of sapphire reached the maximum value, 6.1 nm/min.

At a fixed pressure (300 mTorr) and rf power (150 W) as shown in Fig. 3, the etch rate increased rapidly with increasing helium flow in the range 5–20 sccm. When the flow rate exceeded 20 sccm the etch rate of SiO_2 remain at the same value, of platinum slowly decrease and of sapphire slowly increase. The best selectivity (sapphire–platinum = 3.1, sapphire–SiO_2 = 0.55) has been obtain at flow rate 80 sccm of the helium, at the sapphire etch rate 8.2 nm/min.

The stripes with thickness 420 nm and width 20 μm were fabricated by using the platinum and SiO_2 masks at conditions with high etching selectivity between mask and sapphire together with high etching rate of the sapphire. The rf power, reactor pressure, time of etching, BCl_3 and He flow rate for RIE etching were 150 W, 300 mTorr, 55 minute, 15 sccm and 80 sccm, respectively. The platinum masks with thickness 150 nm were performed by lift off lithography and SiO_2 mask with thickness 890 nm was fabricated by standard wet etching. The etch profile and photo of the stripes, which were carried out by using SiO_2 mask, are in Figs. 4a and 4b, respectively.

Figure 5 shows a plot of logarithm (fluence) versus ablated depth per shot for Ti : sapphire crystal with 0.12 wt % concentration of Ti_2O_3. The majority of data were obtained at relatively high fluence to achieve sufficiently deep craters to allow accurate measurement of the etch depth per pulse averaged over multiple pulse exposure. The linear relationship obtained for measurements shows good agreement with the well-known relationship between the ablated depth h per one pulse and the fluence E:
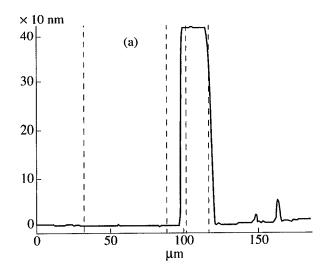
$$h = 1/\alpha \ln(E/E_{th}),$$

where α is the effective absorption coefficient and the E_{th} is the threshold fluence for ablation. The threshold was measured to be 1.36 J/cm², with corresponding absorption coefficient $\alpha = 1.81 \times 10^5$ cm⁻¹.

Figure 6 shows the etch profile (Fig. 6a) measured by alpha step and the photo of one part of the pit ablated in Ti : sapphire (Fig. 6b). As is possible to see from photo and profile, the hole shows rough walls and floor, also the mounds alongside are visible of the height in order of 2 μm. The evident hydrodynamics disturbance also less redeposited materials are presented on the floor and in immediate surroundings of the pit.

4. CONCLUSION

We have studied the BCl_3 : He RIE etching of Ti : sapphire films prepared by pulsed laser deposition.
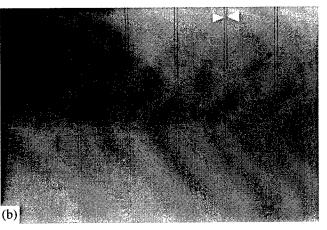
Fig. 4. (a) The etch profile and (b) photo of the stripes fabricated by RIE at the rf power, reactor pressure, time of etching, BCl_3 and He flow rate were 150 W, 300 mTorr, 55 min, 15 sccm, and 80 sccm, respectively. As a mask SiO_2 with thickness 890 nm has been used.
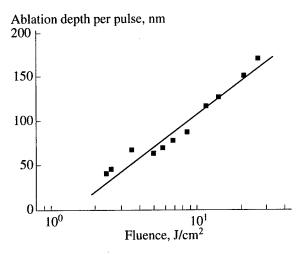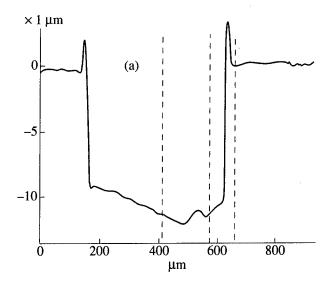
Fig. 5. Dependence of ablation depth per pulse as a function of laser fluence for the irradiation of Ti : sapphire by KrF excimer laser.
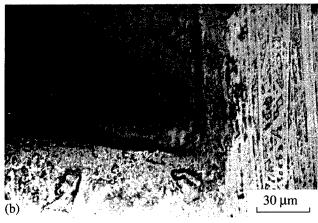
Fig. 6. (a) The etch profile and (b) photo of the etch pit produced in Ti : sapphire by irradiation 248 nm with a fluence 3.57 J/cm² and 150 pulses. The marker bar indicates 30 μm.

The dependence of the etch rate on the RIE process parameters, such as rf power, reactor pressure and helium flow rate, was systematically examined. The etch rate measurement here for RIE shows that it is possible to control surface removal very precisely, on level in order of 1 nm. The suitable masks platinum and SiO_2 were found for sapphire etching. The following optimal etching condition were determined for sapphire patterning by using platinum and SiO_2 masks: reactor pressure 300 mTorr, flow rates BCl_3 and He 15 and 80 sccm respectively, rf power density 0.45 W/cm². At this condition the etch rate of sapphire 11.9 nm/min, selectivities between sapphire and platinum = 3.87 and between sapphire and SiO_2 = 0.55 were achieved. The stripes with thickness 420 nm and width 20 μm have been fabricated by using both platinum and SiO_2 masks. By RIE of Ti : sapphire can produce very high quality structures with smooth surface and precisely defined geometry. The disadvantage of the RIE is the small etch rate, especially for etching of the channel

structures with thickness more than several micrometers some few hours are needed for their fabrication.

KrF laser ablation can produce etched features with high etch rate. The etch rate measurement reported here for Ti : sapphire at 248 nm shows that it is possible to control surface removal at the submicron level by exposure to a fluence exceeding a threshold 1.36 J/cm², but, unfortunately, the quality of the fabricated structures do as not reach the quality of structures fabricated by RIE. On the irradiated surface and in immediate surroundings many disturbances are visible. The improvement would be achieved by using ArF laser instead KrF laser [16] and by homogenization of the laser beam or ultrasonic removing of some large particles after etching [17].

In spite of some problems, the RIE and laser patterning are potentially attractive for the fabrication of microstructures in this active laser material for preparation channel waveguide laser.

ACKNOWLEDGMENTS

REFERENCES

1. Pelec, D., Chambaz, B., Chartier, I., *et al.*, *Opt. Commun.*, **115**, 491.
2. Hanna, D.C., Large, A.C., Shepherd, D.P., *et al.*, 1993, *Appl. Phys. Lett.*, **5**, 7.
3. Jelínek, M., Eason, R.W., Lančok, J., 1996, *Proc. SPIE*, **2888**, 51.
4. Brinkmann, R., Sohler, W., and Suche, H., 1991, *Electronics Let*, **27**, 415.
5. Suche, H., Wessel, R., Westenhofer, S., *et al.*, 1995, *Opt Let.*, **20**, 596.
6. Hickey, L.M.B., Anderson, A.A., and Wilkinson, J.S., 1997, *Europ. Conf. Int. Opt. Stockholm*, Paper PDC-1.
7. Field, S.J., Hanna, D.C., Shepherd, D.P., *et al.*, 1991, *IEEE*, **27**, 428.
8. Field, S.J., Hanna, D.C., Large, A.C., *et al.*, 1992, *Opt Lett.*, **17**, 52.
9. Lallier, E., Pocholle, J.P., Papuchon, M., *et al.*, 1990, *Opt Lett.*, **15**, 682.
10. Sugimoto, N., Ohishi, Y., Katoh, Y., *et al.*, 1995, *Appl. Phys. Lett.*, **67**, 582.
11. Marcuse, D., 1969, *Bell Syst. Tech. J.*, **48**, 3187.
12. Tamir, T., 1988, *Guided-Wave Optoelectronics*, Springer Series in Electronics and Photonics, 26 (Springer).
13. Field, S.J., Hanna, D.C., Large, A.C., *et al.*, 1992, *Opt Lett*, **17**, 52.
14. Field, S.J., Hanna, D.C., Large, A.C., *et al.*, 1991, *Electron. Lett.*, **27**, 2375.
15. Park, J.S. and Milne, W.I., 1996, *Jpn. J. Appl. Phys.*, **35**, 1550.
16. Dyer, P.E., Jackson, S.J., Key, P.H., *et al.*, 1996, *Appl. Surf Sci.*, **96–98**, 849.
17. Jackson, S.J., Metheringham, W.J., and Dyer, P.E., 1995, *Appl. Surf Sci.*, **86**, 223.

Mechanistic Aspects of Excimer Laser Restoration of Painted Artworks

S. Georgiou, V. Zafiropulos, V. Tomari, and C. Fotakis

Foundation for Research and Technology-Hellas, Institute of Electronic Structure and Laser,
P.O. Box 1527, Heraklion, Crete, 71110 Greece
e-mail: sgeorgiu@iesl.forth.gr
Received September 5, 1997

Abstract—The use of excimer laser ablation for the restoration of painted artworks is reviewed with emphasis on the plausible short- and long-term effects of the procedure on the state of the paintings. The dependence of the efficiency of the process and of the surface morphology on laser parameters is discussed. The importance of photochemical effects is addressed by chromatographic analysis of irradiated realistic samples for the detection of photoproducts. It is shown that varnish plays a critical role for the success of the technique. The importance of varnish is further examined in experiments on model samples with photosensitive dopants incorporated. Factors responsible for the "protecting" role of the varnish are proposed. Finally, the potential consequences of laser-induced photomechanical effects are addressed via the use of holographic interferometry. In all, these experiments indicate that optimal fluence ranges can be defined for a highly selective and effective cleaning with minimal or insignificant damaging effects to the substrate.

1. INTRODUCTION

Recently, there has been much interest in the potential of lasers for meeting demanding cleaning applications and in particular for the removal of submicron particles [1]. For instance, in semiconductor industry, because of the ever shrinking dimensions, clearances and tolerances of the devices, the removal of smaller and smaller particulates is critical for their proper functioning. In this application, the laser irradiation provides essentially the energy for overcoming the physical forces for the adherence of the particulates to the surface.

We have demonstrated previously [2–4] that excimer laser ablation affords a highly effective method for the restoration of painted artworks. This application constitutes a different variant of laser cleaning, being more akin to the use of excimers for the patterning of polymers [5] or for the excision of tissues in medicine [6]. It relies on the high absorptivity of materials employed in paintings for effecting efficient and clean etching (i.e., removal of the degraded material) with minimal light penetration to the sublayers.

There are at least two major needs in the restoration of painted artworks [7, 8]: (a) cleaning of the painting surface (varnish) and/or of the support material (canvas, wood, etc.) from accumulated pollutants, photodegradation products, dirt etc. In this case, cleaning is necessary for maintaining the aesthetics of the artwork and prolonging its lifetime, but it is important that this aim is achieved without affecting the authenticity (and, of course, the integrity) of the work. (b) removal of overpaintings in order to recover the original painting.

The traditional methods of dealing with these conservation problems rely on the use of mechanical or chemical means [7]. Because these processes are difficult to control, extensive expertise is necessary to achieve an optimal result. For instance, chemical solvents may penetrate the painting and result in irreversible damage to the pigments and media. On the other hand, use of mechanical means could lead to inadvertent removal of material from the work or to the destruction of the texture of the painted surface. In comparison with these techniques, laser-based cleaning can offer the advantages of automation, selectivity and, most importantly, a high degree of control, through interfacing with a variety of in-situ detection laser-based analytical techniques. Indeed, there are now several examples of demanding restoration problems in which the use of excimer lasers has proven most effective [2–4, 9].

2. ABLATION CHARACTERISTICS

A typical painting consists of several paint layers (each $\approx$20 to 50 μm thick) on a rather thick primer or ground layer that has been applied to the substrate (canvas, wood, etc.). On top of the paint layer, varnish is applied (typically 50–80 μm thick), serving both as a color enhancing and as a protecting layer. It is on top of this layer that accumulation of dirt, pollutants, degradation etc. take place mostly. Thus, much of painting restoration focuses on the cleaning of varnish.

The basic unit of varnish is usually a tetracyclic or pentacyclic organic compound with carbonyl or hydroxyl groups and, possibly, additional functional groups and/or double bonds in the side chains [10]. As its aging progresses, it polymerizes in a three dimensional manner, while, in parallel, natural oxidation [11, 12] takes place, especially at its outer layers.

Etch depth, μm/pulse
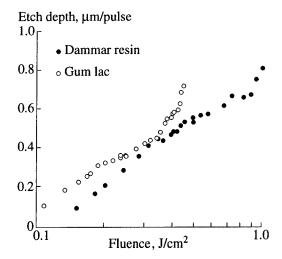
Fig. 1. Etch rates for the ablation of model samples of dammar and gum lac aged varnish with 248 nm irradiation.

The various functional groups of varnish and of its degradation products absorb strongly in the UV and provide for the efficient coupling of the laser irradiation into the substrate. Figure 1 illustrates etching rate curves for the ablation of model samples of oxidized varnish at 248 nm with fluences up to ≈ 1 J/cm^2. Of course, in practice, the optimal laser parameters (i.e., wavelength, fluence, repetition rate, pulse overlap) are case specific, depending on type of materials used, nature and extent of degradation products, etc. Generally, the optimal fluences for painting cleaning are found to be in the range of 200–600 mJ/cm^2, while the removal of overpaintings requires fluences ≈ 2 to 3 times higher. At any rate, it is clear from Fig. 1 that contaminated surface layers of 10's μm thick can be removed by excimer laser ablation with a resolution of 0.1 to 1 μm per pulse. Thus, excimer laser cleaning can be a highly selective process, surpassing by far the degree of selectivity afforded by either mechanical or chemical techniques.

Besides KrF, ArF laser (193 nm) has also been used for aged varnish removal with excellent results. However, the ablation efficiency has been found to be relatively low, which in combination with the low output power of the ArF laser, makes its use extremely lengthy and expensive. Furthermore, the use of shorter pulses has been examined with promising results [14].

In practice, the laser cleaning is performed on a specifically designed workstation, comprised of a computer controlled x–y–z mechanical translator for properly mounting and moving the painting, suitable optics for laser beam delivery and focusing, and several diagnostic modules for the on-line monitoring of the cleaning procedure, thereby enabling on-line control and safeguarding against damage. Monitoring can, in principle, be achieved by a variety of optical and laser-based spectroscopic techniques that have been developed previously in the framework of industrial, environmental or medical applications. Two techniques, in particular, have proven most effective, namely broadband reflectance spectroscopy and/or imaging and Laser Induced Breakdown Spectroscopy (LIBS), as discussed in detail elsewhere [15–17].

3. ASSESSMENT OF THE LASER-INDUCED EFFECTS

Broadly speaking, the plausible effects induced by the irradiation process to the substrate can be delineated in three types, namely thermal, photochemical and photomechanical.

Thermal effects are primarily determined by the thermal diffusivity parameters of the material processed and the laser pulse duration and wavelength. Given the paucity of information (and the variation) for the thermodynamic properties of the materials employed in paintings, elaborate theoretical approaches [18–22] such as sometimes used in the description of the UV ablation of polymers are not expected to be of any accuracy herein. Approximating simply the thermal properties of varnishes with those of simple amorphous organic compounds and/or polymers, we estimate the heat affected zone for typical ns pulses to be ≈ 90–200 nm, i.e., smaller or at most comparable to the optical penetration depth at 248 nm. Indeed, optical microscopic examination of model samples after irradiation demonstrates "clean" etching for ablation at 248 nm. In contrast, irradiation at 308 nm appears to result in a significant thermal load to the remaining material. This difference is consistent with the lower absorption coefficient of the varnish at 308 nm than at 248 nm [11]. We can reasonably argue that because of the very high absorptivity at 248 nm, absorption is localized close to the surface and destruction in the bulk is minimal. Furthermore, two-photon or even higher order absorption processes are expected to be highly probable, thereby resulting in photochemical decompositions with minimization of the energy dissipation to the surrounding medium.

On the other hand, the argument advanced above suggests that photochemical modifications may be expected to be the main source of side-effects of the cleaning procedure. The radicals and ions that are produced by the ablation are expected to be highly reactive and form photo-oxidation products either during the irradiation process itself or in the long run.

To address this issue, model samples of cinnabar red pigment (HgS) in linseed oil covered with varnish were prepared and artificially aged. Then, most of the varnish was removed by using different KrF excimer laser fluences and the remaining pigment/medium was analyzed by chromatographic techniques (GC/MS). The results indicate absence of oxidation products when at least a thin varnish layer is left intact. In contrast, when all varnish is removed and the laser directly irradiates the pigment medium, various oxidation products are observed in the remaining material. It appears that

extensive photodissociation of the pigments occurs and the produced radicals react with the ambient oxygen and/or with the medium. For this reason, in the cleaning of paintings, great attention is paid so that the original painted surface is never exposed to the laser irradiation. For instance, in the cleaning of aged varnish, a thin layer of clean varnish (usually, 5 to 10 μm thick) is always left intact on the pigment medium.
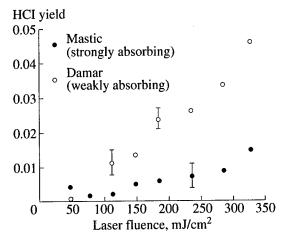
For elucidating the factors responsible for the "protecting" role of the varnish findings, model systems based on solid mixtures of a varnish and chlorobenzene (C_6H_5Cl) were studied under ablation by a KrF laser. C_6H_5Cl has a well known photochemistry in the gas phase and in solution. Upon excitation at 248 nm, it dissociates exclusively by C–Cl bond scission, to give Cl and C_6H_5 fragments. Its photodissociation quantum yield in the gas-phase is quite large (0.4) [23]. In this way, the study of its photolysis and of the reactivity of the produced fragments provides a sensitive probe of photochemical processes occurring during laser illumination. Furthermore, the ablation of liquid samples [24] and of condensed films of C_6H_5Cl [25, 26] has been examined previously by a number of different techniques, thus providing background information for the analysis and the comparison of the results herein.

For monitoring the photoproducts, time-of-flight quadrupole mass spectrometry was employed on an experimental setup that has been described in detail elsewhere [25]. Figure 2 shows the yield of HCl, as a function of laser fluence for C_6H_5Cl dissolved in dammar, which is a relatively weak absorber, and mastic, which is a strong absorber at 248 nm. The observed HCl derives evidently from the Cl fragments produced by the C_6H_5Cl photolysis reacting via H-atom abstraction:

$$Cl + C_xH_y \longrightarrow HCl + C_xH_{y-1}.$$

Addition reactions of Cl to give $C_xH_{y-1}Cl$ species are generally less efficient [27] and thus, the probed HCl is expected to reflect almost quantitatively the degree of photolysis of the incorporated C_6H_5Cl.

In the case of the strongly absorbing varnish, C_6H_5Cl photofragmentation is found to be minimal for fluences up to 350 mJ/cm² (highest fluence examined). In fact, the photolysis yield is indicated to be lower than that in the gas phase by one to two orders of magnitude. This finding has an interesting parallel to the previous observation [28] of Masuhara and coworkers that aromatic molecules embedded in a polymer hardly decompose during ablation. However, it should be noted that their dopants are less photosensitive than the one employed herein. In the present case, we consider the observed low yield to reflect largely the effect of the highly absorptivity of the varnish. In other words, the varnish layer acts as a filter, preventing the light from reaching the pigments and binding media. An additional factor involved may relate to the influence of the "cage effects" resulting in efficient radical recombination, as discussed in detail elsewhere [26] and illustrated in Fig. 3. According to this hypothesis, a number
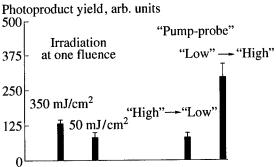
Fig. 2. (a) The plot illustrates the photolysis yield, as measured by the [HCl]/([HCl] + [C_6H_5Cl]) ratio, in the UV ablation of C_6H_5Cl-enriched model samples of damar and mastic. C_6H_5Cl was dissolved in the varnish (≈5% by weight), the samples were left to solidify and were subsequently fixed to a liquid N_2-cooled sample holder. The error bars represent 2σ, as determined from four measurements. (b) "Pump–probe" experiments on the (C_6H_5)₂ photoproducts observed in the UV ablation of C_6H_5Cl-enriched model mastic samples at two different fluences (filled symbols: $F_{LASER} \approx 250$ mJ/cm², unfilled: $F_{LASER} \approx 50$ mJ/cm²). The bars on the left side represent the signals recorded for the photoproduct in the irradiation of films at a single laser fluence, while the ones on the right side illustrate the signal recorded for films that have been first irradiated at one laser fluence ("pump") and then at the other one ("probe"). It is clear that previous irradiation at the low fluence results in a much enhanced signal at the higher one, evidently because of the contribution of the photoproduct accumulated in the film during irradiation at low fluence.

of chromophores do photodissociate, but depending on the reactivity with the surrounding resin, a large number of the fragments may recombine, thereby reforming the parent molecule.

In contrast to what found for mastic, photolysis and accumulation of the chromophore in the irradiation of the weakly absorbing dammar turns out to be significant. Notwithstanding chemical differences between the two varnishes, the reason for the difference appears to relate to the much lower absorptivity of dammar at 248 nm. In this substrate, photolysis occurs at high depth and evidently part of the photoproducts fail to

Fig. 3. Schematics illustrating (a) the "protective" role of the strongly absorbing mastic as compared with that of the weakly absorbing dammar (the indicated circles represent the incorporated chromophores), and (b) the competition between radical recombination to reform the parent molecule and reactivity with the surrounding molecules.

the ejected plume. This is further confirmed in pump–probe experiments, illustrated in Fig. 2b. It appears that the irradiated area attains a high degree of "fluidity" or flexibility so that photoproducts, at least those of small molecular size or of high volatility, can easily desorb. This effect may be a significant factor behind the success of laser cleaning techniques, since it suggests minimal interference from the smaller, highly reactive fragments or products.

We have attempted to complement the examination of the photolysis of C_6H_5Cl with a corresponding examination of the varnish itself, but the desorbate mass spectra deriving from the substrate are too complex to assign and interpret. There is no doubt that during irradiation, a large number of radicals are produced. Depending on their relative number, cross-linking or depolymerization may predominate. It is highly plausible that the empirically found optimal fluence range corresponds to the first condition, i.e., of partial cross-linking, thereby regenerating the initial or a similar 3D structure. Examination by other techniques (such as transient absorption spectroscopy, fluorescence, etc.) is under way for addressing this aspect. At any rate, as the experiments with these model systems strongly indicate, optimal irradiation conditions can be defined under which deleterious photochemical effects to the substrate are minimal.

Considering finally the photomechanical effects induced by the laser irradiation, previous studies [29–31] have demonstrated the development of stress waves with amplitudes of several hundred bars in the excimer laser ablation of tissue and polymers. The effect of these waves can be significant, especially when high laser fluences are employed. On the other hand, when removing aged varnish with fluences generally well below 1 J/cm^2, the shock wave mechanism is expected to be of lesser importance. Nevertheless, the conse-

escape, accumulating instead in the film. In contrast, in the case of the strongly absorbing substrate, photoproduct accumulation is significant only at low fluences (~50 mJ/cm^2), especially for the heavier $(C_6H_5)_2$. At higher fluences such as those used for laser cleaning, there is hardly any evidence for accumulation, evidently because of entrainment of the photoproducts in

Fig. 4. Holographic interferometric examination of model painting (painted wood sample) undergone laser cleaning. Interferograms of the substrate (a) before irradiation, (b) 24 and (c) 54 h after KrF irradiation.

quences of the induced stress pulses will depend on the substrate's mechanical properties, presence and type of interfaces, etc.

To address this issue, we have employed holographic interferometric techniques to examine the formation of cracks, detachments or of other mechanical defects in the cleaning of model systems. Figure 4 depicts double exposure interferograms of the surface of painted wood before and after laser cleaning. The shifts in the observed fringe patterns indicate the formation of defects for laser fluences in the range of 0.8–1.5 J/cm^2. The defects, in the form of delaminations, develop mainly in the interface between the painting and the substrate, probably as a result of the different abilities of the two materials in accommodating the laser-induced stresses.

Although the observation of defect formation is somewhat disturbing, it must be noted that the examination required the use of rather high laser fluences that in practice are avoided. Thus, the specific example represents a rather extreme case. Furthermore, there is indication that after sufficient time, the laser-induced delaminations start gradually to relax, which suggests that their formation may be partly reversible. This issue, i.e., the degree of reversibility of the laser-induced defects, is currently under investigation.

4. CONCLUSIONS

In summary, despite the chemical and structural complexity of painted artworks, excimer lasers can be applied successfully for their restoration. As the studies described in the previous section show, irradiation conditions can be defined under which potentially damaging side effects to the substrate are minimal or at least inconsequential. Certainly, several experimental parameters must be carefully optimized in order to achieve proper cleaning. Furthermore, on-line monitoring is essential for the success of the technique. With these precautions, control over the cleaning process is achieved to a degree that is simply not possible with mechanical or chemical methods. In all, excimer laser ablation affords a most promising approach for meeting demanding restoration problems that are not amenable to traditional methods.

Finally, though outside the scope of this article, there is also great interest in the potential of adapting laser-based analytical techniques to art diagnostics. Several of the existing optical and laser spectroscopic techniques present significant advantages over the traditional analytical methods employed in the art conservation field, in particular as far as sensitivity, non-destructiveness, in situ capabilities, and ease of applicability are concerned. Thus, Raman spectroscopy has already found use for the characterization of pigments [32], while fluorescence is indicated [33, 34] to hold significant merit for the identification of overpaintings, etc. Similarly, LIBS provides [35] for the virtually non-

destructive elemental in-depth profiling of artworks, while the implementation of tunable lasers (i.e., optical parametric techniques) as light sources in IR-reflectography can enhance considerably the capabilities of this technique for the layer by layer imaging and mapping of paintings. Other novel applications of lasers, such as the microetching of holograms [35] for authentication and security purposes, are also under investigation.

In all, the transfer and adaptation of established laser material processing and analytical techniques to art conservation appears to be particularly promising.

ACKNOWLEDGMENTS

REFERENCES

1. Tam, A.C., Leung, W.P., Zapka, W., and Ziemlich, W., 1992, *J. Appl. Phys.*, **71**, 3515; Heroux, J.B., Boughaba, S., Ressejac, I., *et al.*, 1996, *J. Appl. Phys.*, **79**, 2857 and references therein; Mann, K., Wolff-Rottke, B., Muller, F., 1996, *Appl. Surf. Sci.*, **96–98**, 463.
2. Fotakis, C., Anglos, D., Balas, C., *et al.*, 1997, *OSA TOPS on Lasers and Optics for Manufacturing*, Tam, A.C., Ed. (Washington, DC; Optical Society of America), vol. 9, p. 99.
3. Fotakis, C., 1995, *Opt. Photon. News*, **6**, 30.
4. Friberg, T.R., Zafiropulos, V., Kalaitzaki, M., *et al.*, 1997, *Lasers Med. Sci.*, **12**, 55.
5. Srinivasan, R.,1994, *Laser Ablation. Principles and Applications*, Springer Ser. Mater. Sci., Miller, J.C., Ed. (Berlin: Springer), vol. 28, p.107.
6. Azema, A.G.,1994, *Excimer Lasers*, Laude L.D., Ed. (Dordrecht: Kluwer Academic) p. 447 and references therein.
7. Wolbers, R., Sterman, R.N., and Stavroudis, C., 1990, *Notes for Workshop on New Methods in the Cleaning of Paintings* (Marina del Rey, CA: The Getty Conservation Inst.).
8. Asmus, J.F., 1986, *IEEE Circuits and Devices Magazine*, **26**.
9. Watkins, K.G., Larson, J.H., Emmony, D.C., and Steen, W.M., 1995, in *Proceedings of the NATO Advanced Study Institute on Laser Processing: Surface Treatment and Film Deposition* (Dordrecht: Kluwer Academic), p. 907.
10. Mills, J.S., 1956, *J. Chem. Soc.*, **2196**.
11. De la Rie, E.R., 1988, *Studies in Conservation*, **33**, 53.
12. De la Rie, E.R., 1989, *Anal. Chem.*, **61**, 1228 A.
13. Preuss, S., Spath, M., Zhang, Y., and Stuke, M., 1993, *Appl. Phys. Lett.*, **62**, 3049 and references therein.
14. Kautek, W., Pentzien, S., Kruger, J., and Koning, E., 1997, *Restauratoblatter.*
15. Balas, C., 1997, *IEEE Trans. Biomed. Eng.*, **44**, 1.

16. Gobernado-Mitre, I., Prieto, A.C., Zafiropulos, V., *et al.*, 1997, *Appl. Spectrosc.*, **51** (in press).

17. Zafiropulos, V. and Fotakis, C., 1997, *Laser Cleaning in Conservation: an Introduction*, Cooper, M., Ed. (Oxford: Butterworth Heinemann).

18. Mahan, G.D., Cole, H.S., Lin, Y.S., and Philipp, H.R., 1988, *Appl. Phys. Lett.*, **53**, 2377.

19. Sutscliffe, E. and Srinivasan, R., 1986, *J. Appl. Phys.*, **60**, 3315.

20. Pettit, G.H. and Sauerbrey, R., 1993, *Appl. Phys. A*, **5651**.

21. Kuper, S., Brannon, J., and Brannon, K., 1993, *Appl. Phys. A*, **56**, 43.

22. Luk'yanchulk, B., Bityurin, N., Anisimor, S., and Bauerle, D., 1993, *Appl. Phys. A*, **57**, 367.

23. Ichimura, T., Mori, Y., Shinohara, H., and Nishi, N., 1994, *Chem. Phys.*, **189**, 117 and references therein.

24. Tsuboi, Y., Hatanaka, K., Fukumura, H., and Masuhara, H., 1994, *J. Phys. Chem.*, **98**, 11237.

25. Georgiou, S., Koubenakis, A., Syrrou, M., and Kontoleta, P., 1997, *Laser Chem.*, **17**, 73.

26. Georgiou, S., Koubenakis, A., Syrrou, M., and Kontoleta, P., 1997, *Chem. Phys. Lett.*, **270**, 491.

27. Hendry, D.G., Mill, T., and Piszkiewicz, L., 1974, *J. Phys. Chem. Ref. Dat.*, **3**, 937.

28. Fukumura, H., Mibuka, N., Eura, S., *et al.*, 1993, *J. Phys. Chem.*, **97**, 13761.

29. Zweig, A.D. and Deutsch, T.F., 1992, *Appl. Phys. B*, **54**, 76.

30. Dyer, D.E. and Srinivasan, R., 1986, *Appl. Phys. Lett.*, **48**, 445.

31. Gorodetsky, G., Kazyaka, T.G., Melcher, R.L., and Srinivasan, R., 1985, *Appl. Phys. Lett.*, **46**, 828.

32. Anglos, D., Solomidou, M., Zergioti, I., *et al.*, 1996, *Appl. Spectrosc.*, **50**, 1331.

33. Miyoshi, T., Ikeya, M., Kinoshita, S., and Kushida, T., 1982, *Jpn. J. Appl. Phys.*, **21**, 1032.

34. Anglos, D., Couris, S., and Fotakis, C., 1997, *Appl. Spectrosc.*, **51** (in press).

35. Vainos, N.A., Mailis, S., Pissadakis, S., *et al.*, 1996, *Appl. Opt.*, **35**, 6304.

Direct Microdeposition of Diffractive Structures Using Femtosecond Excimer Laser

I. Zergioti*, S. Mailis*, N. A. Vainos*, C. P. Grigoropoulos**, and C. Fotakis*

* *Foundation for Research and Technology–Hellas, Institute of Electronic Structure and Laser, FORTH-IESL,*
P.O. Box 1527, 71110 Greece
e-mail: fotakis@iesl.forth.gr

** *Department of Mechanical Engineering, University of California, Berkeley, California, 94720 USA*
Received September 5, 1997

Abstract—A study of the microdeposition of thin Cr diffractive structures using femtosecond ultraviolet laser radiation in a forward transfer mode is presented. A KrF excimer laser ($\lambda = 248$ nm) having 500 fs pulse duration coupled to a high-power image projection micromachining workstation is used. The ablated material is transferred onto a receiving target glass substrate placed parallel to the source film. Experiments are carried out in a miniature vacuum cell under a low vacuum pressure 10^{-1} Torr. The distance between the source and target surfaces is variable from near-contact to several hundreds of microns. High definition metal diffractive patterns are produced via a direct mask projection scheme, and first results on optical interconnect hologram reconstruction are presented.

INTRODUCTION

Laser-induced thin film forward transfer (LIFT) [1] utilizes pulsed lasers to remove material from a transparent support to a substrate. The film is precoated on a quartz sample and is transferred using a single laser pulse onto a receiving substrate placed against to the source film.

The LIFT process as reported by Bohandy *et al.* [1, 2] was producing direct writing of 50 μm wide Cu lines using single ns excimer laser pulses (193 nm) under high vacuum (10^{-6} Torr). Wagal *et al.* [3] have also reported deposition of diamond-like carbon films using Nd-glass laser in a UHV chamber. In several other studies [4–6] direct writing of 20 μm metal lines under air or helium ambient conditions using ns laser pulses is reported. LIFT has also been used by Pimenov *et al.* [7] as a technique for selective prenucleation with ultrafine diamond powder for subsequent diamond deposition via a CVD process.

The ability to deposit, spots, lines and patterns, with a resolution of the order of μm or less, has direct important applications in the microelectronics and tribology and introduces new concepts in the area of optoelectronics as well. Conventional methods of surface patterning are Chemical Vapor Deposition (CVD), Plasma CVD and sputtering deposition, which may present certain disadvantages such as the inclusion of unwanted collateral products and the contamination of coatings. Among the advantages of the LIFT technique over the coventional methods is that there is no need for complicated and expensive gas handling/vacuum systems. In addition, the properties of the surface are not influenced by either the process, or the purity of the deposition, but most importantly, the method, applied under suitable conditions, as presented herein, pertains the inherent potential and uniqueness in microstructure fabrication.

The aim of this work is to demostrate, for the first time to our knowledge, selective microdeposition of thin Cr films and the direct fabrication of examplar metal holographic patterns using femtosecond excimer lasers.

EXPERIMENTAL

The material used as a "target" for the microdeposition experiments was thin Cr film with thicknesses of 400, 800 and 2000 Å, on quartz samples. The Cr films were uniform and well adherent on quartz substrates. They prepared by sputtering and e-beam evaporation. Corning Glass plates were used as "receiver surfaces." The distance between the target and the receiver surface was variable from near contact to 1000 μm with a 5 μm accuracy.

The target–receiver surface pair was placed into an especially constructed miniature vacuum cell under a pressure of 10^{-1} mbar using a rotary pump. This miniature cell was placed on a computer controlled x–y translation stage, allowing 25×25 mm movement at maximum, by means of piezoelectric motors (Burleigh, Inchworm model), along the x- and y-axes, with a 50 nm resolution determined by optical encoders. In this way, serial writing of metal lines and isolated dots were achieved. In addition, fabrication of computer generated complicated diffractive structures was performed.

A schematic diagram of the excimer laser microdeposition setup is depicted in Fig. 1. The lasers used, was a distributed-feedback dye laser-based fs excimer laser
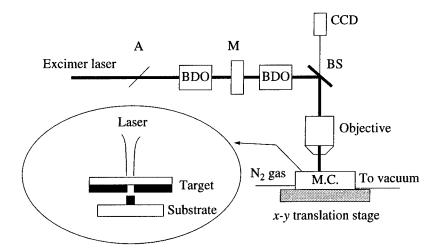
Fig. 1. Schematic diagram of the optical setup for excimer laser microdeposition: A, attenuator; BDO, beam delivery optics; M, mask; BS, beam image/splitter; CCD, camera; MC, microdeposition cell.

100 μm
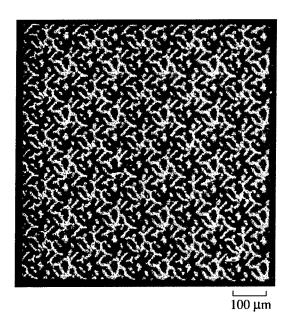
Fig. 2. Scanning Electron Microscopy of Cr Microdeposition on glass. The diffractive structures are deposited by direct mask projection from a 400 Å target source at an energy density of 370 mJ/cm^2.

Fig. 3. Reconstruction of the fs excimer laser microdeposited holographic pattern using a He–Ne. The diffracted scheme is an 8 × 8 array of beamlets representing an optical intercommect matrix.

system (248 nm, 13 mJ pulse energy, 500 fs pulse duration, 1–10 pps repetition rate, 30 × 10 mm beam size). The laser beam was focused onto the target surface through a high power image projection micromachining system [8], based on an inverse microscope, which has been modified to achieve projection of a mask on a large-reduction basis (X30) onto the target. During the deposition process the target area can be viewed through an imaging system, including a CCD camera and microscope ocular lenses. The characterization of the deposited samples was performed using Optical Microscopy, Scanning Electron Microscopy and surface profilometry (Perphometer model).

RESULTS AND DISCUSSION

The optical absorption of the Cr film to be transferred, influences the threshold fluence above which, one pulse leads to the removal of the film onto the receiver surface. The absorption depth of the Cr at 248 nm is 220 Å. The Forward Ablation threshold, is defined as the single pulse energy density value capable for material ablation and transfer occurring with the ablates co-propagating to the laser beam. This is seen to be influenced by the thickness of the target. At 2000 Å thickness there is no deposition using a single pulse even at the maximum available energy density (500 mJ/cm^2).

The Forward Ablation threshold of 800 and 400 Å targets is 100 mJ/cm^2 ($\pm 20\%$) and 80 mJ/cm^2 ($\pm 20\%$), respectively, while the best quality of the deposited dots in terms of the uniformity was obtained for the thinner Cr target, with minimal thermal effects and melted area. The spread of the ablated material was observed depending on the target-substrate distance and energy density level.

Computer generated holograms were fabricated by direct microdeposition via projection of a master hologram mask on the thin film target surface. The pattern is thus deposited in one-step onto the receiving surface. Figure 2 depicts the deposition morphology of direct mask projection holographic pattern from a 400 Å target source at an energy density of 370 mJ/cm^2. The reconstruction of the deposited holographic structure is shown in Fig. 3 depicting an 8 × 8 array of beamlets representing an optical interconnect matrix. In this type of application reconstruction can be performed by using a He Ne laser. Neither materials thickness or reconstruction wavelength have been optimised. Nevertheless, a faithful optical reconstruction is obtained. The binary amplitude nature of the hologram results in a relatively large DC component (Bright peak) appearing in the centre of the patterns as expected. For this application operation in a reflection configuration or deposition of dielectric structures is more appropriate. However, the unique potential of the scheme is outlined.

CONCLUSIONS

Selective deposition of micron-size metal features is demonstrated for the first time in a direct forward transfer mode using a 500 fs KrF excimer laser. The unique potential of the method to perform selective microdeposition is demonstrated by the fabrication of complicated computer generated holographic patterns. The high accuracy and quality of results is verified by hologram reconstruction despite the use of a not optimized configuration. The present scheme introduces a new concept in microstructure fabrication and further work is in progress in order to understand the process and exploit the unique features of the scheme presented.

ACKNOWLEDGMENTS

REFERENCES

1. Bohandy, J., Kim, B.F., and Adrian, F.J., 1986, *J. Appl. Phys.*, **60**, 1538.
2. Bohandy, J., Kim, B.F., Adrian, F.J., and Jette, A.N., 1988, *J. Appl. Phys.*, **63**, 1158.
3. Wagal, S.S., Juengermann, E.M., and Collins, C.B., 1988, *Appl. Phys. Lett.*, **53**, 187.
4. Poon, C. C., and Tam, A. C.,1996, *CLEO Digest*, p. 377.
5. Esrom, H., Zhang, J.-Y., Kogelschatz, U., and Pedraza, A.J., 1995, *Appl. Surf. Sci.*, **86**, 202.
6. Kantor, Z., Toth, Z., and Szorenyi, T., 1992, *Appl. Phys. A*, **54**, 170.
7. Pimenov, S.M., Shafeev, G.A., Smolin, A.A., *et al.*, 1995, *Appl. Surf. Sci.*, **86**, 208.
8. Vainos, N.A., Mailis, S., Pissadakis, S., *et al.*, 1996, *Appl. Opt.*, **35**, 6304.

LASERS AND PHYSICS
OF THIN FILMS

Femtosecond Spectroscopy of Semiconductor Microcavity Polaritons

E. A. Vinogradov*, V. M. Farztdinov*, A. L. Dobryakov*, S. A. Kovalenko*,**,
Yu. E. Lozovik*, and Yu. A. Matveets*

*Institute of Spectroscopy, Russian Academy of Sciences, Troitsk, Moscow oblast, 142092 Russia
e-mail: evinogr@isan.msk.su
**Max-Planck-Institut fur Biophysikalishe Chemie, P.O. Box 2841, Gottingen, D-3400 Germany
Received September 15, 1997

Abstract—Dynamics of semiconductor microcavity modes in ZnSe-metal structure was investigated by femtosecond pump–supercontinuum probe spectroscopy in a wide spectral region of 300–800 nm. The powerful laser pump pulse excites electrons of metal (i.e., boundary of the microcavity) and of ZnSe layer (by two-photon absorption and absorption of second-harmonic generated photon). Nonequilibrium carriers of metal penetrate through Schottky electron barrier into the semiconductor and change its dielectric function. This leads to a shift of frequencies of cavity modes to red region of spectrum. Energy relaxation of charge carriers leads to the heating of the structure and to a shift of the cavity modes in the opposite direction. The generation of coherent phonon oscillations (LO-phonon mode 250 cm^{-1} and TO-phonon mode 200 cm^{-1}) in ZnSe was detected.

1. INTRODUCTION

Nonlinear optical nanostructures now attract growing attention not only because they provide interesting phenomena for the study of nonequilibrium systems, but because they constitute the basis of numerous promising phenomena suitable to all-optical signal-processing schemes [1, 2]. There is considerable interest in understanding of nonlinear optics of thin film planar resonator structure (nonlinear Fabry–Perot resonator). These structures are the simplest physical systems to consider the change of boundary conditions of microcavity during a propagation of ultrashort laser pulses through planar resonator structure and to elucidate the role of nonlinear processes and coherent interaction. The systems of this type are also prospective for study of nonstationary Casimir effect, i.e., parametric photons and other excitations generation due to laser pulse induced instant change of the boundary (see [3] and references therein).

2. EXPERIMENTAL TECHNIQUE

ZnSe films with thickness of 400 and 820 nm on chromium-coated quartz substrate were used as planar resonator structures. The metal film was thick and opaque. The excitation and relaxation of ZnSe film cavity modes was investigated by femtosecond pump–supercontinuum probe technique. The experimental setup and the theory of measurements with a supercontinuum probe have been reported elsewhere [4, 5]. The structures are excited with optical pulses of ≈50 fs duration centered at $\hbar\omega_{pu} = 2.34$ eV. Pump energy was 1.5 μJ. A spot diameter of the pump pulse was measured to be of 150 μm. The supercontinuum probe, covering the spectral range of 1.6–3.2 eV, is dispersed by a polychromator with a resolution of ≈1 nm (3 meV) and registered by a photodiode array with 512 pixels. The pump–probe cross-correlation was ≈70 fs (FWHM) at all probe wavelengths, providing a time resolution of ≈40 fs. A spot diameter of the probe was of 100 μm.

A temporal evolution of the photoinduced reflectivity response $\Delta D_R(\hbar\omega)$ $\{D_R(\hbar\omega) = -\log_{10}[R(\hbar\omega)]\}$ was followed by varying the pump–probe delay in 7 fs steps, up to a maximum time delay of 3 ps. The transient signal is averaged over eight measurements with a repetition rate of 2 Hz. Because the supercontinuum is chirped, the measured spectra were time-corrected [4, 5]. We estimate an accuracy of the time correction as ±15 fs.
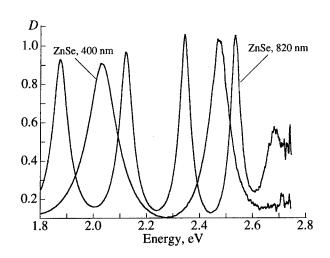
Fig. 1. Linear response $D_R(\hbar\omega) = -\log_{10}[R(\hbar\omega)]$ of ZnSe film on Cr–quartz substrate.
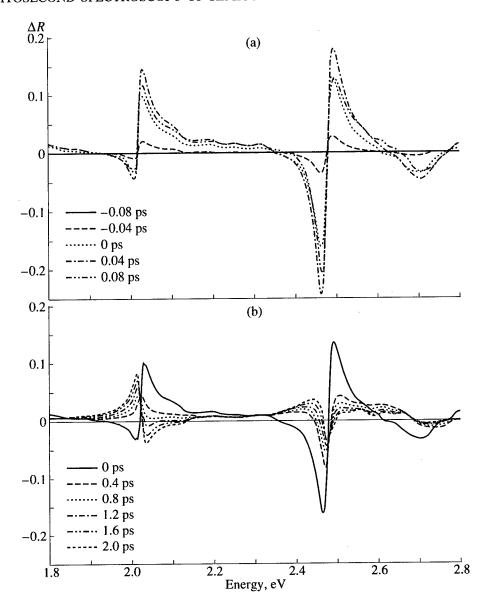
Fig. 2. Temporal evolution of $\Delta D_R(\hbar\omega)$ of ZnSe (400 nm) film on Cr–quartz substrate: (a) time delays from –80 to 80 fs with 40 fs step, (b) time delays from 0 to 2 ps with 0.40 ps step.

3. EXPERIMENTAL RESULTS

The linear reflectivity spectra of the ZnSe/Cr/(quartz substrate) structures are shown in Fig. 1 (for ZnSe films with thickness of 400 and 820 nm). It is seen that for the structure with ZnSe of 400 nm the pumping energy falls in the region of high reflection while for the second structure (with ZnSe of 820 nm) it falls into the low-reflection region. Note that ZnSe film is transparent in the frequency region of pump $\hbar\omega_{pu} = 2.34$ eV and only the two-photon absorption is possible (energy gap for ZnSe is ≈2.67 eV at 300 K).

The photoinduced reflectivity spectra at different time delays are shown in Figs. 2 and 3. The spectral dependence of photoinduced response for long time delays $\tau_D > 1$ ps differs from that for short time delays.

There are two time stages of the photoinduced response temporal evolution: fast stage (with characteristic time of the order of pump pulse duration) and slow stage (with characteristic time of the order of 1 ps). Temporal behavior of the photoinduced response–fast increase on a time scale of pump pulse and consequent fast relaxation—points out that the main contribution to the change of optical response occurs on a time scale determined by the electronic response of the system.

4. DISCUSSION

Now let us consider the physical processes that can lead to the photoinduced reflectivity response of the structures under investigation and characteristic time scales of these processes.
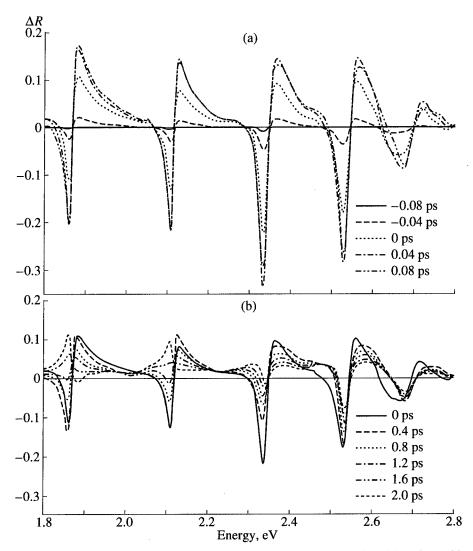
Fig. 3. Temporal evolution of $\Delta D_R(\hbar\omega)$ of ZnSe (820 nm) film on Cr–quartz substrate: (a) time delays from −80 to 80 fs with 40 fs step, (b) time delays from 0 to 2 ps with 0.40 ps step.

(1) The excitation of electrons in metal (i.e., the boundary of microcavity). In the course of pumping pulse absorption the nonequilibrium distribution of charge carriers (electrons above the Fermi level and holes below the Fermi level) in the wide energy region of $E_f \pm \hbar\omega_{p_u}$ is created in the surface layers of Cr. The thickness of this layer can be estimated as $l_{ex} \sim 2/\alpha(\hbar\omega_{p_u}) = 18$ nm. Chromium is a $3d$ transition metal, its wide d bands are approximately half-filled and overlap with s–p bands at the Fermi level. There is no optical gap for direct interband transitions, as, for example, for Cu. Supposing that the change of dielectric function of Cr can be described as the change of Drude contribution we can write

$$\Delta\varepsilon_m = -\frac{(\hbar\omega_p + \Delta\hbar\omega_p)^2}{\hbar\omega(\hbar\omega + i(\gamma + \Delta\gamma))} + \frac{\hbar\omega_p^2}{\hbar\omega(\hbar\omega + i\gamma)}.$$

Here, $\Delta\hbar\omega_p$ is the change of metal plasma frequency $\hbar\omega_p$ (= 6.27 eV according to [6]) and $\Delta\gamma$ is the change

of electrons relaxation rate γ (= 0.063 eV [6]). The change of dielectric function of metal leads to the ultrafast change of the effective boundary conditions on ZnSe/Cr interface for eigenmodes of microcavity. By electron–electron interaction the quasi-equilibrium state is established. The typical time of establishment of quasi-equilibrium electron state is the time of order of tenth fs. We can consider that electron temperature is 10^3 K at this time.

(2) The tunneling of nonequilibrium charge carriers into semiconductor. The part of excited in metal nonequilibrium charge carriers will penetrate ballistically and/or tunnel through Schottky barrier into semiconductor. Supposing that the velocity of carriers is $\sim 10^8$ cm/s the time of flight through the excited region in metal (~ 20 nm, see above) will be ~ 20 fs. During the time of the order of pumping pulse duration the excited carriers will penetrate into the ZnSe layer on a depth of hundreds of Å.

The appearance of carriers in semiconductor layer will modify its dielectric function by free-carrier absorption $\Delta\varepsilon_{fc}$, the states filling in conduction and valence bands $\Delta\varepsilon_{sf}$, and the screening of excitonic transition $\Delta\varepsilon_{ex}$:

$$\Delta\varepsilon_{fc} = -\frac{(\hbar\omega_{ps} + \Delta\hbar\omega_{ps})^2}{\hbar\omega(\hbar\omega + i(\gamma_s + \Delta\gamma_s))} + \frac{\hbar\omega_{ps}^2}{\hbar\omega(\hbar\omega + i\gamma_s)},$$

$$\Delta\varepsilon_{sf}(\omega) = -\Delta\left\{ 8\pi e^2 \sum_k |r_{vc}(\mathbf{k})|^2 \right.$$

$$\times [1 - f_F(\varepsilon_c(\mathbf{k})) - f_F(\varepsilon_v(\mathbf{k}))]\frac{|\varphi_k(\mathbf{r} = 0)|^2}{\hbar\omega - E_k + i\hbar\gamma_k} \right\},$$

$$\Delta\varepsilon_{ex} = \frac{\Delta_{ex}(N)(\hbar\omega_{ex})^2}{(\hbar\omega_{ex})^2 - \hbar\omega(\hbar\omega + i(\gamma_{ex} + \Delta\gamma_{ex}))}$$
$$- \frac{\Delta_{ex}(N_0)(\hbar\omega_{ex})^2}{(\hbar\omega_{ex})^2 - \hbar\omega(\hbar\omega + i\gamma_{ex})}.$$

Here $\hbar\omega_{ps}$ is the plasma frequency of semiconductor, $\Delta\hbar\omega_{ps}$ is its change due to the injection of charge carriers, γ_s is the charge carriers decay constant, Δ_{ex} is the exciton oscillator strength, and γ_{ex} is the exciton decay constant. The changes in dielectric function from free-carrier absorption (negative refraction index change) will be most prominent in the low-energy region $\hbar\omega <$ 1 eV, while the band states filling and screening of excitonic transition (also negative refractive index change in the subgap energy region) will change the dielectric function in the region of absorption threshold $\hbar\omega \sim E_g$.

The height of the Schottky electron barrier for Cr/ZnSe is not known exactly but its typical value is ~1 eV. Supposing that the density of donors is ~10^{16} cm^{-3} the width of this barrier will be ~80 nm. After the establishment of quasi-equilibrium in the electron subsystem of metal the Schottky barrier becomes impenetrable for most of quasi-equilibrium electrons. The holes from semiconductor will penetrate back to the metal. Photoinduced changes of semiconductor dielectric function transform the boundary condition.

(3) Two-photon absorption in semiconductor layer. Another contribution (during the time of order of pulse duration) is connected with two-photon absorption. It is interesting to note that the generation of second harmonic on the metal/semiconductor interface is possible and hence one-quanta absorption of this radiation may be essential too.

The two-photon absorption comes along with the change of the real part of dielectric function of ZnSe film which is negative in the subgap energy region. This change leads to the modification of difference reflectivity and qualitatively agrees with the experimental signal (see Figs. 2, 3). It is interesting to note that the time of establishment of the microcavity modes τ_e (of the

order of the round-trip time of the microcavity $t_{rt} \approx 15$ fs for 820-nm ZnSe film) may be larger than the time of observed difference spectra evolution in the time region considered above. This fact may be important, in principle, for the observation of nonstationary Casimir effect [3] and other phenomena of quantum electrodynamics (see, e.g., [7] and references therein)

(4) The heating of the structure. The energy relaxation of charge carriers due to electron–phonon interaction will lead to the heating of lattice. The resulting lattice temperature rise (on a time scale of the order of 1 ps) leads to a decrease of the band gap energy. The corresponding changes of dielectric function (positive refractive index change in the subgap region) leads to a large shift of cavity modes and to establishment of the new spectral position of these modes.

To reveal the processes that make the main contribution to the observed temporal behavior of photoinduced reflectivity spectra we have calculated the reflectance spectra of our samples $D_R(\hbar\omega) = -\log_{10}[R(\hbar\omega)]$ along with their derivatives on the change of dielectric function of semiconductor and metal layers: $dD_R(\hbar\omega)/dn_s$, $dD_R(\hbar\omega)/d\kappa_s$, $dD_R(\hbar\omega)/dn_m$, $dD_R(\hbar\omega)/d\kappa_m$. The comparison with the experimental difference spectra shows that the main contribution comes from the change of refractive index of ZnSe. The change of Cr dielectric function was calculated within the Drude model. Supposing that the plasma frequency does not change upon excitation, we find out a for the reflectance change to be of the same order as the experimental one the increase of relaxation rate $\Delta\gamma$ should be unrealistically high, of the order of 2 eV. Therefore, the influence of the change of Cr dielectric function is small and can be neglected. This conclusion is also supported by the measurement of reflectivity change of Cr film under femtosecond excitation where the absence of the signal (within the accuracy of measurements) was observed.

Next, consider the change of ZnSe dielectric function. In the energy region far below the absorption threshold only the change of refractive index will be observable. Therefore, for this energy region the change of ZnSe refractive index can be calculated from the relation $\Delta n_s(\hbar\omega) = \Delta D_R^{exp}(\hbar\omega)/[dD_R(\hbar\omega)/dn_s]$. Its spectral behavior for different time delays is shown in Fig. 4. One can see that the refractive index change is most pronounced in the near subgap energy region and decreases with decrease of energy. For long time delays more than ~1 ps the refractive index change becomes positive practically for all energies excluding the narrow subgap (2.5 eV–E_g) energy where it stay negative. Such a behavior is consistent with the refractive index change due to the injection of charge carriers and subsequent energy transfer from charge carriers to the lattice discussed above.

The use of ultrashort pulses has allowed us to observe the coherent oscillations [8], modulating the change of dielectric function and thus varying the transmitted or
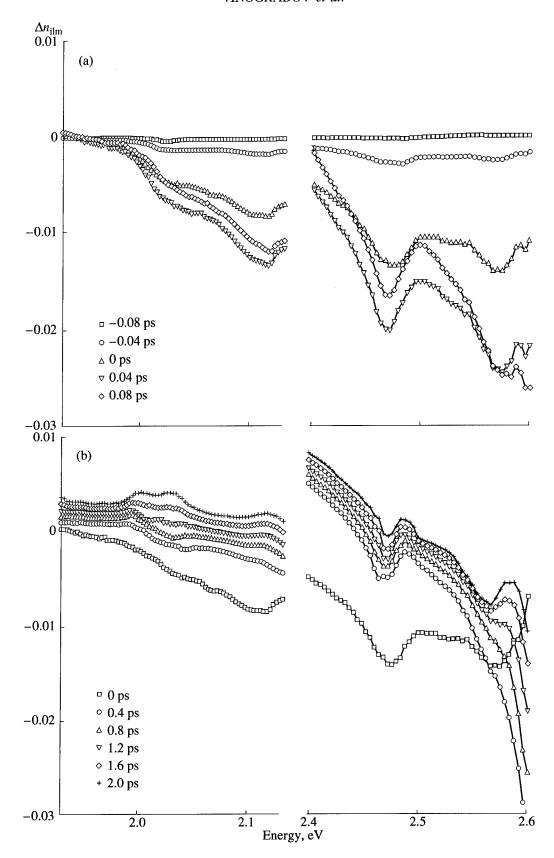
Fig. 4. Temporal evolution of refraction coefficient $\Delta n_{ZnSe}(\hbar\omega)$ extracted from $\Delta D_R(\hbar\omega)$ of ZnSe (400 nm) film on Cr–quartz substrate: (a) time delays from –80 to 80 fs with 40 fs step, (b) time delays from 0 to 2 ps with 0.40 ps step.

reflected light intensity for time-delayed probe pulses. From a Fourier analysis of the time-dependent photoinduced reflectivity response ΔD_R^{exp} (t, $\hbar\omega$), we determine characteristic frequencies of lattice vibrations in the 60–300 cm^{-1} range with a resolution of about 10 cm^{-1}. The resulting spectra $I(\nu_{osc}$, $\hbar\omega$) are corrected to account for the convolution of the optical response with the pump and probe pulse shape. As a result, the generation of coherent phonon oscillations in ZnSe was detected (LO-phonon mode at 250 cm^{-1} and TO-phonon mode at 200 cm^{-1}) across the entire spectral area of probing $\hbar\omega_{probe}$ = 1.8–2.8 eV. Note that the spectral dependence of amplitude of these oscillations is similar to the linear response $D_R(\hbar\omega)$.

There are different possible mechanisms of this generation. One of them is connected with parametric pumping due to nonstationary Casimir effect. The other one may be from the transient electric field localized near the ZnSe–Cr interface. This field is created by the penetration of excited electrons and holes from metal into semiconductor. The relaxed electrons cannot move backward due to the Schottky barrier, while the holes cannot penertate deeply into the semiconductor and are relaxed into the free states in metal. Another one may be connected with laser pulse stimulated Raman scattering.

5. CONCLUSION

In conclusion, note that femtosecond laser pulses make it possible to manipulate the boundary conditions for microcavity modes and to modify the temporal, spectral, and spatial properties of specially chosen semiconductor–metal structures. This is promising for possible applications of the method used for all-optical processing. Particularly, femtosecond spectroscopy of nanostructures permits one to investigate the processes of parametric pumping of cavity modes, coherent phonon generation etc.

ACKNOWLEDGMENTS

REFERENCES

1. Vinogradov, E.A., 1992, *Phys. Rep.*, **217**, 159.
2. Gibbs, H.M., 1985, *Optical Bistability: Controlling Light with Light* (Orlando: Academic).
3. Lozovik, Yu.E., Tsvetus, V.G., and Vinogradov, E.A., 1995, *Phys. Scr.*, **52**, 184.
4. Kovalenko, S.A., Ernsting, N.P., and Ruthmann, J., 1996, *Chem. Phys. Lett.*, **258**, 445.
5. Farztdinov, V.M., Dobryakov, A.L., Kovalenko, S.A., *et al.*, 1997, *Phys. Rev. B*, **56**, 4176.
6. Mazin, I.I., Maksimov, E.G., Rashkeev, C.N., and Uspenskii, Yu.A., 1988, *Proc. of P.N. Lebedev Physical Inst.* (Moscow: Nauka) (in Russia), vol. 190, p. 4.
7. Lozovik, Yu.E., 1986, *Proc. 1st Sov. Britain Symp. on Ion Spectroscopy*, (Troitsk); Belov, A.A., Lozovik, Yu.E., and Pokrovsky, V.L., 1989, *J. Phys. B*, **22**, L101; 1989, *Zh. Eksp. Teor. Fiz.*, **96**, 552.
8. See, for example, review by Merlin, R., 1997, *Solid State Commun.*, **102**, 207.

Multistability of Optical Patterns in a Nonlinear Thin Film due to the Interaction of Hopf Modes

N. A. Loiko and Yu. A. Logvin

Institute of Physics, Belarus Academy of Sciences, F. Skaryna Ave. 70, Minsk, 220072 Belarus
e-mail: nloiko@dragon.bas-net.by
Received August 3, 1997

Abstract—It is demonstrated that multistability of different patterns occurs in a nonlinear optical system consisting of a thin film and feedback mirror. This is a consequence of an interplay between diffraction and delay effects, which leads to the excitation of different spatiotemporal Hopf modes. The Hopf triads satisfying conditions of spatiotemporal matching form a variety of structures which differ in a form, size, and direction of motion.

In the last years, the interest in the transverse pattern formation in nonlinear optical systems (laser, photorefractive oscillator, parametric oscillator, and others) has increased considerably [1]. From one side, it is connected with the fact that the corresponding order parameter equations have been successfully derived. This allows one to consider optical systems in the context of other pattern-forming systems, such as hydrodynamical, chemical, and biological ones. From the other side, studies of optical transverse patterns revealed a rich variety of phenomena, including hexagonal patterns, rolls, spirals, quasi-crystal structures, vortex dynamics, and many others, that lead to novel practical implications of such devices especially in optical information systems. One of the desirable properties for applications is the multistability of patterns. The property gives a possibility to create optical information processors which could be used for pattern recognition and classification purposes with high speed and efficiency. Moreover, the large-aperture optical systems allow a large amount of parallel-processed information.

The purpose of this paper is to show that a simple nonlinear optical scheme (a thin film with a mirror) may produce a rich variety of patterns. It was shown earlier [2, 3] that a time delay in the feedback loop leads to the appearance of the Hopf instabilities besides the static one existing at zero delay. We show in this paper that the longer is the delay time, the more Hopf modes can be excited. Being excited, Hopf modes can build triadic resonant construction satisfying the condition of spatiotemporal phase matching. These resonant Hopf triads produce drifting transverse structures of hexagonal, rhombic, or rhomboidal symmetry.

We use a two-level model for a nonlinear medium described by the Bloch equations

$$\dot{r} = \gamma(-1 + i\delta)r + i\gamma ew, \qquad (1)$$

$$\dot{w} = -(w+1) + i(e^*r - r^*e)/2, \qquad (2)$$

where $r(\mathbf{r}_\perp, t)$ is the normalized polarization emitted by the two-level centers in the film, w is the population dif-

ference, e is the amplitude of the field in the film, δ is the frequency detuning between the incident field and the two-level transition, and $\gamma = T_1/T_2$ is the ratio between the transverse and longitudinal relaxation times.

We assume also that a film of two-level centers has a thickness much less than the wavelength of incident light. This allows us to neglect diffraction and delay during light propagation inside the film. In this case, the transmitted and external incident fields are related as [4]

$$e_t(\mathbf{r}_\perp, t) = e_0 - i \times 2Cr(\mathbf{r}_\perp, t), \qquad (3)$$

where e_t is the amplitude of the transmitted field, C is the bistability parameter [5], $\mathbf{r}_\perp = \{x, y\}$, and e_0 is the amplitude of the incident plane-wave light field.

After transmission through the layer, light is fed back by a mirror which is set parallel to the layer at a distance d. Coupling between the transmitted and the reflected (amplitude e_r) fields is given by the diffractional paraxial operator $\hat{F}$:

$$e_r(\mathbf{r}_\perp, t) = \hat{F}e_t(\mathbf{r}_\perp, t - \tau) \equiv e^{-i\frac{d}{k}\Delta_\perp} e_t(\mathbf{r}_\perp, t - \tau), \qquad (4)$$

where k is the light wavenumber, $\Delta_\perp$ is the Laplacian over transverse coordinates $\mathbf{r}_\perp = \{x, y\}$. It is supposed that the mirror reflectivity is equal to unity, and the distance d contains an integer number of light half-wavelengths.

The expression for the field e driving the centers in the film is given by

$$e(\mathbf{r}_\perp, t) = e_0 + e_r(\mathbf{r}_\perp, t) - i \times 2Cr(\mathbf{r}_\perp, t). \qquad (5)$$

It is seen that the total field in the film consists of two fields illuminating the layer from both sides, as well as of the superradiance field proportional to the polarization r.

In the system, an instability of the homogeneous steady-state solution appears when the bistability parameter C (which is proportional to the optical den-

sity) is considerably large [2]. This may be realized in the films made of semiconductor materials [6, 7]. Taking into account that, in the case of semiconductor, the parameter $\gamma = 10^3$–10^4, the polarization variable r can be adiabatically eliminated from (1), i.e., $r = ew(i - \delta)/(1 + \delta^2)$. Below, we present the results of stability analysis and the data of numerical simulation of (1)–(5) with adiabatically eliminated polarization.

Let us consider Fig. 1, which is the key picture for the understanding of interplay between diffraction and delay effects in our system. Neutral stability curves for static instability ($\text{Re}(\lambda) = 0$, $\text{Im}(\lambda) \equiv \Omega = 0$) are marked in Fig. 1a by closed solid lines. These static zones are independent from the delay time τ. In its turn, Hopf instability is absent at $\tau = 0$ and appears above some threshold value of τ [3, 2] within the same e_0 interval as the static instability. The boundaries of Hopf instability are marked by dots in Fig. 1a at $\tau = 18$. Due to the transcendental structure, the characteristic equation of the linearized delay system has several roots $\text{Re}(\lambda_i) > 0$, $\Omega_i \neq 0$, the number of which grows with increasing τ. A consequence of this can be seen in Fig. 1a, where the secondary Hopf zones are dipped into the primary ones. Frequencies corresponding to the Hopf boundaries in Fig. 1a are plotted versus diffractional parameter θ in Fig. 1b. Equidistant horizontal lines show average Hopf frequencies. Here, $\Omega = 2\pi/T$ is the fundamental frequency. Note that the period T approaches 2τ with increasing τ, which often occurs in systems with delay [8–11]. Vertical dashed lines denote critical values of θ at a certain chosen incident light amplitude ($e_0 = 4.25$). Thus, any excited mode is characterized by a "knot" (θ_i, Ω_i) of a lattice in Fig. 1b. The delay parameter τ and the diffraction parameter θ enter the characteristic equation of the linearized system through the phase factor $e^{i\theta - i\Omega\tau}$ [2]. If at some θ static instability occurs, this instability takes place also at $\theta + 2\pi n$, where n is an integer. θ_2 and θ_4 in Fig. 1 show θ values for static instability. If we assume that the phase slippage $2\pi n$ is achieved on account of $\Omega\tau$, we obtain a family of Hopf instabilities with even frequencies

$$\Omega_n = \frac{2\pi}{T}2n, \quad n = \pm 1, \pm 2, \ldots. \qquad (6)$$

To obtain another family of the Hopf modes, we should make two shifts in π: one shift along a horizontal line in Fig. 1b (e.g., from θ_2 to θ_1) and another shift along a vertical line. Thus, the frequencies of odd modes are

$$\Omega_n = \frac{2\pi}{T}(2n + 1), \quad n = 0, \pm 1, \pm 2, \ldots. \qquad (7)$$

Having in mind that each θ-zone implies an annulus of unstable wave vectors on the (k_x, k_y) plane, we can find a variety of combinations satisfying conditions of three-wave mixing.

Note that the triadic Hopf–static patterns [3] (i.e., patterns creating by two Hopf and one static modes) are particular cases of such mixing. It is natural to suppose
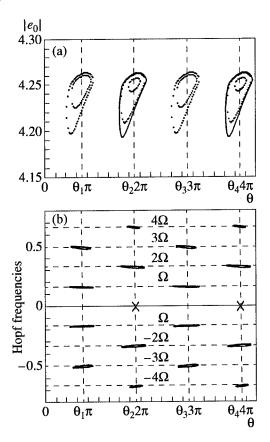
Fig. 1. (a) Neutral stability curves for $C = 3.5$, $\delta = -2$, and $\tau = 18$. Solid (dotted) curves limit the domains of static (Hopf) instability. (b) Hopf frequencies on the boundaries shown in Fig. 1a. Points of static instability are marked with X.

that, by a special choice of initial conditions, we can realize different triadic Hopf structures in our system. Below, we demonstrate this by means of numerical simulations.

To obtain stable resonant Hopf triads, we manipulated the Fourier image of the pattern in the feedback loop. It should be noted that selection and control of patterns by manipulating their Fourier transform is natural for optical systems because of a property of a simple lens [12]. Namely, having a triadic Hopf static pattern [3] at disposal, we filtered static components from the 2D spatial Fourier spectrum and re-addressed the Hopf mode from one $k_\perp$ site to another permitting the building of pure Hopf resonant constructions. Note that all structures obtained for the set of parameters ($e_0 = 4.25$) close to the upper instability boundary see Fig. 1a are asymptotically stable patterns which correspond to own solutions of the system when any filtering is omitted.

Figures 2–4 illustrate drifting triadic Hopf patterns obtained at $\tau = 18$. They differ in the form, size, and direction of motion. The patterns in Figs. 2a–2c are the snapshots of light intensity transmitted through the film. The time interval between the subsequent snapshots is $\tau/2$, which corresponds to approximately a quarter of the full period. The wave vectors of three
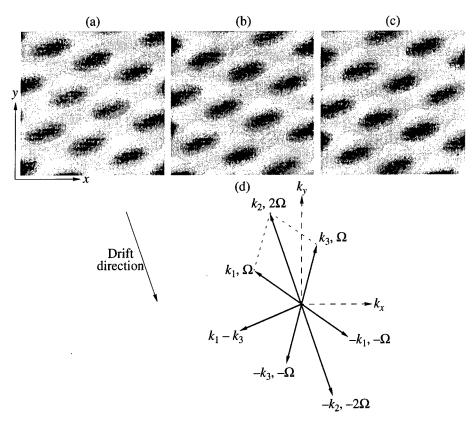
Fig. 2. (a–c) Snapshots of drifting triadic Hopf pattern obtained at three successive moments of time for the parameters of Fig. 1 and $|e_0| = 4.25$ and (d) instantaneous 2D Fourier spectrum.
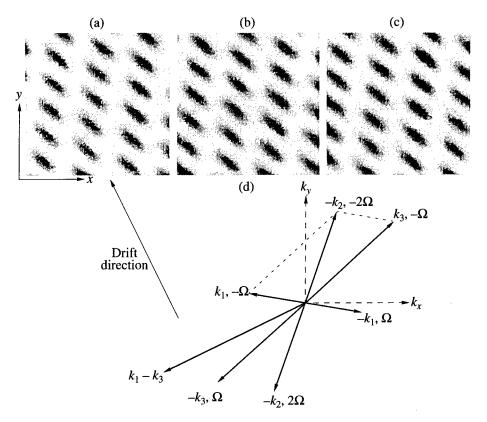
Fig. 3. Triadic Hopf pattern composed by the modes with three different k_i and obtained at the same parameters as the pattern in Fig. 2: (a–c) three snapshots and (d) instantaneous 2D Fourier spectrum.
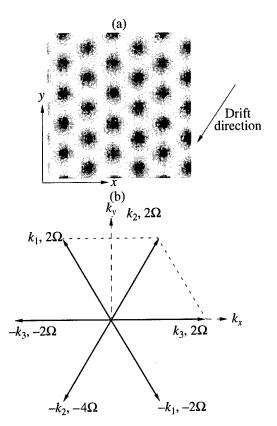
Fig. 4. (a) Triadic Hopf structure in the form of drifting hexagons and (b) its Fourier image.

Hopf modes composing the pattern are shown in the (k_x, k_y) plane in Fig. 2d. The modes with the wave vectors $\mathbf{k}_1$ and $\mathbf{k}_3$ oscillating with the frequency Ω belong to the θ_1 band of Fig. 1, whereas the $(\mathbf{k}_2, 2\Omega)$ mode is excited due to instability θ_2 band. One can see that spatiotemporal phase matching is fulfilled. Of special importance is the sum of the phases of the $(\mathbf{k}_1, +\Omega)$, $(\mathbf{k}_3, +\Omega)$, and $(-\mathbf{k}_2, -2\Omega)$ modes, which form resonant triad. Our analysis shows that this sum is close to $\pm\pi$. Analogously with the cases of static hexagons [13] and of the triadic Hopf–static patterns [3], we could refer to our structure as negative or π triadic Hopf structures if the sum would be exactly $\pm\pi$ (i.e., dark spots on the light background is an attribute of negative triadic structures). Obviously, because of a symmetry of the system, any other resonant triad obtained from the one drawn in Fig. 2d by rotation around the origin is also possible. It means that the direction of motion is determined by the initial conditions.

Another kind of the triadic Hopf structure obtained for the same parameters is presented in Fig. 3. Similar to the previous picture, three snapshots are shown in time interval $\tau/2$. Here, the distinction from the previous case is that all three wave vectors $\mathbf{k}_i$ (see Fig. 3d) have different lengths (i.e., three Hopf modes belong to different θ bands of Fig. 1). Because of this, the pattern has a rhomboidal symmetry. Like in Fig. 2, the pattern

in Fig. 3 performs a drifting motion in the direction perpendicular to $\mathbf{k}_1 - \mathbf{k}_3$. Again, the sum of the phases of three modes composing a resonant triad is close but not exactly equal to $\pm\pi$.

Hopf modes can also build the structures of hexagonal symmetry. For this, three wave vectors must be of equal length, i.e., they should belong to the same instability θ band in Fig. 1. However, not every θ band is suitable for the generation of drifting hexagon patterns. Let us note that the composition of two Hopf modes with odd frequencies $(2n + 1)\Omega$ will give a mode with an even frequency. Therefore, for the creation of Hopf hexagons, the θ_i zones with even subscripts i should be used. In Fig. 4a, a snapshot of a drifting hexagon structure is shown. The velocity and direction of motion are evident from consideration of Fig. 4b, i.e., the pattern runs in the direction of the vector $-\mathbf{k}_2$ with the velocity $2\Omega/|\mathbf{k}_2|$.

Thus, we have demonstrated that the system consisting of a nonlinear film and a feedback mirror can display multistability of transverse patterns of different symmetry. Switching from one pattern to another can be achieved by manipulating the Fourier image. We have not had an aim in this paper to reveal all possible states of the system, but evidently the number of possible stable triadic Hopf patterns grows with increasing time delay in a feedback loop.

REFERENCES

1. 1994, *Chaos, Solitons and Fractals*, Special Issue on Nonlinear Optical Structures, Patterns, Chaos, Lugiato, L.A., Ed., **4**, 383.

2. Loiko, N.A., Logvin, Yu.A., and Samson, A.M., 1996, *Opt. Commun.*, **124**, 383.

3. Logvin, Yu.A., Samson, B.A., Afanas'ev, A.A., *et al.*, 1996, *Phys. Rev. E*, **54**, R4548.

4. Benedikt, M.J. and Trifonov, E.D., 1988, *Phys. Rev. A*, **38**, 2854.

5. Logvin, Yu.A. and Samson, A.M., 1993, *Opt. Commun.*, **96**, 107.

6. Pankov, J.I., 1971, *Optical Processes in Semiconductor* (Englewood Cliffs, NJ: Prentice-Hall).

7. Gremenok, V.F., Zaretskaya, E.P., Kindyak, V.V., *et al.*, 1994, *Pis'ma Zh. Tekh. Fiz.*, **20**, 49 [1994, *Tech. Phys. Lett.*, **20**, 24].

8. Ikeda, K., Kondo, K., and Akimoto, O., 1982, *Phys. Rev. Lett.*, **49**, 1467.

9. Ikeda, K. and Matsumoto, K., 1987, *Physica D*, **29**, 223.

10. Loiko, N.A. and Samson, A.M., 1994, *Kvantovaya Elektron.*, **21**, 713 [1994, *Sov. J. Quantum Electron.*, **21**, 657].

11. Grigorieva, E.V., Kashchenko, S.A., Loiko, N.A., and Samson, A.M., 1992, *Physica D*, **59**, 297.

12. Martin, R., Scroggie, A.J., Oppo, G.-L., and Firth, W.J., 1996, *Phys. Rev. Lett.*, **77**, 4007.

13. Ciliberto, S., Coullet, P., Lega, J., *et al.*, 1990, *Phys. Rev. Lett.*, **65**, 2370.

Growth and Performance of Pulsed Laser Deposited Indium Oxide Thin-Film Holographic Recorders

C. Grivas*, S. Mailis*, L. Boutsikaris*, D. S. Gill*,1, N. A. Vainos*, and P. J. Chandler**

* *Foundation for Technology and Research-Hellas (FO.R.T.H.), Institute of Electronic Structure and Laser (I.E.S.L),*
Laser and Applications Division, P.O. Box 1527, Heraklion, GR-71110 Crete, Greece
e-mail: drig@iesl.forth.gr
** *Physics Department, University of Sussex, Falmer, East Sussex, BN1 9QH United Kingdom*
Received September 05, 1997

Abstract—We report the growth of indium oxide (InO_x) holographic recorders on glass substrates by Pulsed Laser Deposition (PLD). Deposition runs were carried out using pure indium targets at various oxygen ambient pressures. Microstructural and compositional properties of the films grown were studied by X-Ray Diffraction analysis (XRD) and Rutherford Backscattering Spectroscopy (RBS). Dynamic recording of holographic gratings is observed in these films by using a HeCd laser emitting at $\lambda = 325$ nm. A strong dependence of the recording characteristics on the film microstructure was observed. This suggests that the crystalline structure and/or the presence of oxygen vacancies are factors influencing the recording mechanism. The potential control of the response and storage time in this material by the growth conditions is of extreme interest in the holographic information storage and processing applications.

1. INTRODUCTION

Indium oxide has attracted an increasing interest in the optoelectronics sector during the last two decades due to its high values for both the electrical conductivity and optical transmission in the visible and near infrared [1] as well as its relatively high refractive index ($n > 1.8$) [2]. These favourable properties make InO_x suitable for a wide spectrum of applications such as liquid crystal displays, solar cells and switching devices [3]. Fabrication of indium oxide in the form of thin films has been proven to be viable with many of the established growth techniques, comprising ion beam sputtering [4], reactive evaporation [5], reactive ion platting [6], DC magnetron sputtering [7], metalorganic chemical vapour deposition [8], electron beam evaporation [9] and spray pyrolysis [10].

To successfully address applications in the area of holographic information storage there is great need for new improved holographic materials with properties such as long term and high information density storage as well as high diffraction efficiency. In contrast, for dynamic information processing applications apart from high density storage and diffraction efficiency, it is necessary to develop low noise holographic materials exhibiting fast response. In this context Pulsed Laser Deposition (PLD) provides very promising flexible means in the growth of InO_x thin films with holographic recording properties tailored to the particular application of interest.

This work concentrates on the fabrication of indium oxide layers on glass substrates in reactive oxygen atmosphere by pulsed laser ablation of pure indium tar-

gets. The feasibility of dynamic holographic recording in the ultraviolet has been demonstated in [12]. Although work concerning growth on crystalline substrates from sintered indium oxide targets has been presented [11] this is to our knowledge, the first report on PLD growth of InO_x thin films with a view to developing holographic recorders.

2. EXPERIMENTAL PROCEDURE

Two different experimental setups were used, one for the deposition of InO_x thin films and the second for the holographic recording of gratings in these films. The experimental apparatus employed for the preparation of the indium oxide layers is shown in Fig. 1 and comprised a stainless steel vacuum chamber which could be evacuated down to a pressure of 5×10^{-4} Pa. Depositions were performed by means of a KrF excimer laser (Lambda Physik, Model LPX200) with a pulse duration of ~20 ns. The laser was operated at 10 Hz and the deposition runs were carried out using various laser energy densities (1–4 J/cm^2). Fabrication of indium oxide thin films was performed on glass substrates of enhanced quality (Corning 7059) and at different substrate–target distances (5–12 cm). The glass substrates were heated by means of CO_2 laser irradiation (Synrad, Model 57-1). This technique presents the significant advantage over other conventional methods (i.e., halogen lamps, resistance heaters etc.) that the heating can be limited on the small area of the substrate, thus, over-heating of the chamber's walls that could lead to out-gassing from walls surface and contamination of the deposited film is avoided. For achieving homogeneous heating over the whole substrate area, the CO_2 laser beam was passed through a copper homogeniser.

---

1 Present address: Optoelectronics Research Centre, Southampton, SO17 1BJ UK
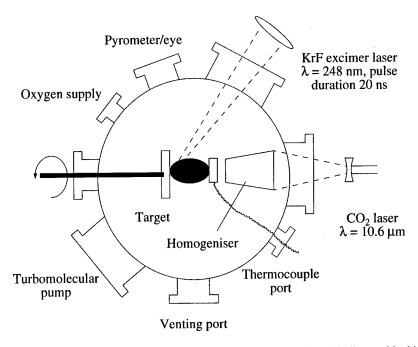
Fig. 1. Experimental apparatus employed for the Pulsed Laser Deposition of indium oxide thin films.

A typical holographic setup was used for the recording of gratings in indium oxide thin films (Fig. 2). It consisted of two lasers a HeCd and a HeNe emitting at 325 and 632.8 nm, respectively. In this configuration, the UV beam originating from the HeCd laser was split by means of a dielectric beam splitter into two parts each having an intensity of 300 mW. The two coherent beams intersected on the film surface forming an interference pattern and producing a refractive index holographic grating by causing microstructural changes in the material. To monitor the evolution of the grating being recorded, a 5.7 mW HeNe beam was employed at normal incidence to the InO_x sample. Two scattered beams $S_{\pm 1}$ of the HeNe probe beam were observed corresponding to the first order diffraction of the recorded sinusoidal grating. Higher order of diffracted beams $S_{\pm m}$ were also resulting from the hologram saturation at the intensity levels used. On-line monitoring of one of the first order diffraction beams was achieved by means of an optical powermeter. A storage oscilloscope was connected to the latter to enable the investigation of the recording characteristics.

Fig. 2. Typical experimental setup employed for holographic recording of gratings in pulsed laser deposited indium oxide thin films. S_{+1}, S_{-1} corresponds to the first order diffraction of the HeNe probe beam, PM is for the powermeter head, ID for the iris diaphragm and SO for the storage oscilloscope. $S_{\pm m} = \pm 1, \pm 2$ correspond to higher order diffracted beams.

3. RESULTS AND DISCUSSION

The microstructural properties of the (InO_x) films were examined by means of X-ray Diffraction analysis (XRD) using $CuK\alpha$ irradiation, while compositional analysis was carried out by Rutherford Backscattering Spectroscopy (RBS). The influence of both the substrate temperature and the oxygen ambient pressure during the deposition runs on the films' crystallinity were investigated. Figure 3 presents θ–2θ XRD recordings for films prepared at different temperatures and at

an oxygen pressure of 5 Pa. The laser energy density employed was 2 J/cm^2 and the distance between substrate and target was 7 cm. XRD patterns obtained from layers grown at room temperature reveal the presence of only metallic indium phases (Fig. 3a). No peaks corresponding to indium oxide phases were observed in the spectra. However a broad feature that appears in the angle region between 20° and 32° implies the presence

Intensity × 10³, cps
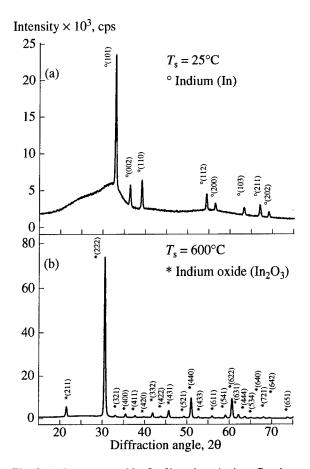
Fig. 3. XRD patterns of In_2O_3 films deposited on Corning (7059) glass substrates at an oxygen ambient pressure of 5 Pa. The substrate temperature T_s employed was as follows: (a) 25°C and (b) 600°C. The In and In_2O_3 diffraction peaks are indicated by different symbols: (o) In and (*) In_2O_3.
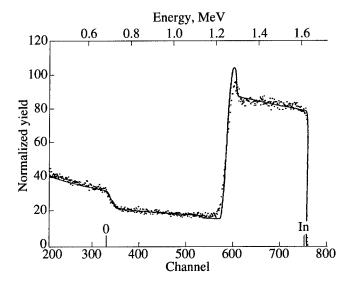
Fig. 4. Rutherford backscattering spectrum of a InO_x film grown on glass substrate at an oxygen pressure of 5 Pa. The points correspond to the experimental results and the full line represents the best fit to the experimental data and was obtained by assuming a stoichiometry of ratio $In_2O_{2.7}$.

of an amorphous phase of either metallic indium or indium oxide. With increasing substrate temperature at constant oxygen ambient pressure constant at 5 Pa growth of pure polycrystalline indium oxide was observed at a temperature of 600°C (Fig. 3b). Presence of only indium oxide phases and growth with preferential orientation parallel to the (222) plane is observed. For this specific oxygen pressure setting of 5 Pa, the onset of indium oxide polycrystalline growth was observed at a substrate temperature of 150°C. Evidence of polycrystalline indium oxide growth was also obtained for films fabricated at room temperature and at oxygen pressure settings $P(O_2) \geq 20$ Pa.

Films obtained at room temperature and at an oxygen pressure of 5 Pa were further analysed by RBS to investigate whether the amorphous phase which appears in the XRD patterns corresponds to metallic indium or indium oxide. Figure 4 shows an RBS spectrum of a 680 nm thick film obtained under these conditions. The points correspond to the experimental data obtained while the curve represents a fit to the point distribution. The best fit was obtained when a composition of $In_2O_{2.7}$ is assumed which implies that the film is oxygen deficient.

Holographic recording of gratings in pulsed laser deposited InO_x films shows a dynamic behaviour. Figure 5 shows typical diffraction efficiency temporal development curves for holographic gratings recorded in 220 nm thick indium oxide films grown at different conditions. Two phases can be distinguished in the recording procedure. During the first phase, the sample
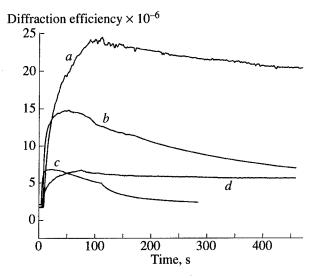
Fig. 5. Typical development of holographic recording of gratings in In_2O_3 films grown at various oxygen ambient pressures $P(O_2)$ and substrate temperatures (T_s). The settings employed for these two parameters were (a) $T_s = 25$°C, $P(O_2) = 5$ Pa; (b) $T_s = 25$°C, $P(O_2) = 7.5$ Pa; (c) $T_s = 25$°C, $P(O_2) = 25$ Pa; and (d) $T_s = 150$°C, $P(O_2) = 5$ Pa, respectively. Films had the same thickness of $h = 220$ nm. Diffraction efficiency values uncorrected for Fresnel losses.

is illuminated by the two UV beams and grating recording in the film is performed. After the onset of the irradiation, a steep increase of the diffraction efficiency is observed. Within few seconds the diffraction efficiency reaches a maximum and immediately after this the UV illumination of the sample was interrupted. In the absence of UV recording beams a decay of the recorded grating is observed. The evolution of the holograms in the PLD fabricated films were found to be strongly dependent on the microstructural properties of the layer.

Figure 5 (curves $a-c$) correspond to films obtained at an oxygen ambient pressure of 5, 7.5, and 25 Pa respectively. In all three cases the substrate temperature during the deposition was 25°C while the laser energy density and the substrate–target distance employed were 2 J/cm^2 and 7 cm respectively. We observe that with increasing oxygen pressure, the diffraction efficiency drops and at 25 Pa ($\eta = 6.7 \times 10^{-6}$) where evidence of polycrystalline growth was observed, it is one order of magnitude lower than that obtained at 5 Pa ($\eta = 2.5 \times 10^{-5}$). The same effect has been observed by varying the temperature. Figure 5 (curve d) shows the temporal behaviour of a grating recorded in an InO$_x$ film that has been prepared at a substrate temperature of 150°C. A laser energy density of 2 J/cm^2 and an oxygen ambient pressure of 5 Pa were used while the substrate–target distance was 7 cm. It can been seen that the diffraction efficiency is again one order of magnitude lower ($\eta = 6.8 \times 10^{-6}$) in comparison with that obtained for the film fabricated at room temperature (Fig. 5 (curve a)). With increasing growth temperature, the diffraction efficiency decreases further and finally, for growth at substrate temperatures above 400°C recording of gratings could not be performed.

The effect of the growth temperature on the temporal characteristics of the holograms was also studied. Figure 6 shows the dark decay time of recorded gratings as a function of the substrate temperature during growth. The decay time constant values were obtained by single exponential decay curves that were fit well to the experimental data. With increasing temperature, a systematic decrease of the decay time constant was observed. Although at room temperature the value obtained was $\tau = 295$ s, this value decreases down to $\tau = 105$ s when the growth temperature was increased to 150°C. For substrate temperatures around 400°C, shorter decay times (~5 s) were obtained. It is clear that growth conditions allow alteration of holographic properties and fabrication of materials suitable to specific application needs.

As for the nature of the recorded holographic gratings, the fact that no darkening or coloration on the surface of the films has been observed after the UV irradiation implies formation of primarily refractive index gratings. We would suggest two effects which may potentially explain the behavior of the recorded gratings in PLD fabricated indium oxide thin films. First
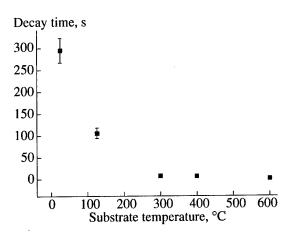
Fig. 6. Holographic grating decay time as a function of the film growth temperature. Films were obtained at an oxygen ambient pressure of $P(O_2) = 5$ Pa and had a thickness of $h = 220$ nm.

the feasibility of grating recording in the absence of perfectly polycrystalline material and the dependence of the recording characteristics on the microstructural properties indicate that the size of the crystalline grain plays an important role. In the case of amorphous or not perfectly polycrystalline material the small crystalline size is responsible for very efficient recording and higher decay time constant values. The involvement of such effects is also supported by results obtained on the holographic recording in DC magnetron sputtering fabricated (InO$_x$) films [12]. However, the recording behavior in these films is contradictory to the one observed in PLD fabricated layers, since it was proven that, despite their highly polycrystalline nature the DC magnetron sputtering ones were suitable for holographic recording probably due to their different grain size. Work is currently in progress to further investigate the microstructure of the grown films by Transmission Electron Microscopy (TEM). Second, the presence of active centers such as oxygen vacancies in the film may be responsible for recording. The number of the oxygen vacancies depends strongly on the fabrication conditions and is expected to be higher when amorphous growth occurs. Alteration of these centers with UV irradiation and relaxation to their previous state is a factor which determines the development of grating recording in indium oxide films. This is supported by the fact that recording of gratings is possible when amorphous InO$_x$ phases are present which implies abundance in oxygen vacancies. We note here, that both grain size and oxygen vacancies may be interrelated, while other effects such as oxygen inclusion and activation which may participate are currently under investigation.

4. SUMMARY

In summary, we have demonstrated the viability of the PLD technique in the growth of indium oxide thin film holographic recorders. The grown InO$_x$ layers are

exhibiting sensitivity in the UV and are promising candidates for high resolution holographic applications. This holographic recording of gratings using UV irradiation is here demonstrated for the first time to our knowledge in PLD grown InO_x films. The recorded gratings present a dynamic behavior and most importantly, their characteristics including diffraction efficiency and decay time were found to be tunable through control of materials growth parameters. This fact constitutes a great advance towards the utilization of the material and the applied fabrication technique in the holographic information storage and information processing sectors as specific demands concerning long storage time or fast response and high diffraction efficiency can be easily met by precisely tailoring material properties.

ACKNOWLEDGMENTS

REFERENCES

1. Vossen, J.L., 1977, *Phys. Thin Films*, **9**, 1.
2. Chen, R.T. and Robinson, D., 1992, *Appl. Phys. Lett.*, **60**, 1541.
3. Franqvist, C.G., 1993, *Appl. Phys. A*, **57**, 19.
4. Bellingham, J.R., Phillips, W.A., and Adkins, C.J., 1990, *J. Phys.: Condens. Matter*, **2**, 6207.
5. Korobov, V., Leibovitch, M., and Shapira, Y., 1994, *Appl. Phys. Lett.*, **65**, 2290.
6. Jeong, J., Moon, J., Hong, J., *et al.*, 1994, *Appl. Phys. Lett.*, **64**, 1215.
7. Xirouhaki, C., Kyriakidis, G., Pedersen, T.F., and Fritzsche, H., 1996, *J. Appl. Phys.*, **79**, 1.
8. Maruyama, T. and Kitamura, T., 1989, *Jpn. J. Appl. Phys. B*, **28**, 1096.
9. Balasubramanian, A., Radhakrishnan, M., and Balasubramanian, C., 1990, *Thin Solid Films*, **193**, 981.
10. Mirzapour, S., Rozati, S.M., Takwale, M.G., *et al.*, 1992, *Mater. Lett.*, **13**, 275.
11. Tarsa, E.J., English, J.H., and Speck, J.S., 1993, *Appl. Phys. Lett.*, **62**, 232.
12. Mailis, S., Boutsikaris, L., Vainos, N.A., *et al.*, 1996, *Appl. Phys. Lett.*, **69**, 2459.

LASERS AND PHYSICS
OF THIN FILMS

Impulse Laser Deposition of Selected Organic Substances

V. Myslik*, M. Vrňata*, F. Vyslouzil*, and M. Jelínek**

Institute of Chemical Technology, Department of Solid-State Engineering, Prague 6, 166 28 Czech Republic
*** Czech Academy of Science, Na Slovance 2, Prague 8, 180 00 Czech Republic*
Received August 5, 1997

Abstract—The contribution is concerned with the preparation of polymer thin layers employing laser ablation and subsequent deposition (LAD technology). A description is given of the procedure of forming the layers using LAD technology and the effect of the basic technological parameters on the properties of layers prepared from polytetrafluorethylene (PTFE) and tin acetyl-acetonate (SnAcAc) targets. The properties of layers evaluated on the basis of FTIR spectra exhibit a good agreement with those of initial substance. The conductivity of layers prepared from SnAcAc depends strongly on the composition of the surrounding atmosphere, permitting applications in sensor technology.

1. INTRODUCTION

The principle of LAD technology utilizes the process of laser-stimulated ablation of the initial substances pressed from the target. When the composition and pressure of the surrounding atmosphere are suitable, a plasma plume is formed above the exposed target area, extending to a distance of several tens of mm. Substances passing from the target into the plasma are deposited on a substrate exposed to the action of the plasma plume. This technology has been investigated both theoretically and experimentally and has been successfully used in the deposition of thin layers of many organic substances, such as ferroelectrics, supracon-ductors, and special ceramic and biocompatible materials. The main advantage of the LAD method is the retention of the stoichiometry (chemical composition) of the initial and deposited layers and precise control of the deposition process including complicated layered structures deposition [1].

At the beginning of the nineties, the first informations were published on the possibility of depositing some organic substances [2, 3]. The authors state in their work that they employed LAD technology to obtain layers similar to the initial substance. However, in the light of the character of organic substances composition, it is necessary to expect that problems will be met both in the selection of suitable substances and also in optimization of the deposition conditions (irradiation density, wavelength, deposition medium, substrate temperature, etc.). It can be expected that, in this case, the ability of the substance to depolymerize to form the monomers without significant degradation of the bonds within the monomer unit and the ability to prepare the pure initial substance in the form of a suitable source target will be important properties.

The work described in this article was motivated by the idea of depositing layers of organic substances that can be used in microelectronics and especially in sensor technology. Due to their simpler composition, PTFE and SnAcAc were selected. In parallel, experi-

ments were also carried out with deposition of polyphenylensulfide (PPS), which has a more complicated chemical structure. This substance was selected in order to evaluate and test the possibility of depositing organic substances with more complex chemical structures.

2. DESCRIPTION OF THE LAD TECHNOLOGY

The technological setup employed (Fig. 1) utilizes radiation from an excimer KrF laser with a wavelength of 248 nm and energy of up to 190 mJ/pulse. The FWHM is about 15 ns at a repetition rate of 5 Hz. After focusing and passing through an aperture, the laser radiation passes through a fused silica window into the working chamber and is incident on a target prepared from the source substance. The rotating motion of the target suppressed formation of a deep hole, which
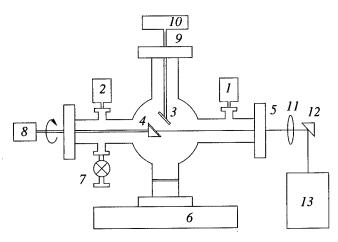
Fig. 1. Deposition chamber: (*1*) Penning gauge, (*2*) Piranni gauge, (*3*) substrate holder, (*4*) target holder, (*5*) input quartz window, (*6*) vacuum stand, (*7*) inert gas outlet, (*8*) rotary equipment, (*9*) heat input, (*10*) heating unit and thermometer, (*11*) quartz lens, (*12*) quartz prism, (*13*) excimer KrF laser, (*14*) filters.

Transmittance, %
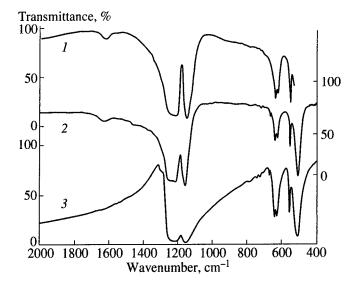
Fig. 2. FTIR spectra of bulk (*2*) and laser-ablated PTFE (*3*). Both can be compared to spectrum *1*, published by Hummel-Scholl IR spectra atlas.

appears as a result of repeated exposure of a single site on the target. The substrate holder can be heated to a temperature of about 300°C. The vacuum system permits evacuation of the deposition chamber to a residual pressure of 10^{-4} Pa and subsequent filling with a working Ar atmosphere at a pressure ranging from 1 to 100 Pa.

3. CHOICE OF MATERIALS AND PREPARATION OF THE EXPERIMENT

In the first phase the LAD method was used in the deposition of PTFE. This material has broad application capabilities. In chemical sensors, thin PTFE layers are used, e.g., as membranes increasing the selectivity of chemical sensors. Because of the relatively simple chemical structure and optimistic reports published in [2, 3], there was a justified expectation that successful transport of the material would occur with retention of the original stoichiometry. In order to evaluate the suitability of the LAD method, experiments were carried out in parallel, based on the deposition of polyphenylensulfide (PPS), which has a more complex basic structural unit compared with PTFE.

In the second case, experiments were concerned with the preparation of layers from the SnAcAc target. This substance and further metal acetylacetonates (e.g., In, Ti, Zn) have already been employed [4] in RF plasma deposition of layers sensitive to both reducing and oxidizing atmospheres.

Targets of the initial substance were prepared in both cases by pressing the pure powder with characteristic particle dimension of about 9 μm to form a target with a diameter of 15 mm. The pressing was carried out at a pressure of about 1 GPa. Part of the tablets were pressed at an elevated temperature of 195°C.

Because of analysis of the deposited layers by FTIR spectroscopy, KBr substrates were employed for the deposition. For measurement of the electrical properties, layers were simultaneously deposited on ceramic substrates fitted on one side with a set of interdigital contacts and on the other side with a heating circuit.

4. DEPOSITION OF PTFE LAYERS

After initial testing of the apparatus, PTFE layers were deposited on KBr and sapphire substrates. The density of the laser radiation varied in the range 0.7–3.2 J cm^{-2}; the Ar working pressure was 40 Pa. The substrate temperature was adjusted in the range 20–250°C. The distance between the target and the substrate could be adjusted in the range 25–60 mm. Figure 2 depicts examples of spectra obtained by the FTIR method. Spectrum *1* corresponds to this one published by Hummel-Scholl IR spectra atlas, spectrum *2* is the spectrum of the initial substance, and *3* is the spectrum of PTFE layer obtained by the LAD method. Below the limit of 1400 cm^{-1}, two bands can be observed on the spectra, with maximum absorbance at 1207 and 1152 cm^{-1}, corresponding to the symmetric and asymmetric vibration modes of the –CF$_2$– group. The further two absorption maxima at 553 and 500 cm^{-1} can be assigned to the vibration modes of PTFE macromolecular chain.

The overall evaluation reveals good agreement of the spectra of the initial substance (*3*) and the deposited substances (*1*). It is also significant that the spectra of the layers deposited by the LAD method do not contain the absorption maxima at 1342, 913, and 1407 cm^{-1} corresponding to the C$_2$F$_4$ monomer unit.

It was found on the basis of gravimetric measurements and evaluation of the intensity of the FTIR spectra that the deposition rate of PTFE begins to saturate at an energy density of about 1.5 J cm^{-2}. The deposition rate at an Ar pressure of 5 Pa then varied around a value of 20 nm s^{-1}. The smoothness of the surface of deposited layers monitored by optical and electron microscopy increased with increasing substrate temperature. Thus, the substrate temperature was maintained at 210°C during the deposition.

In contrast to PTFE, for the deposition of PPS were not found conditions under which transport of this substance from the target to the substrate would occur. Because of the extent of the experiments and the wide range of deposition conditions, it can be concluded that PPS is one of the materials for which it will be difficult or impossible to find suitable deposition conditions. This can be explained by the fact that, when the density of the laser radiation is increased above the threshold for the occurrence of ablation, bond degradation also occurs inside of the monomer units, with irreversible destruction of the material. The energy of the C–S bonds is much smaller than that of the C–F bonds.

5. DEPOSITION OF SnAcAc

Interest in deposition from SnAcAc targets and from similar substrates (InAcAc, TiOAcAc, ZnAcAc) is based on the known ability of thin layers of this substance to absorb and desorb O_2 according to oxidizing or reducing nature of surrounding atmosphere. On the basis of introductory experiments, a laser radiation density between 0.1 and 2.1 J cm^{-2} was employed in deposition of layers from the SnAcAc targets. The exposure time was chosen in the interval 120–1200 s and the working pressure was maintained at 5 Pa. The substrate temperature was not increased by heating.

The deposition yielded a translucent to light yellow–brown layer of the substance. At a distance between the substrate and target of 40 mm, the rate of growth of the layer varied in the range 0.2 to 0.4 nm s^{-1}. The layers were characterized on the basis of spectra obtained by the FTIR method and electrical measurement of the layer conductivity. For this purpose, the layers were deposited on KBr substrates and on ceramic substrates formed on the basis of Al_2O_3.

Figure 3 depicts the IR spectra of four layers. Layer *1* was prepared by the LAD method from the initial SnAcAc target at an energy density of 1.5 J cm^{-2} with subsequent annealing at a temperature of 350°C, spectrum *2* corresponds to SnAcAc prepared in RF plasma (taken from [4]), spectrum *3* depicts the layer deposited by the LAD method without annealing, and spectrum *4* corresponds to the initial substance. Measurement of the electrical conductivity confirmed that, after activation of the layers by annealing, the layers have semiconductive character and the conductivity changes in the presence of a reducing atmosphere. The layers have similar properties to layers prepared purely on the basis of SnO_2; however, the sensitivity to reducing gases is demonstrably greater.

The positions of the individual absorption bands of the spectra given in Fig. 3 indicate the presence of a number of groups. The strong absorption band around 3450 cm^{-1} corresponds to the stretching vibration of bonded -OH groups and the band at 1617 cm^{-1} corresponds to the deformation vibration of –CH= in the –CH=CH$_2$ group. The peak at a wavenumber of 1032 cm^{-1} corresponds to the stretching vibration of the –C–O– bond and the peak at 987 cm^{-1} corresponds to the deformation vibration of the C–H bond in the –CH=CH$_2$ functional group. The broad, intense band with maximum at 570 cm^{-1} corresponds to the bonding arrangement of the Sn–O–Sn group. Spectra *2–4* indicate that there is a characteristic band arrangement that is typical for structural coordination between the tin atom and the acetyl–acetonate ligand in all cases. In spectrum *1*, an increase in the absorbance corresponding to the organic phase.

Electrical measurements were evaluated on the basis of changes in the conductivities of the activated layers. A temperature of 400°C was used for the activation. Then the sensors were exposed to H$_2$, CH$_4$, and
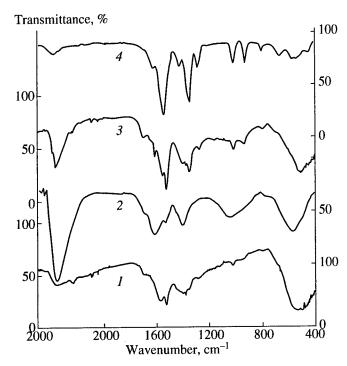
Fig. 3. The IR spectra of four layers. Layer *1* was prepared by the LAD method from the initial SnAcAc target at an energy density of 1.5 J cm^{-2} with subsequent annealing at a temperature of 350°C, spectrum *2* corresponds to SnAcAc prepared in RF plasma (taken from [4]), spectrum *3* depicts the layer deposited by the LAD method without annealing, and spectrum *4* corresponds to the initial substance.
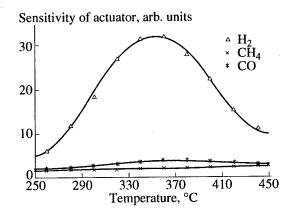
Fig. 4. The relationship between the ratio of the conductivities of layers for exposure to dry synthetic air containing 1000 ppm of reducing gases.

CO atmospheres. The relationship between the ratio of the conductivities of the layers for exposure to dry synthetic air containing 1000 ppm of reducing gases and the initial conductivity in air is depicted in Fig. 4. The ratio of the conductivity plotted for the temperature range 250–450°C indicates that the maximum values were attained for H$_2$ and CO at a temperature of about 360°C; for CH$_4$ the maximum is flat and is shifted to higher values. Comparison of the properties of layers

prepared by laser deposition and layers prepared by the conventional thick-layer technology indicates that the change in the conductivity of the layers prepared by the LAD method is 2× to 6× greater at the maximum, depending on the gas detected.

6. DISCUSSION OF THE RESULTS

On the basis of a set of experiments including a wide range of deposition conditions it was demonstrated that the LAD method can be used for the deposition of a certain group of macromolecular organic substances. Satisfactory results were obtained in the deposition of layers from initial PTFE and SnAcAc targets. On the other hand, suitable deposition conditions were not found for PPS. It can thus be concluded in general that the ability of LAD to deposit a particular organic substance will depend on the character of the basic structural units. The ability of the substance to depolymerize to the undecomposed basic monomer units is apparently also all important factor. It can thus be expected that the search for suitable deposition conditions will be more complicated task for substances with more complex chemical structures and lower bonding energy between atoms within the monomer unit. However, it should be noted that these conclusions are based on a set of experiments carried out using radiation of a single wavelength of 248 nm.

The following important information follows from characterization of the deposited PTFE and SnAcAc layers, based on observation of the FTIR spectra of distinct layers and on the measurement of the growth rate:

(i) The deposited substance has a chemical composition similar to the initial substance. As mentioned in the previous part, good agreement of the chemical composition is apparent for PTFE. It can be concluded from IR spectrum *1* in Fig. 3 for SnAcAc, obtained from the deposited SnAcAc layer, that the original coordination-covalent arrangement of the bonds between the Sn atoms and the CH_3–CO–CH_2–CO–CH_3 organic ligands changes during the deposition to SnO_2 and a nonexactly defined organic phase containing numerous double bonds in the hydrocarbon chain (see spectrum in Fig. 3). The remainder part of the substance retains the original bonds between Sn and the ligand. This is of great importance in the deposition of active layers of chemical sensors, as SnO_2 is a semiconductor and the system of double bonds in the organic phase can be readily polarized; both these newly formed "components" greatly change their electrical properties in the presence of redox (either oxidizing or reducing gases). The process of decomposition of the organic complex further progresses with subsequent thermal formation of layers after deposition (see spectrum *3* in Fig. 3).
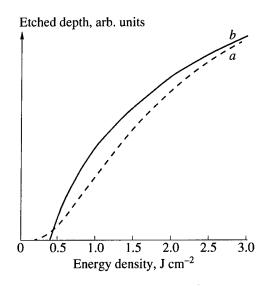
It should be emphasized that, in the preparation of active layers of chemical sensors, a great advantage of the LAD method is the easy exchange of the target during deposition and thus the creation of layered structures with various thicknesses and doping levels in the sensor structures.

(ii) The rate of deposition changes greatly with the chemical composition of the substance. It can be assumed that the deposition rate is directly proportional to the rate of ablation of the target material. The ablation process involves multiphoton absorption on particular chemical bonds of the substance—chromophores. If, for simplicity, only two energy states of these chromophores are assumed, ground state 0 and excited state 1, and if the population density of chromophores in these levels is denoted as p_0 and p_1, respectively, the incident energy density as F_0, the energy density for at the ablation threshold as F_T, and the number of photons participating in the multiphoton process as n, then the etched depth x_{etch} and the thickness of the deposited layer x_{dep} will be given by the relationship

$$x_{etch} \sim x_{dep} \sim 2\lambda(F_0 - F_T)np_0hc, \qquad (1)$$

in which λ is the wavelength of the radiation, h is Planck's constant, and c is the speed of light in vacuum. Thus, the efficiency of the process increases over a certain interval proportional to the radiation wavelength. The rate of decrease of the energy density in the target material from the values incident at the surface, i.e., from F_0 to the ablation threshold value F_T, depends on

(1) the number of photons participating in the multiphoton process, i.e., n;

(2) the history of the system (on whether a laser pulse has already been incident at the site and the time interval from such incidence), i.e., on fraction p_1/p_0;

(3) on the effective cross section for absorption of a photon σ, which is also connected with the energy of the bonds between the atoms in the chain.

Etched depth, arb. units

Fig. 5. A comparison of etching depths calculated for (*a*) photothermal mode, (*b*) photochemical mode.

(iii) On an increase in the energy density of the laser radiation responsible for the formation of the plasma, saturation of the growth rate occurs. In our experiments, the energy of a single pulse attained values of up to 190 mJ and the laser trace had dimensions of 2 × 3 mm, corresponding to a density of the laser radiation of 3.2 J cm^{-2}.

Laser ablation can occur through two mechanisms: photochemical and photothermal. According to [5], calculation of the depth etched by the laser ablation in PTFE yields the dependence depicted in Fig. 5, where curve a describes the dependence for the photochemical model and curve b for the photothermal model. It is apparent from the results of the calculations given in Fig. 5 that, assuming the validity of the photochemical model of the ablation, the rate of sputtering of the PTFE target (and thus also the rate of deposition) will decrease monotonously with increasing energy density—this is the first derivative of curve a in Fig. 5.

In contrast, when employing the photothermal mode [curve b] there is a relatively broad interval of energy densities around the inflection point, in which the rate of sputtering of the target and, thus, also the rate of deposition are constant. It can thus be concluded that, under our conditions, the laser ablation of the target material occurs through the photothermal mechanism and, at higher energy density of the incident laser pulses, the experiment enters the region around the inflection point of curve b.

REFERENCES

1. Chrisey, D.B. and Hubler, G.K., 1994, *Pulsed Laser Deposition of Thin Films* (New York: John Wiley).

2. Blanchet, G.B., Fincher, C.R., Jackson, C.L., *et al.*, 1993, *Appl. Phys. Lett.*, **62**, 1026.

3. Kleinschmidt, J. and Watler, J.U., 1992, *Phys. Status Solidi A*, **131**, 167.

4. Inagaki, N., Tasaka, S., and Suzuki, K., 1990, *J. Appl. Polym. Sci., Appl. Polym. Symp.*, **46**, 173.

5. Metal, M., 1996, *The Employment of Laser Technology in the Creation of Thin Polymer Layer* (Prague: Inst. of Chemical Technology).

Temperature Changes Induced by Low-Energy CO$_2$ Laser Irradiation in Enamel

P. Přech*, A. Jančárek*, P. Gavrilov*, and P. H. Key**

* *CTU, Fac. of Nucl. Sci. & Phys. Eng., Dept. of Physical Electronics, V Holešovičkách 2, Praha 8, 180 00 Czech Republic*
e-mail: prech@troja.fjfi.cvut.cz
** *Dept. of Applied Physics, University of Hull, Hull, UK*
Received August 7, 1997

Abstract—Studies by Stern [1964, *J. Dent. Res.*, 43 (Suppl.), p. 873 (Abs. 307)] demonstrated that a laser could be used to heat the surface of human enamel, increasing enamel resistance to surface demineralisation. Recent studies have shown the CO$_2$ laser to be suitable in preventive dentistry. Because the mechanism of inhibition is not still exactly known we have focused on finding the relation between energy density, wavelength and induced surface temperature. We worked with a tunable TEA CO$_2$ laser using 9.3, 9.6, 10.3, 10.6 μm wavelength and energy density between 0.1 and 2 J/cm^2. This corresponded to the temperature range of 100 to 4000 °C. We prepared a 200 μm thick enamel slide which we irradiated from the front side. The temperature was measured at the opposite side with a microthermometer and the front side temperature was obtained by heat-transfer equation calculation.

1. INTRODUCTION

Several studies have shown that CO$_2$ lasers can be effectively used to modify the chemical composition and surface morphology of dental enamel. This allows the possibility of inhibition of the process of subsurface caries-like lesions [1]. From studies by Featherstone *et al.* [2, 3] we can see that inhibition was wavelength-dependent in the range from 9.3 to 10.6 μm and that these wavelengths are more effective than visible and near IR. The visible range is ineffective because of low absorption in enamel and the near IR has strong absorption in OH$^-$ ions which produced cracks at the surface of the enamel. Absorption in the range 9.3 to 10.6 μm is also strong but the process is thermal in nature. The mechanism of inhibition is unfortunately still unknown but some information of the processes in dental enamel during heating is available [4] and it was found that there are three temperature ranges (100–650°C, 650–1100°C, >1100°C) for principal different chemical and morphological changes. CW CO$_2$ lasers are also not suitable because the interaction time is longer than the thermal relaxation time of enamel (~100 μs) and the absorbed laser energy is conducted away from the enamel surface into the interior of the tooth. This is undesirable because of the possibility of damage to the pulp of the tooth. By the use of pulsed CO$_2$ laser it is possible to produce a temperature rise (>1000°C) at the surface to fuse and melt enamel crystals. This surface melt zone was deep (5 μm) and the interaction region about 10–40 μm deep. It is important to know which energy density induced which temperature because the processes are sensitive to the temperature.

2. EXPERIMENTAL

The experimental setup is shown in Fig. 1. A Lumonix CO$_2$ pulse laser was used for the experiments. A 100–ns pulse width was used with wavelengths of 9.3, 9.6, 10.3 and 10.6 μm. The laser output was directed through a system with iris, mirrors, and lens to develop the beam to Gaussian profile. The pulse energy was monitored using a beam splitter and pyroelectric detector. We used a second detector in the forward direction and a mask with micrometer adjustment for beam profile measurements. For the experiments we prepared enamel slides by polishing to a thickness of about 200 μm. These were mounted together with a microthermocouple of Nickel–Chromium Vs. Copper–Nickel (Omega type E) at the back side of sample with good thermal contact. The enamel slide was irradiated from the front side and the temperature was measured at the back side by the thermocouple. The signal from the thermocouple was amplified and digitised by digital storage oscilloscope and was transferred to personal computer for subsequent analysis.
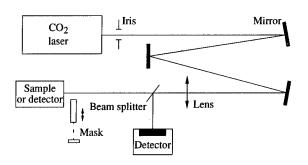
Fig. 1. Setup of temperature measurement.

Relative temperature, °C
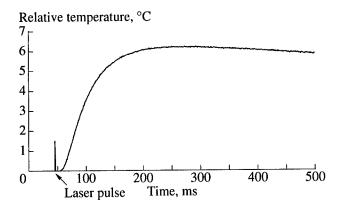
Fig. 2. Time profile of temperature at the back of sample, magnify to see heating part of curve.

Relative temperature, °C

Fig. 3. Time profile of temperature at the back of sample.

The temperature at the surface was calculated by the heat–transfer equation. The model used was for an infinite disk with insulated ends. The solution of heat-transfer equation is given by

$$\vartheta(x, t) = \frac{1}{l}\int_0^l f(x')dx'$$

$$+ \frac{2}{l}\sum_{n=1}^{\infty} e^{\frac{-\kappa n^2 \pi^2 t}{l^2}} \cos\frac{n\pi x}{l}\int_0^l f(x')\cos\frac{n\pi x'}{l}dx', \tag{1}$$

where $f(x)$ is the initial temperature function, t is time, l is thickness of sample, κ is diffusivity, x is axis ($x = 0$ is surface of sample). Because the input energy is from laser irradiation we approximate the initial temperature according to Beers law:

$$f(x) = Fe^{-\alpha x}, \tag{2}$$

where F is the initial surface temperature, α is absorption coefficient. Using this approximation we can write

$$\vartheta(x, t) = \frac{F}{\alpha l} - \frac{F}{\alpha l e^{\alpha l}}$$

$$+ 2F\alpha l \sum_{n=1}^{\infty} e^{-\left(\alpha l + \frac{-\kappa n^2 \pi^2 t}{l^2}\right)} \frac{e^{\alpha l} - (-1)^n}{\alpha^2 l^2 + n^2 \pi^2}\cos\frac{n\pi x}{l}. \tag{3}$$

From this we can express the limit:

$$\text{for } t \longrightarrow \infty \Rightarrow \vartheta = \frac{F}{\alpha l} + \frac{F}{\alpha l e^{\alpha l}} \equiv A, \tag{4}$$

where we defined A as the back surface temperature after thermodynamic equilibrium which could be measured by thermocouple. Because the initial surface temperature was defined by F, we can calculate F from (4) as

$$\vartheta(0, 0) = F = A\frac{1}{\frac{1}{\alpha l} - \frac{1}{\alpha l e^{\alpha l}}} \tag{5}$$

$$\text{for } \alpha l \gg 1 \quad \vartheta(0, 0) = F = A\alpha l.$$
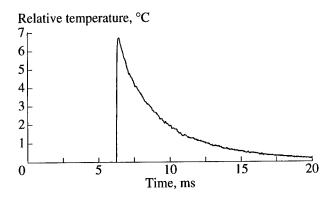
We also use the approximation $\alpha l \gg 1$ because of the strong absorption of enamel.

Scanning electron microscope (SEM) micrographs of irradiated enamel show changes in the surface morphologies. From the size of spot we can calculate the energy density which is needed to melt the surface (>1300°C) and we can compare this to the measurements.

3. RESULTS

The temperature profile on the back side of the sample is shown in Figs. 2 and 3 from which it can be seen that the temperature reaches a maximum. Figure 2 shows the heating and Fig. 3 shows the cooling part of curve. We assume that the air is thermally insulating in comparison to the high thermal conductivity in enamel, so we can define that the maximum of the temperature curve corresponds to $t \longrightarrow \infty$. In this way we can easily calculate the surface temperature given by (5) and the known absorption coefficients from Table 1 [5, 6]. We measured four wavelengths (10.6, 10.3, 9.6, 9.3 μm)

Table 1. Table of reflectance and absorption in enamel

Wavelength, μm	10.6	10.3	9.6	9.3
Reflectance, %	13.8 ± 0.5	16.4 ± 1.0	48.7 ± 1.0	37.7 ± 2.0
Absorption, cm⁻¹	5200	6500	31300	18500

Table 2

Wave-length, μm	10.6	10.3	9.6	9.3
C, °C cm² J⁻¹	870 ± 94	1132 ± 227	3675 ± 274	2092 ± 225

PŘECH *et al.*

Temperature, °C
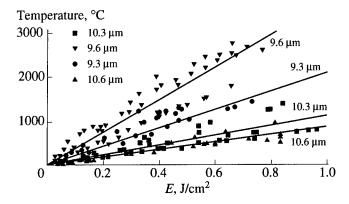
Fig. 4. Dependence between energy density and induced surface temperature.

with energy density from 0.05 to 1 J/cm². The measured points were fitted by a linear curve $\vartheta = CE$ where ϑ is temperature at the surface, E is energy density, and C is the constant of proportionality between E and induced surface temperature. Results are shown at Fig. 4 and summarised in Table 2.

From the SEM we can measure a spot with diameter of 480 μm. We irradiated the enamel with 9.6 μm wavelength and total energy about 4.03 mJ. From the measured beam profile we calculated the energy which was incident on the spot to be 74%. Table 1 shows that the reflectance is about 0.487. We have calculated that the energy absorbed in the spot is about 815 mJ/cm². If we compare this with the temperature measurement (see Fig. 4) we find a corresponding temperature of 3000°C.
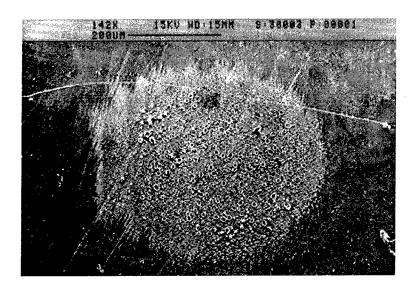
Fig. 5. SEM observation of irradiated spot at enamel surface.
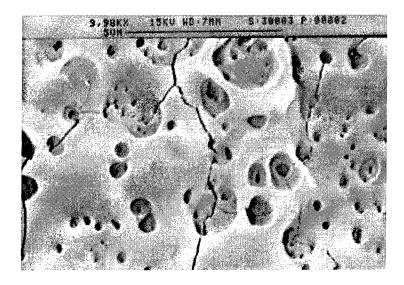
Fig. 6. SEM observation of irradiated spot at enamel surface with magnification.

Because we do not know the latent heat of fusion we have a higher temperature than 1300°C.

4. DISCUSSION

CO_2 laser radiation is strongly absorbed in the range 9.3–10.6 μm. From Fig. 4 we can see that the most effective wavelength is 9.6 μm (on the basis of absorption coefficient). For this application it is important that a range is used where the surface is not heated over 1300°C since that could induce cracks (see Fig. 6) at the surface which would be detrimental to the tooth. To induce a temperature rise at the surface between 100–1300°C we need a fluence in the range 50 to 350 mJ/cm^2. In this regime we can see that there is a good agreement with the SEM observations and the temperature measurements.

REFERENCES

1. Fox, J.L., 1992, *Caries Res.*, **26**, 333.
2. Nelson, D.G.A., 1986, *Caries Res.*, **20**, 289.
3. Nelson, D.G.A., 1986, *New Zealand Dental Journal*, **82**, 74.
4. Wigdor, H.A., 1995, *Lasers in Surgery and Medicine*, **16**, 103.
5. Fried, D., 1994, *Proc. SPIE*, **2128**, 319.
6. Duplain, G., 1987, *Appl. Opt.*, **26**, 4447.

Laser Technology to Contacts Formation of III–V Semiconductors for Measuring Use

L. Hudec, P. Macháč, V. Myslík, and M. Vrňata

Department of Solid State Engineering, Institute of Chemical Technology, Technická 5, Prague 6, 166 28 Czech Republic
e-mail: Petr.Machac@vscht.cz
Received August 5, 1997

Abstract—The contribution describes a technological process of ohmic contact preparation based on a power YAG : Nd laser. Advantages of the laser annealing of ohmic contacts have been employed. To them it may belong a temperature load minimization in connection with a local action and a possibility to contact a buried layer without etching necessity, as well. Some concrete results are published in the contribution, being reached with our procedure. The contacts formation on n-type GaAlAs layers, n-type InP substrates, and GaAs structure with δ-dotted layers is discussed.

1. INTRODUCTION

Annealing is a key step in ohmic contacts preparation and is carried out using various technologies. The most frequently used methods include classical furnace alloying, RTA, and laser annealing. Laser annealing has the basic advantage that it permits very short exposure times, during which only a thin surface layer is heated and the area subjected to thermal strain corresponds to the size of the laser beam spot. In addition, the extremely high cooling rates permit the introduction of dopant concentration that exceeds the equilibrium solubility. Laser technology also enables one to make contacts to two-dimensional layers, which are located deep under the surface of a structure [1]. These contacts cannot be made effectively by conventional furnace alloying, as undesirable out-diffusion of dopants in such a structure may occur during the alloying process [2]. By contrast, this structure is not heat-stressed outside the contact region when annealed by laser. When classical alloying technologies are employed, it is necessary to etch the surface-covering layer and prepare a mesastructure. The thin two-dimensional layer is then contacted through sides of the mesastructure. Current approach to this problem is to prepare a subcontact semiconductor layer with high doping level and small band gap [3, 4] on a working structure. When the subcontact layer is too thick there is necessity to etch it at the area of the future contact [5].

Measuring of basic properties of individual layers is an important step during the semiconductive structures preparation with the help of epitaxial technologies. Sometimes it has been done with buried layers covered by a deposit from another material. Most diagnostic methods need good ohmic contacts on studied layers. The formation of those must be relatively simple and may not cause a degradation of the layer properties. It is the purpose of this work to provide a description of our process for ohmic contact preparation.

2. PROCESS OF CONTACT PREPARATION

The following process has been realized at our department for ohmic contacts preparation in connection with measurements mentioned above:

(1) The demanded contacts morphology has been reached by lift-off technology.

(2) If there is a mask at disposal the classical optical contact lithography is used for the contact patterns preparation.

(3) In special cases the lithography is realized with the straight writing by focused beam radiation generated by a mercurial gas tube in a resist layer.

(4) Contact structure materials have been deposited by a high-vacuum sputtering method.

(5) The contacts have been annealed with the help of the Q-switched YAG : Nd laser.

(6) The annealed process optimization (a suitable density of radiative energy setting, mainly) has been reached by ohmic resistances measurements of the testing contact patterns by four-pointed modified method or by TLM method with respect to a type of the structure. The first one is employed for contacts on bulk semiconductor plates and the second is used for contacts prepared on thin layers or on layered structures.

A power YAG : Nd laser working in the Q-switching regime has been used for our purpose. The laser has operated at fundamental harmonic frequency of radiation (wavelength 1064 nm) and has produced about 350 ns pulses at the repetition rate ranging from 50 to 5000 Hz with the peak power 10 kW. The laser radiation has been focused to a diameter of 40 μm (density of radiation up to 0.3 J/cm²). The setup of the technological laser is depicted in Fig. 1. The laser annealing and the other possible technological processes, including lithography realized with the straight writing by focused and formed beam radiation generated by the mercurial lamp, are provided into the work chamber with inert atmosphere. The chamber scanning is real-

Fig. 1. The setup of the technological laser.

Fig. 2. The contact resistivity of W + Ti/Au/Ge/InP contacts as a function of laser radiation energy density during annealing.
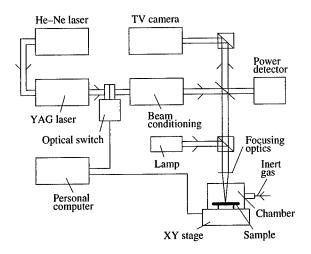
ized by PC-controlled XY stage. There are introduced an optical switch, beam conditioning, two optical splitters, and a focusing optics into the optical path of the YAG : Nd laser radiation. A He–Ne laser is employed as a supporting tool for monitoring of the power IR radiation spot on a surface of a sample in the work chamber by a TV camera.

Some concrete results are published in the contribution, being reached with our described procedure. The contacts formation on n-type GaAlAs layers, n-type InP substrates, and GaAs structure with δ-dotted layers is discussed.

3. CONTACTS ON AlGaAs LAYERS

Samples for these experiments were prepared by epitaxial growth by MOCVD method on semi-insulated GaAs plates. W/In/Ge metallization was applied. The individual layers in the contact have the following significance: the surface layer of tungsten (thickness 100 nm) exhibits good absorption properties for the radiation employed with a wavelength of 1060 nm, indium (thickness 40 nm) produces narrowing of the band gap of the semiconductor in the subcontact area as a consequence of the formation of a ternary semiconductor of the GaInAs type, and the lower layer of germanium with a thickness of 40 nm is used as a dopant to increase the doping of the subcontact layer. The deposition of the contact materials was made by high-vacuum sputtering method.

Main parameters of the samples are given in the table (mole fraction of Al in AlGaAs layer, thickness of the layer, and concentration of dopants). Annealing of the contacts was carried out by power YAG laser (see Section 2). The results of alloying are summarized in the table, which presents the best values of contact resistivity measured by TLM method and the optimal density of radiation energy. The Sample no. 87B has, in agreement with theoretical presumption (smaller band
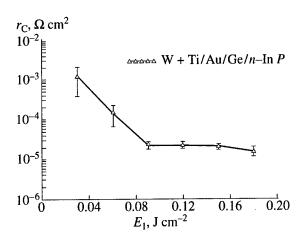
gap and higher level of doping), a lower value of contact resistivity.

4. W + Ti/Au/Ge CONTACTS ON InP
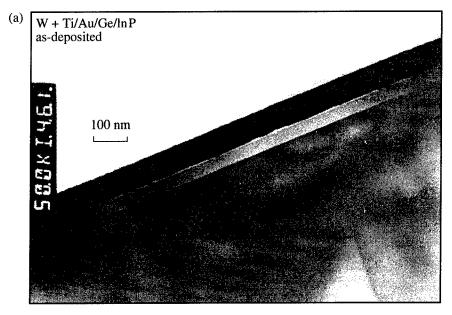
Ohmic contacts to InP-based materials are essential for electronic devices such as some types of transistors as well as for laser diodes and light-emitting diodes. We show here laser annealing of W + Ti(100 nm)/Au(80 nm)/Ge(40 nm) contacts on n-type of InP as an example of ohmic contacts preparation in this field. The reason of W + Ti layer is the same as in the case of contacts on AlGaAs. Au and Ge layers produce a gold–germanium eutectic film that is very frequently used for ohmic contacts on n-type semiconductors [6]. InP was doped to $N_d = 7 \times 10^{17}$ cm^{-3}.

The contact resistivity of W + Ti/Au/Ge/InP contacts as a function of energy density of laser radiation during annealing is depicted in Fig. 2. The function has monotonic dependence and the contact resistivity is practically independent on energy density above value of 0.09 J/cm^2. This behavior offers the possibility to anneal these contacts by energy density slightly above this value.

Transmission electron microscopy (TEM) micrographs of W + Ti/Au/Ge/InP contacts are presented in Fig. 3. The structure of the sample has been analyzed by EDS spectroscopy. Figure 3a depicts a TEM micrograph of as-deposited contact. The upper layer (dark region) contains tungsten, titanium, and gold. The bottom lighter layer contains gold and germanium (probably the

Main parameters of AlGaAs samples and obtained results

No. of the sample	Mole fraction of Al	Thickness of GaAlAs layer [nm]	r_C [Ω cm^2]	E_L [J cm^{-2}]
87B	21	700	1.34×10^{-3}	0.12
101B	30	1100	2.65×10^{-2}	0.09
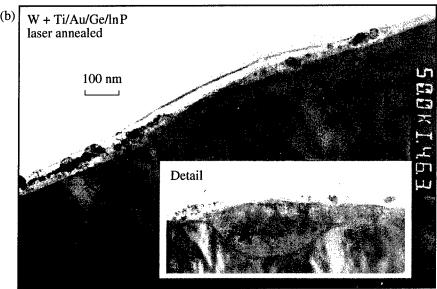
Fig. 3. TEM micrographs of W + Ti/Au/Ge/InP contacts: (a) as deposited, (b) laser annealed by $E_L = 0.12$ J/cm^2.

eutectic alloy). The TEM micrograph of laser-annealed contact (E_L = 0.12 J/cm^2) is presented in Fig. 3b. The formed metallization is inhomogeneous as there are grains grown into the substrate. There is a thin polycrystalline layer on the whole surface that contains beside InP gold and germanium. The composition of the grains (see Detail in Fig. 3b) is practically the same as those of the polycrystalline layer.

5. CONTACT TO A GaAs STRUCTURE WITH δ-DOTTED LAYER

The experiment was carried out using layer structure designated as V85, prepared by the MBE method. Its vertical structure is depicted in Fig. 4. We used the fol-

lowing composition of the metallization of the contact: W-Ti (100 nm)/In (40 nm)/Pd (20 nm) [7]. The reason of W + Ti and In layers is the same as in the case of contacts on AlGaAs: Pd serves as an adhesive material.

Square contacts with dimensions of 500 × 500 μm, with a distance between contacts in square configuration of 5 mm were formed on the sample surface (these contacts are used for Hall mobility measurements). The resistance was measured between all neighboring pairs of contacts prior and after alloying (E_L = 0.12 J/cm^2). As-deposited contacts had mean value of this resistance 1.7 MΩ, after alloying the resistance decreased to the value of 2.65 kΩ. It can be seen that the contacts became connected to the buried δ-doped layer because the laser annealing led to a decrease in the resistance

Cap		GaAs 250 nm
δ		Si
Buffer		GaAs 250 nm
Substrate		GaAs:Cr
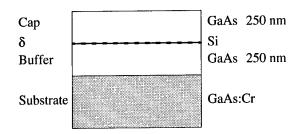
Fig. 4. Vertical structure of the GaAs sample with δ-dotted layer.

between contacts by approximately three orders of magnitude. In addition, subsequent measurement of the parameters of the buried δ layer indicated that the laser annealing did not substantially change the properties of the layer itself (especially the mobility of electrons), while previous attempts to carry out annealing in a furnace led to their irreversible degradation [2].

6. CONCLUSIONS

The main advantages of laser technology compared with classical methods of forming contacts are several:

(1) this is a one-step technological process; it is not necessary to etch the semiconductor in the area of the contact;

(2) the impact of heat is very localized, leading to suppression of thermal strain on the structure outside of the contact area;

(3) focusing of the laser beam permits formation of deep contacts and localized interconnection of multilayer structures.

On the basis of these results we have proposed our technological process of ohmic contacts preparation. The contribution gives some examples of using this technological process.

ACKNOWLEDGMENT

REFERENCES

1. Vrňata, M., Myslík, V., and Macháč, P., 1995, *Proceedings of EDS'95 Conference* (Brno: VUT), 159.
2. Mares, J.J., Oswald, J., Kristofik, J., *et al.*, 1994, *Solid State Commun.*, **89**, 925.
3. Zwicknagl, P., Mukherjee, S.D., Capani, P.M., *et al.*, 1986, *J. Vac. Sci. Technol. B*, **4**(2), 476.
4. Tardy, J., Rojo-Romeo, P., Viktorovitch, P., *et al.*, 1996, *Solid-State Electronics*, **39**, 225.
5. Wu, Ch., Hsu, W., Shieh, H., *et al.*, 1995, *IEEE Electron Device Lett.*, **16**, 112.
6. Shen, T.C., Gao, G.B., and Mokroc, H., 1992, *J. Vac. Sci. Technol. B*, **10**, 2113.
7. Vrňata, M., Myslík, V., and Macháč, P., *J. of Materials Science: Materials in Electronics*, to be published.

The Thickness of the Subcontact Modified Layer of Laser-Annealed WInGe Contacts to GaAs

P. Machác, V. Myslík, and M. Vrňata

Department of Solid State Engineering, Institute of Chemical Technology, Technicka 5, Prague 6, 166 28 Czech Republic
e-mail: Petr.Machac@vscht.cz
Received August 5, 1997

Abstract—It is the purpose of this work to provide a description of determining a thickness of a modified subcontact GaAs layer for WInGe contacts annealed by radiation from power YAG : Nd laser (wavelength 1060 nm). A direct method is based on selective etching of fracture surfaces under the contact and on using an electron microscope. An indirect method is based on formation of contacts on undoped semiconductor layers with various thicknesses. The thickness of the modified subcontact layer at the optimum annealed energy density of 0.09 J cm^{-2} attains value of 500 nm.

1. INTRODUCTION

The formation of ohmic contacts is a very important step in the technology of semiconductor components. In the vast majority of cases, these contacts are formed by annealing of the contact system deposited on the semiconductor surface. In addition to cleaning of the semiconductor surface and deposition, annealing is the most important step in the technology and determines the resultant properties of the prepared contacts. Alloying in a furnace is standardly used, along with rapid thermal annealing (RTA). In some cases, annealing with a power laser is employed, in which a high energy value can be transferred to a very small area. Laser technology has the following basic advantages:

(i) The exposure times for the actual annealing are very short, permitting one to attain overcritical doping values in the subcontact area.

(ii) The high-temperature region remains localized near the surface of the structure and does not produce degradation of the physical parameters of the component.

(iii) The laser radiation can also be localized over the surface, thus limiting the thermal loading of the structure in the lateral direction outside of the actual contact area.

A specific sphere of application of laser annealing lies in situations where the active contact area of the component is located relatively deep below the surface. Here, intense, localized annealing with a power laser can be employed, modifying the sub-contact area of the semiconductor to a considerable depth (up to 500 nm). When classical alloying technologies are employed, it is necessary to etch the surface covering layer at the area of the future contact [1].

In order to form contacts on n-type GaAs and on structures based on GaAs/GaAIAs, a number of multilayer contacts are used. The most frequently employed include AuGe eutectic alloy and a number of modifications based on this substance [1–4]. These contacts exhibit very low contact resistance, but have the disadvantage of poorer stability at higher working temperatures [5]. For this reason, a further group of contact structures is employed, such as the Pd–Ge [6] and AI–Ge [7] systems.

The submitted work is based on experience gained in the preparation of W/In/Ge contacts to GaAs, which exhibit good properties when laser annealing is employed [8]. The individual layers have the following significance: the surface layer of tungsten (thickness 100 nm) exhibits good absorption properties for the radiation employed with a wavelength of 1060 nm, indium (thickness 40 nm) produces narrowing of the forbidden band of the semiconductor in the subcontact area as a consequence of the formation of a ternary semiconductor of the GaInAs type, and the lower layer of germanium with a thickness of 40 nm is used as a dopant to increase the doping of the subcontact layer.

In the creation of deep contacts on layered semiconductor structures, it is essential to know the thickness of the subcontact area. This consists of a layer of semiconductor that is modified as a consequence of the laser annealing (fusion and subsequent recrystallization occurs, accompanied by high diffusion in the liquid phase). The thickness of this layer determines the maximum depth of the buried layers that can be connected with the surface through laser annealing of the ohmic contact.

It is the purpose of this work to provide a description of a direct method of determining the thickness of the modified subcontact area for W/In/Ge contacts on n-GaAs annealed by radiation from a power YAG : Nd laser. The method employed is based on formation of contacts on a conductive semiconductor covered by a defined layer of undoped semiconductor. The contact resistance was evaluated on a set of samples with various thicknesses of the covering layer and variable density of the laser radiation during annealing. An electron
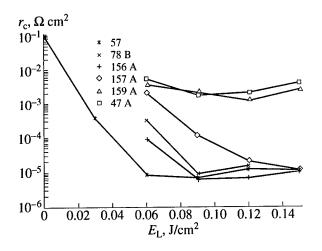
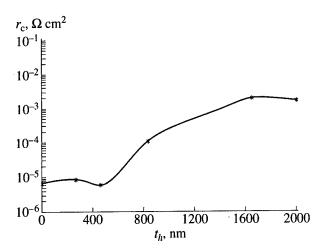**Fig. 1.** The dependence of the contact resistivity r_c on the energy density of the laser radiation E_L.

Fig. 2. The dependence of the contact resistivity r_c on the thickness of the undoped GaAs layer t_h at $E_L = 0.09$ J cm^{-2}.

microscope was used as an auxiliary diagnostic instrument.

2. SAMPLE PREPARATION

A set of semiconductor structures was prepared for the experiments by the MOCVD epitaxial growth method. The individual samples had a layer of undoped pure GaAs of various thicknesses formed on the n-type GaAs substrate (see Table 1). For comparison, one conductive GaAs plate without the epitaxial layer, denoted by number 57, was employed in the experiments.

The testing structures for measuring the contact resistance were formed on the surface of the plate using optical contact lithography (resist SCR 17.1, Lachema Blansko, CR) and by the lift-off method. W/In/Ge contact metallization was applied by the TTS Co. Ltd. (CR) in a PLASMAVAC apparatus. The samples were first cleaned *in situ* by sputtering with Ar$^+$ ions with an energy of 200 eV (current density of the beam of 1 mA/cm^2). The actual deposition was carried out by the high-frequency technique (13 MHz, 600 W, voltage of 3.5 kV). The rate of growth of the deposited layers varied, in dependence on the kind of metal, from 5 to 30 nm/min.

Annealing of the contacts was carried out using radiation from a power YAG : Nd laser working in the Q-switching regime. The wavelength of the radiation was 1060 nm, impulse length 350 ns, pulse energy variable in the range from 0 to 0.3 J/cm^2, the repetition frequency was selected at 500 Hz on the basis of optimization [9, 10], and the rate of shift of the stage with the sample during annealing equaled 0.4 mm/s. The annealing was carried out in an argon atmosphere. A description of the workplace can be found, e.g., in [11].

3. MEASURING THE CONTACT RESISTIVITY

The determination of the depth of the annealed contacts was based on measuring the contact resistivity using a modified four-point method. Figure 1 depicts the values of the contact resistivity of all the samples plotted against the energy density of the laser radiation during alloying. Comparison sample no. 57 and also samples 78B and 156A exhibit minimum contact resistivity in the range $6-8 \times 10^{-6}$ Ω cm^2 at an energy density of 0.09 J cm^{-2}. In sample 157A, this minimum was shifted to an energy density of 0.15 J cm^{-2} as a result of the thicker layer of undoped GaAs. Samples 159A and 47A do not exhibit similar minima and have contact resistivities in the range $1-5 \times 10^{-3}$ Ω cm^2.

Table 1. Main parameters of samples used in experiments

Sample no.	Structure of sample	Thickness of epi. layer [nm]
57	GaAs : Te	0
78B	GaAs : Te/GaAs nondoped	270
156A	GaAs : Te/GaAs nondoped	465
157A	GaAs : Te/GaAs nondoped	830
159A	GaAs : Te/GaAs nondoped	1650
47A	GaAs : Te/GaAs nondoped	2000

Table 2. The best obtained results of contact resistivities

Sample no.	Thickness of epi. layer [nm]	r_c, Ω cm^2	E_L, J cm^{-2}
57	0	6.72×10^{-6}	0.09
78B	270	8.58×10^{-6}	0.09
156A	465	6.14×10^{-6}	0.09
157A	830	1.09×10^{-5}	0.15
159A	1650	1.15×10^{-3}	0.12
47A	2000	1.73×10^{-3}	0.09

Fig. 3. The fracture surface of the sample 47A under the WInGe contact annealed at $E_L = 0.09$ J cm^{-2}.

Table 2 gives a survey of the results obtained. The first column of the table gives the sample numbers, the second lists the thickness of the undoped layers, the third gives the minimum attained contact resistance, and the fourth corresponds to the energy density of the laser radiation during the annealing. The actual annealing was carried out at a radiation density in the range from 0.03 to 0.15 J cm^{-2}. It can be seen from the table that connection with the highly doped substrate occurred for samples with a thickness of the undoped layer of up to 830 nm. The high values of the contact resistivity obtained for samples 159A and 47A indicate that the contacts are formed in the weakly doped semi-conductor and that the sample surface was not inter-connected with the substrate. This theory can be verified by calculations based on the data given in [5]. Contacts formed on the GaAs substrate with donor concentration of 10^{18} cm^{-3} (doping of the substrate plates) have a contact resistivity of $r_c = 6.72 \times 10^{-6}$ Ω cm^2; calculations for contacts with a contact resistivity of 2×10^{-3} Ω cm^2 (this value corresponds to the contacts on samples 159A and 47A) yield a value for the donor concentration in the subcontact area of approximately 6.5×10^{15} cm^{-3}. This value corresponds very well to the concentration of donors in the undoped layers of both of the above samples and thus laser annealing does not lead to connection of the surface with the substrate.

Figure 2 depicts the relationship between the contact resistivity r_c and the thickness of the layer of pure
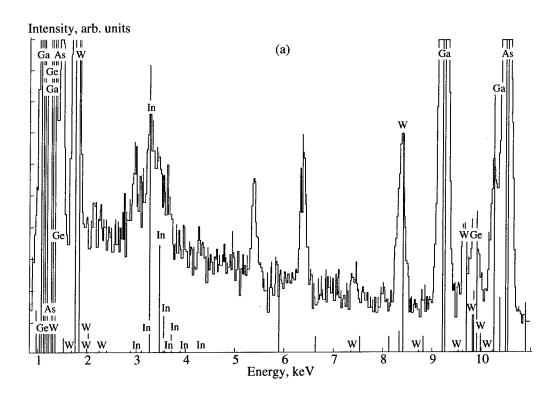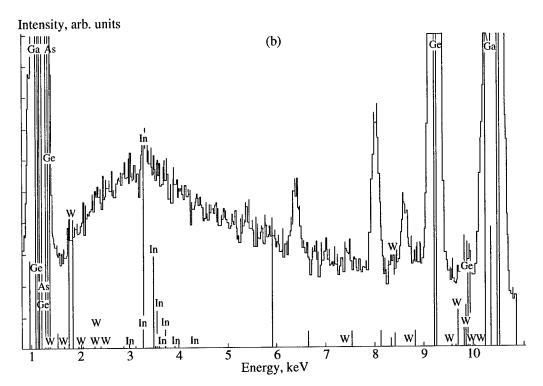
Fig. 4. X-ray electron microprobe spectra of the fracture surface of the sample 47A: (a) area of the residues of metallization, (b) centre of the subcontact layer and (c) epitaxial layer.
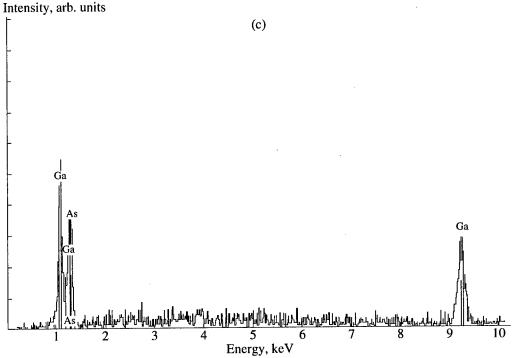
Fig. 4. (Contd.)

GaAs t_h for annealing at an energy density of $E_L = 0.09$ J cm^{-2} (at this value of the energy density, the contact resistivity attained its optimum value for most samples). As expected, this dependence is an increasing function and the surface became connected with the substrate at this energy density only in samples 57, 78B, and 156A.

4. DETERMINATION OF THE THICKNESS OF THE SUBCONTACT LAYERS USING AN ELECTRON MICROSCOPE

The thickness of the subcontact layers was determined directly using selective etching of the fracture surfaces under the contact using AB etching solution (10 ml H$_2$O, 40 mg AgNO$_3$, 5 g CrO$_3$, 8 ml HF) and a

Jeol 733 Superprobe electron microscope. The electron microprobe of this microscope was used to analyze the individual parts of the fracture surfaces.

These experiments were carried out using sample 47A with the thickest epitaxial layer and contact structure annealed at the optimal energy density E_L = 0.09 J cm^{-2}. Figure 3 depicts the fracture surface of this sample etched for 5 s using AB etching solution. Residues of the contact materials can be seen on the surface, followed by the lighter subcontact layer with a thickness of about 500 nm; the grey line at a depth of 2000 nm under the surface corresponds to the boundary between the substrate and the epitaxial layer.

Figure 4 depicts the X-ray spectra measured by the electron microprobe at significant points on the fracture surface. Figure 4a depicts the spectrum of the area of residues of metallization on the sample surface. In addition to gallium and arsenic, all of the metallization elements are present here. The spectrum taken from the centre of the subcontact layer is depicted in Fig. 4b. Tungsten was not found here, but indium and germanium are clearly present. Only gallium and arsenic are present in the epitaxial layer (Fig. 4c).

5. CONCLUSIONS

It is apparent from the results that reliable connection between the surface and the substrate occurs for the selected metallization and annealing regime over the range of thicknesses of the undoped layer up to about 500 nm. At higher thicknesses, it is necessary to increase the energy density of the laser beam which, however, has a detrimental impact on the quality of the surface of the annealed contact. Connection of the surface with the substrate was not possible for samples with undoped layers thicker than 1600 nm. The thickness of the modified subcontact layer during annealing of W/In/Ge contacts on *n*-type GaAs at the optimum energy density of 0.09 J/cm^2 attains values of 500 nm.

REFERENCES

1. Wu, C., Hsu, W., Shien, H., *et al.*, 1995, *IEEE Electron Device Lett.*, **16**, 112.
2. Messica, A., Meirav, U., and Shtrikman, H., 1995, *Thin Solid Films*, **257**, 54.
3. Bühlmann, H.J. and Ilegems, M., 1991, *J. Electrochem. Soc.*, **138**, 2795.
4. Zwicknagl, P., Mukherjee, S.D., Capani, P.M., *et al.*, 1986, *J. Vac. Sci. Technol. B*, **4**, 476.
5. Shen, T.C., Gao, G.B., and Mokroc, H., 1992, *J. Vac. Sci. Technol. B*, **10**, 2113.
6. Tardy, J., Rojo-Roméo, P., Viktorovitch, P., *et al.*, 1996, *Solid-State Electron.*, **39**, 225.
7. Lin, X.V., Lampert, W.V., Swider, W., *et al.*, 1994, *Thin Solid Films*, **253**, 490.
8. Hudec, L., Macháč, P., Myslík, V., *et al.*, 1995, *Proc. Int. Conf. EDS'95* (VUT Brno, Czech Republic).
9. Macháč, P., Myslík, V., and Vrňata, M., 1994, *Electron. Lett.*, **30**, 1185.
10. Macháč, P., Myslík, V., and Vrňata, M., 1996, *Acta Polytechnica, CTU Prague*, **36**, 93.
11. Hudec, L., Macháč, P., and Myslík, V., 1995, *J. Electrical Eng.*, **46**, 25.

Powder Alloying of Low–Carbon Steel by CO₂ Laser

H. Chmelíčková*, L. Kucharičová**, and J. Grézl***

* Joint Laboratory of Optics of Palacky University and Institute of Physics of the Academy of Sciences of Czech Republic Olomouc, 17. listopadu 50, Olomouc, 772 07 Czech Republic
e-mail: chmelh@risc.upol.cz
** Faculty of Natural Sciences, Palacky University, tř. Svobody 26, Olomouc, 772 00 Czech Republic
*** LASERTECH ltd., Vejdovského 6, Olomouc, 772 00 Czech Republic
Received August 7, 1997

Abstract—Alloying is one of several methods of surface treatment by laser beam. Results of this application are wear-resistant, corrosion-resistant and high-temperature oxidation-resistant coatings on substrates, for instance, low–carbon steel. This method is based on the melting of the substrate surface and introducing of additional material. In cooperation with firm LASERTECH, ltd. Olomouc, we have made an experiment with low–carbon steel 0.2%C and two powders: metal powder K 55 and ceramic powder SiC. Results of the experiment are introduced and illustrated by graphs and photos.

1. INTRODUCTION

Laser surface treatment is divided into several methods: transformation hardening, melting, alloying, and cladding. Each of them is characterized by set of process parameters (power, diameter, transverse speed), which determine results of application. Laser alloying and cladding both need melting of component surface and introduction of additional material. This material can be in powder or solid form and can be preplaced or fed during melting process. Applied surface layer is usually 0.5–2.0 mm.

2. EXPERIMENT

We made an experiment with specimen from low–carbon steel 0.2% C and two kinds of powders: metal powder K 55 and ceramic powder SiC. The parameters of these powders are introduced in Table 1. Powders were fed into a melting pool by means of a powder feeding tube of powder feeder TWIN Compact, that stands as near as possible by worktable of CO₂ laser Control ltd. with maximum power 2500 W (Fig. 1).

Process parameters remained constant for four values of transverse speed:

Power:	2200 W
Beam diameter:	0.4 mm
Focal distance:	150 mm
Transverse speeds:	100, 400, 800, 1200 mm/min

Table 1. Parameters of metal powder K 55 and ceramic powder SiC

Material	Composition	Temperature of melting	Grain size (μm)
K 55	Ni, Cr, Si, B, W, Mo	1303 K	100
SiC	Si, C	2973 K	63

We applied three traces with overlap 50% and one control trace for each speed. Alloying samples were than cut in YZ plane, ground, and etched. Cross sections of affected zones were measured and documented by means of device NEOPHOT 2.

3. RESULTS

There are all values of dimensions of affected zones in Table 2. The dependence of the dimensions of melted zone on transverse speed is illustrated in

Table 2. Experiment resolution: dimensions of affected zones

Powder traces	Number of sample	Width (mm)	HIGH (mm)
K 55–1 trace	2	4.4	3.6
	4	1.78	1.87
	6	1.35	1.61
	8	0.96	1.22
K 55–3 trace	1	8.61	4.01
	3	4.03	1.89
	5	2.59	2.25
	7	2.31	2
SiC–1 trace	11	3.9	2.87
	13	2.36	2.16
	15	2.33	1.53
	17	1.13	1.88
SiC–3 trace	10	8.8	2.93
	12	5.4	2.73
	14	3.14	2.47
	16	2.1	2.01
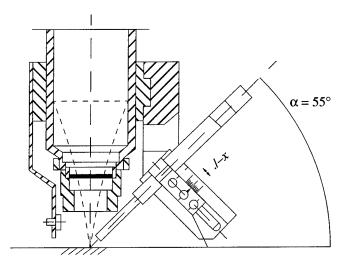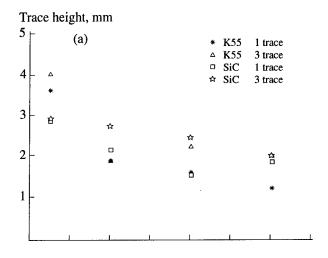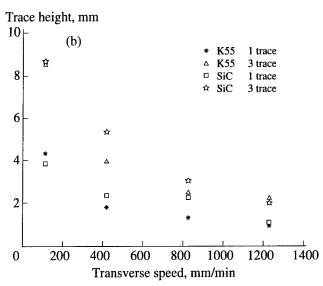
Fig. 1. Scheme of powder feeding.

Fig. 2. Trace high and width as a function of transverse speed.

graphs on Fig. 2. We can see that width and height both fall down with increasing speed.

Vickers hardness test was made with test load 98.07 during time 10 s (10 Hv). Average values are

Specimen	116
Trace K 55	383
Trace SiC	336

We can see that the hardness of surface layer increased three times. Transverse speed has also effect on quality of affected zone, that is nonuniform for
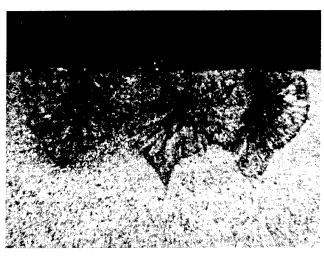
Fig. 3. Sample no. 3, K 55, $v = 400$ mm/min, magnified 15.6×.

Fig. 4. Sample no. 7, K 55, $v = 1200$ mm/min, magnified 25×.
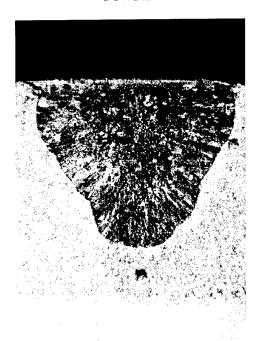
Fig. 5. Sample no. 2, K 55, $v = 100$ mm/min, magnified 12.5×.

speeds less than 400 mm/min and insufficient for speed greater than 800 mm/min.

There are photographs of four various samples on Figs. 3–5. We can see different character of affected zone of three traces K 55 for speed 400 mm/min (Fig. 3), and the uneven affected zone for the biggest speed 1200 mm/min (Fig. 4). Figure 5 shows 12.5× magnified one trace of K 55 for the smallest speed 100 mm/min.

4. CONCLUSION

The conclusion of our work follows from the obtained results: experiment in smaller speed interval 400–800 mm/min will be made with more kinds of powder materials to gain optimal results.

REFERENCES

1. Wearasinghe, V.M., 1984, Laser Cladding of Flat Plates, *PhD Thesis* (University of London).
2. Craffer, R.C. and Oakley, P.J., 1985, *Process and Physical Aspects of Continuous Wave Laser Processing, International Course on Applied Laser Tooling* (Vigo, Spain).

Laser Deposition and Characterization of Optical Layers

J. Bulíř, M. Jelínek, E. Masetti*, and R. Larciprete**

Institute of Physics, Academy of Sciences of the Czech Republic, Na Slovance 2, Prague 8, 180 40 Czech Republic
e-mail: bulir@fzu.cz
* *ENEA, C.R. Casaccia via Anguillarese, 301, S.M. Di Galeria, Roma, 00060 Italy*
** *ENEA, C.R. Frascati, via Enrico Fermi, 45, Frascati (Roma), 00044 Italy*
Received August 18, 1997

Abstract—In this work is presented study of optical properties of the HfO_2, LaF_3, Al_2O_3, CeO_2, Yttrium-stabilized ZrO_2 deposited by Pulsed Laser Deposition. The results were compared with magnetron sputtered Al_2O_3 and Ta_2O_5. The experimental arrangement consists of the KrF excimer laser and stainless-steel chamber where the rotating target and heated substrate holder are placed. The laser beam is focused by the lens onto the target of required material The films were deposited on fused silica substrate (Suprasil). For correct stoichiometry, the oxide films were deposited in oxygen atmosphere. The films were studied by spectroscopy in the UV–Visible and infrared ranges and by spectroscopic ellipsometry. The ellipsometric real-time procedure was used to characterize thin films and for the detection of possible changes on the samples induced by high-power radiation. Al_2O_3 coatings deposited by magnetron sputtering had porosity degrees of 14%. The fraction of pores was calculated by Bruggeman model of effective media. PLD-deposited Al_2O_3 was more compact. However, this film possessed inhomogenious refractive index profile. Some films deposited by PLD (especially fluorides) possess high absorption background caused by small particles on the surface that originate from deposition process. The multilayer structure Ta_2O_5 were deposited without breaking vacuum due to multitarget carousel. One was made by two films Ta_2O_5 and the other coating was made by five couples of Ta_2O_5. Absorption on the interfaces between the layers was studied on these multilayers.

1. INTRODUCTION

Aluminum oxide crystallizes in the corundum (α-Al_2O_3) rhombohedral structure. It is also known as sapphire. The system is unaxial and optical properties measured on a single crystal are therefore anisotropic. The structure of oxygen sublattice is close-packed. Aluminum oxide is useful material for optical coating, namely, in UV spectra because of its wide region of spectral transmission (the absorption edge in the UV region starts at 7 eV) and high hardness and chemical resistance. The refractive index changes from 1.75 to 1.8 in visible region.

Tantalum oxide (Ta_2O_5) is suitable material for the optical layers because of its high refractive index being around 2.4. It is suitable namely for the multilayer systems of dielectric mirrors where there are altered layers of low refractive index with layers with high refractive index.

The rare-earth oxides are potentially useful materials for various optical and electronic applications. One of such rare-earth materials is cerium dioxide (CeO_2) with the fluorite CaF_2 structure. CeO_2 has an ionic bond. The material is very stable even at a very high temperature. The affinity of the cerium with oxygen is very high and the cubic phase can be deposited in an ultrahigh vacuum condition.

Zirconia (Zirconium oxide, ZrO_2) is thermodynamically stable at room temperature but transforms reversibly to the tetragonal crystallographics system on heating above 1173°C. The crystal structures are unusual in that the structure becomes more symmetric on heating; thus, the monoclinic form first transforms and at 2450°C the cubic fluoride phase becomes stable. The higher temperature phases may be stabilized against destructive phase transformation by the addition into solid solution of specific cubic oxides, for example, a few mole percent of yttria (Y_2O_3) can create yttria-stabilized zirconia (YSZ, $(ZrO_2)_{1-x}(Y_2O_3)_x$). Yttria additive, when incorporated into monoclinic phase, first stabilizes the tetragonal form and with further addition, the cubic phase. The cubic fluorite structure is maintained over the composition range $x \approx 0.04$–0.3. YSZ has an index of refraction of 1.98 at 632.8 nm, and 5-eV band gap. The YSZ is not suitable material for UV application because the strong electronic absorption begins around 400 nm.

Optical coating for lasers must meet different requirements depending on the laser system. A common performance requirement is high laser damage resistance which depends on a number of factors involving optical mechanical, thermal, and structural properties of the coating. Most of these characteristics are affected by the deposition process. These properties which are related to film density and microstructure are often different from the ideal bulk values and have been observed to depend on ambient conditions, especially in films with low packing density or high porosity. The film structure also controls the surface morphology, which needs to be smooth to prevent light scattering.

Coatings, especially of high melting temperature materials (as HfO_2, Al_2O_3, CeO_2 and YSZ) deposited by conventional evaporation techniques (i.e., evaporation from a heated crucible and by electron beam) have varying degrees of porosity depending on the material and deposition conditions. Moisture penetrating through pores alters the optical and mechanical properties of the coatings, in an irreversible fashion. The optical effects are due to filling of the pores with water, which has a higher refractive index (1.33 in visible region) than air, and due to changes in the polarizability of the grain boundary surfaces due to adsorption of polar molecules. Moisture also induces compressive or tensile stress depending on the material and grain boundary surface chemistry. The packing density is therefore an important parameter in the final performance of the optical thin film.

Pulsed laser deposition is one of techniques, where energetic ions are generated in the laser-induced plasma. It was shown that films with high packing density and high refractive index compared to conventionally evaporated films are achievable [1]. The higher energy of laser-evaporated species (around 50 eV) compared to thermal evaporation (0.1–1 eV) affects to enhance the surface mobility and provides crystallization at a lower temperature. Owing to the high surface mobility of the film-forming species and resputtering of loosely bound particles, the structure becomes more compact. The main disadvantage of the pulsed laser deposition is low thickness homogeneity of the film and creation of droplets on the film surface. This effect is observed namely at low-temperature melting materials. The droplets on the surface of the film cause scattering of incident light and debase the quality of the optical device. Both disadvantages could be eliminated by modification of the deposition method.

In this work are presented optical properties of the HfO_2, LaF_3, Al_2O_3, CeO_2, YSZ deposited by PLD and Al_2O_3 and Ta_2O_5 deposited by magnetron sputtering. Laser-deposited multilayers HfO_2/SiO_2 were also studied.

2. EXPERIMENTAL DETAILS

The experimental arrangement of the deposition system consists of KrF excimer laser and deposition chamber. The KrF excimer laser beam was focused by lens onto a rotating target of required material. The laser beam fluence was changed by the laser spot size depending on focus of the lens. The laser beam strokes the target at angle of 45° to the normal. Ablated particles caught the heated substrate at distance of 5 cm from the target. The films were deposited on fused silica substrate (Suprasil).

The stainless-steel vacuum chamber pumped by turbomolecular pump produced a base pressure of 10^{-3} Pa. For correct stoichiometry the deposition of oxides films was carried out in oxygen ambient and the pressure was controlled by the needle valve. The experimental con-

Table 1. Summary of deposition conditions of pulsed-laser-deposited films

Material	HfO_2	Al_2O_3	CeO_2	YSZ
Substrate temperature (°C)	550	690	520	520
Oxygen pressure (Pa)	0.5	10^{-2}	5×10^{-2}	5×10^{-2}
Laser fluence (Jcm^{-1})	2.2	19	8.8	8.8
Film thickness (nm)	104	262	252	180
Deposition rate (nm/pulse)	5.8×10^{-3}	7.3×10^{-3}	2.1×10^{-2}	1.5×10^{-2}

Table 2. Summary of deposition conditions of magnetron sputtered films

Material	Al_2O_3	Ta_2O_5
Total pressure (Pa)	7×10^{-1}	5×10^{-1}
Oxygen pressure (Pa)	7×10^{-2}	1.8×10^{-1}
Film thickness (nm)	184	185
Deposition rate (nm/min)	10.8	14.2

Table 3. Summary of deposition conditions of pulsed-laser-deposited multilayers HfO_2/SiO_2

Coating structure	5 couples of HfO_2/SiO_2		single couple of HfO_2/SiO_2	
Material of target	HfO_2	Si	HfO_2	Si
Substrate temperature (°C)	690	690	690	690
Oxygen pressure (Pa)	0.5	0.5	0.5	0.5
Laser fluence (Jcm^{-1})	3.2	13	3.2	13
Film thickness (nm)	50	50	250	250
Total coating thickness (nm)	500		500	

ditions of PLD and magnetron sputtered films are summarized in Tables 1 and 2, respectively.

The fluorides were deposited at base pressure of 10^{-3} Pa. Their deposition process was optimized in order to achieve film without droplets. However, some amount of droplets remained on the surface. Low value of melting temperature is the main reason of droplets creation. The fluorides films were omitted of the study of optical properties because of their low optical quality.

The multilayer structure HfO_2/SiO_2 were deposited without breaking vacuum due to multitarget carousel. In order to distinguish between absorption at the interface and absorption in the film bulk it was deposited two sets of coatings having the same thickness but different structure: one was made by two films HfO_2/SiO_2

and the other coating was made by five couples of HfO_2/SiO_2, each film with a thickness that is 1/5 with respect to the previous case. The deposition conditions are shown in Table 3.

For optical study was used ellipsometer of null type and photospectrometer Lambda9-Perklin Elmer. The photospectrometer was used in tree configurations: for measuring of transmitted, of reflected, and of scattered light. The setup for measuring of scattered light consists of "white" chamber collecting all scattered light. The light from monochromator is directed through this chamber and incident on the measured sample inside the chamber. The transmitted and reflected beam is absorbed by black surface. Only the scattered light is reflected on the collecting sides of the chamber and contributes to the increase of the measured signal.

The damage threshold was studied by the KrF laser working on 248 nm. The laser beam was homogenized and focused on the studied sample. The size of the spot was 4×4 mm. The energy density in the spot was
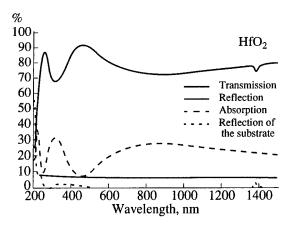
Fig. 1. Optical spectra of HfO_2 film deposited on fused silica substrate (Suprasil) by PLD. Absorption is obtained as the rest of the photo energy to 100%. The absorption at 1380 nm is from the substrate.
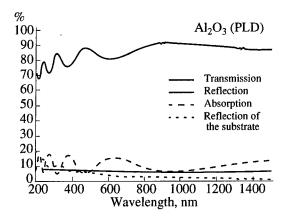
changed from 0.5 to 0.78 J/cm^2. The film was treated by a number of shots of the same energy in the same place. Changes of the film surface were studied after each shot. A real-time four-detector ellipsometer [2] was used for the determination of the damage threshold. The measuring He–Ne laser beam working on 633 nm was incident on the same spot as KrF laser beam at angle of 63.6°.

3. RESULTS

3.1. Optical Spectroscopy

At first the layers were studied by the optical spectroscopy in order to get information of thickness, refractive index, inhomogeneity of refractive index, and absorption. Absorption was calculated from the transmission and reflection spectra as a rest to the 100%. The absorption curves of some materials show strong edge in UV region. Ta_2O_5 and YSZ possess the edge above 300 nm. Consequently, they are not suitable for UV optics. However, in near-IR region these two material are well transparent. The HfO_2 (Fig. 1) film have absorption edge below 250 nm. So, both could be applicable for the most frequently used UV excimer laser, KrF laser working at 248 nm. Al_2O_3 was deposited by two methods: pulsed laser deposition and magnetron sputtering. The absorption edge was not found in the border of measured region. In addition, the laser-deposited Al_2O_3 (Fig. 2) possess high absorption background increasing from several percent in IR region to 15% at measured limit in UV region. The surface of this film is covered by small particles originating from deposition process. The target surface is melted during laser pulse and the drops are erupted from the target. These particles on the surface could be reason of the absorption background. The incident light can be scattered on the surface roughness. The scattered light was measured but it was ascertained that only small part of light is scattered (see Fig. 4). In the spectroscopic graphs, there is also shown a reflectivity curve of the clear substrate.

Fig. 2. Optical spectra of Al_2O_3 film deposited on fused silica substrate (Suprasil) by PLD. Absorption is obtained as the rest of the photo energy to 100%.
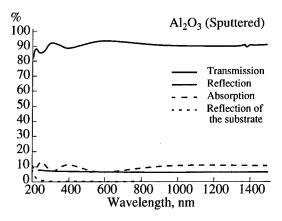
Fig. 3. Optical spectra of Al_2O_3 film deposited on fused silica substrate (Suprasil) by magnetron sputtering. Absorption is obtained as the rest of the photo energy to 100%.
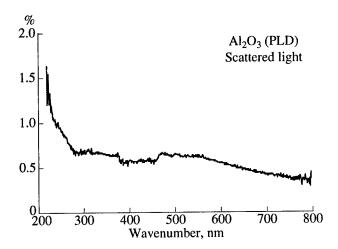
Fig. 4. The fraction of light scattered on the surface roughness of Al_2O_3 film deposited by PLD.

As results from theory for homogeneous monolayer on the substrate, the minima of peaks of samples should lie on this curve. However, for some samples, the minima lie under the substrate reflectivity (Fig. 1) or above the substrate reflectivity. This effect can be caused by inhomogeneity of the refractive index profile. The inhomo-

geneous films can be adopted by models with analytical refractive index profiles, such as linear, exponential, or parabolic profile [3]. A number of papers are interested in the evaluation of the film inhomogeneity [4]. A coefficient of homogeneity of linear profile is defined by the

term $\delta = \dfrac{n_0 - n_i}{\sqrt{n_0 n_i}}$, where n_0 is refractive index near the

surface of the film and n_i is refractive index of the film near the substrate. The coefficient was determined from distance between minima of reflection curves of samples and substrate. For PLD Al_2O_3 film it was about 0.1.

The refractive index and thickness were calculated by envelope method from the minima and the maxima of peaks of the reflectivity curves. The obtained points of refractive index were fitted by the Cauchy dispersion

$n^2 = A + \dfrac{B}{\lambda^2} + \dfrac{C}{\lambda^4}$. The thickness and curves of refrac-

tive indices are shown on Fig. 5.

As it is clear from Fig. 5, the refractive index of the magnetron sputtered Al_2O_3 film is much lower than that of the bulk Al_2O_3. It could be caused by high degree of porosity of the film. Air and moisture penetrate through the pores. This mixture of Al_2O_3 and air or water can be
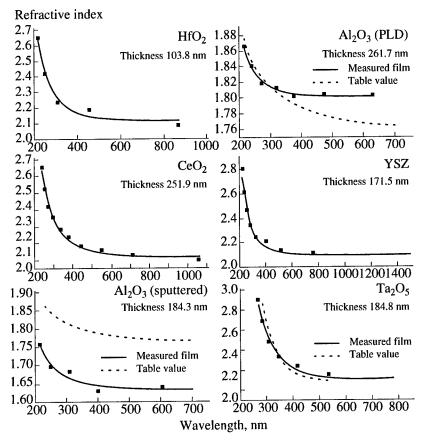
Fig. 5. Refractive index of laser-deposited HfO_2, Al_2O_3, CeO_2, and Yttrium-stabilized ZrO_2 films and magnetron sputtered Al_2O_3 and Ta_2O_5 films on Suprasil. The values were calculated by envelope method from reflectivity spectra. The obtained points were fitted by Cauchy dispersion model.
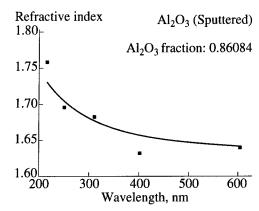
Fig. 6. Refractive index of magnetron sputtered Al_2O_3 film. The points are fitted by Bruggeman model of effective medium consisting of Al_2O_3 and air mixture.
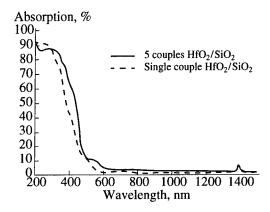
Fig. 7. Absorption of two multilayers consisting of couples of HfO_2/SiO_2. The total thickness of both coatings is about 500 nm.

Fig. 8. A change of ellipsometric angles during the irradiation by KrF excimer laser. The energy density on the spot was 0.75 J cm^{-2}. He–Ne laser beam (633 nm) was incident on the measured film at angle of 63.6°. After each shot 10 measurements were accomplished.

considered to make up effective medium. Bruggeman [5] suggested the effective medium approximation:

$$f_1 \frac{\tilde{N}_1^2 - \tilde{N}_e^2}{\tilde{N}_1^2 + 2\tilde{N}_e^2} + f_2 \frac{\tilde{N}_2^2 - \tilde{N}_e^2}{\tilde{N}_2^2 + 2\tilde{N}_e^2} = 0,$$

where N_1, N_2 are the complex refractive indices of the two compounds, f_1, f_2 are their volume fractions, and N_e is the complex refractive index of the effective medium.

The points of refractive index were fitted by the Bruggeman model. A mixture of Al_2O_3 with table value of refractive index and air having refractive index equal to 1 was considered. As a result, 0.14 fraction of air in this effective medium was obtained.

Two structures of multilayer were measured by photospectrometer. The absorption of both coatings is compared on Fig. 7. It is clear that the absorption of the coating consisting of ten layers possesses higher absorption than the one consisting of two layers even the thickness of both coating is the same. The absorption edge of the former coatings is shifted to the lower photon energies than that of latter coating. Conse-

quently, the light is absorbed mainly on the interfaces between the layers.

The HfO_2 film was treated for damage threshold study. The damage of the film started in the center of the irradiated zone and then it gradually spread over the whole tested area. The change of the ellipsometric angles due to KrF laser irradiation with energy density of 0.78 J cm^{-2} is shown on Fig. 8. The changes start after the fifth shot and the layer is totally damaged till the fifteenth shot. Changes during irradiation with 0.68 J cm^{-2} began to reveal after the tenth shot. No damage was observed during irradiation with energy density of 0.5 J cm^{-2}.

4. CONCLUSION

This work demonstrates that PLD is possible method for deposition of the optical thin layers and multilayers. The films of good optical materials can be prepared at room temperature, which could play an important role in some applications. The films deposited by PLD are more compact than those deposited by magnetron sputtering. For high-power optical applica-

tions it is necessary that the films possess low absorption and smooth surface. However, the laser-deposited films have usually the small droplets on the surface. This is the main disadvantage of the PLD method. The second disadvantage is low homogeneity of the film thickness over large coated area. Even these two disadvantages make the PLD method less suitable for good quality optical films, both could be eliminated by optimization of the deposition process eventually by improving of experimental setup.

ACKNOWLEDGMENTS

REFERENCES

1. Reise, G., Weissmantel, S., Steiger, B., et al., 1995, Appl. Surf. Sci., **86**, 107.

2. Masetti, E. and de Silva, M.P., 1994, Thin Solid Films, **246**, 47.

3. Montecchi, M., 1995, Pure Appl. Opt., **4**, 831.

4. Montecchi, M., Masetti, E., and Emiliani, G., 1995, Pure Appl. Opt., **4**, 15.

5. Bruggeman, D.A.G., 1935, Ann. Phys. (Leip.), **24**, 636.

Study of Nitrogenated Carbon Coating Deposited by PLD

J. Bulíř, M. Jelínek, V. Vorlíček, and K. Jurek

Institute of Physics, Academy of Sciences of the Czech Republic, Na Slovance 2, Prague 8, 180 40 Czech Republic

e-mail: jelinek@fzu.cz

Received August 8, 1997

Abstract—The interest of amorphous carbon (a-C) and carbon nitride films is stimulated by the search of new protective coatings of the mechanical tools due to their high hardness and low friction coefficient. The series of nitrogenated amorphous carbon films (a-C : N) were grown in nitrogen atmosphere from graphite target by pulsed laser deposition method. A KrF excimer laser (200 mJ, 5 Hz) was used. The fused silica and steel substrates were placed at distance of 4 cm from the target. A high voltage of +2100 or –2100 V was applied between substrate and target. A capacitor connected to the target and substrate holder was charged by this voltage. An additional dc discharge is ignited by each laser shot in the deposition chamber. The effect of the discharge on the C–N stoichiometry and on the chemical bonding was studied by electron microprobe X-ray photoemission measurement, and by Raman spectroscopy. The N/C ratio reached a value around 0.2 at the nitrogen pressure above 10 Pa. The nitrogen molecules were dissociated by applied dc discharge in the deposition chamber in order to increase the reactivity of nitrogen.

1. INTRODUCTION

Investigation of nitrogenated carbon became after Liu and Cohen predicted theoretically the superior hardness of the hypothetical β-C_3H_4 material [1].

A nitrogenated amorphous carbon (a-C : N) has been deposited by several deposition methods. a-C : N films deposited by pulsed laser deposition (PLD) from graphite target in nitrogen atmosphere usually contained lower percentage of nitrogen incorporated in the film comparing with other methods [2, 3]. The main reason is low reactivity of molecular nitrogen.

Several experiments with additional arc discharge have been used in conventional pulsed laser deposition to produce additional reactive species [4, 5]. A dc bias voltage applied to the substrate accelerates and attracts the positively or negatively charged ionic species. In addition, the arc-discharge-induced plasma has significantly higher degree of ionization than the laser plasma [4, 6]. In that way, the reactivity of nitrogen can increase.

Raman spectra of a-C and a-C : N were compared in [7]. The D/G ratio of the nitrogenated films was observed to be much higher than that of the a-C films. The narrowing of the G band of nitrogenated films was also observed. It is believed that the increase of D band intensity of a-C : N films does not represent increasing disorder in the structure; however, the decreasing of bandwidth indicates the removal of bond angle and bond disorder [8]. The increase of the ratio D/G indicates increase of the number and/or size of graphitic domains in the films.

In this work, series of nitrogenated amorphous carbon films was deposited by pulsed laser deposition. The influence of additional electrical discharge in a nitrogen atmosphere on the structure of a-C : N films was studied. Main idea of this study is to obtain as high as possible concentration of nitrogen atoms incorporated in the structure. Concurrently with this criteria the structure should be dense and compact.

2. EXPERIMENTAL DETAILS

2.1. Preparation of Samples

The experimental setup consists of a KrF excimer laser (EAK, type ELI-94) and vacuum chamber, in which a substrate holder is placed in the distance of 4 cm from a graphite target. The laser beam (pulse duration 20 ns, repetition rate 5 Hz) was focused by the fused silica lens on the target at an angle of 45°. The target was rotated during deposition in order to avoid a drilling effect. The power density of the beam on the target was around 2×10^8 W cm^{-2}.

The films were deposited on silicon substrate. The substrates were optically polished and cleaned in acetone, toluene, and ethanol before deposition.

At first, the vacuum chamber was pumped out to a pressure of 2×10^{-3} Pa by an oil diffusion pump. Films were deposited on silicon under nitrogen atmosphere of pressure p_N from 0.1 to 100 Pa. During deposition process, temperature of the substrate, T_S, was set on 20 or 370°C. In the arc discharge deposition experiment, the target and substrate holder was electrically connected with a high-voltage source so that the laser-induced plasma initiates the arc discharge. A 0.25-µF capacitor placed outside of the vacuum chamber was coupled to the electrodes. The capacitor was charged to a high voltage, V_{S-T}, of +2100 or –2100 V before every laser pulse by a stabilized dc source. Some of the samples were deposited without the additional arc discharge so that the effect of the discharge could be studied. Plasma plume produced only by laser shot on graphite target (without additional discharge) was usually small, only

a few millimeters in height. The arc discharge enlarged the plasma plume to the full space between the target and substrate such that the ionization of the atoms had significantly higher degree and the nitrogen molecules were more dissociated. A process of capacitor discharging was observed on storage scope. The time of the full discharging of capacitor was between 20 and 30 μs.

2.2. Characterization of the Films

Coatings were analyzed on electron probe X-ray microanalyzer JXA 733 of JEOL. Energy of primary electrons was 3 keV and WD spectrometer with NiC X-ray mirror was used for C, N, and O radiation measurement. Full area of spectral peaks was measured on both, specimens and standards. As standards cubic electrically conductive BN and carbon-coated SiO_2 were used. The spectra of the thinnest film show very high background arising from the silicon substrate. The very high background degraded the accuracy of measurement. All peaks intensities were normalized to the intensities of appropriate standards. k-ratios were converted to weight percentage using program STRATA by Pouchou and Pichoir. This software was supplied by KEVEX-Fison company.

Raman spectra were measured in near-backscattering geometry using 514-, 488-, and 457-nm line of Ar-ion laser with the power of 70 mW. The scattered light was analyzed by the double-grating spectrometer (Spex 14018) and detected by a Quantacon photomultiplier (RCA C31034) operating in the photon-counting regime. The spectral slitwidth never exceeded 6 cm⁻¹. All spectra were fitted by two Gaussians positioned near 1360 and 1560 cm⁻¹ for D and G band, respectively.

3. RESULTS

The thickness of each film was measured by the alphastep. It ranged from 50 to 200 nm.

The graph on Fig. 1 shows the effect of the additional arc discharge on a deposition rate of the film. The deposition rate of film deposited without bias is 0.2 nm/pulse for both substrate temperatures. The negative bias U_{S-T} has only weak effect on increase of the deposition rate while the positive bias U_{S-T} strongly influences an increase of the deposition rate which is twice more than that without bias. The high deposition rate is associated with mass density of the films. The films deposited without arc discharge possess mass density of 2 g cm⁻³. The density of films deposited with positive and negative bias U_{S-T} is reduced to value of 1.4 g cm⁻³ and 1.6 g cm⁻³ (see Fig. 2)

An influence of the arc discharge on the N/C ratio is shown on Fig. 3. The values have comparative meaning because of very low accuracy of the measurement. No nitrogen peak was found in spectra of films deposited without the arc discharge. The additional discharge significantly increased the amount of nitrogen incorporated
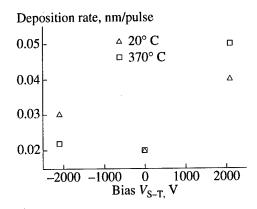
Fig. 1. Deposition rate of the a-C : N films deposited at two different substrate temperatures vs. substrate–target bias.
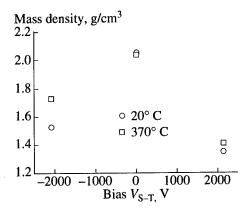
Fig. 2. Mass density of the a-C : N films deposited at two different substrate temperatures vs. substrate–target bias.
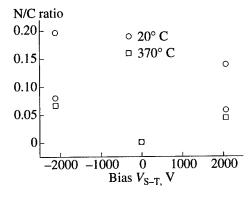
Fig. 3. The N/C ratio of the a-C : N films deposited at two substrate temperatures with positive and negative bias, and without bias. The values have comparative meaning only.

in the structure. The spectra also revealed a relatively high amount of oxygen contained in the film. The main contribution can be attributed to air oxygen or water adsorbed by the films which exhibit an imperfect density.

Raman spectra of the samples deposited at substrate temperature 20 and 370°C are shown on Figs. 4a and 4b, respectively. There are seen a comparison of spectra of
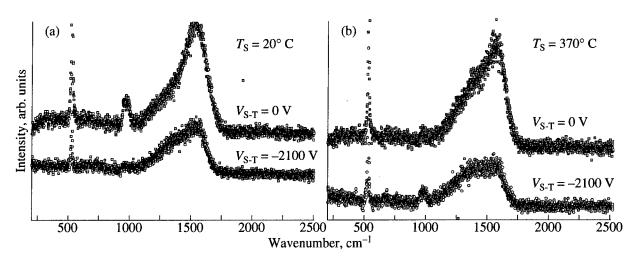
Fig. 4. Raman spectra of two samples deposited at (a) 20°C and (b) 370°C. The uppers were deposited without arc discharge and the lowers with negatively biased arc discharge. The spectra were measured at 514-nm line of argon laser.
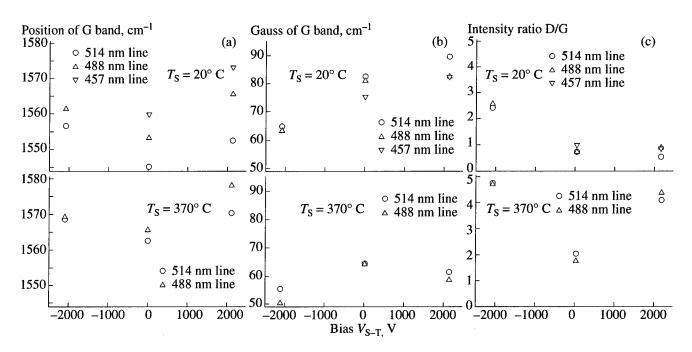
Fig. 5. Results of Raman spectra fitting versus substrate–target bias, V_{S-T}. The spectra were measured at three different wavelengths of exciting light. The samples were prepared at substrate temperature of 20 and 370°C.

a-C : N film deposited without arc discharge and those with arc discharge deposited a-C : N film. The both spectra of arc-deposited films are weaker than the spectra of a-C : N films deposited without arc discharge. Especially, the G band part of these spectra is reduced thereby the D/G intensity ratio is enhanced. No peaks assigned to triple-bonded nitrogen to carbon atom were found near 2220 cm⁻¹. The peaks positioned at 520 and 970 cm⁻¹ are associated with first and second order of silicon substrate.

The arc discharge addition influenced a shift of Raman G band position up to higher wavenumber (see Fig. 5a) as well as the narrowing of the G band (see

Fig. 5b) and enhance of the D/G ratio (Fig. 5c). Especially, negatively biased arc discharge has significant effect on the narrowing of the G band and increase of D/G ratio. Only the a-C : N film deposited at room temperature with positively biased substrate shows weak influence of the arc discharge on the G band width and on the D/G ratio. The effect of the discharge is the same as that of enhance of the substrate temperature T_S.

4. CONCLUSION

It was confirmed that the reactivity of nitrogen gas is enhanced by the electrical dc discharge. It was

revealed by the enhanced concentration of nitrogen in the a-C : N structure. The samples deposited at low nitrogen pressure of around 0.2 Pa have usually no nitrogen observed. However, the a-C : N films made in the dc discharge possess sufficient amount of nitrogen which does not act as terminator bonds. This effect is accompanied by the reduction of mass density of the a-C : N films. The Raman spectra of those samples did not show any peak at 2200 cm^{-1} corresponding to triple bonding C–N. However, the presence of nitrogen caused any changes of broad D–G band that reveal some order takes on. The intensity of graphitic peak at 1575 cm^{-1} is lowered by the presence of nitrogen in the structure.

ACKNOWLEDGMENTS

REFERENCES

1. Liu, A.M. and Cohen, M.L., 1989, *Science*, **245**, 841.

2. Fulin Xiong, Chang, R.P.H., and White, C.W., 1993, *Mat. Res. Soc. Symp. Proc.*, **285**, 587.

3. Zhao, X.-A., Ong, C.W., Tsang, Y.C., *et al.*, 1995, *Appl. Phys. Lett.*, **66**, 2652.

4. Pompe, W., Sheibe, H.-J., Siemroth, P., *et al.*, 1992, *Thin Solid Films*, **208**, 11.

5. Krishnaswamy, J., Rengan, A., Narayan, J., *et al.*, 1989, *Appl. Phys. Lett.*, **54** (24), 2455.

6. Miller, H.C., 1979, *J. Phys. D.*, **12**, 1293.

7. Jeansong Shiao and Hoffman, R.W., 1996, *Thin Solid Films*, **283**, 145.

8. Dillon, R.O., Woollam, J.A., and Katkanant, V., 1984, *Phys. Rev. B*, **29** (6), 3482.

== **COMMENTS**

On the Paper "Micromaser and Laser with Competitive One- and Two-Photon Processes" by A. Joshi (*Laser Physics*, 1997, 7, 68)

T. Gantsog, G. M. Meyer, M. O. Scully, and H. Walther

Max-Planck-Institut fur Quantenoptik, Hans-Kopfermann-Str. 1, D-85748 Garching, Germany
e-mail: herbw@mste.laser.physik.uni-muenchen.de

In [1], Joshi presents the theory of the micromaser and laser operating on three-level atoms with energy levels *a*, *b*, and *c*. The transition between *a* and *b* is a one-photon transition, the one between *b* and *c* is assumed to be a two-photon transition. The case of both transitions being one-photon transitions had been treated at length previously in [2]. Whereas [1] was submitted on 23 July 1996, [2] had already been published on 15 March 1996 and circulated as a preprint since 11 July 1995.

The two-photon transition is described by a slightly different interaction Hamiltonian than the one-photon transition. However, we would like to point out that the calculation in [1] follows exactly the same lines as the one in [2] and the results are qualitatively the same. The reader may judge in how far [1] resembles or copies [2]. As a matter of fact, Joshi does not give any credit to [2], although he obviously used it as his main source of inspiration.

REFERENCES

1. Joshi, A., 1997, *Laser Phys.*, **7**, 68.
2. Gantsog, T., Meyer, G.M., Scully, M.O., and Walther, H., 1996, *Opt. Commun.*, **124**, 579.

7th INTERNATIONAL WORKSHOP ON LASER PHYSICS (LPHYS'98)

(Berlin, July 6–10, 1998)

The seventh annual International Workshop on Laser Physics (LPHYS'98) will be held from July 6 to July 10, 1998 in Berlin, Germany.

This conference continues a series of Workshops held in Dubna 1992, Moscow/Volga river tour 1993, New York 1994, Moscow/Volga river tour (jointly with NATO SILAP Workshop) 1995, Moscow 1996 and Prague 1997.

The total number of Workshop participants is expected to be about 200. In the past, participation was typically from over 20 countries.

The Workshop is being organized by:

- General Physics Institute, Russian Academy of Sciences, Moscow, Russia
- international journal Laser Physics
- Max Born Institute for Nonlinear Optics and Short Pulse Spectroscopy, Berlin, Germany

CHAIRMAN:

Alexander M. Prokhorov (General Physics Institute, Russian Academy of Sciences, Moscow, Russia)

DEPUTY CHAIRMAN:

Pavel P. Pashinin (General Physics Institute, Russian Academy of Sciences, Moscow, Russia)

STEERING COMMITTEE:

Joseph H. Eberly (University of Rochester, Rochester, USA)
Mikhail V. Fedorov (General Physics Institute, Russian Academy of Sciences, Moscow, Russia)
Sven R. Hartmann (Columbia University, New York, USA)
Jamal T. Manassah (The City University of New York, New York, USA)
Pavel P. Pashinin (General Physics Institute, Russian Academy of Sciences, Moscow, Russia)
Kirill A. Prokhorov (General Physics Institute, Russian Academy of Sciences, Moscow, Russia)
Wolfgang Sandner (Max Born Institute for Nonlinear Optics and Short Pulse Spectroscopy, Berlin, Germany)
Herbert Walther (Max Planck Institute of Quantum Optics, Garching, Germany)
Valery M. Yermachenko (Moscow State Engineering Physics Institute, Moscow, Russia)
Igor V. Yevseyev (Moscow State Engineering Physics Institute, Moscow, Russia)

ADVISORY & PROGRAM COMMITTEE:

S.N. Bagayev (Institute of Laser Physics, Novosibirsk, Russia)
V.S. Bagnato (University de San Paulo, Brazil)
J. Baudon (Universite Paris-Nord, Paris, France)
W. Becker (Max Born Institute for Nonlinear Optics and Short Pulse Spectroscopy, Berlin, Germany)
S.L. Chin (Laval University, Quebec, Canada)
F. De Martini (University of Rome, Rome, Italy)
A. Dudelzak (Canadian Space Agency, Quebec, Canada)
A.M. Dykhne (Kurchatov Institute of Atomic Energy, Moscow, Russia)
G. Ferrante (Palermo University, Italy)
C. Fotakis (Foundation for Research and Technology-Hellas, Heraklion, Greece)
S.A. Gonchukov (Moscow State Engineering Physics Institute, Moscow, Russia)
G. Huber (Hamburg University, Hamburg, Germany)
M. Jelinek (Institute of Physics, Czech Academy of Sciences, Prague, Czech Republic)
N.I. Koroteev (Moscow State University, Russia)

N. Kroo (Central Research Institute for Physics, Budapest, Hungary)
P. Leiderer (University of Konstanz, Germany)
G.J. Müller (Institute of Laser and Medicine Technology, Berlin, Germany)
S. Nakai (Osaka University, Japan)
V.V. Osiko (General Physics Institute, Russian Academy of Sciences, Moscow, Russia)
P.M. Saari (Tartu Institute of Physics, Tartu, Estonia)
V.V. Samartsev (Kazan Physics Technical Institute, Russian Academy of Sciences, Russia)
W.P. Schleich (Ulm University, Ulm, Germany)
I.A. Shcherbakov (General Physics Institute, Russian Academy of Sciences, Moscow, Russia)
R.W. Solarz (Lawrence Livermore National Laboratory, Livermore, USA)
R. Steiner (Institute of Laser Technologies in Medicine, Ulm, Germany)
E.A. Vinogradov (Institute of Spectroscopy, Russian Academy of Sciences, Troitsk, Russia)
V.P. Yakovlev (Moscow State Engineering Physics Institute, Moscow, Russia)

LOCAL ORGANIZING COMMITTEE (BERLIN, GERMANY)

Chairman:
Wolfgang Sandner (Max Born Institute for Nonlinear Optics and Short Pulse Spectroscopy)

Members:
W. Becker (Max Born Institute for Nonlinear Optics and Short Pulse Spectroscopy)
T. Elsässer (Max Born Institute for Nonlinear Optics and Short Pulse Spectroscopy)
P.-V. Nickles (Max Born Institute for Nonlinear Optics and Short Pulse Spectroscopy)
H. Weber (Berlin Technical University and LMTB Company)

Secretary:
S. Szlapka (Max Born Institute for Nonlinear Optics and Short Pulse Spectroscopy)

SCIENTIFIC SEMINARS:

- **Modern Trends in Laser Physics** (including far IR, X-ray and gamma lasers)
  Co-Chairs: Paul Leiderer (Germany), Jamal T. Manassah (USA), and Kirill A. Prokhorov (Russia)
- **Strong Field Phenomena**
  Co-Chairs: Wilhelm Becker (Germany), Joseph H. Eberly (USA), and Mikhail V. Fedorov (Russia)
- **Laser Spectroscopy**
  Co-Chairs: Sven R. Hartmann (USA), Herbert Walther (Germany), and Valery M. Yermachenko (Russia)
- **Laser Cooling and Atom Optics**
  Co-Chairs: Jaques Baudon (France), Wolfgang P. Schleich (Germany), and Valery P. Yakovlev (Russia)
- **Physics of Solid State Lasers**
  Co-Chairs: Gunter Huber (Germany), Sadao Nakai (Japan), and Ivan A. Shcherbakov (Russia)
- **Laser Methods in Medicine**
  Co-Chairs: Sergey A. Gonchukov (Russia), Gerhard J. Müller (Germany), and Rudolf Steiner (Germany)

SCIENTIFIC PROGRAM

The program consists of invited lectures, contributed and poster reports followed by discussion. The details will be published in later announcements.
The official Workshop language will be English.

ABSTRACTS

A one-page abstract should contain: title; list of authors (the principal author first); affiliations; addresses for correspondence including phones, faxes, e-mails; and the text of abstract. Abstracts should be sent to the following Co-Chairs of the scientific seminars:

- **Modern Trends in Laser Physics**
  Kirill A. Prokhorov
  E-mail: cyrpro@kapella.gpi.ru

- **Strong Field Phenomena**
  Wilhelm Becker
  E-mail: wbecker@mbi-berlin.de
  Mikhail V. Fedorov
  E-mail: fedorov@theor.msk.ru

- **Laser Spectroscopy**
  Valery M. Yermachenko
  E-mail: yerm@mzs.mephi.msk.su

- **Laser Cooling and Atom Optics**
  Wolfgang P. Schleich
  E-mail: schleich@physik.uni-ulm.de
  Valery P. Yakovlev
  E-mail: yakovlev@theor.mephi.msk.su

- **Physics of Solid State Lasers**
  Ivan A. Shcherbakov
  E-mail: ivan@lazkr1.mail.gpi.ru

- **Laser Methods in Medicine**
  Sergey A. Gonchukov
  E-mail: gonch@quanel.mephi.ru

PROCEEDINGS

The Workshop materials accepted by the Steering and Advisory & Program Committees (both invited and contributed) will be published in the international journal Laser Physics. The rules of the manuscripts' preparation can be found in every issue after Issue 3 of 1995 or on the Laser Physics web site:

http://www.maik.rssi.ru/journals/lasphys.htm.

For further information, please contact:

Dr. Andrey N. Kapitanov
Workshop Secretary
Department of Theoretical Physics,
Moscow State Engineering Physics Institute,
31 Kashirskoe Shosse, Moscow,
115409 Russia
Phone: +7-095-390-0947
Fax: +7-095-148-2780
E-mail: LasPhys@meta.msk.ru

Prof. Wolfgang Sandner
Chairman, Local Organizing Committee
Max Born Institute for Nonlinear Optics and
Short Pulse Spectroscopy
Rudower Str. 6
D-12489 Berlin, Germany
Phone: +49-30-6392-1300
Fax: +49-30-6392-1309
E-mail: sandner@mbi-berlin.de

Abstract deadline: March 4, 1998

ACCESS THE LASER PHYSICS WEB SITE FOR INFORMATION ON THE ANNUAL INTERNATIONAL WORKSHOP ON LASER PHYSICS (LPHYS)

http://www.gpi.ru/lphys/lphys97.html

ACCESS THE WEB SITE FOR INFORMATION ON LPHYS'98

http://www.mbi-berlin.de/lphys98/

Announcement

Special Issue "Lasing without Inversion and Interference Phenomena in Atomic Systems," *Laser Physics*, volume 9, no. 3, 1999

A Special Issue of the international journal *Laser Physics* on "Lasing without Inversion and Interference Phenomena in Atomic Systems" will be edited in 1999, # 3. The Guest Editors of the Issue are:

Olga Kocharovskaya
Institute of Applied Physics
Russian Academy of Sciences
46 Ulyanov Str.
Nizhny Novgorod, 603600
Russia
E-mail: kochar@appl.sci-nnov.ru

Paul Mandel
University Libre de Bruxelles
Campus Plaine C.P. 231
1050 Bruxelles
Belgium
E-mail: pmandel@ulb.ac.be

Marlan O. Scully
Texas A&M University
Department of Physic
Center for Theoretical Physics
College Station
Texas, 77843
USA
E-mail: rost@chaos.tamu.edu

Both progress-report and review papers are invited. The deadline for submission of papers is December 1, 1998. The papers have to be mailed to one of the Guest Editors.

Information for Authors

Laser Physics publishes papers dealing with fundamental and application aspects of laser radiation, critical reviews, requested reviews, and letters to the Editor. The following topics will receive particular attention:

Solid State and Liquid Lasers;
Semiconductor Lasers;
Gas Lasers;
Plasma and X-ray Lasers;
Free-Electron Lasers and Laser Accelerators;
Laser Spectroscopy;
Interaction of Laser Radiation with Matter;
Multiphoton Processes in Atoms, Molecules, and Solids;
Coherent Phenomena and Holography;
Nonlinear and Quantum Optics;
Ultrafast Optics and Strong Field Physics;
Fiber Optics;
Methods of Laser Radiation Control;
Novel Laser Materials;
Surface Phenomena;
Application of Lasers for Information Storage and Processing;
Laser Methods in Chemistry, Biology, and Medicine;
Application of Lasers in Ecology;
Novel Methods of Laser Technologies.

Fees will be paid for papers commissioned by the editors; original papers and letters to the Editor will be published without payment.

Manuscripts should be mailed or may be sent by Express Mail to the following address:

Prof. Igor V. Yevseyev, Department of Theoretical Physics, Moscow Engineering Physics Institute, Kashirskoe Shosse 31, Moscow, 115409 Russia

Instructions for Manuscript Preparation

1. GENERAL

1.1. Manuscripts should be submitted in English or Russian. An original and one copy of the manuscript are required.

1.2. Manuscripts should be typed using a laser, jet, or dot-matrix printer or a typewriter.

1.3. The first page of the manuscript should include the title of the paper; initials and the surnames of authors (even if the manuscript is submitted in Russian, the authors should indicate their initials and surnames in English); the mailing addresses of authors (even if the manuscript is submitted in Russian, the authors should indicate their addresses in English); e-mail address of the corresponding author; abstract of the paper; and the topic from the above list to which, in the authors' opinion, the paper can be assigned. The main text of the paper should begin on the second page of the manuscript. The text of the paper should be completed with the References section. The manuscript should also include table, figure, and photograph captions and tables, figures, and photographs. All pages in the manuscript should be consecutively numbered (including tables, figures, and figure and table captions). A separate sheet at the end of the manuscript should contain the following information about the corresponding author: initials and surname, office and home telephone numbers, fax number, and e-mail address (which is highly appreciated).

1.4. In certain cases, the Editorial Board promptly publishes letters to the Editor. The length of a letter to the Editor should not exceed 10 pages, including the abstract, the text of the manuscript, the list of references, figures, photographs, tables, and table and figure captions.

1.5. The Editorial Board considers the submission of a manuscript and an official application to publish this manuscript in the *Laser Physics* journal as intent of the authors to transfer the copyright for a single publication of this paper in the *Laser Physics* journal.

2. PUBLICATION STAGES

2.1. Upon receipt of a manuscript, the Editorial Board informs the authors using e-mail.

2.2. Upon receipt of a manuscript from a reviewer, the Editorial Board informs the authors about the time of publishing of the manuscript using e-mail.

2.3. Authors receive one copy of page proofs, which should be inspected and returned to the Editorial Board within two days. To avoid delays, the Editorial Board may decide not to send page proofs of certain papers to the authors. In this case, the Technical Editor of the journal carries out the proofreading of the paper.

2.4. Authors can order reprints of their paper from МАИК Наука/Interperiodica Publishing for an additional charge. The minimum order is 50 copies of any article. The prices are as follows:

Number of pages in reprint	Cost if 50 copies are ordered	Cost if 100 copies are ordered
2	$12.00	$14.00
4	$15.50	$21.00
6	$17.50	$25.00
8	$19.50	$29.00
10	$21.50	$33.00
12	$23.50	$37.00
14	$25.50	$41.00
16	$27.50	$45.00

All reprints will be printed on 60# uncoated paper, on separate 8 1/2 × 11" sheets. If there is more than one sheet of paper in reprint, the article will be stapled at the top left-hand corner. These prices do not include freight. For reprints ordered three or more months past the original publication date, photo quality cannot be guaranteed.

Orders for reprints for an additional charge should be submitted to RR Donnelley & Sons Company / ComCom, 924 Marcon Blvd., Allentown, PA 18103 USA; Phone: (610) 231-5603, Fax: (610) 231-5635 (contact person Ms. Lynne McCready).

2.5. The authors will receive reprints free of charge as soon as they are available.

3. GENERAL REQUIREMENTS FOR PREPARING MANUSCRIPTS

3.1. Formulas should be numbered in the order of their appearance throughout the manuscript. Formulas are labeled with Arabic numbers in parentheses on the right.

3.2. Footnotes should be numbered in the order of their appearance throughout the manuscript.

3.3. The literature cited should be formatted as a single list at the end of the manuscript rather than as footnotes (references should be given in English even if the authors submit a manuscript in Russian). Within the text, references should appear as consecutive numbers in square brackets (e.g., [1]). The list of references should be given in the order of the first appearance of references in the text. The list of references should be formatted as follows.

3.3.1. For articles in journals, indicate the surnames and initials of the authors, the year, the title of the journal, the volume number, and the number of the first page of the reference, for example,

1. Smith, A.M., Hant, G., and Fenton, I., 1990, *Laser Phys.*, **1**, 123.

3.3.2. For books, indicate the surnames and initials of the authors, the year, the full title of the book, and the city and the publisher (in parentheses), for example,

2. Polyakova, S.S., Morgan, S., and Charlton, P., 1990, *Quantum Mechanics* (New York: Allen).

In references, if the number of authors of the cited article or book is less than or equal to four, then cite the names of all the authors. If the number of authors is greater than four, then cite only the first three authors and use *et al.* in place of the names of the other authors.

3.4. All figures and drawings should be legible and should be prepared in a format that ensures a clear understanding of all the details. This is especially important for photographs. Drawings should be presented separately from the text of the manuscript. Never paste drawings onto the original. All the figures should be properly captioned. Figure captions should be typed on a separate numbered sheet. The surname of the first author, the title of the paper, and the figure number should be indicated on the face side of figures and drawings at the bottom of the sheet in its free area.

Wherever possible, replace lettering in figures by numbers or symbols, which should be identified in figure captions or within the text. If it is impossible to replace lettering by numbers or symbols, provide lettering in English (even for articles submitted in Russian).

Black-and-white photographs should be glossy and free of defects. Each photograph should be identified on the back by the surname of the first author, the title of the paper, and the number of the photograph written in a soft black pencil.

Use a black pencil to indicate places within the text where figures, tables, and photographs should be positioned.

3.5. In manuscripts submitted in Russian, provide English spelling of proper names in parentheses as these names appear for the first time in the text (except for names of common knowledge, e.g., names that can be found in an encyclopedia, and names that are cited in the list of references); if authors use special uncommon terminology, then it is recommended to provide an English translation for such terms on a separate sheet.

3.6. The authors of review articles requested by the Editorial Board should enclose glossy black-and-white 6×9-cm photographs of each of the authors and brief biographies of each of the authors.

4. PREPARING MANUSCRIPTS USING LASER OR JET PRINTERS

4.1. All mathematical expressions should be carefully written and checked, so that the compositor can easily follow the copy. Vectors and matrices are set in special type style and must be identified for the compositor. Authors are requested to provide a list of vectors and matrices appearing in their manuscripts or to explain in the margin any symbols that they have used to identify those vectors and matrices. All letters and numbers whose identity might be unclear should be identified in the margin. When Greek letters are handwritten, they should be spelled out when they first appear.

5. PREPARING MANUSCRIPTS USING A DOT-MATRIX PRINTER

5.1. Requirements for mathematical expressions are given in Section 4.1.

5.2. If the manuscript is submitted in English, it is desirable to provide a diskette with the text of the manuscript in ASCII codes.

5.3. Do not use a dot-matrix printer for producing figures and drawings. If a dot-matrix printer is used, figures and drawings should be redrawn in order to exclude distortion of the information due to dot structures characteristic of dot-matrix printers.

6. PREPARING MANUSCRIPTS USING A TYPEWRITER

6.1. A manuscript in English or Russian should be typed double-spaced on one side of the page with the left margin no less than 3.5 cm. At the beginning of the manuscript, the title of the paper is typed in English or Russian. Below, type the initials, surnames, and mailing addresses of authors in English (even for manuscripts submitted in Russian).

6.2. Formulas should be legible, properly spaced, and appropriately large. In writing formulas, use India or black ink. Special attention should be given to careful writing of indices and exponents: subscripts should never be written on the same level as main symbols, a prime should be distinguishable from unity, and unity should be distinguishable from comma. Wherever possible, avoid cumbersome notations and simplify composition of formulas

[e.g., replacing e^x by $\exp(x)$ and using ab^{-1} or a/b instead of $\frac{a}{b}$].

6.3. To avoid errors during composition, in writing formulas, clearly differentiate between upper- and lower-case characters. In those cases when upper- and lower-case characters have similar outlines and differ only by their sizes (V and v, U and u, W and w, O and o, K and k, S and s, P and p), upper-case characters should be doubly underlined in a black pencil (e.g., $\underline{\underline{S}}$), whereas lower-case characters should be marked with two dashes above the character (e.g., $\overline{\overline{s}}$). One should clearly differentiate between the letters e and l and the numeral 1 (e should be written as e, and l should be written as l). One should also clearly differentiate between upper-case O, lower-case o, and 0 (zero). For this purpose, mark O and o with two dashes using a black pencil and do not underline zero. Finally, one should differentiate between I and J. For this purpose, write in the manuscript I as a Roman unity.

6.4. Use a red pencil to underline Greek letters with a straight line. Use a blue pencil to underline vectors with a wavy line.

6.5. Use a blue pencil to underline scalar characters typed within the text with a straight line.

6.6. Handwritten and gothic symbols should be defined in the margin when they first appear in the text.

6.7. Indices and exponents should be indicated using a black pencil. Subscripts (e.g., in I_2) should be indicated as $I_{\boxed{2}}$, whereas superscripts and exponents (e.g., in I^2) should be indicated as $I^{\boxed{2}}$. Use this system for identifying characters and symbols both in the original and in the copy.

The e-mail addresses of the Editorial Board are

yevseyev@theor.mephi.msk.su   or   *LasPhys@meta.msk.ru*

GLASS PHYSICS AND CHEMISTRY

Editor-in-Chief
Oleg V. Mazurin
Professor, Russian Academy of Sciences

Published by the Russian Academy of Sciences and the Institute of Silicate Chemistry, **GLASS PHYSICS AND CHEMISTRY** presents the results of research in inorganic glass science by Russian and international authors. Articles cover a diverse number of problems including kinetics in glass, electrical conductivity in glass, spectroscopic study of glasses and crystals, chemical structure of glasses, and thermal analysis.

Scope:
- *Glass structure*
- *Glassy state*
- *Glass formation*
- *Properties of glasses and glass-forming liquids*
- *Theoretical bases of glass technology*

PLASMA PHYSICS REPORTS

A translation, published by the American Institute of Physics, beginning with 1975 issues of *Fizika Plasmy*. Beginning with 1994 issues, it is translated and published by МАИК Наука/Interperiodica Publishing and distributed by the American Institute of Physics. This is the principal journal reporting plasma research performed in leading Russian universities and government institutions.

In 1998 Vol. 24 (English version), a total of 12 issues consisting of approximately 1100 pages, will be published.

Laser Physics
(international journal)

SCOPE

Laser Physics is an international journal published in cooperation with institutes involved in laser research. The renowned Russian laser physicist and Nobel Prize winner, Academician Alexander M. Prokhorov, is Editor-in-Chief. Established in 1990, this journal offers a comprehensive view of theoretical and experimental laser research and applications by top authors. Articles cover every aspect of modern laser physics and quantum electronics, emphasizing physical effects in various media (solid, gaseous, liquid) leading to the generation of laser radiation; peculiarities of propagation of laser radiation; problems involving the impact of laser radiation on various substances and the emerging physical effects, including coherent ones; the applied use of lasers and laser spectroscopy; the processing and storage of information; etc. (Please see list of topics below.) An important part of the journal is devoted to reviews, supplemented by biographical briefs of authors. In addition to original papers and reviews, the journal contains proceedings of international conferences, symposia, and seminars. This journal is a valuable resource for scholars and scientists, laboratories and libraries. The rapid publication, distribution, and delivery of Laser Physics assures recipients timely delivery of current news and research.

- *Solid State and Liquid Lasers*
- *Semiconductor Lasers*
- *Gas Lasers*
- *Plasma and X-ray Lasers*
- *Free-Electron Lasers and Laser Accelerators*
- *Laser Spectroscopy*
- *Interaction of Laser Radiation with Matter*
- *Multiphoton Processes in Atoms, Molecules, and Solids*
- *Coherent Phenomena and Holography*
- *Nonlinear and Quantum Optics*

- *Ultrafast Optics and Strong Field Physics*
- *Fiber Optics*
- *Methods of Laser Radiation Control*
- *Novel Laser Materials*
- *Surface Phenomena*
- *Application of Lasers for Information Storage and Processing*
- *Laser Methods in Chemistry, Biology, and Medicine*
- *Application of Lasers in Ecology*
- *Novel Methods of Laser Technologies*
- *Fundamental Problems*

ACCESS THE LASER PHYSICS WEB SITE FOR CURRENT CONTENTS INFORMATION
http://www.maik.rssi.ru/journals/lasphys.htm

ANNUAL INTERNATIONAL WORKSHOPS ON LASER PHYSICS

In 1992, the Laser Physics Editorial Board decided to hold the first of an Annual International Workshop on Laser Physics. The aim of the Workshop is to give top scientists in the field an opportunity to exchange ideas, discuss results of research, and outline directions for future study.

The format of these workshops is a series of seminars. We welcome your ideas on future seminar topics, as well as suggestions for workshop venues. Please address your comments and suggestions to Prof. Igor V. Yevseyev at: yevsey@lasphys.msk.ru

ACCESS THE LASER PHYSICS WEB SITE FOR INFORMATION
ON THE ANNUAL INTERNATIONAL WORKSHOP ON LASER PHYSICS (LPHYS)
http://www.gpi.ru/lphys/lphys97.html